

POLYOXOMETALATES IN CATALYSIS, BIOLOGY, ENERGY AND MATERIALS SCIENCE

EDITED BY: Soumyajit Roy, Debbie C. Crans and Tatjana N. Parac-Vogt
PUBLISHED IN: Frontiers in Chemistry





frontiers

Frontiers eBook Copyright Statement

The copyright in the text of individual articles in this eBook is the property of their respective authors or their respective institutions or funders. The copyright in graphics and images within each article may be subject to copyright of other parties. In both cases this is subject to a license granted to Frontiers.

The compilation of articles constituting this eBook is the property of Frontiers.

Each article within this eBook, and the eBook itself, are published under the most recent version of the Creative Commons CC-BY licence.

The version current at the date of publication of this eBook is CC-BY 4.0. If the CC-BY licence is updated, the licence granted by Frontiers is automatically updated to the new version.

When exercising any right under the CC-BY licence, Frontiers must be attributed as the original publisher of the article or eBook, as applicable.

Authors have the responsibility of ensuring that any graphics or other materials which are the property of others may be included in the CC-BY licence, but this should be checked before relying on the CC-BY licence to reproduce those materials. Any copyright notices relating to those materials must be complied with.

Copyright and source acknowledgement notices may not be removed and must be displayed in any copy, derivative work or partial copy which includes the elements in question.

All copyright, and all rights therein, are protected by national and international copyright laws. The above represents a summary only. For further information please read Frontiers' Conditions for Website Use and Copyright Statement, and the applicable CC-BY licence.

ISSN 1664-8714

ISBN 978-2-88963-233-6

DOI 10.3389/978-2-88963-233-6

About Frontiers

Frontiers is more than just an open-access publisher of scholarly articles: it is a pioneering approach to the world of academia, radically improving the way scholarly research is managed. The grand vision of Frontiers is a world where all people have an equal opportunity to seek, share and generate knowledge. Frontiers provides immediate and permanent online open access to all its publications, but this alone is not enough to realize our grand goals.

Frontiers Journal Series

The Frontiers Journal Series is a multi-tier and interdisciplinary set of open-access, online journals, promising a paradigm shift from the current review, selection and dissemination processes in academic publishing. All Frontiers journals are driven by researchers for researchers; therefore, they constitute a service to the scholarly community. At the same time, the Frontiers Journal Series operates on a revolutionary invention, the tiered publishing system, initially addressing specific communities of scholars, and gradually climbing up to broader public understanding, thus serving the interests of the lay society, too.

Dedication to Quality

Each Frontiers article is a landmark of the highest quality, thanks to genuinely collaborative interactions between authors and review editors, who include some of the world's best academicians. Research must be certified by peers before entering a stream of knowledge that may eventually reach the public - and shape society; therefore, Frontiers only applies the most rigorous and unbiased reviews. Frontiers revolutionizes research publishing by freely delivering the most outstanding research, evaluated with no bias from both the academic and social point of view. By applying the most advanced information technologies, Frontiers is catapulting scholarly publishing into a new generation.

What are Frontiers Research Topics?

Frontiers Research Topics are very popular trademarks of the Frontiers Journals Series: they are collections of at least ten articles, all centered on a particular subject. With their unique mix of varied contributions from Original Research to Review Articles, Frontiers Research Topics unify the most influential researchers, the latest key findings and historical advances in a hot research area! Find out more on how to host your own Frontiers Research Topic or contribute to one as an author by contacting the Frontiers Editorial Office: researchtopics@frontiersin.org

POLYOXOMETALATES IN CATALYSIS, BIOLOGY, ENERGY AND MATERIALS SCIENCE

Topic Editors:

Soumyajit Roy, Indian Institute of Science Education & Research Kolkata, India

Debbie C. Crans, Colorado State University, United States

Tatjana N. Parac-Vogt, KU Leuven, Belgium

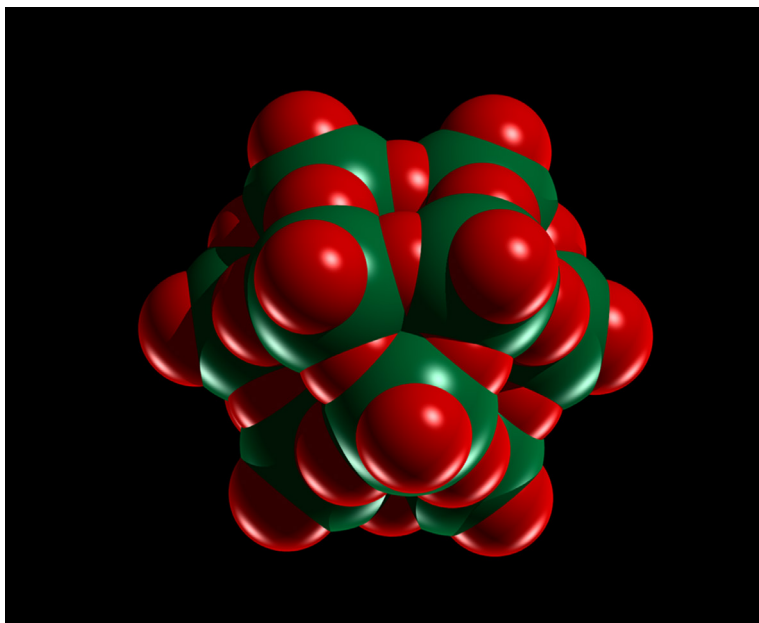


Image of a Polyoxometalate. Image Credit: Shounik Paul.

Citation: Roy, S., Crans, D. C., Parac-Vogt, T. N., eds. (2019). Polyoxometalates in Catalysis, Biology, Energy and Materials Science. Lausanne: Frontiers Media SA.
doi: 10.3389/978-2-88963-233-6

Table of Contents

SECTION I

05 Editorial: Polyoxometalates in Catalysis, Biology, Energy and Materials Science

Soumyajit Roy, Debbie C. Crans and Tatjana N. Parac-Vogt

SECTION II

OVERVIEWS ON OXOMETALATES

07 Keggin Structure, Quō Vādis?

Aleksandar Kondinski and Tatjana N. Parac-Vogt

14 Toward Exploiting the Behavior of Niobium-Containing Mesoporous Silicates vs. Polyoxometalates in Catalysis

Agata Wawrzynczak, Izabela Nowak and Agnieszka Feliczak-Guzik

29 Multi-Tasking POM Systems

Kevin P. Sullivan, Qiushi Yin, Daniel L. Collins-Wildman, Meilin Tao, Yurii V. Geletii, Djamaladdin G. Musaev, Tianquan Lian and Craig L. Hill

SECTION III

POLYOXOMETALATES IN CATALYSIS

39 Photoinduced Oxygen Evolution Catalysis Promoted by Polyoxometalate Salts of Cationic Photosensitizers

Joaquín Soriano-López, Fangyuan Song, Greta R. Patzke and J. R. Galan-Mascaros

47 A Supramolecular Catalyst Self-Assembled From Polyoxometalates and Cationic Pillar[5]arenes for the Room Temperature Oxidation of Aldehydes

Mengyan Zeng, Kun Chen, Junyan Tan, Jie Zhang and Yongge Wei

SECTION IV

POLYOXOMETALATES IN BIOLOGY

55 Decavanadate Inhibits Mycobacterial Growth More Potently Than Other Oxovanadates

Nuttaporn Samart, Zeyad Arhouma, Santosh Kumar, Heide A. Murakami, Dean C. Crick and Debbie C. Crans

71 Antibacterial Activity of Polyoxometalates Against Moraxella catarrhalis

Nadiia I. Gumerova, Emir Al-Sayed, Lukáš Krivosudský, Hana Čipčič-Paljetak, Donatella Verbanac and Annette Rompel

80 Decavanadate Salts of Cytosine and Metformin: A Combined Experimental-Theoretical Study of Potential Metallodrugs Against Diabetes and Cancer

Eduardo Sánchez-Lara, Samuel Treviño, Brenda L. Sánchez-Gaytán, Enrique Sánchez-Mora, María Eugenia Castro, Francisco J. Meléndez-Bustamante, Miguel A. Méndez-Rojas and Enrique González-Vergara

98 Selective Targeting of Proteins by Hybrid Polyoxometalates: Interaction Between a Bis-Biotinylated Hybrid Conjugate and Avidin

Valeria A. Zamolo, Gloria Modugno, Elisa Lubian, Alessandro Cazzolaro, Fabrizio Mancin, Livia Giotto, Disma Mastrogioacomo, Ludovico Valli, Alessandra Sacconi, Silke Krol, Marcella Bonchio and Mauro Carraro

108 Effective in Vitro Photokilling by Cell-Adhesive Gold Nanorods

Álvaro Artiga, Sonia García-Embid, Laura De Matteis, Scott G. Mitchell and Jesús M. de la Fuente

118 Evidence That Speciation of Oxovanadium Complexes Does not Solely Account for Inhibition of Leishmania Acid Phosphatases

Benjamin M. Dorsey, Craig C. McLauchlan and Marjorie A. Jones

129 Selectivity and Reactivity of Zr^{IV} and Ce^{IV} Substituted Keggin Type Polyoxometalates Toward Cytochrome c in Surfactant Solutions

Thomas Quanten, Tessa De Mayaer, Pavletta Shestakova and Tatjana N. Parac-Vogt

SECTION V

POLYOXOMETALATES IN ENERGY AND MATERIALS SCIENCE

142 A Molecular CO_2 Reduction Catalyst Based on Giant Polyoxometalate $\{Mo_{368}\}$

Santu Das, Tuniki Balaraju, Soumitra Barman, S. S. Sreejith, Ramudu Pochamoni and Soumyajit Roy

153 Large Magnetic Polyoxometalates Containing the Cobalt Cubane $[Co^{III}Co_3^{II}(OH)_3(H_2O)_{6-m}(PW_9O_{34})]3^-$ ($m = 3$ or 5) as a Subunit

Yan Duan, Juan M. Clemente-Juan, Carlos Giménez-Saiz and Eugenio Coronado

165 Strategic Isolation of a Polyoxocation Mimicking Vanadium(V) Oxide Layered-Structure by Stacking of $[H_2V_2O_8]^{4-}$ Anions Bridged by (1,4,7-Triazacyclononane)Co(III) Complexes

Sugiarto, Keisuke Kawamoto and Yoshihito Hayashi

173 A Versatile Polyoxovanadate in Diverse Cation Matrices: A Supramolecular Perspective

Srinivasa Rao Amanchi and Samar K. Das

188 A Multifunctional Dual-Luminescent Polyoxometalate@Metal-Organic Framework $EuW_{10}@UiO-67$ Composite as Chemical Probe and Temperature Sensor

William Salomon, Anne Dolbecq, Catherine Roch-Marchal, Grégoire Paille, Rémi Dessapt, Pierre Mialane and Hélène Serier-Brault

196 Photoluminescence Properties of Two Closely Related Isostructural Series Based on Anderson-Evans Cluster Coordinated With Lanthanides $[Ln(H_2O)_7\{X(OH)_6Mo_6O_{18}\}] \cdot yH_2O$, $X = Al, Cr$

Shailabh Tewari, Mohammad Adnan, Balendra, Vineet Kumar, Gaurav Jangra, Gaddam Vijaya Prakash and Arunachalam Ramanan

215 Redox Reaction Triggered Nanomotors Based on Soft-Oxometalates With High and Sustained Motility

Apabrita Mallick, Abhrajit Laskar, R. Adhikari and Soumyajit Roy



Editorial: Polyoxometalates in Catalysis, Biology, Energy and Materials Science

Soumyajit Roy^{1,2*}, Debbie C. Crans^{3*} and Tatjana N. Parac-Vogt^{4*}

¹ Eco-Friendly Applied Materials Laboratory, Department of Chemical Sciences, Materials Science Center, Indian Institute of Science Education and Research Kolkata, Kolkata, India, ² College of Chemistry, Central China Normal University, Wuhan, China, ³ Department of Chemistry, Colorado State University, Fort Collins, CO, United States, ⁴ Department of Chemistry, KU Leuven, Leuven, Belgium

Keywords: polyoxometalates (POMs), soft-oxometalates (SOMs), biology, catalysis, medicine, materials science

Editorial on the Research Topic

Polyoxometalates in Catalysis, Biology, Energy and Materials Science

The chemistry of polyoxometalates/polyoxidometalates (POMs) continues to evolve and has resulted in Nobel prizes (Janell et al., 2001) and several technological advances (Hill, 1998; Cronin and Mueller, 2012; Galán-Mascarós and Kortz, 2018; Pope et al., 2019; Roy and Crans, 2016). The present Research Topic of Frontiers in Chemistry is a celebration of evolution of that ever-exciting chemistry. Though it is impossible to sample the growth of such an active area in the span of Research Topic of the journal Frontiers in Chemistry, it is still possible to give the reader a taste of where this chemistry is now and where it is heading. With this objective in view we have chosen four thematic topics in which this chemistry is evolving: Biology, Catalysis, Energy, and Materials Science. To chart the developments and to put the present trend in perspective, it is apt to archive the history of this field. Thus, to set the stage, arching back to the beginning, Kondinski and Vogt map the efforts of James Fargher Keggin and thereby connect the field to Bragg and Pauling as well as to modern times, showing how structural studies have shaped this field and its developments over time to date. Thereafter, we continue our journey with catalysis and energy harvesting with a review by Sullivan et al. highlighting POM-containing multi-hydrogen-bonding polymers that undergo gelation upon exposure to select organic liquids and simultaneously catalyze reactions along with their use in photoelectrocatalytic water splitting for energy harvesting. A third review by the Nowak group (Wawrzynczak et al.) outlines different catalytic applications of polyoxoniobates in water oxidation, hydrogen evolution, and allied reactions and gives a comparison with niobium containing mesoporous silicates. The Patzke and Galan-Mascaros group (Soriano-López et al.) show pre-catalytic incorporation of the cationic photosensitizer into the anionic polyoxometalate as in RuCo₉, which significantly improves oxygen evolution. Such an effect elegantly demonstrates facilitated electron transfer due to photosensitizer-polyoxometalate pairing in solid-state, enhancing the long-term stability of the photo-sensitizer. By coupling water-oxidation with CO₂ reduction, the Roy group (Das et al.) shows that using Muellerene type {Mo₃₆₈} giant polyoxometalates, efficient energy harvesting homogenous catalytic systems can be realized. In another work, the Zhang and Wei group (Zeng et al.) show that nanospherical self-assembled Anderson type {CrMo₆} polyoxometalate and pillar[5]arenes can oxidize aldehydes to carboxylic acids.

As we move from Catalysis to Materials Science, we come across the one pot synthesis of a magnetic polyoxometalate containing one or two subunits of [Co^{III}Co^{II}₃O₄] cubane by the Coronado group (Duan et al.). In another work the Hayashi group (Sugiarto et al.) uses Cobalt as four [fac-{Co(tacn)}³⁺] units capping a distorted cubane-like V₄O₄ to contain the

OPEN ACCESS

Edited and reviewed by:

Luis D. Carlos,
University of Aveiro, Portugal

*Correspondence:

Soumyajit Roy
roy.soumyajit@gmail.com
Debbie C. Crans
debbie.crans@colostate.edu
Tatjana N. Parac-Vogt
tatjana.vogt@kuleuven.be

Specialty section:

This article was submitted to
Inorganic Chemistry,
a section of the journal
Frontiers in Chemistry

Received: 01 September 2019

Accepted: 09 September 2019

Published: 01 October 2019

Citation:

Roy S, Crans DC and Parac-Vogt TN
(2019) Editorial: Polyoxometalates in
Catalysis, Biology, Energy and
Materials Science.
Front. Chem. 7:646.
doi: 10.3389/fchem.2019.00646

growth of polyoxometalate with far-reaching consequences in studying and trapping of synthetic intermediates in POM research. The Mialane and Serier-Braut group (Salomon et al.) has in another work shown that incorporation of a luminescent europium polyoxotungstate into the cavities of a luminescent zirconium metal organic frameworks results in a multifunctional dual-luminescent material. The Prakash and Ramanan group (Tewari et al.) reports the synthesis and photoluminescent properties of two closely related series of lanthanide containing POM structures. From luminescence and magnetic properties, we move to supramolecular water clusters, which are reported by the Das group (Amanchi and Das) in the context of the synthesis and supramolecular chemistry of seven decavanadate containing compounds. In some of the crystal structures, the authors found that the non-covalent interactions between the lattice water molecules and metal coordinated water molecules lead to the formation of supramolecular water clusters. Can oxometalate architectures move and can such movement be observed? The Roy and Adhikari group (Mallick et al.) shows such motility in soft-matter states of oxometalates or soft-oxometalates exploiting the redox reaction on the surface of such states. From active matter we now move to biological matter, where POMs are extremely active.

Ranging from potential therapeutic agents for Leishmaniasis, photothermal therapy to medicines for diabetes and cancer, the issue explores various facets of POMs for biological applications. The collaborative efforts of the McLauchlan and Jones group (Dorsey et al.) demonstrate from the standpoint of vanadium concentration and speciation of decavanadate and orthovanadate as an inhibitor for phosphatases which translates to being effective as a therapeutic agent targeting the secreted acid phosphatase (SAP) from *Leishmania*. Furthermore, using ^{51}V NMR studies the Crans group (Samart et al.) shows that from the analysis of speciation in oxo-vanadate solutions, decavanadate is a more potent growth inhibitor of two Mycobacterial strains than other oxovanadates. The activity of decavanadates against diabetes is further explored by the group of González-Vergara (Sánchez-Lara et al.), who show synthesis and structural features

of decavanadate salts of Cytosine and Metformin as a potential metallodrug against diabetes and cancer. In a very detailed study, (Gumerova et al.) explore the antibacterial activity of a set of 29 POMs against *Moraxella catarrhalis*. For these bacteria, the Preyssler type POM and the Dawson-type POM were found to be most potent oxometalates and surpass the activity of the Keggin and Anderson types of POMs. Covalently modifying a Keggin type POM, the group of Bonchio and Carraro (Zamolo et al.) obtains a bis-biotinylated conjugate with Avidin to show “selective targeting of proteins by hybrid POMs.” The group of De Matteis and Mitchell (Artiga et al.) achieves cellular internalization of gold nanorods inside a biocompatible and cell-adhesive chitosan hydrogel matrix using Keggin-type polyoxometalate (POM) as an inorganic gelator for “effective *in-vitro* photokilling.” In a work that brings biology, materials science, and catalysis closer, the group of Parac-Vogt (Quanten et al.) explores how selectivity and reactivity of Ce^{IV} and Zr^{IV} substituted Keggin type POMs are affected by various surfactant solutions in the hydrolysis of Cytochrome c, a α helical protein with haem group. With the aid of a series of experiments, the authors show the role of surfactant in facilitating the unfolding of Cytochrome c and in turn dictates the ease of hydrolysis of the protein. With all these works the science of polyoxometalates becomes a melting pot where biology, soft-matter, material science and catalysis science meet, and this Research Topic of Frontiers in Chemistry captures part of the progress in this area.

It has been a privilege for us all as editors working with all the contributors and reviewers in curating the Research Topic, and we thank all—including the Frontiers team—for making this journey a pleasant and timely one. We hope it will bring joy to readers and savor the examples of progress as they are nucleated together. It is our hope that the present Research Topic will ignite, initiate and illuminate the minds of many toward new and unexplored frontiers of polyoxometalate science.

AUTHOR CONTRIBUTIONS

SR, DC, and TP-V curated this special issue together.

REFERENCES

- Cronin, L., and Mueller, A. (2012). Themed collection: polyoxometalate cluster science. *Chem. Soc. Rev.* 41, 7325–7648.
- Galán-Mascarós, J. R., and Kortz, U. (2018). Special issue on polyoxometalates. *Acta Cryst. C* 74, 1180–1181. doi: 10.1107/S2053229618015188
- Hill, C. L. (1998). Thematic issue on polyoxometalates. *Chem. Rev.* 1:98.
- Janell, D., Tocilj, A., Kolln, I., Schlunzen, F., Gluehmann, M., Hansen, H. A., et al. (2001). “Ribosomal crystallography and heteropolytungstates”, in *Polyoxometalate Chemistry*, eds M. T. Pope and A. Mueller (Dordrecht: Kluwer Academic Publishers), 391–415.
- Pope, M. T., Sadakane, M., and Kortz, U. (2019). Special issue: celebrating polyoxometalates (cluster issue). *Eur. J. Inorg. Chem.* 2019, 336–549. doi: 10.1002/ejic.201801543

Roy, S., and Crans, D. C. (2016). Themed collection: emergent polyoxometalates and soft-oxometalates. *New J. Chem.* 40, 882–984. doi: 10.1039/C6NJ90006B

Conflict of Interest: The authors declare that the research was conducted in the absence of any commercial or financial relationships that could be construed as a potential conflict of interest.

Copyright © 2019 Roy, Crans and Parac-Vogt. This is an open-access article distributed under the terms of the Creative Commons Attribution License (CC BY). The use, distribution or reproduction in other forums is permitted, provided the original author(s) and the copyright owner(s) are credited and that the original publication in this journal is cited, in accordance with accepted academic practice. No use, distribution or reproduction is permitted which does not comply with these terms.



Keggin Structure, Quō Vādis?

Aleksandar Kondinski* and Tatjana N. Parac-Vogt

Laboratory of Bioinorganic Chemistry, Department of Chemistry, KU Leuven, Leuven, Belgium

Working under the supervisor of William Lawrence Bragg at the University of Manchester and being under the direct personal and scientific influence by Linus Pauling, Dr. James Fargher Keggin some 85 years ago published a highly unique discovery—the structure of phosphotungstic acid (Nature 1933, 131, 908–909). This structure sparked the reports of other related polyanions from Keggin's contemporaries, marking the true beginnings of structural polyoxometalate chemistry. In this perspective article, we unveil some aspects and applications of Keggin's structure and discuss how it has shaped the course of our understanding of polyoxometalate chemistry and nanomolecular metal oxides/hydroxides in general.

Keywords: polyoxometalates, Keggin structure, structural chemistry, metal oxides, kegginoid, clathrates

OPEN ACCESS

Edited by:

Federico Cesano,
Università degli Studi di Torino, Italy

Reviewed by:

Kenji Nomiya,
Kanagawa University, Japan
Ira Alan Weinstock,
Ben-Gurion University of the Negev,
Israel
Rafael Acerete,
Universitat de València, Spain

*Correspondence:

Aleksandar Kondinski
aleksandar.kondinski@kuleuven.be

Specialty section:

This article was submitted to
Inorganic Chemistry,
a section of the journal
Frontiers in Chemistry

Received: 24 May 2018

Accepted: 24 July 2018

Published: 14 August 2018

Citation:

Kondinski A and Parac-Vogt TN
(2018) Keggin Structure, Quō Vādis?
Front. Chem. 6:346.
doi: 10.3389/fchem.2018.00346

INTRODUCTION

Over human history, many increments in the understanding of the properties of metal oxides have led directly to cultural and technological advancements (Brock, 1993; Arns, 1998; Sass, 2011). In the contemporary era of advanced materials (Heine, 2014), confinement of metal oxides/hydroxides to the nanoscale led to the emergence of cluster materials with unique physicochemical properties (Roy, 2011). Polyoxometalates (POMs) (Pope, 1983), also known as (hetero/iso)polyacids, are one of the earliest discovered metal-oxo nanoclusters with a documented scientific history of over two centuries (Baker and Glick, 1998; Gouzerh and Che, 2006). POMs are typically comprised of early transition metals in high oxidation states (mainly V, Mo, W, Nb, and Ta) and they have been attracting research attention due to their actual and potential applications in catalysis (Kozhevnikov, 2009; Wang and Yang, 2015), molecular magnetism (Gatteschi et al., 1993; Müller et al., 1998; Clemente-Juan et al., 2012) and life sciences (Rhule et al., 1998; Absillis et al., 2008; Bijelic and Rompel, 2015; Ly et al., 2015).

Much of the modern POM chemistry is centered around the concept of the “Keggin structure,” which historically is representative for many heteropolymolybdates and heteropolytungstates. One of the earliest reports on these compounds dates back to 1826, when Berzelius reported the synthesis of phosphomolybdic acid (Berzelius, 1826). However, the structure of these species remained unknown for over a century. By late 1920's some of the renowned chemists working with POMs have attempted to apply Alfred Werner's coordination chemistry approach, which is based on covalent bonding between all constituents, to describe possible structural models (Baker and Glick, 1998). This has changed in 1928 when then a young professor Linus Pauling offered an unconventional solution to tackle the problem by introducing a structure (Figure 1A) that resembles what nowadays we refer to as a “host-guest” systems (Pauling, 1929a). Considering that Pauling's proposal preceded the foundation of modern supramolecular chemistry, at the time his model of the 12-heteropolyacids appeared as highly fascinating and controversial. In this model, a central {XO₄} group is encapsulated by a neutral shell of {W₁₂(OH)₃₆O₁₈} (also written as {W(OH)₃O_{1.5}}₁₂). The shell of {W(OH)₃O_{1.5}}₁₂ can be described as a virtual truncated tetrahedron constructed by twelve W and eighteen O centers defining the vertices and the edges respectively.

Each of the twelve metal centers exhibits octahedral coordination and coordinates to three bridging oxo/oxido ligands and three terminal hydroxo/hydroxido ligands (Baker and Glick, 1998).

From the preserved written communications of Linus Pauling, it is clear that after the submission of his proposal (Pauling, 1929a) he contributed a significant effort to attract crystallographic interest to the problem (Pauling, 1928). As the X-ray crystallography was still in its early stage and very challenging to apply to large molecular systems, Pauling attempted to attract the interest of the Bragg's group at the University of Manchester, which at the time was globally the most prominent group on the powder crystal structure elucidation method. In 1930 Pauling visited Bragg's laboratory with the main purpose to discuss crystal structure elucidation of various compounds including the heteropolyacids (Pauling, 1929b).

During his visit at Manchester, Pauling met with Dr. James Fargher Keggin, which eventually sparked a turning point in the history of POM chemistry (Ayass and Kortz, 2018; Pütt et al., 2018). Dr. Keggin (31.12.1905–11.04.1993), born in the Isle of Man, was a physics graduate from University of Liverpool who performed synthetic and crystallographic experiments in Bragg's laboratory (**Figure 1B**). After the meeting with Pauling, Keggin's research focused on the study of the heteropolyacids. Within a couple of years, Keggin successfully resolved the positions of the tungsten and phosphorus atoms and estimated the relative position of oxygen atoms. Keggin's work was communicated in *Nature* in 1933 (Keggin, 1933a,b) while all details of the complete work appeared in 1934 (Keggin, 1934). Considering the complexity of the discovered structure, Keggin described the tungstophosphic acid as an overall tetrahedral species constituting of twelve $\{\text{MO}_6\}$ octahedra grouped in three triads of $\{\text{M}_3\text{O}_{15}\}$ that connect in corner-sharing fashion around the single central $\{\text{XO}_4\}$ unit (**Figure 1C**). Over the decades, this topology became commonly referred to as the Keggin structure, while more recently in Keggin's honor, a naturally occurring POM mineral $\text{Pb}_3\text{Ca}_3[\text{AsV}_{12}\text{O}_{40}(\text{VO})]\cdot 20\text{H}_2\text{O}$ with Keggin-like motif became known as *kegginite* (Kampf et al., 2017).

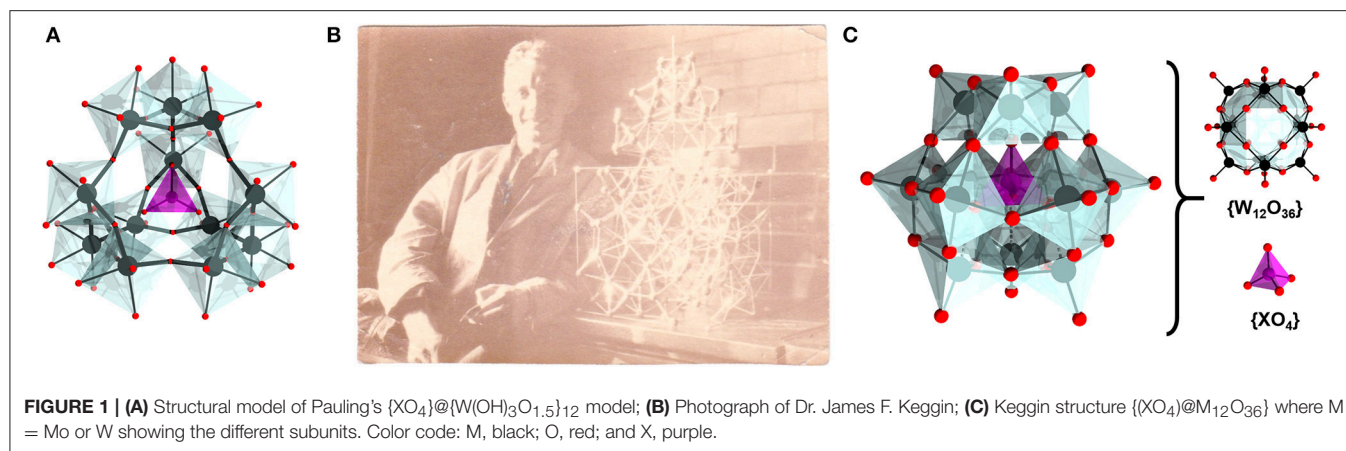
Within the next two decades, a handful of other structures have been proposed and structurally elucidated which laid the foundation of the modern field. However, besides the crystallographic elucidations, the attempts to predict structural topologies by some leading structural chemists at the time such as John Start Anderson (Imperial College London) and Alexander Frank Wells (University of Cambridge) are also very fascinating from the contemporary point of view. Anderson's proposal on the $[\text{IMo}_6\text{O}_{24}]^{5-}$ structure representing a segment of typical double layer metal hydroxide $\text{M}(\text{OH})_2$ (Anderson, 1937), laid in general a correct prediction which was first confirmed for the $[\text{TeMo}_6\text{O}_{24}]^{6-}$ analog (Evans, 1948). On the other hand, Wells' structural predictions were based on an approach that relates to the conceptual construction of polyhedral molecules such as metal-organic polyhedra (Tranchemontagne et al., 2008). Wells' proposal acknowledged the non-uniformity in chemical bonding among different molecular "aggregates" which include the heterogroup and the metal-oxo shell (Wells, 1940). In this regard, he proposed rational stepwise increase of the nuclearity of the molecular metal-oxo shells, while making it clear that

$[\text{MO}_3]_n$ and their terminal-oxo free derivative $[\text{MO}_2]_n$ follow the same building up trend. In Wells' view, the Keggin structure can be described as a $\{\text{M}_{12}\text{O}_{36}\}$ shell with cuboctahedral and rhombocuboctahedral networks defined by the positions of the M and O atoms respectively that hosts a heterogroup. Following the step wise building up, he envisioned that a $[\text{MO}_3]_{18}$ shell should provide sufficient room for two heterogroups leading to the $\{\text{P}_2\text{W}_{18}\text{O}_{68}\}$ structure. This structural proposal was confirmed a decade later by Barrie Dawson (Dawson, 1953; Mathieson, 1975).

When examining the $\{\text{MO}_6\}$ "octahedra" in the Mo^{VI} and W^{VI} -based Keggin structures, the non-uniformity to which Wells was referring to becomes apparent. Although many detailed bonding studies exist (Mingos, 1999), one easily marks the large discrepancy in the M–O bond lengths which are ca. 1.7 and 1.9 Å from the addenda to the terminal and the bridging μ_2 -O atoms respectively, but ca. 2.4 Å from the addenda centers to the interior O atoms attached to the heterogroup. With the emergence of supramolecular chemistry, the non-uniformity in bonding gave rise to the clathrate-model in late 1980's and early 1990's (Pope and Müller, 1991), which later became a useful model for discussing the electronic properties of Keggin derivatives on the basis of computational chemistry (Maestre et al., 2001; Neiwert et al., 2002; López et al., 2006).

APPLICATIONS OF THE "CLASSICAL" KEGGIN CLATHRATES

The Keggin structure, as originally elucidated, is primarily representative for hetero-12-molybdates and hetero-12-tungstates. In this regard, multiple tetrahedral heterogroups $\{\text{XO}_4\}$ where X = P, Ge, Si, or As (but also many other different cations) have been reported to be encapsulated within the $\{\text{M}_{12}\text{O}_{36}\}$ shell (Pope, 1983; Anyushin et al., 2014). The Mo^{VI} - and W^{VI} -based Keggin anions can be easily reduced forming blue and brown colored solutions respectively, due to the intense charge transfer processes. In this context, already starting from the nineteenth century there has been an application of this property in the colorimetric detection and quantification of phosphate anions by the so-called molybdenum blue method (Holman, 1943; Baker and Glick, 1998). Indeed, this redox-responsive and reversible change in color has made the Mo-based Keggin structure recently applicable for preparation of rewritable paper (Sun et al., 2015). The reduction of the Mo-based Keggin structure impressively undergoes up to 24 electrons process without disintegration of the structure (Wang et al., 2012), as the reduction also increases the formation of metal-metal bonding between the addenda centers (Nishimoto et al., 2014). It has been noted that the reversible redox processes of these polyanions are also very useful in the preparation of electrolytes suitable for light-driven artificial hydrogen evolution (Symes and Cronin, 2013). Typical Mo- and W-based Keggin structures exhibit thermal stability up ca. 300°C, making them catalytically attractive also at elevated temperatures (Moffat, 2002). As redox active polynuclear superacids they provide a reactive surface for a variety of (electro)catalytic

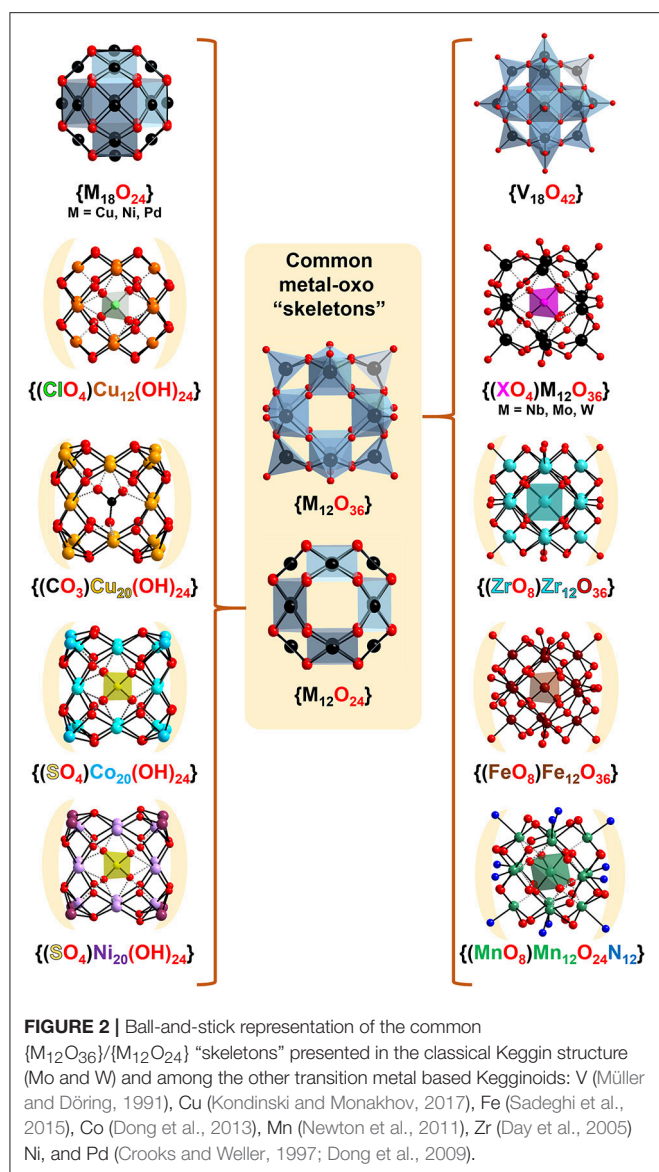


transformations (Kozhevnikov, 2009). The high number of heavy elements and overall molecular surface covered by terminal oxo atoms makes the Keggin species also very suitable for applications in protein crystallography (Bijelic and Rompel, 2015).

The “Achilles heel” of the Mo- and W-based Keggin is that their stability is pH dependent. As the pH increases the Mo- and W-based Keggin gradually disintegrate. This property was one of the main challenges that in the early twentieth century made the assignment of overall charge to these polyanions very difficult as the resulting “unsaturated” or “lacunary” structures exhibit higher negative charges per addendum than the parent Keggin anion (Baker and Glick, 1998). However, later it was realized that the lacunary polytungstates encapsulating $\{PO_4\}$, $\{SiO_4\}$, $\{GeO_4\}$, $\{AsO_3\}$, $\{SbO_3\}$, and $\{BiO_3\}$ heterogroups can be effectively isolated and used as polydentate all-inorganic ligands (Pope, 1983; Baker and Glick, 1998). Typically, the former Keggin-derived lacunary POMs include the monolacunary species $\{XO_4\}W_{11}O_{35}\}$ which are generated by a formal loss of single $\{MO\}$ unit and a set of trilacunary heteropolytungstate conformers $\{XO_4\}W_9O_{30}\}$ and $\{XO_3\}W_9O_{30}\}$, obtained by the loss of $\{MO_2\}_3$ unit. Such materials exhibit defect sites with available nucleophilic O centers that interact with any cation in solution which can be exemplified by their recent application in ultrahigh water purification of toxic metal cations (Herrmann et al., 2017). The lacunary W-based Keggin are typically prepared at higher pH (ca. 7–9) and have been employed as all-inorganic ligands in the preparation of many organometallic (Proust et al., 2012), lanthanide (Boskovic, 2017) and transition metal containing (Zheng and Yang, 2012) polyanions which show potential and actual applications in catalytic oxidations of organics (Proust et al., 2008), luminescence (Binnemans, 2009; Yamase, 2009), hydrolysis of biomolecules (Ly et al., 2015), stabilization of nanoparticles (Mitchell and de la Fuente, 2012), design of hybrid materials (Proust et al., 2008, 2012), smart surfactants (Landsmann et al., 2012; Polarz et al., 2014) molecular magnetism (Gatteschi et al., 1993; Clemente-Juan et al., 2012) and design of supercapacitors (Gómez-Romero et al., 2003).

THE “UNIQUENESS” OF THE KEGGIN STRUCTURE AND THE RISE OF MOLECULAR KEGGINOIDS

Already from the mid-1960's to the end of 1970's it became well-established that hetetrometals (M') can substitute one or more addenda centers of the $\{M_{12}O_{36}\}$ shell leading to mixed-addenda $\{(XO_4)M'_xM_{12-x}O_{36}\}$ Keggin anions (Smith and Pope, 1973; Pope and Scully, 1975; Pope et al., 1976). These studies combined with the findings that other elements such as aluminum (Johansson, 1960) and germanium (Bradley et al., 1990) can form cationic assemblies similar to the Keggin structure, opened up the way for Baker-Figgis concept of Keggin configomers (Baker and Figgis, 1970), which implies that in principle the overall $\{M_{12}O_{36}\}$ shell can adopt a variety of topologies that differ mainly on the ratio of edge-sharing vs. corner-sharing polyhedra. These studies were hinting that other elements may mimic POM topologies and in particular produce Keggin-like (Kondinski and Monakhov, 2017), “extended” Keggin (Müller and Döring, 1991) or as we herein refer to *kegginoidal* topologies (Figure 2). One of the early visions in this directions came from Müller and coworkers who recognized the relationship between “classical” Keggin structure and “extended” Keggin structure $[X@V_{18}O_{42}]^{n-}$ ($X = SO_4^{2-}$ and VO_4^{3-}) (Müller and Döring, 1991). These structures indeed can be virtually derived by addition of $\{MO\}$ cations at the unoccupied square faces of the virtual rhombocubocthedron constructed by the 24 bridging oxo ligands of the $[MO_3]_{12}$ shell. In the case of vanadium, the necessity of additional vanadyl cations is clear because the hypothetical fully-oxidized shell $[V_{12}O_{36}]^{12-}$ is expected to be highly negative and thus highly reactive. Therefore, the virtual addition of vanadyl cations is supposed to charge-stabilize the overall structure. In the case of vanadium's heavier congener niobium, highly charged polyanions of the type $[(XO_4)Nb_{12}O_{36}]^{16-}$ ($X = Si$ and Ge) (Nyman et al., 2004) exhibit very strong interactions with the counteractions in solution and in the solid state. Due to the high negative charge, the Nb-Keggin derivatives are also highly reactive with vanadyl cations producing kegginoidal $[(PO_4)Nb_{12}O_{36}(VO)_6]^{3-}$ structure



(Shen et al., 2014) representing mixed addenda derivatives of the $\{V_{18}O_{42}\}$ structure.

However, besides recognizing the relationship between the classical and the “extended” Keggin shell system, in early 1990’s Müller and coworkers also recognized the similarity between the kegginoidal $\{V_{18}O_{42}\}$ and its polyoxocuprate analog that misses terminal oxo atoms $[Cu_{18}O_{24}]^{12-}$ (see **Figure 2**; Kipka and Müller-Buschbaum, 1977). The kegginoidal topology of the former is also adopted by the polyoxopalladate $[Pd_{18}O_{24}]^{12-}$ and the polyoxonickelate $[Ni_{18}O_{24}]^{12-}$ (Crooks and Weller, 1997). These pioneering discoveries including number of reports of related heteropoly structures constitute the foundation of late transition metals based POMs (Ni, Pd, Pt, Cu, and Au) (Izarova et al., 2012; Kondinski and Monakhov, 2017) which exhibits potential in revealing insights into precious metal catalysis (Goloboy and Klemperer, 2009) and in building molecular

nanomagnets with relevance to quantum computing (Baldoví and Kondinski, 2018).

The conceptual transitioning from $\{MO_3\}_{12}$ to $\{MO_2\}_{12}$ is an effective methodology that can assist in recognizing structural trends among a diversity of reported topologies. In this regard, copper(II) hydroxide which in the bulk shows characteristic chain structure (von Jaggi and Oswald, 1961), once confined to the nanoscale by stabilizing cations forms kegginoidal $[Cu(OH)_2]_{12}$ clusters (Kondinski and Monakhov, 2017). Normally, six or eight symmetrically arranged cations can stabilize the 24 labile hydroxo ligands. For instance, the naturally occurring $[Cu(OH)_2]_{12}$ kegginoid in the cavities of the zeolitic Tschörtnerite mineral is stabilized by eight Ca^{2+} cations (Effenberger et al., 1998). As synthetically it is challenging to mimic the environment of Tschörtnerite, many tenths of other synthetically reported kegginoidal polyoxocuprates exhibit metal-hydroxo cores where the local coordination of each individual copper(II) center besides square planar $\{CuO_4\}$ may adopt square pyramidal $\{CuO_5\}$ or octahedral $\{CuO_6\}$, leading to large variety of structures with local differences, form which some to great extent mimic the classical Keggin (Kondinski and Monakhov, 2017).

There is a number of other structures that have been already recognized or that can be recognized as molecular kegginoids. For instance, the mineral murataite (Ericit and Hawthorne, 1995) exhibits kegginoidal $\{(ZnO_4)@Ti_{12}O_{36}\}$ motifs, which has been recognized and considered as a viable synthetic target (Nomiya et al., 2011). On the other hand, many polyalkoxotitanates resemble the structure of the $\{V_{18}O_{42}\}$ kegginoid (Rozes and Sanchez, 2011). Titanium’s heavier congener zirconium forms polyoxo/alkoxozirconate kegginoids which encapsulate a complete $\{ZrO_8\}$ unit (Morosin, 1977; Day et al., 2005). Nickel(II) and cobalt(II) based kegginoids $[Ni_{20}(OH)_2(MMT)_{12}(SO_4)]^{2+}$ (Dong et al., 2009) and $[Co_{20}(OH)_2(MMT)_{12}(SO_4)]^{2+}$ (Dong et al., 2013; Mu et al., 2016) have been isolated in presence of MMT = 2-mercapto-5-methyl-1,3,4-triazole ligands. These polyoxocations exhibit $\{M_{20}(OH)_{24}\}$ cores that can be derived by formal stabilization of the $\{M_{12}(OH)_{24}\}$ topology by additional eight cations (**Figure 2**). In the case of manganese, mixed-valence kegginoid $[Mn^{III}_{12}Mn^{IV}_6(OH)_2(OMe)_4(bemp)_6]^{4+}$ (where $H_3bemp = 2,6$ -bis[N-(2-hydroxyethyl)iminomethyl]-4-methylphenol) has been isolated and showed impressive solution and electrochemical stability and single molecule magnet behavior (Newton et al., 2011). Finally, among the most influential works on molecular kegginoids remains Nyman’s “iron Keggin” $[Fe^{III}O_4@Bi^{III}_6Fe^{III}_{12}O_{12}(OH)_{12}(Cl_3CCOO)_{12}]^+$ which has been successfully isolated and proposed as a good structural model of the naturally occurring ferrihydrite (Sadeghi et al., 2015).

All of these studies appearing over the past few decades require us to adopt a more inclusive vision of the Keggin structure and its role in the chemistry of nanomolecular metal oxides and hydroxides. In this light, the Keggin structure and its related molecular kegginoids unveil large opportunities for a conceptual approach to some practically important metal-oxo/hydroxo compounds. The conceptual approach proposes that structure-stability trends observed among Mo, W and V

based kegginoids can be transferred and *in silico* explored for a variety of costly late transition noble metals. Such strategies could pave the way toward a rational synthesis of a variety of novel mixed-addenda, heterogroup substituted and even hybrid organic-inorganic kegginoids. Those approaches can also assist to shed light into the structure of some catalytically active metal oxides/hydroxides such as the Pearlman's catalyst ($\text{Pd}(\text{OH})_2/\text{C}$) (Albers et al., 2015).

CONCLUSION AND OUTLOOK

The discovery of the Keggin structure some 85 years ago was a turning point for structural POM chemistry. Over the past decades, global efforts have expanded the scope of applications of this structure, but more importantly, they have widened up our understanding of nanomolecular metal oxides. The structural similarities of the Mo- and W- based Keggin structure with many emerging metal-oxo/hydroxo/alkoxo clusters hint at the existence of common metal-oxo "skeletons," which subsequently loosen the traditional boundaries of POM chemistry. So then where is the Keggin structure going? Considering that many metal cations may take a role as addenda centers or as stabilizing units, the landscape of molecular kegginoids that includes

possible mixed-addenda, semimetal, and hybrid functionalized derivatives is limitless. Thus, with the ever-growing synthetic and theoretical insights into these systems, rational design and atom-economic preparation of novel kegginoids with desired properties are eminent.

AUTHOR CONTRIBUTIONS

AK wrote the perspective. TP-V initiated and revised the perspective. Both authors have read and agreed with the final version of the perspective.

FUNDING

AK thanks the Research Foundation Flanders (FWO) for the post-doctoral fellowship (166497/12Y9218N LV 5457).

ACKNOWLEDGMENTS

Mr. James Keggin (Isle of Man) is thanked for providing the historical photograph which has enriched this perspective. KU Leuven is thanked for providing research support.

REFERENCES

- Absillis, G., Cartuyvels, E., Van Deun, R., and Parac-Vogt, T. N. (2008). Hydrolytic cleavage of an RNA-model phosphodiester catalyzed by a highly negatively charged polyoxomolybdate $[\text{Mo}_7\text{O}_{24}]^{6-}$ cluster. *J. Am. Chem. Soc.* 130, 17400–17408. doi: 10.1021/ja804823g
- Albers, P. W., Mobus, K., Wieland, S. D., and Parker, S. F. (2015). The fine structure of Pearlman's catalyst. *Phys. Chem. Chem. Phys.* 17, 5274–5278. doi: 10.1039/C4CP05681G
- Anderson, J. S. (1937). Constitution of the polyacids. *Nature* 140, 850. doi: 10.1038/140850a0
- Anyushin, A. V., Smolentsev, A. I., Mainichev, D. A., Vicent, C., Gushchin, A. L., Sokolov, M. N., et al. (2014). Synthesis and characterization of a new Keggin anion: $[\text{BeW}_{12}\text{O}_{40}]^{6-}$. *Chem. Commun.* 50, 9083–9085. doi: 10.1039/C4CC02456G
- Arns, R. G. (1998). The other transistor: early history of the metal-oxide semiconductor field-effect transistor. *Eng. Sci. Educ. J.* 7, 233–240. doi: 10.1049/esej:19980509
- Ayass, W. W., and Kortz, U. (2018). Remember the Keggin Ion? *ChemViews Mag.* 2018. doi: 10.1002/chemv.201800009
- Baker, L. C. W., and Figgis, J. S. (1970). New fundamental type of inorganic complex: hybrid between heteropoly and conventional coordination complexes. Possibilities for geometrical isomerisms in 11-, 12-, 17-, and 18-heteropoly derivatives. *J. Am. Chem. Soc.* 92, 3794–3797. doi: 10.1021/ja00715a047
- Baker, L. C. W., and Glick, D. C. (1998). Present general status of understanding of heteropoly electrolytes and a tracing of some major highlights in the history of their elucidation. *Chem. Rev.* 98, 3–49. doi: 10.1021/cr960392l
- Baldoví, J. J., and Kondinski, A. (2018). Exploring high-symmetry lanthanide-functionalized polyoxopalladates as building blocks for quantum computing. *Preprints*. 2018:2018060369. doi: 10.20944/preprints201806.0369.v1
- Berzelius, J. J. (1826). Beitrag zur näheren Kenntniss des Molybdäns. *Ann. Phys.* 82, 369–392.
- Bijelic, A., and Rempel, A. (2015). The use of polyoxometalates in protein crystallography – an attempt to widen a well-known bottleneck. *Coord. Chem. Rev.* 299, 22–38. doi: 10.1016/j.ccr.2015.03.018
- Binnemans, K. (2009). Lanthanide-based luminescent hybrid materials. *Chem. Rev.* 109, 4283–4374. doi: 10.1021/cr8003983
- Boskovic, C. (2017). Rare earth polyoxometalates. *Acc. Chem. Res.* 50, 2205–2214. doi: 10.1021/acs.accounts.7b00197
- Bradley, S. M., Kydd, R. A., and Yamdagni, R. (1990). Detection of a new polymeric species formed through the hydrolysis of gallium(III) salt solutions. *J. Chem. Soc., Dalton Trans.* 413–417. doi: 10.1039/dt9900000413
- Brock, W. H. (1993). *The Norton History of Chemistry*. New York, NY: W.W. Norton & Co Inc.
- Clemente-Juan, J. M., Coronado, E., and Gaita-Arino, A. (2012). Magnetic polyoxometalates: from molecular magnetism to molecular spintronics and quantum computing. *Chem. Soc. Rev.* 41, 7464–7478. doi: 10.1039/c2cs35205b
- Crooks, R. J., and Weller, M. T. (1997). The syntheses and structures of the complex oxide carbonates $\text{Ba}_{11}\text{Pd}_{11}\text{O}_{20}(\text{CO}_3)_2$ and $\text{Ba}_{88}\text{Ni}_{87}\text{O}_{156}(\text{CO}_3)_{19}$. *J. Solid State Chem.* 128, 220–227. doi: 10.1006/jssc.1996.7191
- Dawson, B. (1953). The structure of the 9(18)-heteropoly anion in potassium 9(18)-tungstophosphate, $\text{K}_6(\text{P}_2\text{W}_{18}\text{O}_{62}) \cdot 14\text{H}_2\text{O}$. *Acta Crystallogr.* 6, 113–126. doi: 10.1107/S0365110X53000466
- Day, V. W., Klemperer, W. G., and Pafford, M. M. (2005). Methyltriskaidecaborates, molecular forms of zirconia. *Inorg. Chem.* 44, 5397–5404. doi: 10.1021/ic048307c
- Dong, L., Huang, R., Wei, Y., and Chu, W. (2009). A remarkable member of the polyoxometalates: the eight-nickel-capped α -keggin polyoxoazoniclate. *Inorg. Chem.* 48, 7528–7530. doi: 10.1021/ic9012872
- Dong, L., Li, X., Cao, J., Chu, W., and Huang, R. (2013). An α -Keggin polyoxometalate completely constructed from the late transition metal Co^{II} as poly atom. *Dalton Trans.* 42, 1342–1345. doi: 10.1039/C2DT31896B
- Effenberger, H., Giester, G., Krause, W., and Bernhardt, H. (1998). Tschörtnerite, a copper-bearing zeolite from the Bellberg volcano, Eifel, Germany. *Am. Mineral.* 83, 607–617. doi: 10.2138/am-1998-5-620
- Ercit, T. S., and Hawthorne, F. C. (1995). Murataite, A UB12 derivative structure with condensed Keggin molecules. *Can. Mineral.* 33, 1223–1229.
- Evans, H. T. Jr. (1948). The crystal structures of ammonium and potassium molybdatellurates. *J. Am. Chem. Soc.* 70, 1291–1292. doi: 10.1021/ja01183a521
- Gatteschi, D., Pardi, L., Barra, A. L., and Müller, A. (1993). Polyoxovanadates: the missing link between simple paramagnets and bulk magnets? *Mol. Eng.* 3, 157–169. doi: 10.1007/BF00999630

- Goloboy, J. C., and Klemperer, W. G. (2009). Are particulate noble-metal catalysts metals, metal oxides, or something in-between? *Angew. Chem. Int. Ed.* 48, 3562–3564. doi: 10.1002/anie.200805382
- Gómez-Romero, P., Chojak, M., Cuentas-Gallegos, K., Asensio, J. A., Kulesz, P. J., Casañ-Pastor, N., et al. (2003). Hybrid organic–inorganic nanocomposite materials for application in solid state electrochemical supercapacitors. *Electrochem. Comm.* 5, 149–153. doi: 10.1016/S1388-2481(03)00010-9
- Gouzerh, P., and Che, M. (2006). From Scheele and Berzelius to Müller. Polyoxometalates (POMs) revisited and the “missing link” between the bottom up and top down approaches. *Actual. Chim.* 298, 9–22. Available online at: <https://www.lactualitechimique.org/De-Scheele-et-Berzelius-a-Muller-les-polyoxometallates-POMs-revisites-et-le-chainon-manquant-entre>
- Heine, T. (2014). Grand challenges in computational materials science: from description to prediction at all scales. *Front. Mater.* 1:7. doi: 10.3389/fmats.2014.00007
- Herrmann, S., De Matteis, L., de la Fuente, J. M., Mitchell, S. G., and Streb, C. (2017). Removal of multiple contaminants from water by polyoxometalate supported ionic liquid phases (POM-SILPs). *Angew. Chem. Int. Ed.* 56, 1667–1670. doi: 10.1002/anie.201611072
- Holman, W. I. M. (1943). A new technique for the determination of phosphorus by the molybdenum blue method. *Biochem. J.* 37, 256–259. doi: 10.1042/bj0370256
- Izarova, N. V., Pope, M. T., and Kortz, U. (2012). Noble metals in polyoxometalates. *Angew. Chem. Int. Ed.* 51, 9492–9510. doi: 10.1002/anie.201202750
- Johansson, G. (1960). The crystal structure of some basic aluminum salts. *Acta Chem. Scand.* 14, 771–773. doi: 10.3891/acta.chem.scand.14-0771
- Kampf, A. R., Hughes, J. M., Nash, B. P., and Marty, J. (2017). Kegginite, $\text{Pb}_3\text{Ca}_3[\text{As}_5\text{O}_{40}(\text{VO})] \cdot 2\text{H}_2\text{O}$, a new mineral with a novel ϵ -isomer of the Keggin anion. *Am. Mineral.* 102, 461. doi: 10.2138/am-2017-5834
- Keggin, J. F. (1933a). Structure of the molecule of 12-phosphotungstic acid. *Nature* 131, 908–909.
- Keggin, J. F. (1933b). Structure of the crystals of 12-phosphotungstic acid. *Nature* 132, 351.
- Keggin, J. F. (1934). Structure and formula of 12-phosphotungstic acid. *Proc. R. Soc. A* 144, 75–100. doi: 10.1098/rspa.1934.0035
- Kipka, R., and Müller-Buschbaum, H. K. (1977). Über oxocuprate, XX ein erdalkalioxocuprat(II) mit geschlossenen baugruppen: BaCuO_2 /about oxocuprates, XX alkaline-earth oxocuprate(ii) with closed structural groups: BaCuO_2 . *Z. Naturforsch.* 32b, 124–126. doi: 10.1515/znbs-1977-0201
- Kondinski, A., and Monakhov, K. Y. (2017). Breaking the gordian knot in the structural chemistry of polyoxometalates: copper(II)-oxo/hydroxo clusters. *Chem. Eur. J.* 23, 7841–7852. doi: 10.1002/chem.201605876
- Kozhevnikov, I. (2009). “Sustainable heterogeneous acid catalysis by heteropoly acids,” in *Handbook of Green Chemistry - Green Catalysis, Vol 2: Heterogeneous Catalysis*, eds P. T. Anastas and R. H. Crabtree (Weinheim: Wiley-VCH), 153–174.
- Landsmann, S., Wessig, M., Schmid, M., Cölfen, H., and Polarz, S. (2012). Smart inorganic surfactants: more than surface tension. *Angew. Chem. Int. Ed.* 51, 5995–5999. doi: 10.1002/anie.201200139
- López, X., Fernández, J. A., and Poblet, J. M. (2006). Redox properties of polyoxometalates: new insights on the anion charge effect. *Dalton Trans.* 1162–1167. doi: 10.1039/B507599H
- Ly, H. G., Absillis, G., Janssens, R., Proost, P., and Parac-Vogt, T. N. (2015). Highly amino acid selective hydrolysis of myoglobin at aspartate residues as promoted by zirconium(IV)-substituted polyoxometalates. *Angew. Chem. Int. Ed.* 54, 7391–7394. doi: 10.1002/anie.201502006
- Maestre, J. M., Lopez, X., Bo, C., Poblet, J., and Casañ-Pastor, N. (2001). Electronic and magnetic properties of α -Keggin anions: a DFT study of $[\text{XM}_{12}\text{O}_{40}]^{n-}$, ($\text{M} = \text{W}, \text{Mo}; \text{X} = \text{Al}^{\text{III}}, \text{Si}^{\text{IV}}, \text{P}^{\text{V}}, \text{Fe}^{\text{III}}, \text{Co}^{\text{II}}, \text{Co}^{\text{III}}$) and $[\text{SiM}_{11}\text{VO}_{40}]^{m-}$ ($\text{M} = \text{Mo}$ and W). *J. Am. Chem. Soc.* 123, 3749–3758. doi: 10.1021/ja003563j
- Mathieson, A. McL. (1975). Barrie Dawson, 1925–1974. *Acta Cryst. A* 31, 269–270. doi: 10.1107/S0567739475000563
- Mingos, D. M. P. (1999). Bonding and charge distribution in polyoxometalates: a bond valence Approach. 93, 340.
- Mitchell, S. G., and de la Fuente, J. M. (2012). The synergistic behavior of polyoxometalates and metal nanoparticles: from synthetic approaches to functional nanohybrid materials. *J. Mater. Chem.* 22, 18091–18100. doi: 10.1039/c2jm33128d
- Moffat, J. B. (2002). *Metal-Oxygen Clusters: The Surface and Catalytic Properties of Heteropoly Oxometalates*. Boston, MA: Springer.
- Morosin, B. (1977). Molecular configuration of a tridecazirconium oxide-methoxide complex. *Acta Crystallogr. B* 33, 303–305. doi: 10.1107/S056774087700346X
- Mu, B., Wang, Q., and Huang, R. (2016). Photocatalysis from a series of polyoxoazocobaltate high-nuclearity nanoclusters. *RSC Adv.* 6, 12114–12122. doi: 10.1039/C5RA26978D
- Müller, A., and Döring, J. (1991). Topologisch und elektronisch bemerkenswerte “reduzierte” Cluster des Typs $[\text{V}_{18}\text{O}_{42}(\text{X})]^{n-}$ ($\text{X} = \text{SO}_4, \text{VO}_4$) mit T_d -Symmetrie und davon abgeleitete Cluster $[\text{V}_{(18-p)}\text{As}_{2p}\text{O}_{42}(\text{X})]^{m-}$ ($\text{X} = \text{SO}_3, \text{SO}_4, \text{H}_2\text{O}; p = 3, 4$). *Z. Anorg. Allg. Chem.* 595, 251–274.
- Müller, A., Peters, F., Pope, M. T., and Gatteschi, D. (1998). Polyoxometalates: very large clusters - nanoscale magnets. *Chem. Rev.* 98, 239–271. doi: 10.1021/cr9603946
- Neiwerth, W. A., Cowan, J. J., Hardcastle, K. I., Hill, C. L., and Weinstock, I. A. (2002). Stability and Structure in α - and β -Keggin Heteropolytungstates, $[\text{X}^n+\text{W}_{12}\text{O}_{40}]^{(8-n)-}$, $\text{X} = p$ -Block Cation. *Inorg. Chem.* 41, 6950–6952. doi: 10.1021/ic026023r
- Newton, G. N., Yamashita, S., Hasumi, K., Matsuno, J., Yoshida, N., Nihei, M., et al. (2011). Redox-controlled magnetic $\{\text{Mn}_{13}\}$ keggins systems. *Angew. Chem. Int. Ed.* 50, 5716–5720. doi: 10.1002/anie.201100515
- Nishimoto, Y., Yokogawa, D., Yoshikawa, H., Awaga, K., and Irle, S. (2014). Super-reduced polyoxometalates: excellent molecular cluster battery components and semipermeable molecular capacitors. *J. Am. Chem. Soc.* 136, 9042–9052. doi: 10.1021/ja5032369
- Nomiya, K., Sakai, Y., and Matsunaga, S. (2011). Chemistry of group IV metal ion-containing polyoxometalates. *Eur. J. Inorg. Chem.*, 2011, 179–196. doi: 10.1002/ejic.201000712
- Nyman, M., Bonhomme, F., Alam, T. M., Parise, J. B., and Vaughan, G. M. B. (2004). $[\text{SiNb}_{12}\text{O}_{40}]^{16-}$ and $[\text{GeNb}_{12}\text{O}_{40}]^{16-}$: highly charged keggins ions with sticky surfaces. *Angew. Chem. Int. Ed.* 43, 2787–2792. doi: 10.1002/anie.200353410
- Pauling, L. (1928). Letter from Linus Pauling to W. L. Bragg. October 22, 1928. 2015. Available online at: <http://scarc.library.oregonstate.edu/coll/pauling/bond/corr/corr30.1-lp-bragg-19281022.html>
- Pauling, L. (1929a). The molecular structure of the tungstosilicates and related compounds. *J. Am. Chem. Soc.* 51, 2868–2880.
- Pauling, L. (1929b). Letter from Linus Pauling to W. L. Bragg. July 15, 1929. 2015. Available online at: <http://scarc.library.oregonstate.edu/coll/pauling/bond/corr/corr30.1-lp-bragg-19290715.html>
- Polarz, S., Landsmann, S., and Klaiber, A. (2014). Hybrid surfactant systems with inorganic constituents. *Angew. Chem. Int. Ed.* 53, 946–954. doi: 10.1002/anie.201303159
- Pope, M. T. (1983). *Heteropoly and Isopoly Oxometalates*. Berlin; Heidelberg: Springer-Verlag.
- Pope, M. T., and Müller, A. (1991). Polyoxometalate chemistry: an old field with new dimensions in several disciplines. *Angew. Chem. Int. Ed.* 30, 34–48. doi: 10.1002/anie.199100341
- Pope, M. T., O'Donnell, S. E., and Prados, R. A. (1976). Electron exchange between pairs of vanadium atoms in novel geometric isomers of heteropoly tungstates. *Adv. Chem. Ser.* 150, 85–94. doi: 10.1021/ba-1976-0150.ch008
- Pope, M. T., and Scully, T. F. (1975). Geometrical isomerism arising from partial substitution of metal atoms in isopoly and heteropoly complexes. Possibilities for the Keggin structure. *Inorg. Chem.* 14, 953–954. doi: 10.1021/ic50146a052
- Proust, A., Matt, B., Villanneau, R., Guillemot, G., Gouzerh, P., and Izzet, G. (2012). Functionalization and post-functionalization: a step towards polyoxometalate-based materials. *Chem. Soc. Rev.* 41, 7605–7622. doi: 10.1039/c2cs35119f
- Proust, A., Thouvenot, R., and Gouzerh, P. (2008). Functionalization of polyoxometalates: towards advanced applications in catalysis and materials science. *Chem. Commun.* 1837–1852. doi: 10.1039/b715502f
- Pütt, R., Kondinski, A., and Monakhov, K. (2018). Die “klassischen” Polyoxometallate. *Chem. Unserer Zeit.* 52. doi: 10.1002/ciuz.201800818
- Rhule, J. T., Hill, C. L., Judd, D. A., and Schinazi, R. F. (1998). Polyoxometalates in Medicine. *Chem. Rev.* 98, 327–358. doi: 10.1021/cr960396q
- Roy, S. (2011). “Soft Oxometalates” (SOMs): a very short introduction. *Comm. Inorg. Chem.* 32, 113–126. doi: 10.1080/02603594.2011.608443

- Rozes, L., and Sanchez, C. (2011). Titanium oxo-clusters: precursors for a Lego-like construction of nanostructured hybrid materials. *Chem. Soc. Rev.* 40, 1006–1030. doi: 10.1039/c0cs00137f
- Sadeghi, O., Zakharov, L. N., and Nyman, M. (2015). Aqueous formation and manipulation of the iron-oxo Keggin ion. *Science* 347, 1359–1362. doi: 10.1126/science.aaa4620
- Sass, S. L. (2011). *The Substance of Civilization: Materials and Human History from the Stone Age to the Age of Silicon*. New York, NY: Arcade Publishing.
- Shen, J., Zhang, Y., Zhang, Z., Li, Y., Gao, Y., and Wang, E. (2014). Polyoxoniobate-based 3D framework materials with photocatalytic hydrogen evolution activity. *Chem. Commun.* 50, 6017–6019. doi: 10.1039/c3cc49245a
- Smith, D. P., and Pope, M. T. (1973). Heteropoly 12-metallophosphates containing tungsten and vanadium. Preparation, voltammetry, and properties of mono-, di-, tetra-, and hexavanado complexes. *Inorg. Chem.* 12, 331–336. doi: 10.1021/ic50120a018
- Sun, H., Gao, N., Ren, J., and Qu, X. (2015). Polyoxometalate-based Rewritable Paper. *Chem. Mater.* 27, 7573–7576. doi: 10.1021/acs.chemmater.5b03711
- Symes, M. D., and Cronin, L. (2013). Decoupling hydrogen and oxygen evolution during electrolytic water splitting using an electron-coupled-proton buffer. *Nat. Chem.* 5, 403–409. doi: 10.1038/nchem.1621
- Tranchemontagne, D. J., Zheng, N., O’Keeffe, M., and Yaghi, O. M. (2008). Reticular chemistry of metal–organic polyhedra. *Angew. Chem. Int. Ed.* 47, 5136–5147. doi: 10.1002/anie.200705008
- von Jaggi, H., and Oswald, H. R. (1961). Die Kristallstruktur des Kupferhydroxids $\text{Cu}(\text{OH})_2$. *Acta Crystallogr.* 14, 1041–1045. doi: 10.1107/S0365110X61003016
- Wang, H., Hamanaka, S., Nishimoto, Y., Irle, S., Yokoyama, T., Yoshikawa, H., et al. (2012). In operando X-ray absorption fine structure studies of polyoxometalate molecular cluster batteries: polyoxometalates as electron sponges. *J. Am. Chem. Soc.* 134, 4918–4924. doi: 10.1021/ja2117206
- Wang, S. S., and Yang, G. (2015). Recent advances in polyoxometalate-catalyzed reactions. *Chem. Rev.* 115, 4893–4962. doi: 10.1021/cr500390v
- Wells, A. F. (1940). Finite complexes in crystals: a classification and review. *Philos. Mag. (1798-1977)* 30, 103–134. doi: 10.1080/14786444008520702
- Yamase, T. (2009). Luminescence of polyoxometallolanthanoates and photochemical nano-ring formation. *Handb. Phys. Chem. Rare Earths* 39, 297–356. doi: 10.1016/S0168-1273(08)00003-2
- Zheng, S. T., and Yang, G. (2012). Recent advances in paramagnetic-TM-substituted polyoxometalates (TM = Mn, Fe, Co, Ni, Cu). *Chem. Soc. Rev.* 41, 7623–7646. doi: 10.1039/c2cs35133a

Conflict of Interest Statement: The authors declare that the research was conducted in the absence of any commercial or financial relationships that could be construed as a potential conflict of interest.

Copyright © 2018 Kondinski and Parac-Vogt. This is an open-access article distributed under the terms of the Creative Commons Attribution License (CC BY). The use, distribution or reproduction in other forums is permitted, provided the original author(s) and the copyright owner(s) are credited and that the original publication in this journal is cited, in accordance with accepted academic practice. No use, distribution or reproduction is permitted which does not comply with these terms.



Toward Exploiting the Behavior of Niobium-Containing Mesoporous Silicates vs. Polyoxometalates in Catalysis

Agata Wawrzynczak, Izabela Nowak* and Agnieszka Feliczak-Guzik

Faculty of Chemistry, Adam Mickiewicz University in Poznań, Poznań, Poland

OPEN ACCESS

Edited by:

Debbie C. Crans,
Colorado State University,
United States

Reviewed by:

Tilo Sönnel,
University of Auckland, New Zealand
Craig L. Hill,
Emory University, United States

*Correspondence:

Izabela Nowak
nowakiza@amu.edu.pl

Specialty section:

This article was submitted to
Inorganic Chemistry,
a section of the journal
Frontiers in Chemistry

Received: 22 June 2018

Accepted: 29 October 2018

Published: 21 November 2018

Citation:

Wawrzynczak A, Nowak I and
Feliczak-Guzik A (2018) Toward
Exploiting the Behavior of
Niobium-Containing Mesoporous
Silicates vs. Polyoxometalates in
Catalysis. *Front. Chem.* 6:560.
doi: 10.3389/fchem.2018.00560

Classification of polyoxometalates (POMs) is based on their chemical composition, basically represented by two general formulae: a) $[M_mO_y]^{p-}$ b) $[X_xM_mO_y]^{q-}$, where M is the main transition metal, O is the oxygen atom and X can be a non-metal atom such as Si. Additionally, in the most cases, the structure of the polyoxometalates is derived from a combination of octahedral units MO_6 with a central metal atom M and the oxygen atoms placed at their corners. In such octahedra, oxygen atoms allow the condensation between two octahedral units, while one oxygen atom (or max. two atoms) makes double bond with the central metal atom and is not shared with other metal atoms within the complex (terminal oxygens). On the other hand, niobium-containing mesoporous silicates contain mainly MO_4 tetrahedra and reveal superior activity in heterogeneous catalysis. Thus, the proper coordination of niobium is crucial for the catalytic activity and will be deeply discussed. The similarity in the catalytic behavior of niobium-polyoxometalates and heterogeneous niobium single-site catalysts in selective oxidations will be demonstrated.

Keywords: PONbs, catalytic oxidation, H_2 evolution, base catalysis, Knoevenagel condensation

INTRODUCTION

The family of polyoxometalates (POMs) consist of different anionic polynuclear metal-oxygen clusters which comprise the edge-sharing and corner-sharing pseudo-octahedral MO_6 units that form an ionic core and cover mainly early transition metals (Gumerova and Rompel, 2018). Up till now many compounds falling into this category have been synthesized in a great number of shapes and sizes, with the Lindqvist (1953) and Keggin (1933) geometries being the foremost studied. POMs can be also sub-categorized as isopolyanions, containing no heterometals, or additional metals (with Lindqvist ion as an example) and heteropolyanions enclosing heterometals (like in the Keggin ion) (Long et al., 2010).

The Lindqvist ion (hexametalate, of the formula $[M_6O_{19}]^{p-}$) can be characterized as a superoctahedron created from 6 edge-sharing octahedra with every octahedral metal connected to the oxygen atoms (Figure 1). On the other hand, the Keggin ion with a formula $[XM_{12}O_{40}]^{q-}$ contains a central tetrahedral oxoanion (e.g., PO_4 , SiO_4 , AlO_4) in which each oxygen is the terminal atom for three edge-sharing MO_6 octahedra (Nyman, 2011). In the case of α -Keggin polymorph the four MO_6 trimers share corners, whereas in other isomers (labeled with the prefixes β -, γ -, δ - and ϵ -) these units are linked together in different ways (Baker and Figgis, 1970).

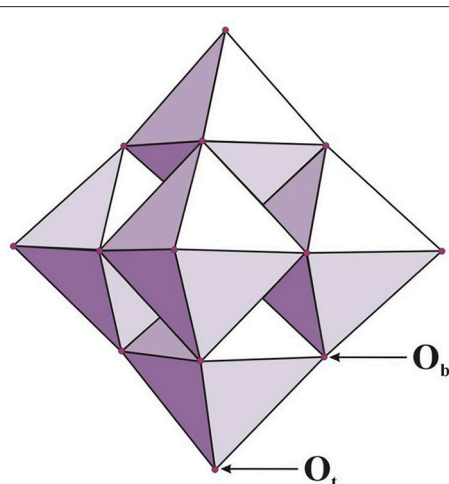


FIGURE 1 | The Lindqvist anion of $[M_6O_{19}]^{p-}$ type (for $M = Mo, W$ $p = 2$ and for $M = Nb, Ta$ $p = 8$); O_b and O_t depicts bridging (e.g., $Nb-O_b-Nb$) and terminal (e.g., $Nb-O_t$) oxygen atoms, respectively (adopted from Bontchev and Nyman, 2006).

In literature a great exertion has been devoted to the synthesis and characterization of various POM structures (Pope and Kortz, 2012; Hutin et al., 2013), nevertheless these materials are also attractive regarding their applications, namely in catalysis (Lv et al., 2012; Wang et al., 2015), bio- and nanotechnology (Yamase and Pope, 2002), medicine (Sarafianos et al., 1996; Rhule et al., 1998; Zhang et al., 2014), material sciences (Proust et al., 2008; Tong and Ye, 2010), macromolecular crystallography (Bijelic and Rompel, 2015) or electrochemistry (Sadakane and Steckhan, 1998). Many of these applications are based on the redox potential of POMs, since they possess high capacity to release and bear electrons (Botar et al., 2009; Su et al., 2017). Polyoxometalates may be considered as weak Lewis bases due to the presence of surface oxoligands that may attach Lewis acids. Nevertheless, one has to bear in mind that the basicity of these surface oxygens is very low. Still, the addenda metals present in polyanion skeletons may possess unoccupied orbitals and thus can generate Lewis acidic sites at the outside of POMs (Wang et al., 2015).

When polyoxometalates-related chemistry is concerned, it seems to be restricted mainly to group VI of the periodic table, whereas group V elements (V, Nb and Ta) do not find such high coverage in the literature. In general, polyoxoniobates (PONbs) can be divided into two categories, namely isopolyniobates (IPONbs) and heteropolyniobates (HPONbs). Toward the end of the Twentieth century, polyoxoniobates involved mainly $[Nb_6O_{19}]^{8-}$ structures (Lindqvist ion) isolated as single or mixed Cs, K, Na, Li salts (Filowitz et al., 1979; Ozeki et al., 1994; Nyman et al., 2006; Anderson et al., 2007) or some coordination complexes thereof (i.e. $Mn[Nb_6O_{19}]_2^{12-}$) (Flynn and Stucky, 1969a). Also the related decaniobate $[Nb_{10}O_{28}]^{6-}$ has been reported (Graeber and Morosin, 1977). In 1969, Flynn et al. determined the structure of IPONbs modified with transition metals and ethylenediamine ligand

(Flynn and Stucky, 1969b) and started a series of studies on TM-containing IPONbs. Subsequently, in 2006 Yagasaki et al. isolated a crystalline tetra-n-butylammonium salt of icosaniobate $[Nb_{20}O_{54}]^{8-}$ and contributed to a group of isopolyniobates (IPONbs) with samples possessing potential application as building blocks or precursors for constructing new niobate clusters (Maekawa et al., 2006). As a result, other groups initiated studies on the synthesis and characterization of unique PONb clusters, with Nyman's $\{Nb_{24}O_{72}H_9\}^{15-}$ (Bontchev and Nyman, 2006), Cronin's $[HnNb_{27}O_{76}]^{16-}$ or $[H_{10}Nb_{31}O_{93}(CO_3)]^{23-}$ (Tsunashima et al., 2010) and more recently Wang's $KNa_2[Nb_{24}O_{72}H_{21}] \cdot 38H_2O$, $K_2Na_2[Nb_{32}O_{96}H_{28}] \cdot 80H_2O$, and $K_{12}[Nb_{24}O_{72}H_{21}]_4 \cdot 107H_2O$ as examples (Huang et al., 2012a). Recently, the largest and the highest nuclearity polyoxoniobate, i.e., protein-sized (ca. $4.2 \times 4.2 \times 3.6$ nm³) inorganic molecule $\{Nb_{288}O_{768}(OH)_{48}(CO_3)_{12}\}$ containing up to 288 niobium atoms was obtained (Wu et al., 2018).

On the other hand, from among HPONbs, Keggin-type nioboaxalates are the most widely studied and used as efficient precursors for creating functional materials. The first Keggin-type HPONb $[SiNb_{12}O_{40}]^{16-}$ was synthesized in the presence of titanium cations, where a Ti_2O_2 dimer was applied as a linker to connect the Keggin type units into a one dimensional chain-like framework (Nyman et al., 2002). Up till now a series of HPONbs have been synthesized in the presence of P, V, Ge, Si, and As, resulting in compounds like $[V_3Nb_{12}O_{42}]^{9-}$ (Son et al., 2013a) $[PV_2Nb_{12}O_{42}]^{9-}$ (Son et al., 2013b) $\{GeNb_{12}V_2^{IV}O_{42}\}$ (Zhang et al., 2014) or $[H_6Ge_4Nb_{16}O_{56}]^{10-}$ (Shen et al., 2013), as well as $[Si_4Nb_{16}O_{56}]^{16-}$ (Abramov et al., 2017). Lately also series of niobium-tungsten-lanthanide heterometallic polyoxometalates have been prepared with Y, La, Sm, Eu, and Yb cations (Jin et al., 2016). However, it is still challenging to find papers broadening PONbs applications, beyond the Lindqvist ion, due to the limitations of chemistry in aqueous synthesis of PONbs (requirement of alkaline solution, lack of appropriate precursors) (Nyman, 2011).

Additionally, a new possibility will be exploited soon, i.e., the encapsulation of polyoxoniobates in inorganic substrates and the application in catalysis of the resulting materials can be expected. There are already examples of other than niobium-based polyoxometalates (Lefebvre, 2013). Only recently a functionalized polyoxoniobate/g- C_3N_4 nanoporous material has been synthesized with carbon nitride (g- C_3N_4) and hexaniobate ($K_8Nb_6O_{19} \cdot 10H_2O$) as starting materials (Gan et al., 2018).

Contrary, niobium-containing mesoporous silicates receive great attention due to the well-studied and convenient synthesis procedures in aqueous solutions. Moreover, they possess very attractive structural, textural, and morphological surface properties, like highly ordered structures, high surface areas, narrow pore size distributions as well as tunable pore sizes and structures, affecting their activity in catalysis, sorption, and separations (Nowak, 2012).

The best known mesoporous material is MCM-41. The synthesis of this material was described by scientists at the Mobil Oil Company in 1992. This procedure was realized by the application of surfactant micelles as structure determining agents

in a sol-gel method. The surfactants (amphiphilic) organize themselves into cylindrical micelles that are encapsulated by silicate compounds. Finally, calcination process is applied in order to eliminate the organic surfactant without changes in a hexagonal organization of mesopores (Beck et al., 1992; Kresge et al., 1992). Sol-gel technology concerns the creation of a solid phase through the gelation of a colloidal suspension-sol (Lev et al., 1997). Two possible routes for this process are known: inorganic and organic ones. Inorganic route is the hydrothermal technique that includes the creation of a sol from the inorganic, silicon-containing starting material. In the organic route the starting material possess an organic component, e.g., tetraethyl orthosilicate (TEOS) which is hydrolyzed to form a gel. The liquid crystal templating process employed by the Mobil Oil Company in 1992, engaged the dissolution of a various surfactant species in the pre-hydrolyzed inorganic precursor. This mechanism is highly influenced by electrostatic and steric interactions between the solvent, inorganic precursor and the self-assembled organic surfactants. In the synthesis of mesoporous materials, a wide variety of surfactants with various properties could be used, e.g., anionic, lipid, zwitterionic even two-tailed species. Surfactants are used to create the mesopores. The metal precursor could be added during the synthesis of materials or by wet impregnation (Huo et al., 1994). As a source of niobium, ammonium niobium oxalate $\text{NH}_4[\text{NbO}(\text{C}_2\text{O}_4)_2(\text{H}_2\text{O})_2] \cdot 3\text{H}_2\text{O}$, potassium niobate $\text{K}_8\text{Nb}_6\text{O}_{19}$ or niobium chloride NbCl_5 were commonly used (Yan et al., 2018).

There are several aspects that influence the synthesis of Nb-containing mesoporous molecular sieves, namely silicon and niobium source, their molar ratio, surfactant type, synthesis environment (pH, the presence of counterions), etc. General methodologies for the synthesis of niobium catalysts on mesoporous materials are based on the use of the hydrothermal method, e.g., Ziolek's and Nowak's groups described incorporation of niobium during the synthesis of mesoporous materials using hydrothermal method (Ziolek and Nowak, 1997; Kilos et al., 2004; Nowak and Jaroniec, 2005; Feliczak-Guzik et al., 2009; Nowak, 2012). An overall procedure for the synthesis of various mesoporous materials is shown in **Figure 2**.

For the purposes of this review, we will focus only on the papers on the catalytic activity of polyoxometalates and niobium-containing mesoporous silicates published in the last decade.

CATALYSIS ON POLYOXONIOMATES

To date the great number of studies on POMs have been dedicated to the synthesis and characterization procedures. So far, in latest scientific literature a progress in investigating the applications of POMs in catalysis may be noticed. It is the most probably stimulated by the attractive features of these materials, comprising adjustable acidity and redox properties, fundamental resistance to the oxidative decomposition, significant thermal stability, and remarkable susceptibility to light and electricity.

These outstanding features have a strong connection to the structures and compositions of POMs (Wang and Yang, 2015).

Several POM systems, in both oxidized and reduced forms, can be used as robust catalysts due to their significant thermal- and photostability. Moreover, they can also be simply transformed to reactive forms by applying light and electricity (Gumerova and Rompel, 2018). The applications of polyoxometalate clusters as catalysts are many and varied, nonetheless they include mostly green H_2O_2 -based epoxidation systems (Zhou et al., 2015), catalytic approaches to sustainable splitting of water (Long et al., 2010), and also photocatalysis in various photoredox systems e.g., the oxidation of alkanes, alkenes or alcohols as well as in the light-induced mineralization of several organic and inorganic contaminants (Shen et al., 2009; Streb, 2012; Wang et al., 2017; Gan et al., 2018; Li et al., 2018).

When catalytic reactions are taken under consideration, PONbs are foremost less studied than their counterparts containing Mo, W, or V. Among others, it can be observed for epoxidation reactions, particularly those based on H_2O_2 catalyzed by POMs, which have been thoroughly discussed by groups of Neumann or Hill in many papers from the 1980's (e.g., Duncan et al., 1995; Vasylyev and Neumann, 2004). Quite challenging chemistry of Nb-based polyoxometalates could be one of the possible reasons, since the solution interactions of isopolyoxoniobates are strongly pH-dependent and dominated by $[\text{H}_x\text{Nb}_{10}\text{O}_{28}]^{(6-x)-}$ ion at pH close to neutral and by $[\text{H}_x\text{Nb}_6\text{O}_{19}]^{(8-x)-}$ ion at higher pH values.

Greater catalytic activity of polyoxoniobates may be achieved, for example, by its functionalization with transition metals, but one has to bear in mind that PONbs are quite challenging materials because of insufficient recognition of their solution behavior, since they can be present only in strong alkaline aqueous solutions, whereas most of the transition metals (TM) cations precipitate as a result of the creation of respective oxides or hydroxides. Though, cations as Cu, V, Ti, W, Zn, Cr, Ni, Co, and Pt, have been successfully introduced into the PONb systems (Ohlin et al., 2008a; Chen et al., 2010; Niu et al., 2010, 2011; Guo et al., 2011, 2012; Huang et al., 2012b; Son et al., 2013b; Abramov et al., 2015a,b; Liu et al., 2017). Some examples of applications of TM-modified polyoxoniobates as catalysts will be also covered in this review.

Catalytic Splitting of Water

Last decades clearly showed that a transfer of energy sources to renewable and sustainable systems is essential, since the global warming induced by the so called greenhouse gases has become a vital issue. Photochemical systems, permitting the conversion of solar energy to useful chemical reactivity, appear to be quite promising in this respect. Particular effort has been made to the designing photocatalytic processes which can easily proceed in the presence of polyoxometalates with improved photoactivity. The photoactivity of POMs has been already acknowledged in literature, but it is focused mainly on Mo-based salts containing organoammonium counter ions that can easily undergo photoredox-reactions in the solid state (Streb, 2012).

Generally speaking, polyoxometalates are a class of highly redox-active compounds with semiconductor-like

photochemical properties that may be involved in the light-induced photoredox reactions with direct environmental impact. Their reactivity can result in the substrate reduction or oxidation, depending on the type of the used cluster (Figure 3).

Polyoxometalates have been involved in the conversion of a wide range of molecules that may proceed mostly with two types of photoreductive reactions, i.e., the homogeneous photoreductive activation of CO₂ or production of hydrogen, the latter one being the reductive aspect of the water splitting process, as well as with visible-light induced substrate oxidation (Streb, 2012).

Water Oxidation on PONbs

Water oxidation is a crucial step in the water splitting reaction. It can be used to produce H₂ toward application as a sustainable energy carrier. In order to reach the shortest way in conversion of solar light into its storable energy counterparts it is fundamental to create catalytic systems straightforwardly powered by sunlight and based on stable and economically feasible catalysts.

A few years ago, Feng et al. reported the synthesis procedure for obtaining a photoactive catalyst based on polyoxoniobate cluster $\{[\text{Nb}_2(\text{O})_2(\text{H}_2\text{O})_2]\{\text{SiNb}_{12}\text{O}_{40}\}\}^{10-}$. In this structure, which consists of infinite 1D chains created from Nb-based Keggin clusters interconnected by dinuclear $\{\text{Nb}_2(\text{O})_2(\text{H}_2\text{O})_2\}$ moieties, it is possible to coordinate water molecule to each of the two bridging Nb sites. The Nb⁵⁺ site in the linking $\{\text{Nb}_2(\text{O})_2(\text{H}_2\text{O})_2\}$ unit is seven-coordinated with four O²⁻ anions from the Keggin unit, two bridging O²⁻ sites, which are connected to another Nb⁵⁺, and one H₂O molecule. This specific seventh coordination of niobium atoms strongly affects the local coordination geometry of Nb⁵⁺ as well as the chain arrangement and spatial packing. All these features establish K₁₀[Nb₂O₂(H₂O)₂][SiNb₁₂O₄₀]·12H₂O as a potential catalyst for efficient water oxidation (Zhang et al., 2011).

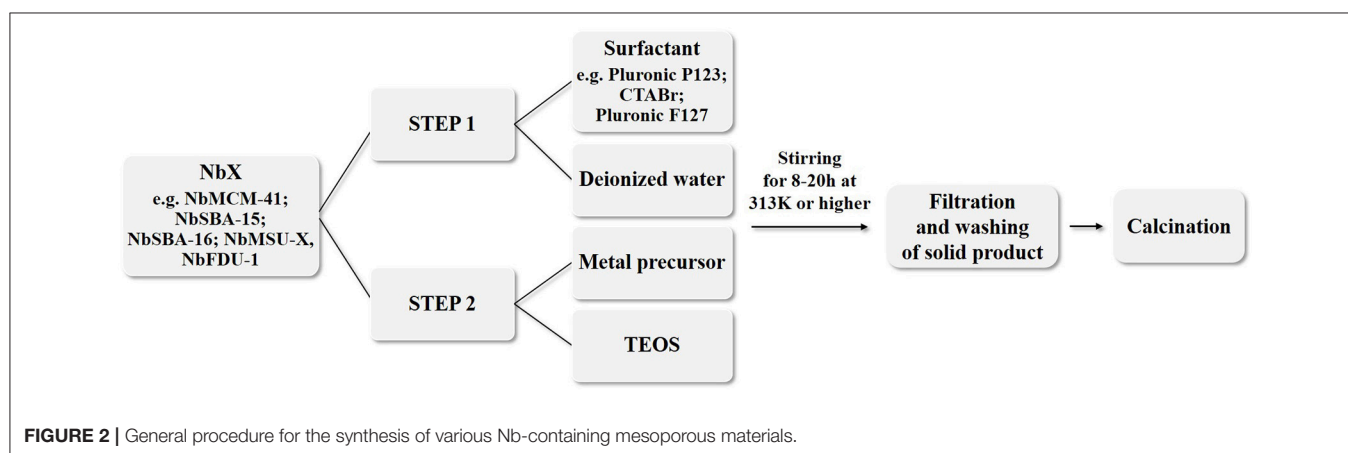
PONbs may also serve as compounds supporting the synthesis of water oxidation catalysts. Zhang and co-workers have developed an efficient method for electrodeposition of cobalt and nickel nanostructures in the presence of the Lindqvist ion [Nb₆O₁₉]⁸⁻. ICP-MS analysis revealed that the elemental ratio of Co:Nb and Ni:Nb was 1:1 and 1:3, respectively.

Raman spectra confirmed the presence of both [Nb₆O₁₉]⁸⁻ and Co(OH)₂/Ni(OH)₂ species. Further study indicated that Lindqvist ion provided electrostatic stabilization to Co(OH)₂ or Ni(OH)₂ and hence the films show exceptional stability and efficiency for electrocatalytic oxidation of water in the alkaline solution (Liu et al., 2015).

Four polyoxoniobates [Nb₆O₁₉]⁸⁻, [Nb₁₀O₂₈]⁶⁻, [Ti₂Nb₈O₂₈]⁸⁻ and [H₂Si₄Nb₁₆O₅₆]¹⁴⁻ have been tested by Qian et al. in order to evaluate their activity in the water oxidation. They found out that the studied compounds were active electrochemical catalysts under basic condition with a high catalytic current. Computational methods were applied as well to estimate photoluminescence of these compounds. It was found that the calculated values are in a good agreement with the experimental data. The obtained results proved also the impact of clusters size and addenda atoms on the catalytic and fluorescent properties of PONbs (Ye et al., 2013).

Casey's group have examined how isopolyoxoniobates, namely [H_xNb₆O₁₉]^{(8-x)-} and [H_xNb₁₀O₂₈]^{(6-x)-} ions, react with hydrogen peroxide. By using ESI-MS and ¹⁷O NMR spectroscopy the scientists could observe the differences in the behavior of hexaniobate and decaniobate anions in the presence of H₂O₂ molecules. The reaction with the hexaniobate Lindqvist ion proceeds quite slowly, while with the decaniobate anion it completes almost immediately. In addition, contrary to the hexaniobate, the decaniobate anions dissociate in the presence of peroxide, yielding in peroxohexaniobate species. These results are of particular importance when it comes to the use of PONbs as water-splitting catalysts, as the oxygen atoms bound to the terminal Nb atom can be easily substituted with peroxy groups, which are a product of water oxidation (Ohlin et al., 2008b). It is also worth mentioning that similar studies were also performed for molybdenum and tungstate-based polyoxometalates (e.g., Duncan et al., 1995; Vasylyev and Neumann, 2004).

Casey et al. have synthesized a new pentaphosphate niobate polyoxometalate cluster in the form of highly soluble and stable over a wide pH range tetramethylammonium (TMA) salt: (TMA)₉H₃Nb₉P₅O₄₁·28H₂O. The researchers proved that this compound could be reversibly converted into the peroxo form when H₂O₂ is added. This novel cluster may be regarded as a



molecular form of the niobium-phosphate solid, which is suitable for many catalytic applications, among others for the oxidation reactions (Son and Casey, 2015).

H₂ Evolution on PONbs

POMs may be considered as efficient functional modules for assembling molecular photocatalysts, since they can undergo stepwise, fast, and reversible reactions based on multielectron-transfer with no changes in their structures. As yet, several polyoxometalate catalysts containing mainly W and Mo have been exploited for light-driven H₂ evolution. Still, one always has to bear in mind that most of these POM-based catalysts cannot act as photocatalyst alone. Usually co-catalyst, such as Pt, NiO, and Co complexes, are necessary to lower the overpotential for H₂ evolution (Wang et al., 2015).

In the last years, the progress in PONbs chemistry was focused primarily on the synthesis and characterization procedures of novel types of polyoxoniobate compounds. However, Nb-based compounds such as niobates and niobium oxides have been already used as efficient photocatalysts and extensively studied in the water-splitting process for H₂ generation. Particular attention to the polyoxoniobates as photocatalysts has been paid in the last decade (Wu et al., 2015).

Feng et al. have synthesized two compounds belonging to a group of photocatalytically active polyoxoniobates, namely K₁₀[Nb₂O₂(H₂O)₂][SiNb₁₂O₄₀].12H₂O, that contains bridging units with highly unsymmetrical seven-coordinated Nb⁵⁺ sites, and Na₁₀[Nb₂O₂][SiNb₁₂O₄₀].xH₂O with the octahedral coordination of Nb⁵⁺. During photocatalytic tests, performed in the presence of these two PONbs and several co-catalyst (e.g., Pt, NiO), they observed significant differences in the amounts of evolved hydrogen. The higher activity of K₁₀[Nb₂O₂(H₂O)₂][SiNb₁₂O₄₀].12H₂O was attributed primarily to specific structure of the bridging unit, where H₂O molecules can be bonded directly to Nb species. Moreover, the

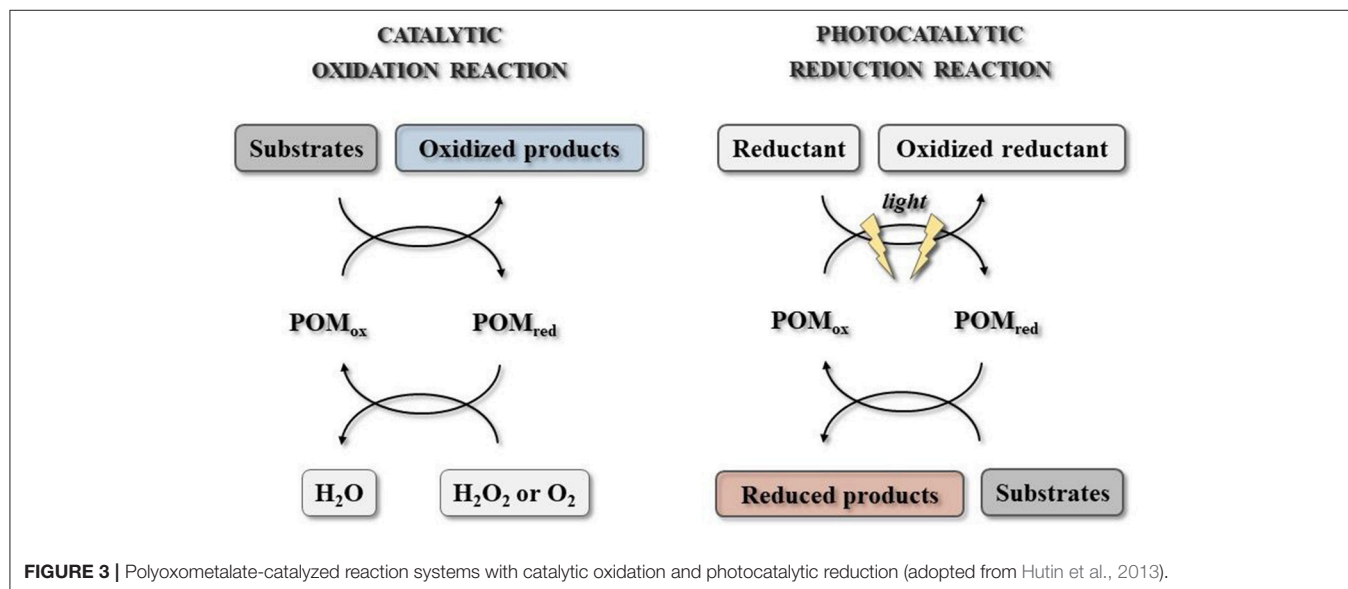
distorted configuration of NbO₇ unit may generate a substantial dipole moment which facilitates the electron-hole charge separation (Zhang et al., 2011).

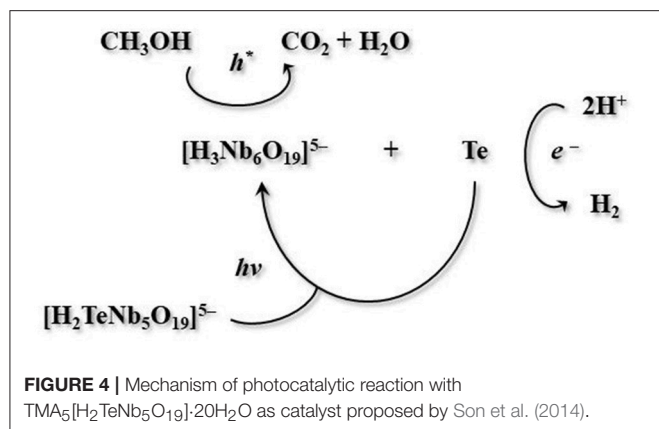
A few years ago Wang's group developed three novel polyoxoniobates based on {Nb₂₄O₇₂}, {Nb₃₂O₉₆}, and {K₁₂Nb₉₆O₂₈₈} clusters built from [Nb₇O₂₂]⁹⁻ fundamental unit. These compounds, denoted as KNa₂[Nb₂₄O₇₂H₂₁].38H₂O, K₂Na₂[Nb₃₂O₉₆H₂₈].80H₂O, and K₁₂[Nb₂₄O₇₂H₂₁]₄.107H₂O, and possessing molecular triangle, square, and cuboctahedral cage geometries, respectively, were successfully applied in the UV-light photocatalytic H₂ evolution. Catalytic systems involved also Co^{III}(dmgH)₂pyCl or Pt as co-catalysts and triethylamine as a sacrificial donor of electrons (Huang et al., 2012a).

An interesting survey of the photocatalytic activity of polyoxoniobates was presented by Son and co-workers. They synthesized TMA₅[H₂TeNb₅O₁₉].20H₂O (TMA⁺ = tetramethylammonium cation), a new tellurium-substituted polyoxoniobate based on a Lindqvist-type [H₂TeNb₅O₁₉]⁵⁻ anion. A water-methanol solution of this cluster under Xe lamp irradiation showed an outstanding activity in H₂-evolution. In-depth research demonstrated that this cluster decomposes upon irradiation, leading to the formation of [H₃Nb₆O₁₉]⁵⁻ anion and metallic tellurium in mostly nanowire morphology. The same authors suggested that hexaniobate cluster and metallic tellurium, formed as photodecomposition products, act as co-catalyst. Furthermore, they proposed a mechanism of the studied photocatalytic reaction system (Figure 4).

It should be specified, that the reported TMA salt of the TeNb₅ molecule, when compared to an analogous Nb₆ unit, exhibits a similar solid-state structure and pH stability. Though, it reveals much higher H₂-evolution activity due to a photodecomposition route to Nb₆-based anion and Te(0) nanowires (Son et al., 2014).

It is worth mentioning that polyoxoniobates containing transition metals (TM-PONbs) are much less studied, as their synthesis procedures are quite problematic and may be





performed only in the narrow pH range suitable for the PONbs precursors. Nonetheless, many groups explore this problem, trying to design and synthesize new TM-PONbs, since these compounds are potentially attractive materials e.g., in water photolysis, base-catalyzed decomposition of biocontaminants and nuclear waste treatment (Wu et al., 2015).

Su et al. have employed TM cations (Cr³⁺ and Fe³⁺) to react with the [Si(NbO₂)₃W₉O₃₇]⁷⁻ anion, resulting in three TM-containing nanoclusters: [(Si₂W₁₈Nb₆O₇₈)Cr(H₂O)₄]⁷⁻, [(Si₂W₁₈Nb₆O₇₈)Cr₂(H₂O)₈]⁴⁻, and [(Si₂W₁₈Nb₆O₇₈)FeCl₂(H₂O)₂]⁹⁻. According to the same authors, these are the first W/Nb mixed-addendum POM photocatalysts with a visible-light-driven activity for the H₂ production (Huang et al., 2013).

A year later the same group synthesized under hydrothermal conditions a tetrameric PONb Cs₁₉K₂[Nb₄O₆(SiW₉Nb₃O₄₀)₄]Cl·27H₂O by employing trivacant Keggin-type polysilicotungstates as a carrier for niobium species. The synthesis procedure involved the self-assembly of W/Nb mixed-addendum POM [SiW₉(NbO₂)₃O₃₇]⁷⁻. This compound may be viewed as four {SiW₉O₃₄} units supported on {Nb₁₆O₃₀} cluster and it demonstrated high photocatalytic activity for H₂ evolution in the presence of Pt species as a co-catalyst (Yang et al., 2014).

In the group of Wang a novel compound, based on Lindqvist polyoxoniobate substituted by transition-metal cation (K₁₀[(Nb₆O₁₉)Cr^{III}(H₂O)₂]₂·28H₂O), was obtained by using a new two-pot synthesis procedure. X-ray structure analysis showed that [(Nb₆O₁₉)Cr^{III}(H₂O)₂]₂¹⁰⁻ polyanion is a dinuclear dimeric polyoxoniobate, built of fundamental building blocks [Nb₆O₁₉]⁸⁻ sandwiched by two {Cr^{III}(H₂O)₂} groups. The synthesized PONb was tested as a catalyst in the photocatalytic evolution of hydrogen in the presence of Pt or Co^{III}(dmgH)₂pyCl and methanol as a co-catalyst and sacrificial electron donor, respectively. K₁₀[(Nb₆O₁₉)Cr^{III}(H₂O)₂]₂·28H₂O proved to be active in the studied catalytic system, especially in the presence of Pt species as a co-catalyst (Liang et al., 2015).

By means of a combination of hydrothermal and diffusional procedures, the same group obtained also a one-dimensional polyoxoniobate K₅[H₂AgNb₆O₁₉]₂·11H₂O, in which Lindqvist polyanions [Nb₆O₁₉]⁸⁻ are connected to each other by silver

cations forming an infinite chain. As reported by the above authors, this compound represents the first example of PONb in which an Ag atom is grafted on a hexaniobate anion. Moreover, photocatalytic tests revealed that it also enables acquiring high amounts of H₂ (Wang et al., 2015).

Some time ago, Wang et al. assembled two phosphoniobate-based materials with 3D framework, built of [PNb₁₂O₄₀(VO)₆]³⁻ building blocks and copper-organic linkers: [Cu(en)₂]₄[PNb₁₂O₄₀(VO)₆]₃·(OH)₅·8H₂O, (en = 1,2-ethylenediamine), and [Cu(enMe)₂]₄[PNb₁₂O₄₀(VO)₆]₃·(OH)₅·6H₂O, (enMe = 1,2-diaminopropane). Due to the presence of vanadium atoms supporting the activation of surface oxygen atoms of heteropolyniobate-based frameworks, these compounds exhibit photocatalytic activity in the hydrogen evolution (Shen et al., 2014).

Polyoxoniobates modified with organic ligands also show potential in the visible-light-driven catalysis. In order to extend the light absorbed by oxoniobium clusters to the visible region, Cu(en)₂ (en = ethylenediamine) complex may be introduced into the structure of PONbs. The resulting dimer [Cu(en)₂]₁₁K₄Na₂[KNb₂₄O₇₂H₉]₂·120H₂O benefits with strong absorption from the UV to visible light region and therefore can be used in H₂ evolution systems comprising Co^{III}(dmgH)₂pyCl or Pt as co-catalyst. According to Wang and co-workers, a satisfying catalytic performance is associated with the synergistic effect of the oxoniobium clusters and Cu(en)₂ complex, which occurs during the photoexcitation step (Wang et al., 2012). Moreover, the results with [Cu(en)₂]₁₁K₄Na₂[KNb₂₄O₇₂H₉]₂·120H₂O catalyst are noticeably better than those obtained with the Cu-connected polyoxomolybdates (Fu et al., 2012).

Quite an interesting example of polyoxoniobate-based catalytic systems for H₂ evolution was presented by a group of Li and Xu. They synthesized a low-cost and stable K₇HNb₆O₁₉-NiS/Cd_{0.65}Zn_{0.35}S photocatalytic system and proved that the presence of K₇HNb₆O₁₉ polyoxoniobate and NiS as co-catalysts affects strongly catalytic activity of Cd_{0.65}Zn_{0.35}S, increasing it to 3.4 times of that obtained with non-modified Cd_{0.65}Zn_{0.35}S. This improvement was ascribed to the positive synergistic effect between Nb₆ species and NiS in the co-catalysts, serving as electron collectors and adsorption active sites (Ma et al., 2014).

Epoxidation Reactions

Epoxidation of allylic alcohols with hydrogen peroxide as the oxidizing agent is a convenient method for obtaining epoxide alcohols, which are important final products or intermediates in the fine chemicals industry. PONbs, mostly functionalized with transition metals, have been also investigated as catalyst in the epoxidation process due to their exceptional features of great basicity and surface charge.

Wang et al. have synthesized a pseudosandwich-type PONb-based organic-inorganic hybrid material, Na₈{Ni[Ni(en)₂Nb₁₀O₃₂]}·28H₂O (en = ethanediamine), using K₇HNb₆O₁₉·13H₂O as a precursor. This material is the first example of a trinuclear nickel-containing polyoxoniobate, which is composed of a {Ni[Ni(en)₂]}₂ unit coordinated by two

monolacunary $[\text{Nb}_5\text{O}_{18}]^{11-}$ units. Additionally, the Ni^{2+} ions at both ends of the $\{\text{Ni}[\text{Ni}(\text{en})_2]\}$ cluster are functionalized by ethanediamine molecules. The synthesized samples were investigated as catalyst in the epoxidation of allylic alcohols in the assistance of H_2O_2 at room temperature in aqueous solution. Epoxidation of 3-methyl-2-buten-1-ol, which was selected as a model substrate, resulted in high conversion (98%) and selectivity (94%) at mild reaction conditions (25°C, 5 min). Comparative studies with $\text{K}_7\text{HfNb}_6\text{O}_{19}\cdot 13\text{H}_2\text{O}$ as a catalyst showed that the conversion of allylic alcohols was lower than that of $\text{Na}_8\{\text{Ni}[\text{Ni}(\text{en})_2]\text{Nb}_{10}\text{O}_{32}\}\cdot 28\text{H}_2\text{O}$. According to the same authors, it suggests that Nb atoms play crucial role in the considered epoxidation reactions. Furthermore, catalytic tests involving recycling of the catalyst have also been performed. The catalytic activity of PONb-based organic-inorganic hybrid compound stayed almost unchanged even after the sixth catalytic run. On the other hand, the catalytic activity of $\text{K}_7\text{HfNb}_6\text{O}_{19}\cdot 13\text{H}_2\text{O}$ was decreased already in the second run. Comparison of the FT-IR spectra of the fresh and reused catalysts showed noticeable differences at the peaks of 1,388 and 668 cm^{-1} , that could be attributed to bridging Nb–O_b vibrations from Lindqvist hexaniobate structure. These results suggests that the framework of the catalyst was subjected to the partial decomposition and peroxidation by H_2O_2 (Li et al., 2017).

Epoxidation of styrene is an essential reaction for the production of styrene oxide, a key organic intermediate for producing valuable products such as surfactants, paints and epoxy resins. However, simultaneous achievement of significant conversion of the substrate and selectivity to the epoxide is quite challenging.

Researchers from Cui group have studied the epoxidation of styrene to styrene oxide in a batch reactor heated to 80°C, with aqueous tert-butyl hydroperoxide (TBHP) and CH_3CN as an oxidizing agent and solvent, respectively. Three new organic-inorganic hybrid vanadium-bicapped Si centered PONb clusters based on $[\text{SiNb}_{12}\text{V}_2\text{O}_{42}]^{12-}$ unit, namely $[\text{Cu}(\text{en})_2]_4[\text{Cu}(\text{en})_2(\text{H}_2\text{O})_2]_2[\text{SiNb}_{12}\text{V}_2\text{O}_{42}]\cdot 14\text{H}_2\text{O}$, $[\text{Cu}(\text{en})_2]_2[\text{Cu}(\text{en})_2(\text{H}_2\text{O})_4]_4[\text{SiNb}_{12}\text{V}_2\text{O}_{42}]\cdot 4\text{H}_2\text{O}$ and $[\text{Cu}(\text{en})_2(\text{H}_2\text{O})_2]_4[\text{Cu}(\text{en})_2(\text{H}_2\text{O})]_2[\text{SiNb}_{12}\text{V}_2\text{O}_{42}]\cdot 11\text{H}_2\text{O}$ (en = ethanediamine), served as catalysts in this reaction. As proved by the results, all the three compounds were excellent catalysts for the epoxidation of styrene with conversion close to 99% and selectivity varying between 80.46 and 86.63%. Comparison with the isopolyniobate $\text{K}_6\text{H}_2\text{Nb}_6\text{O}_{19}\cdot 17\text{H}_2\text{O}$, which exhibits a 3-D structure created from $[\text{Nb}_6\text{O}_{19}]^{8-}$ and potassium clusters, indicated that the compound structure and the presence of other elements influence the catalytic effect of PONbs. Reusing of catalysts in styrene epoxidation proved good stability in catalytic experiments. As evidenced from FT-IR measurements, the characteristic bands attributed to $\nu(\text{Nb}-\text{O}_t)$ and $\nu(\text{Nb}-\text{O}_b-\text{Nb})$ were located at 852 and 696 cm^{-1} , respectively, and could be observed both for Nb_6O_{19} -based isopolyniobate and organic-inorganic hybrid PONb clusters, confirming the Lindqvist hexaniobate-related composition of the second group of compounds (Zhang et al., 2017).

Base Catalysis

Base-catalyzed reactions such as the C–C bond creating ones (e.g., aldol condensation, Knoevenagel condensation, Michael addition, Henry reaction), chemical fixation of CO_2 , cyanosilylation of carbonyl compounds, oxidation, hydrogenation, isomerization of alkenes/alkynes, (trans)esterification or the Tishchenko reaction are very important to the bulk and fine chemicals industry (Kamata and Sugahara, 2017). In recent years much effort has been devoted to the activity of polyoxometalates in the acid-, photo-, and oxidation-catalysis, but base catalysis on these compounds has hardly been investigated (Wang et al., 2015). Nevertheless, new aspects of mono- and polyoxometalate base catalysts have also found coverage in literature.

The base catalysis by polyoxometalates may be attributed to the negativity of the surface oxygen atoms, mostly due to the great charge densities of the clusters. Thus, POMs possessing oxygen atoms with a higher negative charge density will reveal stronger base properties. The value of $-n/y$ in $[\text{M}_x\text{O}_y]^{n-}$ units characterizes a negative charge averaged over all oxygen atoms, but it was obtained not taking into account the electronic charge transfer from metal to oxygen. Consequently, this value delivers only a lower limit of the oxygen atom negativity. Polyoxoniobates, like hexaniobate $[\text{Nb}_6\text{O}_{19}]^{8-}$ and decaniobate $[\text{Nb}_{10}\text{O}_{28}]^{6-}$ cluster, have more negative $-n/y$ values than polyoxotungstates (POWs) (Nyman, 2011; Wu et al., 2015). Assuming that the $-n/y$ ratio may be considered as a quantification of the basicity of POMs, one can say that compounds with group V metals (V, Nb, Ta) are more favorable in base catalysts than their counterparts with group VI elements (Mo, W). Therefore, Tsukuda et al. have applied $(\text{TMA})_6[\text{Nb}_{10}\text{O}_{28}]\cdot 6\text{H}_2\text{O}$ ($\text{TMA}^+ =$ tetramethylammonium cation) as a homogeneous catalyst for the Knoevenagel condensation between benzaldehyde and various nitrile compounds having different pK_a values. Knoevenagel condensation is a vital process among coupling reaction leading to the formation of new C=C bonds. It proceeds between carbonyl compounds (acceptors) and active methylene compounds (donors) such as nitriles. The key step in this reaction is abstraction of proton from donors performed by base catalysts, therefore a proper selection of catalyst is crucial for high yields of products. The results obtained by the group of Tsukuda showed that decaniobate cluster $[\text{Nb}_{10}\text{O}_{28}]^{6-}$ may act as a robust homogeneous catalyst not only for Knoevenagel condensation between benzaldehyde and p-methoxyphenylacetonitrile but also for Claisen-Schmidt condensation of benzaldehyde and acetophenone. This substantial catalytic activity was related to the high negative charge at the oxygen sites (−0.79 to −0.87) that originates primarily from the high over-all negative charge on the cluster. Density functional theory calculations, particularly natural bond orbital (NBO) analysis, were applied in order to obtain localized charge on the oxygen atoms. It was proved that NBO charge of O_b (−0.873) in $[\text{Nb}_{10}\text{O}_{28}]^{6-}$ was the lowest through the composing oxygen atoms and thus the tetraalkylammonium salts of decaniobate cluster could

successfully serve as catalysts in the Knoevenagel condensation and CO₂ fixation to epoxides (Hayashi et al., 2016, 2017).

Similarly, Zhou, Wang and coworkers have revealed that the NBO charges of the O_t atoms in [SiNb₁₂O₄₀]¹⁶⁻ cluster are inferior when compared with those of other polyoxometalates, though the difference in the basicity among oxygen atoms has not been explained so far. Nevertheless, it was shown that the sodium salt of dodecaniobate Keggin type PONb, Na₁₆[SiNb₁₂O₄₀], can perform as an effective heterogeneous catalyst for the Knoevenagel condensation of benzaldehyde and ethyl cyanoacetate as well as for cycloaddition of CO₂ to epichlorohydrin under relatively mild and solvent-free conditions (Ge et al., 2016).

On the other hand, the paper published lately by Niu and Wang describes the exceptional basicity of negatively charged Lindqvist type PONb (K₇HNb₆O₁₉·13H₂O). Theoretical NBO calculations confirmed that the most negative NBO charge of oxygen in this compound equals -1.001. This value indicates outstanding basicity, since it is significantly higher than those reported in other polyoxoniobates. Thus, K₇HNb₆O₁₉·13H₂O is likely to be used as a strong base catalyst. Experimental study, performed under mild conditions, confirmed that it can effectively catalyze Knoevenagel condensation of benzaldehyde with ethyl cyanoacetate, disregarding the steric and electronic effect of aromatic aldehydes (Xu et al., 2018).

Although, it is worth mentioning that most of the above described catalytic systems for Knoevenagel condensation exhibit quite low relevance due to a narrow range of active methylene compounds with low pK_a values. Hence, only a few papers on catalytic systems which may be applied to unreactive substrates have been published so far. It reveals that strongly negative NBO charges of PONbs play a crucial role in the Knoevenagel condensation (Kamata and Sugahara, 2017).

Synthesis of 4*H*-pyrans from an aldehyde, malononitrile and a β-dicarbonyl compound is an example of reaction in which a basic catalysts is required. In most cases this multicomponent process lead to extended reaction times and tiresome catalyst retrieval. Several categories of basic solids like mesoporous Ca-MCM, oxides or hydrotalcites have been employed in this reaction. Quite often microwave radiation is used in order to decrease the reaction times by causing a direct energy transfer to the reagents and initiating instant superheating. The study published by Martínez et al. focuses on the new application of the compound based on decaniobate [Nb₁₀O₂₈]⁶⁻, namely [N(CH₃)₄]₆[Nb₁₀O₂₈].6H₂O. It was successfully used as basic solid catalyst in multi-reagent, microwave-assisted and solvent-free reaction to obtain several 4*H*-pyran derivatives. Different aldehydes with various electron-withdrawing or electron donor functionalities were tested, showing that the former ones favor shorter reaction times. The reuse of the catalyst, that could be

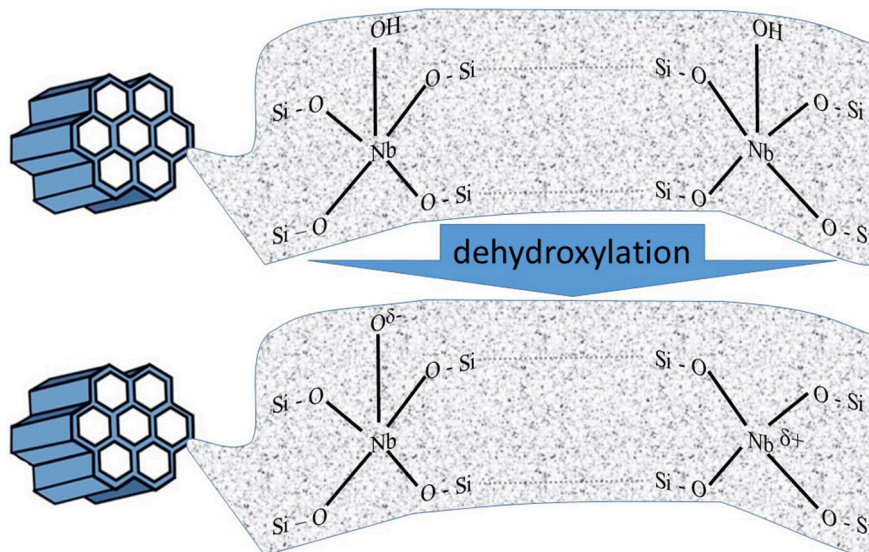


FIGURE 5 | Schematic representation of active centers created after dehydroxylation of ordered mesoporous niobosilicates (adopted from Nowak, 2012).

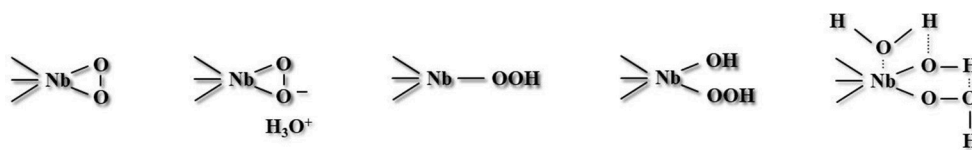
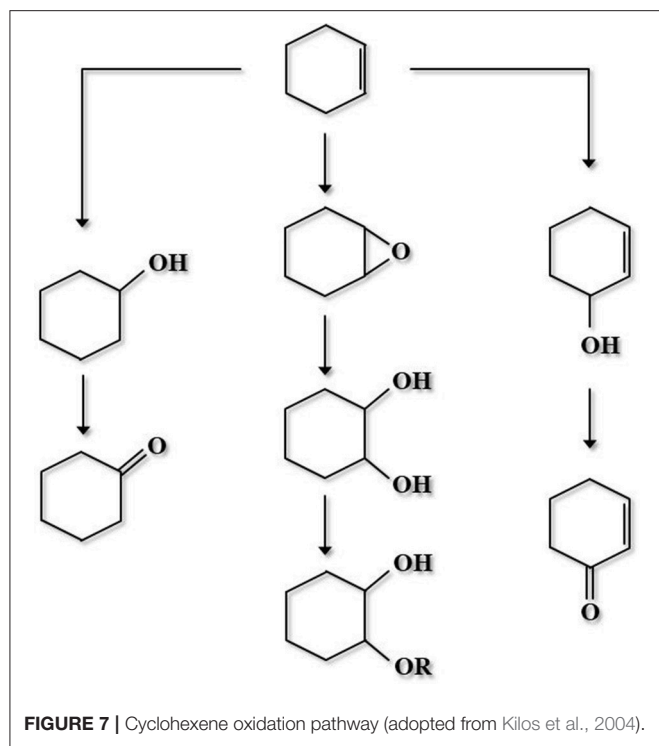


FIGURE 6 | Possible arrangements of peroxo and hydroperoxo Nb species discussed in literature (adopted from Ivanchikova et al., 2017).



easily isolated from the reaction mixture, was evaluated as well. It was proved that the catalyst retained its initial activity and almost unchanged structure after four cycles of the reaction. FT-IR analysis exhibited that the representative bands of the decaniobate unit were maintained but with reduced intensity, what was perhaps caused by the adsorption of the substrate on the surface of the catalyst. It was also demonstrated that a low basicity is sufficient to promote the synthesis of 4*H*-pyrans, thus the reaction takes place disregarding the quantity of decaniobate phase in the catalyst's structure. Moreover, under microwave irradiation and solvent-free conditions the desired products were obtained in shorter reaction times (Gutierrez et al., 2018).

CATALYSIS ON NIOBIUM-CONTAINING MESOPOROUS SILICATES

Among abundant applications of metal-modified mesoporous materials, those containing niobium are preferred in catalytic processes. Mesoporous silicas are an ideal platform for providing an appropriate distribution of Nb species and may work as active and environment-friendly heterogeneous catalysts in conversion of quite large organic molecules. Introduction of Nb atoms to siliceous matrix is favored, as both lattice are matching to each other in nucleation and particle evolution. Consequently, the content of niobium in the framework can be enlarged without creating extra-framework Nb species. However, it is important to specify that the replacement of Nb(V) with Si(IV) in mesoporous silica creates in the lattice an excessive positive charge, which is presumed to be stabilized by the charge of $-OH$ groups (e.g., Nowak, 2004, 2012). Only dehydroxylation of such material generates active species, as it is shown in Figure 5.

The presence of oxidative species ($Nb-O^{\delta-}$) and Lewis acid sites ($Nb^{\delta+}$) was confirmed on the basis of ESR and NO/FTIR measurements, as well as catalytic tests. It was assumed that the detected oxidative properties of Nb-containing mesoporous sieve were caused by the occurrence of active lattice oxygen created during the dehydroxylation of the Nb-modified molecular silica. One should bear in mind, that the generation of this active lattice oxygen always goes along with the formation of Lewis acid sites (Nowak, 2012).

Oxidation of Various Unsaturated Compounds

Epoxidation of unsaturated compounds constitutes one of the principal transformations in the industry of fine chemicals (Sheldon and van Vliet, 2001; Cavani and Teles, 2009; Ivanchikova et al., 2017). Conventionally, epoxidation of organic compounds, such like alkenes or various alcohols is realized by oxidation in the presence of organic peracids or by the chlorohydrin method. Nowadays, the elimination of the use of hazardous substrates and reduction of wastes is a great challenge in the modern organic synthesis. For this reason, many scientists have been applying aqueous H_2O_2 as an oxidant, as it generates only water as the byproduct (Grigoropoulou et al., 2003; Lane and Burgess, 2003; Sheldon et al., 2007; Clerici and Kholdeeva, 2013).

Recently, the catalysts containing niobium have drawn much attention in the field of the oxidation reactions. Mesoporous Nb-containing silicates obtained by various procedures have been active catalysts for epoxidation of olefins in the presence of hydrogen peroxide as an oxidizing agent (Nowak et al., 2003; Kilos et al., 2005; Nowak and Ziolek, 2005; Feliczak et al., 2009; Feliczak-Guzik and Nowak, 2009; Selvaraj et al., 2009; Nowak, 2012; Gallo et al., 2013; Tiozzo et al., 2014, 2015; Ivanchikova et al., 2015; Thornburg et al., 2015; Turco et al., 2015).

The activity of niobium-containing silicates in epoxidation reactions is related mainly to the occurrence of isolated Nb(V) sites in tetrahedral coordination, then the type of the acidity of the surface niobium species imposes the stability of formed reaction products (Ramanathan and Subramaniam, 2018). For example, the Lewis acid sites created by NbO_4 tetrahedra promote epoxidation, whereas the Brønsted acid sites, originating from distorted NbO_6 octahedra or nano-domains of Nb_2O_5 (Turco et al., 2015), induce decomposition of hydrogen peroxide and promote the ring opening reaction of epoxide (Di Serio et al., 2012; Yan et al., 2014). Additionally, isolated and undercoordinated Nb(V) species are strongly engaged in the significant catalytic activity of materials containing niobium in selective oxidation with H_2O_2 (Aronne et al., 2008; Thornburg et al., 2016).

Different oxidizing species were suggested as active forms accountable for liquid-phase selective oxidation over materials containing niobium. According to literature, radical forms, including HO^\bullet , were observed (Ziolek et al., 2015), as well as superoxo $Nb^V O_2^\bullet$ (Ziolek et al., 2011), $Nb^{IV}-(O_2)^-$ (Bregante et al., 2017), and species designated as $Nb-O^-$ (Ziolek et al., 2000, 2001). In addition, non-radical forms, such as side-on peroxo $Nb(\eta^2-O_2)$ (Shima et al., 2009; Chagas et al., 2013), and end-on hydroperoxo (Somma et al., 2005; Aronne et al., 2008; Thornburg et al., 2016) species were detected. Different structures suggested

for the non-radical peroxo niobium species (Ivanchikova et al., 2017) are shown in **Figure 6**.

Different types of mesoporous materials containing niobium have been prepared and tested in oxidation reactions with H₂O₂ (Nowak et al., 2003; Nowak and Ziolek, 2005; Somma and Strukul, 2006; Feliczak-Guzik et al., 2009; Gallo et al., 2013; Tiozzo et al., 2014; Ivanchikova et al., 2015, 2017; Ramanathan et al., 2015; Thornburg et al., 2015; Dworakowska et al., 2017; Thornburg and Notestein, 2017).

Very interesting property of the niobium catalysts is regioselectivity toward epoxidation of the less electron-rich exocyclic C=C bond in terpenes (Gallo et al., 2013; Tiozzo et al., 2014). Ivanchikova et al. have confirmed that a very important factor in the regioselectivity of epoxidation of limonene over mesoporous niobium silicates is the nature of the solvent (Ivanchikova et al., 2015). The highest ratio of exo/endo epoxides was obtained in acetonitrile as solvent.

Nowak et al. described the selective oxidation of terpenes and terpenoids, such as geraniol, limonene, α -terpineol using H₂O₂ as an oxidant over NbMSU-X-catalysts (Feliczak-Guzik et al., 2009), which are characterized by a 3D interconnecting network of “worm-like” pores (Feliczak and Nowak, 2007). The oxidation of terpenes/terpenoids was performed in glass batch reactor upon dynamic stirring at 313 K for 23 h. Products of reaction were evaluated by GC and GC-MS. The oxidations of terpenes exhibited good site- and chemoselectivity, resulting in monoepoxides as the main products, e.g., geraniol can be epoxidized to epoxy- or diepoxygeraniol, limonene to 1,2- and 8,9-epoxylimonene.

The catalytic activity of niobium-containing materials (NbMCM-41) was studied also in oxidation of m-toluidine to

m-aminobenzoic acid and m-aminobenzaldehyde with CO₂-free air at 472–673 K (Nowak, 2012).

A niobium-containing mesoporous molecular sieve (e.g., NbMCM-41, NbSBA-15 or NbFDU-1) showed great activity in direct transformation of cyclohexene into cyclohexene epoxide and 1,2-cyclohexanediol, at mild temperature in the presence of H₂O₂ (Feliczak-Guzik et al., 2015). Cyclohexene oxidation pathway is shown in **Figure 7** (Kilos et al., 2004), whereas **Table 1** presents the application of various Nb-functionalized mesoporous silica-based catalysts, oxidants, and solvents in the catalytic oxidation reactions not mentioned above.

Knoevenagel Condensation

Knoevenagel condensation is a catalytic process, which requires the presence of basic active centers. Their activity and the selectivity of the reaction depend on the type of reagents used. This reaction states one of the most frequently used C–C forming processes (Corma and Martín-Aranda, 1991). The final products of this reaction could be used in perfumes, cosmetics, herbicides, insecticides, pharmaceuticals, polymers, etc. (Calvino Casilda et al., 2010).

In general, the Knoevenagel condensation is carried out in the presence of different catalysts, including carbonyl compounds, aldehydes or ketones, and active methylene compounds. Lewis acid catalysts such as LaCl₃ (Narsaiah and Nagaiah, 2003), piperidine and alkali metal supported catalysts (Leelavathi and Kumar, 2004; Martín-Aranda et al., 2005; Perozo-Rondon et al., 2006), ionic liquids (Moriel et al., 2010), or alkali modified metal oxides (Calvino-Casilda et al., 2009), zeolites (Wada and Suzuki, 2003) and mesoporous materials (Zienkiewicz et al., 2009) or

TABLE 1 | Nb-containing ordered mesoporous silica catalysts, oxidants, and solvents in the catalytic oxidation reactions.

Catalyst	Reaction	Oxidant	Solvent	References
Nb-MMM-E	Alkene epoxidation	H ₂ O ₂ or TBHP	MeCN	Ivanchikova et al., 2015
Nb/SiO ₂	Epoxidation of limonene	H ₂ O ₂ or TBHP	MeCN	Gallo et al., 2013
Nb/SiO ₂ ; Nb ₂ O ₅ /SBA-15; CINbS; CINbS-AC Nb-silicates – EISA (evaporation-induced self-assembly) Nb SBA-16	Oxidation of cyclohexene	H ₂ O ₂	MeCN	Ivanchikova et al., 2017
				Kondo et al., 2018 Padula et al., 2018 Ramanathan et al., 2018 Kholdeeva et al., 2018 Ramanathan et al., 2015
The niobium(V)-grafted silica catalysts	Selective epoxidation of rapeseed oil (triglyceride) and two mixtures of vegetable-derived methyl esters	H ₂ O ₂	Not mentioned	Dworakowska et al., 2017
Nb-HMS-X	Ethylbenzene oxidation	TBHP	MeCN	Rahman et al., 2016
Nb-MCM-41	Oxidation of geraniol	H ₂ O ₂	MeOH	Marin-Astorga et al., 2012
Nb-TUD-1	Propylene epoxidation	H ₂ O ₂	MeOH	Liu et al., 2003; Yan et al., 2018
		N ₂ O	Not mentioned	Held and Florczak, 2009
Nb-KIT-6, Nb-KIT-5, Nb-MCM-48, Nb-TUD-1	Ethylene epoxidation	H ₂ O ₂	MeOH	Ramanathan et al., 2018
				Yan et al., 2016

polymer-supported catalysts (Tamami and Fadavi, 2005) were used as catalysts.

Bifunctional heterogeneous catalysts established on the basis of SBA-15 samples, modified with various metals, such as Zr, Nb, and Mo and functionalized with aminopropylsiliceous species were interesting materials in this reaction (Calvino-Casilda et al., 2016). According to literature, the role of amine group as basic centers was significant. Ziolek et al. described the application of imidazole as a source of basicity, loaded on mesoporous silicas and niobosilicates in Knoevenagel reaction (Kryszak et al., 2017a) as Lewis acid site involved in the above reaction.

Experimental study, concerning the development of basicity on different mesoporous metallosilicates (Nb- and Ce-) and silicas, has been reported by Ziolek et al. Their results proved a significant role of the catalyst structure, amount and nature of metal in the supports, and category of organic, nitrogen-containing modifying agent in adjusting catalysts' activity and selectivity in Knoevenagel condensation. It was also evidenced that niobium and cerium assumed different locations within the siliceous matrix: Nb was almost completely incorporated into the silica skeleton, while cerium was placed in pores in the form of crystalline CeO₂. This led to entirely divergent performance of catalysts in the test reaction, since Nb-containing supports showed Lewis acidity, whereas cerium modified supports exhibited redox properties. These acidic and redox properties are vital in promoting Knoevenagel condensation, because Lewis acidity strongly supports this reaction via acid-base cooperation (the ion-pair mechanism) and redox properties play an important role in the enhancement of the support basicity. Moreover, the presence of niobium, contrary to ceria, improved the thermal stability of the nitrogen containing compounds attached to the silicas' surface by the chemical cooperation between niobium species (Lewis acid sites) and nitrogen compounds (source of basic sites) (Kryszak et al., 2017b).

Similar results were obtained in the catalytic tests with silica matrices of various chemical compositions and consequently with different acidity. It was proved that selectivity to the Knoevenagel products depends considerably on the nature of the support for each anchored amine, mostly due to the participation of acid sites in the withdrawing of hydroxyl groups from the reaction's intermediate (Blasco-Jiménez et al., 2010).

Further studies, involving catalytic tests of mesoporous silica with different Nb content and loaded aminosilane, proved that the chemical composition of the mesoporous supports strongly impact the basicity of the catalyst. The amino-grafted samples based on supports with high niobium-content revealed much higher activity in catalytic reactions (Knoevenagel condensation and Michael addition) than their counterparts with no incorporated niobium species (Blasco-Jiménez et al., 2009).

SUMMARY

The distinctive chemical properties of niobium designate it as a valuable promoter, active phase or support in numerous catalytic

systems, e.g., niobium species are key factors in the liquid phase oxidation in the presence of H₂O₂ as the oxidizing agent.

Materials containing niobium have been used in catalytic processes over the last few decades. At present, such materials may be considered as a substitute to the routinely used Ti- or Zr-based catalysts in several applications. The addition of niobium often increases surface redox properties in catalysts.

Nonetheless, it is crucial to point out that the behavior of Nb species strongly depends on the location and type of material into which it is incorporated. Polyoxometalates and niobium-containing mesoporous silicates are good examples illustrating the effects of niobium atoms localization and the character of matrix to which they are incorporated on the properties of particular materials. In POMs niobium occurs in octahedral units MO₆, while in the silica matrix it prefers MO₄ tetrahedra. These different coordination types play a vital role in the catalytic activity. Therefore, PONbs are tested mainly in the photocatalytic systems, whereas Nb-containing mesoporous silicates are remarkably active catalysts in the oxidation/epoxidation reactions.

At present, the research concerning polyoxometalates, especially polyoxoniobates, seems to be entering a new exciting phase. On the basis of this review one can see that POM-based chemistry is aiming further than the synthesis and structural characterization of new clusters. The evolution of functionalized compounds, employing, among others, self-assembly aspects and intrinsic chemical and electronic properties, encourages to bring about gradually more complex molecular structures that could operate as tools with several adjustable utilities.

On the other hand, Nb-functionalized mesoporous silicates proved to be active in selective transformations of variety of reagents. They may be preferably employed in oxidation reactions, but after additional adjustment, they can serve as basic, acidic, bifunctional, and reducible or non-reducible catalysts. What is more, substantial correlations of niobium with other lattice components make Nb-containing mesoporous molecular sieves more stable and active even in the gas phase reactions.

The growing attention paid to Nb-based chemistry permits us to believe that further development, especially in the field of polyoxoniobates, may be expected and the performed study will bring exciting outcomes for the future in the area of catalysis and other applications.

AUTHOR CONTRIBUTIONS

AW, IN, AF-G contributed to the design of the paper layout, implementation of the bibliographical research and to the writing of the manuscript.

ACKNOWLEDGMENTS

The authors wish to thank the National Center for Science for financial support of the studies reported within the research project HARMONIA-5 (no. DEC-2013/10/M/ST5/00652).

REFERENCES

- Abramov, P. A., Davletgildeeva, A. T., and Sokolov, M. N. (2017). Formation of silicon-containing polyoxoniobates from hexaniobate under high temperature conditions. *J. Clust. Sci.* 28, 735–744. doi: 10.1007/s10876-016-1121-9
- Abramov, P. A., Sokolov, M. N., and Vicent, C. (2015a). Polyoxoniobates and polyoxotantalates as ligands – revisited. *Inorganics* 3, 160–177. doi: 10.3390/inorganics3020160
- Abramov, P. A., Vicent, C., Kompankov, N. B., Gushchin, A. L., and Sokolov, M. N. (2015b). Platinum polyoxoniobates. *Chem. Commun.* 51, 4021–4023. doi: 10.1039/C5CC00315F
- Anderson, T. M., Thoma, S. G., Bonhomme, F., Rodriguez, M. A., Park, H., Parise, J. B., et al. (2007). Lithium polyniobates. A Lindqvist-supported lithium-water adamantane cluster and conversion of hexaniobate to a discrete Keggin complex. *Cryst. Growth Des.* 7, 719–723. doi: 10.1021/cg0606904
- Aronne, A., Turco, M., Bagnasco, G., Ramis, G., Santacesaria, E., Di Serio, M., et al. (2008). Gel derived niobium-silicon mixed oxides: characterization and catalytic activity for cyclooctene epoxidation. *Appl. Catal. A* 347, 179–185. doi: 10.1016/j.apcata.2008.06.011
- Baker, L. C. W., and Figgis, J. S. (1970). A new fundamental type of inorganic complex: hybrid between heteropoly and conventional coordination complexes. Possibilities for geometrical isomerisms in 11-, 12-, 17-, and 18-heteropoly derivatives. *J. Am. Chem. Soc.* 92, 3794–3797. doi: 10.1021/ja00715a047
- Beck, J. S., Vartuli, J. C., Roth, W. J., Leonowicz, M. E., Kresge, C. T., Schmitt, K. D., et al. (1992). New family of mesoporous molecular sieves prepared with liquid crystal templates. *J. Am. Chem. Soc.* 114, 10834–10843. doi: 10.1021/ja00053a020
- Bijelic, A., and Rempel, A. (2015). The use of polyoxometalates in protein crystallography - an attempt to widen a well-known bottleneck. *Coord. Chem. Rev.* 299, 22–38. doi: 10.1016/j.ccr.2015.03.018
- Blasco-Jiménez, D., López-Peinado, A. J., Martín-Aranda, R. M., Ziolek, M., and Sobczak, I. (2009). Sonocatalysis in solvent-free conditions: an efficient eco-friendly methodology to prepare N-alkyl imidazoles using amino-grafted NbMCM-41. *Catal. Today* 142, 283–287. doi: 10.1016/j.cattod.2008.11.028
- Blasco-Jiménez, D., Sobczak, I., Ziolek, M., López-Peinado, A. J., and Martín-Aranda, R. M. (2010). Amino-grafted metallosilicate MCM-41 materials as basic catalysts for eco-friendly processes. *Catal. Today* 152, 119–125. doi: 10.1016/j.cattod.2010.04.031
- Bontchev, R. P., and Nyman, M. (2006). Evolution of polyoxoniobate cluster anions. *Angew. Chem., Int. Ed.* 45, 6670–6672. doi: 10.1002/anie.200602200
- Botar, B., Ellern, A., Hermann, R., and Kögerler, P. (2009). Electronic control of spin coupling in keplerate-type polyoxomolybdates. *Angew. Chem. Int. Ed.* 48, 9080–9083. doi: 10.1002/anie.200903541
- Bregante, D. T., Priyadarshini, P., and Flaherty, D. W. (2017). Kinetic and spectroscopic evidence for reaction pathways and intermediates for olefin epoxidation on Nb in *BEA. *J. Catal.* 348, 75–89. doi: 10.1016/j.jcat.2017.02.008
- Calvino Casilda, V., Perez-Mayoral, E., Bañares, M. A., and Lozano Diz, E. (2010). Real-time Raman monitoring of dry media heterogeneous alkylation of imidazole with acidic and basic catalysts. *E. Chem. Eng. J.* 161, 371–376. doi: 10.1016/j.ccej.2010.01.028
- Calvino-Casilda, V., Martín-Aranda, R. M., Lopez-Peinado, A. J., Sobczak, I., and Ziolek, M. (2009). Catalytic properties of alkali metal-modified oxide supports for the Knoevenagel condensation: kinetic aspects. *Catal. Today* 142, 278–282. doi: 10.1016/j.cattod.2008.08.023
- Calvino-Casilda, V., Olejniczak, M., Martín-Aranda, R., and Ziolek, M. (2016). The role of metallic modifiers of SBA-15 supports for propyl-amines on activity and selectivity in the Knoevenagel reactions. *Micropor. Mesopor. Mater.* 224, 201–207. doi: 10.1016/j.micromeso.2015.11.027
- Cavani, F., and Teles, J. H. (2009). Sustainability in catalytic oxidation: an alternative approach or a structural evolution? *ChemSusChem* 2, 508–534. doi: 10.1002/cssc.200900020
- Chagas, P., Oliveira, H. S., Mambrini, R., Le Hyaric, M., de Almeida, M. V., and Oliveira, L. C. A. (2013). A novel hydrophobic niobium oxyhydroxide as catalyst: selective cyclohexene oxidation to epoxide. *Appl. Catal. A* 454, 88–92. doi: 10.1016/j.apcata.2013.01.007
- Chen, G., Wang, C., Ma, P., Wang, J., and Niu, J. (2010). A novel organic-inorganic hybrid polyoxoniobate constructed from $[\text{Cu}(\text{en})(\text{H}_2\text{O})][\text{HfNb}_6\text{O}_{19}]^{5-}$ polyoxoanions and methane-like $[\text{K}_4\text{Na}]^{5+}$ cations. *J. Clust. Sci.* 21, 121–131. doi: 10.1007/s10876-010-0296-8
- Clerici, M. G., and Kholdeeva, O. A. (eds.). (2013). *Liquid Phase Oxidation Via Heterogeneous Catalysis: Organic Synthesis and Industrial Applications*. New Jersey, NJ: John Wiley and Sons.
- Corma, A., and Martín-Aranda, R. M. (1991). Alkaline-substituted sepiolites as a new type of strong base catalyst. *J. Catal.* 130, 130–137. doi: 10.1016/0021-9517(91)90097-N
- Di Serio, M., Turco, R., Pernice, P., Aronne, A., Sannino, F., and Santacesaria, E. (2012). Valuation of $\text{Nb}_2\text{O}_5\text{-SiO}_2$ catalysts in soybean oil epoxidation. *Catal. Today* 192, 112–116. doi: 10.1016/j.cattod.2012.03.069
- Duncan, D. C., Carlisle Chambers, R., Hecht, E., and Hill, C. L. (1995). Mechanism and Dynamics in the $\text{H}_3[\text{PW}_{12}\text{O}_{40}]$ -catalyzed selective epoxidation of terminal Olefins by H_2O_2 . Formation, Reactivity, and Stability of $[\text{PO}_4\{\text{WO}(\text{O}_2)_2\}_4]^{3-}$. *J. Am. Chem. Soc.* 117, 681–691. doi: 10.1021/ja00107a012
- Dworakowska, S., Tiozzo, C., Niemczyk-Wrzeszcz, M., Michorczyk, P., Ravasio, N., Psaro, R., et al. (2017). Mesoporous molecular sieves containing niobium(V) as catalysts for the epoxidation of fatty acid methyl esters and rapeseed oil. *J. Clean. Prod.* 166, 901–909. doi: 10.1016/j.jclepro.2017.08.098
- Feliczak, A., and Nowak, I. (2007). Controlled synthesis of mesoporous NbMSU-X: influence of the preparation route. *Stud. Surf. Sci. Catal.* 170, 519–524. doi: 10.1016/S0167-2991(07)80886-X
- Feliczak, A., Walczak, K., Wawrzynczak, A., and Nowak, I. (2009). The use of mesoporous molecular sieves containing niobium for the synthesis of vegetable oil-based products. *Catal. Today* 140, 23–29. doi: 10.1016/j.cattod.2008.07.012
- Feliczak-Guzik, A., and Nowak, I. (2009). Mesoporous niobosilicates serving as catalysts for synthesis of fragrances. *Catal. Today* 142, 288–292. doi: 10.1016/j.cattod.2008.11.027
- Feliczak-Guzik, A., Wawrzynczak, A., and Nowak, I. (2009). Studies on mesoporous niobosilicates synthesized using F127 triblock copolymer. *Adsorption* 15, 247–253. doi: 10.1007/s10450-009-9184-7
- Feliczak-Guzik, A., Wawrzynczak, A., and Nowak, I. (2015). Selective catalytic oxidations of cyclohexene, thioether and geraniol with hydrogen peroxide. Sensitivity to the structure of mesoporous niobosilicates. *Micropor. Mesopor. Mater.* 202, 80–89. doi: 10.1016/j.micromeso.2014.09.051
- Filowitz, M., Ho, R. K. C., Klemperer, W. G., and Shum, W. (1979). Oxygen-17 nuclear magnetic resonance spectroscopy of polyoxometalates. 1. Sensitivity and resolution. *Inorg. Chem.* 18, 93–103. doi: 10.1021/ic50191a021
- Flynn, C. M., and Stucky, G. D. (1969a). Crystal structure of sodium 12-niobomanganate(IV), $\text{Na}_{12}\text{MnNb}_{12}\text{O}_{38} \cdot 50\text{H}_2\text{O}$. *Inorg. Chem.* 8, 335–344. doi: 10.1021/ic50072a030
- Flynn, C. M., and Stucky, G. D. (1969b). Sodium 6-niobo(ethylenediamine)cobaltate(III) and its chromate(III) analog. *Inorg. Chem.* 8, 178–180. doi: 10.1021/ic50071a048
- Fu, H., Lu, Y., Wang, Z., Liang, C., Zhang, Z.-M., and Wang, E. (2012). Three hybrid networks based on octamolybdate: ionothermal synthesis, structure and photocatalytic properties. *Dalton Trans.* 41, 4084–4090. doi: 10.1039/c2dt11912a
- Gallo, A., Tiozzo, C., Psaro, R., Carniato, F., and Guidotti, M. (2013). Niobium metallocenes deposited onto mesoporous silica via dry impregnation as catalysts for selective epoxidation of alkenes. *J. Catal.* 298, 77–83. doi: 10.1016/j.jcat.2012.11.015
- Gan, Q., Shi, W., Xing, Y., and Hou, Y. (2018). A polyoxoniobate/g- C_3N_4 nanoporous material with high adsorption capacity of methylene blue from aqueous solution. *Front. Chem.* 6:7. doi: 10.3389/fchem.2018.00007
- Ge, W., Wang, X., Zhang, L., Du, L., Zhou, Y., and Wang, J. (2016). Fully-occupied Keggin type polyoxometalate as solid base for catalyzing CO_2 cycloaddition and Knoevenagel condensation. *Catal. Sci. Technol.* 6, 460–467. doi: 10.1039/C5CY01038A
- Graeber, E. J., and Morosin, B. (1977). The molecular configuration of the decaniobate ion ($\text{Nb}_{17}\text{O}_{28}^{6-}$). *Acta Crystallogr. Sect. B* 33, 2137–2143. doi: 10.1107/S0567740877007900
- Grigoropoulou, G., Clark, J. H., and Elings, J. A. (2003). Recent developments on the epoxidation of alkenes using hydrogen peroxide as an oxidant. *Green Chem.* 5, 1–7. doi: 10.1039/B208925B
- Gumerova, N. I., and Rempel, A. (2018). Synthesis, structures and applications of electron-rich polyoxometallates. *Nat. Rev. Chem.* 2:0112. doi: 10.1038/s41570-018-0112

- Guo, G., Xu, Y., Cao, J., and Hu, C. (2011). An unprecedented vanadoniobate cluster with 'trans-vanadium' bicapped Keggin-type $\{V_{Nb}_{12}O_{40}(VO)_2\}$. *Chem. Commun.* 47, 9411–9413. doi: 10.1039/c1cc12329g
- Guo, G., Xu, Y., Cao, J., and Hu, C. (2012). The $\{V_4Nb_6O_{30}\}$ cluster: a new type of vanadoniobate anion structure. *Chem. Eur. J.* 18, 3493–3497. doi: 10.1002/chem.201103390
- Gutierrez, L. F., Nope, E., Rojas, H. A., Cubillos, J. A., Sathicq, Á. G., Romanelli, G. P., et al. (2018). New application of decaniobate salt as basic solid in the synthesis of 4H-pyrans by microwave assisted multicomponent reactions. *Res. Chem. Intermed.* 44, 5559–5568. doi: 10.1007/s11164-018-3440-y
- Hayashi, S., Yamazoe, S., Koyasu, K., and Tsukuda, T. (2016). Application of group V polyoxometalate as an efficient base catalyst: a case study of decaniobate clusters. *RSC Adv.* 6, 16239–16242. doi: 10.1039/C6RA00338A
- Hayashi, S., Yamazoe, S., Koyasu, K., and Tsukuda, T. (2017). Lewis base catalytic properties of $[Nb_{10}O_{28}]^{6-}$ for CO_2 fixation to epoxide: Kinetic and theoretical studies. *Chem. Asian J.* 12, 1635–1640. doi: 10.1002/asia.201700534
- Held, A., and Florczak, P. (2009). Vanadium, niobium and tantalum modified mesoporous molecular sieves as catalysts for propene epoxidation. *Catal. Today* 142, 329–334. doi: 10.1016/j.cattod.2008.07.030
- Huang, P., Qin, C., Su, Z. M., Xing, Y., Wang, X. L., Shao, K. Z., et al. (2012a). Self-assembly and photocatalytic properties of polyoxoniobates: $\{Nb_{24}O_{72}\}$, $\{Nb_{32}O_{96}\}$, and $\{K_{12}Nb_6O_{288}\}$ Clusters. *J. Am. Chem. Soc.* 134, 14004–14010. doi: 10.1021/ja303723u
- Huang, P., Qin, C., Wang, X.-L., Sun, C.-Y., Jiao, Y.-Q., Xing, Y., et al. (2013). Self-assembly and visible-light photocatalytic properties of W/Nb mixed-addendum polyoxometalate and transition-metal cations. *ChemPlusChem* 78, 775–779. doi: 10.1002/cplu.201300175
- Huang, P., Qin, C., Wang, X.-L., Sun, C.-Y., Yang, G.-S., Shao, K.-Z., et al. (2012b). An unprecedented organic-inorganic hybrid based on the first $\{Nb_{10}V_4O_{40}(OH)_2\}^{12-}$ clusters and copper cations. *Chem. Commun.* 48, 103–105. doi: 10.1039/C1CC15684E
- Huo, I., Margolese, D. I., Ciesla, U., Demuth, D. G., Feng, P., Gier, T. E., et al. (1994). Organisation of organic molecules with inorganic molecular species into nanocomposite biphasic arrays. *Chem. Mater.* 6, 1176–1191. doi: 10.1021/cm00044a016
- Hutin, M., Rosnes, M. H., Long, D.-L., and Cronin, L. (2013). "Polyoxometalates: synthesis and structure – from building blocks to emergent materials," in *Comprehensive Inorganic Chemistry II*, Vol. 2, eds J. Reedijk and K. Poeppelmeier (Oxford: Elsevier), 241–269.
- Ivanchikova, I. D., Maksimchuk, N. V., Skobelev, I. Y., Kaichev, V. V., and Kholdeeva, O. A. (2015). Mesoporous niobium-silicates prepared by evaporation-induced self-assembly as catalysts for selective oxidations with aqueous H_2O_2 . *J. Catal.* 332, 138–148. doi: 10.1016/j.jcat.2015.10.003
- Ivanchikova, I. D., Skobelev, I. Y., Maksimchuk, N. V., Paukshtis, E. A., Shashkov, M. V., and Kholdeeva, O. A. (2017). Toward understanding the unusual reactivity of mesoporous niobiumsilicates in epoxidation of C=C bonds with hydrogen peroxide. *J. Catal.* 356, 85–99. doi: 10.1016/j.jcat.2017.09.011
- Jin, L., Li, X.-X., Qi, Y.-J., Niu, P.-P., and Zheng, S.-T. (2016). Giant hollow heterometallic polyoxoniobates with sodalite-type lanthanide-tungsten-oxide cages: discrete nanoclusters and extended frameworks. *Angew. Chem. Int. Ed.* 55, 1–6. doi: 10.1002/anie.201608113
- Kamata, K., and Sugahara, K. (2017). Base catalysis by mono- and polyoxometalates. *Catalysts* 7, 345–369. doi: 10.3390/catal7110345
- Keggin, J. F. (1933). Structure of the molecule of 12-phosphotungstic acid. *Nature* 131, 908–909. doi: 10.1038/131908b0
- Kholdeeva, O. A., Ivanchikova, I. D., Maksimchuk, N. V., and Skobelev, I. Y. (2018). H_2O_2 -based selective epoxidations: Nb-silicates versus Ti-silicates. *Catal. Today In press*. doi: 10.1016/j.cattod.2018.04.002
- Kilos, B., Aouine, M., Nowak, I., Ziolek, M., and Volta, J. C. (2004). The role of niobium in the gas- and liquid-phase oxidation on metallosilicate MCM-41-type materials. *J. Catal.* 224, 314–325. doi: 10.1016/j.jcat.2004.03.002
- Kilos, B., Nowak, I., Ziolek, M., Tuel, A., and Volta, J. C. (2005). Transition metal containing (Nb, V, Mo) SBA-15 molecular sieves - synthesis, characteristic and catalytic activity in gas and liquid phase oxidation. *Stud. Surf. Sci. Catal.* 158, 1461–1468. doi: 10.1016/S0167-2991(05)80498-7
- Kondo, J. N., Hiyoshia, Y., Otsuga, R., Ishikawa, A., Wang, Y.-H., and Yokoi, T. (2018). Thin (single-triple) niobium oxide layers on mesoporous silica substrate. *Micropor. Mesopor. Mater.* 262, 191–198. doi: 10.1016/j.micromeso.2017.11.032
- Kresge, C. T., Leonowicz, M. E., Roth, W. J., Vartuli, J. C., and Beck, J. S. (1992). Ordered mesoporous molecular sieves synthesised by a liquid crystal template mechanism. *Nature* 359, 710–712. doi: 10.1038/359710a0
- Kryszak, D., Stawicka, K., Calvino-Casilda, V., Martin-Aranda, R., and Ziolek, M. (2017a). Imidazole immobilization in nanopores of silicas and niobosilicates SBA-15 and MCF. A new concept towards creation of basicity. *Appl. Catal.* 531, 139–150. doi: 10.1016/j.apcata.2016.10.028
- Kryszak, D., Stawicka, K., Trejda, M., Calvino-Casilda, V., Martin-Aranda, R., and Ziolek, M. (2017b). Development of basicity in mesoporous silicas and metallosilicates. *Catal. Sci. Technol.* 7, 5236–5248. doi: 10.1039/C7CY00927E
- Lane, B. S., and Burgess, K. (2003). Metal-catalyzed epoxidations of alkenes with hydrogen peroxide. *Chem. Rev.* 103, 2457–2474. doi: 10.1021/cr020471z
- Leelavathi, P., and Kumar, S. R. (2004). Niobium (V) chloride catalyzed Knoevenagel condensation: an efficient protocol for the preparation of electrophilic alkenes. *J. Mol. Catal. A* 240, 99–102. doi: 10.1016/j.molcata.2005.06.026
- Lefebvre, F. (2013). "Polyoxometalates encapsulated in inorganic materials: applications in catalysis," in *New and Future Developments in Catalysis: Hybrid Materials, Composites, and Organocatalysts*, 265–288. doi: 10.1016/B978-0-444-53876-5.00011-8
- Lev, O., Wu, Z., Bharathi, S., Glezer, V., Modestov, A., Gun, J., et al. (1997). Sol-gel materials in electrochemistry. *Chem. Mater.* 9, 2354–3375. doi: 10.1021/cm970367b
- Li, L., Niu, Y., Dong, K., Ma, P., Zhang, C., Niu, J., et al. (2017). A Ni-containing decaniobate incorporating organic ligands: synthesis, structure, and catalysis for allylic alcohol epoxidation. *RSC Adv.* 7, 28696–28701. doi: 10.1039/C7RA03254D
- Li, X., Dong, J., Liu, H., Sun, X., Chi, Y., and Hu, C. (2018). Recoverable amphiphilic polyoxoniobates catalyzing oxidative and hydrolytic decontamination of chemical warfare agent simulants in emulsion. *J. Hazard. Mater.* 344, 994–999. doi: 10.1016/j.jhazmat.2017.11.061
- Liang, Z., Zhang, D., Liu, Q., Ma, P., Niu, J., and Wang, J. (2015). A novel transition-metal-linked hexaniobate cluster with photocatalytic H_2 evolution activity. *Inorg. Chem. Commun.* 54, 19–20. doi: 10.1016/j.inoche.2015.01.033
- Lindqvist, I. (1953). The structure of the hexaniobate ion in $7Na_2O \cdot 6Nb_2O_5 \cdot 32H_2O$. *Arkiv for Kemi* 5, 247–250.
- Liu, B.-X., Cai, Z.-W., Yang, T., Li, X.-X., Yang, G.-Y., and Zheng, S.-T. (2017). A rare polyoxometalate based on mixed niobium-based polyoxoanions $[GeNb_{18}O_{54}]^{14-}$ and $[Nb_3W_3O_{19}]^{5-}$. *Inorg. Chem. Commun.* 78, 56–60. doi: 10.1016/j.inoche.2017.02.014
- Liu, Y. P., Guo, S.-X., Ding, L., Ohlin, C. A., Bond, A. M., and Zhang, J. (2015). Lindqvist polyoxoniobate ion-assisted electrodeposition of cobalt and nickel water oxidation catalysts. *ACS Appl. Mater. Interfaces* 7, 16632–16644. doi: 10.1021/acsami.5b04219
- Liu, Y. Y., Murata, K., and Inaba, M. (2003). Synthesis and catalytic activity of niobium-containing hexagonal mesoporous silica. *Chem. Lett.* 32, 992–993. doi: 10.1246/cl.2003.992
- Long, D.-L., Tsunashima, R., and Cronin, L. (2010). Polyoxometalates: building blocks for functional nanoscale systems. *Angew. Chem. Int. Ed.* 49, 1736–1758. doi: 10.1002/anie.200902483
- Lv, H., Geletii, Y. V., Zhao, C., Vickers, J. W., Zhu, G., Luo, Z., et al. (2012). Polyoxometalate water oxidation catalysts and the production of green fuel. *Chem. Soc. Rev.* 41, 7572–7589. doi: 10.1039/C2CS35292C
- Ma, L., Li, F., Sun, Z., Liu, M., Wang, Y., and Xu, L. (2014). Synergetic effect of polyoxoniobate and NiS as cocatalysts for enhanced photocatalytic H_2 evolution on $Cd_{0.65}Zn_{0.35}S$. *RSC Adv.* 4, 21369–21372. doi: 10.1039/C4RA01827C
- Maekawa, M., Ozawa, M. Y., and Yagasaki, Y. A. (2006). Icosaniobate: a new member of the isoniobate family. *Inorg. Chem.* 45, 9608–9609. doi: 10.1021/ci0601788
- Marin-Astorga, N., Martinez, J. J., Borda, G., Cubillos, J., Suarez, D. N., and Rojas, H. (2012). Control of the chemoselectivity in the oxidation of geraniol over lanthanum, titanium and niobium catalysts supported on mesoporous silica MCM-41. *Top. Catal.* 55, 620–624. doi: 10.1007/s11244-012-9840-0
- Martin-Aranda, R. M., Ortega-Cantero, E., Rojas-Cervantes, M. L., Vicente Rodríguez, M. A., and Bañares-Muñoz, M. A. (2005). Ultrasound-activated

- Knoevenagel condensation of malononitrile with carbonylic compounds catalysed by alkaline-doped saponites. *J. Chem. Tech. Biotech.* 80, 234–238. doi: 10.1002/jctb.1174
- Moriel, P., García-Suárez, E. J., Martínez, M., García, A. B., Montes-Morán, M. A., Calvino-Casilda, V., et al. (2010). Synthesis, characterization, and catalytic activity of ionic liquids based on biosources. *Tetrahedron Lett.* 51, 4877–4881. doi: 10.1016/j.tetlet.2010.07.060
- Narsaiah, A. V., and Nagaiah, K. (2003). An efficient Knoevenagel condensation catalyzed by $\text{LaCl}_3 \cdot 7\text{H}_2\text{O}$ in heterogeneous medium. *Synth. Commun.* 21, 3825–3832. doi: 10.1081/SCC-120025194
- Niu, J., Wang, G., Zhao, J., Sui, Y., Ma, P., and Wang, J. (2011). Zero- or one-dimensional organic-inorganic hybrid polyoxoniobates constructed from decanionic units and transition-metal complexes. *Cryst. Growth Des.* 11, 1253–1261. doi: 10.1021/cg1014829
- Niu, J.-Y., Chen, G., Zhao, J.-W., Ma, P.-T., Li, S.-Z., Wang, J.-P., et al. (2010). Two novel copper-undecaniobates decorated by copper-organic cations $[\{\text{Cu}(\text{H}_2\text{O})\text{L}\}_2\{\text{CuNb}_{11}\text{O}_{35}\text{H}_4\}]^{5-}$ ($\text{L}=1,10\text{-phenanthroline}$, $2,2'\text{-bipyridine}$) consisting of plenary and monolacunar Lindqvist-type isopolyoniobate fragments. *Chem. Eur. J.* 16, 7082–7086. doi: 10.1002/chem.201000824
- Nowak, I. (2004). Textural and structural properties of niobium-containing micro-, meso- and macroporous molecular sieves. *Coll. Surf. Sci. Physicochem. Eng. Aspects* 241, 103–111. doi: 10.1016/j.colsurfa.2004.04.036
- Nowak, I. (2012). Frontiers in mesoporous molecular sieves containing niobium: from model materials to catalysts. *Catal. Today* 192, 80–88. doi: 10.1016/j.cattod.2012.05.048
- Nowak, I., and Jaroniec, M. (2005). Three-dimensional cubic mesoporous molecular sieves of FDU-1 containing niobium: Dependence of niobium source on structural properties. *Langmuir* 21, 755–760. doi: 10.1021/la048157i
- Nowak, I., Kilos, B., Ziolk, M., and Lewandowska, A. (2003). Epoxidation of cyclohexene on Nb-containing meso- and macroporous materials. *Catal. Today* 78, 487–498. doi: 10.1016/S0920-5861(02)00332-2
- Nowak, I., and Ziolk, M. (2005). Effect of texture and structure on the catalytic activity of mesoporous niobosilicates for the oxidation of cyclohexene. *Micropor. Mesopor. Mater.* 78, 281–288. doi: 10.1016/j.micromeso.2004.10.010
- Nyman, M. (2011). Polyoxoniobate chemistry in the 21st century. *Dalton Trans.* 40, 8049–8058. doi: 10.1039/c1dt10435g
- Nyman, M., Alam, T. M., Bonhomme, F., Rodriguez, M. A., Frazer, C. S., and Welk, M. E. (2006). Solid-state structures and solution behavior of alkali salts of the $[\text{Nb}_6\text{O}_{19}]^{8-}$ Lindqvist ion. *J. Cluster Sci.* 17, 197–219. doi: 10.1007/s10876-006-0049-x
- Nyman, M., Bonhomme, F., Alam, T. M., Rodriguez, M. A., Cherry, B. R., Krumhansl, J. L., et al. (2002). A general synthetic procedure for heteropolyoniobates. *Science* 297, 996–998. doi: 10.1126/science.1073979
- Ohlin, C. A., Villa, E. M., Fetting, J. C., and Casey, W. H. (2008a). The $[\text{Ti}_{12}\text{Nb}_6\text{O}_{44}]^{10-}$ ion – a new type of polyoxometalate structure. *Angew. Chem. Int. Ed.* 47, 5634–5636. doi: 10.1002/anie.200801883
- Ohlin, C. A., Villa, E. M., Fetting, J. C., and Casey, W. H. (2008b). Distinctly different reactivities of two similar polyoxoniobates with hydrogen peroxide. *Angew. Chem. Int. Ed.* 120, 8375–8378. doi: 10.1002/anie.200803688
- Ozeki, T., Yamase, T., Naruke, H., and Sasaki, Y. (1994). X-Ray structural characterization of the protonation sites in the dihydrogen hexaniobate anion. *Bull. Chem. Soc. Jpn.* 67, 3249–3253. doi: 10.1246/bcsj.67.3249
- Padula, I. D., Chagas, P., Furst, C. G., and Oliveira, L. C. A. (2018). Mesoporous niobium oxyhydroxide catalysts for cyclohexene epoxidation reactions. *Appl. Sci.* 8, 881–890. doi: 10.3390/app8060881
- Perozo-Rondon, E., Calvino-Casilda, V., Casal, B., Martín-Aranda, R. M., and Rojas-Cervantes, M. L. (2006). Catalysis by basic carbons: preparation of dihydropyridines. *Appl. Surf. Sci.* 252, 6080–6083. doi: 10.1016/j.apsusc.2005.11.017
- Pope, M. T., and Kortz, U. (2012). “Polyoxometalates,” in *Encyclopedia of Inorganic and Bioinorganic Chemistry*, ed R. A. Scott, (Hoboken, NJ; New York, NY: John Wiley and Sons, Ltd.), 1–14. doi: 10.1002/9781119951438.eibc0185.pub2
- Proust, A., Thouvenot, R., and Gouzerh, P. (2008). Functionalization of polyoxometalates: towards advanced applications in catalysis and materials science. *Chem. Commun.* 2008, 1837–1852. doi: 10.1039/B715502F
- Rahman, S., Shah, S., Santra, C., Sen, D., Sharma, S., Pandey, J. K., et al. (2016). Controllable synthesis of niobium doped mesoporous silica materials with various morphologies and its activity for oxidative catalysis. *Micropor. Mesopor. Mater.* 226, 169–178. doi: 10.1016/j.micromeso.2015.12.049
- Ramanathan, A., and Subramaniam, B. (2018). Metal-incorporated mesoporous silicates: tunable catalytic properties and applications. *Molecules*, 23, 263–276. doi: 10.3390/molecules23020263
- Ramanathan, A., Zhu, H., Maheswari, R., and Subramaniam, B. (2018). Remarkable epoxidation activity of neat and carbonized niobium silicates prepared by evaporation-induced self-assembly. *Micropor. Mesopor. Mater.* 261, 158–163. doi: 10.1016/j.micromeso.2017.10.049
- Ramanathan, A., Zhu, H., Maheswari, R., Thapa, P. S., and Subramaniam, B. (2015). Comparative study of Nb-incorporated cubic mesoporous silicates as epoxidation catalysts. *Ind. Eng. Chem. Res.* 54, 4236–4242. doi: 10.1021/ie504386g
- Rhule, J. T., Hill, C. L., Judd, D. A., and Schinazi, R. F. (1998). Polyoxometalates in medicine. *Chem. Rev.* 98, 327–358. doi: 10.1021/cr960396q
- Sadakane, M., and Steckhan, E. (1998). Electrochemical properties of polyoxometalates as electrocatalysts. *Chem. Rev.* 98, 219–238. doi: 10.1021/cr960403a
- Sarafianos, S. G., Kortz, U., Pope, M. T., and Modak, M. J. (1996). Mechanism of polyoxometalate-mediated inactivation of DNA polymerases: an analysis with HIV-1 reverse transcriptase indicates specificity for the DNA-binding cleft. *Biochem. J.* 319, 619–626. doi: 10.1042/bj3190619
- Selvaraj, M., Kawi, S., Park, D. W., and Ha, C. S. (2009). A merit synthesis of well-ordered two-dimensional mesoporous niobium silicate materials with enhanced hydrothermal stability and catalytic activity. *J. Phys. Chem. C* 113, 7743–7749. doi: 10.1021/jp811334r
- Sheldon, R., Arends, I. W. C. E., and Hanefeld, U. (2007). *Green Chemistry and Catalysis*. Weinheim: Wiley-VCH.
- Sheldon, R. A., and van Vliet, M. C. A. (2001). *Fine Chemicals through Heterogeneous Catalysis*. Weinheim: Wiley-VCH.
- Shen, J.-Q., Yao, S., Zhang, Z.-M., Wu, H.-H., Zhang, T.-Z., and Wang, E.-B. (2013). Self-assembly and photocatalytic property of germanoniobate $[\text{H}_6\text{Ge}_4\text{Nb}_{16}\text{O}_{56}]^{10-}$: encapsulating four $[\text{GeO}_4]$ tetrahedra within a $[\text{Nb}_{16}]$ cage. *Dalton Trans.* 42, 5812–5817. doi: 10.1039/c3dt32855d
- Shen, J. Q., Wu, Q., Zhang, Y., Zhang, Z. M., Li, Y. G., Gao, Y. Q., et al. (2014). Polyoxoniobate-based 3D framework materials with photocatalytic hydrogen evolution activity. *Chem. Commun.* 50, 6017–6019. doi: 10.1039/C3CC49245A
- Shen, L., Xu, Y.-Q., Gao, Y.-Z., Cui, F.-Y., and Hu, C.-W. (2009). 3D extended polyoxoniobates/tantalates solid structure: Preparation, characterization and photocatalytic properties. *J. Mol. Struct.* 934, 37–43. doi: 10.1016/j.molstruc.2009.06.018
- Shima, H., Tanaka, M., Imai, H., Yokoi, T., Tatsumi, T., and Kondo, J. N. (2009). IR observation of selective oxidation of cyclohexene with H_2O_2 over mesoporous Nb_2O_5 . *J. Phys. Chem. C* 113, 21693–21699. doi: 10.1021/jp906422z
- Somma, F., Canton, P., and Strukul, G. (2005). Effect of the matrix in niobium-based aerogel catalysts for the selective oxidation of olefins with hydrogen peroxide. *J. Catal.* 229, 490–498. doi: 10.1016/j.jcat.2004.11.028
- Somma, F., and Strukul, G. (2006). Niobium Containing Micro-, Meso- and Macroporous Silica Materials as Catalysts for the Epoxidation of Olefins with Hydrogen Peroxide. *Catal. Lett.* 107, 73–81. doi: 10.1007/s10562-005-9733-y
- Son, J.-H., and Casey, W. H. (2015). A new Keggin-like niobium-phosphate cluster that reacts reversibly with hydrogen peroxide. *Chem. Commun.* 51, 12744–12747. doi: 10.1039/C5CC03782D
- Son, J.-H., Ohlin, C. A., Johnson, R. L., Yu, P., and Casey, W. H. A. (2013b). Soluble phosphorus-centered Keggin polyoxoniobate with bicapping vanadyl groups. *Chem. Eur. J.* 19, 5191–5197. doi: 10.1002/chem.201204563
- Son, J.-H., Wang, J., Osterloh, F. E., Yub, P., and Casey, W. H. (2014). A tellurium-substituted Lindqvist-type polyoxoniobate showing high H_2 evolution catalyzed by tellurium nanowires via photodecomposition. *Chem. Commun.* 50, 836–838. doi: 10.1039/C3CC47001F
- Son, J. H., Ohlin, C. A., Larson, E. C., Yu, P., and Casey, W. H. (2013a). Synthesis and characterization of a soluble vanadium-containing Keggin polyoxoniobate by ESI-MS and ^{51}V NMR: $(\text{TMA})_9[\text{V}_3\text{Nb}_{12}\text{O}_{42}]\cdot 18\text{H}_2\text{O}$. *Eur. J. Inorg. Chem.* 10–11, 1748–1753. doi: 10.1002/ajic.201201056
- Streb, C. (2012). New trends in polyoxometalate photoredox chemistry: From photosensitisation to water oxidation catalysis. *Dalton Trans.* 41, 1651–1659. doi: 10.1039/C1DT11220A

- Su, X.-F., Zhu, B., Wu, C.-X., Yan, L.-K., and Su, Z.-M. (2017). Theoretical studies on Lindqvist polyoxometalates $[M_6O_{19}]^{p-}$ ($M = Mo, W, p=2; M = V, Nb, Ta, p=8$) and derivatives: Electronic structures, stability and bonding. *J. Theor. Comput. Chem.* 16, 1750054/1-1750054/11. doi: 10.1142/S0219633617500547
- Tamami, B., and Fadavi, A. (2005). Amino group immobilized on polyacrylamide: an efficient heterogeneous catalyst for the Knoevenagel reaction in solvent-free and aqueous media. *Catal. Commun.* 6, 747–751. doi: 10.1016/j.catcom.2005.07.012
- Thornburg, N. E., Nauert, S. L., Thompson, A. B., and Notestein, J. M. (2016). Synthesis structure-function relationships of silica-supported niobium(V) catalysts for alkene epoxidation with H_2O_2 . *ACS Catal.* 6, 6124–6134. doi: 10.1021/acscatal.6b01796
- Thornburg, N. E., and Notestein, J. M. (2017). Rate and selectivity control in thioether and alkene oxidation with H_2O_2 over phosphonate-modified niobium(V)-silica catalysts. *ChemCatChem* 9, 3714–3724. doi: 10.1002/cctc.201700526
- Thornburg, N. E., Thompson, A. B., and Notestein, J. M. (2015). Periodic trends in highly dispersed groups IV and V supported metal oxide catalysts for alkene epoxidation with H_2O_2 . *ACS Catal.* 5, 5077–5088. doi: 10.1021/acscatal.5b01105
- Tiozzo, C., Bisio, C., Carniato, F., and Guidotti, M. (2014). Grafted non-ordered niobium-silica materials: versatile catalysts for the selective epoxidation of various unsaturated fine chemicals. *Catal. Today* 235, 49–57. doi: 10.1016/j.cattod.2014.02.027
- Tiozzo, C., Palumbo, C., Psaro, R., Bisio, C., Carniato, F., Gervasini, A., et al. (2015). The stability of niobium-silica catalysts in repeated liquid-phase epoxidation tests: a comparative evaluation of in-framework and grafted mixed oxides. *Inorg. Chim. Acta* 431, 190–196. doi: 10.1016/j.ica.2015.01.048
- Tong, H., and Ye, J. (2010). Building niobate nanoparticles with hexaniobate Lindqvist ions. *Eur. J. Inorg. Chem.* 1473–1480. doi: 10.1002/ejic.200901133
- Tsunashima, R., Long, D. L., Miras, H. N., Gabb, D., Pradeep, C. P., and Cronin, L. (2010). The construction of high-nuclearity isopolyoxoniobates with pentagonal building blocks: $[HnNb_{27}O_{76}]^{16-}$ and $[H_{10}Nb_{31}O_{93}(CO_3)]^{23-}$. *Angew. Chem., Int. Ed.* 49, 113–116. doi: 10.1002/anie.200903970
- Turco, R., Aronne, A., Carniti, P., Gervasini, A., Minieri, L., Pernice, P., et al. (2015). Influence of preparation methods and structure of niobium oxide-based catalysts in the epoxidation reaction. *Catal. Today* 254, 99–103. doi: 10.1016/j.cattod.2014.11.033
- Vasylyev, M. V., and Neumann, R. (2004). New Heterogeneous Polyoxometalate Based Mesoporous Catalysts for Hydrogen Peroxide Mediated Oxidation Reactions. *J. Am. Chem. Soc.* 126, 884–890. doi: 10.1021/ja036702g
- Wada, S., and Suzuki, H. (2003). Calcite and fluorite as catalyst for the Knoevenagel condensation of malononitrile and methyl cyanoacetate under solvent-free conditions. *Tetrahedron Lett.* 44, 399–401. doi: 10.1016/S0040-4039(02)02431-0
- Wang, H., Liang, Z., Liu, Q., Zhang, D., and Wang, J. (2015). Synthesis, structure and photocatalytic hydrogen evolution of a silver-linked hexaniobate Lindqvist chain. *Inorg. Chem. Commun.* 61, 157–159. doi: 10.1016/j.inoche.2015.09.010
- Wang, Q., Chapleski, J. R., Plonka, A. M., Gordon, W. O., Guo, W., et al. (2017). Atomic-level structural dynamics of polyoxoniobates during DMMP decomposition. *Sci. Rep.* 7, 773. doi: 10.1038/s41598-017-00772-x
- Wang, S. S., and Yang, G. Y. (2015). Recent advances in polyoxometalate-catalyzed reactions. *Chem. Rev.* 115, 4893–4962. doi: 10.1021/cr500390v
- Wang, Z. L., Tan, H. Q., Chen, W. L., Li, Y. G., and Wang, E. B. (2012). A copper(II)-ethylenediamine modified polyoxoniobate with photocatalytic H_2 evolution activity under visible light irradiation. *Dalton Trans.* 41, 9882–9884. doi: 10.1039/c2dt30663h
- Wu, H.-L., Zhang, Z.-M., Li, Y.-G., Wang, X.-L., and Wang, E.-B. (2015). Recent progress in polyoxoniobates decorated and stabilized via transition metal cations or clusters. *Cryst. Eng. Comm.* 17, 6261–6268. doi: 10.1039/C5CE00909J
- Wu, Y.-L., Li, X.-X., Qi, Y.-J., Yu, H., Jin, L., and Zheng, S.-T. (2018). $[Nb_{288}O_{768}(OH)_{48}(CO_3)_{12}]$: a macromolecular polyoxometalate with close to 300 niobium atoms. *Angew. Chem.* 57, 8572–8576. doi: 10.1002/anie.201804088
- Xu, Q., Niu, Y., Wang, G., Li, Y., Zhao, Y., Singh, V., et al. (2018). Polyoxoniobates as a superior Lewis base efficiently catalyzed Knoevenagel condensation. *Mol. Catal.* 453, 93–99. doi: 10.1016/j.mcat.2018.05.002
- Yamase, T., and Pope, M. T. (2002). *Polyoxometalate Chemistry for Nano-Composite Design*. New York, NY: Springer Science and Business Media.
- Yan, W., Ramanathan, A., Ghanta, M., and Subramaniam, B. (2014). Towards highly selective ethylene epoxidation catalysts using hydrogen peroxide and tungsten- or niobium-incorporated mesoporous silicate (KIT-6). *Catal. Sci. Technol.* 4, 4433–4439. doi: 10.1039/C4CY00877D
- Yan, W., Ramanathan, A., Patel, P. D., Maiti, S. K., Laird, B. B., Thompson, W. H., et al. (2016). Mechanistic insights for enhancing activity and stability of Nb-incorporated silicates for selective ethylene epoxidation. *J. Catal.* 336, 75–84. doi: 10.1016/j.jcat.2015.12.022
- Yan, W., Zhang, G., Yan, H., Liu, Y., Chen, X., Feng, X., et al. (2018). Liquid-phase epoxidation of light olefins over W and Nb nanocatalysts. *ACS Sustainable Chem. Eng.* 6, 4423–4452. doi: 10.1021/acssuschemeng.7b03101
- Yang, Z.-X., Huang, P., Zhao, L., Zhang, M., Zhang, Y.-T., and Su, Z.-M. (2014). Self-assembly and photocatalytic hydrogen evolution of a niobium-containing polyoxometalate. *Inorg. Chem. Commun.* 44, 195–197. doi: 10.1016/j.inoche.2014.03.022
- Ye, Y. C., Chen, C., Feng, H., Zhou, J., Ma, J., Chen, J., et al. (2013). Visible photoluminescence of polyoxoniobates in aqueous solution and their high electrocatalytic activities for water oxidation. *OJIC* 3, 59–69. doi: 10.4236/ojic.2013.33009
- Zhang, T.-T., Zhang, X., Lü, Y., Li, G.-D., Xiao, L.-N., Cui, X.-B., et al. (2017). New organic-inorganic hybrid compounds based on $[SiNb_{12}V_2O_{42}]^{12-}$ with high catalytic activity for styrene epoxidation. *Inorg. Chem. Front.* 4, 1397–1404. doi: 10.1039/C7QI00318H
- Zhang, Y., Shen, J.-Q., Zheng, L.-H., Zhang, Z.-M., Li, Y.-X., and Wang, E.-B. (2014). Four polyoxoniobate-based inorganic-organic hybrids assembly from bicapped heteropolyoxoniobate with effective antitumor activity. *Cryst. Growth Des.* 14, 110–116. doi: 10.1021/cg401227g
- Zhang, Z. Y., Lin, Q. P., Kurunthu, D., Wu, T., Zuo, F., Zheng, S. T., et al. (2011). Synthesis and photocatalytic properties of a new heteropolyoxoniobate compound: $K_{10}[Nb_2O_2(H_2O)_2][SiNb_{12}O_{40}] \cdot 12H_2O$. *J. Am. Chem. Soc.* 133, 6934–6937. doi: 10.1021/ja201670x
- Zhou, Y., Guo, Z., Hou, W., Wang, Q., and Wang, J. (2015). Polyoxometalate-based phase transfer catalysis for liquid-solid organic reactions: a review. *Catal. Sci. Technol.* 5, 4324–4335. doi: 10.1039/C5CY00674K
- Zienkiewicz, Z., Calvino-Casilda, V., Sobczak, I., Ziolek, M., Martín-Aranda, R. M., and Lopez-Peinado, A. J. (2009). The possible use of alkali metal modified NbMCM-41 in the synthesis of 1,4-dihydropyridine intermediates. *Catal. Today* 142, 303–307. doi: 10.1016/j.cattod.2008.10.022
- Ziolek, M., Decyk, P., Sobczak, I., Trejda, M., Florek, J., Golinska, H., et al. (2011). Catalytic performance of niobium species in crystalline and amorphous solids-gas and liquid phase oxidation. *Appl. Catal. Gen.* 391, 194–204. doi: 10.1016/j.apcata.2010.07.022
- Ziolek, M., and Nowak, I. (1997). Synthesis and characterization of niobium-containing MCM-41. *Zeolites* 18, 356–360. doi: 10.1016/S0144-2449(97)00027-4
- Ziolek, M., Sobczak, I., Decyk, P., Sobanska, K., Pietrzyk, P., and Sojka, Z. (2015). Search for reactive intermediates in catalytic oxidation with hydrogen peroxide over amorphous niobium(V) and tantalum(V) oxides. *Appl. Catal.* 164, 288–296. doi: 10.1016/j.apcata.2014.09.024
- Ziolek, M., Sobczak, I., Lewandowska, A., Nowak, I., Decyk, P., Renn, M., et al. (2001). Oxidative properties of niobium-containing mesoporous silica catalysts. *Catal. Today* 70, 169–181. doi: 10.1016/S0920-5861(01)00416-3
- Ziolek, M., Sobczak, I., Nowak, I., Decyk, P., Lewandowska, A., and Kujawa, J. (2000). Nb-containing mesoporous molecular sieves – a possible application in the catalytic processes. *Micropor. Mesopor. Mater.* 35, 195–207. doi: 10.1016/S1387-1811(99)00220-6

Conflict of Interest Statement: The authors declare that the research was conducted in the absence of any commercial or financial relationships that could be construed as a potential conflict of interest.

Copyright © 2018 Wawrzynczak, Nowak and Felicjak-Guzik. This is an open-access article distributed under the terms of the Creative Commons Attribution License (CC BY). The use, distribution or reproduction in other forums is permitted, provided the original author(s) and the copyright owner(s) are credited and that the original publication in this journal is cited, in accordance with accepted academic practice. No use, distribution or reproduction is permitted which does not comply with these terms.



Multi-Tasking POM Systems

Kevin P. Sullivan¹, Qiushi Yin¹, Daniel L. Collins-Wildman¹, Meilin Tao¹, Yurii V. Geletii¹,
Djamaladdin G. Musaev^{1,2}, Tianquan Lian¹ and Craig L. Hill^{1*}

¹ Department of Chemistry, Emory University, Atlanta, GA, United States, ² Emerson Center for Scientific Computation, Emory University, Atlanta, GA, United States

Polyoxometalate (POM)-based materials of current interest are summarized, and specific types of POM-containing systems are described in which material facilitates multiple complex interactions or catalytic processes. We specifically highlight POM-containing multi-hydrogen-bonding polymers that form gels upon exposure to select organic liquids and simultaneously catalyze hydrolytic or oxidative decontamination, as well as water oxidation catalysts (WOCs) that can be interfaced with light-absorbing photoelectrode materials for photoelectrocatalytic water splitting.

Keywords: Polyoxometalates (POMs), heterogeneous catalysis, multi-functional polymers, catalytic water oxidation, photoelectrochemical water splitting

OPEN ACCESS

Edited by:

Debbie C. Crans,
Colorado State University,
United States

Reviewed by:

Enrique González-Vergara,
Benemérita Universidad Autónoma de
Puebla, Mexico
Yoshihito Hayashi,
Kanazawa University, Japan

*Correspondence:

Craig L. Hill
chill@emory.edu

Specialty section:

This article was submitted to
Inorganic Chemistry,
a section of the journal
Frontiers in Chemistry

Received: 29 June 2018

Accepted: 30 July 2018

Published: 21 August 2018

Citation:

Sullivan KP, Yin Q,
Collins-Wildman DL, Tao M, Geletii YV,
Musaev DG, Lian T and Hill CL (2018)
Multi-Tasking POM Systems.
Front. Chem. 6:365.
doi: 10.3389/fchem.2018.00365

POM PROPERTIES THAT MAKE THEM EFFECTIVE IN MATERIALS APPLICATIONS

Materials chemistry has evolved to the point where rational design of multifunctional systems with synergistic capabilities is possible. POMs are very effective as components of materials owing to their great synthetic tunability, allowing for many physical and chemical properties to be tailored to specific applications. Incorporating POMs into heterogeneous systems therefore allows for a bottom-up approach to the development of multifunctional materials (Miras et al., 2012; He et al., 2014; Zhang et al., 2014).

Polyoxometalates are useful in catalysis and other applications owing to their redox potentials, acidities, polarities, negative charge densities on surface oxygens and other parameters (Hill, 1998; Wang and Yang, 2015). Several reviews can be consulted for early studies of fundamental structure and reactivity (Pope, 1983, 2004; Hill, 2004; Yamase and Pope, 2006; Wang and Yang, 2015). The polyanion can be extensively modified by substitution of surface metal-oxo units (addenda or surface metal-oxo units) with many first-row transition-metal and other redox-active metal ions as well as organometallic groups. Of the large number of polyanion structural families, derivatives of the two most common families, Keggin and Wells-Dawson, still dominate fundamental studies of the impact of polyanion substitution and modification on the chemistry of POMs (Coronado and Gómez-García, 1995; Hill, 1998; Borrás-Almenar et al., 2001; Long et al., 2010). The fact that POMs are polyoxoanions with several counterions balancing the charge allows this huge and growing class of inorganic cluster compounds to be highly versatile; both the polyanion and the counterions can be altered, impacting the factors that make POMs useful in catalysis and other applications. This variability allows for small changes to be made in the POM systematically, facilitating the study and optimization of the resulting material.

The redox potentials of POMs are key to the reactions that feature prominently in many applications. POM potentials are controlled by the redox-active metals in the POM framework, by transition metal substituted into addenda (outside) structural sites, and by the charge density and geometry of the POM. Different POM geometries have intrinsically different charge densities on the framework metals and the oxygens bridging these metals, thus both the framework and substituted transition metals have altered potentials when present in different POM structural families. In addition to the framework metal and/or substituted transition metal, the nature and type of the counterion can also impact POM potentials (Hill, 2004). Ever more studies have demonstrated that POM counterions impact nearly every property of POMs that feature in their applications (Grigoriev et al., 2000, 2001).

The relative ease of incorporating POMs into heterogeneous matrices is another reason they are particularly well-suited for construction of functional materials. Several strategies exist for the immobilization of POMs including electrostatic attraction, solvophobic interactions, or covalent linkages (Proust et al., 2012; Hill and Kholdeeva, 2013; Xiao et al., 2016). Immobilization of POMs through electrostatic and solvophobic interactions is the most common and simple method, owing to the high negative charge of the POMs and ease of counter cation exchange (to produce insoluble salts) (Proust et al., 2012). Attaching POMs to materials covalently leads to the most stable products, however relatively few methods exist to achieve this covalent linkage while retaining all of the desired properties of the POM. As such, the development of covalently functionalized materials remains a very active area of research. Many studies have focused on the development of POM-based polymers to enable easier processing and facilitate the creation of POM-based devices and advanced materials. The tuning of flexible organic ligands and polyanions in POM-hybrids also allows for the engineering of POM-based compounds and materials with specific desired topologies (Taleghani et al., 2016). Most commonly, covalent incorporation of POMs and other inorganic compounds into polymer matrices is achieved through side-chain functionalization either before or after the polymerization process (Hu et al., 2012; Rieger et al., 2012; Macdonell et al., 2015; Wu et al., 2016). Both the self-assembly of POM-organic hybrids and their incorporation into polymers have been reviewed recently (Carraro and Gross, 2014; Wu et al., 2016).

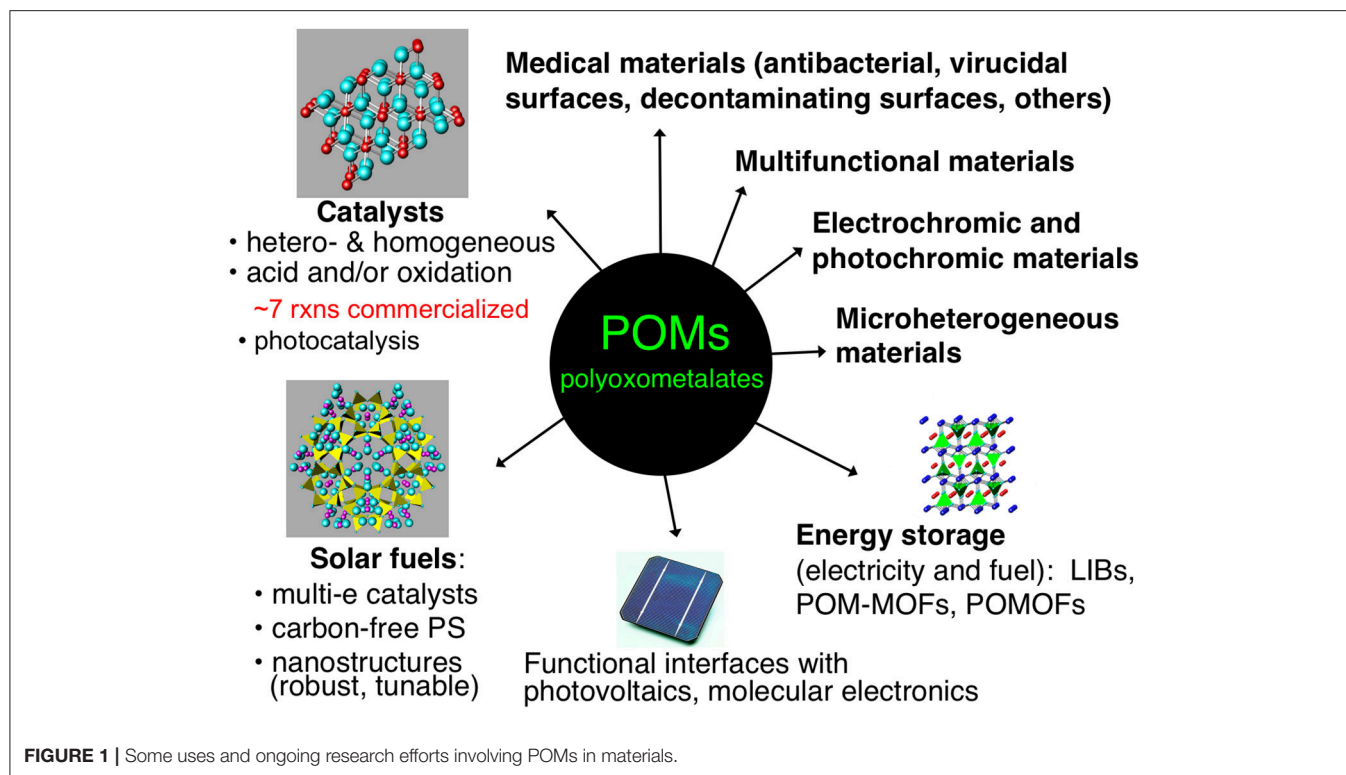
SURVEY OF POM MATERIALS APPLICATIONS

Figure 1 illustrates several applications of POMs in materials. Some of these topics, such as catalysis of organic transformations, are more mature than others, but substantial research continues in all these areas. Several heterogeneous and homogeneous processes catalyzed by POMs have had commercial applications, such as in the hydration of alkenes or polymerization of tetrahydrofuran (Kozhevnikov, 1998). These industrial processes primarily

involve the use of heteropolyacids as acid catalysts or more complex, mixed-metal POM derivatives as oxidation catalysts (Hill and Prosser-McCartha, 1995; Okuhara et al., 1996; Kozhevnikov, 1998, 2002; Mizuno and Misono, 1998; Moffat, 2001).

Several recent reviews have been published covering applications of POMs in heterogeneous catalysis (Long et al., 2007; Nlate and Jahier, 2012; Ren et al., 2015; Wang and Yang, 2015; Patel et al., 2016). One area of significant interest in POM-based materials has been the incorporation of POMs into metal-organic frameworks (MOFs) (Du et al., 2014). MOFs have attained a very high profile in the field of heterogeneous materials, as their high surface area and modifiable topologies allow for the design of a variety of very active functional materials (Corma et al., 2010; Furukawa et al., 2013). Combining the versatility of function of POMs with the high surface area of MOFs has led to several interesting and highly active materials. Song et al. reported the synthesis and characterization of a MOF (MOF-199) containing the Keggin-type POM $[\text{CuPW}_{11}\text{O}_{39}]^{5-}$ within its pores. This POM-MOF exhibited substantially increased catalytic aerobic oxidation of sulfides and thiols to deodorized products compared to the POM or the MOF alone (Song et al., 2011). Ma et al. carried out a similar study in which a POM $[\text{PW}_{12}\text{O}_{40}]^{3-}$ was used as a template during the synthesis of the MOF (NENU-11), aiding in its formation during a simple one-step hydrothermal synthesis. The resulting POM-MOF was then shown to be active towards the adsorption and hydrolysis of dimethyl methylphosphonate, an analog of organophosphonate chemical warfare agents, demonstrating synergistic roles of both the POM and the MOF in the composite material (Ma et al., 2011).

As mentioned previously, POM organic/inorganic hybrids are highly attractive for developing processable materials that incorporate the functionality of POMs. Research on POM organic/inorganic hybrids has developed into an extensive field with applications in many disciplines (Zonnevijlle and Pope, 1979; Gouzerh and Proust, 1998; Qi and Wu, 2009; Dolbecq et al., 2010; Proust et al., 2012; Song and Tsunashima, 2012). These include POM-modified organic/inorganic nanocomposites for energy applications (which will be discussed in greater depth later in this article) (Genovese and Lian, 2015; Ji et al., 2015), green synthesis (Omwoma et al., 2015; Zhou et al., 2015), photochemical and electrochemical properties (Walsh et al., 2016), environmental remediation (Sivakumar et al., 2012), among others. These POM materials often exhibit multiple synergistic functions. For example, Haimov et al. reported the synthesis of a cross-linked polyethyleneimine polymer containing $[\text{ZnWZn}_2(\text{H}_2\text{O})_2(\text{ZnW}_9\text{O}_{34})_2]^{12-}$ POMs. The hydrophilic domains of the polymer contained both the POMs and the 2-alkanol substrates, and the lipophilic domain affects the solubility of the substrate in the hydrophilic domain. When the material was used to catalyze the hydrogen peroxide-based oxidation of the 2-alkanol substrates to the corresponding ketones, the material had the dual role of enhancing the reaction rate by bringing the POM and substrate in closer proximity and imparting a liposelectivity component to the reaction rate as a



function of the hydrophobic nature of the substrate (Haimov and Neumann, 2006).

Another class of POM-based materials that warrant note are POMs intercalated into layered double hydroxides (LDHs). POM-LDH systems date back to Pinnavaia's early studies (Kwon et al., 1988), and have expanded to become an active field within POM materials chemistry (Omwoma et al., 2014; Li T. et al., 2017). An example by Zhao et al. demonstrates the synergistic effect of intercalating various sandwich-structure POMs into LDHs. They tested these materials on the mild and solvent-free oximation of aromatic aldehydes by the POM and observed substantial selectivity enhancements due to the ability of the LDH to suppress the formation of byproducts. Additionally, the heterogeneous support facilitated easy recovery and reuse of the material (Zhao S. et al., 2011).

Many types of POMs lend themselves to energy applications, such as energy storage and solar fuel generation. The ability of certain categories of POMs (most polytungstates, polymolybdates, and polyvanadates) to be reduced by many electrons, first dramatically noted in a study by Launay and co-workers (Launay, 1976) has led to intriguing studies of POM-based batteries and energy storage assemblies (Wang et al., 2012; Pratt et al., 2013; Genovese and Lian, 2015). One study published by Suárez-Guevara et al. uses electrodes made from activated carbon and the POM, $\text{H}_3\text{PW}_{12}\text{O}_{40}$, in which the POM exhibits multiple functions: it increases the capacitance, operating voltage, and energy density of the battery. Additionally, the POM protects the activated carbon electrode from oxidation, allowing for the cell to have a high capacitance retention after a large

number of charge-discharge cycles (Suárez-Guevara et al., 2014). An example of an energy application in which a POM has four planned and realized functions is a POM-Pt-MOF material that facilitates visible-light-driven catalytic H_2 evolution and does this far more effectively than any of the 3 components alone. In this material, the POMs (1) catalyze reduction of platinum salts to Pt(0) nanoparticles, (2) stabilize the Pt nanoparticles and prevent them from aggregating, (3) induce a strong electrostatic association of the negatively charged Pt NPs with the protonated $\text{NH}_2\text{-MIL-53}$ sites on the MOF particle surfaces, and (d) helps catalyze the H_2 evolution reaction (Guo et al., 2016).

We now focus on two types of POM-based materials that illustrate the broad utility landscape of such materials. One involves the incorporation of a POM into the main chain of a polymer, resulting in a material which sequesters and decontaminates toxic or odorous compounds. The other involves immobilization of POM catalysts in photoelectrode assemblies in which the POM undergoes multiple photoinduced electron transfer processes and also carries the many steps involved in the oxidation of water molecules to O_2 .

POM-CONTAINING NETWORK MATERIALS THAT PHYSICALLY ENTRAP AND CATALYZE DEGRADATION

Very recently we reported the design and synthesis of a POM-based polymer that demonstrates the advantages of combining the rich chemistry of POMs with properties obtained from

incorporating the POM unit into a material. We synthesized and characterized a polymer composed of hexavanadate (V_6O_{19}) POM units and 1,3,5-benzenetricarboxamide-based linkers (trisBTA), with the formula $[(n-C_4H_9)_4N]_{2n}[(V_6O_{13})_n\{((OCH_2)_3CNHCO)_3C_6H_3\}_x\{((OCH_2)_3CNHCO)_2((HOCH_2)_3CNHCO)C_6H_3\}_y\{(OCH_2)_3CNHCO((HOCH_2)_3CNHCO)_2C_6H_3\}_z]$ (**TBA-polyV₆**, x = triply bound trisBTA, y = doubly-bound trisBTA, z = singly-bound trisBTA) (**Figure 2**) (Sullivan et al., 2017). This class of materials exhibits several functions: it forms gels within seconds after contact with polar aprotic organic liquids, catalyzes the oxidative or hydrolytic degradation of toxins and odorants under mild conditions, and exhibits color change during select oxidation reactions. This combination of properties was made possible through the incorporation of the POMs (capable of catalyzing oxidation and hydrolysis) and the organic linkers to form a polymeric material. The design of this polymer material from modular components allowed us to tailor the multiple functions to be useful for the entrapment and removal of toxic substances, including chemical warfare agent (CWA) analogs.

Polyoxometalate-organic hybrid species can oxidize a variety of organic substrates (Dolbecq et al., 2010), with hexavanadates

demonstrating particular activity for oxidation of sulfides (Hill et al., 2006; Han and Hill, 2007). Thus, redox-active **TBA-polyV₆** facilitates color-change detection and oxidative decontamination. To demonstrate the applicability of **TBA-polyV₆** for air-based oxidative removal reactions, we conducted studies on the catalytic oxidation of 1-propanethiol (PrSH), as thiols are a major class of odorants in human environments. This representative thiol is fully oxidized to the corresponding non-odorous disulfide, and oxygen reoxidizes the reduced POM units (**Figure 3a**). The material is red in its powder state and reddish-orange when dispersed in solvent, indicative of the oxygen-to-metal charge transfer absorption manifold of a fully-oxidized $[V_6^V O_{13}(OR)_6]^{2-}$ core (R = trisBTA linkers). Upon reduction of the POM, **TBA-polyV₆** becomes dark green as a broad peak between 600 and 900 nm increases, attributed to intervalence charge-transfer bands in the reduced POM (Chen et al., 1992). The persistent observation of a green reduced hexavanadate species during the reaction provides colorimetric detection capabilities for this polymeric material (**Figure 3**). In addition to aerobic oxidation of thiols, **TBA-polyV₆** catalyzes the oxidation of sulfides by hydrogen peroxide, including 2-chloroethyl ethyl sulfide, an analog of the CWA sulfur mustard. The sulfide is completely oxidized within 30 min after adding

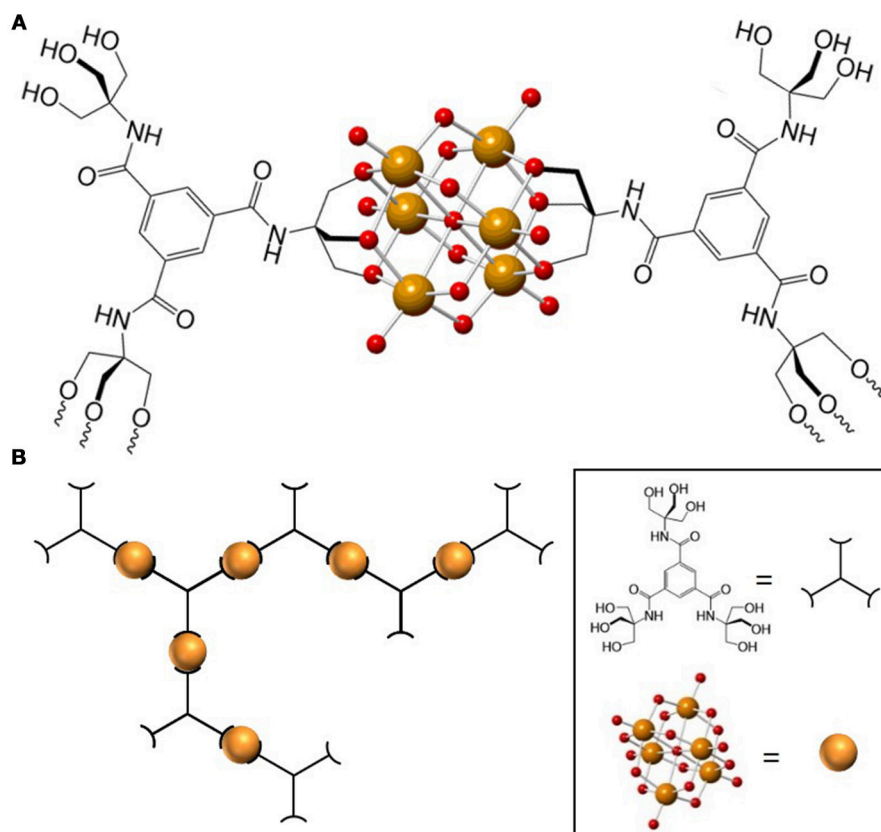


FIGURE 2 | (A) Representation of a monomeric **TBA-polyV₆** unit. **(B)** Representation of the **TBA-polyV₆** polymer. Orange and red spheres represent V(V) and O²⁻, respectively. Reproduced from (Sullivan et al., 2017) with permission from the Royal Society of Chemistry.

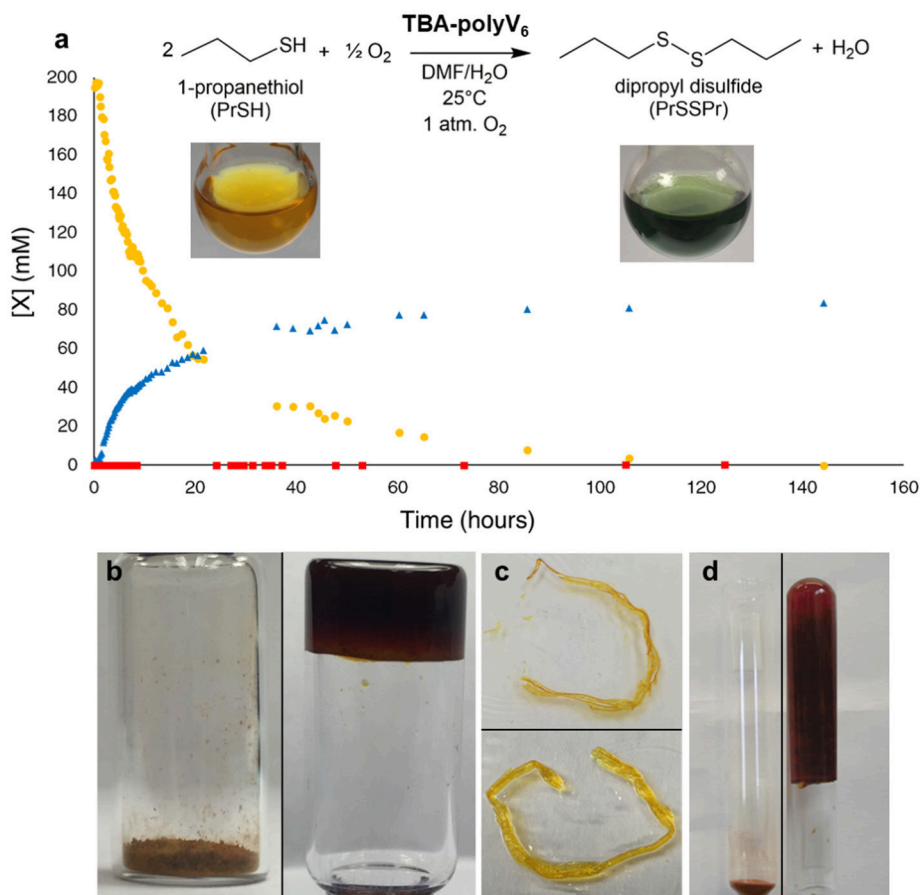


FIGURE 3 | Aerobic oxidation catalyzed by **TBA-polyV₆**. **(a)** Oxidation of 1-propanethiol (●) to dipropyl disulfide (▲) catalyzed by **TBA-polyV₆**. The molar ratio was 127 1-propanethiol: 1 V₆. A control reaction (■) was run under identical conditions but without **TBA-polyV₆**. **Inset:** A yellow dispersion of **TBA-polyV₆** in DMF before (left) and after (right) addition of 1-propanethiol (**Figure 4**). **(b)** Swelling of **TBA-polyV₆** (left) in the presence of dimethyl methyl phosphonate (DMMP) (right). **(c)** A strand of **TBA-polyV₆** before (above) and after (below) addition of DMSO. **(d)** Swelling of **TBA-polyV₆** (left) in the presence of DMF (right). **(d)** Swelling behavior measured in mL of liquid per gram of material after 24-hour exposure. Reproduced from (Sullivan et al., 2017) with permission from the Royal Society of Chemistry.

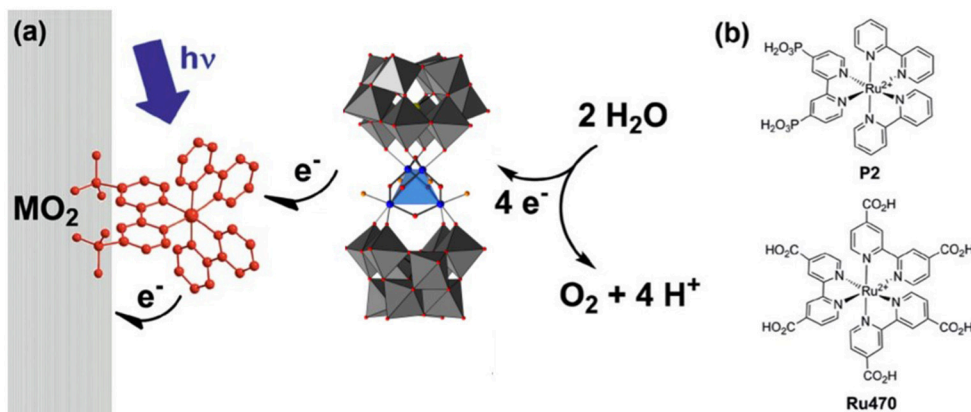


FIGURE 4 | **(a)** Principle of operation of a triadic water-oxidizing photoanode incorporating both Ru₄Si₂ and a dye. **(b)** Structures of the dyes which have been used in triads with Ru₄Si₂ (Xiang et al., 2013). Adapted with permission from J. Phys Chem. C., 2013, 117 (2), pp 918–926. Copyright 2013, American Chemical Society.

H_2O_2 , whereas a reaction run without catalyst requires multiple hours to go to completion.

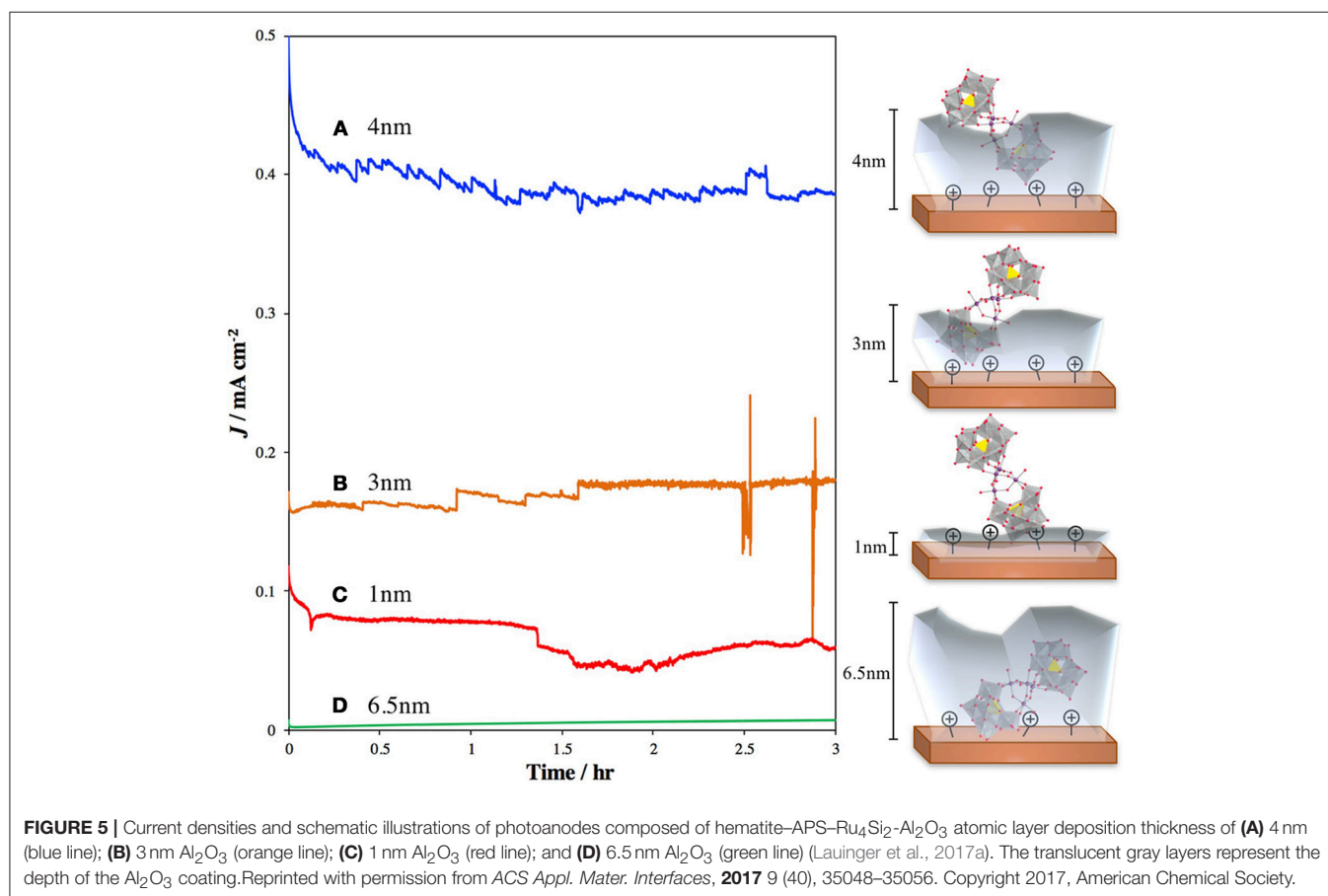
Recent studies have demonstrated both polyoxometalate-catalyzed hydrolysis of phosphoester bonds as well as hydrogen bond donor-catalyzed hydrolysis of organophosphate (OP) CWAs (Steens et al., 2010; Barba-Bon et al., 2013; Sambrook and Notman, 2013; Kinnan et al., 2014). Additionally, Zr-based MOFs and POMs have received a great deal of attention for their high activities toward hydrolysis of organophosphates, including OP nerve agents (Mondloch et al., 2015; Luong et al., 2016; Collins-Wildman et al., 2018). To demonstrate that **TBA-polyV₆** is highly modular in nature, we synthesized a new polymer through simple cation exchange with zirconyl chloride, affording **Zr-polyV₆**, which exhibits high activity for catalytic hydrolysis of dimethyl *p*-nitrophenylphosphate (DMNP). We again show how the chemical and physical properties of the multifunctional POM-based polymer can be readily tuned to achieve targeted applications.

After demonstrating that the catalytic capabilities of the POM units remain intact in the heterogeneous material, we examined the gelation capabilities of the polymers. Studies of compounds containing 1,3,5-benzenetricarboxamides have shown them to be capable of forming gels through the presence of extensive hydrogen-bonding networks through the amide units, as well as π -stacking between adjacent aromatic groups (Sambrook and Notman, 2013). This property is preserved

in **TBA-polyV₆**, demonstrated by organogelation resulting from the addition of polar aprotic liquids to the material (Figures 3b–d). Significantly, we observed that **TBA-polyV₆** can form gels when exposed to OP agent analogs. Addition of the nerve agent analog dimethyl methyl phosphonate DMMP results in immobilization of a substantial amount of the liquid with rapid swelling kinetics. We demonstrate, therefore, that incorporating multiple functionalities to this POM-based polymer has allowed us to develop the first examples of materials that are potentially capable of both immobilizing and decontaminating CWAs.

HETEROGENEOUS POLYOXOMETALATE WATER OXIDATION CATALYSTS (WOCs) AND THEIR USE IN PHOTOELECTROCATALYTIC WATER SPLITTING

The applications of POMs or POM-based materials to solar fuels (artificial photosynthesis) is now a substantial category by itself. POMs have been examined in several functional roles for solar fuel generation. The first of these is broad-spectrum and intense visible light absorption with charge separation. Some POM derivatives have high extinction coefficients for charge transfer absorption (Zhao C. et al., 2011; Zhao et al., 2013), and while



the charge-transfer excited-state lifetimes are highly variable, most are too short to result in high-quantum-yield chemical capture. However, POMs are quite active as catalysts for multi-electron reduction (reduction of H_2O to H_2 or CO_2 to carbon-based fuel molecules) (Wang et al., 2016; Gumerova and Rompel, 2018). Several POMs that are efficient water reduction catalysts under visible-light-driven or dark conditions have been reported (Lv et al., 2014, 2015, 2016), and some POMs facilitate CO_2 reduction under appropriate conditions (Ettedgui et al., 2010; Wang et al., 2016). One of the primary applications that has been the subject of extensive research within the field of POMs has been the catalysis of water oxidation. Since the original reports of a POM water oxidation catalyst (WOC), namely the tetra-ruthenium sandwich polytungstate, $[\{\text{Ru}_4\text{O}_4(\text{OH})_2(\text{H}_2\text{O})_4\}(\gamma\text{-SiW}_{10}\text{O}_{36})_2]^{10-}$ (Ru_4Si_2) (Geletii et al., 2008; Sartorel et al., 2008), and the first publication on a POM WOC of all earth-abundant elements (Yin et al., 2010), there have been scores of papers on POM WOCs (Lauinger et al., 2017b; Li J. et al., 2017).

The issue of the true active catalyst species is always one of great interest in any catalytic system (Vickers et al., 2013; Wu et al., 2015). Polyoxometalate WOCs have been of particular concern in this regard (Stracke and Finke, 2011, 2014; Vickers et al., 2013; Folkman and Finke, 2017). This is due to the fact that POMs are essentially molecular metal oxides and could potentially have extensive speciation equilibria in solution (Sumliner et al., 2014; Sara et al., 2015; Lauinger et al., 2017b; Nyman, 2017). Some of the species that could be present include the metal aqua complexes as well as the corresponding metal oxide nanoparticles, all of which could also be active as WOCs (Stracke and Finke, 2014; Sumliner et al., 2014; Folkman and Finke, 2017; Lauinger et al., 2017b; Suen et al., 2017). It is therefore essential that any POM species is demonstrated to be stable and active under experimental conditions. POMs have been immobilized on photoanodes to make photocatalytic water oxidizing electrodes, allowing careful tailoring of POMs during their synthesis to be combined with the stabilizing effects of a heterogeneous material. Heterogeneous systems involving POMs are generally more stable than their molecular counterparts due to the limiting of solution phase equilibria involving the POM, preventing speciation that could lead to a shift in the composition of the catalytic POM cluster (Lauinger et al., 2017b). Heterogeneous WOCs are also advantageous because both half reactions involved in water splitting are spatially separated, preventing product recombination or the collection of an explosive mixture of hydrogen and oxygen. In addition, heterogeneous architectures enable efficient charge transfer and separation between photosensitizer and catalyst. In a homogeneous setup, the two components must diffuse to one another leaving time for charge recombination or breakdown of unstable intermediates, lowering the overall system efficiency.

In general, studies of POMs immobilized on photoelectrodes are of three types: electrostatic binding to a surface-bound photosensitizer dye, electrostatic immobilization on semiconductor photoanodes, and partial encapsulation of POM WOCs on photoanodes via metal oxide nanofilm deposition. Studies done by Xiang et al. used ultrafast transient absorption spectroscopy to probe electron transfer between the Ru_4Si_2 WOC, photosensitizer dye $[\text{Ru}(\text{bpy})_2(\text{dppbpy})]^{2+}$, and various

metal oxide electrode surfaces (**Figure 4**) (Xiang et al., 2013). A similar study was also reported by Bonchio, Scandola and co-workers in which illumination of the POM-dye-metal oxide triad resulted in a rapid (10 ns) electron injection which occurs from the catalyst to sensitizer, generating a long lived (0.5 μs) charge-separated state (Orlandi et al., 2010). This proved to be an effective strategy for water oxidation as Fielden et al. later demonstrated with oxygen measurements on a similar triad (Fielden et al., 2015), however, a limitation in both cases was the stability of the dye on the surface.

Several studies have focused on direct binding of the POM to photoactive metal oxides, such as TiO_2 and hematite. Recently, our group published a report in which we treated TiO_2 with 3-aminopropyltrimethoxysilane (APS) to generate a cationic surface that strongly bound the highly negatively charged POM WOC, Ru_4Si_2 (Lauinger et al., 2015). This was effective for surface immobilization of the POM and light driven water oxidation. To improve this system by moving the observed catalysis from the UV into the visible range, we examined surface treatment of hematite with Ru_4Si_2 as the POM WOC to achieve visible-light-driven water oxidation (Lauinger et al., 2017a). In this system, atomic layer deposition (ALD) of Al_2O_3 was used to provide stabilization through partial encapsulation of the POM. The thickness of the ALD layer was optimized to prevent desorption of the catalyst without greatly reducing the efficiency of electron injection from Ru_4Si_2 into the hematite electrode (**Figure 5**).

Perhaps most impressive of recent efforts to turn known homogeneous POM WOCs into functional heterogeneous electrocatalysts involves the immobilization of a septa-cobalt POM into a graphite matrix using a carbon paste electrode (Blasco-Ahicart et al., 2017). By formulating the POM cluster in combination with Ba^{2+} and a stable graphite matrix, Blasco-Ahicart et al. observed a dramatic synergistic effect of both increased stability and catalytic performance. This was the first reported example of a stable discrete complex with earth-abundant elements for water oxidation in strongly acidic media. At certain current densities, this heterogeneous composition even manages to have a lower overpotential than the long-running state-of-the-art iridium oxide and ruthenium oxide WOC films. Having a concrete understanding of how this type of synergistic effect between the hydrophobic carbon paste framework and the POM occurs could yield substantial improvements in the WOC field (Yin and Hill, 2017).

CONCLUSIONS

The field of POM-based materials has been expanding rapidly and is likely to remain fruitful as ever more applications are explored. The ease of tunability and high activity of POMs combined with the processability, stability, or other physical advantages of heterogeneous systems allows for extraordinary versatility in application of these materials. These efforts have led many scientists traditionally working on homogeneous systems towards materials chemistry, and vice versa. Thus, there is an imperative to combine the vast knowledge base of each of these fields and foster collaboration to aid in the production of high

quality research towards the development and characterization of new hybrid POM systems.

AUTHOR CONTRIBUTIONS

KS and CH oversaw all writing. QY, DC-W, MT, YG all contributed to the writing of the WOC section. DM and TL provided input.

REFERENCES

- Barba-Bon, A., Costero, A. M., Parra, M., Gil, S., Martínez-Máñez, R., Sancenón, F., et al. (2013). Neutral 1,3-diindolylureas for nerve agent remediation. *Chem. Eur. J.* 19, 1586–1590. doi: 10.1002/chem.201202028
- Blasco-Ahicart, M., Soriano-López, J., Carbó, J. J., Poblet, J. M., and Galán-Mascaros, J. R. (2017). Polyoxometalate electrocatalysts based on earth-abundant metals for efficient water oxidation in acidic media. *Nat. Chem.* 10, 24–30. doi: 10.1038/nchem.2874
- Borrás-Almenar, J. J., Clemente-Juan, J. M., Clemente-Leon, M., Coronado, E., Galán-Mascaros, J. R., and Gómez-García, C. J. (2001). “Molecular materials from polyoxometalates,” in *Polyoxometalate Chemistry From Topology Via Self-Assembly to Applications*, eds M. T. Pope and A. Müller (Dordrecht: Kluwer), 231.
- Carraro, M., and Gross, S. (2014). Hybrid materials based on the embedding of organically modified transition metal oxoclusters or polyoxometalates into polymers for functional applications a review. *Materials* 7, 3956–3989. doi: 10.3390/ma7053956
- Chen, Q., Goshorn, D. P., Scholes, C. P., Tan, X. L., and Zubietta, J. (1992). Coordination compounds of polyoxovanadates with a hexametallate core. Chemical and structural characterization of $[V_6O_{13}\{(OCH_2)_3CR\}_2]^{2-}$, $[V_6O_{11}(OH)_2\{(OCH_2)_3CR\}_2]$, $[V_4V_2O_9(OH)_4\{(OCH_2)_3CR\}_2]^{2-}$, and $[V_6O_7(OH)_6\{(OCH_2)_3CR\}_2]^{2-}$. *J. Am. Chem. Soc.* 114, 4667–4681. doi: 10.1021/ja00038a033
- Collins-Wildman, D. L., Kim, M., Sullivan, K. P., Plonka, A. M., Frenkel, A. I., Musaev, D. G., et al. (2018). Buffer-induced acceleration and inhibition in polyoxometalate-catalyzed organophosphorus ester hydrolysis. *ACS Catal.* 8, 7068–7076. doi: 10.1021/acscatal.8b00394
- Corma, A., García, H., and Llabrés i Xamena, F. X. (2010). Engineering metal organic frameworks for heterogeneous catalysis. *Chem. Rev.* 110, 4606–4655. doi: 10.1021/cr9003924
- Coronado, E., and Gómez-García, C. J. (1995). Polyoxometalates From magnetic clusters to molecular materials. *Comments Inorg. Chem.* 17, 255–281. doi: 10.1080/02603599508032707
- Dolbecq, A., Dumas, E., Mayer, C. R., and Mialane, P. (2010). Hybrid organic-inorganic polyoxometalate compounds from structural diversity to applications. *Chem. Rev.* 110, 6009–6048. doi: 10.1021/cr1000578
- Du, D. Y., Qin, J. S., Li, S. L., Su, Z. M., and Lan, Y. Q. (2014). Recent advances in porous polyoxometalate-based metal-organic framework materials. *Chem. Soc. Rev.* 43, 4615–4632. doi: 10.1039/C3CS60404G
- Ettegui, J., Diskin-Posner, Y., Weiner, L., and Neumann, R. (2010). Photoreduction of carbon dioxide to carbon monoxide with hydrogen catalyzed by a rhenium(I) phenanthroline-polyoxometalate hybrid complex. *J. Am. Chem. Soc.* 132, 188–190. doi: 10.1021/ja1078199
- Fielden, J., Sumlin, J. M., Han, N., Geletii, Y. V., Xiang, X., Musaev, D. G., et al. (2015). Water splitting with polyoxometalate-treated photoanodes enhancing performance through sensitizer design. *Chem. Sci.* 6, 5531–5543. doi: 10.1039/C5SC01439E
- Folkman, S. J., and Finke, R. G. (2017). Electrochemical water oxidation catalysis beginning with Co(II) polyoxometalates the case of the precatalyst Co₄V₂W₁₈O₆₈. *ACS Catal.* 7, 7–16. doi: 10.1021/acscatal.6b
- Furukawa, H., Cordova, K. E., O’Keeffe, M., and Yaghi, O. M. (2013). The chemistry and applications of metal-organic frameworks. *Science* 341:1230444. doi: 10.1126/science.1230444

FUNDING

The multi-functional POM-based polymer work was funded by the Defense Threat Reduction Agency (grant # HDTRA1-16-1-0029), and the catalytic water oxidation work was funded by the U.S. Department of Energy, Office of Basic Energy Sciences, Solar Photochemistry program (grant # DE-FG02-07ER 15906).

- Geletii, Y. V., Botar, B., Kögerler, P., Hillesheim, D. A., Musaev, D. G., and Hill, C. L. (2008). An all-inorganic, stable, and highly active tetraruthenium homogeneous catalyst for water oxidation. Selected as the VIP Article by the reviewers and editor. *Angew. Chem. Int. Ed.* 47, 3896–3899. doi: 10.1002/anie.200705652
- Genovese, M., and Lian, K. (2015). Polyoxometalate modified inorganic-organic nanocomposite materials for energy storage applications: a review. *Curr. Opin. Solid State Mater. Sci.* 19, 126–137. doi: 10.1016/j.cossms.2014.12.002
- Gouzerh, P., and Proust, A. (1998). Main-group element, organic, and organometallic derivatives of polyoxometalates. *Chem. Rev.* 98, 77–111. doi: 10.1021/cr960393d
- Grigoriev, V. A., Cheng, D., Hill, C. L., and Weinstock, I. (2001). A. role of alkali metal cation size in the energy and rate of electron transfer to solvent-separated 1:1 [(M⁺)(Acceptor)] (M⁺) Li⁺, Na⁺, K⁺) ion pairs. *J. Am. Chem. Soc.* 123, 5292–5307. doi: 10.1021/ja010074q
- Grigoriev, V. A., Hill, C. L., and Weinstock, I. (2000). A. role of cation size in the energy of electron transfer to 1:1 polyoxometalate ion pairs {(M⁺)(Xⁿ⁺VW₁₁O₄₀)}⁽⁸⁻ⁿ⁾⁻ (M = Li, Na, K). *J. Am. Chem. Soc.* 122, 3544–3545. doi: 10.1021/ja993862c
- Gumerova, N. I., and Rompel, A. (2018). Synthesis, structures and applications of electron-rich polyoxometalates. *Nat. Rev. Chem.* 2, 1–20. doi: 10.1038/s41570-018-0112
- Guo, W., Lv, H., Chen, Z., Sullivan, K. P., Lauinger, S. M., Chi, Y., et al. (2016). Self-assembly of polyoxometalates, Pt nanoparticles and metal-organic frameworks into a hybrid material for synergistic hydrogen evolution. *J. Mater. Chem. A* 4, 5952–5957. doi: 10.1039/C6TA00011H
- Haimov, A., and Neumann, R. (2006). An example of lipophiloselectivity the preferred oxidation, in water, of hydrophobic 2-Alkanols catalyzed by a cross-linked polyethyleneimine-polyoxometalate catalyst assembly. *J. Am. Chem. Soc.* 128, 15697–15700. doi: 10.1021/ja064294l
- Han, J. W., and Hill, C. L. (2007). A coordination network that catalyzes O₂-based oxidations. *J. Am. Chem. Soc.* 129, 15094–15095. doi: 10.1021/ja069319v
- He, W. W., Li, S. L., Zang, H. Y., Yang, G. S., Zhang, S. R., Su, Z. M., et al. (2014). Entangled structures in polyoxometalate-based coordination polymers. *Coord. Chem. Rev.* 279, 141–160. doi: 10.1016/j.ccr.2014.03.022
- Hill, C. L. (1998). Introduction polyoxometalates—multicomponent molecular vehicles to probe fundamental issues and practical problems. *Chem. Rev.* 98, 1–2. doi: 10.1021/cr960395y
- Hill, C. L. (2004). “Polyoxometalates reactivity,” in *Comprehensive Coordination Chemistry-II From Biology to Nanotechnology Comprehensive Coordination Chemistry II*, eds A. G. Wedd (Oxford: Elsevier Ltd) 4, 679–759. doi: 10.1002/chin.200440228
- Hill, C. L., Anderson, T. M., Han, J., Hillesheim, D. A., Geletii, Y. V., Okun, N. M., et al. (2006). New complexes and materials for O₂-based oxidations. *J. Mol. Catal. A Chem.* 251, 234–238. doi: 10.1016/j.molcata.2006.02.046
- Hill, C. L., and Kholdeeva, O. A. (2013). “Selective liquid phase oxidations in the presence of supported polyoxometalates,” in *Liquid Phase Oxidation via Heterogeneous Catalysis Organic Synthesis and Industrial Applications*, eds M. G. Clerici, and O. A. Kholdeeva (Hoboken, NJ: John Wiley and Sons, Inc), 263–319.
- Hill, C. L., and Prosser-McCarthy, C. M. (1995). Homogeneous catalysis by transition metal oxygen anion clusters. *Coord. Chem. Rev.* 143, 407–455.
- Hu, M.-B., Xia, N., Yu, W., Ma, C., Tang, J., Hou, Z.-Y., et al. (2012). A click chemistry approach to the efficient synthesis of

- polyoxometalate-polymer hybrids with well-defined structures. *Polym. Chem.* 3:617. doi: 10.1039/c2py00546h
- Ji, Y., Huang, L., Hu, J., Streb, C., and Song, Y.-F. (2015). Polyoxometalate-functionalized nanocarbon materials for energy conversion, energy storage and sensor systems. *Energy Environ. Sci.* 8, 776–189. doi: 10.1039/C4EE03749A
- Kinnan, M. K., Creasy, W. R., Fullmer, L. B., Schreuder-Gibson, H. L., and Nyman, M. (2014). Nerve agent degradation with polyoxoniobates. *Eur. J. Inorg. Chem.* 2014, 2361–2367. doi: 10.1002/ejic.201400016
- Kozhevnikov, I. V. (1998). Catalysis by heteropoly acids and multicomponent polyoxometalates in liquid-phase reactions. *Chem. Rev.* 98, 171–198. doi: 10.1021/cr960400y
- Kozhevnikov, I. V. (2002). *Catalysis by Polyoxometalates*. Chichester: Wiley.
- Kwon, T., Tsigdinos, G. A., and Pinnavaia, T. J. (1988). Pillaring of layered double hydroxides (LDHs) by polyoxometalate anions. *J. Am. Chem. Soc.* 110, 3653–3654. doi: 10.1021/ja00219a048
- Lauinger, S. M., Piercy, B. D., Li, W., Yin, Q., Collins-Wildman, D. L., Glass, E. N., et al. (2017a). Stabilization of polyoxometalate water oxidation catalysts on hematite by atomic layer deposition. *ACS Appl. Mater. Interfaces* 9, 35048–35056. doi: 10.1021/acsami.7b12168
- Lauinger, S. M., Sumliner, J. M., Yin, Q., Xu, Z., Liang, G., Glass, E. N., et al. (2015). High stability of immobilized polyoxometalates on TiO₂ nanoparticles and nanoporous films for robust, light-induced water oxidation. *Chem. Mater.* 27, 5886–5891. doi: 10.1021/acs.chemmater.5b01248
- Lauinger, S. M., Yin, Q., Geletii, Y. V., and Hill, C. L. (2017b). “Polyoxometalate multielectron catalysts in solar fuel production,” in *Advances in Inorganic Chemistry Polyoxometallate Chemistry, 1st Edn*, eds L. Cronin and R. V. Eldik (Oxford: Elsevier), 69, 117–154.
- Launay, J. P. (1976). Reduction of the metatungstate ion. high levels of reduction of H₂W₁₂O₄₀⁶⁻, derivatives of the ion HW₁₂O₄₀⁷⁻, and general discussion. *J. Inorg. Nucl. Chem.* 38, 807–816. doi: 10.1016/0022-1902(76)80361-2
- Li, J., Güttinger, R., Moré, R., Song, F., Wan, W., and Patzke, G. R. (2017). Frontiers of water oxidation the quest for true catalysts. *Chem. Soc. Rev.* 46, 6124–6147. doi: 10.1039/C7CS00306D
- Li, T., Miras, H. N., and Song, Y.-F. (2017). Polyoxometalate (POM)-layered double hydroxides (LDH) composite materials design and catalytic applications. *Catalysis* 7:260. doi: 10.3390/catal7090260
- Long, D. L., Burkholder, E., and Cronin, L. (2007). Polyoxometalate clusters, nanostructures and materials: from self assembly to designer materials and devices. *Chem. Soc. Rev.* 36, 105–121. doi: 10.1039/B502666K
- Long, D. L., Tsunashima, R., and Cronin, L. (2010). Polyoxometalates building blocks for functional nanoscale systems. *Angew. Chem. Int. Ed.* 49, 1736–1758. doi: 10.1002/anie.200902483
- Luong, T. K. N., Shestakova, P., Absillis, G., and Parac-Vogt, T. N. (2016). Detailed mechanism of phosphonohydride bond hydrolysis promoted by a binuclear Zr^{IV}-substituted keggin polyoxometalate elucidated by a combination of ³¹P, ³¹P DOSY, and ³¹P EXSY NMR spectroscopy. *Inorg. Chem.* 55, 4864–4873. doi: 10.1021/acs.inorgchem.6b00385
- Lv, H., Chi, Y., Leusen, J. V., Kögerler, P., Chen, Z., Bacsá, J., et al. (2015). [(Ni₄(OH)₃AsO₄)₄(B-α-PW₉O₃₄)₄]²⁸⁻ A new polyoxometalate structural family with catalytic hydrogen evolution activity. *Chem. Eur. J.* 21, 17363–17370. doi: 10.1002/chem.201503010
- Lv, H., Gao, Y., Guo, W., Lauinger, S. M., Chi, Y., Bacsá, J., et al. (2016). A Cu-based polyoxometalate catalyst for efficient catalytic hydrogen evolution. *Inorg. Chem.* 55, 6750–6758. doi: 10.1021/acs.inorgchem.6b01032
- Lv, H., Guo, W., Wu, K., Chen, Z., Bacsá, J., Musaev, D. G., et al. (2014). A noble-metal-free, tetra-nickel polyoxotungstate catalyst for efficient photocatalytic hydrogen evolution. *J. Am. Chem. Soc.* 136, 14015–14018. doi: 10.1021/ja5084078
- Ma, F. J., Liu, S. X., Sun, C. Y., Liang, D. D., Ren, G. J., Wei, F., et al. (2011). A sodalite-type porous metal-organic framework with polyoxometalate templates: adsorption and decomposition of dimethyl methylphosphonate. *J. Am. Chem. Soc.* 133, 4178–4181. doi: 10.1021/ja109659k
- Macdonell, A., Johnson, N. A., Surman, A. J., Cronin, L. (2015). Configurable nanosized metal oxide oligomers via precise “Click” coupling control of hybrid polyoxometalates. *J. Am. Chem. Soc.* 137, 5662–5665. doi: 10.1021/jacs.5b02466
- Miras, H. N., Yan, J., Long, D. L., and Cronin, L. (2012). Engineering polyoxometalates with emergent properties. *Chem. Soc. Rev.* 41, 7403–7430. doi: 10.1039/c2cs35190k
- Mizuno, N., and Misono, M. (1998). Heterogeneous catalysis. *Chem. Rev.* 98, 199–218. doi: 10.1021/cr960401q
- Moffat, J. B. (2001). *Metal-Oxygen Clusters The Surface and Catalytic Properties of Heteropoly Oxometalates*. New York, NY: Kluwer Academic/Plenum Publishers.
- Mondloch, J. E., Katz, M. J. III, William, C. I. III, Ghosh, P., Liao, P., Bury, W., et al. (2015). Destruction of chemical warfare agents using metal-organic frameworks. *Nat. Mater.* 14, 512–516. doi: 10.1038/nmat4238
- Nlate, S., and Jahier, C. (2012). Dendritic polyoxometalate hybrids: efficient and recoverable catalysts for oxidation reactions. *Eur. J. Inorg. Chem.* 2013, 1606–1619. doi: 10.1002/ejic.201201129
- Nyman, M. (2017). Small-angle X-ray scattering to determine solution speciation of metal-oxo clusters. *Coord. Chem. Rev.* 352, 461–472. doi: 10.1016/j.ccr.2016.11.014
- Okuhara, T., Mizuno, N., and Misono, M. (1996). Catalytic chemistry of heteropoly compounds. *Adv. Catal.* 41, 113–252. doi: 10.1016/S0360-0564(08)60041-3
- Omwoma, S., Chen, W., Tsunashima, R., and Song, Y.-F. (2014). Recent advances on polyoxometalates intercalated layered double hydroxides from synthetic approaches to functional material applications. *Coord. Chem. Rev.* 258–259, 58–71. doi: 10.1016/j.ccr.2013.08.039
- Omwoma, S., Gore, C. T., Ji, Y., Hu, C., and Song, Y.-F., (2015). Environmentally benign polyoxometalate materials. *Coord. Chem. Rev.* 286, 17–29. doi: 10.1016/j.ccr.2014.11.013
- Orlandi, M., Argazzi, R., Sartorel, A., Carraro, M., Scorrano, G., Bonchio, M., et al. (2010). Ruthenium polyoxometalate water splitting catalyst very fast hole scavenging from photogenerated oxidants. *Chem. Commun.* 46, 3152–3154. doi: 10.1039/b926823e
- Patel, A., Narkhede, N., Singh, S., and Pathan, S. (2016). Keggin-type lacunary and transition metal substituted polyoxometalates as heterogeneous catalysts: a recent progress. *Catal. Rev.* 58, 337–370. doi: 10.1080/01614940.2016.1171606
- Pope, M. T. (1983). *Heteropoly and Isopoly Oxometalates*. Berlin: Springer-Verlag.
- Pope, M. T. (2004). “Polyoxo anions synthesis and structure,” in *Comprehensive Coordination Chemistry II From Biology to Nanotechnology Comprehensive Coordination Chemistry II*, ed A. G. Wedd (Oxford: Elsevier Ltd), 635–678.
- Pratt, H. D. III., Hudak, N. S., Fang, X., and Anderson, T. M. (2013). A polyoxometalate flow battery. *J. Pow. Sour.* 236, 259–264. doi: 10.1016/j.jpowsour.2013.02.056
- Proust, A., Matt, B., Villanneau, R., Guillemot, G., Gouzerh, P., and Izzet, G. (2012). Functionalization and post-functionalization a step towards polyoxometalate-based materials. *Chem. Soc. Rev.* 41, 7605–7622. doi: 10.1039/c2cs35119f
- Qi, W., and Wu, L. (2009). Polyoxometalate / polymer hybrid materials fabrication and properties. *Polym. Int.* 58, 1217–1225. doi: 10.1002/pi.2654
- Ren, Y., Wang, M., Chen, X., Yue, B., and He, H. (2015). Heterogeneous catalysis of polyoxometalate based organic-inorganic hybrids. *Materials* 8, 1545–1567. doi: 10.3390/ma8041545
- Rieger, J., Antoun, T., Lee, S. H., Chenal, M., Pembouong, G., de la Haye, J. et al. (2012). Synthesis and characterization of a thermoresponsive polyoxometalate-polymer hybrid. *Chem. Eur. J.* 18, 3355–3361. doi: 10.1002/chem.201101771
- Sambrook, M. R., and Notman, S. (2013). Supramolecular chemistry and chemical warfare agents from fundamentals of recognition to catalysis and sensing. *Chem. Soc. Rev.* 42, 9251–9267. doi: 10.1039/c3cs60230c
- Sara, G.-F., Joaquín, S.-L., Ramón, G.-M. J., and May, N. (2015). Solution speciation and stability of cobalt-polyoxometalate water oxidation catalysts by X-ray scattering. *Eur. J. Inorg. Chem.* 2015, 2833–2840. doi: 10.1002/ejic.201500404
- Sartorel, A., Carraro, M., Scorrano, G., Zorzi, R. D., Geremia, S., McDaniel, N. D., et al. (2008). Polyoxometalate embedding of a tetraruthenium(IV)-oxo-core by template-directed metalation of [γ-SiW₁₀O₃₆]⁸⁻ a totally inorganic oxygen-evolving catalyst. *J. Am. Chem. Soc.* 130, 5006–5007. doi: 10.1021/ja077837f
- Sivakumar, R., Thomas, J., and Yoon, M. (2012). Polyoxometalate-based molecular/nano composites: advances in environmental remediation by photocatalysis and biomimetic approaches to solar energy conversion. *J. Photochem. Photobiol. C Photochem. Rev.* 13, 277–298. doi: 10.1016/j.jphotochemrev.2012.08.001

- Song, J., Luo, Z., Britt, D., Furukawa, H., Yaghi, O. M., Hardcastle, K. I., et al. (2011). A multi-unit catalyst with synergistic stability and reactivity A polyoxometalate-metal organic framework for aerobic decontamination. *J. Am. Chem. Soc.* 133, 16839–16846. doi: 10.1021/ja203695h
- Song, Y. F., and Tsunashima, R. (2012). Recent advances on polyoxometalate-based molecular and composite materials. *Chem. Soc. Rev.* 41, 7384–7402. doi: 10.1039/c2cs35143a
- Steens, N., Ramadan, A. M., Absillis, G., and Parac-Vogt, T. N. (2010). Hydrolytic cleavage of DNA-model substrates promoted by polyoxovanadates. *Dalton Trans.* 39, 585–592. doi: 10.1039/B913471A
- Stracke, J. J., and Finke, R. G. (2011). Electrocatalytic water oxidation beginning with the cobalt polyoxometalate $[\text{Co}_4(\text{H}_2\text{O})_2(\text{PW}_9\text{O}_{34})_2]^{10-}$ identification of heterogeneous CoOx as the dominant catalyst. *J. Am. Chem. Soc.* 133, 14872–14875. doi: 10.1021/ja205569j
- Stracke, J. J., and Finke, R. G. (2014). Distinguishing homogeneous from heterogeneous water oxidation catalysis when beginning with polyoxometalates. *ACS Catal.* 4, 909–933. doi: 10.1021/cs4011716
- Suárez-Guevara, J., Ruiz, V., and Gomez-Romero, P. (2014). Hybrid energy storage high voltage aqueous supercapacitors based on activated carbon-phosphotungstate hybrid materials. *J. Mater. Chem. A* 2, 1014–1021. doi: 10.1039/C3TA14455K
- Suen, N.-T., Hung, S.-F., Quan, Q., Zhang, N., Xu, Y.-J., and Chen, H. (2017). M. Electrocatalysis for the oxygen evolution reaction recent development and future perspectives. *Chem. Soc. Rev.* 46, 337–365. doi: 10.1039/C6CS00328A
- Sullivan, K. P., Neiwert, W. A., Zeng, H., Mehta, A. K., Yin, Q., Hillesheim, D. A., et al. (2017). Polyoxometalate-based gelating networks for entrapment and catalytic decontamination. *Chem. Commun.* 53, 11480–11483. doi: 10.1039/C7CC05657E
- Sumliner, J. M., Lv, H., Fielden, J., Geletii, Y. V., Hill, C. L. (2014). Polyoxometalate multi-electron-transfer catalytic systems for water splitting. *Eur. J. Inorg. Chem.* 2014, 635–644. doi: 10.1002/ejic.201301573
- Taleghani, S., Mirzaei, M., Eshtiagh-Hosseini, H., and Frontera, A. (2016). Tuning the topology of hybrid inorganic-organic materials based on the study of flexible ligands and negative charge of polyoxometalates A crystal engineering perspective. *Coord. Chem. Rev.* 309, 84–106. doi: 10.1016/j.ccr.2015.10.004
- Vickers, J. W., Lv, H., Sumliner, J. M., Zhu, G., Luo, Z., Musaev, D. G., et al. (2013). Differentiating homogeneous and heterogeneous water oxidation catalysis confirmation that $[\text{Co}_4(\text{H}_2\text{O})_2(\alpha\text{-PW}_9\text{O}_{34})_2]^{10-}$ is a molecular water oxidation catalyst. *J. Am. Chem. Soc.* 135, 14110–14118. doi: 10.1021/ja4024868
- Walsh, J. J., Bond, A. M., Forster, R. J., and Keyes, T. E. (2016). Hybrid polyoxometalate materials for photo(electro-) chemical applications. *Coord. Chem. Rev.* 306, 217–234. doi: 10.1016/j.ccr.2015.06.016
- Wang, H., Hamanaka, S., Nishimoto, Y., Irle, S., Yokoyama, T., Yoshikawa, H., et al. (2012). In operando X-ray absorption fine structure studies of polyoxometalate molecular cluster batteries polyoxometalates as electron sponges. *J. Am. Chem. Soc.* 134, 4918–4924. doi: 10.1021/ja2117206
- Wang, M.-Y., Ma, R., and He, L.-N. (2016). Polyoxometalate-based ionic liquids-promoted CO_2 conversion. *Sci. China Chem.* 59, 507–516. doi: 10.1007/s11426-016-5560-9
- Wang, S. S., and Yang, G. Y. (2015). Recent advances in polyoxometalate-catalyzed reactions. *Chem. Rev.* 115, 4893–4962. doi: 10.1021/cr500390v
- Wu, H., Yang, H.-K., and Wang, W. (2016). Covalently-linked polyoxometalate-polymer hybrids optimizing synthesis, appealing structures and prospective applications. *New J. Chem.* 40, 886–897. doi: 10.1039/C5NJ01257K
- Wu, X., Li, F., Zhang, B., and Sun, L. (2015). Molecular complexes in water oxidation Pre-catalysts or real catalysts. *J. Photochem. Photobiol. C Photochem. Rev.* 25, 71–89. doi: 10.1016/j.jphotochemrev.2015.07.002
- Xiang, X., Fielden, J., Rodríguez-Córdoba, W., Huang, Z., Zhang, N., Luo, Z., et al. (2013). Electron transfer dynamics in semiconductor-chromophore-polyoxometalate catalyst photoanodes. *J. Phys. Chem. C* 117, 918–926. doi: 10.1021/jp312092u
- Xiao, Z., Chen, K., Wu, B., Li, W., Wu, P., and Wei, Y. (2016). An easy way to construct polyoxovanadate-based organic-inorganic hybrids by stepwise functionalization. *Eur. J. Chem.* 2016, 808–811. doi: 10.1002/ejic.201501297
- Yamase, T., and Pope, M. T. (2006). *Polyoxometalate Chemistry for Nano-Composite Design* New York, NY: Kluwer Academic Publishers.
- Yin, Q., and Hill, C. L. (2017). Passing the acid test. *Nat. Chem.* 10, 6–7. doi: 10.1038/nchem.2921
- Yin, Q., Tan, J. M., Besson, C., Geletii, Y. V., Musaev, D. G., Kuznetsov, A. E., et al. (2010). A fast soluble carbon-free molecular water oxidation catalyst based on abundant metals. *Science* 328, 342–345. doi: 10.1126/science.1185372
- Zhang, B., Yin, P., Haso, F., Hu, L., and Liu, T. (2014). Soft matter approaches for enhancing the catalytic capabilities of polyoxometalate clusters. *J. Cluster Sci.* 25, 695–710. doi: 10.1007/s10876-013-0643-7
- Zhao, C., Huang, Z., Rodríguez-Córdoba, W., Kambara, C. S., O'Halloran, K. P., Hardcastle, K. I., et al. (2011). Synthesis and characterization of a metal-to-polyoxometalate charge transfer molecular chromophore. *J. Am. Chem. Soc.* 133, 20134–20137. doi: 10.1021/ja209360x
- Zhao, C., Rodríguez-Córdoba, W., Kaledin, A. L., Yang, Y., Geletii, Y. V., Lian, T. et al. (2013). An inorganic chromophore based on a molecular oxide supported metal carbonyl cluster $[\text{P}_2\text{W}_{17}\text{O}_{61}\{\text{Re}(\text{CO})_3\}_3\{\text{ORb}(\text{H}_2\text{O})\}(\mu_3\text{-OH})]^{9-}$. *Inorg. Chem.* 52, 13490–13495. doi: 10.1021/ic4018823
- Zhao, S., Xu, J., Wei, M., and Song, Y.-F. (2011). Synergistic catalysis by polyoxometalate-intercalated layered double hydroxides oximation of aromatic aldehydes with large enhancement of selectivity. *Green Chem.* 13, 384–389. doi: 10.1039/c0gc00664e
- Zhou, Y., Guo, Z., Hou, W., Wang, Q., and Wang, J. (2015). Polyoxometalate-based phase transfer catalysis for liquid-solid organic reactions: a review. *Catal. Sci. Technol.* 5, 4324–4335. doi: 10.1039/C5CY00674K
- Zonnevijlle, F., and Pope, M. T. (1979). Attachment of organic groups to heteropoly oxometalate anions. *J. Am. Chem. Soc.* 101, 2731–2732. doi: 10.1021/ja00504a040

Conflict of Interest Statement: The authors declare that the research was conducted in the absence of any commercial or financial relationships that could be construed as a potential conflict of interest.

Copyright © 2018 Sullivan, Yin, Collins-Wildman, Tao, Geletii, Musaev, Lian and Hill. This is an open-access article distributed under the terms of the Creative Commons Attribution License (CC BY). The use, distribution or reproduction in other forums is permitted, provided the original author(s) and the copyright owner(s) are credited and that the original publication in this journal is cited, in accordance with accepted academic practice. No use, distribution or reproduction is permitted which does not comply with these terms.



Photoinduced Oxygen Evolution Catalysis Promoted by Polyoxometalate Salts of Cationic Photosensitizers

Joaquín Soriano-López^{1,2}, Fangyuan Song³, Greta R. Patzke^{3*} and J. R. Galan-Mascaros^{1,4*}

¹ Institute of Chemical Research of Catalonia, Barcelona Institute of Science and Technology, Tarragona, Spain,

² Departament de Química Física i Inorgànica, Universitat Rovira i Virgili, Tarragona, Spain, ³ Department of Chemistry, University of Zurich, Zurich, Switzerland, ⁴ ICREA, Passeig Lluís Companys, Barcelona, Spain

OPEN ACCESS

Edited by:

Soumyajit Roy,
Indian Institute of Science Education
and Research Kolkata, India

Reviewed by:

Graham Newton,
University of Nottingham,
United Kingdom
Samar Kumar Das,
University of Hyderabad, India

*Correspondence:

Greta R. Patzke
greta.patzke@chem.uzh.ch
J. R. Galan-Mascaros
jrgalan@icicq.es

Specialty section:

This article was submitted to
Inorganic Chemistry,
a section of the journal
Frontiers in Chemistry

Received: 30 April 2018

Accepted: 03 July 2018

Published: 14 August 2018

Citation:

Soriano-López J, Song F, Patzke GR
and Galan-Mascaros JR (2018)
Photoinduced Oxygen Evolution
Catalysis Promoted by
Polyoxometalate Salts of Cationic
Photosensitizers. *Front. Chem.* 6:302.
doi: 10.3389/fchem.2018.00302

The insoluble salt $\text{Cs}_{15}\text{K}[\text{Co}_9(\text{H}_2\text{O})_6(\text{OH})_3(\text{HPO}_4)_2(\text{PW}_9\text{O}_{34})_3]$ (**CsCo₉**) is tested as heterogeneous oxygen evolution catalyst in light-induced experiments, when combined with the homogeneous photosensitizer $[\text{Ru}(\text{bpy})_3]^{2+}$ and the oxidant $\text{Na}_2\text{S}_2\text{O}_8$ in neutral pH. Oxygen evolution occurs in parallel to a solid transformation. Post-catalytic essays indicate that the **CsCo₉** salt is transformed into the corresponding $[\text{Ru}(\text{bpy})_3]^{2+}$ salt, upon cesium loss. Remarkably, analogous photoactivated oxygen evolution experiments starting with the $[\text{Ru}(\text{bpy})_3]_{(5+x)}\text{K}_{(6-2x)}[\text{Co}_9(\text{H}_2\text{O})_6(\text{OH})_3(\text{HPO}_4)_2(\text{PW}_9\text{O}_{34})_3] \cdot (39+x)\text{H}_2\text{O}$ (**RuCo₉**) salt demonstrate much higher efficiency and kinetics. The origin of this improved performance is at the cation-anion, photosensitizer-catalyst pairing in the solid state. This is beneficial for the electron transfer event, and for the long-term stability of the photosensitizer. The latter was confirmed as the limiting process during these oxygen evolution reactions, with the polyoxometalate catalyst exhibiting robust performance in multiple cycles, upon addition of photosensitizer, and/or oxidant to the reaction mixture.

Keywords: water splitting, oxygen evolution, polyoxometalates, photosensitizer, cobalt

INTRODUCTION

Sunlight is the preferred carbon-neutral energy source for competing with fossil fuels for energy production, because solar radiation is readily accessible at almost any location on the surface of the Earth (Cook et al., 2010). Artificial photosynthesis aims to mimic natural photosynthesis, where sunlight is stored in the form of chemical bonds through reduction of CO_2 into sugars, employing H_2O as the ultimate source of electrons (Mcevoy and Brudvig, 2006). Therefore, an artificial photosynthesis device would convert sunlight into spatially separated electron/hole pairs and store its energy subsequently into chemical bonds by means of water splitting, obtaining hydrogen as a clean fuel together with oxygen as the only side product (Lewis and Nocera, 2006; Balzani et al., 2008; Barber, 2009). Unfortunately, the market introduction of commercial artificial photosynthesis devices is still hampered by the lack of robust, inexpensive and efficient water oxidation catalysts (WOCs) (Dau et al., 2010; Seh et al., 2017).

Over the last decades, scientists have reported a wide variety of new WOCs. Homogeneous organometallic compounds work at fast oxygen evolution rates and offer good processability (Concepcion et al., 2008, 2009; Bozoglian et al., 2009; Blakemore et al., 2010; Xu et al., 2010; Lloret-Fillol et al., 2011; Mccool et al., 2011; Barnett et al., 2012; Duan et al., 2012; Liu and Wang, 2012; Zhang et al., 2013; Goberna-Ferrón et al., 2014). However, they often suffer from limited long-term stability due to oxidative degradation of the organic ligands in the harsh working conditions needed for water oxidation. Precious-metal-based WOCs, for instance Ir-, and Ru-based materials, have shown superior performance and stability for water oxidation catalysis (Pillai et al., 2000; Youngblood et al., 2009; Blakemore et al., 2010; Duan et al., 2012). Unfortunately, the high production price due to metal scarcity questions their viable implementation into commercial devices. Earth abundant transition metal oxides and perovskites are a robust alternative, but exclusively in alkaline media (Galán-Mascarós, 2015). Therefore, alternatives to the current state-of-the-art catalysts are needed.

Polyoxometalates (POMs) have recently appeared as a promising new catalyst class (Geletii et al., 2008; Sartorel et al., 2008). When employed as WOCs, they combine the most appealing features of homogeneous and heterogeneous materials, and many of them can be obtained from inexpensive raw materials. They are all-inorganic molecular clusters with high stability under strongly oxidizing conditions. At the same time, their molecular nature provides access to the tunability and superior processing capabilities of homogeneous catalysts for their easier implementation into devices (Pope, 1983; Pope and Müller, 2001). POMs have shown high catalytic activity in water oxidation over a remarkable pH range (0-10), and they retain their catalytic activity under heterogeneous conditions as their corresponding insoluble salts, or when anchored onto solid supports (Wu et al., 2012; Guo et al., 2013; Quintana et al., 2013; Soriano-López et al., 2013).

Among polyoxometalates, the cobalt-containing POMs (Co-POMs) have emerged as the most promising WOCs due to their high efficiency and kinetics (Goberna-Ferrón et al., 2012; Lv et al., 2012, 2014; Evangelisti et al., 2013). After Hill et al. reported the OER activity of the $[\text{Co}_4(\text{H}_2\text{O})_2(\text{PW}_9\text{O}_{34})_2]^{10-}$ polyanion (Yin et al., 2010; Huang et al., 2011; Stracke and Finke, 2011, 2013, 2014), we turned our attention to the high nuclearity $[\text{Co}_9(\text{H}_2\text{O})_6(\text{OH})_3(\text{HPO}_4)_2(\text{PW}_9\text{O}_{34})_3]^{16-}$ (Goberna-Ferrón et al., 2012, 2015; Soriano-López et al., 2013; **Co₉**, **Figure 1**). **Co₉** shows good activity for photo-assisted water oxidation in homogeneous conditions, exhibiting fast charge transfer kinetics with the model $[\text{Ru}(\text{bpy})_3]^{2+}$ photosensitizer (bpy = 1,2-dipyridyl; Natali et al., 2017). It is also active in the solid state when processed as an insoluble salt with alkaline metal counteranions (Soriano-López et al., 2013).

In this work we report the next required step on the road to technological applications for **Co₉** in an artificial photosynthesis platform, namely its combination with a photosensitizer in a light-induced process in heterogeneous conditions. These essays have been very successful with other POMs and

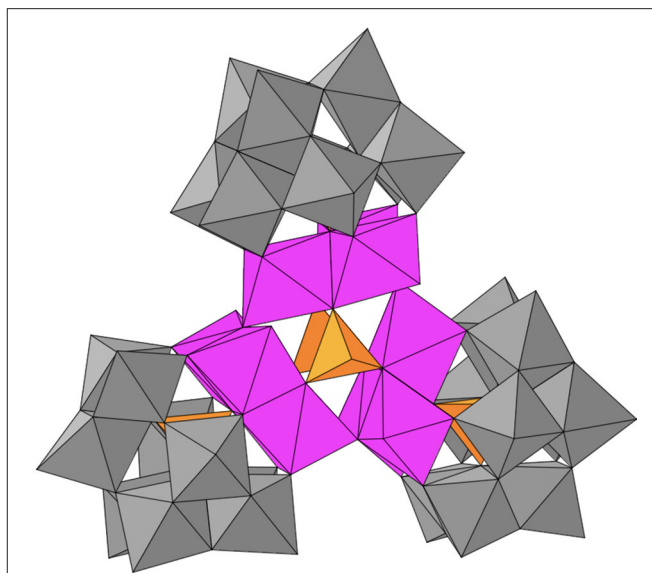


FIGURE 1 | Polyhedral representation of the polyanion $[\text{Co}_9(\text{H}_2\text{O})_6(\text{OH})_3(\text{HPO}_4)_2(\text{PW}_9\text{O}_{34})_3]^{16-}$ (**Co₉**); WO_6 , gray octahedra; PO_4 , orange tetrahedra; CoO_6 , pink octahedra.

water oxidation catalysts to assess photo-induced catalytic performance, mechanistic considerations, and stability issues (Puntoriero et al., 2010; Gao et al., 2013; Sartorel et al., 2013; Al-Oweini et al., 2014; Xiang et al., 2014; Natali et al., 2017). Our experiments confirm the efficient electron transfer between catalyst and sensitizer, even when both species are combined into an insoluble salt. The latter opens up interesting possibilities for future combinations of cationic photosensitizers with polyanionic WOCs for the construction of compact functional photoelectrodes.

EXPERIMENTAL SECTION

Materials and Synthesis

Tris(2,2'-bipyridyl)dichlororuthenium(II) hexahydrate and sodium persulfate were purchased from TCI and Sigma-Aldrich (>99% purity) and used without further purification. The synthesis of $\text{Cs}_{15}\text{K}[\text{Co}_9(\text{H}_2\text{O})_6(\text{OH})_3(\text{HPO}_4)_2(\text{PW}_9\text{O}_{34})_3] \cdot 39\text{H}_2\text{O}$ (**CsCo₉**) was already reported (Soriano-López et al., 2013). $[\text{Ru}(\text{bpy})_3]_{(5+x)}\text{K}_{(6-2x)}[\text{Co}_9(\text{H}_2\text{O})_6(\text{OH})_3(\text{HPO}_4)_2(\text{PW}_9\text{O}_{34})_3] \cdot (39+x)\text{H}_2\text{O}$ (**RuCo₉**) was prepared by metathesis: A stoichiometric excess of $[\text{Ru}(\text{bpy})_3]\text{Cl}_2$ was added to a solution containing $\text{Na}_8\text{K}_8[\text{Co}_9(\text{H}_2\text{O})_6(\text{OH})_3(\text{HPO}_4)_2(\text{PW}_9\text{O}_{34})_3] \cdot 43\text{H}_2\text{O}$ (**KCo₉**). **RuCo₉** immediately precipitated as an orange powder. It was filtered, washed with water and acetone, and air-dried.

Material Characterizations

Elemental CHN analysis was performed with an Elemental Microanalyzer Flash model 1112. Detection of Co, Ru, and W was performed on an inductively coupled plasma atomic emission spectrometer iCap 6500 (Thermo Fisher Scientific), and

K was detected on a 2,380 atomic absorption spectrophotometer (Perkin-Elmer), both by Mikroanalytisches Labor Pascher (Remagen/Germany). Thermogravimetric analyses were performed with powder samples using a TGA/SDTA851 Mettler Toledo with a MT1 microbalance. Dynamic light scattering was used to measure the particle size distribution employing a Malvern NanoZS analyzer. FT-IR spectra were collected in the $3600\text{--}400\text{ cm}^{-1}$ range with a Bruker Optics FTIR Alpha spectrometer equipped with a DTGS detector and a KBr beamsplitter at 4 cm^{-1} resolution. Raman measurements were acquired using a Renishaw inVia Reflex Raman confocal microscope (Gloucestershire, UK) equipped with a diode laser emitting at 785 nm at a nominal power of 300 mW , and a Peltier-cooled CCD detector (-70°C) coupled to a Leica DM-2500 microscope. X-ray photoelectron spectroscopy (XPS) (K-ALPHA, Thermo Scientific SSTTI at University of Alicante) was used to analyze the surface of the samples. All spectra were collected using Al-K_{α} radiation (1486.6 eV), monochromatized by a twin crystal monochromator, yielding a focused X-ray spot with a diameter of $400\text{ }\mu\text{m}$, at $3\text{ mA} \times 12\text{ kV}$. The alpha hemispherical analyzer was operated in the whole energy band, and 50 eV in a narrow scan to selectively measure the particular elements.

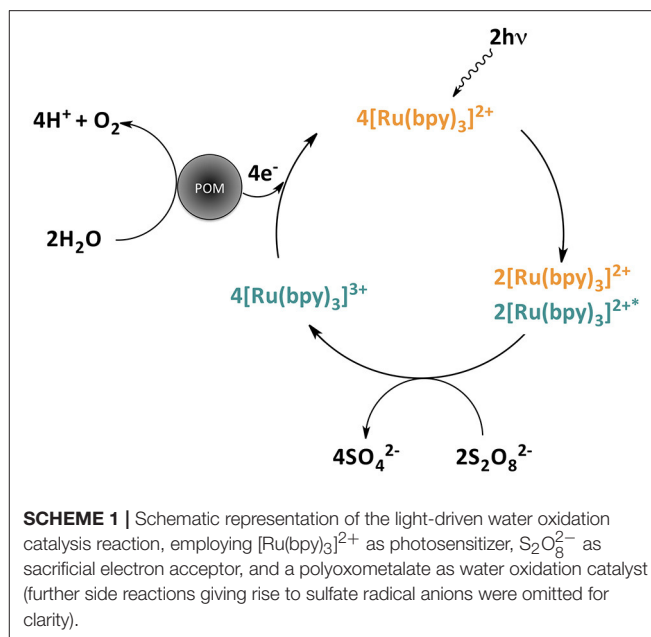
Photoinduced Water Oxidation Catalysis

Oxygen evolution experiments were performed in a 6.7 mL headspace Schlenk tube sealed with a rubber septum (PFTE). The Schlenk tube was covered with aluminum foil, in order to avoid an early light-induced reaction of the system, and filled with 1 mM (9.4 mg) $[\text{Ru}(\text{bpy})_3]\text{Cl}_2$, 5 mM (14.9 mg) $\text{Na}_2\text{S}_2\text{O}_8$, the desired amount of catalyst, and 12.5 mL of 40 mM KP_1 buffer solution at $\text{pH } 7.0$. Experiments employing the RuCo_9 salt as catalyst were performed with and without addition of $[\text{Ru}(\text{bpy})_3]\text{Cl}_2$, the former for comparison in the same conditions required for Co_3O_4 experiments. Suspensions were completely deaerated by purging with nitrogen. A baseline of 20 min was recorded to ensure that no oxygen leakage or side reactions took place. Next, the system was exposed to the light of a blue LED lamp (wavelength at peak emission = 465 nm ; OSRAM Opto Semiconductors) working at 0.20 A and 11.4 V . The concentration of oxygen in the headspace was measured by employing a O_2 -sensor probe (Ocean Optics NeoFOX oxygen-sensing system equipped with a FOXY probe). Turnover number (TON) and turnover frequency (TOF) were estimated per Co_9 content as obtained from chemical analyses on fresh compounds (see SI).

RESULTS AND DISCUSSION

Visible-Light-Driven Water Oxidation by CsCo_9 in Heterogeneous Conditions

Water oxidation experiments were carried out with $[\text{Ru}(\text{bpy})_3]^{2+}$ as a model photosensitizer and $\text{S}_2\text{O}_8^{2-}$ as sacrificial electron acceptor, in a suspension of the insoluble salt $\text{Cs}_{15}\text{K}[\text{Co}_9(\text{H}_2\text{O})_6(\text{OH})_3(\text{HPO}_4)_2(\text{PW}_9\text{O}_{34})_3]$ (CsCo_9). Light irradiation ($\lambda > 400\text{ nm}$) of this mixture



promotes oxygen evolution, which was monitored using a fluorescence O_2 -sensor probe for increasing amounts of CsCo_9 ($1\text{--}50\text{ mg}$). The proposed net reaction mechanism for light-driven water oxidation catalyzed by POMs is depicted in **Scheme 1**. No oxygen evolution was detected in the absence of any of the components.

The reaction starts with fast kinetics immediately after light irradiation, and slows down until oxygen evolution stops reaching a plateau after 2 h . We analyzed the oxygen production as a function of catalyst content (**Figure 2** and **Table 1**). The highest values of turnover number (TON) and turnover frequency (TOF) obtained were 14.2 and 10.8 h^{-1} , for the minimum quantity used (1 mg , $\approx 0.1\text{ }\mu\text{mol}$). In terms of chemical yield (CY, see SI), a maximum 9.2% was reached for intermediate CsCo_9 contents (10 mg , $\approx 1\text{ }\mu\text{mol}$) in the investigated range. After oxygen evolution, CsCo_9 was recovered from the reaction vessel to perform structural characterization. The FT-IR spectrum shows the typical Co_9 bands within the $1,100\text{--}400\text{ cm}^{-1}$ range, identical to those observed with the freshly made CsCo_9 . We also found additional bands in the region between $1,200$ and $1,600\text{ cm}^{-1}$, which can be attributed to the bipyridyl (bpy) ligand (**Figure S1**). The same information is obtained from the Raman spectra (**Figure S2**). Moreover, comparison of the XPS spectra (**Figure S3**) showed the appearance of intense Ru peaks in the recovered CsCo_9 , and disappearance of the expected Cs peak (**Figure S4**). The data in their entirety suggest that cation exchange occurred under turnover conditions, i.e., Cs^+ cations are replaced by $[\text{Ru}(\text{bpy})_3]^{2+}$ cations. Indeed, the Raman spectrum of the recovered CsCo_9 is reminiscent of the corresponding Raman spectrum of the salt obtained by addition of an excess of $[\text{Ru}(\text{bpy})_3]\text{Cl}_2$ to an aqueous K_{16}Co_9 solution (**Figure S9**).

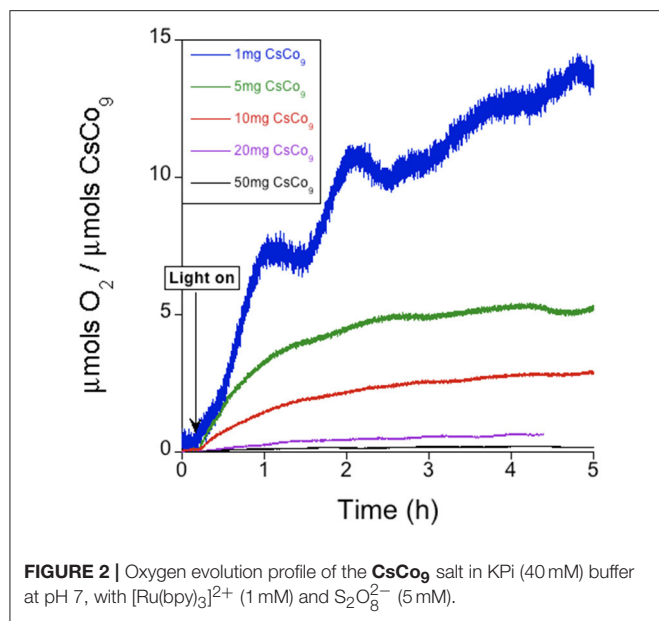


FIGURE 2 | Oxygen evolution profile of the **CsCo₉** salt in KPi (40 mM) buffer at pH 7, with [Ru(bpy)₃]²⁺ (1 mM) and S₂O₈²⁻ (5 mM).

TABLE 1 | Comparison of visible-light-driven oxygen evolution performance of **CsCo₉** and **RuCo₉** catalysts^(a).

POM	Catalyst (mg)	1	5	10	20	50
CsCo ₉ (first run)	TON	14.2	5.3	2.9	0.7	0.2
	TOF (h ⁻¹)	10.8	4.0	1.4	0.3	0.2
	CY (%)	4.4	8.4	9.2	4.0	3.6
RuCo ₉	TON	27.3	20.3	16.7	7.2	2.7
	TOF (h ⁻¹)	19.1	11.9	17.0	9.0	4.3
	CY (%)	7.6	28.4	47.6	42.4	36.4
POM	Catalyst (μm)	0.1	0.5	1	2	5

^aTON, total turnover number after completion of the reaction; TOF, slope of the oxygen evolution curve at the starting time; CY, total chemical yield after completion of the reaction.

Visible-Light-Driven Water Oxidation by RuCo₉ in Heterogeneous Conditions

Addition of an excess of [Ru(bpy)₃]Cl₂ to an aqueous KCo₉ solution forms immediately an insoluble precipitate. The presence of the [Ru(bpy)₃]²⁺ cation and the [Co₉(H₂O)₆(OH)₃(HPO₄)₂(PW₉O₃₄)₃]¹⁶⁻ anion were confirmed by FT-IR spectroscopy (Figure S8) with the signature bands for both molecular species. However, the exact stoichiometry was difficult to completely assess. We carried out elemental CHN analyses, and metal ICP analyses, along with thermogravimetry analyses, and they were not fully consistent (Table S1). It is worthy to note at this point that our attempts to crystallize this compound in order to accurately characterize its composition and structure failed, because slow diffusion between solutions of cation and anion produce insoluble single crystals of the compound [Ru(bpy)₃]₂K₁₂[Co₉(H₂O)₆(OH)₃(HPO₄)₂(PW₉O₃₄)₃]_xH₂O

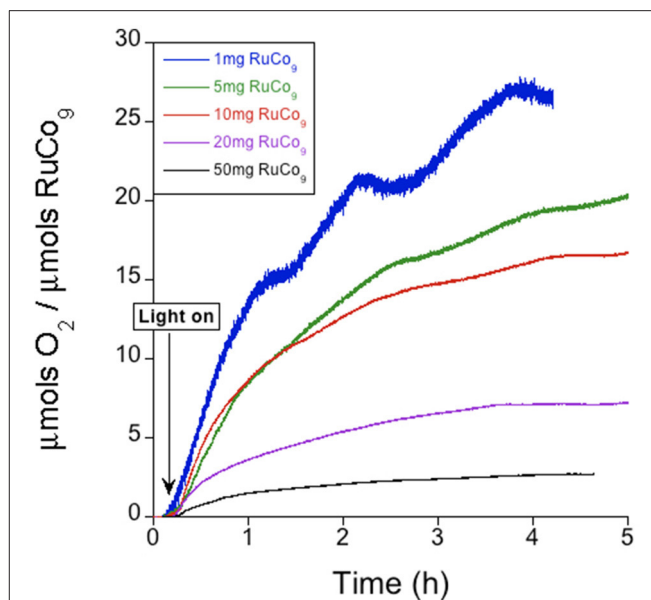


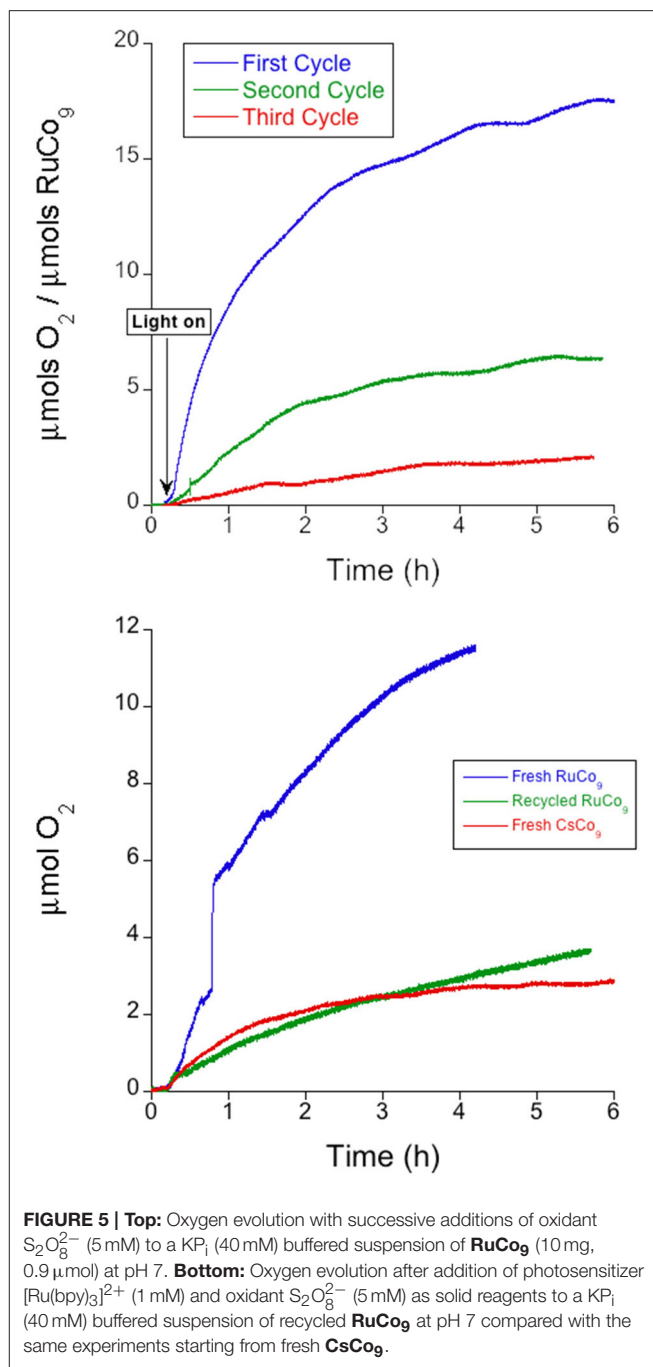
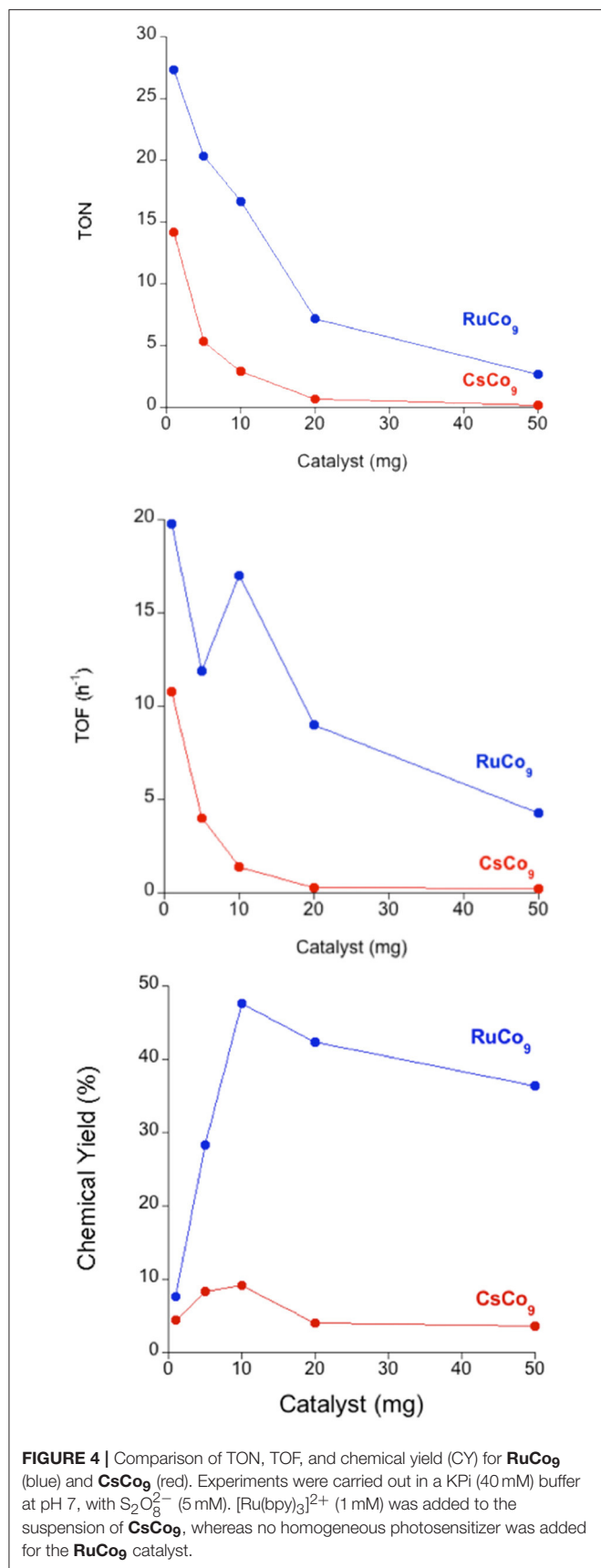
FIGURE 3 | Oxygen evolution profile for solid **RuCo₉** in KPi (40 mM) buffer at pH 7 with S₂O₈²⁻ (5 mM).

(Table S2, Figure S13). This Ru/POM stoichiometry is far too low in comparison with our **RuCo₉** analyses (Table S1), and thus it is not representative of the **RuCo₉** catalyst. The obtention of this crystalline phase, though, precludes the isolation of other salts with higher [Ru(bpy)₃]²⁺ content, closer to the present **RuCo₉** solid. The most plausible explanation is that **RuCo₉** actually consists of a mixture of different [Ru(bpy)₃]/Co₉ salts, and their slightly different solubility and composition gives small deviations depending on the given analytical technique. With all the analytical data taken into account (Table S1), we assign an average stoichiometry [Ru(bpy)₃]_(5+x)K_(6-2x)[Co₉(H₂O)₆(OH)₃(HPO₄)₂(PW₉O₃₄)₃]₁·(39+x)H₂O (**RuCo₉**), where -1 < x < 1 (see Table S1 and Figure S5). This powder is insoluble in water at room temperature with an average particle size of 374 nm (Figure S6).

When a suspension of **RuCo₉** in a solution of S₂O₈²⁻ is irradiated (λ > 400 nm), oxygen evolution starts. In this case, the proposed reaction mechanism is analogous to that depicted in Scheme 1, but with photosensitizer and catalyst bound together in the solid state through electrostatic cation-anion interactions. Remarkably, the measured oxygen evolution in these conditions (Figure 3) is significantly superior to the first run starting from photosensitizer in solution (Table 1 and Figure 4). The maximum TON (27.3) and TOF (19.1 h⁻¹) values are doubled, and the CY showed a remarkable increase up to 47.6%. Pulsed experiments confirmed that oxygen evolves exclusively when the light source is switched on (Figure S7).

Stability of the RuCo₉ System

In order to determine the limiting agent in the photo-assisted oxygen evolution reaction, we carried out different tests.



Successive additions of $\text{S}_2\text{O}_8^{2-}$ to the as-used RuCo_9 suspension indicate that oxygen evolution activity is severely affected after each cycle (Figure 5 and Table 2), i.e., the system can barely perform three cycles before reaching complete deactivation. After deactivation, addition of an aliquot containing the photosensitizer $[\text{Ru}(\text{bpy})_3]^{2+}$ and $\text{S}_2\text{O}_8^{2-}$ to the reaction vessel restarts oxygen evolution, with rates and yields comparable to those obtained with CsCo_9 (Figure 5). This behavior can only be explained with deactivation of the photosensitizer in RuCo_9 recycling experiments, probably due to oxidative degradation of

TABLE 2 | Comparison of the **RuCo₉**-catalyzed light-driven oxygen evolution performance obtained for successive addition of $S_2O_8^{2-}$ (5 mM) to the reaction vessel^a.

	TON	TOF (h ⁻¹)	CY (%)
1st cycle	16.7	17.0	47.6
2nd cycle	6.4	2.7	17.6
3rd cycle	2.1	0.7	5.6

^aTON, total turnover number at the final reaction time; TOF, slope of the oxygen evolution curve at the starting time; CY, total chemical yield at the final reaction time.

the organic ligands, during the harsh working conditions. The catalytic POM appears to be robust, since its performance is maintained during successive cycles.

Analysis of Adventitious CoO_x Formation

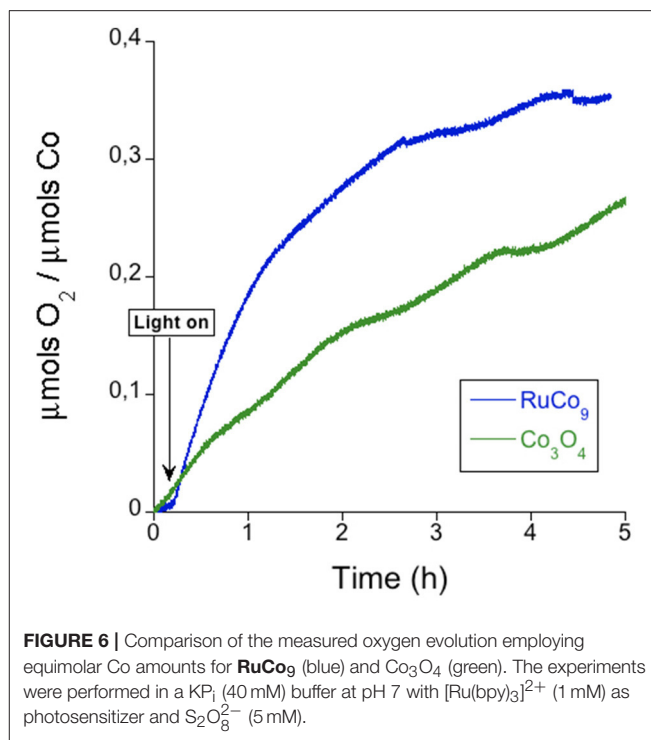
In water oxidation with cobalt-based catalysts, it is fundamental to rule out the *in situ* formation of cobalt oxide CoO_x, a competent heterogeneous WOC. This could occur through Co²⁺ leaching from the **RuCo₉** salt, and the subsequent formation of CoO_x under oxidative conditions. Thus, we analyzed the as-used **RuCo₉** with different experimental techniques in the search for traces of CoO_x.

RuCo₉ was recovered from the reaction vessel after the visible-light-driven water oxidation experiments. The signature FT-IR and Raman bands of the **Co₉** cluster remain identical when compared with pristine **RuCo₉**, suggesting that the bulk POM structure is maintained during the experiments. Raman spectroscopy is particularly suited to detect even traces of CoO_x due to its high surface sensitivity, but no bands that could be assigned to a CoO_x species are present (**Figures S8–S10**).

As with fresh **RuCo₉**, the elemental and ICP analyses showed small deviations, making difficult to confirm final stoichiometry. The numbers are not too different from the original stoichiometry (**Table S1**). However, we need to point out that these analyses show a decrease for all elements, except for W that increases. We assign this surprising result to the deterioration of the compounds during working conditions [triggered by the [Ru(bpy)₃]²⁺ decomposition], making them even more insoluble, and untractable.

Another powerful surface-sensitive technique is XPS. Pristine and recovered **RuCo₉** salts display analogous XPS spectra (**Figure S11**). The presence of CoO_x should include the appearance of a typical Co³⁺ peak below 780 eV (Chuang et al., 1976; Tan et al., 1991; Hara et al., 2000). Close analysis of the Co and O edges in search of such features that could be assigned to the presence of an CoO_x phase were negative. XPS spectra of **RuCo₉** before and after oxygen evolution show intense bands only in the 780–783 eV range, which differ from those expected for CoO_x (**Figure S12**). This indicates that no cobalt oxide amounts are formed during turnover conditions within the detection limit of these techniques.

In order to gather additional indirect proof of the absence of the significant participation of cobalt oxide impurities, we compared the photo-induced oxygen evolution reaction starting from the **RuCo₉** salt to the Co₃O₄ catalyst (**Figure 6** and

**FIGURE 6** | Comparison of the measured oxygen evolution employing equimolar Co amounts for **RuCo₉** (blue) and Co₃O₄ (green). The experiments were performed in a KP_i (40 mM) buffer at pH 7 with [Ru(bpy)₃]²⁺ (1 mM) as photosensitizer and $S_2O_8^{2-}$ (5 mM).**TABLE 3** | Comparison of the light-driven oxygen evolution data catalyzed by **RuCo₉** and by Co₃O₄ under the same reaction conditions^{a,b}.

Catalyst	TON	TOF (h ⁻¹)	CY (%)
RuCo₉	3.2	2.3	17.2
Co ₃ O ₄	0.9	0.3	12.8

^aTON, total turnover number at the final reaction time; TOF, slope of the oxygen evolution curve at the starting time; CY, total chemical yield at the final reaction time.

^bThe experiments were performed in a KP_i (40 mM) buffer at pH 7 with [Ru(bpy)₃]²⁺ (1 mM) as photosensitizer, $S_2O_8^{2-}$ (5 mM) as sacrificial electron acceptor, and with 13.99 μmols of Co in the form of **RuCo₉** or Co₃O₄.

Table 3). For equimolar conditions, **RuCo₉** displays an overall better performance, with faster onset kinetics and a higher efficiency. This is incompatible with the attribution of the catalytic activity observed for **RuCo₉** to very small traces of CoO_x, which may be below the detection limit of Raman or XPS techniques.

CONCLUSIONS

We compared the heterogeneous catalytic activity of two different **Co₉** starting materials under visible-light-driven water oxidation conditions at neutral pH. Direct combination of **CsCo₉** with a homogeneous photosensitizer yields a maximum turnover number (TON) of 14.2 and a maximum turnover frequency (TOF) of 10.8 h⁻¹ with oxygen yields around 10%. Pre-catalytic incorporation of the cationic photosensitizer into the polyoxometalate salt through substitution of the alkali metal improves the oxygen

evolution notably, affording chemical yields close to 50%. We associate this improvement to two beneficial effects of photosensitizer immobilization. On the one hand, the closer cation-anion (photosensitizer/catalyst) interaction in the solid state facilitates electron transfer, and therefore enhances the oxygen evolution kinetics. Additionally, the incorporation of the photosensitizer into the solid state partially improves its stability, an additional benefit to increase the efficiency of the overall process.

Our experimental data indicate that oxygen evolution eventually stops due to decomposition of the photosensitizer. Successive additions of photosensitizer re-start the water oxidation reaction at consistent rates, supporting the stable catalytic performance of **Co₉**. We carried out careful surface analyses on the as-used catalyst in the search of traces of cobalt oxide. Neither Raman nor XPS spectroscopy showed any feature that could be associated with CoO_x species. Additionally, **RuCo₉** exhibits superior catalytic performance than Co₃O₄. Thus, the hypothetical presence of undetectable CoO_x traces cannot be responsible for the observed catalytic activity. This supports the genuine catalytic activity of **RuCo₉** for photo-induced water oxidation as the first example, to the best of our knowledge, of an effective photosensitizer/catalyst electron transfer in an ionic salt. The superior performance of this ionic composite opens up interesting perspectives for the use of such materials in the development of compact photoanodes for artificial photosynthesis.

REFERENCES

- Al-Oweini, R., Sartorel, A., Bassil, B. S., Natali, M., Berardi, S., Scandola, F., et al. (2014). Photocatalytic water oxidation by a mixed-valent Mn^{III}Mn^{IV}O₃ manganese oxo core that mimics the natural oxygen-evolving center. *Angew. Chem. Int. Ed.* 53, 11182–11185. doi: 10.1002/anie.201404664
- Balzani, V., Credi, A., and Venturi, M. (2008). Photochemical conversion of solar energy. *ChemSusChem* 1, 26–58. doi: 10.1002/cssc.200700087
- Barber, J. (2009). Photosynthetic energy conversion: natural and artificial. *Chem. Soc. Rev.* 38, 185–196. doi: 10.1039/B802262N
- Barnett, S. M., Goldberg, K. I., and Mayer, J. M. (2012). A soluble copper-bipyridine water-oxidation electrocatalyst. *Nat. Chem.* 4, 498–502. doi: 10.1038/nchem.1350
- Blakemore, J. D., Schley, N. D., Balcells, D., Hull, J. F., Olack, G. W., Incarvito, C. D., et al. (2010). Half-sandwich iridium complexes for homogeneous water-oxidation catalysis. *J. Am. Chem. Soc.* 132, 16017–16029. doi: 10.1021/ja104775j
- Bozoglian, F., Romain, S., Ertem, M. Z., Todorova, T. K., Sens, C., Mola, J., et al. (2009). The Ru-Hbpy water oxidation catalyst. *J. Am. Chem. Soc.* 131, 15176–15187. doi: 10.1021/ja9036127
- Chuang, T. J., Brundle, C. R., and Rice, D. W. (1976). Interpretation of the x-ray photoemission spectra of cobalt oxides and cobalt oxide surfaces. *Surf. Sci.* 59, 413–429. doi: 10.1016/0039-6028(76)90026-1
- Concepcion, J. J., Jurss, J. W., Brennaman, M. K., Hoertz, P. G., Patrocinio, A. O., Murakami Iha, N. Y., et al. (2009). Making oxygen with ruthenium complexes. *Acc. Chem. Res.* 42, 1954–1965. doi: 10.1021/ar9001526
- Concepcion, J. J., Jurss, J. W., Templeton, J. L., and Meyer, T. J. (2008). One site is enough. catalytic water oxidation by [Ru(tpy)(bpm)(OH₂)]²⁺ and [Ru(tpy)(bpz)(OH₂)]²⁺. *J. Am. Chem. Soc.* 130, 16462–16463. doi: 10.1021/ja8059649
- Cook, T. R., Dogutan, D. K., Reece, S. Y., Surendranath, Y., Teets, T. S., and Nocera, D. G. (2010). Solar energy supply and storage for the legacy and nonlegacy worlds. *Chem. Rev.* 110, 6474–6502. doi: 10.1021/cr100246c
- Dau, H., Limberg, C., Reier, T., Risch, M., Roggan, S., and Strasser, P. (2010). The mechanism of water oxidation: from electrolysis via homogeneous to biological catalysis. *ChemCatChem* 2, 724–761. doi: 10.1002/cctc.201000126
- Duan, L., Bozoglian, F., Mandal, S., Stewart, B., Privalov, T., Llobet, A., et al. (2012). A molecular ruthenium catalyst with water-oxidation activity comparable to that of photosystem II. *Nat. Chem.* 4, 418–423. doi: 10.1038/nchem.1301
- Evangelisti, F., Car, P.-E., Blacque, O., and Patzke, G. R. (2013). Photocatalytic water oxidation with cobalt-containing tungstobismutates: tuning the metal core. *Catal. Sci. Technol.* 3, 3117–3129. doi: 10.1039/c3cy00475a
- Galán-Mascarós, J. R. (2015). Water oxidation at electrodes modified with earth-abundant transition-metal catalysts. *ChemElectroChem* 2, 37–50. doi: 10.1002/celec.201402268
- Gao, J., Cao, S., Tay, Q., Liu, Y., Yu, L., Ye, K., et al. (2013). Molecule-based water-oxidation catalysts (WOCs): Cluste-size-dependent dye-sensitized polyoxometalates for visible-light-driven O₂ evolution. *Sci. Rep.* 3:1853. doi: 10.1038/srep01853
- Geletii, Y. V., Botar, B., Köeğerler, P., Hillesheim, D. A., Musaev, D. G., and Hill, C. L. (2008). An all-inorganic, stable, and highly active tetra-ruthenium homogeneous catalyst for water oxidation. *Angew. Chem. Int. Ed.* 47, 3896–3899. doi: 10.1002/anie.200705652
- Goberna-Ferrón, S., Peña, B., Soriano-López, J., Carbó, J. J., Zhao, H., Poblet, J. M., et al. (2014). A fast metal-metal bonded water oxidation catalyst. *J. Catal.* 315, 25–32. doi: 10.1016/j.jcat.2014.04.010
- Goberna-Ferrón, S., Soriano-López, J., Galán-Mascarós, J. R., and Nyman, M. (2015). Solution speciation and stability of cobalt-polyoxometalate water oxidation catalysts by X-ray scattering. *Eur. J. Inorg. Chem.* 2015, 2833–2840. doi: 10.1002/ejic.201500404
- Goberna-Ferrón, S., Vígara, L., Soriano-López, J., and Galán-Mascarós, J. R. (2012). Identification of a nonanuclear [Co₉^{II}] polyoxometalate cluster as a homogeneous catalyst for water oxidation. *Inorg. Chem.* 51, 11707–11715. doi: 10.1021/ic301618h

AUTHOR CONTRIBUTIONS

GP and JRG-M proposed the concept. GP, JRG-M, and JS-L designed the experiments. JS-L and FS carried out the experiments. All authors analyzed the data and contributed to the manuscript writing.

FUNDING

We would like to acknowledge the financial support from the Spanish Ministerio de Economía y Competitividad (MINECO) through project CTQ2015-71287-R and the Severo Ochoa Excellence Accreditation 2014-2018 SEV-2013-0319; and the Generalitat de Catalunya (2017-SGR-1406 and the CERCA Programme). GP and FS are grateful for financial support by the Swiss National Science Foundation (Sinergia Grant No. CRSII2_160801/1) and by the University Research Priority Program Solar Light to Chemical Energy Conversion (URPP LightChEC) of the University of Zurich. This collaboration took place in the context of the COST PoCheMoN action supported by the European Research Area.

SUPPLEMENTARY MATERIAL

The Supplementary Material for this article can be found online at: <https://www.frontiersin.org/articles/10.3389/fchem.2018.00302/full#supplementary-material>

- Guo, S.-X., Liu, Y., Lee, C.-Y., Bond, A. M., Zhang, J., Geletii, Y. V., et al. (2013). Graphene-supported $[\{\text{Ru}_4\text{O}_4(\text{OH})_2(\text{H}_2\text{O})_4\}(\gamma\text{-SiW}_{10}\text{O}_{36})_2]^{10-}$ for highly efficient electrocatalytic water oxidation. *Energy Environ. Sci.* 6, 2654–2663. doi: 10.1039/c3ee41892h
- Hara, M., Waraksa, C. C., Lean, J. T., Lewis, B. A., and Mallouk, T. E. (2000). Photocatalytic water oxidation in a buffered tris(2,2'-bipyridyl)ruthenium complex-colloidal IrO_2 system. *J. Phys. Chem. A* 104, 5275–5280. doi: 10.1021/jp000321x
- Huang, Z., Luo, Z., Geletii, Y. V., Vickers, J. W., Yin, Q., Wu, D., et al. (2011). Efficient light-driven carbon-free cobalt-based molecular catalyst for water oxidation. *J. Am. Chem. Soc.* 133, 2068–2071. doi: 10.1021/ja109681d
- Lewis, N. S., and Nocera, D. G. (2006). Powering the planet: chemical challenges in solar energy utilization. *Proc. Natl. Acad. Sci. U.S.A.* 103, 15729–15735. doi: 10.1073/pnas.0603395103
- Liu, X., and Wang, F. Y. (2012). Transition metal complexes that catalyze oxygen formation from water: 1979–2010. *Coord. Chem. Rev.* 256, 1115–1136. doi: 10.1016/j.ccr.2012.01.015
- Lloret-Fillol, J., Codolà, Z., Garcia-Bosch, I., Gómez, L., Pla, J. J., and Costas, M. (2011). Efficient water oxidation catalysts based on readily available iron coordination complexes. *Nat. Chem.* 3, 807–813. doi: 10.1038/nchem.1140
- Lv, H., Geletii, Y. V., Zhao, C., Vickers, J. W., Zhu, G., Luo, Z., et al. (2012). Polyoxometalate water oxidation catalysts and the production of green fuel. *Chem. Soc. Rev.* 41, 7572–7589. doi: 10.1039/c2cs35292c
- Lv, H., Song, J., Geletii, Y. V., Vickers, J. W., Sumlin, J. M., Musaev, D. G., et al. (2014). An exceptionally fast homogeneous carbon-free cobalt-based water oxidation catalyst. *J. Am. Chem. Soc.* 136, 9268–9271. doi: 10.1021/ja5045488
- McCool, N. S., Robinson, D. M., Sheats, J. E., and Dismukes, G. C. (2011). A Co_4O_4 “cubane” water oxidation catalyst inspired by photosynthesis. *J. Am. Chem. Soc.* 133, 11446–11449. doi: 10.1021/ja203877y
- Mcevoy, J. P., and Brudvig, G. W. (2006). Water-splitting chemistry of photosystem II. *Chem. Rev.* 106, 4455–4483. doi: 10.1021/cr0204294
- Natali, M., Bazzan, I., Goberna-Ferrón, S., Al-Oweini, R., Ibrahim, M., Bassil, B. S., et al. (2017). Photo-assisted water oxidation by high-nuclearity cobalt-oxo cores: tracing the catalyst fate during oxygen evolution turnover. *Green Chem.* 19, 2416–2426. doi: 10.1039/C7GC00052A
- Pillai, K. C., Kumar, A. S., and Zen, J.-M. (2000). Nafion- RuO_2 - $\text{Ru}(\text{bpy})_3^{2+}$ composite electrodes for efficient electrocatalytic water oxidation. *J. Mol. Catal. A* 160, 277–285. doi: 10.1016/S1381-1169(00)00262-4
- Pope, M. T. (1983). *Heteropoly and Isopoly Oxometalates*. Berlin: Springer.
- Pope, M. T., and Müller, A. (2001). *Polyoxometalate Chemistry From Topology via Self-Assembly to Applications*. Dordrecht: Kluwer Academic Publishers.
- Punteriero, F., La Ganga, G., Sartorel, A., Carraro, M., Scorrano, G., Bonchio, M., et al. (2010). Photo-induced water oxidation with tetra-nuclear ruthenium sensitizer and catalyst: a unique 4×4 ruthenium interplay triggering high efficiency with low-energy visible light. *Chem. Commun.* 46, 4725–4727. doi: 10.1039/c0cc00444h
- Quintana, M., López, A. M., Rapino, S., Toma, F. M., Iurlo, M., Carraro, M., et al. (2013). Knitting the catalytic pattern of artificial photosynthesis to a hybrid graphene nanotexture. *ACS Nano* 7, 811–817. doi: 10.1021/nn305313q
- Sartorel, A., Bonchio, M., Campagna, S., and Scandola, F. (2013). Tetrametallic molecular catalysts for photochemical water oxidation. *Chem. Soc. Rev.* 42, 2262–2268. doi: 10.1039/C2CS35287G
- Sartorel, A., Carraro, M., Scorrano, G., De Zorzi, R., Geremia, S., McDaniel, N. D., et al. (2008). Polyoxometalate embedding of a tetra-ruthenium(IV)-oxo-core by template-directed metalation of $[\gamma\text{-SiW}_{10}\text{O}_{36}]^{8-}$: a totally inorganic oxygen-evolving catalyst. *J. Am. Chem. Soc.* 130, 5006–5007. doi: 10.1021/ja077837f
- Seh, Z. W., Kibsgaard, J., Dickens, C. F., Chorkendorff, I., Nørskov, J. K., and Jaramillo, T. F. (2017). Combining theory and experiment in electrocatalysis: insights into materials design. *Science* 355:eaad4998. doi: 10.1126/science.aad4998
- Soriano-López, J., Goberna-Ferrón, S., Vigara, L., Carbó, J. J., Poblet, J. M., and Galán-Mascarós, J. R. (2013). Cobalt polyoxometalates as heterogeneous water oxidation catalysts. *Inorg. Chem.* 52, 4753–4755. doi: 10.1021/ic4001945
- Stracke, J. J., and Finke, R. G. (2011). Electrocatalytic water oxidation beginning with the cobalt polyoxometalate $[\text{Co}_4(\text{H}_2\text{O})_2(\text{PW}_9\text{O}_{34})_2]^{10-}$: identification of heterogeneous CoO_x as the dominant catalyst. *J. Am. Chem. Soc.* 133, 14872–14875. doi: 10.1021/ja205569j
- Stracke, J. J., and Finke, R. G. (2013). Water oxidation catalysis beginning with $2.5 \mu\text{M} [\text{Co}_4(\text{H}_2\text{O})_2(\text{PW}_9\text{O}_{34})_2]^{10-}$: investigation of the true electrochemically driven catalyst at $\geq 600 \text{ mV}$ overpotential at a glassy carbon electrode. *ACS Catal.* 3, 1209–1219. doi: 10.1021/cs400141t
- Stracke, J. J., and Finke, R. G. (2014). Distinguishing Homogeneous from heterogeneous water oxidation catalysis when beginning with polyoxometalates. *ACS Catal.* 4, 909–933. doi: 10.1021/cs4011716
- Tan, B. J., Klabunde, K. J., and Sherwood, P. M. A. (1991). XPS studies of solvated metal atom dispersed (SMAD) catalysts. Evidence for layered cobalt-manganese particles on alumina and silica. *J. Am. Chem. Soc.* 113, 855–861. doi: 10.1021/ja00003a019
- Wu, J., Liao, L., Yan, W., Xue, Y., Sun, Y., Yan, X., et al. (2012). Polyoxometalates immobilized in ordered mesoporous carbon nitride as highly efficient water oxidation catalysts. *ChemSusChem* 5, 1207–1212. doi: 10.1002/cssc.201100809
- Xiang, R., Ding, Y., and Zhao, J. (2014). Visible-light-induced water oxidation mediated by a mononuclear-cobalt(II)-substituted silicotungstate. *Chem. Asian J.* 9, 3228–3237. doi: 10.1002/asia.201402483
- Xu, Y., Fischer, A., Duan, L., Tong, L., Gabrielsson, E., Åkermark, B. (2010). Chemical and light-driven oxidation of water catalyzed by an efficient dinuclear ruthenium complex. *Angew. Chem. Int. Ed.* 49, 8934–8937. doi: 10.1002/anie.201004278
- Yin, Q., Tan, J. M., Besson, C., Geletii, Y. V., Musaev, D. G., Kuznetsov, A. E., et al. (2010). A fast soluble carbon-free molecular water oxidation catalyst based in abundant metals. *Science* 328, 342–345. doi: 10.1126/science.1185372
- Youngblood, W. J., Lee, S. H. A., Kobayashi, Y., Hernandez-Pagan, E. A., Hoertz, P. G., Moore, T. A., et al. (2009). Photoassisted overall water splitting in a visible light-absorbing dye-sensitized photoelectrochemical cell. *J. Am. Chem. Soc.* 131, 926–927. doi: 10.1021/ja809108y
- Zhang, M. T., Chen, Z., Kang, P., and Meyer, T. J. (2013). Electrocatalytic water oxidation with a copper(II) polypeptide complex. *J. Am. Chem. Soc.* 135, 2048–2051. doi: 10.1021/ja3097515

Conflict of Interest Statement: The authors declare that the research was conducted in the absence of any commercial or financial relationships that could be construed as a potential conflict of interest.

Copyright © 2018 Soriano-López, Song, Patzke and Galan-Mascaros. This is an open-access article distributed under the terms of the Creative Commons Attribution License (CC BY). The use, distribution or reproduction in other forums is permitted, provided the original author(s) and the copyright owner(s) are credited and that the original publication in this journal is cited, in accordance with accepted academic practice. No use, distribution or reproduction is permitted which does not comply with these terms.



A Supramolecular Catalyst Self-Assembled From Polyoxometalates and Cationic Pillar[5]arenes for the Room Temperature Oxidation of Aldehydes

Mengyan Zeng^{1†}, Kun Chen^{1†}, Junyan Tan², Jie Zhang^{2*} and Yongge Wei^{1*}

¹ Key Lab of Organic Optoelectronics & Molecular Engineering of Ministry of Education, Department of Chemistry, Tsinghua University, Beijing, China, ² Beijing National Lab for Molecular Sciences, Key Lab of Polymer Chemistry and Physics of Ministry of Education, College of Chemistry and Molecular Engineering, Peking University, Beijing, China

OPEN ACCESS

Edited by:

Soumyajit Roy,
Indian Institute of Science Education
and Research Kolkata, India

Reviewed by:

Scott George Mitchell,
Instituto de Ciencia de Materiales de
Aragón (ICMA), Spain
Carsten Streb,
Universität Ulm, Germany
Lixin Wu,
Jilin University, China

*Correspondence:

Jie Zhang
jz10@pku.edu.cn
Yongge Wei
yonggewei@tsinghua.edu.cn

[†]These authors have contributed
equally to this work

Specialty section:

This article was submitted to
Inorganic Chemistry,
a section of the journal
Frontiers in Chemistry

Received: 30 April 2018

Accepted: 13 September 2018

Published: 16 October 2018

Citation:

Zeng M, Chen K, Tan J, Zhang J and
Wei Y (2018) A Supramolecular
Catalyst Self-Assembled From
Polyoxometalates and Cationic
Pillar[5]arenes for the Room
Temperature Oxidation of Aldehydes.
Front. Chem. 6:457.
doi: 10.3389/fchem.2018.00457

Oxidizing aldehydes to generate carboxylic acids is a crucial reaction in nature and in chemical industry. The aldehyde oxidation, an easily achieved process in liver cells, is inert toward autoxidation in industrial production and difficultly achieved under enzymatic condition (in water, at pH 7, at room temperature). Herein, we prepared a supramolecular catalyst which are nanospheres assembled in aqueous media by chromium centered Anderson polyoxometalates $\text{Na}_3[\text{CrMo}_6\text{O}_{18}(\text{OH})_3]$ (namely, CrMo_6) and cationic pillar[5]arenes (namely, P5A) with 10 positive charges which can be used as the phase transfer catalysts (PTCs). This supramolecular catalyst was exploited on aldehydes oxidation under enzymatic condition with relatively good conversion. Through DLS monitoring, the diameters of nanospheres were variable while changing the charge ratios of the ionic complexes (P5A-CrMo_6), and it is probably because of the closer charge ratios causing the more compact assemblies. Also, the nano-morphologies were monitored by TEM and SEM, and the nanostructures were characterized by zeta potential, the X-ray energy-dispersive spectroscopy (EDS), elemental analysis.

Keywords: pillar[5]arenes, chromium centered Anderson polyoxometalates, nanospheres, supramolecular catalyst, aldehyde oxidation

INTRODUCTION

Rational design of functional nanobuilding blocks with well-defined nanostructure and specific functionality is very important. Polyoxometalates (POMs) are well-defined early transition metal-oxygen anionic clusters with various chemical composition and nanosized architecture (Müller and Pope, 1991; Dolbecq et al., 2010; Miras et al., 2012). The potential applications range from catalysis (Mizuno et al., 2005), electronics (Kawasaki et al., 2011), magnetism (Poblet et al., 2003), and photochemistry (Li et al., 2011), to medicines (Rhule et al., 1998). POMs possesses the assembly ingredients for forming different kinds of nanostructures (Li et al., 2017). Spontaneous self-assembly of weak electrolyte type POMs into vesicle-like supramolecular structures has been confirmed by Liu et al. (Liu, 2002; Liu et al., 2003; Liu and Liu, 2005a,b). The assistance from grafting groups or counterions has been demonstrated to be more effective in constructing POM self-assemblies (Zhang et al., 2008; Landsmann et al., 2010; Yin et al., 2013; Zhu et al., 2013).

Compared with the covalent modification of POM with grafting groups, utilization of electrostatic interactions between anionic POMs and cationic amphiphiles may be more versatile for the hierarchical self-assembly of POM clusters (Ishiba et al., 2017; Li et al., 2017; Cheng et al., 2018).

Pillararenes, as a new generation of macrocyclic host, with hydroquinone as units linked at para position, have attracted much attention since its first report by Ogoshi (Ogoshi et al., 2008). Compared with the other macrocycles such as crown ethers, cyclodextrin, calixarene, and cucurbituril, pillararenes possess a columnar shape with a p-electron rich cavity, having unique characteristics, such as easy and facile synthesis, various modification sites, pillar architectures, making them favorable building blocks in developing self-assembly for constructing vesicles, molecular machines, artificial transmembrane channels and so on (Xue et al., 2012; Tan and Yang, 2015; Ogoshi et al., 2016).

Oxidizing aldehydes to produce carboxylic acids is a crucial reaction in nature and in chemical industry (Latchman, 1995; Crabb et al., 2004). In living cells, oxidizing aldehydes into acids is conducted at body temperature using oxygen as oxidizing agent and dehydrogenase as the catalyst in neutral aqueous solution (Crabb et al., 2004). There are relatively few examples of models performing under enzymatic condition (in water, at pH 7, at room temperature) (Marinescu and Bols, 2006; Raynal et al., 2014). Generally, despite being prone to autoxidation, most kinds of aldehydes are relatively stable (Liu and Li, 2016; Zhang et al., 2017). The majority of these oxidation reactions in modern industry require stoichiometric amounts of hazardous oxidants such as KMnO_4 (Kleiderer, 1930; Ruhoff, 1936), CrO_3 (Sandborn, 1929), KHSO_5 (Mo, 2006), KIO_4 (Travis et al., 2003), etc., and often take place in organic solvents. Since Li et al. sequentially reported first homogeneous silver- and copper- catalysis of aerobic aldehyde oxidation in water (Liu et al., 2015; Liu and Li, 2016), Wei et al. reported a single-sided triol-functionalized iron centered Anderson POM catalysis (Yu et al., 2017). POMs combine high reactivity and stability in oxidation catalysis (Lechner et al., 2016). Phase transfer catalysts (PTCs) provide easy, inexpensive and versatile solutions for organic reactions (Maruoka and Ooi, 2003; Hashimoto and Maruoka, 2008). It accelerates the reaction rate by improving the solubility of the reactants isolated in different liquid phases. Herein, we used cationic pillar[5]arenes (namely, P5A) as PTCs and exploited the P5A- CrMo_6 supramolecular complex (Figure 1) assembled by the chromium centered polyoxometalates $\text{Na}_3[\text{CrMo}_6(\text{OH})_3]$ (namely, CrMo_6) and P5A under aqueous conditions. When applied to catalyze aldehydes into carboxylic acids, this supramolecular catalysis (Leeuwen, 2008) offered better catalytic effect than CrMo_6 or P5A alone with air as the oxidant in water under enzymatic conditions as a result of synergy effect that combined advantage of CrMo_6 and P5A.

EXPERIMENTAL SECTION

Materials and Methods

Boron trifluoride diethyl etherate, and 1,4-Dibromo butane were purchased from Aladdin. All the other chemicals were purchased

from Sinopharm Chemical Reagent Co., Ltd. All the reagents were used without further purification.

$\text{Na}_3[\text{Cr}(\text{OH})_6\text{Mo}_6\text{O}_{18}]$ were prepared according to previously reported procedures (Wu et al., 2011). Na_2MoO_4 (12 g, 57.5 mmol) was dissolved in water (10 mL). Keeping 80 °C, concentrated nitric acid (4.5 mL) was added to the solution. Then stop the heating equipment, and $\text{Cr}(\text{NO}_3)_3$ (3.2 g) was slowly added to the solution. When a large amount of red precipitates appeared in the solution, the reaction was stopped. After cooled down to room temperature, the solution was filtered, and 8.9 g of the red solid was collected as the product. Yield: 84% based on Mo.

The cationic water-soluble pillar[5]arene (P5A) were prepared according to previously reported procedures (Ma et al., 2011; Yao et al., 2012, 2014) (Supplementary Figure 1). $^1\text{H-NMR}$ (400 MHz, D_2O) δ (ppm) (Supplementary Figure 2): 6.73 (s, 10H), 3.80 (s, 30H), 3.10 (s, 20H), 2.91 (s, 90H), 1.59 (s, 40H). $^{13}\text{C-NMR}$ (400 MHz, D_2O) δ (ppm) (Supplementary Figure 3): 166.98, 150.21, 129.32, 66.13, 57.91, 52.91, 25.84, 19.54. HRESI-MS (Supplementary Figure 4): m/z calcd for $[\text{M}-2\text{Br}]^{2+}$ 1196.36002; $[\text{M}-3\text{Br}]^{3+}$ 770.60389; $[\text{M}-4\text{Br}]^{4+}$ 557.72439; $[\text{M}-5\text{Br}]^{5+}$ 430.39624; $[\text{M}-6\text{Br}]^{6+}$ 345.17750; $[\text{M}-7\text{Br}]^{7+}$ 284.59296, $[\text{M}-8\text{Br}]^{8+}$ 239.06875; $[\text{M}-9\text{Br}]^{9+}$ 203.59118.

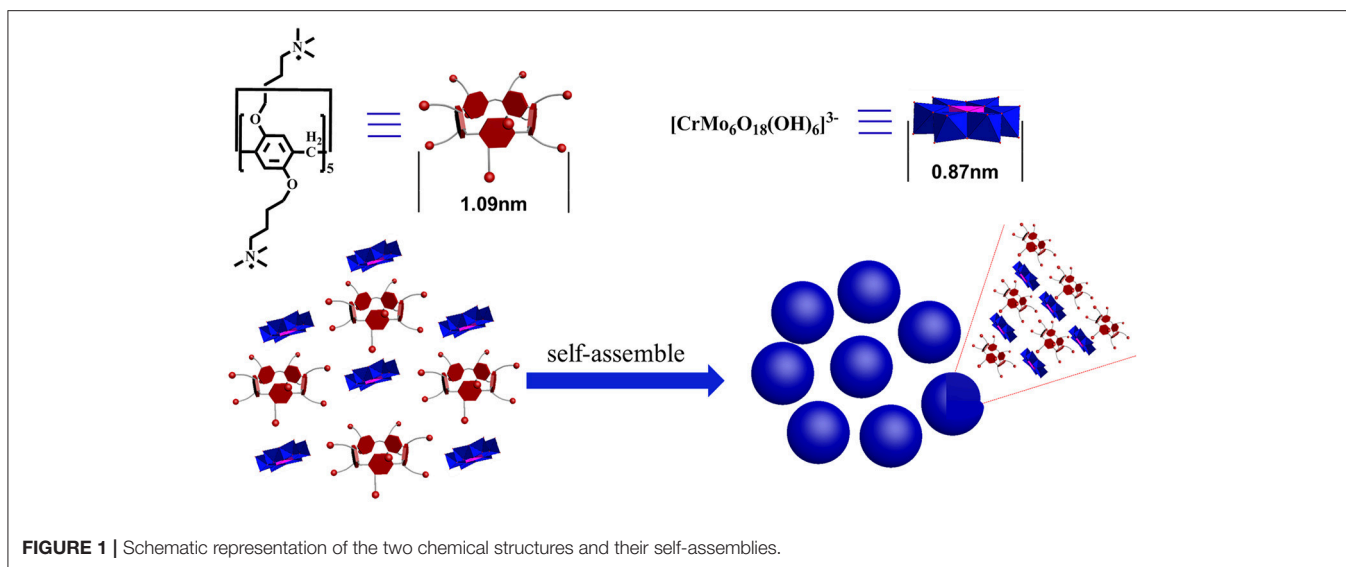
The preparation of the nanospheres were by mixing different charge ratios of cationic P5A and anionic CrMo_6 in water solution, with the concentration of P5A and CrMo_6 kept constant at 0.05 mg/mL.

NMR: $^1\text{H-NMR}$ and $^{13}\text{C-NMR}$ were performed on JNM-ECA400 equipment. **TEM:** TEM images were obtained on a JEMO 2010 Electron microscopy with an operational acceleration voltage of 120 kV. The samples were prepared by fishing the carbon coated copper grid into the aqueous solution and then dried in air at 25°C for 30 min. **HPLC:** HPLC was performed on a Waters 2695 with a UV detector and refractive index detector. The gradient elution was performed with 8 mM $(\text{NH}_4)_2\text{HPO}_4$ at a rate of 0.7 mL/min. Fifty microliter of prepared sample or standard solution was injected. **HRESI-MS:** HRESI-MS was performed on a Flash EA 1112 full-automatic mass spectrometer, and the experiment was carried out in the positive-ion mode using CHCl_3 as the solvent. **SEM:** SEM was performed on Hitachi SU-8010 Electron microscopy with an operational acceleration voltage of 200 V–50 KV. The preparation of samples was by dropping about 20 μL of the solution on a cleaved silicon surface. The gold spraying time is 30 seconds. **FT-IR:** IR was carried out on a Perkin Elmer Spectrum. The solid samples were prepared by vacuum drying at 50°C.

Catalytic Experiments

General Procedure for the Oxidation of Aldehydes

Prepare 1.0 mM P5A, 1.0 mM CrMo_6 aqueous solution, respectively. Pipette 43 μL P5A (1.0 mM), 144 μL CrMo_6 (1.0 mM), and 4770 μL water into a PE tube. After ultrasonic bath for 1 min, the nanosphere (P5A- CrMo_6) solids were collected though high speed centrifugation (14,000 rpm, 25°C, 5 min), washed with pure water, and purified by centrifugation. Then the collected colloids were dried at 50°C under vacuum to obtain the products. Dry weight: 0.2 mg. Yield: 81.1% based on P5A and CrMo_6 . The catalytic system contains P5A- CrMo_6



(0.2 mg, 0.002 mmol, 0.2 mol %), benzaldehyde (101 μ L, 1 mmol), air (using air pump to control the flow velocity), H_2O (5 mL). The mixture was stirred at 30°C , and the reaction progress was monitored by HPLC. After 12 h, 3×5 mL ethyl ether was added by extracting three times to give the organic phase, and the solid catalyst was isolated by filtration. Then the organic phase was diluted 100 times by acetonitrile. The diluted samples were loaded into sample vials and detected by HPLC, using acetonitrile and water as mobile phase, non-polar C18 as separation column, UV and refractive index detector as detector.

RESULTS AND DISCUSSION

The supramolecular amphiphiles (SA) (Wang et al., 2010; Han et al., 2011; Zhang and Wang, 2011) was prepared by mixing different charge ratios of cationic P5A and anionic CrMo_6 in water solution, with the concentration of P5A and CrMo_6 kept constant at $0.05 \text{ mg} \cdot \text{mL}^{-1}$. After the samples were mixed, the assembling process took place rapidly. Dynamic light scattering (DLS) was used to monitor size evolution of these assemblies with different charge ratios. We define the compositional formation of the charge ratio (r) between P5A and CrMo_6 , $r = (3 \text{ P5A}^{10+}) : (10 \text{ CrMo}_6^{3-})$. The DLS count rates, shown in **Figure 2A**, were very low until r reached 0.4. When $0.4 \leq r \leq 1.0$, the DLS count rates were more than 100 kcps. But when $1.0 < r$, the DLS count rates were also low (even less than 10 kcps), indicating no detectable assemblies in the solution. When $r < 0.4$, the charge ratio of P5A and CrMo_6 is greatly unmatched, and the size of assemblies is big and thermodynamically unstable. A small amount of precipitates was found at the bottom of the bottle in a very short time. That is why the DLS count rate is low when $r < 0.4$. As the charge ratios of P5A and CrMo_6 became closer, the hydrodynamic radii (R_h) of assemblies in aqueous solution become smaller, because of the more compact assembly due to the closer charge ratios. Average size of the nanospheres was obtained by dynamic light scattering, shown in **Figure 2B**. For charge

ratios at 4:10, 6:10, 8:10, 10:10, the hydrodynamic radius is 567, 295, 130, and 75 nm, respectively. Combined with relative TEM images, shown in **Supplementary Figure 5**, the closer charge ratios caused the more compact assemblies. However, for $r > 1.0$, these solutions were clear during the 17 days of testing time, and almost no regular aggregates can be observed for TEM testing, which indicated that there were no convinced assemblies. It is convinced that the size of these aggregates are molar ratios dependently.

In this investigation, the system of $r = 10:10$ was chose as the research object, named P5A- CrMo_6 , which has the highest DLS count rate and thermodynamically stable R_h at ~ 75 nm, shown in **Figure 2B**. The hydrodynamics radius of the aggregates in the aqueous solution slowly increased over time, shown in **Figure 3A**. During the first 17 days, there is still no precipitate in the solution, which confirms the stability of the aggregates. The hydrodynamic radii of nanospheres grows with time. The average hydrodynamic radii became bigger from 75 nm on first day to 87 nm on the 17th day, as shown in **Figure 3A**. This is because more and more compounds (POM or P5A) aggregated on the outer surface of the nanospheres, as time goes by. And the nanospheres diameters of the 1st day, the 8th day, the 17th day were also counted from TEM images (**Figures 3C,D** and **Supplementary Figures 6A,C,E**). By analyzing the size-dispersion histogram of nanospheres (**Supplementary Figures 6B,D,F**), the average diameters are 99, 111, and 150 nm, respectively. Compared with the DLS data, all the statistical sizes of the nanospheres in TEM images are a litter smaller which is directly caused by the removing hydration layer of nanospheres under drying (**Supplementary Figure 7**). Furthermore, X-ray energy-dispersive spectroscopy (EDS) coupled with HRTEM shows that both molybdenum, chromium, bromine, nitrogen, and oxygen elements exist throughout the assemblies, shown in **Supplementary Figure 8**. The molybdenum and chromium elements are attributed to CrMo_6 , and the bromine and nitrogen elements are attributed to P5A.

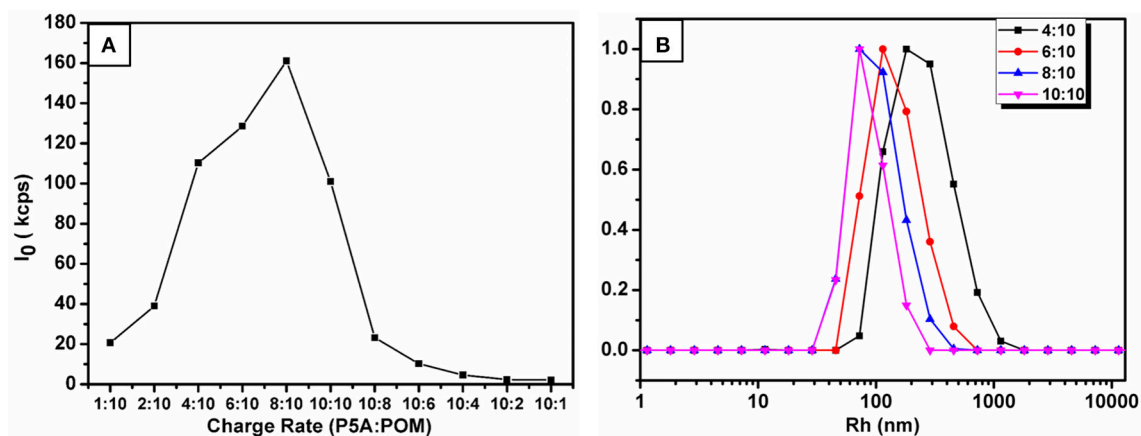


FIGURE 2 | (A) DLS total scattered intensity I of the P5A-CrMo₆ complex at different charge ratios. From left to right, the charge rate of P5A:CrMo₆ is 1:10, 2:10, 4:10, 6:10, 8:10, 10:10, 10:8, 10:6, 10:4, 10:2, 10:1. The concentration of (P5A-CrMo₆) was controlled at 0.05 mg/mL. **(B)** The size distribution at different charge ratios obtained by a CONTIN analysis with normalized counts by DLS.

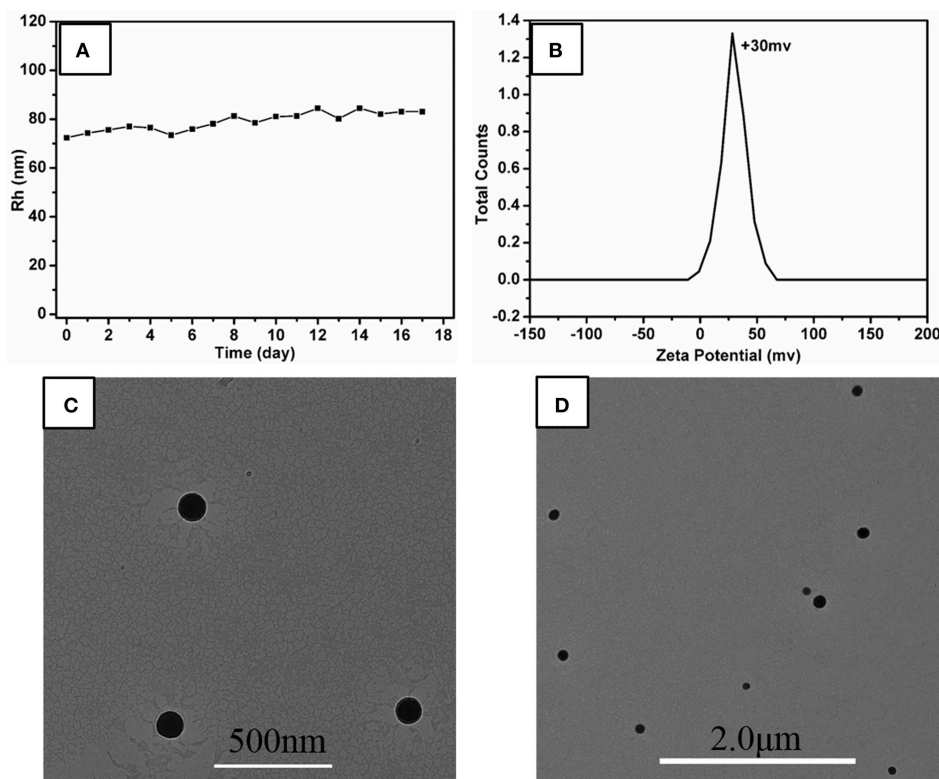


FIGURE 3 | (A) Change of hydrodynamic radii (R_h) of P5A-CrMo₆ in water solution with time. Charge ratio of P5A-CrMo₆ is 10:10. The concentration of P5A-CrMo₆ is 0.05 mg/mL. **(B)** Zeta potential of the P5A-CrMo₆ self-assemblies with charge ratio 10:10 at 0.05 mg/mL in water solution. **(C)** TEM image of the self-assemblies immediately after mixed together. **(D)** TEM images of self-assemblies after 17th day.

In order to explore the assembly structure, scanning electron microscopy (SEM) and zeta potential were taken. As shown in **Supplementary Figure 9**, the sphere aggregates were solid structure. And the zeta potential of the aggregates was determined to be +30 mV, shown in **Figure 3B**, indicating that the outer surface of these aggregates is covered by cations,

probably the cationic P5A. The composition of these nanospheres determined by elemental analysis was CrMo₆:P5A = 3.3:1, which indicated that the CrMo₆ anion is surrounded by P5A in the form of P5A·(CrMo₆)_{3.3}, shown in **Supplementary Table S1**. The structure was still maintained as supported by FTIR spectra, shown in **Supplementary Figure 10**. The peaks at 908 cm⁻¹

n ($\text{Mo}-\text{O}_b-\text{Mo}$) and 945 cm^{-1} ($\text{Mo}-\text{O}_d$, O_d = terminal oxygen) are consistent with the structure of CrMo_6 , indicating the Anderson-type structure is maintained during assembling. Herein, the diameter of P5A (10.0 Å) by DFT calculation is larger than CrMo_6 (8.7 Å). The surface occupation of CrMo_6 is greater than 2/3. As a result, no classical reverse bilayer can be formed (Volkmer et al., 2000; Bu et al., 2002, 2005; Qi et al., 2008; Li et al., 2017). The tight packing of rigid balls instead of classical reverse bilayer were the probably formed state. It is consistent with solid aggregates detected by SEM and TEM. The assembled structure assumed be arranged as shown in **Figure 1**.

Catalytic oxidations of aldehydes into carboxylic were investigated to further explore the function of the P5A- CrMo_6 nanospheres, shown in **Figure 4**. Air as oxidant was simply flushed into the reaction flask (with a balloon) under aqueous reaction conditions. Through optimizing the catalytic

reaction temperature conditions, we chose 30°C as the reaction temperature. Taking catalytic oxidation benzaldehyde to benzoic acid as the key research example, the reaction kinetics was monitored by liquid chromatography at different time points, shown as **Figure 5A**. For nanospheres, after 3 h, the yield of benzoic acid has reached more than 96%. According to the control experiments, when the catalyst is Anderson-type POMs $\text{Na}_3[\text{CrMo}_6\text{O}_{18}(\text{OH})_3]$ alone, the yield reaching 90% needs at least 4 h. When only cationic P5A is used as catalyst, reaching above 90% of yield needs at least 6 h. Since the aldehydes oxidation is an auto-oxidation process, when there is no catalyst, the benzaldehyde can also be oxidized, however, reaching above 90% yield needs at least 8 h. In general, most kinds of aldehydes are stable, despite being prone to autooxidation, requiring a long reaction time. Water, the most environmental benign solvent, was chosen as the solvent in this oxidation process. Unfortunately, most of aldehydes can't be dissolved in water, for example, the lauric aldehyde. The cationic pillararenes are a new kind of phase transfer catalysis similar to TBABr, which can drag the insoluble organic aldehyde into water. It is the key factor to improve the contact area between catalyst and substrate. As heterogeneous catalysts, the nanospheres have the synergistic catalytic effect of Anderson type POM CrMo_6 and organic cationic P5A which acts as phase transfer catalyst.

In order to explore the scope and functional-group compatibility of these nanospheres, a number of functionalized aldehydes were used as substrates to carry out the reaction under the optimized conditions, shown in **Figure 6**. Aromatic aldehyde bearing a methyl group was oxidized in quantitative yields above 99% (products 2) after 12 h. Halogen-substituted aldehydes such as 4-bromobenzaldehyde were tolerated under the optimized reaction conditions and the corresponding carboxylic acids were obtained in quantitative yields above 99% (products 3). However, when aromatic aldehydes bearing electron-withdrawing groups such as 4-nitrobenzaldehydes, 4-hydroxybenzaldehyde, 2-hydroxybenzaldehyde, 4-methoxybenzaldehyde, the obtained oxidized carboxylic acid yields are low (products 4–7). Because of the water-solubility of 4-hydroxybenzaldehyde

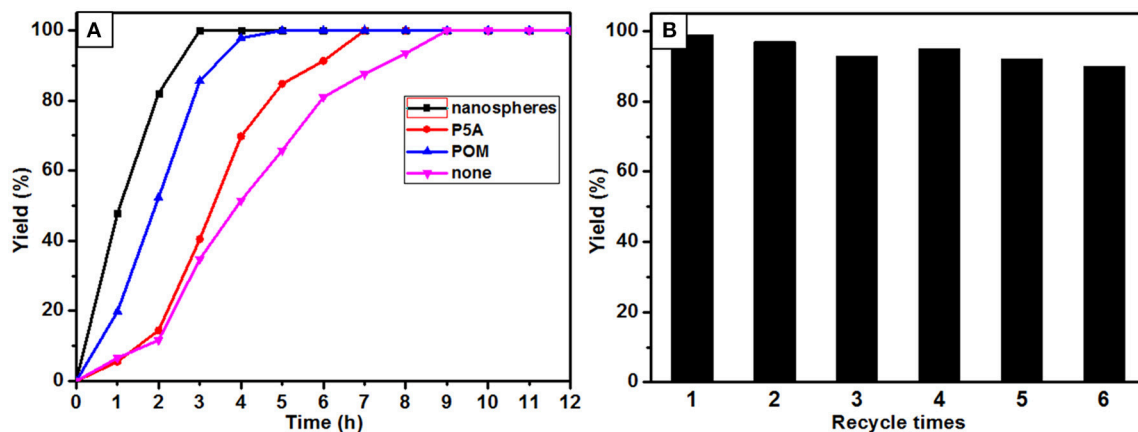
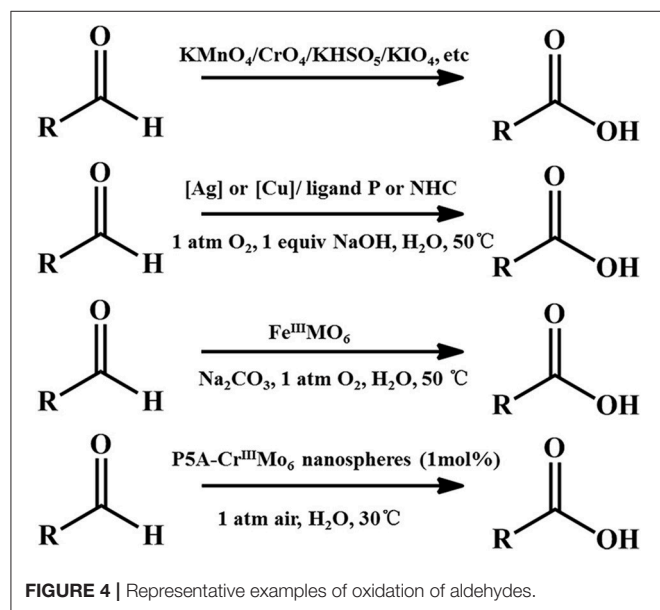


FIGURE 5 | Reaction dynamics (A) and catalytic experiment of recycled of nanospheres (B).

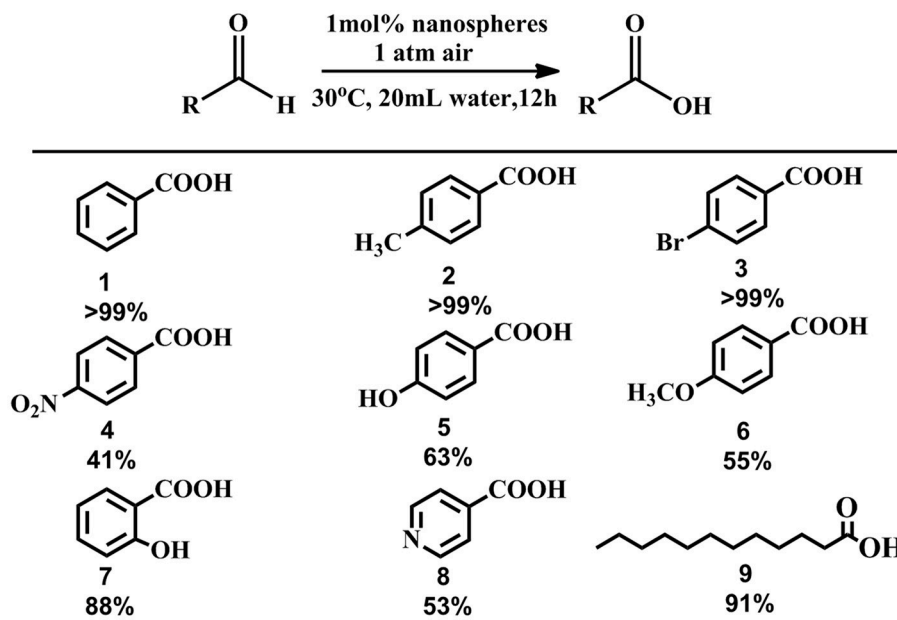


FIGURE 6 | Investigation of substrate scope.

and 2-hydroxybenzaldehyde, their oxidation yields are relatively higher compared with 4-nitrobenzaldehyde and 4-methoxybenzaldehyde. Heterocyclic aromatic aldehyde such as 4-pyridinecarboxaldehyde was also oxidized with a yield about 53% (products 8). The aliphatic aldehyde such as lauric aldehyde was also tested. Interestingly, the oxidation yield is surprisingly high, with an essentially quantitative yield of 91% (products 9). The strong host-guest interaction between the cationic pillar[5]arenes and lauric aldehyde or lauric acid might result in water-insoluble lauric aldehyde penetrating the positive pillar[5]arenes because of electrostatic interaction, hydrogen bond interaction and CH/ π interaction, and then lauric aldehyde might be more susceptible to be oxidized.

The recycling and stability of the nanosphere catalysts were also evaluated. After six cycles, the catalytic yield of nanospheres is still above 80%, shown in Figure 5B. The structure of the catalyst is basically unchanged after six reaction cycles as confirmed by FT-IR spectrum, shown in Supplementary Figure 10. Unfortunately, the spherical aggregates unable to maintain their original morphology after the second cycle of experiments, but the aggregates are still kept in nanosized, shown in Supplementary Figure 11. This result explained why the catalytic activity still maintained after six cycles.

CONCLUSION

In summary, we exploited the co-assembly of polyanionic functional chromium centered POM $[\text{CrMo}_6\text{O}_{18}(\text{OH})_3]^{3-}$ and polycationic functional pillar[5]arenes in aqueous solution. Interestingly, the nanospheres were formed and their diameters were variable along with the changing of charge ratios of

$\text{CrMo}_6\text{:P5A}$ in ionic complexes. The regularity of the assembly of different charge ratio was detected through DLS, and the morphology of these nanospheres were observed by SEM and TEM. Combined with zeta potential, we presumed a structural model to this system. The well-defined nanospheres were explored as the catalyst for catalytic oxidation of aldehydes into carboxylic acids. Synergy effect which combined both advantages of $[\text{CrMo}_6\text{O}_{18}(\text{OH})_3]^{3-}$ and P5A offers better catalytic effect with relatively good conversion. Future directions of this work are aimed at continuing to find amazing nanostructures, probing the mechanism and exploiting different applications.

AUTHOR CONTRIBUTIONS

MZ did most experiments and data collection work, and wrote the manuscript. KC helped some key data analysis and revised the manuscript. JT helped to do the DLS experiments and revise the manuscript. JZ and YW guided the entire experiments and revised the manuscript.

ACKNOWLEDGMENTS

This work was supported by the National Natural Science Foundation of China (NSFC Nos. 21471087, 21631007, and 21225103). We thank our colleagues, Dr. Qiang Han and Dr. Dejin Zang for experimental assistances and helpful discussions.

SUPPLEMENTARY MATERIAL

The Supplementary Material for this article can be found online at: <https://www.frontiersin.org/articles/10.3389/fchem.2018.00457/full#supplementary-material>

REFERENCES

- Bu, W., Fan, H., Wu, L., Hou, X., Hu, C., Gang, Z., et al. (2002). Surfactant-encapsulated polyoxoanion: structural characterization of its langmuir films and langmuir-blodgett films. *Langmuir* 18, 6398–6403. doi: 10.1021/la020085c
- Bu, W., Li, H., Sun, H., Shengyan Yin, A., and Wu, L. (2005). Polyoxometalate-based vesicle and its honeycomb architectures on solid surfaces. *J. Am. Chem. Soc.* 127, 8016–8017. doi: 10.1021/ja042980j
- Cheng, N., Chen, Y., Wu, X., and Liu, Y. (2018). 2D organic-inorganic nanosheets via self-assembly of a pillar[6]arene and polyoxometalate for enhanced degradation efficiency. *Chem. Commun.* 54, 6284–6287. doi: 10.1039/C8CC03306D
- Crabb, D.W., Matsumoto, M., Chang, D., and You, M. (2004). Overview of the role of alcohol dehydrogenase and aldehyde dehydrogenase and their variants in the genesis of alcohol-related pathology. *Proc. Nutr. Soc.* 63, 49–63. doi: 10.1079/PNS2003327
- Dolbecq, A., Dumas, E., Mayer, C.R., and Mialane, P. (2010). Hybrid organic-inorganic polyoxometalate compounds: from structural diversity to applications. *Cheminform* 41, 6009–6048. doi: 10.1002/chin.201052225
- Han, P., Li, S., Wang, C., Xu, H., Wang, Z., Zhang, X., et al. (2011). UV-responsive polymeric superamphiphile based on a complex of malachite green derivative and a double hydrophilic block copolymer. *Langmuir* 27, 14108–14111. doi: 10.1021/la203486q
- Hashimoto, T., and Maruoka, K. (2008). Recent development and application of chiral phase-transfer catalysts. *Chem. Rev.* 39, 5656–5682. doi: 10.1021/cr068368n
- Ishiba, K., Noguchi, T., Iguchi, H., Morikawa, M.A., Kaneko, K., and Kimizuka, N. (2017). Photoresponsive nanosheets of polyoxometalates formed by controlled self-assembly pathways. *Angew. Chem. Int. Ed.* 56, 2974–2978. doi: 10.1002/anie.201612473
- Kawasaki, N., Wang, H., Nakanishi, R., Hamanaka, S., Kitauro, R., Shinohara, H., et al. (2011). Nanohybridization of polyoxometalate clusters and single-wall carbon nanotubes: applications in molecular cluster batteries. *Angew. Chem. Int. Ed.* 50, 3471–3474. doi: 10.1002/anie.201007264
- Kleiderer, R.L.S., a.E.C. (1930). Piperonylic acid. *Org. Synth.* 10, 82–83. doi: 10.15227/orgsyn.010.0082
- Landsmann, S., Lizandarapueyo, C., and Polarz, S. (2010). A new class of surfactants with multinuclear, inorganic head groups. *J. Am. Chem. Soc.* 132, 5315–5321. doi: 10.1021/ja1011178
- Latchman, D.S. (1995). Biochemistry (4th edn). *Trends Biochem. Sci.* 20, 488. doi: 10.1016/S0968-0004(00)89112-4
- Lechner, M., Guttel, R., and Streb, C. (2016). Challenges in polyoxometalate-mediated aerobic oxidation catalysis: catalyst development meets reactor design. *Dalton Trans.* 45, 16716–16726. doi: 10.1039/C6DT03051C
- Leeuwen, P. W. N. M. V. (2008). *Supramolecular Catalysis*. Weinheim: Wiley-VCH.
- Li, B., Li, W., Li, H., and Wu, L. (2017). Ionic complexes of metal oxide clusters for versatile self-assemblies. *Acc. Chem. Res.* 50, 1391–1399. doi: 10.1021/acs.accounts.7b00055
- Li, H., Pang, S., Wu, S., Feng, X., Müllen, K., and Bubeck, C. (2011). Layer-by-layer assembly and UV photoreduction of graphene-polyoxometalate composite films for electronics. *J. Am. Chem. Soc.* 133, 9423–9429. doi: 10.1021/ja201594k
- Liu, G., and Liu, T. (2005a). Strong attraction among the fully hydrophilic $\{\text{Mo}_7\text{Fe}_3\}$ macroanions. *J. Am. Chem. Soc.* 127, 6942–6943. doi: 10.1021/ja0510966
- Liu, G., and Liu, T. (2005b). Thermodynamic properties of the unique self-assembly of $\{\text{Mo}_7\text{Fe}_3\}$ inorganic macro-ions in salt-free and salt-containing aqueous solutions. *Langmuir* 21, 2713–2720. doi: 10.1021/la047897o
- Liu, M., and Li, C.J. (2016). Catalytic fehling's reaction: an efficient aerobic oxidation of aldehyde catalyzed by copper in water. *Angew. Chem. Int. Ed.* 128, 10964–10968. doi: 10.1002/ange.201604847
- Liu, M., Wang, H., Zeng, H., and Li, C.J. (2015). Silver(I) as a widely applicable, homogeneous catalyst for aerobic oxidation of aldehydes toward carboxylic acids in water—“silver mirror”: From stoichiometric to catalytic. *Sci. Adv.* 1, 1500020–1500030. doi: 10.1126/sciadv.1500020
- Liu, T. (2002). Supramolecular structures of polyoxomolybdate-based giant molecules in aqueous solution. *J. Am. Chem. Soc.* 124, 10942–10943. doi: 10.1021/ja027045f
- Liu, T., Diemann, E., Li, H., Dress, A.W., and Müller, A. (2003). Self-assembly in aqueous solution of wheel-shaped Mo_{154} oxide clusters into vesicles. *Nature* 426, 59–62. doi: 10.1038/nature02036
- Ma, Y., Ji, X., Xiang, F., Chi, X., Han, C., He, J., et al. (2011). A cationic water-soluble pillar[5]arene: synthesis and host-guest complexation with sodium 1-octanesulfonate. *Chem. Commun.* 47, 12340–12342. doi: 10.1039/c1cc15660h
- Marinescu, L.G., and Bols, M. (2006). Very high rate enhancement of benzyl alcohol oxidation by an artificial enzyme. *Angew. Chem. Int. Ed.* 45, 4590–4593. doi: 10.1002/anie.200600812
- Maruoka, K., and Ooi, T. (2003). Enantioselective amino acid synthesis by chiral phase-transfer catalysis. *Chem. Rev.* 103, 3013–3028. doi: 10.1021/cr020020e
- Miras, H.N., Yan, J., Long, D.L., and Cronin, L. (2012). Engineering polyoxometalates with emergent properties. *Chem. Soc. Rev.* 41, 7403–7430. doi: 10.1039/c2cs35190k
- Mizuno, N., Yamaguchi, K., and Kamata, K. (2005). Epoxidation of olefins with hydrogen peroxide catalyzed by polyoxometalates. *Coord. Chem. Rev.* 249, 1944–1956. doi: 10.1016/j.ccr.2004.11.019
- Mo, H. (2006). Carboxylic acids from primary alcohols and aldehydes by a pyridinium chlorochromate catalyzed oxidation. *Cheminform* 37, 2487–2490. doi: 10.1002/chin.200607040
- Müller, A., and Pope, M. T. (1991). Polyoxometalate chemistry: an old field with new dimensions in several disciplines. *Angew. Chem. Int. Ed.* 30, 34–48. doi: 10.1002/anie.199100341
- Ogoshi, T., Kanai, S., Fujinami, S., Yamagishi, T.A., and Nakamoto, Y. (2008). para-Bridged symmetrical pillar[5]arenes: their Lewis acid catalyzed synthesis and host-guest property. *J. Am. Chem. Soc.* 130, 5022–5025. doi: 10.1021/ja711260m
- Ogoshi, T., Yamagishi, T.A., and Nakamoto, Y. (2016). Pillar-shaped macrocyclic hosts pillar[n]arenes: new key players for supramolecular chemistry. *Chem. Rev.* 47, 7937–8002. doi: 10.1021/acs.chemrev.5b00765
- Poblet, J.M., Lopez, X., and Bo, C. (2003). Ab initio and DFT modeling of complex materials: towards the understanding of electronic and magnetic properties of polyoxometalates. *Chem. Soc. Rev.* 32, 297–308. doi: 10.1039/B109928K
- Qi, W., Li, H., and Wu, L. (2008). Stable photochromism and controllable reduction properties of surfactant-encapsulated polyoxometalate/silica hybrid films. *J. Phys. Chem. B* 112, 8257–8263. doi: 10.1021/jp801188e
- Raynal, M., Ballester, P., Vidalferran, A., and Van, P.L. (2014). Supramolecular catalysis. Part 2: artificial enzyme mimics. *Chem. Soc. Rev.* 43, 1734–1821. doi: 10.1039/C3CS60037H
- Rhule, J.T., Hill, C.L., Judd, D.A., and Schinazi, R.F. (1998). Polyoxometalates in medicine. *Chem. Rev.* 98, 327–358. doi: 10.1021/cr960396q
- Ruhoff, J. R. (1936). n-Heptanoic acid. *Org. Synth.* 16:39. doi: 10.15227/orgsyn.016.0039
- Sandborn, L. T. (1929). l-Menthone. *Org. Synth.* 9:52. doi: 10.15227/orgsyn.009.0052
- Tan, L. L., and Yang, Y. W. (2015). Molecular recognition and self-assembly of pillararenes. *J. Inclusion Phenom. Macrocyclic Chem.* 81, 13–33. doi: 10.1007/s10847-014-0441-3
- Travis, B. R., Sivakumar, M., Hollist, G. O., and Borhan, B. (2003). Facile oxidation of aldehydes to acids and esters with oxone. *Org. Lett.* 34, 1031–1035. doi: 10.1021/ol0340078
- Volkmer, D., Chesne, A.D., Kurth, D.G., Schnablegger, H., Lehmann, P., Koop, M.J., et al. (2000). Towards nanodevices: synthesis and characterization of the nanoporous surfactant-encapsulated Keplerate $(\text{DODA})_{40}(\text{NH}_4)_2(\text{H}_2\text{O})_n \subset \text{Mo}_{132}\text{O}_{372}(\text{CH}_3\text{COO})_{30}(\text{H}_2\text{O})_{72}$. *J. Am. Chem. Soc.* 122, 1995–1998. doi: 10.1021/ja992350v
- Wang, C., Chen, Q., Wang, Z., and Zhang, X. (2010). An enzyme-responsive polymeric superamphiphile. *Angew. Chem. Int. Ed.* 49, 8612–8615. doi: 10.1002/anie.201004253
- Wu, P., Yin, P., Zhang, J., Hao, J., Xiao, Z., and Wei, Y. (2011). Single-side organically functionalized Anderson-type polyoxometalates. *Chem. Eur. J.* 17, 12002–12005. doi: 10.1002/chem.201101552
- Xue, M., Yang, Y., Chi, X., Zhang, Z., and Huang, F. (2012). Pillararenes, a new class of macrocycles for supramolecular chemistry. *Acc. Chem. Res.* 45, 1294–1308. doi: 10.1021/ar2003418
- Yao, Y., Li, J., Dai, J., Chi, X., and Xue, M. (2014). A water-soluble pillar[6]arene: synthesis, host-guest chemistry, controllable self-assembly, and application in controlled release. *RSC Adv.* 4, 9039–9042. doi: 10.1039/c3ra46681g

- Yao, Y., Xue, M., Chi, X., Ma, Y., He, J., Abliz, Z., et al. (2012). A new water-soluble pillar[5]arene: synthesis and application in the preparation of gold nanoparticles. *Chem. Commun.* 48, 6505–6507. doi: 10.1039/c2cc31962d
- Yin, P., Zhang, J., Li, T., Zuo, X., Hao, J., Warner, A.M., et al. (2013). Self-recognition of structurally identical, rod-shaped macroions with different central metal atoms during their assembly process. *J. Am. Chem. Soc.* 135, 4529–4536. doi: 10.1021/ja400656j
- Yu, H., Ru, S., Dai, G., Zhai, Y., Lin, H., Han, S., et al. (2017). An efficient iron(III)-catalyzed aerobic oxidation of aldehydes in water for the green preparation of carboxylic acids. *Angew. Chem. Int. Ed.* 56, 3867–3871. doi: 10.1002/anie.201612225
- Zhang, J., Song, Y.F., Cronin, L., and Liu, T. (2008). Self-assembly of organic-inorganic hybrid amphiphilic surfactants with large polyoxometalates as polar head groups. *J. Am. Chem. Soc.* 130, 14408–14409. doi: 10.1021/ja805644a
- Zhang, X., and Wang, C., (2011). Supramolecular amphiphiles. *Chem. Soc. Rev.* 40, 94–101. doi: 10.1039/B919678C
- Zhang, Y., Cheng, Y., Cai, H., He, S., Shan, Q., Zhao, H., et al. (2017). Catalyst-free aerobic oxidation of aldehydes into acids in water under mild conditions. *Green Chem.* 19, 5708–5713. doi: 10.1039/C7GC02983G
- Zhu, Y., Yin, P., Xiao, F., Li, D., Bitterlich, E., Xiao, Z., et al. (2013). Bottom-up construction of POM-based macrostructures: coordination assembled paddle-wheel macroclusters and their vesicle-like supramolecular aggregation in solution. *J. Am. Chem. Soc.* 135, 17155–17160. doi: 10.1021/ja408228b
- Conflict of Interest Statement:** The authors declare that the research was conducted in the absence of any commercial or financial relationships that could be construed as a potential conflict of interest.
- Copyright © 2018 Zeng, Chen, Tan, Zhang and Wei. This is an open-access article distributed under the terms of the Creative Commons Attribution License (CC BY). The use, distribution or reproduction in other forums is permitted, provided the original author(s) and the copyright owner(s) are credited and that the original publication in this journal is cited, in accordance with accepted academic practice. No use, distribution or reproduction is permitted which does not comply with these terms.



Decavanadate Inhibits Mycobacterial Growth More Potently Than Other Oxovanadates

Nuttaporn Samart^{1,2}, Zeyad Arhouma^{1,3}, Santosh Kumar⁴, Heide A. Murakami¹, Dean C. Crick^{3,4} and Debbie C. Crans^{1,3*}

¹ Department of Chemistry, Colorado State University, Fort Collins, CO, United States, ² Department of Chemistry, Rajabhat Rajanagarindra University, Chachoengsao, Thailand, ³ Cell and Molecular Biology Program, Colorado State University, Fort Collins, CO, United States, ⁴ Department of Microbiology, Immunology and Pathology, Colorado State University, Fort Collins, CO, United States

OPEN ACCESS

Edited by:

Christian Hartinger,
University of Auckland, New Zealand

Reviewed by:

Eugenio Garribba,
University of Sassari, Italy
Sanja Grguric-Sipka,
University of Belgrade, Serbia

*Correspondence:

Debbie C. Crans
debbie.crans@colostate.edu

Specialty section:

This article was submitted to
Inorganic Chemistry,
a section of the journal
Frontiers in Chemistry

Received: 24 June 2018

Accepted: 09 October 2018

Published: 20 November 2018

Citation:

Samart N, Arhouma Z, Kumar S,
Murakami HA, Crick DC and
Crans DC (2018) Decavanadate
Inhibits Mycobacterial Growth More
Potently Than Other Oxovanadates.
Front. Chem. 6:519.
doi: 10.3389/fchem.2018.00519

⁵¹V NMR spectroscopy is used to document, using speciation analysis, that one oxometalate is a more potent growth inhibitor of two Mycobacterial strains than other oxovanadates, thus demonstrating selectivity in its interaction with cells. Historically, oxometalates have had many applications in biological and medical studies, including study of the phase-problem in X-ray crystallography of the ribosome. The effect of different vanadate salts on the growth of *Mycobacterium smegmatis* (*M. smeg*) and *Mycobacterium tuberculosis* (*M. tb*) was investigated, and speciation was found to be critical for the observed growth inhibition. Specifically, the large orange-colored sodium decavanadate ($V_{10}O_{28}^{6-}$) anion was found to be a stronger inhibitor of growth of two mycobacterial species than the colorless oxovanadate prepared from sodium metavanadate. The vanadium(V) speciation in the growth media and conversion among species under growth conditions was monitored using ⁵¹V NMR spectroscopy and speciation calculations. The findings presented in this work is particularly important in considering the many applications of polyoxometalates in biological and medical studies, such as the investigation of the phase-problem in X-ray crystallography for the ribosome. The findings presented in this work investigate the interactions of oxometalates with other biological systems.

Keywords: vanadate, speciation, sodium metavanadate, decavanadate, growth inhibition, tuberculosis

INTRODUCTION

Polyoxometalates (POMs) are a class of compounds that have been investigated in a range of biological and biomedical systems, as their effects in cell culture studies and *in vivo* suggest that these compounds have potential for use as therapeutic agents (Moskovitz and Group, 1988; Hill et al., 1990; Rhule et al., 1998; Aureliano and Crans, 2009; Fraqueza et al., 2012; Aureliano et al., 2013, 2016; Wang et al., 2013; Aureliano and Ohlin, 2014; Leon et al., 2014; Kioseoglou et al., 2015; Shah et al., 2015; Sun et al., 2016; Fu et al., 2018; Gumerova et al., 2018). Decavanadate is a homopolyoxometalate anion, and one of the POMs that has been reported to have known biological effects, as documented by studies reported with cells as well as with

isolated enzyme systems. (Pluskey et al., 1996; Aureliano and Crans, 2009; Zhai et al., 2009; Fraqueza et al., 2012; Turner et al., 2012; Aureliano et al., 2013; Kioseoglou et al., 2013; Aureliano, 2014, 2016; Aureliano and Ohlin, 2014). Protein crystal structures have been reported for some protein-POM complexes such as those reported between the ribosome and a Dawson oxometallate (Weinstein et al., 1999; Auerbach-Nevo et al., 2005; Bashan and Yonath, 2008; Noeske et al., 2015). Other protein-POM complexes include protein complexes with smaller oxometalates such as decavanadate (Winkler et al., 2017). The limited stability of decavanadate at neutral pH would suggest that hydrolysis intermediates may form and generate stable complexes with proteins or cellular components. Speciation studies are important in this regard, and different species and possibilities must be considered when investigating the mode of action of systems that are not thermodynamically stable (Aureliano and Crans, 2009; Levina et al., 2017a). Even if the speciation is characterized, the active species and mode of action of these complex systems can be non-trivial to interpret (Willsky et al., 1984b, 1985, 2011; Delgado et al., 2005; Crans et al., 2011; Postal et al., 2016; Jakusch and Kiss, 2017). However, a wide range of activities have been reported depending on the protein, biological system or specific vanadium species (Crans, 2000; Crans et al., 2013; Correia et al., 2015; Postal et al., 2016). Recently, it has become clear that compound uptake is critical to the mode of action because many vanadium compounds are modified during the uptake process (Pessoa and Tomaz, 2010; Crans et al., 2011; Le et al., 2017; Levina et al., 2017a). In the case of a large anion such as decavanadate, the question is simply whether the species is too large to enter through protein channels and thus must be taken up through endocytosis or passive transport mechanisms. The alternative possibility is that the uptake is of the smaller vanadium oxovanadates, such as monomeric vanadate, which then oligomerizes to form decavanadate inside the cell. The formation of decavanadate has been demonstrated in yeast (*S. cerevisiae*) and thus makes this anion a desirable system to understand in greater detail (Willsky et al., 1984b, 1985).

Vanadium is a first-row transition metal ion and is in the group of transition metals that can form POMs (Baes, 1976; Chasteen, 1983; Vilas Boas and Costa Pessoa, 1987; Pope and Müller, 1991; Rehder, 1991; Crans et al., 2004, 2017). Vanadium is particularly prone to forming homopolyoxometalate ions as well (Baes, 1976; Aureliano and Crans, 2009). Indeed, pure crystalline metavanadate and orthovanadate upon dissolution will form several oxovanadate species containing vanadate monomer, V_1 , vanadate dimer, V_2 , vanadate tetramer, V_4 , vanadate pentamer, V_5 and decavanadate, V_{10} (Pettersson et al., 1983, 1985; Crans et al., 1990), **Figure 1**. Some of these species have been characterized using X-ray crystallography and have been found to interconvert in aqueous solution (Evans, 1966; Crans et al., 1990). However, the specifics of the reactions and their conditions vary. For example, vanadate and oligomeric species containing 2, 4, and 5 vanadium atoms are colorless and rapidly convert at neutral pH, **Figure 1A** (Crans et al., 1990). In contrast, decavanadate will form rapidly at acidic pH, but is only kinetically stable at neutral pH, **Figure 1B** (Baes, 1976; Pope and Müller, 1991; Aureliano and

Crans, 2009; Crans et al., 2017). Indeed, the kinetic studies have shown that decamer formation is a rapid process and much faster than the V_{10} decomposition in both neutral and basic solution (Clare et al., 1973a,b; Druskovich and Kepert, 1975; Comba and Helm, 1988; Kustin, 2015; Crans et al., 2017). The decomposition pathways investigated follow several different mechanisms and are dependent on the concentrations of H^+ and OH^- and the other counter ions present in solution (Clare et al., 1973a,b; Druskovich and Kepert, 1975; Comba and Helm, 1988; Kustin, 2015). Information is needed describing how decavanadate interacts with membrane interfaces and cellular systems, including how decavanadates biological activities compare to monomeric vanadate. Specifically, an attractive alternative mode of action to simple decavanadate binding would be the direct delivery of a vanadium atom from decavanadate to a biomolecule resulting in the dissolution of the decavanadate cluster. The X-ray characterization of decavanadate shows that its dimensions are $5.4 \text{ \AA} \times 7.7 \text{ \AA} \times 8.3 \text{ \AA}$, **Figure 1** (Evans, 1966), a large size that cannot be accommodated by many biological transport channels. Therefore, any uptake of decavanadate is likely to be through endocytosis or a passive mechanism. An attractive alternative mode of uptake would involve dissolution of the cluster by direct delivery of vanadium atoms, for example, into a system such as a protein. However, such a mechanism is more difficult to investigate and will require more information regarding the potential interactions of the anion with ligands and interfaces. We have been addressing related questions for some time (Crans et al., 2017) and exploring the interactions of V_{10} with interfaces (Baruah et al., 2006; Crans et al., 2006, 2017; Samart et al., 2014; Sanchez-Lombardo et al., 2016). Indeed, more information is needed to be able to characterize the process of how the decavanadate converts to the vanadate monomer and smaller clusters, but such processes undoubtedly involve the molecular association of structures that form in solution. The work presented in this manuscript compares the effect of decavanadate and oxovanadates on two mycobacterial species. The results of this comparison are related to the questions of uptake of vanadate and will form the background information on which it will be possible to begin to address issues regarding potential delivery of V-atoms as well as uptake of decavanadate compared to monomeric and oligomeric vanadate.

Mycobacteria are particularly resistant to hydrophilic drug penetration, and thus studies with these organisms are of general interest. There have been several studies documenting the possibility that vanadium may affect growth of the bacteria, whether in a stimulatory or inhibitory manner; however, these studies did not consider the speciation of the studied compounds in growth media and in the biological context of the cells. For example, previous studies have been carried out investigating the effects of the simple salt vanadate on the cell growth of mycobacteria in the presence and absence of Tween-80 (Costello and Hedgecock, 1959). These studies investigated the possibility that vanadium may be stimulatory to growth because it would be able to replace Fe^{2+} , Fe^{3+} , or biologically active Mo-atoms (Turian, 1951). Dose response curves reported in cultures in the presence of added metavanadate gave complete growth inhibition

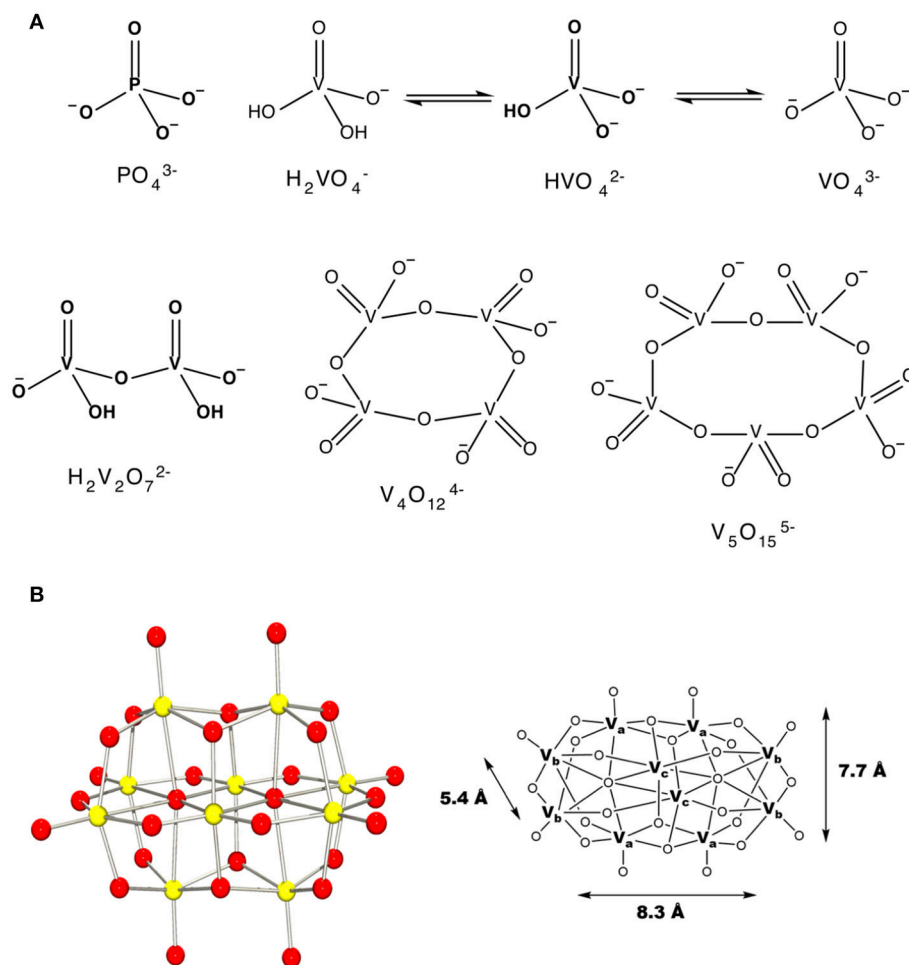


FIGURE 1 | The schematic structures of (A) monomeric vanadate, monomeric and polymeric vanadate series (B) X-ray structure of V_{10} and the three different types of vanadium atoms in this complex ion with indicated dimensions (Evans, 1966). This figure was adapted with permission from Aureliano and Ohlin (2014), Crans et al. (2017).

observed at 5.0 $\mu\text{g/mL}$ V-atom for *M. tb* (H37Rv), at 10 $\mu\text{g/mL}$ V-atom for *Mycobacterium butyricum*, at 50 $\mu\text{g/mL}$ V-atom for *Mycobacterium phlei*, but even at 200 $\mu\text{g/mL}$ V-atom *M. smeg* was not completely inhibited (Costello and Hedgecock, 1959).

Additionally, studies have been carried out on vanadium coordination complexes and their effect on the growth of mycobacteria (Maiti and Ghosh, 1989; David et al., 2005; Correia et al., 2014; Gajera et al., 2015). The studies explore the possibility that a known drug, or drug derivative complexes binding to vanadium, may exert a greater synergetic activity (Correia et al., 2014; Gajera et al., 2015). For example, in a series of hydroxyquinoline (Correia et al., 2014), fluoroquinoline (Gajera et al., 2015) and acid hydrazides (Martins et al., 2015) vanadium(V) complex studies, the complexes were found with micromolar inhibitory potency against *M. tb*. In other systems the vanadium complex was found to have little if any effect on the growth of the bacterium (Maiti and Ghosh, 1989; Gajera et al., 2015). Additionally, a series of vanadium

thiosemicarbazone and hydroquinoline complexes tested against *M. tb* were found to have micromolar inhibition constant against growth, but the ligand was more potent than the complex (Correia et al., 2014; Gajera et al., 2015). In these cases, complexation to the vanadium protected the bacterium. Combined these studies demonstrate that vanadium compounds may be inhibitory or protective, depending on the environment and ligands that may be complexed to it, and thus it is of interest to investigate the effects of simple vanadium complexes prior to formation of a coordination complex.

In this work, we determine the effects of decavanadate and the rapidly exchanging oxovanadates on the growth of two mycobacterial species. These studies directly compare the effects of the two vanadium salt species and in doing so, will allow researchers to address the issue of whether such oxometalate species exert different effects, possibly due to uptake or conversion of the salt under physiological conditions. In our studies with *M. smeg* and *M. tb*, it was discovered

that decavanadate undergoes hydrolysis forming monomeric vanadate in the presence of the cells, suggesting some type of interaction with the bacterial cells or with the material excreted by the bacterial cells. Comparison of metavanadate and decavanadate demonstrates that these two oxovanadate species have very different effects on the growth of these mycobacterial species and depending on species, the potency varies.

MATERIALS AND METHODS

Materials

Sodium metavanadate (99.9% NaVO_3) was purchased from Sigma-Aldrich, hydrochloric acid (36.5–38%, HCl) and citric acid (99% $\text{C}_6\text{H}_8\text{O}_7$) were purchased from Fischer. Deuterium oxide (D_2O , 99.9%) was purchased from Cambridge Isotope Laboratories, Inc. All reagents and other chemicals was purchased from Sigma-Aldrich. Vanadium complexes were prepared according to literature (Samart et al., 2014; Sanchez-Lombardo et al., 2016).

Preparation of Stock Solutions for NMR Spectroscopy Evaluation

Vanadate

Colorless stock solutions of sodium metavanadate (NaVO_3 , 100 mM) were prepared in deuterium oxide (D_2O). The suspension was heated to dissolve the solid, the solution was cooled to room temperature and then the pH was measured (~pH 7–8) (Crans et al., 1990).

Decavanadate

An orange-red solution of sodium decavanadate ($\text{Na}_6\text{V}_{10}\text{O}_{28}$, 100 mM) was prepared from NaVO_3 (1.00 M, 1.22 g). Sodium metavanadate solutions were prepared directly by addition of solid NaVO_3 to D_2O and heating the solution to dissolve the solid. Once the solution was clear, the pH was adjusted to 4.5–5.8 using 6 M DCl (DCl was prepared from 12 M HCl by the addition of D_2O) resulting in an orange colored solution. The V_{10} content in this solution was verified using ^{51}V NMR spectroscopy and assuming the vanadium was all present as $\text{V}(\text{V})$ the concentration of each oxovanadate could be calculated from the integration of the spectra (Crans et al., 1990).

Citric Acid and V-Citrate Complex Solutions

Stock solutions of citric acid (100 mM, pH 2.33) were prepared in deuterium oxide (D_2O). The vanadium-citrate complexes were prepared by adding equimolar amounts of citric acid and vanadium. The solution was diluted to form solutions with 75, 50, 10, and 5.0 mM vanadium(V).

Preparation of Stock Solution to Cell Culture Studies

Stock solutions of vanadate and vanadium complexes were prepared in double distilled water ($\text{DI H}_2\text{O}$), 7H9 media or in 100% DMSO depending on the solubility of these complexes. Specifically, metavanadate, orthovanadate or decavanadate were prepared in double distilled water. Isoniazid (INH) was dissolved in sterile distilled water and used as a positive control.

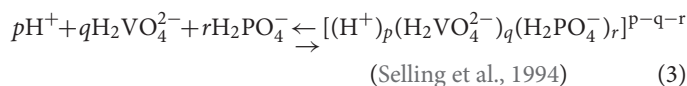
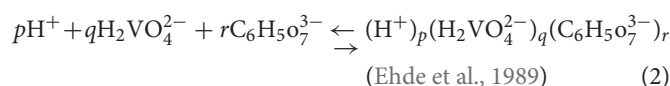
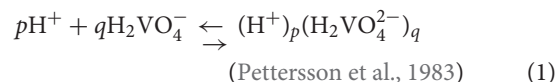
Nuclear Magnetic Resonance (NMR) Measurements

All ^{51}V NMR spectroscopy measurements were taken on a Bruker spectrometer at 78.9 MHz for ^{51}V (400 MHz for ^1H). The chemical shifts were obtained using external reference for ^{51}V NMR of Na_3VO_4 (100 mM, pH 12.9, signals at -535 (V_1) and -559 ppm (V_2)). The samples were prepared fresh to form vanadium-citrate complexes in media and the composition was investigated as a function of time with experiments carried out at time points: 0, 1, 5, and 24 h.

Speciation of vanadium was calculated using the integration of the vanadium peak(s) within the ^{51}V NMR spectra. The concentration of each species was determined using the known added concentration [assuming all vanadium is in the form of $\text{V}(\text{V})$] (Crans et al., 1990), the integration of the vanadium peak(s) in the spectrum and by using the mole fractions for each signal, the concentration of each species could be calculated as shown in Table 1.

Speciation Analysis

The interpretation of the ^{51}V NMR spectral data was supplemented by speciation calculations based on constants measured previously (Pettersson et al., 1983; Ehde et al., 1989; Selling et al., 1994). The species distribution diagrams were calculated by using HySS 2009 software (Alderighi et al., 1999; Carsella et al., 2017) and known speciation constants of the system at hand (Pettersson et al., 1983; Ehde et al., 1989; Selling et al., 1994). The citrate and the phosphate concentrations found in the Middlebrook 7H9 broth medium supplemented with 5% BSA, 2% dextrose, 5% catalase (ADC) enrichment, glycerol (0.2%, v/v), and Tween 80 (0.05%, v/v) were 0.48 and 24 mM, respectively (Bbltm, 2018). The vanadium concentrations that were investigated were concentrations of 5, 3.3, and 10 mM. The speciation diagrams were constructed using the following equilibrium reactions for the binary $\text{H}^+ - \text{H}_2\text{VO}_4^{2-}$ system [see equation (1)] (Pettersson et al., 1983), and two ternary system, $\text{H}^+ - \text{H}_2\text{VO}_4^{2-} - \text{C}_6\text{H}_5\text{O}_7^{3-}$ and $\text{H}^+ - \text{H}_2\text{VO}_4^{2-} - \text{H}_2\text{PO}_4^-$ [see equation (2) (Ehde et al., 1989) and (3) (Selling et al., 1994)]. The alternate formulas were provided in the format of the equations provided for comparison.



As described previously, the equations above describe the nature of the complexes that form. For example, HVO_4^{2-} is described as $\text{H}_2\text{VO}_4^{2-}$ minus H^+ and thus the species is described as $(-1,1)$ where the p being -1 (Pettersson et al., 1983; Ehde et al., 1989).

TABLE 1 | Formation constants of Vanadate species in a 0.6M NaCl system.

(p, q)	log β	Formula	Extended formula
BINARY SYSTEM (H^+-$H_2VO_4^-$) REF (2)			
-1, 1	-7.92	HVO_4^{2-}	$(H^+)_{-1}(H_2VO_4^{2-})$
-2, 2	-15.17	$V_2O_7^{4-}$	$(H^+)_{-2}(H_2VO_4^{2-})_2$
-1, 2	-5.25	$HV_2O_7^{3-}$	$(H^+)_{-1}(H_2VO_4^{2-})_2$
0, 2	2.77	$H_2V_2O_7^{2-}$	$(H_2VO_4^{2-})_2$
-2, 4	-8.88	$V_4O_{13}^{6-}$	$(H^+)_{-2}(H_2VO_4^{2-})_4$
-1, 4	0.22	$HV_4O_{13}^{5-}$	$(H^+)_{-1}(H_2VO_4^{2-})_4$
0, 4	10.0	$V_4O_{12}^{4-}$	$(H_2VO_4^{2-})_4$
0, 5	12.4	$V_5O_{15}^{5-}$	$(H_2VO_4^{2-})_5$
4, 10	52.1	$V_{10}O_{28}^{6-}$	$(H^+)_{-4}(H_2VO_4^{2-})_{10}$
5, 10	58.1	$HV_{10}O_{28}^{5-}$	$(H^+)_{-5}(H_2VO_4^{2-})_{10}$
6, 10	61.9	$H_2V_{10}O_{28}^{4-}$	$(H^+)_{-6}(H_2VO_4^{2-})_{10}$
7, 10	63.5	$H_3V_{10}O_{28}^{3-}$	$(H^+)_{-7}(H_2VO_4^{2-})_{10}$
2, 1	6.96	VO_2^+	$(H^+)_{-2}(H_2VO_4^{2-})_{10}$
(p, q, r) log β Formula Extended formula			
TERNARY SYSTEM (H^+-$H_2VO_4^-$-$C_6H_5O_7^{3-}$) REF (3)			
1, 0, 1	5.217	Cit^{2-}	$(H^+)(Cit^{3-})$
2, 0, 1	9.298	Cit^-	$(H^+)_2(Cit^{3-})$
3, 0, 1	12.067	Cit	$(H^+)_3(Cit^{3-})$
1, 2, 1	12.84	$(H^+)(H_2VO_4^{2-})_2(Cit^{3-})$	
2, 2, 1	19.68	$(H^+)_2(H_2VO_4^{2-})_2(Cit^{3-})$	
3, 2, 1	24.12	$(H^+)_3(H_2VO_4^{2-})_2(Cit^{3-})$	
3, 1, 1	18.35	$(H^+)_3(H_2VO_4^{2-})(Cit^{3-})$	
2, 1, 1	14.1	$(H^+)_2(H_2VO_4^{2-})(Cit^{3-})$	
4, 2, 2	31.3	$(H^+)_4(H_2VO_4^{2-})_2(Cit^{3-})_2$	
5, 2, 2	35.3	$(H^+)_5(H_2VO_4^{2-})_2(Cit^{3-})_2$	
6, 2, 2	39.2	$(H^+)_6(H_2VO_4^{2-})_2(Cit^{3-})_2$	
(p, q, r) log β Formula Extended formula			
TERNARY SYSTEM (H^+-$H_2VO_4^-$-$H_2PO_4^-$) REF (4)			
-2, 0, 1	-17.650	PO_4^{3-}	$[(H^+)_{-2}(H_2PO_4^-)]^{3-}$
-1, 0, 1	-6.418	HPO_4^{2-}	$[(H^+)_{-1}(H_2PO_4^-)]^{2-}$
1, 0, 1	1.772	H_3PO_4	$[(H^+)(H_2PO_4^-)]$
9, 14, 1	90.7	$H_3PV_{14}O_{42}^{6-}$	$[(H^+)_9(H_2VO_4^{2-})_{14}(H_2PO_4^-)]^{6-}$
10, 14, 1	94.84	$H_4PV_{14}O_{42}^{5-}$	$[(H^+)_{10}(H_2VO_4^{2-})_{14}(H_2PO_4^-)]^{5-}$
11, 14, 1	96.41	$H_5PV_{14}O_{42}^{4-}$	$[(H^+)_{11}(H_2VO_4^{2-})_{14}(H_2PO_4^-)]^{4-}$

Bacterial Strains and Culture Conditions

Mycobacterium smegmatis mc²155 was grown in 7H9 Middlebrook Medium supplemented with 0.2% (v/v) glycerol, 10% ADC, 0.05% Tween-80, and incubated at 37°C with shaking for 24 h. The growth of bacteria was monitored to mid-logarithmic growth phase using a spectrophotometer at 600 nm to an optical density of 0.6 (OD_{600nm}) (Bbl™, 2018). Metavanadate (40 mM, pH 8.6) and decavanadate [100 mM V₁₀ (1.0 M V-atoms), pH 3.8] stock solutions and the media with bacteria were added to a 96 well plate in a 3-fold dilution experiment monitored at times 0, 1, 5, and 24 h. The pH of these samples ranged from 5.5 to 6.3 before and after treatment with

V-compounds and growth; see spectra for in supplemental for details (Upadhyay et al., 2015).

Culture supernatant after cell growth generated for ⁵¹V NMR analysis was prepared by running separate growth experiments for the *M. smeg* mc² 155 experiments with a total volume of 5 mL. At each time point, a 1 mL aliquot was removed for NMR analysis. ⁵¹V NMR spectra were run at the time points 0, 1, 5, and 24 h without lock.

M. tb mc² 6230 is a nonpathogenic deletion mutant (Δ RD1 Δ panCD) strain H37Rv that can safely be used in a Biosafety Level 2 conditions (Sambandamurthy et al., 2006). The bacteria were grown in 7H9 Middlebrook medium with the addition of D-pantothenate (24 mg/L) at 37°C to an optical density at 600 nm (OD_{600nm}) of 0.6–0.8. The cultures were diluted and treated with the appropriate metavanadate and decavanadate stock solutions in a 96 well plate in a 3-fold dilution experiment, and incubated at 37°C for the duration of the experiment (5–7 days). The pH values of these samples ranged from 5.6 to 6.8 after growth for 5 days; see spectra for details.

⁵¹V NMR spectra were acquired on culture supernatant without lock (no D₂O in sample) at the beginning and end of the bacterial growth experiment (0 and 5 days) for *M. tb* mc² 6230 growth samples.

RESULTS

Investigating the effects of both vanadate and decavanadate on mycobacterial growth requires information on the speciation of vanadium under the conditions of the growth assay studies. *M. tb* and *M. smeg* were grown in supplemented Middlebrook 7H9 medium. Some of the components of the medium may form vanadium complexes. The major candidates for complex formation based on literature formation constants are phosphate (Gresser et al., 1986), citrate (Pettersson et al., 1985; Levina et al., 2017a), and amino acids (Crans, 2000; Rehder et al., 2002; Esbak et al., 2009). In the following, we investigated whether these complexes formed in the media, **Figure 1**.

Reaction of Vanadate and Decavanadate With Components in Growth Media

⁵¹V NMR studies were carried out with vanadate and decavanadate solutions and Middlebrook 7H9 broth medium supplemented with 10% ADC enrichment (5% BSA, 2% dextrose, 5% catalase), glycerol (0.2%, v/v) and Tween 80 (0.05%, v/v). The mycobacteria grow well at pH 6.8, and decavanadate is known to form between pH 3 to 6.5 (Pope and Müller, 1991; Crans et al., 2004; Baruah et al., 2006; Aureliano and Crans, 2009). V₁₀ is formed at low pH values and the V₁₀ hydrolyzes at neutral pH. When V₁₀ is added to the growth media the pH was increased from pH 7.6 to 6.5/7 by the buffering capacity of the growth media and there is a potential for hydrolysis of V₁₀. Importantly, little hydrolysis is observed in growth media in the absence of mycobacteria. NMR spectra were recorded at a range of pH values because the reactions of vanadate are very sensitive to pH (see **Supplemental Material**); however, the spectra shown in **Figures 2 and 3** are those of direct relevance to observation

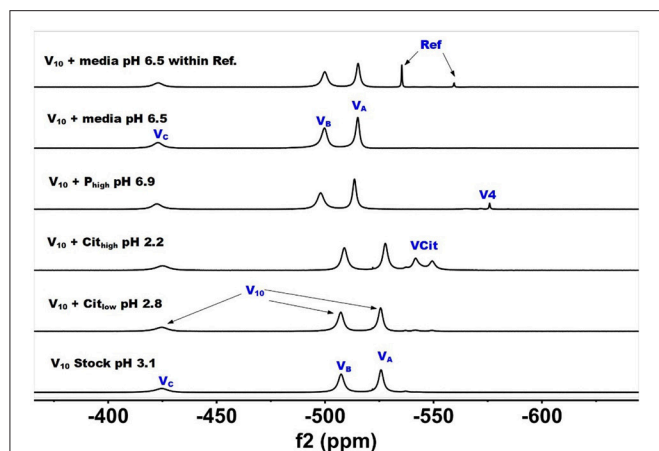


FIGURE 2 | ^{51}V NMR (78.9 MHz) spectra are shown of solution of decavanadate (10 mM V_{10} , 100 mM V-atoms). The samples are from the bottom up diluted V_{10} stock solution (100 mM V-atom) at pH 3.1; 10 mM V_{10} in the presence of 0.48 mM and 0.97 mM citrate at pH 2.8 and 2.2, respectively; 10 mM V_{10} in the presence of 24 mM P_i at pH 6.9; and finally 10 mM V_{10} in the presence of Middlebrook 7H9 broth medium supplemented with 10% ADC enrichment (5% BSA, 2% dextrose, 5% catalase), glycerol (0.2%, v/v) and Tween 80 (0.05%, v/v) recorded both in the absence and the presence of a capillary reference of 100 mM Na_3VO_4 .

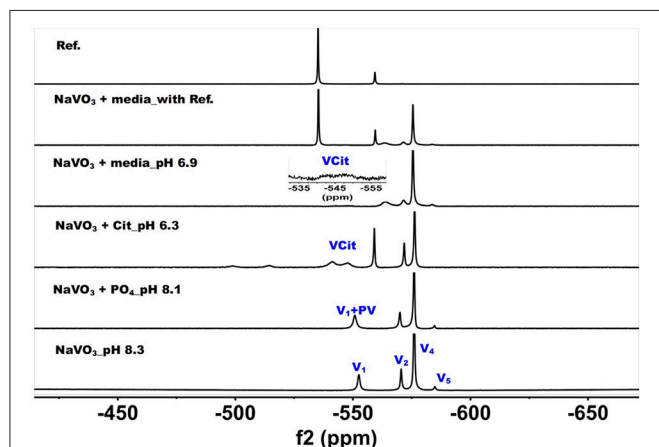


FIGURE 3 | ^{51}V NMR (78.9 MHz) spectra are shown of solution of colorless oxovanadate (40 mM V_1 , 40 mM V-atoms). The samples are from the bottom up diluted V_1 stock solution (40 mM V-atom) at pH 8.3; 10 mM V_{10} in the presence of 24 mM P_i at pH 8.1; 10 mM V_{10} in the presence of 0.48 mM citrate at pH 6.3, and finally 10 mM V_{10} in the presence of Middlebrook 7H9 broth medium supplemented with 10% ADC enrichment (5% BSA, 2% dextrose, 5% catalase), glycerol (0.2%, v/v) and Tween 80 (0.05%, v/v) recorded both in the absence and the presence of a capillary reference of 100 mM Na_3VO_4 . The spectrum labeled Reference is of the capillary reference alone (top spectrum). The key to the signals: V-oligomers, V_1 monomer; V_2 , dimer; V_4 , tetramer; V_5 , pentamer; VCit, V-citrate complex; PV, vanadate-phosphate complex.

and assignment of the species that form in the growth media (see below **Figure 4**). Importantly, all the spectra are referenced against a reference sample (labeled Ref. in **Figure 3**, containing 100 mM Na_3VO_4).

In **Figure 2**, we show the spectra of decavanadate under various conditions. First, we show the spectrum of the stock solution at pH 3.1 with the three characteristic signals for the three different V-atoms in the V_{10} molecule. Next, we show two spectra with added citrate at two concentrations at pH 2.8 and 2.2 where the decavanadate will form VCit complex (two signals at -548 and -552 ppm). The next three spectra at higher pH values are shown first in the presence of phosphate (P_i), demonstrating that the signals for V_{10} shifts as the pH increases from 3 to 6.9. As shown in the final two spectra in **Figure 2**, V_{10} in the presence of media that contains both citrate and P_i did not form any other V-products when all V-atoms are in the form of V_{10} . The spectrum of V_{10} in media is shown both in the presence and absence of a capillary tube filled with Na_3VO_4 and used to reference the spectra (**Figure 2**). All the NMR spectra were referenced in this manner and the other NMR spectra are provided in the **Supplemental Material**. In summary, these spectra shown that when vanadium is present in the form of V_{10} , other vanadium species do not form in the cell media.

The spectra shown in **Figure 2** demonstrated that the V_{10} is stable in the growth media, which is consistent with studies in yeast media reported previously (Willsky et al., 1984a, 1985). The data shown in **Figure 2** demonstrated that at pH 2, the V_{10} forms complexes with citrate but as the pH increased to near neutral pH, V_{10} did not form such products with growth media components (Ehde et al., 1989; Zhou et al., 1999; Crans, 2000; Kaliva et al., 2002, 2003; Chen et al., 2007, 2014; Lodyga-Chruscinska et al., 2008). In contrast, when V_{10} is converted to the oxovanadates or V_1 is the starting form at vanadium, the VCit and PV complexes are formed (this is generally observed in solutions at neutral or more basic pH values, **Figure 3**). However, if the pH of the growth media decreases (that is the acidity increase and pH value decrease), V_{10} hydrolyzes and forms oxometalates that are able to react with media components (see **Figures 2, 3**).

The spectra of solutions from metavanadate (NaVO_3) containing vanadate monomer and other oxovanadates prepared in aqueous solution and in media are shown in **Figure 3**. Since vanadate solutions contain rapidly converting species (Crans et al., 1990) and the composition depends on pH and concentration, the species present is dependent on the solution composition. The first spectrum shows a solution containing the interconverting oxovanadates, V_1 , V_2 , V_4 , and V_5 . In the presence of P_i and at slightly lower pH value, the V_1 signal shifted and the linewidth increased, which is indicative of the formation of a vanadate-phosphate complex (abbreviated PV on the spectra in **Figure 2**) (Gresser et al., 1986; Andersson et al., 2005). Although there are no X-ray structures for these species, the Gresser-Tracey team proposed that there is both a vanadium species that is four or five-coordinate and octahedral based on the chemistry shifts). The formation of the PV species (Gresser et al., 1986; Andersson et al., 2005) is rapid on the NMR time scale, and thus results in shifting of the vanadate monomer (V_1) signal in place of observing two separate signals one for V_1 and one for PV. As the pH decreased to 6.3, V_1 protonates and the monomer signal shifts to about -560 ppm. At these higher pH values, the

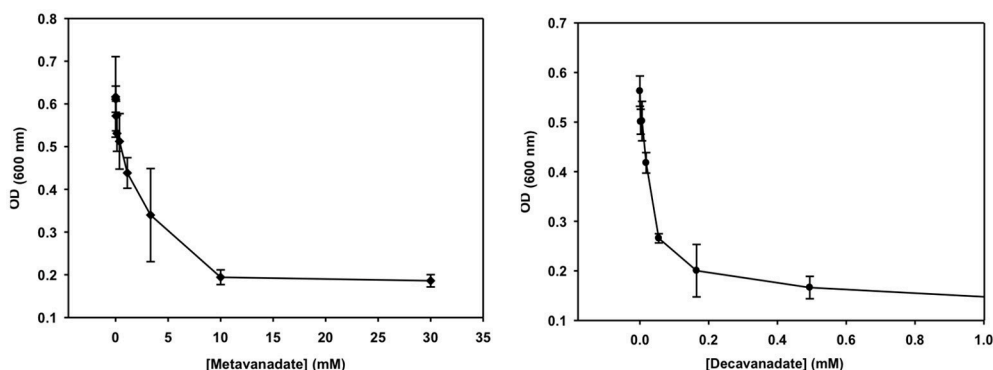


FIGURE 4 | The growth curve is shown for treatment with vanadate (left, prepared from a 40 mM colorless metavanadate solution) and decavanadate [right, prepared from a 100 mM orange decavanadate solution (1.0 M V-atoms) on *M. tb*].

TABLE 2 | The EC₅₀ values for V₁ and V₁₀ treated *Mycobacterium tuberculosis* and *smegmatis*.

	EC ₅₀ (<i>M. tb</i>) (mM)	Stand. error	EC ₅₀ (<i>M. tb</i>) (mM V-atoms)	Stand. error	EC ₅₀ (<i>M. smeg</i>) (mM)	Stand. error	EC ₅₀ (<i>M. smeg</i>) (mM V-atoms)	Stand. error
V ₁	2.0	0.43	2.0	0.43	0.19	0.071	0.19	0.071
V ₁₀	0.029	0.005	0.29	0.05	0.0037	0.0004	0.037	0.004

VCit complex is found to form in solutions containing both V₁ and citrate. Many different VCit complexes are known, however, the broad doublet signal observe for the VCit could be several structures as described in the literature (Ehde et al., 1989; Zhou et al., 1999; Crans, 2000; Kaliva et al., 2002, 2003; Chen et al., 2007, 2014; Lodyga-Chruscinska et al., 2008). The final spectra show the addition of the vanadate stock solution to media, which at pH 6.9 results in a solution that contains a signal of V₁ and PV, V₂, and V₄ and a trace of V₅. The amount of VCit formed is low and it is difficult to see the signal from in the normal growth media spectrum, so we used an increased amplification to show the VCit signal and part of such spectrum is shown in the spectral insert.

In summary, if the growth of the mycobacteria is conducted near pH 6.8, the speciation of vanadium (V) will readily reach thermodynamic control. Solutions prepared from NaVO₃ will contain little to no V₁₀ and solutions containing V₁₀ will be relatively stable. Therefore, growth studies will be carried out with either V₁ or V₁₀ species, and it will be possible to determine if there is a difference in the growth effects on mycobacteria by these two species. That is the growth effects of the V₁ with the oligomeric oxovanadates and V₁₀ are measured in media with known vanadium speciation and under conditions where it is possible to observe the effect of each species.

Growth Inhibition Experiments of Vanadate Monomer and Decavanadate

Growth inhibition experiments were designed to measure the effects of V₁₀ and V₁ each on *M. tb* mc² 6230 and *M. smeg* mc² 155. The measurements monitor growth using absorbance at 600 nm and the concentration of the vanadium compound

was changing with 3-fold dilution experiments. In this manner, the growth of the bacteria was measured over a 2,000-fold range of concentrations of vanadium compound. The results with the *M. tb* are shown in **Figure 4**, and the EC₅₀ (concentration of compound where growth is reduced by half) value calculated for the V₁ experiment was 2.0 mM (2.0 mM V-atoms) and for the V₁₀ experiment 29 μM (0.29 mM V-atoms, **Table 2**).

These results show that V₁₀ is a more potent inhibitor than V₁ by a factor of 100 in terms of concentration and a factor of 10 in terms of concentration of V-atoms. This result demonstrates that the large V₁₀ anion is more inhibitory than the V₁ atom even when counting for the fact that there are 10 V-atoms in each V₁₀ species. As discussed below, ⁵¹V NMR spectroscopy was used to examine the speciation in the solutions and verify that the V₁₀ solution indeed contained V₁₀ (see below for details).

The growth effects were also measured for *M. smeg* mc² 155 for both V₁₀ and V₁ (data not shown). Similarly, the EC₅₀ values were calculated for the V₁ experiment to be 190 μM (0.190 mM V-atoms) and for the V₁₀ experiment to be 3.7 μM (0.037 mM V-atoms). These results show that the V₁₀ is a more potent inhibitor than V₁, by a factor of 100 in terms of concentration and a factor of 10 in terms of concentration of V-atoms as we also observed for *M. tb*.

These results present evidence that the large compact V₁₀-anion is a stronger inhibitor than V₁ of cell growth of the two mycobacterial strains. The more potent inhibition by V₁₀ compared to V₁ shows that the V₁₀ is an inhibitor, and that it is not V₁ formed from hydrolyzed V₁₀. However, it should be mentioned that it is solutions of V₁₀ that are causing the inhibitory growth effect, and we cannot rule out the possibility that the effect is caused by several species including the hydrolysis

products, or some mechanism in which V_{10} delivers the V-atom to the cells. Regardless, these studies demonstrate the effects of simple oxovanadates and the large decavanadate. The fact that V_{10} has a greater effect than V_1 (or 10 V_1 molecules) supports the interpretation that the growth effects observed are not due to V_1 formed from hydrolyzed V_{10} . To support this interpretation, we acquired the ^{51}V NMR spectra of the growth media solutions at various times during the growth experiment.

Speciation Studies in Media of Mycobacteria Treated With Vanadate and Decavanadate

^{51}V NMR Spectra of Media That Have Grown Mycobacteria and Have Been Treated With Metavanadate

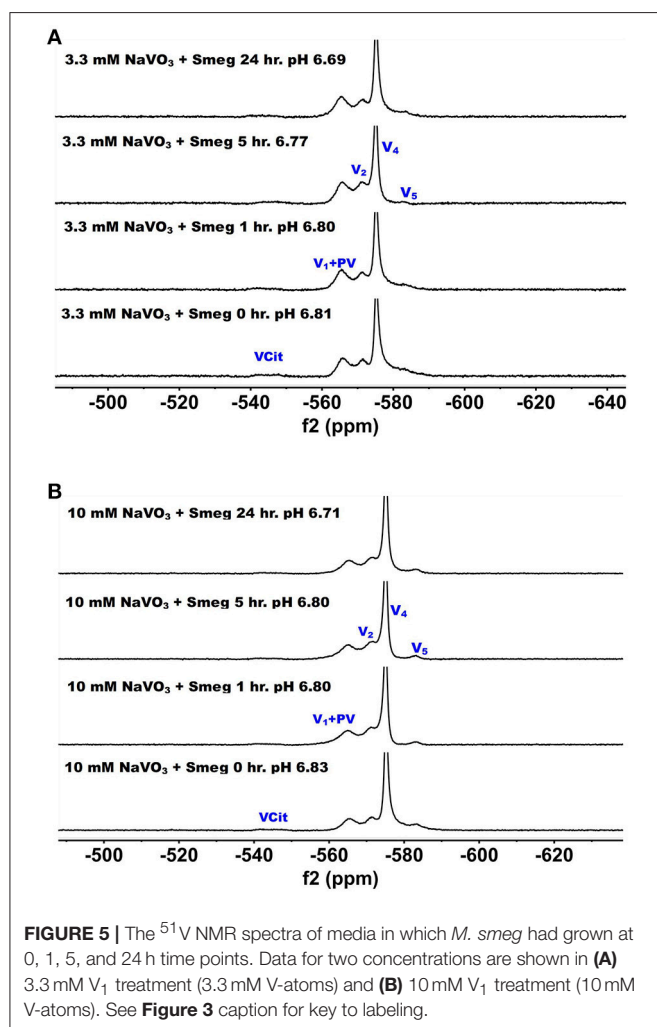
^{51}V NMR spectra were recorded at several concentration and time-points in the growth media in which *M. smeg* had grown because as mentioned above the bacteria were subjected to a 2000-fold concentration range. In **Figure 5**, we show the ^{51}V NMR spectra recorded at 3.3 mM and 10 mM oxometalates,

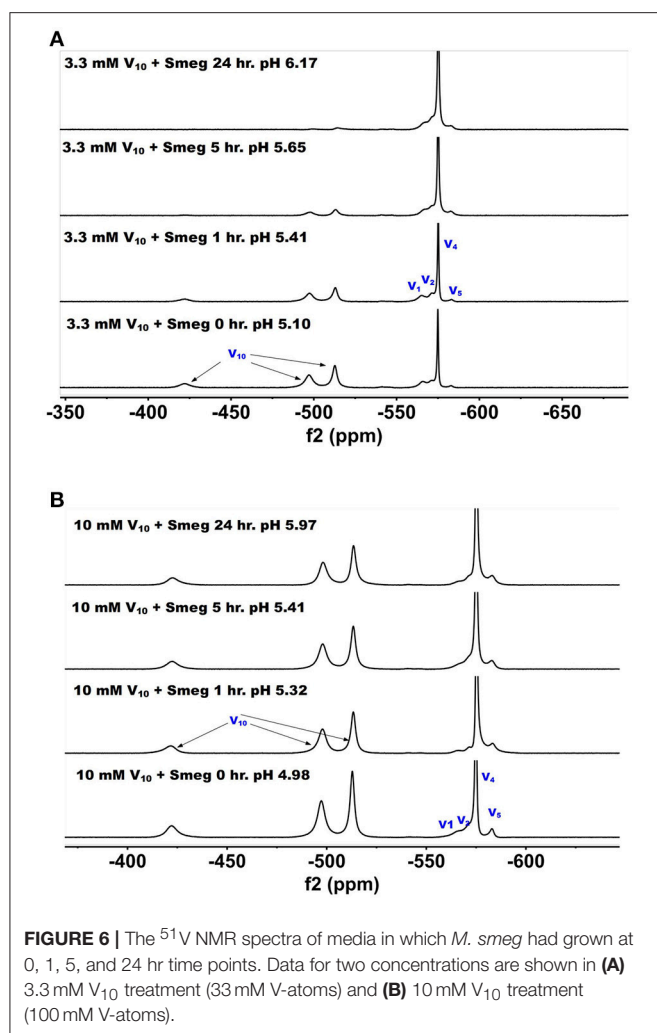
respectively. Both these series show the presence of the different oxometalates (V_1 , V_2 and V_4). In addition, neither series show any evidence for change as the experiment proceeded. This is somewhat surprising, because experiments with other cellular systems, such as yeast, fungi and red blood cells, all showed significant signs of signal reduction (Willsky et al., 1984b, 1985; Crans et al., 2002; Delgado et al., 2005; Jakusch et al., 2014). Since the V_1 or oxovanadate is not a strong inhibitor of growth, it is possible that the simple vanadate system is not getting into the *M. smeg* cells very effectively.

^{51}V NMR Spectra of Media in Which Mycobacteria Have Been Treated With Decavanadate

^{51}V NMR spectra were recorded at several concentrations and time-points in the growth media in which *M. smeg* had grown. In **Figure 6**, we show the ^{51}V NMR spectra recorded at 3.3 and 10 mM, respectively. Both series show the presence of V_{10} . Although the stock solutions and growth media without bacterial cells contains 100% V_{10} (**Figure 2**), the addition of growth media containing cells immediately caused some decomposition of V_{10} (**Figure 6**). NMR spectra were recorded multiple times of the 3.3 mM V and resulted in approximately a 1:1 ratio of V_{10} to oxovanadates as determined by integration of the spectra. As shown in **Figure 6**, after 1 h the composition of the sample was very similar to the content at the beginning of treatment, whereas at the 5 h time point the V_{10} had decreased significantly and at 24 h very little was left. This demonstrates that the V_{10} is not stable in the media in the presence of the *M. smeg* cells at 33 mM total V-atom concentration even though the pH is between 5.8 and 6.8 which is a pH range where there should not have been any hydrolysis of V_{10} according to the known solution chemistry of V_{10} . However, V_{10} treatment may cause signal reduction or the V(V) may interact with large structural components in the mycobacterial cells (or their excretion products) and the ^{51}V NMR signal has broadened beyond detection. Precedent for these possibilities has been reported previously (Willsky et al., 1984b, 1985; Crans et al., 2002). In the series of spectra at 10 mM V_{10} in the media, there is less evidence for V_{10} removal is apparent at the different time points. However, when we integrated the signals a slow decrease in the V_{10} signals compared to the oxovanadate signals was clear. The ratio at time zero was 1:0.71, at time 1 h it was 1:1.08; at time 5 h it was 1:1.18 and at 24 h it was 1:1.24. Thus, providing evidence for a slow decrease in V_{10} content as the experiment progressed. This data is consistent with the possibility that there is some reduction of the vanadium from the POM resulting in hydrolysis and formation of the oxovanadates.

To further investigate whether there was any reduction taking place upon vanadium treatment, we also measured the color change in these samples, **Table 3**. More data and the pH measurements on all the samples shown are provided in the **Supplemental Material**, and the pH values are all in the range from 6.1 to 7.4. Vanadium(V) on reduction is known to change from colorless (V_1 oxovanadates) or yellow/orange (V_{10}) to a green color (Crans et al., 2004, 2010, 2013; Pessoa and Tomaz, 2010; Jakusch et al., 2014). The 7H9 media alone did not cause any reduction as evidenced by the media sample maintained the color prior to treatment, **Table 3**. All the samples containing





media and *M. smegmatis* treated with V_{10} developed a greenish tint as the treatment progressed beyond 5 h time points, whereas the samples treated with V_1 remained colorless, see **Table 3**. This is consistent with reduction of some of the V(V) in the V_{10} salt. Interesting, similar reduction was not observed for the samples treated with the V_1 solutions. These observations are consistent with the selective reduction of the V(V) and that the reduction was more prevalent after longer treatments, higher concentrations of vanadium and V_{10} compared to V_1 . Since the reduction only took place in the presence of V_{10} , this anion induced a response that was not induced by V_1 . Furthermore, the supernatant of a batch of grown *M. smeg.* bacteria and centrifuging down the bacteria and removing them was collected to investigate if the bacteria excrete a component responsible for the observed reduction. The V_{10} and V_1 samples were added to this supernatant and the data are shown in column 4 in **Table 3**. This supernatant also generate the color change from orange to green upon incubation. This experiment showed that the reduction is something that was induced by a material excreted from the *M. smeg.* cells during growth. This suggest that the reduction is likely to come from the excretion

of siderophores (Hider and Kong, 2010) or proteins such as the reported protein tyrosine phosphatases from mycobacteria (Beresford et al., 2009; Dutta et al., 2016). Since we also carried out such studies of supernatant that had been heated (see **Supplemental Material**), such a product is either a very heat stable protein or a siderophore-type of material.

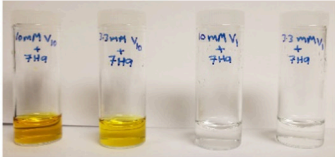
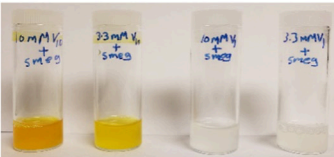
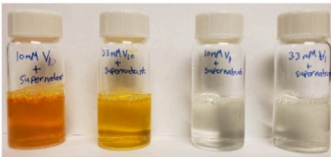
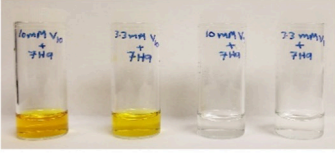
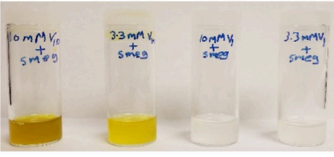
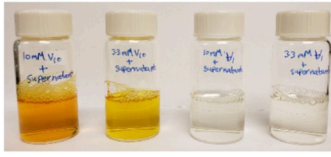



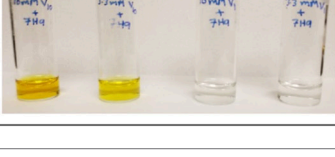


Combined these studies show that there is selectivity in the effects of interactions of vanadium with mycobacteria, and that for these systems the most effective form is not the V_1 , which is a potent phosphatase inhibitor and a common active form of vanadium. These studies show that the V_{10} , a POM is more potent inhibitor of growth of mycobacteria than the well-known phosphatase inhibitor, V_1 . The studies also demonstrate that there is some redox chemistry involved in this process and that the mycobacteria excrete a component that interact with V_{10} and cause the redox chemistry and hydrolysis of the V_{10} . Eventually the V_1 samples would also show the color change consistent with reduction, but this required growth periods beyond several weeks and this process may be different than the reduction, of V_{10} .

Modeling Speciation Vanadium species Distribution in Mycobacteria Media Added Metavanadate

To quantify the V-species that are present in the growth assay media, we carried out speciation analyses modeling experimentally the distribution of vanadium species in the media. This analysis is based on analyzing solutions containing V-species that are governed by thermodynamics and can be calculated the HySS program (Alderighi et al., 1999). This model can analyze the experimental conditions found in solution prepared by the addition of metavanadate and exposed to the conditions of the cell growth assay. We used the reactions reported previously with regard to the exchange of labile oxovanadates (Pettersson et al., 1983, 1985; Gresser et al., 1986; Ehde et al., 1989; Crans et al., 1990, 2000; Crans, 2000, 2005; Andersson et al., 2005; Baruah et al., 2006; Aureliano and Crans, 2009), the formation of the VCit complex (Ehde et al., 1989; Crans, 2000), the formation of the PV complex (Gresser et al., 1986; Andersson et al., 2005), and the thermodynamics relating to the decavanadate deprotonation reactions (Crans, 2005; Baruah et al., 2006; Aureliano and Crans, 2009). The known speciation parameters used for vanadate at various pH values were measured in the presence of 0.6 M NaCl to keep the salt concentration constant for all the components in the system. As shown in **Figure 5**, the species composition for the conditions of three different concentrations of vanadium (0.0050, 3.3, and 10 mM) are illustrated. As discussed above, the vanadium samples prepared with decavanadate will not contain this speciation distribution because all V(V) was converted to V_{10} . The addition of this solution to the media will only slowly hydrolyze the V_{10} species to the equilibrium oxovanadate mixture if above or near pH 7.

The speciation analysis of the conditions observed in the media with freely exchangeable oxovanadate shown in **Figure 3** demonstrate that an observable amount of VCit complex forms. Depending on the concentration of the vanadium, the contribution of VCit is larger percentage-wise at the lower

TABLE 3 | Samples treated with V_{10} and V_1 in 7H9 media, *M. smeg* cultures and supernatant after *M. smeg*.

Time	media7H9	<i>M.smeg</i> in 7H9 media	Supernatant after <i>M.smeg</i> growth (cells removed)
0			
1			
5			
24			

Growth (columns 2, 3, and 4). The yellow or orange V_{10} is shown from the left with 10 and 3.3 mM samples, and the colorless V_1 samples from the left 10 and 3.3 mM in each column. When reduction took place the green color is evident [vanadium (IV)]. See **Supplemental Material** for the pH values of each of these samples.

concentrations of vanadate; for example, at 0.005 and 1.0 mM V-atoms at neutral pH the amount is 75–80% (in terms of mole fraction) of VCit complex. In contrast, at 10 mM V-atoms at neutral pH the amount is ~10%. However, if the amounts are calculated, this would correspond to 0.0004, and 1.0 mM VCit complex in the media. These observations are consistent with the very strong formation constant for VCit. The PV complex, however, is much less stable, and even though there is much more phosphate in the assay, the PV complex is only observed in a significant concentration at high V and P_i concentrations (5 and 24 mM, respective). Although the PV complex is only observed in high concentrations at mM V-treatments the shifting of the V_1 signal attests to the presence of the PV adduct in the assays with *M. tb* and *M. smeg*.

The results shown in **Figure 7** are in general agreement with the experimental data obtained in **Figures 2, 3, 5, 6** with regard to formation of the VCit and PV complexes. **Figure 7** shows that there are four different VCit complexes formed at low vanadium concentration, but at higher concentration and in the presence of phosphate two major VCit complexes formed. There are several assumptions on which these estimations are based, including the differences in ionic strengths, the low concentration of the vanadium used, and the fact that some reduction takes place during the growth experiment to be changing the concentrations somewhat of the VCit and PV complexes. Regardless, our general considerations demonstrate that VCit and PV complexes should form as predicted by the speciation

analysis (Pettersson et al., 1983; Ehde et al., 1989; Selling et al., 1994) and reflect the equilibrium mixture observed by NMR analysis.

DISCUSSION

Vanadium derivatives have been considered as therapeutic agents since 1899 (Lyonnet et al., 1899; Crans et al., 2018). Recent studies demonstrate that vanadium compounds and salts are effective antidiabetic agents (Sakurai, 2002; Thompson and Orvig, 2006; Kiss et al., 2008; Smith et al., 2008; Thompson et al., 2009; Willsky et al., 2011, 2013; Crans, 2015; Trevino et al., 2015; Boulmier et al., 2017; Levina and Lay, 2017b) but their therapeutic properties have been expanded for these materials to be anticancer agents (Lu and Zhu, 2011; Leon et al., 2017; Medina et al., 2017; Crans et al., 2018), immunotherapy agents (Lu and Zhu, 2011; Selman et al., 2018) as well as treatment for other diseases (Zwolak, 2014; Pessoa et al., 2015). Many of the compounds are coordination complexes, which form vanadate during processing after administration (Thompson et al., 2009; Willsky et al., 2011). Considering the ease with which vanadium undergoes redox chemistry (Crans et al., 2010), it is known that some of the vanadium is converted from V(V) to lower oxidation states upon administration (Thompson et al., 2009; Willsky et al., 2011). Furthermore, studies were carried out on the salts prior to investigation of coordination complexes (Sakurai et al., 1990; Goldfine et al., 2000; Willsky et al., 2001,

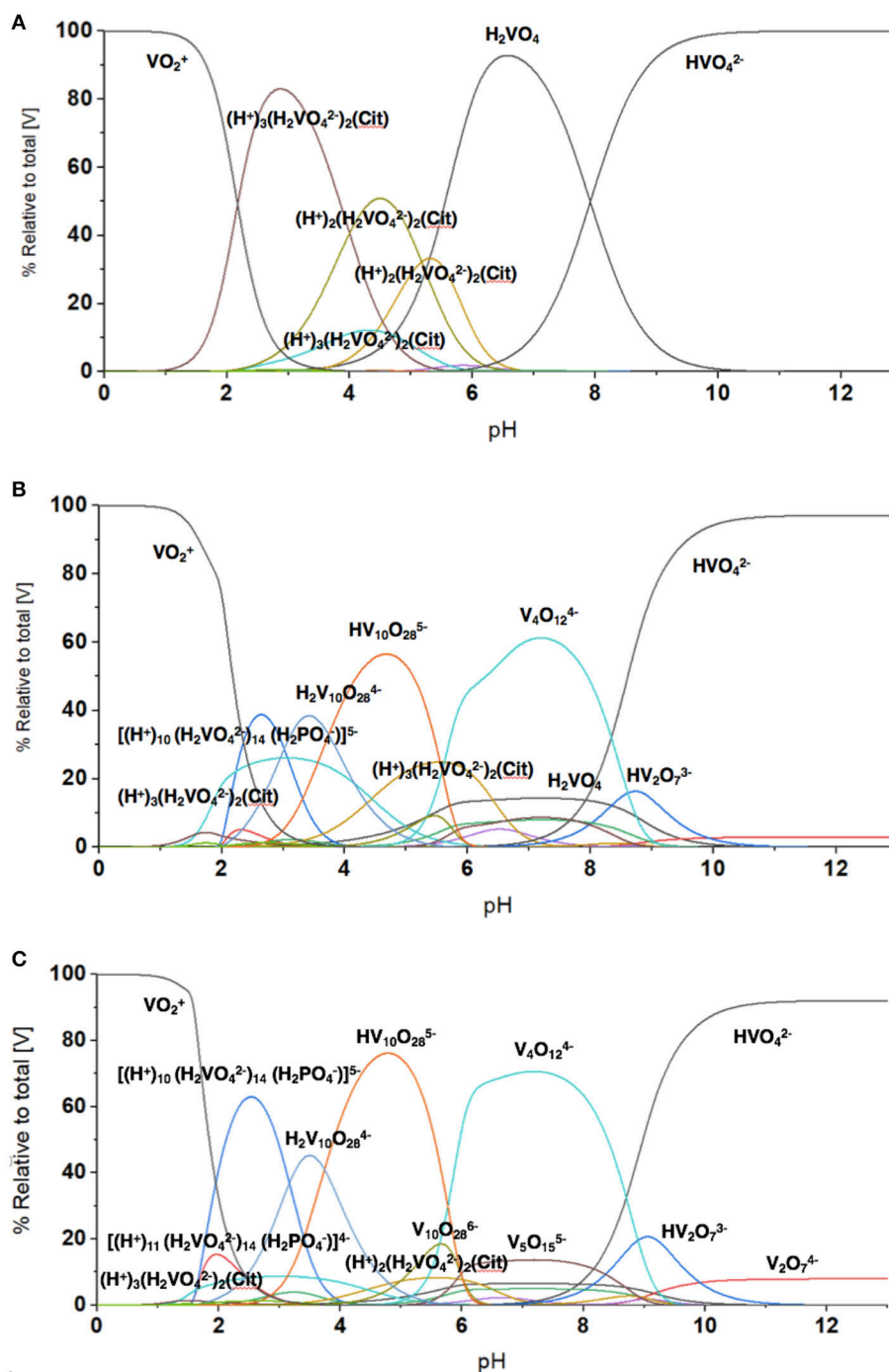


FIGURE 7 | The evaluation of the speciation at different vanadium concentration using HySS Program (vs. 2009) (Alderighi et al., 1999). The speciation diagram shown was calculated at several vanadium (V-atom) concentrations in the presence of 0.48 mM citrate and 24 mM phosphate found in the growth media and **(A)** 5.0 μ M vanadate, **(B)** 3.3 mM vanadate, and **(C)** 10 mM vanadate. Note, the concentrations of different species regardless of nuclearity are here shown in terms of V-atoms.

2013; Smith et al., 2008). The biological activity of homooxovanadates have been of considerable interest considering the varied biological effects depending on the specific vanadium species (Sakurai et al., 1990; Willsky et al., 2001; Postal et al., 2016). Information on cellular uptake by vanadium species is

of interest, and the studies presented here compare the effect of monomeric vanadate and decavanadate. Such direct comparison is important to understand the interconversion between these species, and despite the many reports in the literature (reviewed in Aureliano and Crans, 2009), no similar study showing data for

direct comparison between the two different species have been reported.

Cellular studies have been reported in different types of organisms that consider the uptake of vanadate. Willsky reported studies with yeast (Willsky et al., 1984b, 1985; Crans et al., 2002), and concluded that V_1 was the species entering the cells; however, upon entry processing took place; forming decavanadate in the lysosomes, and forming V(IV) through redox processes. The treatment of the yeast cells with vanadate solutions containing mainly vanadate monomer and oligomers is evidenced by ^{51}V NMR spectroscopy and EPR spectroscopy. These studies were very elegant and truly important, because they documented the formation of decavanadate in cells from monomeric vanadate for the first time (Willsky et al., 1984b). Recently, Zakrzewska and Zivic reported a series of studies in fungi exploring the uptake of both vanadate and V(IV) using ^{51}V and EPR spectroscopy, as well as polarographic studies (Zizic et al., 2013, 2016; Hadzibrahimovic et al., 2017). The initial ^{51}V NMR studies on *Phycomyces blakesleeanus* mycelium were supplemented with polarography, which allowed for the assignment of the signal at -535 ppm accumulating inside the fungi cells to V_1 even though the pH of the system was defined by HEPES buffer at 7.2 where V_1 generally has a peak position at a higher frequency (Zizic et al., 2016). The authors attribute the signal shifting to intracellular complexation of V_1 . Alternatively, these observations are consistent with a hydrophobic environment having been reported in some cases to alter composition and speciation and impact the shifting of observed signals. Combined, these studies showed convincingly that the cell wall is not responsible for reduction of vanadate (Hadzibrahimovic et al., 2017) and these studies also confirm that tetrameric vanadate is not able to enter the cells (Zizic et al., 2016) as reported in yeast as well (Crans et al., 2002) (Willsky et al., 1984a,b.)

Cellular studies in mammalian systems have also been carried out, and many of these studies are linked to the stability and speciation of vanadium compounds in blood (Delgado et al., 2005; Zhang et al., 2006; Li et al., 2009; Jakusch et al., 2011, 2014; Willsky et al., 2013; Sanna et al., 2014, 2017; Jakusch and Kiss, 2017). Although bacterial cells do not contain blood, they do infect mammals and thus the vanadium chemistry in blood is relevant to bacterial infections as well. These studies include detailed investigations into various complexes, and projections based on studies in model systems what would be observed in mammalian systems and *in vivo*. Although such studies remain model studies, they are important because they begin to provide a view of how it will look like in the *in vivo* cells. Studies were also reported by Garner and coworkers using ^1H NMR spin echo and ^{51}V NMR spectroscopy to characterize the uptake of vanadate and subsequent reduction to form V(IV) in erythrocytes (Garner et al., 1997). The reduction of the vanadate was attributed to glutathione as demonstrated in a time-dependent response using both ^{51}V NMR and ^1H spin echo NMR (Garner et al., 1997). The addition of the blocking agent 4,4'-diisothio-cyanatostilbene-2,2b-disulfonic acid (DIDS) specifically blocks the anion transporter preventing the vanadate from entering the erythrocytes. Adding the blocker prevented

vanadate entering, and the depletion of glutathione was arrested. Thus, depletion of intracellular glutathione could be correlated with entering vanadate and the authors proposed that the reduced vanadium [presumably V(IV)] formed complexed with cellular components, because no or little V(IV) formed (Garner et al., 1997).

These studies stand in direct contrast to studies in which decavanadate is associated with proteins and have been characterized by X-ray crystallography (Winkler et al., 2017). However, consideration of both solution and solid state is necessary to characterize both the effects of decavanadate and simple oxovanadates. The studies shown here demonstrate three important findings. First, the fact that decavanadate is a potent inhibitor of growth of two mycobacterial species and more so than monomeric vanadate, which is a known potent phosphatase inhibitor (Crans, 2015; Mclauchlan et al., 2015). Indeed, phosphatase inhibition has recently been reported by V_{10} of the Leishmania acid phosphatase as well as earlier reports (Aureliano and Crans, 2009; Dorsey et al., 2018). Second, the fact that monomeric vanadate is not as potent inhibitor for *M. tb* and *M. smeg*. Third, these studies also demonstrate that under conditions in which the decavanadate would remain stable, in the presence of *Mycobacterium* spp. the decavanadate undergoes hydrolysis. These combined observations suggest that some type of mechanism that involves the bacterium (or something excreted by the bacterium) interacting with the decavanadate and causes the conversion to oxovanadates. This is particularly interesting because similar response is not observed in the media without bacteria.

CONCLUSION

The studies presented demonstrate that decavanadate (V_{10}) inhibits the growth of two mycobacterial species, *M. tb* and *M. smeg*, whereas the oxovanadates prepared from NaVO_3 inhibit growth with 10-100-fold less potency. The inhibition was observed in media containing citrate and phosphate, resulting in the formation of a VCit complex and PV complexes. However, neither of these complexes appeared to interfere with the observed inhibition for V_{10} and the inhibition by V_1 was still 10-100-fold less. The greater inhibitory selectivity of V_{10} (or a component of V_{10}) result is important because it demonstrates that simple vanadium salts can have different effects on cells, and that a vanadium compound other than the potent phosphatase inhibitor, monomeric vanadate (V_1), can inhibit growth. Importantly, these studies suggest that other oxometalates may have the ability to inhibit growth of mycobacteria and other pathogens.

In addition, these studies demonstrated that mycobacteria or some component excreted by the mycobacteria which catalyzes the hydrolysis of V_{10} and the same effect was not observed in media in the absence of growing cells. This process is particularly interesting because it implies that the V_{10} interacts with the some cell component, possibly through some mechanism involving V_{10} delivering a V-atom to such a cell component. This type of mechanism is novel and further investigation into such process

will be of general interest and important for the mode of action of POMs in biological systems.

AUTHOR CONTRIBUTIONS

NS carried out the ^{51}V NMR studies, prepared the figures and wrote part of the manuscript. ZA carried out the growth studies with vanadate and decavanadate and recorded some of the NMR spectra. ZA also collected the experiments with the colors of the various media. HM did the speciation calculations. SK and DCri advised and oversaw the biological studies. DCra combined the chemical and biological components of the work, advised and oversaw the NMR studies and wrote the manuscript with the assistance of NS. All authors contributed to the editing of the manuscript.

FUNDING

NS was funded by Rajabhat Rajanagarindra University to take a summer leave to carry out research. ZA was funded by a fellowship from Libyan Ministry of Education. Supplies were

obtained in part from funds from the Arthur P. Cope Foundation administered by the American Chemical Society (to DCC) and the NSF grant (CHE-1709564) (to DCri and DCra).

ACKNOWLEDGMENTS

We thank the Core Facilities at Colorado State University for their assistance in carrying out the work described in this manuscript. NS thanks Rajabhat Rajanagarindra University for the support to travel and carry out research.

SUPPLEMENTARY MATERIAL

The Supplementary Material for this article can be found online at: <https://www.frontiersin.org/articles/10.3389/fchem.2018.00519/full#supplementary-material>

More figures are included in the supplementary materials showing additional spectra supporting the results presented in the manuscript and include NMR experiments, growth experiments and additional information on the speciation calculations.

REFERENCES

- Alderighi, L., Gans, P., Ienco, A., Peters, D., Sabatini, A., and Vacca, A. (1999). Hyperquad simulation and speciation (HySS): a utility program for the investigation of equilibria involving soluble and partially soluble species. *Coor. Chem. Rev.* 184, 311–318. doi: 10.1016/S0010-8545(98)00260-4
- Andersson, I., Gorzsas, A., Kerezi, C., Toth, I., and Pettersson, L. (2005). Speciation in the aqueous $\text{H}^+/\text{H}_2\text{VO}_4^-/\text{H}_2\text{O}_2/\text{phosphate}$ system. *Dalton Trans.* 22, 3658–3666. doi: 10.1039/b508273k
- Auerbach-Nevo, T., Zarivach, R., Peretz, M., and Yonath, A. (2005). Reproducible growth of well diffracting ribosomal crystals. *Acta Crystallogr. Sec. D.* 61, 713–719. doi: 10.1107/S0907444905006311
- Aureliano, M. (2014). Decavanadate contribution to vanadium biochemistry: *in vitro* and *in vivo* studies. *Inorg. Chim. Acta* 420, 4–7. doi: 10.1016/j.ica.2013.10.010
- Aureliano, M. (2016). Decavanadate toxicology and pharmacological activities: V-10 or V-1, both or none? *Oxid. Med. Cell Longev.* 2016:6103457. doi: 10.1155/2016/6103457
- Aureliano, M., and Crans, D. C. (2009). Decavanadate ($\text{V}_{10}\text{O}_{28}^{6-}$) and oxovanadates: oxometalates with many biological activities. *J. Inorg. Biochem.* 103, 536–546. doi: 10.1016/j.jinorgbio.2008.11.010
- Aureliano, M., Fraqueza, G., and Ohlin, C. A. (2013). Ion pumps as biological targets for decavanadate. *Dalton Trans.* 42, 11770–11777. doi: 10.1039/c3dt50462j
- Aureliano, M., and Ohlin, C. A. (2014). Decavanadate *in vitro* and *in vivo* effects: facts and opinions. *J. Inorg. Biochem.* 137, 123–130. doi: 10.1016/j.jinorgbio.2014.05.002
- Aureliano, M., Ohlin, C. A., Vieira, M. O., Marques, M. P. M., Casey, W. H., and De Carvalho, L. (2016). Characterization of decavanadate and decaniobate solutions by Raman spectroscopy. *Dalton Trans.* 45, 7391–7399. doi: 10.1039/C5DT04176G
- Baer, C. F. (1976). *The Hydrolysis of Cations*. New York, NY: John Wiley & Sons.
- Baruah, B., Roden, J. M., Sedgwick, M., Correa, N. M., Crans, D. C., and Levinger, N. E. (2006). When is water not water? Exploring water confined in large reverse micelles using a highly charged inorganic molecular probe. *J. Am. Chem. Soc.* 128, 12758–12765. doi: 10.1021/ja0624319
- Bashan, A., and Yonath, A. (2008). The linkage between ribosomal crystallography, metal ions, heteropolytungstates and functional flexibility. *J. Mol. Struct.* 890, 289–294. doi: 10.1016/j.molstruc.2008.03.043
- Bbltm, D. (2018). “Middlebrook 7H9 Broth • Middlebrook 7H9 Broth with Glycerol • Middlebrook 7H9 Broth with Polysorbate 80 • Middlebrook ADC Enrichment.” 2nd ed).
- Beresford, N., Mulhearn, D., Szczepankiewicz, B., Liu, G., Johnson, M. E., Fordham-Skelton, A., et al. (2009). Inhibition of MptpB phosphatase from *Mycobacterium tuberculosis* impairs mycobacterial survival in macrophages. *J. Antimicrob. Chemother.* 63, 928–936. doi: 10.1093/jac/dkp031
- Boulmier, A., Feng, X. X., Oms, O., Mialane, P., Riviere, E., Shin, C. J., et al. (2017). Anticancer activity of Polyoxometalate-Bisphosphonate complexes: synthesis, characterization, *in vitro* and *in vivo* results. *Inorg. Chem.* 56, 7558–7565. doi: 10.1021/acs.inorgchem.7b01114
- Carsella, J. S., Sánchez-Lombardo, I., Bonetti, S. J., and Crans, D. C. (2017). Selenium speciation in the Fountain Creek Watershed correlates with water hardness, Ca and Mg levels. *Molecules* 22, 708, 1–16. doi: 10.3390/molecules22050708
- Chasteen, N. D. (1983). “The biochemistry of vanadium,” in *Copper, Molybdenum, and Vanadium in Biological Systems*, eds M. J. Clarke, J. B. Goodenough, J. A. Ibers, C. K. Jørgensen, D. M. P. Mingos, J. B. Neilands, G. A. Palmer, D. Reinen, P. J. Sadler, R. Weiss, and R. J. P. Williams (New York, NY: Springer-Verlag), 105–138. doi: 10.1007/BFb0111304
- Chen, C. Y., Chen, M. L., Chen, H. B., Wang, H. X., Cramer, S. P., and Zhou, Z. H. (2014). α -Hydroxy coordination of mononuclear vanadyl citrate, malate and S-citramalate with N-heterocycle ligand, implying a new protonation pathway of iron-vanadium cofactor in nitrogenase. *J. Inorg. Biochem.* 141, 114–120. doi: 10.1016/j.jinorgbio.2014.08.003
- Chen, C. Y., Zhou, Z. H., Mao, S. Y., and Wan, H. L. (2007). Asymmetric dinuclear hydroxyl and ethoxyl citrate dioxovanadates(V). *J. Coord. Chem.* 60, 1419–1426. doi: 10.1080/00958970601029420
- Clare, B. W., Kepert, D. L., and Watts, D. W. (1973a). Acid decomposition of decavanadate-specific salt effects. *J. Chem. Soc., Dalton Trans.* 22, 2481–2487.
- Clare, B. W., Kepert, D. L., and Watts, D. W. (1973b). Kinetic study of the acid decomposition of decavanadate. *J. Chem. Soc. Dalton Trans.* 22, 2479–2487. doi: 10.1039/dt9730002479
- Comba, P., and Helm, L. (1988). The solution structure and reactivity of decavanadate. *Helv. Chim. Acta* 71, 1406–1420. doi: 10.1002/hlca.19880710605
- Correia, I., Adão, P., Roy, S., Wahba, M., C., M., Maurya, M. R., Marques, F., et al. (2014). Hydroxyquinoline derived vanadium(IV and V) and copper(II) complexes as potential anti-tuberculosis and anti-tumor agents. *J. Inorg. Biochem.* 141, 83–93. doi: 10.1016/j.jinorgbio.2014.07.019

- Correia, I., Roy, S., Matos, C. P., Borovic, S., Butenko, N., Cavaco, I., et al. (2015). Vanadium(IV) and copper(II) complexes of salicylaldehydes and aromatic heterocycles: Cytotoxicity: DNA binding and DNA cleavage properties. *J. Inorg. Biochem.* 147, 134–146. doi: 10.1016/j.jinorgbio.2015.02.021
- Costello, R. L., and Hedgcock, L. W. (1959). Effect of metavanadate ion on the growth *in vitro* of mycobacterium tuberculosis. *J. Bacteriol.* 77, 794–799.
- Crans, D., Yang, L., Haase, A., and Yang, X. (2018). Health benefits of Vanadium and its potential as an anticancer agent. *Met. Ions Life Sci.* 18, 251–279. doi: 10.1515/9783110470734-015
- Crans, D. C. (2000). Chemistry and insulin-like properties of vanadium(IV) and vanadium(V) compounds. *J. Inorg. Biochem.* 80, 123–131. doi: 10.1016/S0162-0134(00)00048-9
- Crans, D. C. (2005). Fifteen years of dancing with vanadium. *Pure Appl. Chem.* 77, 1497–1527. doi: 10.1351/pac200577091497
- Crans, D. C. (2015). Antidiabetic, chemical, and physical properties of organic Vanadates as Presumed transition-state inhibitors for Phosphatases. *J. Org. Chem.* 80, 11899–11915. doi: 10.1021/acs.joc.5b02229
- Crans, D. C., Bedi, H. S., Li, S., Zhang, B., Nomiya, K., Kasuga, N. C., et al. and Willsky, G. R. (2002). “Tetranavanadate, decavanadate, Keggin and Dawson oxotungstates inhibit growth of *S. cerevisiae*” in *Polyoxometalate Chemistry for Nano-Composite Design, [Symposium]* (Honolulu, HI), 181–195.
- Crans, D. C., Peters, B. J., Wu, W., and Mclauchlan, C. C. (2017). Does Anion-Cation Organization in Na⁺-containing X-ray crystal structures relate to solution interactions in inhomogeneous nanoscale environments: Sodium-decavanadate in solid state materials, minerals and microemulsions. *Coord. Chem. Rev.* 344, 115–130. doi: 10.1016/j.ccr.2017.03.016
- Crans, D. C., Rithner, C. D., Baruah, B., Gourley, B. L., and Levinger, N. E. (2006). Molecular probe location in reverse micelles determined by NMR dipolar interactions. *J. Am. Chem. Soc.* 128, 4437–4445. doi: 10.1021/ja0583721
- Crans, D. C., Rithner, C. D., and Theisen, L. A. (1990). Application of time-resolved 51V 2D NMR for quantitation of kinetic exchange pathways between vanadate monomer, dimer, tetramer, and pentamer. *J. Am. Chem. Soc.* 112, 2901–2908. doi: 10.1021/ja00164a009
- Crans, D. C., Smee, J. J., Gaidamauskas, E., and Yang, L. Q. (2004). The chemistry and biochemistry of vanadium and the biological activities exerted by vanadium compounds. *Chem. Rev.* 104, 849–902. doi: 10.1021/cr020607t
- Crans, D. C., Trujillo, A. M., Phalarzyn, P. S., and Cohen, M. D. (2011). How environment affects drug activity: localization, compartmentalization and reactions of a vanadium insulin-enhancing compound, dipicolinatooxovanadium(V). *Coord. Chem. Rev.* 255, 2178–2192. doi: 10.1016/j.ccr.2011.01.032
- Crans, D. C., Woll, K. A., Prusinskas, K., Johnson, M. D., and Norkus, E. (2013). Metal speciation in health and medicine represented by iron and vanadium. *Inorg. Chem.* 52, 12264–12275. doi: 10.1021/ic4007873
- Crans, D. C., Yang, L. Q., Jakusch, T., and Kiss, T. (2000). Aqueous chemistry of ammonium (dipicolinato)oxovanadate(V): the first organic vanadium(V) insulin-mimetic compound. *Inorg. Chem.* 39, 4409–4416. doi: 10.1021/ic9908367
- Crans, D. C., Zhang, B., Gaidamauskas, E., Keramidias, A. D., Willsky, G. R., and Roberts, C. R. (2010). Is Vanadate reduced by thiols under biological conditions? Changing the redox potential of V(V)/V(IV) by complexation in aqueous solution. *Inorg. Chem.* 49, 4245–4256. doi: 10.1021/ic100080k
- David, S., Barrosa, V., Cruzb, C., and Delgado, R. (2005). *In vitro* effect of free and complexed indium(III) against Mycobacterium tuberculosis. *FEMS Microbiol. Lett.* 251, 119–124. doi: 10.1016/j.femsle.2005.07.044
- Delgado, T. C., Tomaz, A. I., Correia, I., Pessoa, J. C., Jones, J. G., Geraldies, C. F., et al. (2005). Uptake and metabolic effects of insulin mimetic oxovanadium compounds in human erythrocytes. *J. Inorg. Biochem.* 99, 2328–2339. doi: 10.1016/j.jinorgbio.2005.08.014
- Dorsey, B. M., McLauchlan, C. C., and Jones, M. A. (2018). Evidence that speciation of oxovanadium complexes does not solely account for inhibition of Leishmania Acid Phosphatases. *Front. Chem.* 8:109. doi: 10.3389/fchem.2018.00109
- Druskovich, D. M., and Kepert, D. L. (1975). Base decomposition of decavanadate. *J. Chem. Soc. Dalton Trans.* 22, 947–851. doi: 10.1039/dt9750000947
- Dutta, N. K., He, R., Pinn, M. L., He, Y., Burrows, F., Zhang, Z.-Y., et al. (2016). Mycobacterial protein tyrosine phosphatase A and B inhibitors augment the bactericidal activity of the standard anti-tuberculosis regimen. *ACS Infect. Dis.* 2, 231–239. doi: 10.1021/acsinfecdis.5b00133
- Ehde, P., Andersson, I., and Pettersson, L. (1989). Multicomponent polyanions. 43. A study of aqueous equilibria in the vanadocitrate system. *Acta Chem. Scand.* 43, 136–143. doi: 10.3891/acta.chem.scand.43-0136
- Esbak, H., Enyedy, E. A., Kiss, T., Yoshikawa, Y., Sakurai, H., Garribba, E., et al. (2009). Aminoacid-derivatised picolinato-oxidovanadium(IV) complexes: characterisation, speciation and *ex vivo* insulin-mimetic potential. *J. Inorg. Biochem.* 103, 590–600. doi: 10.1016/j.jinorgbio.2008.11.001
- Evans, H. T. Jr. (1966). The molecular structure of the isopoly complex ion, decavanadate ($V_{10}O_{28}^{6-}$). *Inorg. Chem.* 5, 967–977. doi: 10.1021/ic50040a004
- Fraqueza, G., De Carvalho, L., Marques, M. P. M., Maia, L., Ohlin, C. A., Casey, W. H., et al. (2012). Decavanadate, decaniobate, tungstate and molybdate interactions with sarcoplasmic reticulum Ca^{2+} -ATPase: quercetin prevents cysteine oxidation by vanadate but does not reverse ATPase inhibition. *Dalton Trans.* 41, 12749–12758. doi: 10.1039/c2dt31688a
- Fu, D. Y., Zhang, S. M., Qu, Z. Y., Yu, X. H., Wu, Y. Q., and Wu, L. X. (2018). Hybrid assembly toward enhanced thermal stability of virus-like particles and antibacterial activity of Polyoxometalates. *ACS Appl. Mater. Interf.* 10, 6137–6145. doi: 10.1021/acsami.7b17082
- Gajera, S. B., Mehta, J. I., and Patel, M. N. (2015). DNA interaction, cytotoxicity, antibacterial and antituberculosis activity of oxovanadium(IV) complexes derived from μ -oroquinolones and 4-hydroxy-5-((4-hydroxyphenyl)diazenyl)thiazole-2(3H)-thione[†]. *RSC Adv.* 5, 21710–21719. doi: 10.1039/C5RA01222H
- Garner, M., Reglinski, J., Smith, W. E., McMurray, J., Abdullah, I., and Wilson, R. (1997). A ¹H spin echo and ⁵¹V NMR study of the interaction of vanadate with intact erythrocytes. *J. Biol. Inorg. Chem.* 2, 235–241. doi: 10.1007/s007750050129
- Goldfine, A. B., Patti, M.-E., Zuberi, L., Goldstein, B. J., Leblanc, R., Landaker, E. J., et al. (2000). Metabolic effects of vanadyl sulfate in humans with non-insulin-dependent diabetes mellitus: *in vivo* and *in vitro* studies. *Metabolism* 49, 400–410. doi: 10.1016/S0026-0495(00)90418-9
- Gresser, M. J., Tracey, A. S., and Parkinson, K. M. (1986). Vanadium(V) oxyanions: the interaction of vanadate with pyrophosphate, phosphate, and arsenate. *J. Am. Chem. Soc.* 108, 6229–6234. doi: 10.1021/ja00280a020
- Gumerova, N., Krivosudsky, L., Fraqueza, G., Breibeck, J., Al-Sayed, E., Tanuhadi, E., et al. (2018). The P-type ATPase inhibiting potential of polyoxotungstates. *Metallomics* 10, 287–295. doi: 10.1039/C7MT00279C
- Hadzibrahimovic, M., Suznjevic, D., Pastor, F., Antic, T. C., Zizic, M., Zakrzewska, J., et al. (2017). The interactions of vanadate monomer with the mycelium of fungus *Phycomyces blakesleeanus*: reduction or uptake? *Anton. V. Leeuw. Inter. J. Gen. Mol. Microb.* 110, 365–373. doi: 10.1007/s10482-016-0808-0
- Hider, R. C., and Kong, X. (2010). Chemistry and biology of siderophores. *Nat. Prod. Rep.* 27, 637–657. doi: 10.1039/b906679a
- Hill, C. L., Hartnup, M., Faraj, M., Weeks, M., Prosser-Mccartha, C. M., Brown, R. B. Jr., et al. (1990). Polyoxometalates as inorganic anti-HIV-1 compounds. Structure-activity relationships. *Adv. Chemotherapy AIDS*, 33–41.
- Jakusch, T., Enyedy, É. A., Kozma, K., Paár, Z., Bényei, A., and Kiss, T. (2014). Vanadate complexes of 3-hydroxy-1, 2-dimethyl-pyridinone: Speciation, structure and redox properties. *Inorg. Chim. Acta* 420, 92–102. doi: 10.1016/j.ica.2013.12.034
- Jakusch, T., and Kiss, T. (2017). *In vitro* study of the antidiabetic behavior of vanadium compounds. *Coord. Chem. Rev.* 351, 118–126. doi: 10.1016/j.ccr.2017.04.007
- Jakusch, T., Pessoa, J. C., and Kiss, T. (2011). The speciation of vanadium in human serum. *Coord. Chem. Rev.* 255, 2218–2226. doi: 10.1016/j.ccr.2011.02.022
- Kaliva, M., Kyriakakis, E., and Salifoglou, A. (2002). Reactivity investigation of dinuclear vanadium(IV,V)-citrate complexes in aqueous solutions. A closer look into aqueous vanadium-citrate interconversions. *Inorg. Chem.* 41, 7015–7023. doi: 10.1021/ic020323r
- Kaliva, M., Raptopoulou, C. P., Terzis, A., and Safifoglou, A. (2003). Systematic studies on pH-dependent transformations of dinuclear vanadium(V)-citrate complexes in aqueous solutions - A perspective relevance to aqueous vanadium(V)-citrate speciation. *J. Inorg. Biochem.* 93, 161–173. doi: 10.1016/S0162-0134(02)00563-9

- Kioseoglou, E., Gabriel, C., Petanidis, S., Psycharis, V., Raptopoulou, C. P., Terzis, A., et al. (2013). Binary Decavanadate-Betaine composite materials of potential anticarcinogenic activity. *Z. Anorg. Allg. Chem.* 639, 1407–1416. doi: 10.1002/zaac.201300144
- Kioseoglou, E., Petanidis, S., Gabriel, C., and Salifoglou, A. (2015). The chemistry and biology of vanadium compounds in cancer therapeutics. *Coord. Chem. Rev.* 301, 87–105. doi: 10.1016/j.ccr.2015.03.010
- Kiss, T., Jakusch, T., Hollender, D., Dornyei, A., Enyedy, E. A., Pessoa, J. C., et al. (2008). Biospeciation of antidiabetic VO(IV) complexes. *Coord. Chem. Rev.* 252, 1153–1162. doi: 10.1016/j.ccr.2007.09.011
- Kustin, K. (2015). Aqueous vanadium ion dynamics relevant to bioinorganic chemistry: a review. *J. Inorg. Biochem.* 147, 32–38. doi: 10.1016/j.jinorgbio.2014.12.009
- Le, M., Rathje, O., Levina, A., and Lay, P. A. (2017). High cytotoxicity of vanadium (IV) complexes with 1, 10-phenanthroline and related ligands is due to decomposition in cell culture medium. *J. Biol. Inorg. Chem.* 22, 663–672. doi: 10.1007/s00775-017-1453-4
- Leon, I. E., Cadavid-Vargas, J. F., Di Virgilio, A. L., and Etcheverry, S. B. (2017). Vanadium, Ruthenium and Copper compounds: a new class of Nonplatinum Metalodrugs with Anticancer activity. *Curr. Med. Chem.* 24, 112–148. doi: 10.2174/0929867323666160824162546
- Leon, I. E., Porro, V., Astrada, S., Egusquiza, M. G., Cabello, C. I., Bollati-Fogolin, M., et al. (2014). Polyoxometalates as antitumor agents: bioactivity of a new polyoxometalate with copper on a human osteosarcoma model. *Chem. Biol. Interact.* 222, 87–96. doi: 10.1016/j.cbi.2014.10.012
- Levina, A., Crans, D. C., and Lay, P. (2017a). Speciation of metal drugs, supplements and toxins in media and bodily fluids controls *in vitro* activities. *Coord. Chem. Rev.* 352, 473–498. doi: 10.1016/j.ccr.2017.01.002
- Levina, A., and Lay, P. A. (2017b). Stabilities and Biological Activities of Vanadium Drugs: What is the Nature of the Active Species?. *Chem. Asian J.* 12, 1692–1699. doi: 10.1002/asia.201700463
- Li, M., Ding, W., Smees, J. J., Baruah, B., Willsky, G. R., and Crans, D. C. (2009). Anti-diabetic effects of vanadium (III, IV, V) - chlorodipicolinate complexes in streptozotocin-induced diabetic rats, *BioMetals* 103, 585–905. doi: 10.1007/s10534-009-9241-4
- Lodyga-Chruscinska, E., Sanna, D., Garribba, E., and Micera, G. (2008). Potentiometric, spectroscopic, electrochemical and DFT characterization of oxovanadium(IV) complexes formed by citrate and tartrates in aqueous solution at high ligand to metal molar ratios: the effects of the trigonal bipyramidal distortion in bis-chelated species and biological implications. *Dalton Trans.* 28, 4903–4916. doi: 10.1039/b803520b
- Lu, L. P., and Zhu, M. L. (2011). Metal-based inhibitors of protein Tyrosine Phosphatases. *Anti Cancer Agents Med. Chem.* 11, 164–171. doi: 10.2174/187152011794941271
- Lyonnet, B., Martz, S., and Martin, E. (1899). L'emploi therapeutique des derives du vanadium. *La Presse Méd.* 1, 191–192.
- Maiti, A., and Ghosh, S. (1989). Synthesis and reactivity of the Oxovanadium(IV) Complexes of Two N-O donors and potentiation of the antituberculosis activity of one of them on Chelation to metal ions: part, I. *V. J. Inorg. Biochem.* 36, 131–139. doi: 10.1016/0162-0134(89)80020-0
- Martins, P. G., Mori, M., Chiaradia-Delatorre, L. D., Menegatti, A. C., Mascarello, A., Botta, B., et al. (2015). Exploring oxidovanadium (IV) complexes as YopH inhibitors: mechanism of action and modeling studies. *ACS Med. Chem. Lett.* 6, 1035–1040. doi: 10.1021/acsmedchemlett.5b00267
- Mclauchlan, C. C., Peters, B. J., Willsky, G. R., and Crans, D. C. (2015). Vanadium-phosphatase complexes: Phosphatase inhibitors favor the trigonal bipyramidal transition state geometries. *Coord. Chem. Rev.* 301–302, 163–199. doi: 10.1016/j.ccr.2014.12.012
- Medina, J. J. M., Naso, L. G., Pérez, A. L., Rizzi, A., Ferrer, E. G., and Williams, P. A. (2017). Antioxidant and anticancer effects and bioavailability studies of the flavonoid baicalin and its oxidovanadium (IV) complex. *J. Inorg. Biochem.* 166, 150–161. doi: 10.1016/j.jinorgbio.2016.11.005
- Moskovitz, B. L., and Group, A. T. H.-C. S. (1988). Clinical trial and tolerance of HPA-23 in patients with acquired immunodeficiency syndrome. *Antimicrob. Agents Chemother.* 32, 1300–1303. doi: 10.1128/AAC.32.9.1300
- Noeske, J., Wasserman, M. R., Terry, D. S., Altman, R. B., Blanchard, S. C., and Cate, J. H. D. (2015). High-resolution structure of the Escherichia coli ribosome. *Nat. Struct. Mol. Biol.* 22, 336–341. doi: 10.1038/nsmb.2994
- Pessoa, J. C., Etcheverry, S., and Gambino, D. (2015). Vanadium compounds in medicine. *Coord. Chem. Rev.* 301, 24–48. doi: 10.1016/j.ccr.2014.12.002
- Pessoa, J. C., and Tomaz, I. (2010). Transport of therapeutic Vanadium and Ruthenium complexes by blood plasma components. *Curr. Med. Chem.* 17, 3701–3738. doi: 10.2174/092986710793213742
- Pettersson, L., Andersson, I., and Hedman, B. (1985). Multicomponent polyanions. 37. A potentiometric and 51V-NMR study of equilibria in the $H^+ - HVO_4^{2-}$ system in 3.0 M-Na(ClO₄) medium covering the range 1E–1G[H⁺]. *Chem. Scr.* 25, 309–317.
- Pettersson, L., Hedman, B., Andersson, I., and Ingri, N. (1983). Multicomponent polyanions. 34. P potentiometric and 51V NMR study of equilibria in the $H^+ - HVO_4^{2-}$ system in the 0.6 M Na(Cl) medium covering the range 1E–1G[H⁺]. *Chem. Scrip.* 22, 254–264.
- Pluskey, S., Mahroof-Tahir, M., Crans, D. C., and Lawrence, D. S. (1996). Vanadium oxoanions and cAMP-dependent protein kinase: an anti-substrate inhibitor. *Biochem. J.* 321, 333–339. doi: 10.1042/bj3210333
- Pope, M. T., and Müller, A. (1991). Polyoxometalate chemistry: an old field with new dimensions in several disciplines. *Angew. Chem. Int. Ed. Engl.* 30, 34–48. doi: 10.1002/anie.199100341
- Postal, K., Maluf, D. F., Valdameri, G., Rüdiger, A. L., Hughes, D. L., de Sá, E. L., et al. (2016). Chemoprotective activity of mixed valence polyoxovanadates against diethylsulphate in *E. coli* cultures: insights from solution speciation studies. *RSC Adv.* 6, 114955–114866. doi: 10.1039/c6ra15826a
- Rehder, D. (1991). The bioinorganic chemistry of vanadium. *Angew. Chem. Int. Ed. Engl.* T 30, 148–167. doi: 10.1002/anie.199101481
- Rehder, D., Pessoa, J. C., Geraldes, C., Castro, M., Kabanos, T., Kiss, T., et al. (2002). *In vitro* study of the insulin-mimetic behaviour of vanadium(IV, V) coordination compounds. *J. Biol. Inorg. Chem.* 7, 384–396. doi: 10.1007/s00775-001-0311-5
- Rhule, J. T., Hill, C. L., Judd, D. A., and Schinazi, R. F. (1998). Polyoxometalates in medicine. *Chem. Rev.* 98, 327–358. doi: 10.1021/cr960396q
- Sakurai, H. (2002). A new concept: the use of vanadium complexes in the treatment of diabetes mellitus. *Chem. Rec.* 2, 237–248. doi: 10.1002/tcr.10029
- Sakurai, H., Tsuchiya, K., Nukatsuka, M., Kawada, J., Ishikawa, S., Yoshida, H., et al. (1990). Insulin-mimetic action of vanadyl complexes. *J. Clin. Biochem. Nutr.* 8, 193–200. doi: 10.3164/jcbn.8.193
- Samart, N., Saeger, J., Haller, K., Manuel Aureliano, M., and Crans, D. (2014). Interaction of decavanadate with interfaces and biological model membrane systems: characterization of soft oxometalate systems. *J. Mol. Eng. Mat.* 2, 1–21. doi: 10.1142/S2251237314400073
- Sambandamurthy, V. K., Derrick, S. C., Hsu, T., Chen, B., Larsen, M. H., Jalapathy, K. V., et al. (2006). Mycobacterium tuberculosis ΔRD1 ΔpanCD: a safe and limited replicating mutant strain that protects immunocompetent and immunocompromised mice against experimental tuberculosis. *Vaccine* 24, 6309–6320. doi: 10.1016/j.vaccine.2006.05.097
- Sanchez-Lombardo, I., Baruah, B., Alvarez, S., Werst, K. R., Segaline, N. A., Levinger, N. E., et al. (2016). Size and shape trump charge in interactions of oxovanadates with self-assembled interfaces: application of continuous shape measure analysis to the decavanadate anion. *New J. Chem.* 40, 962–975. doi: 10.1039/C5NJ01788B
- Sanna, D., Serra, M., Micera, G., and Garribba, E. (2014). Interaction of antidiabetic vanadium compounds with hemoglobin and red blood cells and their distribution between plasma and erythrocytes. *Inorg. Chem.* 53, 1449–1464. doi: 10.1021/ic402366x
- Sanna, D., Ugone, V., Micera, G., Buglyó, P., Bír,ó, L., and Garribba, E. (2017). Speciation in human blood of Metvan, a vanadium based potential anti-tumor drug. *Dalton Trans.* 46, 8950–8967. doi: 10.1039/C7DT00943G
- Selling, A., Andersson, I., Pettersson, L., and Schramm, C. M., S.L., D., and J.H., G. (1994). Multicomponent Polyanions. 47. The aqueous Vanadophosphate system. *J. Inorg. Chem.* 33, 3141–3150. doi: 10.1021/ic00092a021
- Selman, M., Rousso, C., Bergeron, A., Son, H., Krishnan, R., El-Sayes, N., et al. (2018). Multi-modal potentiation of oncolytic virotherapy by Vanadium compounds. *Mol. Ther.* 26, 56–69. doi: 10.1016/j.jymthe.2017.10.014

- Shah, H. S., Joshi, S. A., Haider, A., Kortz, U., Ur-Rehman, N., and Iqbal, J. (2015). Synthesis of chitosan-coated polyoxometalate nanoparticles against cancer and its metastasis. *RSC Adv.* 5, 93234–93242. doi: 10.1039/C5RA18489D
- Smith, D. M., Pickering, R. M., and Lewith, G. T. (2008). A systematic review of vanadium oral supplements for glycaemic control in type 2 diabetes mellitus. *Qjm-an Inter. J. Med.* 101, 351–358. doi: 10.1093/qjmed/hcn003
- Sun, T. D., Cui, W., Yan, M., Qin, G., Guo, W., Gu, H. X., et al. (2016). Target delivery of a novel Antitumor Organoplatinum(IV)-substituted Polyoxometalate Complex for Safer and more effective colorectal cancer therapy *in vivo*. *Adv. Mater.* 28, 7397–7404. doi: 10.1002/adma.201601778
- Thompson, K. H., Lichter, J., Lebel, C., Scaife, M. C., McNeill, J. H., and Orvig, C. (2009). Vanadium treatment of type 2 diabetes: a view to the future. *J. Inorg. Biochem.* 103, 554–558. doi: 10.1016/j.jinorgbio.2008.12.003
- Thompson, K. H., and Orvig, C. (2006). Vanadium in diabetes: 100 years from Phase 0 to Phase, I. *J. Inorg. Biochem.* 100, 1925–1935. doi: 10.1016/j.jinorgbio.2006.08.016
- Trevino, S., Sánchez-Lara, E., Sarmiento-Ortega, V. E., Sánchez-Lombardo, I., Flores-Hernández, J. A., Pérez-Benítez, A., et al. (2015). Hypoglycemic, lipid-lowering and metabolic regulation activities of metforminium decavanadate (H₂Metf)₃ [V₁₀O₂₈]-8H₂O using hypercaloric-induced carbohydrate and lipid deregulation in Wistar rats as biological model. *J. Inorg. Biochem.* 147, 85–92. doi: 10.1016/j.jinorgbio.2015.04.002
- Turian, G. (1951). Action plasmogène du fer chez les Mycobacteries. Le bacille de la fièvre, indicateur biologique du fer. 34, 917–920. *Helv. Chim. Acta* 34, 917–920. doi: 10.1002/hlca.19510340325
- Turner, T. L., Nguyen, V. H., Mclauchlan, C. C., Dymon, Z., Dorsey, B. M., Hooker, J. D., et al. (2012). Inhibitory effects of decavanadate on several enzymes and *Leishmania tarentolae* *in vitro*. *J. Inorg. Biochem.* 108, 96–104. doi: 10.1016/j.jinorgbio.2011.09.009
- Upadhyay, A., Fontes, F., Gonzalez-Juarrero, M., McNeil, M. R., Crans, D. C., Jackson, M., et al. (2015). MenI, a novel menaquinone reductase in *Mycobacterium tuberculosis* is required for survival in macrophages. *ACS Central Sci.* 2015, 1, 292–302. doi: 10.1021/acscentsci.5b00212
- Vilas Boas, L. V., and Costa Pessoa, J. (1987). “Vanadium,” in *Comprehensive Coordination Chemistry. The Synthesis, Reactions, Properties & Applications of Coordination Compounds*, eds G. Wilkinson, Sir, R. D. Gillard, and J. A. McCleverty (New York, NY: Pergamon Press), 453–583.
- Wang, L., Zhou, B. B., and Liu, J. R. (2013). Anticancer Polyoxometalates. *Prog. Chem.* 25, 1131–1141.
- Weinstein, S., Jahn, W., Glotz, C., Schlünzen, F., Levin, I., Janell, D., et al. and Yonath, A. (1999). Metal compounds as tools for the construction and the interpretation of medium-resolution maps of ribosomal particles. *J. Struct. Biol.* 127, 141–151. doi: 10.1006/jsbi.1999.4135
- Willsky, G. R., Chi, L.-H., Godzala, M. III, Kostyniak, P. J., Smee, J. J., Trujillo, A. M., et al. (2011). Anti-diabetic effects of a series of vanadium dipicolinate complexes in rats with streptozotocin-induced diabetes. *Coord. Chem. Rev.* 255, 2258–2269. doi: 10.1016/j.ccr.2011.06.015
- Willsky, G. R., Goldfine, A. B., Kostyniak, P. J., McNeill, J. H., Yang, L. Q., Khan, H. R., et al. (2001). Effect of vanadium(IV) compounds in the treatment of diabetes: *in vivo* and *in vitro* studies with vanadyl sulfate and bis(maltolato)oxovanadium(IV). *J. Inorg. Biochem.* 85, 33–42. doi: 10.1016/S0162-0134(00)00226-9
- Willsky, G. R., Halvorsen, K., Godzala, M. E., Iii, C. H., L.-H., Most, M. J., Kaszynski, P., et al. (2013). Coordination chemistry may explain pharmacokinetics and clinical response of vanadyl sulfate in type 2 diabetic patients. *Metallomics* 5, 1491–1502. doi: 10.1039/c3mt00162h
- Willsky, G. R., Leung, J. O., Offermann, P. V. Jr., Plotnick, E. K., and Dosch, S. F. (1985). Isolation and characterization of vanadate-resistant mutants of *Saccharomyces cerevisiae*. *J. Bacteriol.* 164, 611–617.
- Willsky, G. R., Preischel, D. A., and McCabe, B. C. (1984a). Vanadium metabolism in *S-Cerevisiae*. *Biophys. J.* 45, A76–A76.
- Willsky, G. R., White, D. A., and McCabe, B. C. (1984b). Metabolism of added Ortho-Vanadate to Vanadyl and High- molecular-weight Vanadates by *Saccharomyces-Cerevisiae*. *J. Biol. Chem.* 259, 3273–3281.
- Winkler, P. A., Huang, Y., Sun, W., Du, J., and Lü, W. (2017). Electron cryo-microscopy structure of a human TRPM4 channel. *Nature* 552, 200–204. doi: 10.1038/nature24674
- Zhai, F. Y., Wang, X. H., Li, D. L., Zhang, H., Li, R., and Song, L. S. (2009). Synthesis and biological evaluation of decavanadate Na₄Co(H₂O)(6)V(10)O(28)center dot 18H₂O. *Biomed. Pharmacother.* 63, 51–55. doi: 10.1016/j.biopha.2008.01.006
- Zhang, Y., Yang, X. D., Wang, K., and Crans, D. C. (2006). The permeability and cytotoxicity of insulin-mimetic vanadium (III,IV,V)-dipicolinate complexes, *J. Inorg. Biochem.* 100, 80–87. doi: 10.1016/j.jinorgbio.2005.10.006
- Zhou, Z. H., Zhang, H., Jiang, Y. Q., Lin, D. H., Wan, H. L., and Tsai, K. R. (1999). Complexation between vanadium(V) and citrate: spectroscopic and structural characterization of a dinuclear vanadium(V) complex. *Transit. Metal Chem.* 24, 605–609. doi: 10.1023/A:1006947218366
- Zizic, M., Miladinovic, Z., Stanic, M., Hadzibrahimovic, M., Zivic, M., and Zakrzewska, J. (2016). V-51 NMR investigation of cell-associated vanadate species in *Phycomyces blakesleeanus* mycelium. *Res. Microbiol.* 167, 521–528. doi: 10.1016/j.resmic.2016.04.012
- Zizic, M., Zivic, M., Spasojevic, I., Bogdanovic Pristov, J., Stanic, M., Cvetcic-Antic, T., et al. (2013). The interactions of vanadium with *Phycomyces blakesleeanus* mycelium: enzymatic reduction, transport and metabolic effects. *Res. Microbiol.* 164, 61–69. doi: 10.1016/j.resmic.2012.08.007
- Zwolak, I. (2014). Vanadium carcinogenic, immunotoxic and neurotoxic effects: a review of *in vitro* studies. *Toxicol. Mech. Method.* 24, 1–12. doi: 10.3109/15376516.2013.843110

Conflict of Interest Statement: The authors declare that the research was conducted in the absence of any commercial or financial relationships that could be construed as a potential conflict of interest.

Copyright © 2018 Samart, Arhouma, Kumar, Murakami, Crick and Crans. This is an open-access article distributed under the terms of the Creative Commons Attribution License (CC BY). The use, distribution or reproduction in other forums is permitted, provided the original author(s) and the copyright owner(s) are credited and that the original publication in this journal is cited, in accordance with accepted academic practice. No use, distribution or reproduction is permitted which does not comply with these terms.



Antibacterial Activity of Polyoxometalates Against *Moraxella catarrhalis*

Nadiia I. Gumerova¹, Emir Al-Sayed¹, Lukáš Krivosudský¹, Hana Čipčić-Paljetak², Donatella Verbanac² and Annette Rempel^{1*}

¹ Universität Wien, Fakultät für Chemie, Institut für Biophysikalische Chemie, Wien, Austria, ² Center for Translational and Clinical Research, Croatian Center of Excellence for Reproductive and Regenerative Medicine, School of Medicine, University of Zagreb, Zagreb, Croatia

OPEN ACCESS

Edited by:

Debbie C. Crans,
Colorado State University,
United States

Reviewed by:

Guo-Hong Tao,
Sichuan University, China
Eimer Mary Tuite,
Newcastle University, United Kingdom

*Correspondence:

Annette Rempel
annette.rempel@univie.ac.at

Specialty section:

This article was submitted to
Inorganic Chemistry,
a section of the journal
Frontiers in Chemistry

Received: 23 March 2018

Accepted: 19 July 2018

Published: 14 August 2018

Citation:

Gumerova NI, Al-Sayed E,
Krivosudský L, Čipčić-Paljetak H,
Verbanac D and Rempel A (2018)
Antibacterial Activity of
Polyoxometalates Against *Moraxella*
catarrhalis. *Front. Chem.* 6:336.
doi: 10.3389/fchem.2018.00336

The antibacterial activity of 29 different polyoxometalates (POMs) against *Moraxella catarrhalis* was investigated by determination of the minimum inhibitory concentration (MIC). The Preyssler type polyoxotungstate (POT) $[\text{NaP}_5\text{W}_{30}\text{O}_{110}]^{14-}$ demonstrates the highest activity against *M. catarrhalis* (MIC = 1 $\mu\text{g/ml}$) among all tested POMs. Moreover, we show that the Dawson type based anions, $[\text{P}_2\text{W}_{18}\text{O}_{62}]^{6-}$, $[(\text{P}_2\text{O}_7)\text{Mo}_{18}\text{O}_{54}]^{4-}$, $[\text{As}_2\text{Mo}_{18}\text{O}_{62}]^{6-}$, $[\text{H}_3\text{P}_2\text{W}_{15}\text{V}_3\text{O}_{62}]^{6-}$, and $[\text{AsW}_{18}\text{O}_{60}]^{7-}$ are selective on *M. catarrhalis* (MIC range of 2–8 $\mu\text{g/ml}$). Among the six tested Keggin type based POTs ($[\text{PW}_{12}\text{O}_{40}]^{3-}$, $[\text{H}_2\text{PCoW}_{11}\text{O}_{40}]^{5-}$, $[\text{H}_2\text{CoTiW}_{11}\text{O}_{40}]^{6-}$, $[\text{SiW}_{10}\text{O}_{36}]^{8-}$, $[\text{SbW}_9\text{O}_{33}]^{9-}$, $[\text{AsW}_9\text{O}_{33}]^{9-}$), only the mono-substituted $[\text{H}_2\text{CoTiW}_{11}\text{O}_{40}]^{6-}$ showed MIC value comparable to those of the Dawson type group. Polyoxovanadates (POVs) and Anderson type POMs were inactive against *M. catarrhalis* within the tested concentration range (1–256 $\mu\text{g/ml}$). Four Dawson type POMs $[\text{P}_2\text{W}_{18}\text{O}_{62}]^{6-}$, $[(\text{P}_2\text{O}_7)\text{Mo}_{18}\text{O}_{54}]^{4-}$, $[\text{As}_2\text{Mo}_{18}\text{O}_{62}]^{6-}$, $[\text{H}_3\text{P}_2\text{W}_{15}\text{V}_3\text{O}_{62}]^{6-}$ and the Preyssler POT $[\text{NaP}_5\text{W}_{30}\text{O}_{110}]^{14-}$ showed promising antibacterial activity against *M. catarrhalis* (MICs < 8 $\mu\text{g/ml}$) and were therefore tested against three additional bacteria, namely *S. aureus*, *E. faecalis*, and *E. coli*. The most potent antibacterial agent was $[\text{NaP}_5\text{W}_{30}\text{O}_{110}]^{14-}$, exhibiting the lowest MIC values of 16 $\mu\text{g/ml}$ against *S. aureus* and 8 $\mu\text{g/ml}$ against *E. faecalis*. The three most active compounds ($[\text{NaP}_5\text{W}_{30}\text{O}_{110}]^{14-}$, $[\text{P}_2\text{W}_{18}\text{O}_{62}]^{6-}$, and $[\text{H}_3\text{P}_2\text{W}_{15}\text{V}_3\text{O}_{62}]^{6-}$) show bacteriostatic effects in killing kinetics study against *M. catarrhalis*. We demonstrate, that POM activity is mainly depending on composition, shape, and size, but in the case of medium-size POTs (charge is more than –12 and number of addenda atoms is not being higher than 22) its activity correlates with the total net charge.

Keywords: bioactive polyoxometalates, metal-oxo clusters, Preyssler archetype, Dawson archetype, minimum inhibitory concentration, time-killing analysis, Gram-negative pathogen

INTRODUCTION

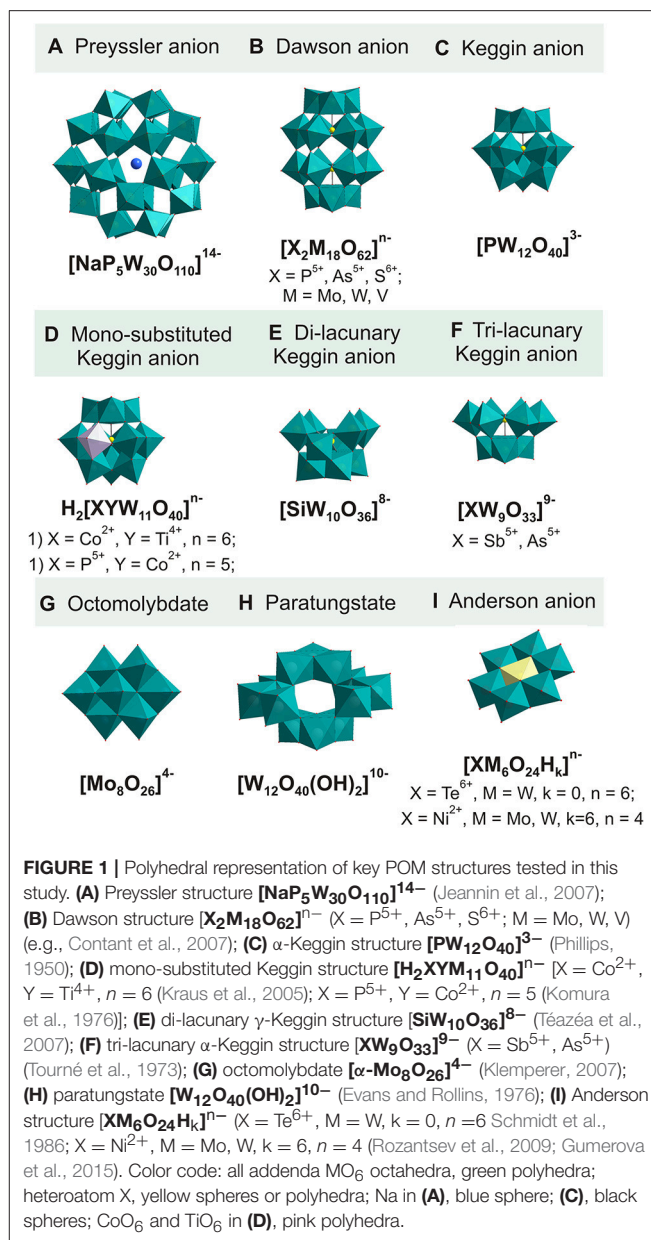
Moraxella catarrhalis is a Gram-negative human mucosal pathogen which causes middle ear infections in infants and children and lower respiratory tract infections in adults with chronic pulmonary disease (Karalus and Campagnari, 2000). *M. catarrhalis* is one of the three major causes of otitis media along with *Streptococcus pneumoniae* and *Haemophilus influenzae*

(Del Beccaro et al., 1992). Based on culture isolation and serological studies, *M. catarrhalis* has been implicated as a cause of sinusitis in both children and adults. In addition, *M. catarrhalis* occasionally causes severe infections such as septic arthritis, bacteremia, cellulitis, osteomyelitis, endocarditis, and pericarditis (Karalus and Campagnari, 2000). The fact that *M. catarrhalis* was not considered as an important human pathogen until recently has contributed to the limited research aimed to find vaccines for prevention or selective antibiotics for the treatment of respiratory tract infections (Karalus and Campagnari, 2000).

Excessive or improper use of antibiotics led to the development of antibacterial resistance worldwide during the last few decades, suggesting the incidence of these infections may continue to rise. Thus, new active classes of antibiotics are urgently needed for the most common community-acquired respiratory pathogens with emerging antimicrobial resistance. Along with new organic compounds, metal oxides have attracted significant interest over the past decade as they offer alternative modes of antimicrobial action (Dizaj et al., 2014). A particularly attractive sub-class of metal oxides is metal oxide anions, the so-called polyoxometalates (POMs) (Pope, 1983). POMs comprise an array of corner- and edge-sharing pseudo-octahedrally coordinated MO_6 (M most often V, Nb, Mo, W) units that form an ionic core and are amenable to a variety of chemical transformations (Figure 1). Alongside with applications of POMs in catalysis (Wang and Yang, 2015), nanotechnology (Yamase and Pope, 2006), electrochemistry (Sadakane and Steckhan, 1998), material sciences (Proust et al., 2008), and molecular magnetism (Clemente-Juan et al., 2012), POMs have also been proven to exhibit remarkable biological activity. Due to the highly negative charge, strong acidity, geometry, their use in macromolecular crystallography (Bijelic and Rompel, 2015, 2017; Molitor et al., 2017) and as antimicrobial (Yamase, 2005; Li et al., 2016; Bijelic et al., 2018), antiviral (Judd et al., 2001), antitumor (Fu et al., 2015), antidiabetes (Nomiya et al., 2001), and anti-amyloid-fibril agents (related to Alzheimer's disease) (Gao et al., 2014) has been reported so far and more attention should be given to the biological and therapeutic effect of POMs.

Polyoxotungstates (POTs), polyoxomolybdates (POMos) and polyoxovanadates (POVs) of different structural types have been shown to exhibit synergy with some conventional antibiotics (Yamase et al., 1996; Tajima, 2001) or direct antibacterial activity (Inoue et al., 2005; Bae et al., 2008) against both Gram-negative and Gram-positive bacteria. In general POVs, especially decavanadate, and large, highly negatively charged POMs exhibit a high activity, whereas for example the activity of Keggin type POMs is bacterial strain dependent (Bijelic et al., 2018).

Thus, in this paper, we determined the antibacterial activity of 18 POTs, seven POMos and four POVs. Mainly we focused on two the most common Keggin and Dawson archetypes with different type of addenda atom and number of lacunas. A few examples of isopolytungstates, -molybdates, and -vanadates, as well as Anderson type anions together with larger Preyssler POT were added to the tested group in order to estimate effect of size and charge of anions. The minimum inhibitory concentration (MIC) against *M. catarrhalis* for each POM



was determined. The five most active compounds based on Dawson and Preyssler archetypes with MIC < 8 $\mu\text{g}/\text{ml}$ were also tested on two Gram-positive organisms *Staphylococcus aureus* and *Enterococcus faecalis* and the Gram-negative bacterium *Escherichia coli*. In addition, time-kill assays were performed against *M. catarrhalis* to study the pharmacodynamics of the POMs of Preyssler and Dawson type with MIC = 1–2 $\mu\text{g}/\text{ml}$ by examining the rate of bactericidal activity at varying POM concentrations over time.

MATERIALS AND METHODS

Materials

The **Preyssler POT** (Figure 1A) $(\text{NH}_4)_{14}[\text{NaP}_5\text{W}_{30}\text{O}_{110}] \cdot 30\text{H}_2\text{O}$ (Jeannin et al., 2007); **heteropolymetalates with Dawson**

structure (Figure 1B): $K_6[P_2W_{18}O_{62}] \cdot 14H_2O$ (Contant et al., 2007), $(NH_4)_6[P_2Mo_{18}O_{62}] \cdot 12H_2O$ (Briand et al., 2002), $[(C_{16}H_{36})_4N]_4[P_4Mo_{18}O_{61}]$ (Kortz and Pope, 1994), $(CH_6N_3)_6[As_2Mo_{18}O_{62}] \cdot 9H_2O$ (Ichida and Sasaki, 1983), $[(CH_3)_4N]_4[S_2Mo_{18}O_{62}]$ (Hori and Himeno, 1987), $Na_{12}[P_2W_{15}O_{56}] \cdot 25H_2O$ (Contant et al., 2007), $[N(CH_3)_4]_6[H_3P_2W_{15}V_3O_{62}] \cdot 6H_2O$ (Finke et al., 1986), $K_6[As_2W_{18}O_{62}] \cdot 14H_2O$ (Bi et al., 2000), $Na_7[AsW_{18}O_{60}] \cdot 16H_2O$ (Jeannin and Martin-Frere, 1979); **heteropolymetalates with Keggin-based structures (Figures 1C-E):** $Na_3[PW_{12}O_{40}] \cdot 12H_2O$ (Phillips, 1950), $(NH_4)_5[H_2PCoW_{11}O_{40}]$ (Komura et al., 1976), $K_6H_2[CoTiW_{11}O_{40}] \cdot 13H_2O$ (Kraus et al., 2005), $K_8[SiW_{10}O_{36}] \cdot 10H_2O$ (Téazéa et al., 2007), $Na_9[SbW_9O_{33}] \cdot 19.5H_2O$ (Tourné et al., 1973); $Na_9[AsW_9O_{33}] \cdot 19.5H_2O$ (Tourné et al., 1973), $K_{14}[As_2W_{19}O_{67}(H_2O)]$ (Kortz et al., 2001); $K_9(C_2H_8N)_5[H_{10}Se_2W_{29}O_{103}] \cdot 30H_2O$ (Gao et al., 2013); **isopolymetalates (Figures 1F,G):** $Na_{10}[W_{12}O_{40}(OH)_2] \cdot 20H_2O$ (Evans and Rollins, 1976), $Na_{12}[H_4W_{22}O_{74}] \cdot 31H_2O$ (Miras et al., 2008), $[(C_4H_9)_4N]_2[Mo_6O_{19}]$ (Klemperer, 2007), $[(C_4H_9)_4N]_4[\alpha-Mo_8O_{26}]$ (Klemperer, 2007), $K_4Na_2[V_{10}O_{28}] \cdot 10H_2O$ (Lee and Joo, 2003), $K_4[V_4O_8(L-tart)_2] \cdot 8H_2O$, tart = $C_4H_2O_6^{4-}$ (Schwendt et al., 2007), $K_4[V_4O_8(D-tart)_2] \cdot 8H_2O$, tart = $C_4H_2O_6^{4-}$ (Schwendt et al., 2007); **heteropolymetalates with Anderson structure (Figure 1I):** $Na_6[TeW_6O_{24}] \cdot 22H_2O$ (Schmidt et al., 1986), $Na_4[Ni(OH)_6W_6O_{18}] \cdot 16H_2O$ (Rozantsev et al., 2009), $Na_4[Ni(OH)_6Mo_6O_{18}] \cdot 16H_2O$ (Gumerova et al., 2015), $Na_2[N(CH_3)_4]_2[Ni(OH)_3W_6O_{18}(OCH_2)_3CCH_2OH] \cdot 9H_2O$ (Gumerova et al., 2016) were synthesized according to procedures published elsewhere. **Table 1** lists the POMs tested in this study together with notation of their abbreviation. **Characterization of POMs.** Compounds were identified by IR measurements on a Bruker Vertex 70 IR Spectrometer equipped with a single-reflection diamond-ATR unit. In case of mono-crystalline sample POMs $((NH_4)_{14}[NaP_5W_{30}O_{110}] \cdot 30H_2O$, $K_6[P_2W_{18}O_{62}] \cdot 14H_2O$, $K_6H_2[CoTiW_{11}O_{40}] \cdot 13H_2O$, $[N(CH_3)_4]_6[H_3P_2W_{15}V_3O_{62}] \cdot 6H_2O$, $Na_{10}[W_{12}O_{40}(OH)_2] \cdot 20H_2O$, $Na_{12}[H_4W_{22}O_{74}] \cdot 31H_2O$, $Na_6[TeW_6O_{24}] \cdot 22H_2O$, $Na_4[Ni(OH)_6W_6O_{18}] \cdot 16H_2O$, $Na_4[Ni(OH)_6Mo_6O_{18}] \cdot 16H_2O$) were also identified by checking unit cell on a Bruker D8 Venture equipped with multilayer monochromator, MoK α INCOATEC micro focus sealed tube and Kryoflex cooling device.

MIC Determination

Minimum inhibitory concentrations (MICs) were determined by the broth microdilution method according to guidelines of the Clinical Laboratory Standards Institute (Wikler, 2009). Double dilutions of tested compounds in 96-well microtiter plates were prepared in the concentration range of 1–256 $\mu\text{g/mL}$. *E. coli* (ECM1556) and *S. aureus* (ATCC 29213) were grown on Mueller-Hinton agar plates (by Becton Dickinson, USA), whereas *E. faecalis* (ATCC29212) and *M. catarrhalis* (ATCC 23246) were grown on Columbia agar with 5% defibrinated sheep blood. Inocula were prepared by direct colony suspension method

and plates were inoculated with $5 \cdot 10^{-4}$ CFU/well. Results were determined by visual inspection after 20–22 h of incubation at 37°C in ambient air. Testing was performed by the standard broth microdilution method with azithromycin (Lode et al., 1996) as the reference antibiotic to assess test validity.

Time-Killing Assay

M. catarrhalis inoculum was prepared by direct colony suspension in sterile saline and the organism density was matched to 1.0 McFarland turbidity standard. The bacterial suspension was further diluted in cation-adjusted Mueller-Hinton Broth in 1:50 ratio to obtain the starting inoculum of $5 \cdot 10^5$ – $5 \cdot 10^6$ colony-forming units (CFU)/mL. Tested POMs were added to tubes containing 6 mL of bacterial suspension, in concentrations corresponding to 1 \times , 5 \times , and 10 \times MIC, while the control antibiotic azithromycin was tested with 1 \times and 10 \times MIC. One tube was used as a drug-free control. After addition of the POMs, tubes were incubated at 37°C for 24 h. Viable colony counts were determined at 0, 2, 4, 6, and 24 h. At each time-point, a 100 μL aliquot was removed from each tube and 10-fold dilutions were prepared in saline, plated on Columbia agar with 5% defibrinated sheep blood in 20 μL aliquots and incubated on 37°C for 24 h. The lower limit for quantifying colony counts was 200 CFU/mL. Bactericidal activity was defined as a ≥ 3 log₁₀ reduction in CFU/mL (Barry et al., 1999).

RESULTS AND DISCUSSION

Antibacterial Activity of Preyssler and Dawson Type POTs and POMs

The antibacterial activity of the 29 POMs against the Gram-negative *M. catarrhalis* was evaluated by means of MIC (**Table 1**). The highest activity with a MIC range of 1–8 $\mu\text{g/mL}$ was observed for POMs with Preyssler type (**Figure 1A**) and Dawson (**Figure 1B**) structure.

Moreover, the most active POM on *M. catarrhalis*, namely the Preyssler anion $P_5W_{30}^{14-}$ (**Figure 1A**) (MIC = 1 $\mu\text{g/mL}$), was additionally tested on the Gram-positive organisms *S. aureus* and *E. faecalis* and the Gram-negative *E. coli*, which are major human pathogens that cause a wide range of clinical infections (**Table 2**). $P_5W_{30}^{14-}$ exhibited good activity against *S. aureus* with MIC = 16 $\mu\text{g/mL}$ and *E. faecalis* with MIC = 8 $\mu\text{g/mL}$, which is the same as for the clinically applied drug azithromycin (Lode et al., 1996), however, it performed inactive against the Gram-negative *E. coli*. The chitosan- P_5W_{30} nanoassembly has already demonstrated high anticancer activity, which is considered to arise due to high number of phosphorous and tungsten atoms (Shah et al., 2014). Remarkably, the Se-containing lacunary anion $Se_2W_{29}^{14-}$, which is of comparable size and equally charged, exhibited significantly lower MICs (64 $\mu\text{g/mL}$). This indicates the importance and the influence of the structure, shape, and composition for the antibacterial activity, justifying more detailed studies to elucidate the structure-activity relationship.

Except for $P_2Mo_{18}^{6-}$, $S_2Mo_{18}^{4-}$, and $As_2W_{18}^{6-}$, all Dawson type POMs (**Figure 1B**) tested in this study exhibited potential antibacterial activity exhibiting a MIC within the range of 2–8 $\mu\text{g/mL}$. Among the Dawson type group, $P_2W_{18}^{6-}$ and its

TABLE 1 | Minimum inhibitory concentration (MIC) of POMs against the *M. catarrhalis* (ATCC 23246).

POM	Abbreviation	Charge number (z)	z/m*	MIC, $\mu\text{g/ml}$
HETEROPOLYANIONS				
Preyssler POT (Figure 1A)				
$(\text{NH}_4)_{14}[\text{NaP}_5\text{W}_{30}\text{O}_{110}]\cdot 30\text{H}_2\text{O}$	$\text{P}_5\text{W}_{30}^{14-}$	−14	0.47	1
Dawson-based (Figure 1B)				
$\text{K}_6[\text{P}_2\text{W}_{18}\text{O}_{62}]\cdot 14\text{H}_2\text{O}$	$\text{P}_2\text{W}_{18}^{6-}$	−6	0.33	2
$[\text{N}(\text{CH}_3)_4]_6[\text{H}_3\text{P}_2\text{W}_{15}\text{V}_3\text{O}_{62}]\cdot 6\text{H}_2\text{O}$	$\text{P}_2\text{W}_{15}\text{V}_3^{6-}$	−6	0.33	2
$[(\text{C}_6\text{H}_5)_4\text{N}]_4[\text{P}_4\text{Mo}_{18}\text{O}_{61}]$	$\text{P}_2\text{O}_7\text{Mo}_{18}^{4-}$	−4	0.22	4
$(\text{CH}_6\text{N}_3)_6[\text{As}_2\text{Mo}_{18}\text{O}_{62}]\cdot 9\text{H}_2\text{O}$	$\text{As}_2\text{Mo}_{18}^{6-}$	−6	0.33	4
$\text{Na}_7[\text{AsW}_{18}\text{O}_{60}]\cdot 16\text{H}_2\text{O}$	AsW_{18}^{7-}	−7	0.39	8
$(\text{NH}_4)_6[\text{P}_2\text{Mo}_{18}\text{O}_{62}]\cdot 12\text{H}_2\text{O}$	$\text{P}_2\text{Mo}_{18}^{6-}$	−6	0.33	>256
$[(\text{CH}_3)_4\text{N}]_4[\text{S}_2\text{Mo}_{18}\text{O}_{62}]$	$\text{S}_2\text{Mo}_{18}^{4-}$	−4	0.22	>256
$\text{Na}_{12}[\text{P}_2\text{W}_{15}\text{O}_{56}]\cdot 25\text{H}_2\text{O}$	$\text{P}_2\text{W}_{15}^{12-}$	−12	0.8	>256
$\text{K}_6[\text{As}_2\text{W}_{18}\text{O}_{62}]\cdot 14\text{H}_2\text{O}$	$\text{As}_2\text{W}_{18}^{6-}$	−6	0.33	>256
Keggin-based (Figures 1C–F)				
$\text{K}_6\text{H}_2[\text{CoTiW}_{11}\text{O}_{40}]\cdot 13\text{H}_2\text{O}$	CoTiW_{11}^{6-}	−6	0.45	16
$\text{K}_8[\text{SiW}_{10}\text{O}_{36}]\cdot 10\text{H}_2\text{O}$	SiW_{10}^{8-}	−8	0.8	32
$\text{Na}_3[\text{PW}_{12}\text{O}_{40}]\cdot 12\text{H}_2\text{O}$	PW_{12}^{3-}	−3	0.25	128
$\text{Na}_9[\text{SbW}_9\text{O}_{33}]\cdot 19.5\text{H}_2\text{O}$	SbW_9^{9-}	−9	1	256
$\text{Na}_9[\text{AsW}_9\text{O}_{33}]\cdot 19.5\text{H}_2\text{O}$	AsW_9^{9-}	−9	1	>256
$(\text{NH}_4)_5[\text{H}_2\text{PCoW}_{11}\text{O}_{40}]$	PCoW_{11}^{5-}	−5	0.45	>256
POTs based on lacunary Keggin units				
$\text{K}_{14}[\text{As}_2\text{W}_{19}\text{O}_{67}(\text{H}_2\text{O})]$	$\text{As}_2\text{W}_{19}^{14-}$	−14	0.74	64
$\text{K}_9(\text{C}_2\text{H}_8\text{N})_5[\text{H}_{10}\text{Se}_2\text{W}_{29}\text{O}_{103}]\cdot 30\text{H}_2\text{O}$	$\text{Se}_2\text{W}_{29}^{14-}$	−14	0.48	64
Anderson-based (Figure 1I)				
$\text{Na}_6[\text{TeW}_6\text{O}_{24}]\cdot 22\text{H}_2\text{O}$	TeW_6^{6-}	−6	1	>256
$\text{Na}_4[\text{Ni}(\text{OH})_6\text{W}_6\text{O}_{18}]\cdot 16\text{H}_2\text{O}$	NiW_6^{4-}	−4	0.67	>256
$\text{Na}_4[\text{Ni}(\text{OH})_6\text{Mo}_6\text{O}_{18}]\cdot 16\text{H}_2\text{O}$	NiMo_6^{4-}	−4	0.67	>256
$\text{Na}_2[\text{N}(\text{CH}_3)_4]_2[\text{Ni}(\text{OH})_3\text{W}_6\text{O}_{18}(\text{OCH}_2)_3\text{CCH}_2\text{OH}]\cdot 9\text{H}_2\text{O}$	$\text{NiW}_6\text{penta}^{4-}$	−4	0.67	>256
ISOPOLYANIONS (FIGURES 1G,H)				
$[(\text{C}_4\text{H}_9)_4\text{N}]_4[\alpha\text{-Mo}_8\text{O}_{26}]$	Mo_8^{4-}	−4	0.5	32
$\text{Na}_{10}[\text{W}_{12}\text{O}_{40}(\text{OH})_2]\cdot 27\text{H}_2\text{O}$	W_{12}^{10-}	−10	0.45	64
$\text{Na}_{12}[\text{H}_4\text{W}_{22}\text{O}_{74}]\cdot 31\text{H}_2\text{O}$	W_{22}^{12-}	−12	0.54	128
$[(\text{C}_4\text{H}_9)_4\text{N}]_2[\text{Mo}_6\text{O}_{19}]$	Mo_6^{2-}	−2	0.33	>256
$\text{K}_4\text{Na}_2[\text{V}_{10}\text{O}_{28}]\cdot 10\text{H}_2\text{O}$	V_{10}^{6-}	−6	0.6	>256
$\text{K}_4[\text{V}_4\text{O}_8(\text{L-tart})_2]\cdot 8\text{H}_2\text{O}$, tart = $\text{C}_4\text{H}_2\text{O}_6^{4-}$	$\text{V}_4\text{-L-tart}^{4-}$	−4	1	256
$\text{K}_4[\text{V}_4\text{O}_8(\text{D-tart})_2]\cdot 8\text{H}_2\text{O}$, tart = $\text{C}_4\text{H}_2\text{O}_6^{4-}$	$\text{V}_4\text{-D-tart}^{4-}$	−4	1	>256
POSITIVE CONTROL				
Azithromycin (Lode et al., 1996)				0.06

POMs combined in groups according to their structural type and within the group listed from higher to lower activity. *m - number of addenda atoms.

triple-protonated equally charged vanadium-substituted analog $\text{P}_2\text{W}_{15}\text{V}_3^{6-}$ (Figure 1B) have proven to be the most promising with a MIC of $2\text{ }\mu\text{g/ml}$ suggesting that VO_6 sites in Dawson type mixed polyoxovanadatotungstates (POVTs) lattice do not have any significant impact on the antibacterial activity, which was observed earlier for Keggin POVTs as they were remarkably

more active against *S. pneumoniae* than their corresponding POTs (Fukuda and Yamase, 1997). In the Dawson pair $\text{P}_2\text{W}_{18}^{6-}$ (MIC = $2\text{ }\mu\text{g/ml}$) and $\text{P}_2\text{Mo}_{18}^{6-}$ (MIC > $256\text{ }\mu\text{g/ml}$), the POMo is considered as inactive, whereas for $\text{As}_2\text{W}_{18}^{6-}$ (MIC > $256\text{ }\mu\text{g/ml}$) and $\text{As}_2\text{Mo}_{18}^{6-}$ (MIC = $4\text{ }\mu\text{g/ml}$) the opposite effect is observed. Dawson related compounds, namely AsW_{18}^{7-} (Figure 2C), with

TABLE 2 | Minimum inhibitory concentration (MIC) of Dawson and Preyssler type POMs against the *M. catarrhalis* strains.

Compound	MIC, $\mu\text{g/ml}$		
	<i>S. aureus</i> (ATCC 29213)	<i>E. faecalis</i> (ATCC29212)	<i>E. coli</i> (ECM1556)
PREYSSLER ANION			
$\text{P}_5\text{W}_{30}^{14-}$	16	8	>256
DAWSON-BASED ANIONS			
$\text{P}_2\text{O}_7\text{Mo}_4^{4-}$	>256	>256	>256
$\text{As}_2\text{Mo}_6^{6-}$	256	>256	>256
$\text{P}_2\text{W}_{15}\text{V}_3^{6-}$	>256	>256	>256
AsW_{18}^{7-}	>256	>256	>256
Azithromycin (positive control)*	1	8	0.25

*MICs for azithromycin were obtained in this study.

one tricoordinated $\text{As}^{\text{III}}\text{O}_3$ unit (Jeannin and Martin-Frere, 1979), and $\text{P}_2\text{O}_7\text{Mo}_4^{4-}$ (Figure 2B), which has a pyrophosphate anion enclosed (Kortz and Pope, 1994), demonstrated higher activity against bacteria (MIC values are 8 and $4\mu\text{g/ml}$, respectively) than classical $\text{As}_2\text{W}_{18}^{6-}$ and $\text{P}_2\text{Mo}_{18}^{6-}$ (Figure 2A). The presence of highly bioactive and toxic arsenic trioxide in the first case should play a significant role, but difference in the coordination of the heteroatoms in both cases leads to a change of the “rugby-ball-shaped” (Figure 2A) Dawson structure to a “hour-glass” shaped anion (Figures 2B,C), which also may be related to discrepancies in antibacterial activity. These anomalies in the activity of isostructural POTs and POMos indicate that both the hetero- and addenda atoms play a significant role in the bioactivity and that the appropriate combination of these atoms must be decisive for the antibacterial activity.

The superiority of the Dawson structure among four different structural groups of polyoxomolybdates in the inhibition of a tartrate-resistant acid phosphatase (ACP) from *Leishmania donovani* and the tartrate-sensitive ACP from human seminal fluid (prostatic ACP) has been reported previously (Saha et al., 1991). $\text{As}_2\text{Mo}_6^{6-}$ was the most potent inhibitor and exhibited the highest degree of selectivity against both ACPs. Here, $\text{As}_2\text{Mo}_{18}^{6-}$ is proved to be a potent antibacterial agent with the third lowest MIC value of $4\mu\text{g/ml}$ against *M. catarrhalis*.

Antibacterial Activity of Keggin- and Anderson Based Type POTs

Keggin type POTs are known to exhibit antibacterial activities, for example, by increasing the susceptibility of certain bacteria strains toward β -lactam antibiotics (Yamase et al., 1996). In this study the strongest activity was shown for the Keggin based CoTiW_{11}^{6-} (Figure 1D) exhibiting a MIC value of $16\mu\text{g/ml}$. Interestingly, despite consisting of the same isomer of Keggin unit, the classical PW_{12}^{3-} (Figure 1C) and the two mono-substituted PCoW_{11}^{5-} and CoTiW_{11}^{6-} (Figure 1D) showed completely different activities. The most negatively charged CoTiW_{11}^{6-} is the most active compound; however, the charge dependency is not observed in the case of the other two Keggin anions- PW_{12}^{3-} with a total charge of -3 exhibited a MIC of

$128\mu\text{g/ml}$ and PCoW_{11}^{5-} with a total charge of -5 exhibited a value $>256\mu\text{g/ml}$. Thus, we assume a decisive role for the accessible TiO_6 unit in CoTiW_{11}^{6-} (Figure 1D) in the activity against *M. catarrhalis*. CoTiW_{11}^{6-} was previously also shown as the most potent NTPDase inhibitor among six different POTs, (Müller et al., 2006).

The dilacurary SiW_{10}^{8-} (Figure 1E) showed much higher activity than the trilacurary anions SbW_9^{9-} and AsW_9^{9-} (Figure 1F; $32\mu\text{g/ml}$ for SiW_{10}^{8-} against $>256\mu\text{g/ml}$ for SbW_9^{9-} and AsW_9^{9-}). Nevertheless, the Keggin and Dawson $\text{P}_2\text{W}_{15}^{12-}$ lacurary anions did not meet the expectation that more negatively charged compounds exhibit higher antibacterial activity.

The inorganic and organically functionalized Anderson type POTs and POMos (Figure 1I) are inactive against *M. catarrhalis* (Table 1). The inactivity of this type of POM was previously observed for *Helicobacter pylori*, which as well as *M. catarrhalis* is most sensitive to larger POMs (Yamase et al., 1996). It is tempting to speculate that the combination of compact size and small charge of Anderson type anion (Blazevic and Rompel, 2016) is the reason of its antibacterial inactivity.

Antibacterial Activity of Isopolymetalates

Among the investigated isopolyanions only two POTs (W_{12}^{10-} (Figure 1H) and W_{12}^{12-}) and octamolybdate Mo_8^{4-} (Figure 1G) showed a MIC value $>256\mu\text{g/ml}$. It should be noted, that decavanadate tested in this study (V_{10}^{6-}) did not show antibacterial activity (MIC $>256\mu\text{g/ml}$), which confirms the selective activity of the most common vanadates V_{10}^{6-} and $\text{V}_4\text{O}_{12}^{4-}$ against *Streptococcus pneumoniae* with MIC values in the range of $4\text{--}32\mu\text{g/ml}$ (positive control with conventional antibiotics: $2\text{--}32\mu\text{g/ml}$; Fukuda and Yamase, 1997). We also included tetranuclear vanadium tartrates ($\text{V}_4\text{-L-tart}^{4-}$ and $\text{V}_4\text{-D-tart}^{4-}$) in our study as they, similarly to V_{10}^{6-} , are one of the few vanadate species with proved stability and hydrolytic immunity in aqueous solutions over time (Schwendt et al., 2007). However, both POTs were inactive toward *M. catarrhalis*.

The Relationship Between the Composition of POMs and Its Activity Against *M. catarrhalis*

By analyzing the data in Table 1, it becomes clear that POMs despite having the same or very close charge and size can demonstrate absolutely different activities (e.g. compare Dawson-based $\text{P}_2\text{W}_{18}^{6-}$ and $\text{P}_2\text{Mo}_{18}^{6-}$ or Keggin-based PCoW_{11}^{5-} and CoTiW_{11}^{6-}). As already noted above, there are at least three factors affecting the antibacterial activity: size, charge, chemical composition, and their combination. In order to understand the structure-activity-relationship (SAR) we minimized the influence of one of these factors and compared the main characteristics for phosphorus-containing Keggin PW_{12}^{3-} (Figure 1C), Dawson $\text{P}_2\text{W}_{18}^{6-}$ (Figure 1B), and Preyssler $\text{P}_5\text{W}_{30}^{14-}$ (Figure 1A) POTs (Table 3). Leastways for these fully saturated (not lacurary) POTs with the same heteroatom PW_{12}^{3-} , $\text{P}_2\text{W}_{18}^{6-}$, and $\text{P}_5\text{W}_{30}^{14-}$ there is a clear dependence in the increase in antibacterial activity with an

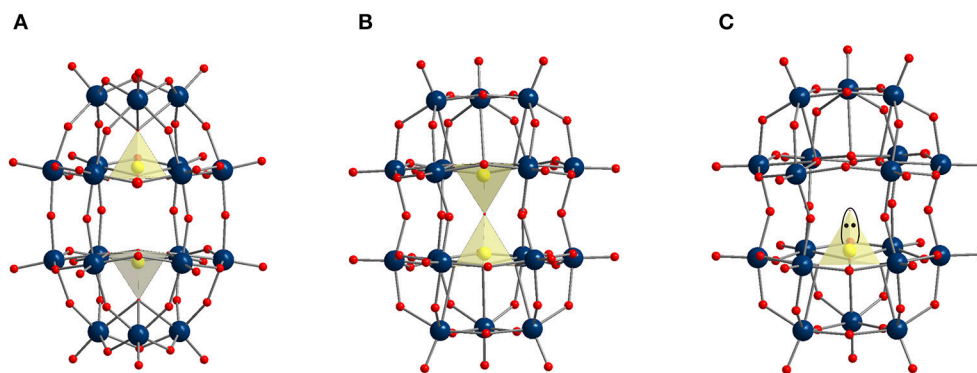


FIGURE 2 | Ball and stick representation of (A) classical Dawson type anion $P_2Mo_6^{6-}$ (Brind et al., 2002); (B) anion in $P_2O_7Mo_4^{4-}$ (Kortz and Pope, 1994); (C) anion in AsW_7^{7-} (Jeannin and Martin-Frere, 1979). Color code: addenda atom Mo (B) or W (C), dark blue spheres; heteroatom P (B) or As (C), yellow spheres; O, red spheres.

TABLE 3 | Dimension and redox characteristics for phosphorus-containing Keggin, Dawson, and Preyssler POTs.

POT	Charge number (z)	Volume/ 10^{-22} cm ^{3**}	Volume charge density/cm ^{-3**}	z/m*	Reduction potential, V**	MIC, μ g/ml
$P_5W_{30}^{14-}$ (Preyssler)	-14	18.48	1,213	0.47	-0.43	1
$P_2W_{18}^{6-}$ (Dawson)	-6	9.995	961.8	0.33	+0.06	2
PW_{12}^{3-} (Keggin)	-3	6.234	771.0	0.25	-0.023	128

*m-number of addenda atoms.

**were taken from López et al. (2006).

increase in charge and size and no correlation with respect to the redox potential.

No simple SAR was found for all tested POMs, however, narrowing the data set only to the largest tested group, namely POTs with a charge <-12 and with a number of addenda atoms not being higher than 22 it became possible to correlate the antibacterial activity and the charge of the POT (Figure 3). The presented dependence may indicate for medium-sized POTs (but not for POTs with number of addenda atoms more than 22) a stronger effect against *M. catarrhalis* of anions exhibiting a charge of -8 to -6 .

Cells of *M. catarrhalis* have on their surface low molecular weight lipopolysaccharides (LPS), also called lipooligosaccharides (LOS), which contribute to the increased hydrophobicity of its outer membrane and to the high susceptibility to hydrophobic antimicrobial agents such as macrolides (Gotoh et al., 1989; Tsujimoto et al., 1999). However, *M. catarrhalis* shows susceptibility not only to hydrophobic agents, but also to hydrophilic agents such as β -lactam antibiotics (Gotoh et al., 1992). The increased susceptibility of these strains toward β -lactams is probably due to the higher permeability of the outer membrane toward these agents. POMs, as examples of super chaotropic anions, can adsorb onto lipid monolayers via electrostatic and/or hydrophobic interaction depending on the charge of the lipid layer (Kobayashi et al., 2017). The model experiments with three differently charged Keggin anions show that dominant interaction equally depends both on the charge density of POMs and on the lipid density (Kobayashi et al., 2017).

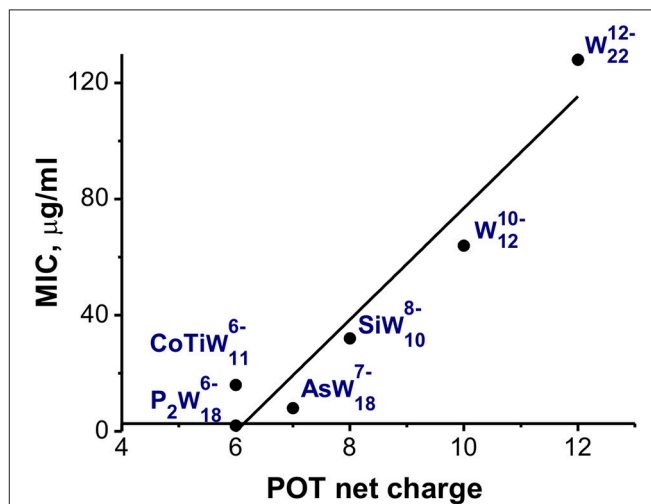


FIGURE 3 | Charge-activity-relationship of POTs against *M. catarrhalis*. POTs $P_2W_{18}^{6-}$ (Figure 1B) and AsW_{18}^{7-} (Figure 2C) demonstrate Dawson structure, $CoTiW_{11}^{6-}$ (Figure 1D) and SiW_{10}^{8-} (Figure 1E) are Keggin-based anions, whereas W_{12}^{10-} (Figure 1H) and W_{22}^{12-} - isopolytungstates (see Table 1).

Time-Killing Studies

In order to assess whether the tested compounds kill the bacteria (bactericidal effect) or prevent its growth (bacteriostatic effect), time-kill study was performed. Killing kinetics for three the most active compounds: Preyssler $P_5W_{30}^{14-}$ (Figure 1A) and two Dawson $P_2W_{18}^{6-}$ and $P_2W_{15}V_3^{6-}$ (Figure 1B) POTs were

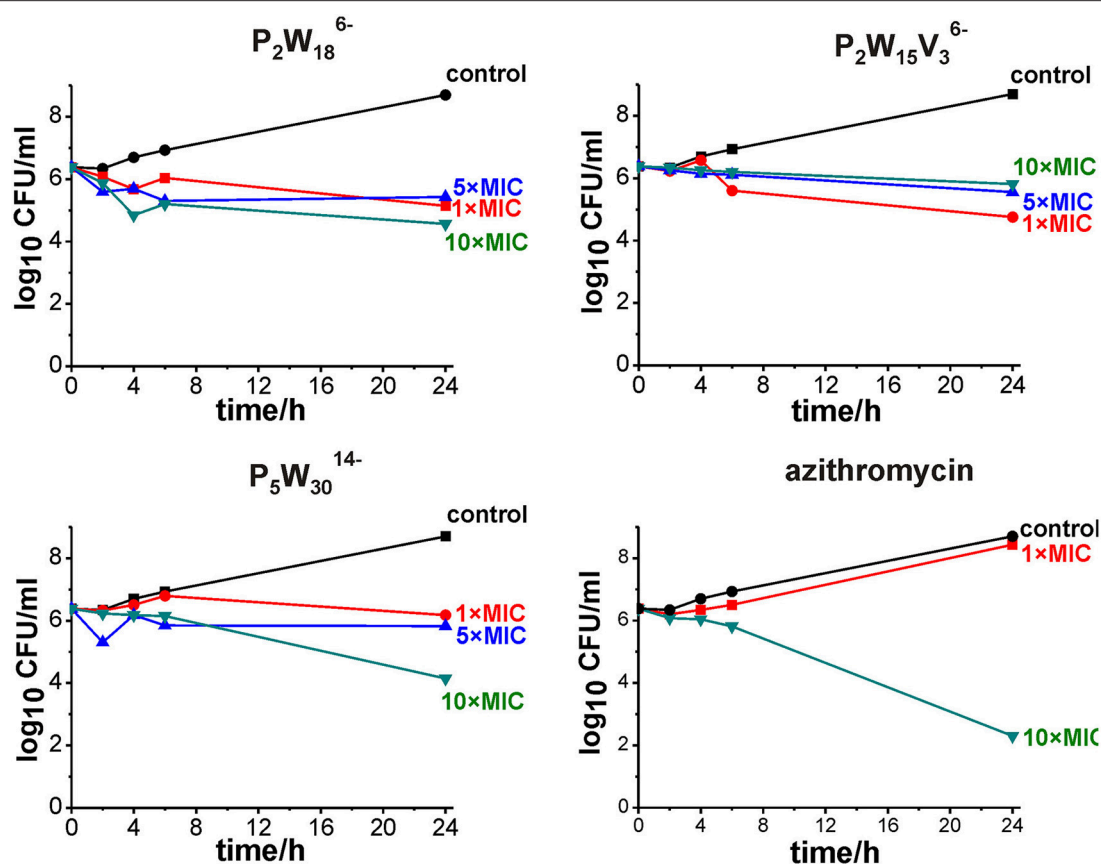


FIGURE 4 | Time-kill curves for Dawson $P_2W_{18}^{6-}$ and $P_2W_{15}V_3^{6-}$, Preyssler $P_5W_{30}^{14-}$ POTs and azithromycin at minimum inhibitory concentration (MIC) (red), 5-fold (blue) and 10-fold MIC concentration (green) against *M. catarrhalis* ATCC23246 strain. Control represents uninhibited bacterial growth (black).

determined against *M. catarrhalis*. POTs were tested at three concentrations, corresponding to 1 \times , 5 \times , and 10 \times MIC. The bactericidal activity of the agents was defined for at least a 3 \log_{10} reduction in viable colony counts. In the control (sample without antibiotic), the numbers of the viable strain were kept within the cultivation of 24 h relative to those at 0 h. **Figure 4** represents time-killing curves for compounds $P_5W_{30}^{14-}$, $P_2W_{18}^{6-}$, and $P_2W_{15}V_3^{6-}$. All tested POMs show bacteriostatic effects, resulting from a little change in viable colony numbers within 24 h despite the concentration being equal to 10-fold MIC (**Figure 4**). Although it would seem preferable for an antibiotic to kill the offending bacteria rather than to merely inhibit it, the clinical importance of an *in vitro* bactericidal action being better than a bacteriostatic action has rarely been documented. The superiority of bactericidal over bacteriostatic action in the treatment of gram-positive bacterial infections is intuitive rather than based on rigorous scientific research (Pankey and Sabath, 2004).

CONCLUSIONS

An important investigation in exploring biological effects of POMs was performed. The antibacterial activity of 29 POTs,

POMos, and POVos against *M. catarrhalis* was investigated by determination of their minimum inhibitory concentrations (MIC) and time-killing kinetics. The following important conclusions were drawn:

- 1) According to their MIC values, Preyssler $P_5W_{30}^{14-}$ (**Figure 1A**) and five Dawson-based $P_2W_{18}^{6-}$, $P_2W_{15}V_3^{6-}$, $P_2O_7Mo_4^{4-}$, $As_2Mo_6^{6-}$, AsW_{18}^{7-} (**Figures 1B, 2**) POMs are promising antibacterial agents against *M. catarrhalis*.
- 2) The Preyssler type POT $P_5W_{30}^{14-}$ (**Figure 1A**) showed the highest antibacterial activity against *M. catarrhalis* (MIC = 1 μ g/ml) and further MIC investigation against *S. aureus* and *E. faecalis* proved its antibacterial potential.
- 3) Based on MIC values, Dawson-type POMs (see **Figure 1B**) exhibited highest activity and selectivity against *M. catarrhalis*.
- 4) Among Keggin-type POMs (see **Figures 1C-E**), only the mono-substituted $CoTiW_{11}^{6-}$ (**Figure 1D**) showed MIC comparable to that of the Dawson-type group.
- 5) POVos and Anderson type POMs (**Figure 1I**) were inactive (MIC > 256 μ g/ml) against *M. catarrhalis* strain.
- 6) According to time-killing studies three the most active POTs (Preyssler $P_5W_{30}^{14-}$ and Dawson $P_2W_{18}^{6-}$

and $P_2W_{15}V_3^{6-}$) showed bacteriostatic effect against *M. catarrhalis*.

- 7) POM activity mainly depends on composition, shape and size, but in the case of medium-size POTs correlates with the total net charge.

AUTHOR CONTRIBUTIONS

NG and AR contributed toward the study design, wrote the manuscript. NG, EA-S, and LK synthesized and characterized POMs. HC-P and DV performed all antibacterial study. All authors read and approved the final version of the manuscript.

REFERENCES

- Bae, E., Lee, J. W., Hwang, B. H., Yeo, J., Yoon, J., Cha, H. J., et al. (2008). Photocatalytic bacterial inactivation by polyoxometalates. *Chemosphere* 72, 174–181. doi: 10.1016/j.chemosphere.2008.01.071
- Barry, A. L., Craig, W. A., Nadler, H., Reller, L. B., Sanders, C. C., and Swenson, J. M. (1999). *Methods for Determining Bactericidal Activity of Antimicrobial Agents: Approved Guideline*. NCCLS document M26-A 19 (18). Wayne, PA: National Committee for Clinical Laboratory Standards.
- Bi, L. H., Wang, E. B., Peng, J., Huang, R. D., Xu, L., and Hu, C. W. (2000). Crystal structure and replacement reaction of coordinated water molecules of the heteropoly compounds of sandwich-type tungstoarsenates. *Inorg. Chem.* 39, 671–679. doi: 10.1021/ic990596v
- Bijelic, A., Aureliano, M., and Rompel, A. (2018). The antibacterial activity of polyoxometalates: structures, antibiotic effects and future perspectives. *Chem. Commun.* 54, 1153–1169. doi: 10.1039/C7CC07549A
- Bijelic, A., and Rompel, A. (2015). The use of polyoxometalates in protein crystallography—An attempt to widen a well-known bottleneck. *Coord. Chem. Rev.* 299, 22–38. doi: 10.1016/j.ccr.2015.03.018
- Bijelic, A., and Rompel, A. (2017). Ten good reasons for the use of the tellurium-centered Anderson-Evans polyoxotungstate in protein crystallography. *Acc. Chem. Res.* 50, 1441–1448. doi: 10.1021/acs.accounts.7b00109
- Blazevic, A., and Rompel, A. (2016). The Anderson-Evans polyoxometalate: from inorganic building blocks via hybrid organic-inorganic structures to tomorrows “Bio-POM”. *Coord. Chem. Rev.* 307, 42–64. doi: 10.1016/j.ccr.2015.07.001
- Briand, L. E., Valle, G. M., and Thomas, H. J. (2002). Stability of the phosphomolybdic Dawson-type ion $P_2Mo_{18}O_{62}^{6-}$ in aqueous media. *J. Mat. Chem.* 12, 299–304. doi: 10.1039/b106769a
- Clemente-Juan, J. M., Coronado, E., and Gaita-Ariño, A. (2012). Magnetic polyoxometalates: from molecular magnetism to molecular spintronics and quantum computing. *Chem. Soc. Rev.* 41, 7464–7478. doi: 10.1039/c2cs35205b
- Contant, R., Klemperer, W. G., and Yaghi, O. (2007). “Potassium octadecatungstodiphosphates(V) and related lacunary compounds,” in *Inorganic Syntheses*, ed A. P. Ginsberg (New York, NY: John Wiley & Sons, Inc.), 104–111.
- Del Beccaro, M. A., Mendelman, P. M., Inglis, A. F., Richardson, M. A., Duncan, N. O., Clausen, C. R., et al. (1992). Bacteriology of acute otitis media: a new perspective. *J. Pediatr.* 120, 81–84. doi: 10.1016/S0022-3476(05)80605-5
- Dizaj, S. M., Lotfipour, F., Barzegar-Jalali, M., Zarrintan, M. H., and Adibkia, K. (2014). Antimicrobial activity of the metals and metal oxide nanoparticles. *Mater. Sci. Eng. C* 44, 278–284. doi: 10.1016/j.msec.2014.08.031
- Evans, H. T., and Rollins, O. W. (1976). Sodium paradodecatungstate 20-hydrate. *Acta Cryst. B* 32, 1565–1567. doi: 10.1107/S00567740876005827
- Finke, R. G., Rapko, B., Saxton, R. J., and Domaille, P. J. (1986). Trisubstituted heteropolytungstates as soluble metal oxide analogs. 3¹. synthesis, characterization, ³¹P, ²⁹Si, ⁵¹V, and 1- and 2-D ¹⁸³W NMR, deprotonation, and proton mobility studies of organic solvent solute forms of $H_xSiW_9V_3O_{40}^{x-7}$ and $H_xP_2W_{15}V_3O_{62}^{x-9}$. *J. Am. Chem. Soc.* 108, 2947–2960. doi: 10.1021/ja00271a025

FUNDING

This research was funded by the Austrian Science Fund (FWF): P27534 (AR), M2203 (NG), and M2200 (LK) and University of Vienna, Austria.

ACKNOWLEDGMENTS

The authors are grateful to Prof. Dr. Gerald Giester for support with X-ray measurements at the Institut für Mineralogie und Kristallographie, Univ. of Vienna and to Dr. Aleksandar Bijelic and Dr. Joscha Breibeck for valuable discussions regarding this work.

- Fu, L., Gao, H., Yan, M., Shouzhui, L., Xinyu, L., Dai, Z., et al. (2015). Polyoxometalate-based organic-inorganic hybrids as antitumor drugs. *Small* 11, 2938–2945. doi: 10.1002/smll.201500232
- Fukuda, N., and Yamase, T. (1997). *In vitro* antibacterial activity of vanadate and vanadyl compounds against *Streptococcus pneumoniae*. *Biol. Pharm. Bull.* 20, 927–930. doi: 10.1248/bpb.20.927
- Gao, J., Yan, J., Beeg, S., Long, D. L., and Cronin, L. (2013). One-pot versus sequential reactions in the self-assembly of gigantic nanoscale polyoxotungstates. *J. Am. Chem. Soc.* 135, 1796–1805. doi: 10.1021/ja309237x
- Gao, N., Sun, H., Dong, K., Ren, J., Duan, T., Xu, C., et al. (2014). Transition-metal-substituted polyoxometalate derivatives as functional anti-amyloid agents for Alzheimer's disease. *Nat. Commun.* 5:3422. doi: 10.1038/ncomms4422
- Gotoh, N., Tanaka, S., and Nishino, T. (1989). Supersusceptibility to hydrophobic antimicrobial agents and cell surface hydrophobicity in *Branhamella catarrhalis*. *FEMS Microbiol. Lett.* 59, 211–213. doi: 10.1111/j.1574-6968.1989.tb03112.x
- Gotoh, N., Tanaka, S., and Nishino, T. (1992). Permeability of the outer membrane of *Moraxella catarrhalis* for β -lactam antibiotics. *J. Antimicrob. Chemother.* 29, 279–285. doi: 10.1093/jac/29.3.279
- Gumerova, N. I., Melnik, N. A., Rozantsev, G. M., Baumer, V. N., and Radio, S. V. (2015). Sodium heteropolyhexamolybdenumnickelate (II) $Na_4[Ni(OH)_6Mo_6O_{18}]\cdot 16H_2O$ with an Anderson anion: synthesis and crystal structure. *J. Struct. Chem.* 56, 926–933. doi: 10.1134/S002247661505157
- Gumerova, N. I., Roller, A., and Rompel, A. (2016). $[Ni(OH)_3W_6O_{18}(OCH_2)_3CCH_2OH]^{4-}$: the first tris-functionalized Anderson-type heteropolytungstate. *Chem. Commun.* 52, 9263–9266. doi: 10.1039/C6CC04326G
- Hori, T., and Himeno, S. (1987). Preparation of a yellow heteropoly molybdosulfate. *Chem. Lett.* 16, 53–56. doi: 10.1246/cl.1987.53
- Ichida, H., and Sasaki, Y. (1983). The structure of hexaguanidinium octadecamolybdiarsenate enneahydrate, $(CH_6N_3)_6[As_2Mo_{18}O_{62}]\cdot 9H_2O$. *Acta Cryst. C* 39, 529–533. doi: 10.1107/S0108270183005363
- Inoue, M., Segawa, K., Matsunaga, S., Matsumoto, N., Oda, M., and Yamase, T. (2005). Antibacterial activity of highly negative charged polyoxotungstates, $K_{27}[KAs_4W_{40}O_{140}]$ and $K_{18}[KSb_9W_{21}O_{86}]$, and Keggin-structural polyoxotungstates against *Helicobacter pylori*. *J. Inorg. Biochem.* 99, 1023–1031. doi: 10.1016/j.jinorgbio.2005.01.010
- Jeannin, Y., and Martin-Frere, J. (1979). X-ray study of $(NH_4)_7[H_2AsW_{18}O_{60}]\cdot 16H_2O$: first example of a heteropolyanion containing protons and arsenic (III). *Inorg. Chem.* 18, 3010–3014. doi: 10.1021/ic50201a013
- Jeannin, Y., Martin-Frere, J., Choi, D. J., and Pope, M. T. (2007). “The sodium pentaphosphato(V)-triacontatungstate anion isolated as the ammonium salt,” in *Inorganic Syntheses*, ed A. P. Ginsberg (New York, NY: John Wiley & Sons, Inc.), 115–118.
- Judd, D. A., Nettles, J. H., Nevins, N., Snyder, J. P., Liotta, D. C., Tang, J., et al. (2001). Polyoxometalate HIV-1 protease inhibitors. A new mode of protease inhibition. *J. Am. Chem. Soc.* 123, 886–897. doi: 10.1021/ja001809e

- Karalus, R., and Campagnari, A. (2000). *Moraxella catarrhalis*: a review of an important human mucosal pathogen. *Microbes Infect.* 2, 547-559. doi: 10.1016/S1286-4579(00)00314-2
- Klemperer, W. G. (2007). "Tetrabutylammonium isopolyoxometalates," in *Inorganic Syntheses*, ed A. P. Ginsberg (New York, NY: John Wiley & Sons, Inc.), 74-85.
- Kobayashi, D., Nakahara, H., Shibata, O., Unoura, K., and Nabika, H. (2017). Interplay of hydrophobic and electrostatic interactions between polyoxometalates and lipid molecules. *J. Phys. Chem. C* 121, 12895-12902. doi: 10.1021/acs.jpcc.7b01774
- Komura, A., Hayashi, M., and Imanaga, H. (1976). Heteropolytungstates containing cobalt (II) or cobalt (III). *Bull. Chem. Soc. Jpn.* 49, 87-91. doi: 10.1246/bcsj.49.87
- Kortz, U., and Pope, M. T. (1994). Polyoxometalate-diphosphate complexes. 2. structure of 18-molybdopyrophosphate, $[(P_2O_7)Mo_{18}O_{54}]^{4-}$, which encloses a linear, eclipsed conformation of the pyrophosphate anion, and preliminary characterization of its one- and two-electron heteropoly blues. *Inorg. Chem.* 33, 5643-5646. doi: 10.1021/ic00103a008
- Kortz, U., Savelieff, M. G., Bassil, B. S., and Dickman, M. H. (2001). A large, novel polyoxotungstate: $[As_6^{III}W_{65}O_{217}(H_2O)_7]^{26-}$. *Angew. Chem. Int. Ed.* 40, 3384-3386. doi: 10.1002/1521-3773(20010917)40:18<3384::AID-ANIE3384>3.0.CO;2-O
- Kraus, W., Stephan, H., Röllich, A., and Reck, G. (2005). $K_6H_2[CoTiW_{11}O_{40}] \cdot 13H_2O$ with a monotitanoundecatungstocobaltate (II) anion. *Acta Cryst. E* 61, i35-i37. doi: 10.1107/S1600536805005180
- Lee, U., and Joo, H. C. (2003). Potassium-sodium double salt of decavanadate, $K_4Na_2[V_{10}O_{28}] \cdot 10H_2O$. *Acta Cryst. E* 59, i122-i124. doi: 10.1107/S1600536803016453
- Li, J., Chen, Z., Zhou, M., Jing, J., Li, W., Wang, Y., et al. (2016). Polyoxometalate-driven self-assembly of short peptides into multivalent nanofibers with enhanced antibacterial activity. *Angew. Chem. Int. Ed.* 55, 2592-2595. doi: 10.1002/anie.201511276
- Lode, H., Borner, K., Koeppel, P., and Schaberg, T. (1996). Azithromycin - review of key chemical, pharmacokinetic and microbiological features. *J. Antimicrob. Chemother.* 37, 1-8.
- López, X., Fernández, J. A., and Poblet, J. M. (2006). Redox properties of polyoxometalates: new insights on the anion charge effect. *Dalton Trans.* 1162-1167. doi: 10.1039/B507599H
- Miras, H. N., Yan, J., Long, D. L., and Cronin, L. (2008). Structural evolution of "S"-shaped $[H_4W_{22}O_{74}]^{12-}$ and "S"-shaped $[H_{10}W_{34}O_{116}]^{18-}$ isopolyoxotungstate clusters. *Angew. Chem. Int. Ed.* 47, 8420-8423. doi: 10.1002/anie.200802109
- Molitor, C., Bijelic, A., and Rempel, A. (2017). The potential of hexatungstotellurate (VI) to induce a significant entropic gain during protein crystallization. *IUCr J.* 4, 34-740. doi: 10.1107/S2052252517012349
- Müller, C. E., Iqbal, J., Baqi, Y., Zimmermann, H., Röllich, A., and Stephan, H. (2006). Polyoxometalates-a new class of potent ecto-nucleoside triphosphate diphosphohydrolase (NTPDase) inhibitors. *Bioorg. Med. Chem. Lett.* 16, 5943-5947. doi: 10.1016/j.bmcl.2006.09.003
- Nomiya, K., Torii, H., Hasegawa, T., Nemoto, Y., Nomura, K., Hashino, K., et al. (2001). Insulin mimetic effect of a tungstate cluster. Effect of oral administration of homo-polyoxotungstates and vanadium-substituted polyoxotungstates on blood glucose level of STZ mice. *J. Inorg. Biochem.* 86, 657-667. doi: 10.1016/S0162-0134(01)00233-1
- Pankey, G. A., and Sabath, L. D. (2004). Clinical relevance of bacteriostatic versus bactericidal mechanisms of action in the treatment of Gram-positive bacterial infections. *Clin. Infect. Dis.* 38, 864-870. doi: 10.1086/381972
- Phillips, M. A. (1950). The preparation of phosphotungstic acid and of sodium and barium phosphotungstates. *J. Chem. Technol. Biotechnol.* 69, 282-284. doi: 10.1002/jctb.5000690906
- Pope, M. (1983). *Heteropoly and Isopoly Oxometalates*, *Inorganic Chemistry Concepts*. Berlin: Springer.
- Proust, A., Thouvenot, R., and Gouzerh, P. (2008). Functionalization of polyoxometalates: towards advanced applications in catalysis and materials science. *Chem. Commun.* 1837-1852. doi: 10.1039/B715502F
- Rozantsev, G. M., Radio, S. V., Gumerova, N. I., Baumer, V. N., and Shishkin, O. B. (2009). Phase formation in the Ni^{2+} - WO_4^{2-} - H^+ - H_2O system ($Z=1.00$). crystal structure and properties of sodium heteropolyhexatungsten nickelate (2+) $Na_4[Ni(OH)_6W_6O_{18}] \cdot 16H_2O$. *J. Struct. Chem.* 50, 296-305. doi: 10.1007/s10947-009-0041-z
- Sadakane, M., and Steckhan, E. (1998). Electrochemical properties of polyoxometalates as electrocatalysts. *Chem. Rev.* 98, 1, 219-238. doi: 10.1021/cr960403a
- Saha, A. K., Crans, D. C., Pope, T. M., Simone, C. M., and Glew, R. H. (1991). Inhibition of human seminal fluid and leishmania donovani phosphatases by molybdate heteropolyanions. *J. Biol. Chem.* 266, 3511-3517.
- Schmidt, K. J., Schrobilgen, G. J., and Sawyer, J. F. (1986). Hexasodium hexatungstotellurate (VI) 22-hydrate. *Acta Cryst. C* 42, 1115-1118. doi: 10.1107/S0108270186093204
- Schwendt, P., Tracey, A. S., Tatiersky, J., Gáliková, J., and Žák, Z. (2007). Vanadium(V) tartrato complexes: speciation in the $H_3O^+(OH^-)/H_2VO_4^-/(2R,3R)$ -tartrate system and X-ray crystal structures of $Na_4[V_4O_8(rac-tart)_2] \cdot 12H_2O$ and $(NEt_4)_4[V_4O_8((R,R)-tart)_2] \cdot 6H_2O$ ($tart = C_4H_2O_4^{4-}$). *Inorg. Chem.* 46, 3971-3983. doi: 10.1021/ic062223h
- Shah, H. S., Al-Oweini, R., Haider, A., Kortz, U., and Iqbal, J. (2014). Cytotoxicity and enzyme inhibition studies of polyoxometalates and their chitosan nanoassemblies. *Toxicol. Rep.* 1, 341-352. doi: 10.1016/j.toxrep.2014.06.001
- Tajima, Y. (2001). Lacunary-substituted undecatungstosilicates sensitize methicillin-resistant *Staphylococcus aureus* to β -lactams. *Biol. Pharm. Bull.* 24, 1079-1084. doi: 10.1248/bpb.24.1079
- Téazéa, A., Hervéa, G., Finke, R. G., and Lyon, D. K. (2007). " α -, β -, and γ -dodecatungstosilicic acids: isomers and related lacunary compounds," in *Inorganic Syntheses*, ed A. P. Ginsberg (New York, NY: John Wiley & Sons, Inc.), 85-96.
- Tourné, C., Revel, A., Tourné, G., and Vendrell, M. (1973). Heteropolytungstates containing elements of phosphorus family with degree of oxidation (III) or (V)-identification of species having composition X_2W_{19} and XW_9 ($X = P, As, Sb, Bi$) and relation to those with composition XW_{11} . *C. R. Acad. Sci. Ser. C* 277, 643-645.
- Tsujimoto, H., Gotoh, N., and Nishino, T. (1999). Diffusion of macrolide antibiotics through the outer membrane of *Moraxella catarrhalis*. *J. Infect. Chemother.* 5, 196-200. doi: 10.1007/s101560050034
- Wang, S. S., and Yang, G. Y. (2015). Recent advances in polyoxometalate-catalyzed reactions. *Chem. Rev.* 115, 4893-4962. doi: 10.1021/cr500390v
- Wikler, M. A. (2009). *Methods for Dilution Antimicrobial Susceptibility Test for Bacteria That Grow Aerobically*. Approved Standard M7-A8. Wayne, PA: Clinical and Laboratory Standards Institute.
- Yamase, T. (2005). Anti-tumor, -viral, and -bacterial activities of polyoxometalates for realizing an inorganic drug. *J. Mater. Chem.* 15, 4773-4782. doi: 10.1039/b504585a
- Yamase, T., Fukuda, N., and Tajima, Y. (1996). Synergistic effect of polyoxotungstates in combination with β -lactam antibiotics on antibacterial activity against methicillin-resistant *Staphylococcus aureus*. *Biol. Pharm. Bull.* 19, 459-465. doi: 10.1248/bpb.19.459
- Yamase, T., and Pope, M. (2006). *Polyoxometalate Chemistry for Nano-Composite Design*. New York, NY: Springer Science & Business Media.

Conflict of Interest Statement: The authors declare that the research was conducted in the absence of any commercial or financial relationships that could be construed as a potential conflict of interest.

Copyright © 2018 Gumerova, Al-Sayed, Krivosudský, Čipčić-Paljetak, Verbanac and Rempel. This is an open-access article distributed under the terms of the Creative Commons Attribution License (CC BY). The use, distribution or reproduction in other forums is permitted, provided the original author(s) and the copyright owner(s) are credited and that the original publication in this journal is cited, in accordance with accepted academic practice. No use, distribution or reproduction is permitted which does not comply with these terms.



Decavanadate Salts of Cytosine and Metformin: A Combined Experimental-Theoretical Study of Potential Metallodrugs Against Diabetes and Cancer

Eduardo Sánchez-Lara¹, Samuel Treviño², Brenda L. Sánchez-Gaytán¹, Enrique Sánchez-Mora³, María Eugenia Castro¹, Francisco J. Meléndez-Bustamante², Miguel A. Méndez-Rojas⁴ and Enrique González-Vergara^{1*}

¹ Centro de Química del Instituto de Ciencias, Benemérita Universidad Autónoma de Puebla, Puebla, Mexico, ² Facultad de Ciencias Químicas, Benemérita Universidad Autónoma de Puebla, Puebla, Mexico, ³ Instituto de Física "Luis Rivera Terrazas", Benemérita Universidad Autónoma de Puebla, Puebla, Mexico, ⁴ Departamento de Ciencias Químico-Biológicas, Universidad de las Américas Puebla, Puebla, Mexico

OPEN ACCESS

Edited by:

Debbie C. Crans,
Colorado State University,
United States

Reviewed by:

Manuel Aureliano,
University of Algarve, Portugal
Samar Kumar Das,
University of Hyderabad, India

*Correspondence:

Enrique González-Vergara
enrique.gonzalez@correo.buap.mx

Specialty section:

This article was submitted to
Inorganic Chemistry,
a section of the journal
Frontiers in Chemistry

Received: 29 June 2018

Accepted: 20 August 2018

Published: 02 October 2018

Citation:

Sánchez-Lara E, Treviño S,
Sánchez-Gaytán BL, Sánchez-Mora
E, Castro ME, Meléndez-Bustamante
FJ, Méndez-Rojas MA and
González-Vergara E (2018)
Decavanadate Salts of Cytosine and
Metformin: A Combined
Experimental-Theoretical Study of
Potential Metallodrugs Against
Diabetes and Cancer.
Front. Chem. 6:402.
doi: 10.3389/fchem.2018.00402

Cytosine, a DNA and RNA building-block, and Metformin, the most widely prescribed drug for the treatment of Type 2 *Diabetes mellitus* were made to react separately with ammonium or sodium metavanadates in acidic aqueous solutions to obtain two polyoxovanadate salts with a 6:1 ratio of cation-anion. Thus, compounds $[\text{HCyt}]_6[\text{V}_{10}\text{O}_{28}] \cdot 4\text{H}_2\text{O}$, **1** and $[\text{HMetf}]_6[\text{V}_{10}\text{O}_{28}] \cdot 6\text{H}_2\text{O}$, **2** (where HCyt = Cytosinium cation, $[\text{C}_4\text{H}_6\text{N}_3\text{O}]^+$ and HMetf = Metforminium cation, $[\text{C}_4\text{H}_{12}\text{N}_5]^+$) were obtained and characterized by elemental analysis, single crystal X-ray diffraction, vibrational spectroscopy (IR and Raman), solution ^{51}V -NMR, thermogravimetric analysis (TGA-DTGA), as well as, theoretical methods. Both compounds crystallized in $P\bar{1}$ space group with $Z' = 1/2$, where the anionic charge of the centrosymmetric ion $[\text{V}_{10}\text{O}_{28}]^{6-}$ is balanced by six Cytosinium and six Metforminium counterions, respectively. Compound **1** is stabilized by π - π stacking interactions coming from the aromatic rings of HCyt cations, as denoted by close contacts of 3.63 Å. On the other hand, guanidinium moieties from the non-planar HMetf in Compound **2** interact with decavanadate μ_2 -O atoms via N-H...O hydrogen bonds. The vibrational spectroscopic data of both IR and Raman spectra show that the dominant bands in the 1000-450 cm^{-1} range are due to the symmetric and asymmetric $\nu(\text{V}-\text{O})$ vibrational modes. In solution, ^{51}V -NMR experiments of both compounds show that polyoxovanadate species are progressively transformed into the monomeric, dimeric and tetrameric oxovanadates. The thermal stability behavior suggests a similar molecular mechanism regarding the loss of water molecules and the decomposition of the organic counterions. Yet, no changes were observed in the TGA range of 540–580°C due to the stability of the $[\text{V}_{10}\text{O}_{28}]^{6-}$ fragment. Dispersion-corrected density functional theory (DFT-D) calculations were carried out to model the compounds in aqueous phase using a polarized continuum model calculation.

Optimized structures were obtained and the main non-covalent interactions were characterized. Biological activities of these compounds are also under investigation. The combination of two therapeutic agents opens up a window toward the generation of potential metalopharmaceuticals with new and exciting pharmacological properties.

Keywords: decavanadate, metformin, cytosine, X-ray crystal structure, vibrational spectroscopy, ^{51}V -NMR, theoretical studies, polyoxovanadates

INTRODUCTION

Vanadium bioinorganic chemistry is becoming a very important topic in the last decades. The information about vanadium in biological systems is increasing in giant steps, so as a guide for our research we have considered many highlights in the history of the field (See **Scheme 1**). In this introduction, relevant information will be presented in a limited way.

Vanadium(IV) and (V) based-compounds have been tested for their potential biomedical use in the treatment of *Diabetes mellitus*, cancer, bacterial diseases and viral infections (Crans, 2000; Rehder, 2008, 2012, 2015a,b). Its therapeutic effects have been attributed mainly to the fact that vanadate has structural and electronic similarities to phosphate. In this sense, vanadium species like vanadate, $(\text{H}_2\text{VO}_4)^-$, can adopt a stable trigonal-bipyramidal geometry similar to that of phosphate transition state in phosphate-metabolizing enzymes, and inhibit its biological activity (Costa-Pessoa et al., 2015; Crans, 2015; Dorsey et al., 2018). Since most of the enzymes inhibited by vanadate participate in key intracellular signaling processes, vanadium has been considered a transition element with relevant medicinal applications (Rehder, 2015a,b; Del Carpio et al., 2018; Selman et al., 2018).

Unlike phosphate, vanadate(V) solutions can form, under specific conditions, **polyoxovanadate** species such as the decavanadate anion, $[\text{V}_{10}\text{O}_{28}]^{6-}$ (Hayashi, 2011). The structure of this oxo-cluster is stable at acidic pH range and structurally contains ten vanadium atoms assembled into a compact structure with unit cell dimensions of $8.3 \text{ \AA} \times 7.7 \text{ \AA} \times 5.4 \text{ \AA}$, where the V^{5+} metal ions occupy the octahedral interstices in the ten $[\text{VO}_6]$ units (Swallow and Barnes, 1964; Aureliano, 2011).

With respect to the biological activity of decameric species, it has been shown that decavanadate induce several changes in biological processes through the interaction with biological systems, such as myosin, actin, and ion pumps, which are major proteins implicated in muscle contraction and its regulation (Aureliano, 2011, 2016, 2017; Winkler et al., 2017). Furthermore, it has been reported that decavanadate has an insulin-enhancing activity in streptozotocin-induced diabetic rats (Pereira et al., 2009) and in murine diabetic models induced by hypercaloric diets or alloxan (Treviño et al., 2015, 2016, 2018). Recently it has been suggested that its *in vitro* anticancer activity may be related to the inhibitory effects on specific enzymes involved in tumor proliferation (Aureliano, 2017; Bijelic et al., 2018). Also, the structure determination of the TRMP4 calcium channel has revealed two binding sites for the decavanadate anions, Thus,

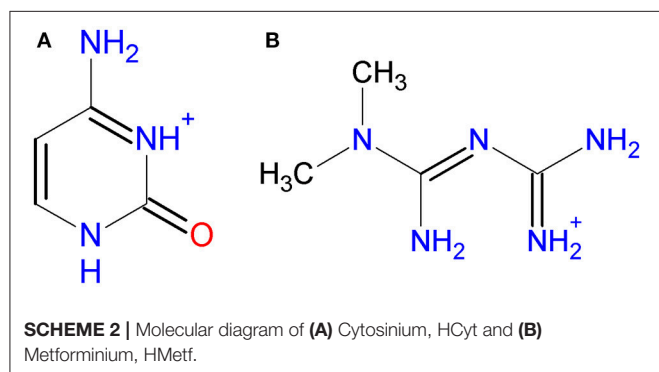
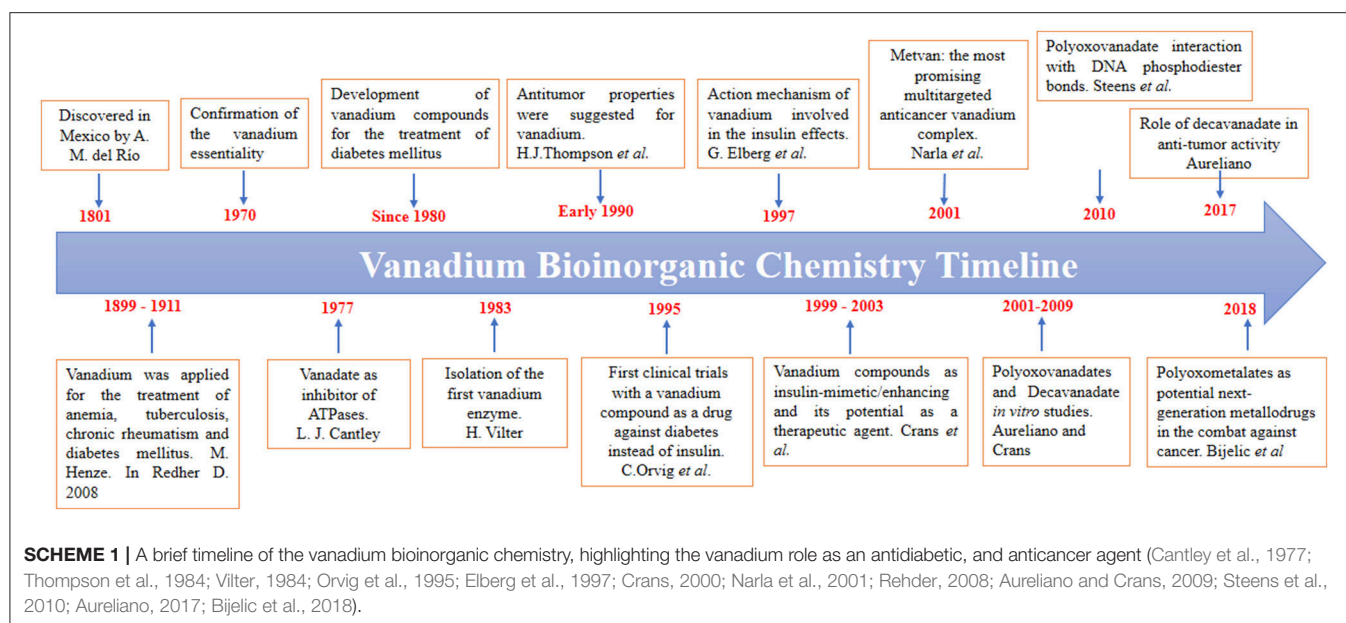
open up new ways for decavanadate biological actions (Winkler et al., 2017).

Because of its high anionic charge, decavanadate is mainly stabilized by counterions through electrostatic interactions and **hydrogen bonds**. In previous works, decavanadate has been combined with a variety of cations, including protons, alkali-metal ions, ammonium, alkylammonium, phosphonium, organic and organometallic cations (Chinea et al., 2000; Lee and Joo, 2003; Correia et al., 2004; Kojima et al., 2011; Bartošová et al., 2012; Kioseoglou et al., 2013; Mal et al., 2013; Sánchez-Lombardo et al., 2014; Crans, 2015; Sánchez-Lara et al., 2015, 2016b). In this work, we combined decavanadate with two biologically relevant molecules Cytosine and Metformin (**Scheme 2**) with the aim to synthesize compounds with potential pharmacological activity.

About the counterions used in this work, Cytosine is one of the naturally occurring nitrogenous bases found in DNA and RNA. Some pyrimidine derivatives exhibit anticancer activity, and some compounds have been used for the treatment of fungal infections (Vermes et al., 2000; Parker, 2009). On the other hand, N,N-dimethylbiguanide or Metformin, as it is known worldwide, is the favorite prescription drug to control the effects of type 2 *D. mellitus* (UK Prospective Diabetes Study (UKPDS) Group., 1998) and is known to affect the cellular housekeeping of copper (Repišćák et al., 2014). Although Metformin is a relatively simple molecule, it possess a versatile behavior as indicated by its capacity of forming salts and coordination compounds in which it participates as a dicationic, monocationic, neutral, and anionic or dianionic species (Zhu et al., 2002).

Besides its role as an insulin sensitizer, new evidence suggests that administration of Metformin may reduce the risk of several types of cancer, including breast, pancreatic and colon cancer (Evans et al., 2005; Libby et al., 2009; Kasznicki et al., 2014). Although the exact molecular mechanism of action for involving Metformin remains unclear, it is known that one of its primary targets is complex I of the mitochondrial electron transport system affecting ATP generation (El-Mir et al., 2000).

Following on from this, the primary focus of this paper is to present two polyoxovanadates-based compounds with potential pharmacological activity. Special emphasis was placed in the compounds' physical and chemical characterization and strengthened with the theoretical analysis. We thus think that the structural study here presented to justify an in-depth biological study to understand, for example, the outcome on the bioactivity of some decavanadate compounds with specific counterions (Yraola et al., 2007; Zorzano et al., 2009; Treviño et al., 2015, 2016, 2018).



at a heating rate of 25 °C/min in alumina pans. An empty pan was used as a reference. Single-crystal X-ray data were recorded with an Agilent Gemini A diffractometer, software SHELX-2014/7 (Sheldrick, 2015). Selected crystal data and details of the structure determination of the compounds are summarized in **Table 1**. CCDC numbers 1850706 (Compound 1) and 1850707 (Compound 2) contain the supplementary crystallographic data for this paper. These data can be obtained for free at <http://www.ccdc.cam.ac.uk/conts/retrieving.html> (or from the CCDC, 12 Union Road, Cambridge CB2 1EZ, UK; Fax: +44-1223-336-033; e-mail address: deposit@ccdc.cam.ac.uk). The supramolecular networks were studied by using *Mercury* CSD (release 3.1.2) (Macrae *et al.*, 2008), which, together with *OLEX-2* (Dolomanov *et al.*, 2009) were used to produce crystallographic artwork.

EXPERIMENTAL SECTION

All manipulations were carried out at room temperature and with no special solvent and reagent purification. Infrared spectra were obtained in KBr pellets in the range from 400–4000 cm^{-1} by using an IR Digilab, Mod. Scimitar FT-IR spectrophotometer. Raman spectra were obtained at room temperature in backscattering configuration using the 633 nm line of a He-Ne laser as an excitation source by using a LabRAM HR-Olympus Micro Raman system. The ^1H , ^{13}C were obtained at 500 MHz and 125 MHz respectively, while the ^{51}V -NMR spectra were recorded at 131.5 MHz with a Bruker AVANCE III 500 MHz spectrometer using deuterated water (D_2O). Chemical shifts were referenced to VOCl_3 as an external standard in the case of ^{51}V -NMR. The elemental analysis was performed by Elemental Analyser CHNS/O Thermo Scientific Flash 2000. Thermogravimetric (TGA) and differential thermal (DTA) analysis were carried out under continuous N_2 flow on an STA 2500 Regulus differential scanning calorimeter (Netzsch Instruments, Burlington, MA). Samples were weighed (~ 10 mg) and heated from 30 to 700 °C,

Computational Methods

The structural and electronic properties of compounds $[\text{HCyt}]_6[\text{V}_{10}\text{O}_{28}] \cdot 4\text{H}_2\text{O}$, **1**, and $[\text{HMet}]_6[\text{V}_{10}\text{O}_{28}] \cdot 6\text{H}_2\text{O}$, **2**, were computed from theoretical calculations based on the density functional theory (DFT) (Hohenberg and Kohn, 1964). Geometry optimization of the asymmetric unit of Compound **1** and **2** was obtained using the pure functional B97-D3 (Grimme *et al.*, 2011). B97-D3 is a Grimme's functional that includes the Becke and Johnson dispersion corrections (BJ-damping), recommended for non-covalent interactions (Grimme *et al.*, 2011). The split-valence 6-31G(d) basis set (Rassolov *et al.*, 1998) used in the C, H, O, and N atoms includes a single set of Gaussian polarization functions. A LanL2MB basis set (Hay and Wadt, 1985) and an effective core potential (ECP) which replaces the effects of the inner core electrons with a pseudopotential specific for transition metal atoms, were used for the V atom. Aqueous solvent effects were calculated with the polarized continuum model using the conductor-like polarizable continuum model (CPCM) (Barone *et al.*, 1998). Calculations were performed with

TABLE 1 | Single crystal data and structure refinement details for [HCyt]₆[V₁₀O₂₈]·4H₂O, **1**, and [HMetf]₆[V₁₀O₂₈]·6H₂O, **2**.

	Compound 1	Compound 2
Empirical formula	C ₂₄ H ₄₄ N ₁₈ O ₃₈ V ₁₀	C ₂₄ H ₈₄ N ₃₀ O ₃₄ V ₁₀
Formula weight	1702.17	1846.61
Crystal system	Triclinic	Triclinic
T (K)	298(2)	298(2)
Space group	<i>P</i> $\bar{1}$	<i>P</i> $\bar{1}$
<i>a</i> [Å]	10.6062(6)	11.5615(6)
<i>b</i> [Å]	12.2173(7)	13.2793(8)
<i>c</i> [Å]	12.4329(7)	13.7694(6)
α (deg)	62.225(6)	96.011(4)
β (deg)	69.091(6)	107.347(4)
γ (deg)	85.817(5)	115.557(6)
<i>V</i> (Å ³)	1323.04(16)	1752.30(18)
<i>Z</i>	1	1
Radiation type	Mo K α , λ = 0.7107 Å	Mo K α , λ = 0.7107 Å
<i>D</i> _{calc} (mg/m ³)	2.136	1.824
μ (mm ⁻¹)	1.806	1.37
Reflections collected	18,005	23,664
Independent reflections	6,464	8,617
Parameters	454	567
Goodness-of-fit on <i>F</i> ²	1.03	1.05
Final R index [<i>I</i> > 2 σ (<i>I</i>)]	0.050	0.051
Largest diff. peak and hole (e/Å ³)	0.80, -0.83	1.01, -0.52
<i>wR</i> ₂ (all data)	0.138	0.163

the Gaussian16 program (Frisch et al., 2016) and visualization of the results was carried out with the GaussianView 6.0.16 program (Dennington et al., 2016).

Synthesis of [HCyt]₆[V₁₀O₂₈]·4H₂O (**1**)

First, 0.5 g of NH₄VO₃ was dissolved in 30 mL of distilled water and heated up to dissolution. Then, three drops of concentrated hydrochloric acid (37 %) were added at room temperature to allow the formation of decavanadate anions. After obtaining an orange solution, 0.111 g (1 mmol) of cytosine previously dissolved in 20 mL of distilled water was added dropwise under stirring, obtaining a crystalline orange precipitate, which was filtered from the mother solution (pH = 5.8). Recrystallization from 20 mL of hot water gave a low yield of block-shaped orange crystals, which have low solubility in water. ⁵¹V NMR (D₂O): -515.84, -500.31, -423.55. IR (KBr, cm⁻¹): 3383, 3321 [$\nu_{\text{as}}(\text{N-H})$], 3170 [$\nu_{\text{s}}(\text{N-H})$], 2984 [$\nu(\text{C-H})$], 1718 [$\nu(\text{C=O})$], 1686 [$\nu(\text{C=C})$], 1656 [$\nu(\text{C=N})$], 1545 [$\delta(\text{N-H})$], 987, 952 [$\nu(\text{V=O})$], 820, 737 [$\nu_{\text{as}}(\text{V-O-V})$], 603, 571 [$\nu_{\text{s}}(\text{V-O-V})$]. Anal. Calc. for C₂₄H₄₄N₁₈O₃₈V₁₀ (MW=1702.17 g/mol) C, 16.93%; H, 2.60%; N, 14.81%. Found: C, 17.23%; H, 2.76%; N, 14.94%.

Synthesis of [HMetf]₆[V₁₀O₂₈]·6H₂O (**2**)

Two 850-mg-Metformin hydrochloride tablets (Alpharma laboratories) were each crushed using a mortar and pestle and added to a solution containing 0.5 g of NaVO₃, previously dissolved in 30 mL of distilled water. Three drops of concentrated

hydrochloric acid (37%) were added by stirring and then filtered. Needle-shaped orange crystals of Compound **2**, were isolated from their mother solution (pH=6.3) and filtered after 3 days. It is important to note that the pH value was a key factor to obtain this compound since the metformin molecule can act as monocationic or dicationic species at different acidic pH values (Chatkon et al., 2014; Sánchez-Lombardo et al., 2014). The slightly acidic medium of the mother solution maintains the monoprotection of the metformin molecule and eventually the formation of Compound **2**. Second, the monoprotectioned metformin is a good hydrogen-bonding donor leading to better solvation in the aqueous medium, therefore, allowing a good solubility of this compound. Yield (based on vanadium): 0.260 g, 35%. ¹H NMR (D₂O): δ = 3.027 (s, 6H, CH₃), ¹³C (D₂O): δ = 37.7 (CH₃), 158.7 (C-NH₂), 160.2 (C=NH₂⁺). ⁵¹V (D₂O): -514.43, -500.02, -422.31. IR (KBr, cm⁻¹): $\tilde{\nu}$ = 3502 [$\nu(\text{O-H})$], 3396-3321 [$\nu_{\text{as}}(\text{N-H})$], 3170 [$\nu_{\text{s}}(\text{N-H})$], 1624, 1569 [$\nu(\text{C=N})$], 1481, 1419 [$\delta(\text{CH}_3)$], 1053 [$\delta(\text{N-H})$], 945 [$\nu_{\text{s}}(\text{V=O})$], 830, 736 [$\nu_{\text{as}}(\text{V-O-V})$], 603, 571 [$\nu_{\text{s}}(\text{V-O-V})$]. Anal. Calc. for C₂₄H₈₄N₃₀O₃₄V₁₀ (MW=1846.61 g/mol) C, 15.61%; H, 4.60%; N, 22.75%. Found: C, 16%; H, 4.5%; N, 22.74%.

RESULTS AND DISCUSSION

Synthetic Strategy

Compound [HCyt]₆[V₁₀O₂₈]·4H₂O, **1**, was isolated from an acidic mother solution of NH₄VO₃ with a pH of around 6, which allowed the protonation of the cytosine molecules and the formation of decavanadate anions. The first attempt to obtain a compound based on [V₁₀O₂₈]⁶⁻ units and cytosine was initially explored by our group using sodium metavanadate salt NaVO₃ as a precursor of polyoxovanadate ions. However, as a result, we obtained a compound previously published, where the sodium ions are present in the crystal structure forming metal-complexes with the cytosine molecules and the [V₁₀O₂₈]⁶⁻ ions (Bošnjakovic-Pavlovic et al., 2009). With the purpose of replacing the Na⁺ ions to get Compound **1**, the starting material NaVO₃ was replaced by NH₄VO₃. In this way, the cytosinium cations were incorporated in the resulting compound, without the presence of NH₄⁺ ions, and the water molecules were occluded during the crystallization process as lattice solvent.

On the other hand, crystals of [HMetf]₆[V₁₀O₂₈]·6H₂O, **2**, were isolated in good yield (35%) from an aqueous solution of sodium metavanadate NaVO₃ at pH 6.3. Again, the pH value and the vanadium source were the key factors to obtain this Compound. The synthetic strategy was, first, take into account that Metformin molecule is a moderately strong base with two pK_a values of 2.8 and 11.5 (Kathuria et al., 2018) and therefore can act as monocationic or dicationic species at different acidic pH values. Second, we needed to avoid the formation of metforminium(2+) decavanadates salts, previously reported by us (Sánchez-Lombardo et al., 2014). From this, we decided to use a slightly acidic medium in order to maintain the monoprotection of the Metformin molecule present in the Metformin hydrochloride tablets, and eventually to get the Compound **2**. Is important to mention herein that the solubility of this compound is very high in contrast with the Compound **1**,

may be due to protonated form of Metformin (HMetf) is a good hydrogen-bonding donor, leading to better solvation in aqueous medium allows, therefore, a good solubility of this compound. This point is particularly relevant to carry out biological testing.

Crystal Structure Description

Single-crystal X-ray structural analysis shows that Compound **1** crystallizes in the centrosymmetric $P\bar{1}$ space group (Table 1) with the asymmetric unit, containing one-half of decavanadate anion placed in an inversion center, three independent HCyt cations in the amino-oxo tautomeric form and two lattice water molecules, each located in general positions are depicted in Figure 1. The structure of the $[V_{10}O_{28}]^{6-}$ cluster is well known and consists of an arrangement of a 10-edge-shared $[VO_6]$ octahedron close to a local D_{2h} symmetry, though the crystallographic symmetry is C_i .

In agreement with the *Mogul* geometry check (Macrae et al., 2008), the V–O bond lengths and the V–O–V angles are found in normal ranges; comparable with other structures containing this oxo-cluster and showed no unusual geometrical parameters. The backbone of the $[V_{10}O_{28}]^{6-}$ anion is a very rigid entity that does not present significant structural changes caused by non-covalent interactions. The (3-)anion charge in the asymmetric unit is therefore stabilized by three HCyt cations, protonated at N2, N12, and N22 sites. All the H-atoms of HCyt were found from the difference-Fourier map and refined isotropically. The residual electronic density is actually low for room temperature data of $0.80 \text{ e}/\text{\AA}^3$. From this, Compound **1** can be formulated as $[\text{HCyt}]_6[V_{10}O_{28}] \cdot 4\text{H}_2\text{O}$.

Ionization of the cytosine molecule in an acid medium leads to the introduction of a third donor group. This protonation causes an increase in the internal C–N–C bond angles of the pyrimidine rings in the three independent organic molecules. For example, the C1–N2–C2 angle of $124.81(3)^\circ$ is larger in cation N1 than in the corresponding value found in the 118.90° -non-protonated cytosine molecule (Lee and Wang, 2010). Also, the short bond

lengths between C2–N3 and N1–C4 of 1.302(5) and 1.358(5) Å, respectively, show a resonance effect of π -electron density on the entire molecule. These values are very similar in the three independent cations.

According to the Cambridge Structural Database (CSD, version 5.39, last updated November 2017; Groom et al., 2016), there are no direct structure precedents of Compound **1** in the crystallographic literature, but some complexes containing HCyt or neutral cytosine interacting with polyoxometalate ions have been structurally characterized by X-ray diffraction. One of these structures is an inorganic hybrid polymer built from $\text{P}_2\text{Mo}_5\text{O}_{23}$ clusters and Cu(II)–cytosine subunits (Weng et al., 2002). There are two structures based on hetero-polyoxometalates, $[\text{SeMo}_5\text{O}_{21}]^{4-}$ and $[(\text{HAsO}_4)\text{Mo}_6\text{O}_{19}]^{6-}$ (Nagazi and Haddad, 2014; Ayed et al., 2015). The last and possibly the closest structure to Compound **1** is a compound co-crystallized with $[V_{10}O_{28}]^{6-}$ and Na^+ ions (Bošnjakovic-Pavlovic et al., 2009). However, a duplex structure containing a cytosine/cytosinium dimer is present in this case. In Compound **1**, dimer formation is disrupted despite a cooperative triple hydrogen bonding of the duplex structure, possibly owing to the low pK_a value of the hydrochloric acid used to adjust the pH that produces the protonation of all the cytosine molecules, avoiding the formation of the hemicytosinium pair (Perumalla et al., 2013).

The supramolecular structure of Compound **1** is dominated by classic N–H...O, O–H...O, C–H...O and π -stacking interaction among heterocyclic rings. In this regard, the independent cations N1 and N11 of HCyt interact with $[V_{10}O_{28}]^{6-}$ through N–H...O hydrogen bonds, which involve protonated pyrimidine rings as donor groups and two μ_2 -O sites of the anion as acceptors, with a N1–H1...O9 distance of 2.77(4) Å and a N11–H11...O12 distance of 2.73(4) Å, as well as N–H...O angles of 169 and 172° , respectively (Table 2). These cations generate π - π contacts characterized by a centroid-to-centroid distance of 3.92(3) Å. The remaining N2 and N3 atoms from cation N1 comprise planar rings represented by $R_2^2(8)$ (Etter et al., 1990) with μ_2 -O decavanadate atoms.

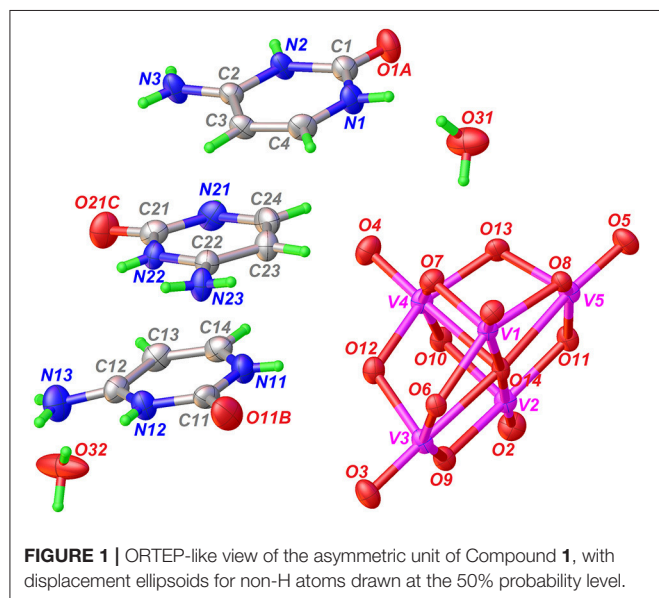


TABLE 2 | Hydrogen bond geometry (Å, °) for Compound **1**.

D–H...A	D–H	H...A	D...A	D–H...A	Symmetry code
N1–H1...O9	0.85 (5)	1.94 (5)	2.777 (4)	169 (5)	$x-1, y, z$
N2–H2...O10	0.70 (5)	1.98 (5)	2.670 (4)	168 (5)	$-x+1, -y+1, -z+1$
N3–H31...O5	0.81 (5)	2.06 (5)	2.813 (4)	156 (5)	$x, y, z-1$
N3–H32...O10	0.81 (5)	2.51 (5)	3.125 (4)	134 (4)	$-x+1, -y+1, -z+1$
N3–H32...O11	0.81 (5)	2.53 (5)	3.249 (4)	149 (5)	$-x+1, -y+1, -z+1$
N11–H11...O12	0.74 (5)	2.00 (5)	2.739 (4)	172 (5)	
N12–H12...O32	0.67 (5)	2.01 (5)	2.679 (5)	174 (6)	
N13–H131...O21C	0.91 (6)	1.92 (6)	2.818 (5)	168 (5)	$-x+2, -y+1$
N21–H21...O31	0.76 (5)	2.16 (5)	2.911 (5)	168 (5)	$-x+1, -y+1, -z+1$
N22–H22...O11	0.75 (4)	2.03 (5)	2.722 (4)	154 (5)	$x, y, z-1$
N23–H231...O11B	0.76 (5)	2.04 (5)	2.791 (5)	173 (5)	$-x+1, -y, -z+1$
N23–H232...O6	0.81 (5)	1.91 (5)	2.708 (5)	166 (5)	$-x+1, -y, -z+1$

On the other hand, N11- and N21-based HCyt cations interact with each other *via* one hydrogen bond between the acceptor O carboxylic atom and the exocyclic amino group, with distance of 2.81(5) Å for O21C...H131–N13 and 2.79(5) Å for O11B...H231–N23, forming a C(12) (Etter et al., 1990) infinite chain extended in the [101] direction, which is stacked through the inversion center coming from the space-group symmetry. In this regard, the π - π parallel-displaced stacking interaction between N11 and N21 cations in the layer is characterized by a centroid-to-centroid distance of 3.63(3) Å and by a displacement angle of approximately 20°. These chains are hydrogen-bonded with decavanadate oxygen atoms forming $R_2^2(8)$ and $R_3^3(10)$ ring motifs (Figure 2). It is important to mention that distances of 3.6–3.8 Å between centroids of the π - π stacking interactions are also found in DNA and RNA structures. The relevance of this phenomena is unclear at the moment. However, it can be hypothesized that polyoxometalates could be used as templates for base-base linkages and base-base pairing in the early development of life (Rehder, 2011; Cafferty et al., 2016).

The molecular formula of Compound 2 has been determined by single-crystal X-ray diffraction as $[\text{HMetf}]_6[\text{V}_{10}\text{O}_{28}] \cdot 6\text{H}_2\text{O}$ (Table 1). This compound also crystallizes in the triclinic $P\bar{1}$ space group with half of the decavanadate anion ($Z' = \frac{1}{2}$), three independent monoprotonated HMetf cations and three lattice water molecules in the asymmetric unit (Figure 3). Therefore, six HMetf neutralize the $[\text{V}_{10}\text{O}_{28}]^{6-}$ anion charge in the unit cell.

In the refinement process, one of the HMetf is split into two sites with refined occupancies of 0.616(5) in part A and 0.382(5) in part B. It is not surprising to detect a positional disorder for this cation because this limited disorder should be a stabilizing

factor for the whole crystal structure. On the other hand, O52, O53, O54, and O55 from water molecules were refined more effectively with an occupancy factor of 1/2. The largest peak in

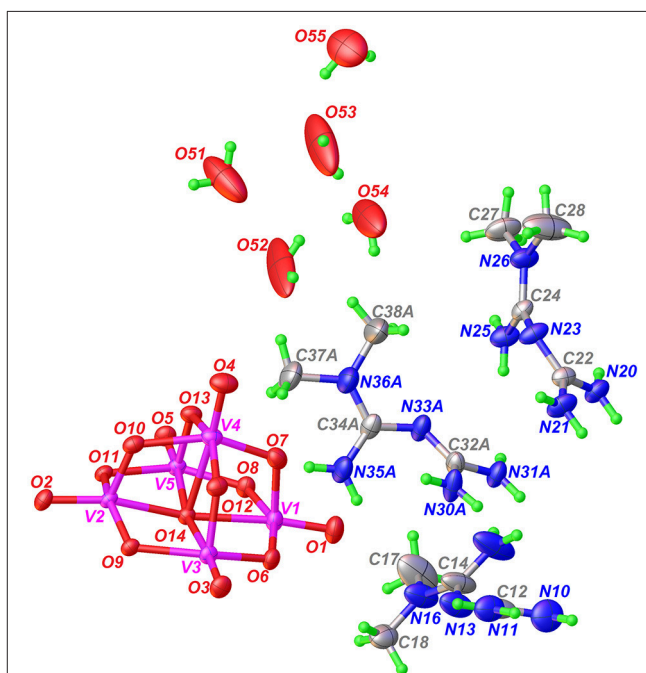


FIGURE 3 | ORTEP-like view of the asymmetric unit of Compound 2, with displacement ellipsoids for non-H atoms drawn at the 50% probability level. Only the major component of disorder for one HMetf is shown.

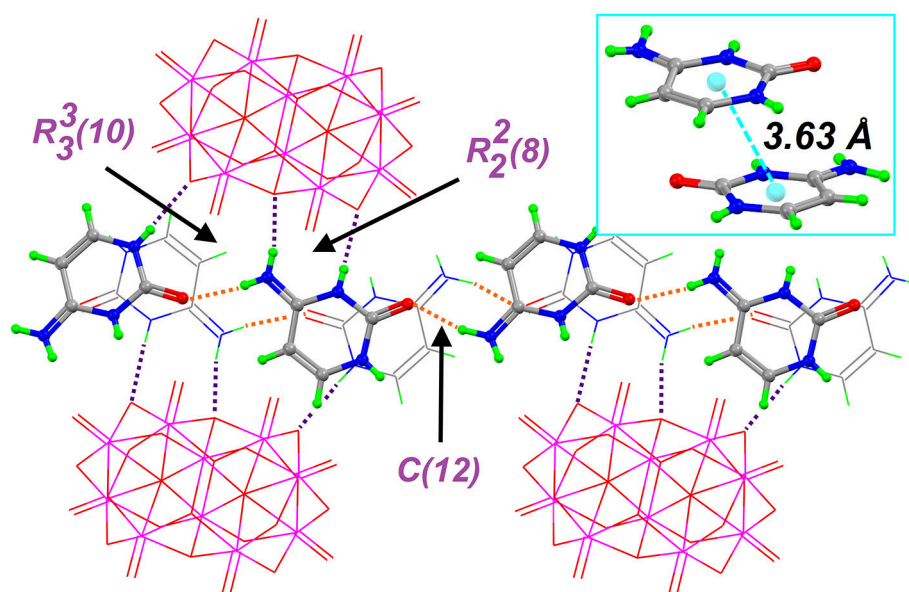


FIGURE 2 | Partial crystal structure of Compound 1, showing the supramolecular network, which is based on the hydrogen bonds (dashed lines) formed between HCyt and decavanadates: Orange H-bonds are used to form the C(12) chain that is connected to $[\text{V}_{10}\text{O}_{28}]^{6-}$ anions by purple H-bonds in the crystal structure. The inset displays the π - π contacts between two non-symmetry related HCyt.

the final difference electron density synthesis was $1.01 \text{ e}/\text{\AA}^3$ and the largest hole was $0.52 \text{ e}/\text{\AA}^3$.

The non-planar HMetf in Compound **2** shows the geometrical features of Metformin hydrochloride (Form B) (Childs et al., 2004), where the orientation of the $-\text{C}(\text{NH}_2)$ and $-\text{N}(\text{CH}_3)_2$ groups are found on the opposite side due to a decrease in van der Waals repulsion. The torsion angles for cations N10, N20 and N30A are $158.3(6)^\circ$, $137.2(4)^\circ$, and $144.7(13)^\circ$, respectively. This type of conformation is observed in several Metforminium(1+) based-salts containing chloride, nitrate, acetate, salicylate, squarate, and carbonate (Zhu et al., 2003; Childs et al., 2004; Olar et al., 2010; Pérez-Fernández et al., 2013; Serb et al., 2014; Dong et al., 2015).

There are some tautomeric forms reported for HMetf in the solid state, all of which are fully delocalized (Scheme 3) (Pérez-Fernández et al., 2013; Kathuria et al., 2018). Cation N10 present in Compound **2** corresponds to tautomer (c), while N30A and N20 cations correspond to tautomer (d). Although the central N atoms can act as acceptor groups, only N23 accepts one hydrogen bond from O55, with a distance $\text{O55} \cdots \text{H55A} \cdots \text{N23}$ of $2.84(11) \text{ \AA}$ (Table 3).

By analyzing the bond lengths in HMetf, we observed that the $\text{N}-(\text{CH}_3)_2$ methyl group bond lengths correspond to single bonds with a distance ranging from $1.44(7)$ to $1.47(9) \text{ \AA}$. For the C–N bonds, the bond distances range from $1.31(7)$ to $1.35(7) \text{ \AA}$ and the central C–N–C angle is reduced to nearly 120° , all of which suggests a π -electron density delocalization across the biguanide group.

Regarding structures crystallized with decavanadate and the anti-diabetic drug Metformin, our research group has previously obtained three decavanadate Metforminium salts at low pH values, all of them characterized by X-ray diffraction (Sánchez-Lombardo et al., 2014). However, in these cases, the Metforminium ions are acting as a dicationic species. Debbie Crans group, on the other hand, has described a water-insoluble double salt containing decavanadate and a mixture of Metforminium(1+) and a protonated guanylurea counterion (Chatkon et al., 2014). The Metformin molecule in the reported

compound presents equal proton distributions and similar structural features to those of HMetf found in Compound **2**.

Further describing the structure of Compound **2**, all guanidinium moieties of HMetf cations are involved in hydrogen bonds with decavanadate anion, through $\text{N}-\text{H} \cdots \text{O}$ with $R_1^2(6)$ and $R_2^2(8)$ ring motifs with distances ranging from $2.89(5)$ to $3.25(7) \text{ \AA}$ and characterized by angles $\text{D}-\text{H} \cdots \text{A} > 140^\circ$ (Figure 4). These guanidinium-decavanadate interactions are also favored by Coulombic forces.

A complete supramolecular analysis of this compound is difficult to attain because one HMetf is split into two fractional parts and the disorder in O51, O52, O53, and O54 affect the water H-bond positions. However, considering only the N10 and N20 cations, we observe the formation of a four-level $R_4^4(20)$ ring involving two non-symmetry related HMetf, that interact with terminal and bridging μ_2 - and μ_3 -O from $[\text{V}_{10}\text{O}_{28}]^{6-}$. This tetramer is formed by $\text{N11}-\text{H11A} \cdots \text{O12}$ $3.10(6) \text{ \AA}$, $\text{N15}-\text{H15B} \cdots \text{O13}$ $2.93(8) \text{ \AA}$, $\text{N20}-\text{H20B} \cdots \text{O3}$ $2.93(6) \text{ \AA}$, and $\text{N21}-\text{H21A} \cdots \text{O11}$ $2.95(5) \text{ \AA}$ hydrogen bonds. Also, a centrosymmetric ring $R_4^4(16)$ is present in this compound. In this case, two inversion-related HMetf cations interact with terminal and bridging μ_3 -O atoms from decavanadate as acceptor groups. This third-level motif with pattern $R(> k < l > k < l)$ shows a chair-like conformation. Both supramolecular patterns are represented in Figure 5. It is important to notice the similarity between the binding sites of TRPM4 calcium channel which are rich in arginine and lysine residues and Compound **2**. In this sense, the interaction of the biguanide Metformin, resembles the interactions of the guanidinium ions in the TRMP4 decavanadate binding sites. (see Figure 4) PDB: 5WP6.

Solid-State Vibrational Spectroscopy

FTIR and Raman spectra of Compounds **1-2** are shown in Figure 6 and can be compared with those of neutral cytosine and Metformin hydrochloride, respectively. Furthermore, the Raman spectra of Compounds **1-2** are compared with that of the ammonium decavanadate salt, $[\text{NH}_4]_6[\text{V}_{10}\text{O}_{28}] \cdot 6\text{H}_2\text{O}$, for a better assignment of the Raman bands.

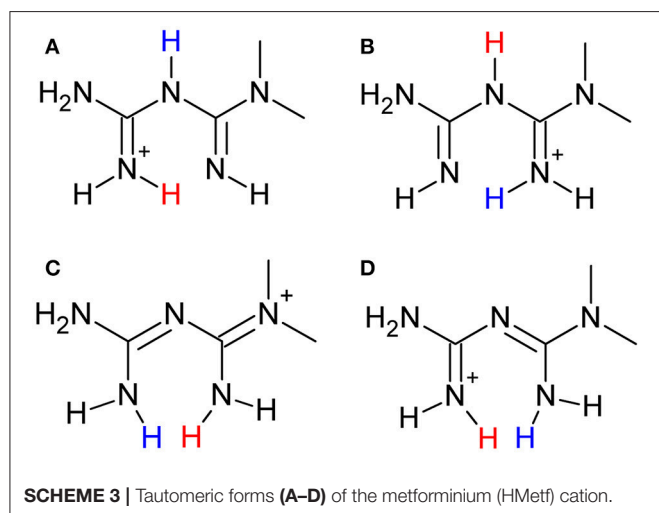


TABLE 3 | Hydrogen bond geometry (\AA , $^\circ$) for Compound **2**.

$\text{D}-\text{H} \cdots \text{A}$	$\text{D}-\text{H}$	$\text{H} \cdots \text{A}$	$\text{D} \cdots \text{A}$	$\text{D}-\text{H} \cdots \text{A}$	Symmetry code
$\text{N10}-\text{H10A} \cdots \text{O12}$	0.86	2.09	$2.894(5)$	155	$-x+1, -y+1, -z+1$
$\text{N11}-\text{H11A} \cdots \text{O7}$	0.86	2.47	$3.251(7)$	151	
$\text{N11}-\text{H11A} \cdots \text{O12}$	0.86	2.37	$3.102(6)$	143	
$\text{N15}-\text{H15B} \cdots \text{O13}$	0.85	2.27	2.931	134	
$\text{N20}-\text{H20A} \cdots \text{O5}$	0.86	2.42	$3.142(5)$	142	
$\text{N20}-\text{H20B} \cdots \text{O3}$	0.86	2.14	$2.932(6)$	153	
$\text{N21}-\text{H21A} \cdots \text{O11}$	0.86	2.12	$2.950(5)$	162	
$\text{N25}-\text{H25A} \cdots \text{O9}$	0.86	2.15	$2.808(4)$	133	$-x, -y+1$
$\text{N30A}-\text{H30A} \cdots \text{O6}$	0.86	2.15	$2.95(2)$	154	
$\text{N31A}-\text{H31B} \cdots \text{O6}$	0.86	2.35	$3.09(3)$	144	
$\text{N35A}-\text{H35A} \cdots \text{O8}$	0.86	2.13	$2.898(6)$	149	
$\text{O(55)}-\text{H55(A)} \cdots \text{N23}$	0.85	$2.11(5)$	$2.841(11)$	$144(5)$	$x-1, y, z$

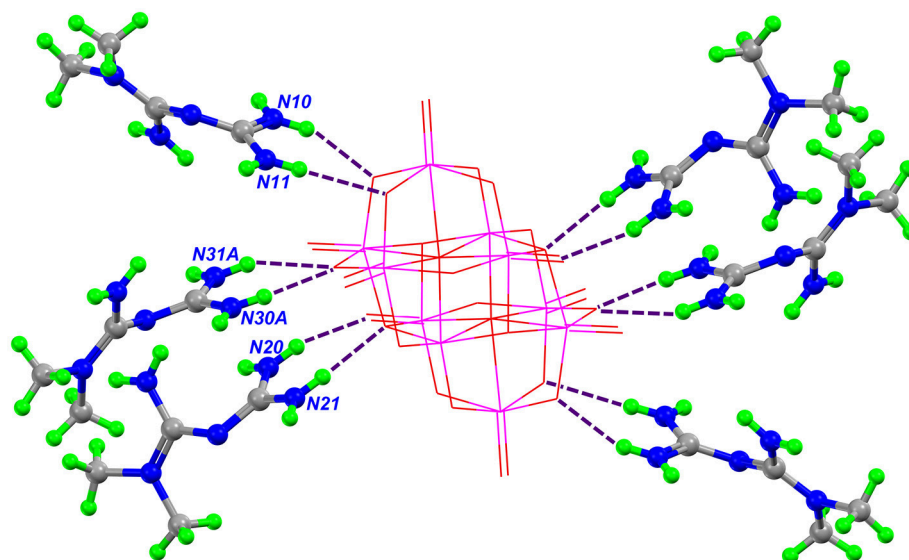


FIGURE 4 | Part of the crystal structure of Compound **2**, showing the interaction between HMetf and $[V_{10}O_{28}]^{6-}$. The main hydrogen bonds between the cations and anion that form the $R_2^2(8)$ and $R_1^2(6)$ rings are shown as purple dashed lines.

The middle IR (**Figure 6A**) of Compound **1** shows a set of peaks in the *high-frequency* region at $3486\text{--}2684\text{ cm}^{-1}$. $\nu_{as}(\text{N-H})$ appears at 3383 and 3321 cm^{-1} , while $\nu_s(\text{N-H})$ appears at 3135 cm^{-1} . $\nu(\text{C}_{sp^2}\text{--H})$ is observed in the range of $2984\text{--}2694\text{ cm}^{-1}$ (Rozenberg et al., 2004). Strong IR vibrations seen at $1,718$, $1,686$, and $1,656\text{ cm}^{-1}$ have been assigned to $\nu(\text{C=O})$, $\nu(\text{C=C})$, and $\nu(\text{C=N})$, respectively. It is known that the position of these bands is shifted upon protonation of the cytosine ring by shortening bond lengths (Rasheed and Ahmad, 2010; Sridhar et al., 2012).

The bands observed at 987 and 952 cm^{-1} in the IR spectra and the corresponding Raman peaks (**Figure 6B**) at 992 and 958 cm^{-1} are assigned to symmetric stretching modes of the terminal V=O bonds of the decavanadate anion. However, the $(V_{10}O_{28})^{6-}$ vibrations are mixed with the corresponding vibrations of the HCyt molecules (see **Table 4**).

The bands at the $833\text{--}737\text{ cm}^{-1}$ region in the infrared spectrum are attributed to the asymmetric stretching modes of (V-O-V) units, overlapped with the cytosine ring “breathing” vibration observed at 792 cm^{-1} in the neutral cytosine molecule. In Raman spectra, the asymmetric stretching mode of (V-O-V) is found at 835 cm^{-1} as a medium-intensity peak, and the intense band at 793 cm^{-1} is due to the ring-breathing mode of the HCyt (Mathlouthi et al., 1986; Frost et al., 2005; Frost and Palmer, 2011; Pavliuk et al., 2014; Madzharova et al., 2016; Sánchez-Lara et al., 2016b).

Two IR intense bands at 572 and 513 cm^{-1} , and the corresponding Raman band at 595 cm^{-1} are observed. These frequencies were assigned to $\nu_s(\text{V-O-V})$. The Raman bands at $423\text{--}320\text{ cm}^{-1}$ may be attributed to the $\delta(\text{V-O-V})$. Bands below 240 cm^{-1} are attributed to V-O bonds and lattice vibrations (Frost et al., 2005; Frost and Palmer, 2011).

For Compound **2**, the medium-intensity bands in the *high-frequency* region in the IR spectra (**Figure 6C**) at $3,395\text{--}3,289$

cm^{-1} are attributed to the $\nu_{as}(\text{N-H})$ bond, while the band corresponding to $\nu_s(\text{N-H})$ is observed in the region of $3,200\text{--}3,170\text{ cm}^{-1}$. On the other hand, the very weak bands at $2,972$ and $2,936\text{ cm}^{-1}$ correspond to the symmetric and asymmetric stretching vibrations of the methyl groups of HMetf, respectively (Gunasekaran et al., 2006). No significant difference between the IR spectra of Compound (**2**) and Metformin hydrochloride were observed possibly because the protonation state remained unchanged.

For Compound **2**, the strong intensity bands in the IR spectrum at $1,624$ and $1,569\text{ cm}^{-1}$ could originate from $\nu(\text{C=N})$. The medium-intensity bands in the IR at $1,481$ and $1,419\text{ cm}^{-1}$ could arise from asymmetric deformations of CH_3 groups (Gunasekaran et al., 2006; Sheela et al., 2010; Ghasemi et al., 2018).

The strong IR vibration at 950 cm^{-1} corresponds to $\nu(\text{V=O})$. The corresponding vibrations appear in the Raman spectrum (**Figure 6D**) at 977 and 952 cm^{-1} . In the same Raman spectrum, an intense peak is observed at 938 cm^{-1} , which can be assigned to $\delta(\text{N-H})$ with a contribution of $\nu_{as}(\text{V-O-V})$ (Frost et al., 2005; Gunasekaran et al., 2006). The IR absorption at 830 and 736 cm^{-1} corresponds to the $\nu_{as}(\text{V-O-V})$ bond. The Raman line at 833 cm^{-1} originated from the same vibration is very weak. Returning to the IR absorption spectrum, medium-intensity bands are observed at 603 and 571 cm^{-1} , which correspond to $\nu_s(\text{V-O-V})$. This band is observed also at 602 cm^{-1} in the Raman spectrum (Frost et al., 2005; Frost and Palmer, 2011; Pavliuk et al., 2014; Sánchez-Lara et al., 2016b). Vibrations below 450 cm^{-1} are quite similar to those found for Compound **1** crystallized with cytosine.

Solution NMR-Spectroscopy

It has been shown that vanadate(V) species in solution can occur simultaneously in equilibrium with a different state of

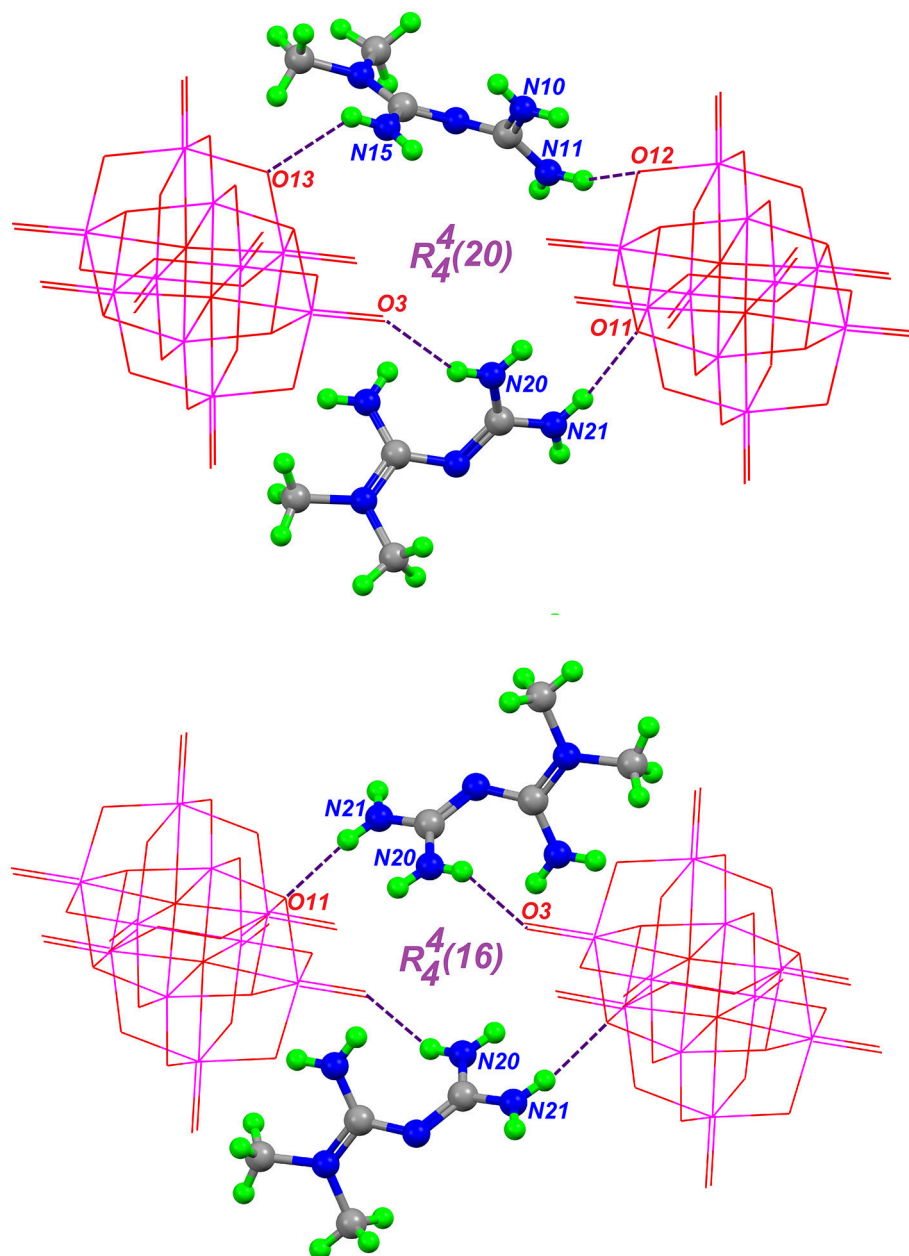


FIGURE 5 | Hydrogen-bond patterns in Compound **2**, formed through hydrogen bonds (purple dashed lines) between two HMetf cations and two symmetry-related $[V_{10}O_{28}]^{6-}$ moieties.

protonation and, in some cases, with different conformations (Aureliano and Ohlin, 2014). These characteristics of the aqueous vanadium(V) chemistry are highly dependent on pH, vanadium concentration and ionic strength (Dorsey et al., 2018). Decavanadate structure in solution, for example, could be decomposed into three species: monomeric $[H_2VO_4]^-$, dimeric $[H_2V_2O_7]^{2-}$ and tetrameric $[V_4O_{12}]^{4-}$ vanadates. This speciation has been studied mainly by ^{51}V -NMR spectroscopy and these findings have significant consequences for toxicology activities and pharmacological applications of decavanadate based-compounds (Soares et al., 2007; Aureliano et al., 2016).

Due to this last, the ^{51}V -NMR spectroscopy for both compounds was carried out. Aqueous solutions of Compound **1** at pH close to 7 display the classical ^{51}V resonance signals ascribed to the three different vanadium atoms of the decavanadate structure, present at: $V10A = -515.88$ ppm, $V10B = -500.31$ ppm, and $V10C = -423.55$ ppm (Figure 7) (Rehder et al., 2007; Rehder, 2015a,b). However, it is known that decavanadate slowly decomposes when the $pH > 6.5$, where it is thermodynamically unstable and it is transformed into the labile monomers and cyclic vanadates (Soares et al., 2007; Aureliano and Crans, 2009). Thus, the sharp signal at $\delta = -560.04$ ppm can be assigned to

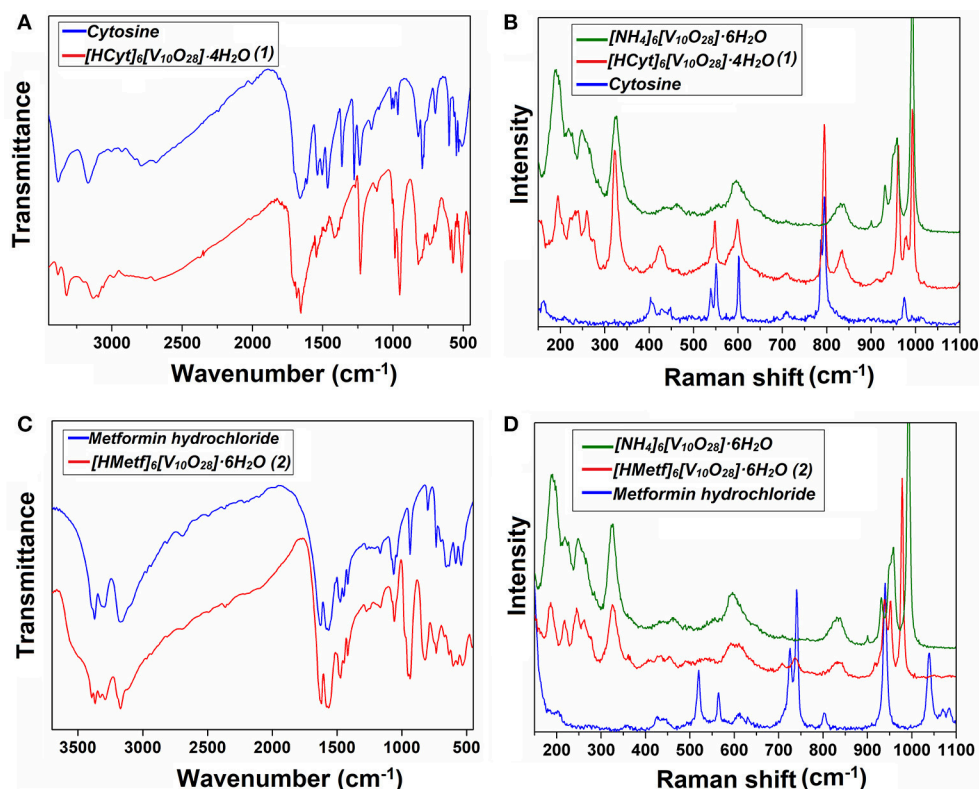


FIGURE 6 | Vibrational spectroscopy of Compounds 1-2 recorded in solid-state. (A) and (B) are the FT-IR and Raman spectra for Cytosine and Compound 1, while (C) and (D) are the FT-IR and Raman spectra for Metformin hydrochloride and Compound 2, respectively.

the biologically active species $[\text{H}_2\text{VO}_4]^-$ (V1), while the signals at $\delta = -572.52$ and -577.06 ppm can be attributed to the divanadate $[\text{H}_2\text{V}_2\text{O}_7]^{2-}$ (V2) and cyclic tetramer $[\text{V}_4\text{O}_{12}]^{4-}$ (V4), respectively (Rehder et al., 2007).

For Compound 2, the shifts for $[\text{V}_{10}\text{O}_{28}]^{6-}$ structure are very similar to those for Compound 1, which are observed at: $\text{V10A} = -514.43$ ppm, $\text{V10B} = -500$, $\text{V10C} = -422.31$ ppm. We also observe the presence of other vanadate species as a consequence of decavanadate hydrolysis, with signals at -560.39 , -572.19 , and -576.80 ppm, which correspond to V1, V2, and V4, respectively (see Figure 7).

On the other hand, the ^{13}C -NMR spectrum (Figure S1) shows one signal at 37.41 ppm corresponding to the equivalent methyl groups of the Metformin molecules, and the two signals observed at 158.43 and 160.12 ppm corresponding to the tertiary guanidyl carbons $\text{C}-\text{NH}_2$ and $\text{C}=\text{NH}_2^+$, respectively (Chatkon et al., 2013; Ibrahim et al., 2015). The ^1H -NMR in water- D_2 shows only one resonance peak at 2.7 ppm due to two equivalent methyl groups (data not shown). The N-H protons were exchanged in D_2O by eliminating the signals at 7.20 and 7.69 ppm, previously observed in $\text{DMSO}-d_6$ (Gadape and Parikh, 2011).

DSC-TGA Analysis

The thermal behavior of $[\text{HCyt}]_6[\text{V}_{10}\text{O}_{28}] \cdot 4\text{H}_2\text{O}$ (1), and $[\text{HMetf}]_6[\text{V}_{10}\text{O}_{28}] \cdot 6\text{H}_2\text{O}$ (2), was assessed by TGA/DTA analysis (Figures S2, S3). For Compound 1, the thermogram shows

a mass loss of around 3-4% corresponding to lattice water molecules in the range of 30–150°C, which fits with four water molecules [% mass, calc. (found): 4.23% (4%)]. An endothermic process occurs around 225°C which may be attributed to the melting of cytosine, followed by a continuous mass loss in the range from 220 to 580°C which may correspond to the thermal degradation of the six cytosinium ions [% mass, calc. (found) for $6 \times \text{C}_4\text{H}_6\text{N}_3\text{O}$: 39.5% (40%)]. For Compound 2, the DTA thermogram shows three well defined endothermic peaks in a temperature range of 37–70°C, all related to the loss of lattice water molecules. This water loss is in agreement with the corresponding mass change observed in the TGA curve suggesting the loss of six uncoordinated water molecules [% mass, calc (found): 5.85% (6%)]. Completion of this stage leads to the anhydrous phase, which shows a significant range of thermal stability extending to ca. 200°C. This thermal behavior has been observed for other polyoxometalates ions with organic moieties (Iyer et al., 2014; Sánchez-Lombardo et al., 2014; Martín-Caballero et al., 2016; Dissem et al., 2018). Considering that the melting point of Metformin hydrochloride is 224°C (Benmessaoud et al., 2016), we can assign the endothermic peaks observed in the DTA thermogram in a temperature range of 190–210°C, to the melting of Metforminium cations (HMetf) present in Compound 2. Above this temperature, an exothermic mass loss takes place that corresponds to the combustion of the metforminium cations per decavanadate unit [%mass, calc.

TABLE 4 | Assignments of IR and Raman abortion bands for Compounds 1-2.

Compound 1			Compound 2		
FT-IR ^a (cm ⁻¹)	FT-Raman (cm ⁻¹)	Vibrational Assignment ^b	FT-IR (cm ⁻¹)	FT-Raman (cm ⁻¹)	Vibrational assignment
3383 (s)		$\nu_{as}(\text{NH}_2)$	3532 (b)		$\nu(\text{O-H})$
3321 (s)		$\nu_{as}(\text{NH}_2)$	3370 (s)		$\nu_{as}(\text{NH}_2)$
3135 (s)		$\nu_s(\text{NH}_2)$	3201(s), 3171(s)		$\nu_s(\text{NH}_2)$
2693 (vw)		$\nu(\text{C-H})$	3171 (vs)		$\nu_s(\text{NH}_2)$
1718 (vs)		$\nu(\text{C=O})$	2970 (vw)		$\nu_{as}(\text{CH}_3)$
1686 (vs)		$\nu(\text{C=C})$	2936 (vw)		$\nu_s(\text{CH}_3)$
1656 (s)		$\nu(\text{N=C})$	1624 (s)		$\nu(\text{C=N})$
1545 (m)		$\nu(\text{N=C}), \beta(\text{Ring})$	1569 (vs)		$\nu(\text{C=N})$
1479 (vw)		(C-N)	1509 (vw)		$\delta(\text{NH})$
1231 (s)		$\nu(\text{C-N}), \beta(\text{C-H}), \beta(\text{N-H})$	1477 (m)		$\delta(\text{CH}_3)$
987 (vs), 952 (vs)	992 (vs), 958 (vs)	$\nu(\text{V=O}), \gamma(\text{C-H}), \nu(\text{ring}), \rho(\text{NH}_2)$	1418 (m)		$\delta(\text{CH}_3)$
820 (s), 737 (m)	835 (vs)	$\nu_{as}(\text{V-O-V}) + \nu(\text{Ring})$	1279 (w), 1165 (w), 1059 (w)	1089 (w), 1048 (w)	$\nu(\text{C-N})$
	793 (vs)	$\nu(\text{Ring})$	950 (vs)	977 (vs), 952 (vs), 937 (vs)	$\nu(\text{V=O}), \omega(\text{N-H})$
572 (s), 513 (s)	595 (vs)	$\nu_s(\text{V-O-V}) + \beta(\text{C=O}), \beta(\text{Ring})$	822 (vs), 735 (vs)	833 (vs), 738 (w)	$\nu_{as}(\text{V-O-V}), \omega(\text{N-H}), \gamma(\text{N-H})$
	421 (s)	$\delta(\text{VO}_3), \gamma(\text{Ring})$	573 (w), 541 (w)	600 (m)	$\nu_s(\text{V-O-V}), \delta(\text{C-N-C})$
	321 (s), 260 (s), 237 (s), 162(w)	$\delta(\text{V-O-V}), \text{Lattice vibrations}, \omega(\text{NH}_2)$		325 (s), 261 (s), 245 (s)	$\delta(\text{V-O-V})$ Lattice vibrations

^a(s) Strong; (vs) very strong; (m) medium; (w) weak; (vw) very weak; (br) broad; (vbr) very broad.

^b(ν) stretching; (ν_s) sym. stretching; (ν_{as}) asym. stretching; (β) in-plane bending; (δ) bending; (ρ) rocking; (ω) wagging; (γ) out-of-plane bending.

(found) for $6 \times \text{C}_4\text{H}_{12}\text{N}_5$: 42.3% (40%)]. In both cases, above 540–580°C no further mass losses are observed, which can be attributed to the remaining inorganic fragment $[\text{V}_{10}\text{O}_{28}]^{6-}$ which is thermally stable event up to 600°C as observed in previously reported decavanadates compounds (Omri et al., 2015; Ortaboy et al., 2018). It may be possible that further thermal treatment of the decavanadate ion may yield other vanadium oxides, possibly V_2O_5 or other mixed-valence oxides (Riou et al., 1998). However, a more in-depth analysis such as thermogravimetry is necessary to confirm the nature of the resulting metal oxides, which may probably consist of vanadium oxide nanoparticles produced by thermal decomposition of the polyoxovanadate systems (Martin-Caballero et al., 2016).

Theoretical Results

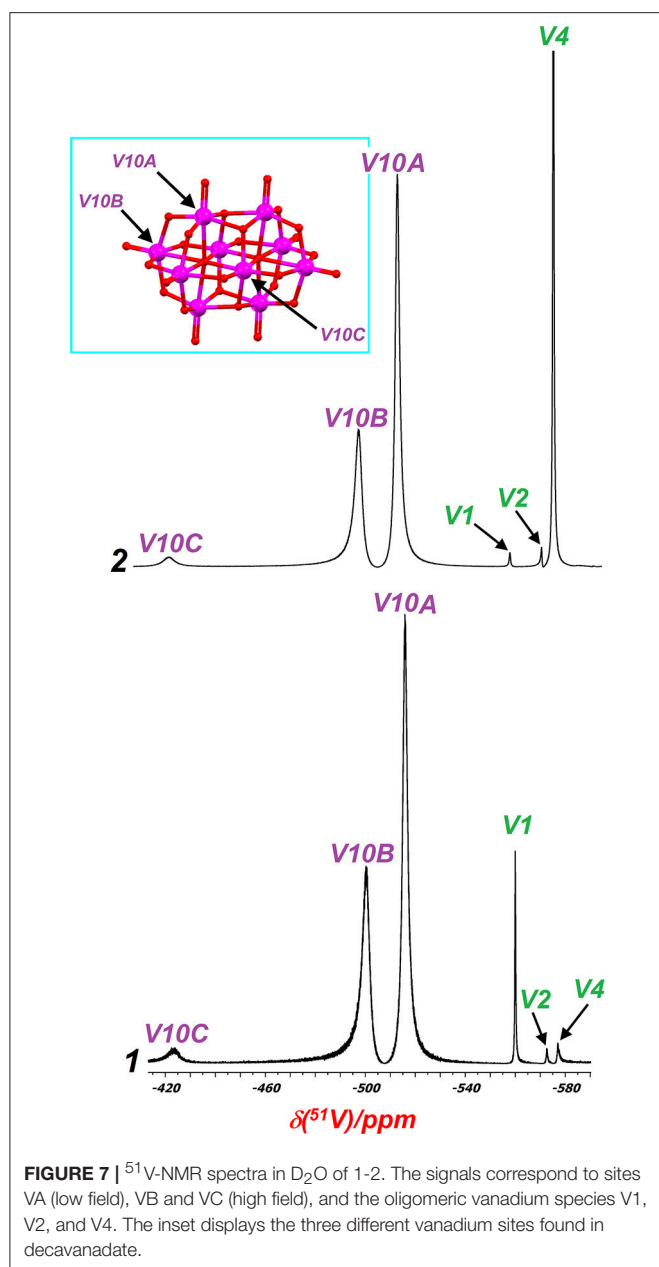
Optimized structures of the asymmetric unit in aqueous solvation phase of Compounds 1 and 2 are shown in Figures 8, 9. It can be seen that the theoretical structures are similar to those mapped from crystallographic data. Selected parameters for the compounds are shown in Tables S1, S2. Selected hydrogen bonds are also reported in Table S3. Atom labels are the same as those used in Figures 1, 3.

Table S1 shows the structural parameters for Compound 1 obtained by the DFT-D methods in solution phase from X-ray crystallographic data used as an initial structure for calculation.

In the aqueous phase, some variations were observed in the dihedral angle values calculated in the decavanadate anion $[\text{V}_{10}\text{O}_{28}]^{6-}$ due to the solvent effect. The group of cytosinium cations ($[\text{C}_4\text{H}_6\text{N}_3\text{O}]^+$) interacting with the decavanadate anion $[\text{V}_{10}\text{O}_{28}]^{6-}$ replicates the behavior in the crystallographic unit cell. Water molecules in Compound 1 form important hydrogen bond interactions.

For Compound 2, the full optimization of the asymmetric unit showed that the intramolecular parameters for the metforminium cations ($[\text{C}_4\text{H}_{12}\text{N}_5]^+$) had significant structural displacements relative to the position of the decavanadate. The decavanadate ion optimized parameters for Compound 2 were obtained with good precision using the crystallographic data as a reference. Moreover, the optimized parameters for the anion structure were similar in both compounds. Contrary to what is observed in 1, where one of the water molecules acts as a water bridge ($\mu_2\text{-O}$) between the cation and the decavanadate, the optimized water molecules in Compound 2 act as a cluster (O51–O55) without any apparent cation-anion interaction (Figure 9).

Including the solvent effect in both compounds was a decisive step for geometry optimization, as well as taking into consideration the non-covalent interactions $\text{N-H}\cdots\text{O}$ and $\text{O-H}\cdots\text{O}$ through the inclusion of the dispersion forces by the DFT-D methods.



The main hydrogen bonds were also theoretically characterized. A previous study about the electronic properties of a cytosine-decavanadate system was carried out by using Atoms in Molecules Topological Analysis (Bošnjakovic-Pavlovic et al., 2009). In this work, the density of $\text{D-H}\cdots\text{A}$ hydrogen bonds were analyzed, suggesting the $\text{N-H}\cdots\text{O}$ as strong hydrogen bonds and $\text{C-H}\cdots\text{O}$ as weak hydrogen bonds in the cytosine-decavanadate system containing sodium cations. In the present work, the non-covalent interactions $\text{N-H}\cdots\text{O}$ were also found using the DFT-D methodology and including a solvent effect by means of the CPCM approach. Values similar to crystallographic data, used as a reference, were obtained for interactions $\text{N-H}\cdots\text{O}$ for Compounds 1 and 2 as reported in Table 2. In addition,

important interactions were calculated between water molecules in both compounds (Table S3).

Figures 10, 11 show the distribution for the frontier molecular orbitals [the highest occupied molecular orbital (HOMO) and the lowest unoccupied molecular orbital (LUMO)], and the molecular electrostatic potential (MEP) for Compounds 1 and 2. When the decavanadate anion $[\text{V}_{10}\text{O}_{28}]^{6-}$ is built together with cytosinium or metforminium cations and water molecules, significant symmetric non-covalent interactions are observed in the resulting compounds. For compound 1, the HOMO was mainly delocalized on all oxygen atoms of $[\text{V}_{10}\text{O}_{28}]^{6-}$ except O1, as shown in Figure 8. Furthermore, the nitrogen atoms and the partially delocalized $\text{C}=\text{C}$ double bonds of Cytosinium cations provide a significant contribution to HOMO. On the other hand, LUMO was mainly delocalized on the nitrogen and carbon atoms of cations $[\text{C}_4\text{H}_6\text{N}_3\text{O}]^+$, (see Figures 10A,B). For compound 2 the HOMO distribution is mainly delocalized on the oxygen atoms of $[\text{V}_{10}\text{O}_{28}]^{6-}$, with contributions from the O1, O3 and O5 atoms (and their symmetric equivalents in decavanadate anion), see Figure 9. Additionally, a significant contribution to HOMO is provided from the atoms forming C-N bonds in Metforminium cations. LUMO is mainly delocalized on nitrogen atoms of cations $[\text{C}_4\text{H}_{12}\text{N}_5]^+$ (see Figures 11A,B). The total electron density was mapped with the electrostatic potential surface (isovalue = 0.004) for both compounds, as shown in Figures 10C, 11C. The qualitative color code indicates red regions with a negative charge, while blue regions indicate positive charge. Yellow and green regions correspond to intermediate values toward negative or positive charges, respectively. The negative charge is gathered mainly on the anion $[\text{V}_{10}\text{O}_{28}]^{6-}$, while counterions $[\text{C}_4\text{H}_6\text{N}_3\text{O}]^+$, and $[\text{C}_4\text{H}_{12}\text{N}_5]^+$ have a positive charge. Non-covalent interactions $\text{N-H}\cdots\text{O}$ and $\text{O-H}\cdots\text{O}$ are located in intermediate regions of electron density. The distribution of charges in both compounds clearly indicate the relevance of Coulombic interactions.

CONCLUSIONS

This paper focused on the structural description and characterization of two new decavanadate salts, obtained at acidic pH under mild conditions by a combination of ammonium and sodium metavanadates with pharmacologically active counterions from Cytosine and Metformin. In summary, the preparation and complete characterization by elemental analysis, XRD single crystal analysis, spectroscopy and thermal analysis of these new compounds was reported. Also, theoretical studies were carried out to analyze the molecular structure and characterize the intermolecular interactions of these hybrid compounds.

About the crystal structures, we observed that molecular packing in these compounds is predominantly driven by strong hydrogen bonds, as well as Coulombic interactions between cations and decavanadate cluster, building interesting supramolecular networks that have been described herein. The solid-state spectroscopy analyses (FT-IR and Raman) confirmed the presence of $[\text{V}_{10}\text{O}_{28}]^{6-}$ and the characteristic vibrations

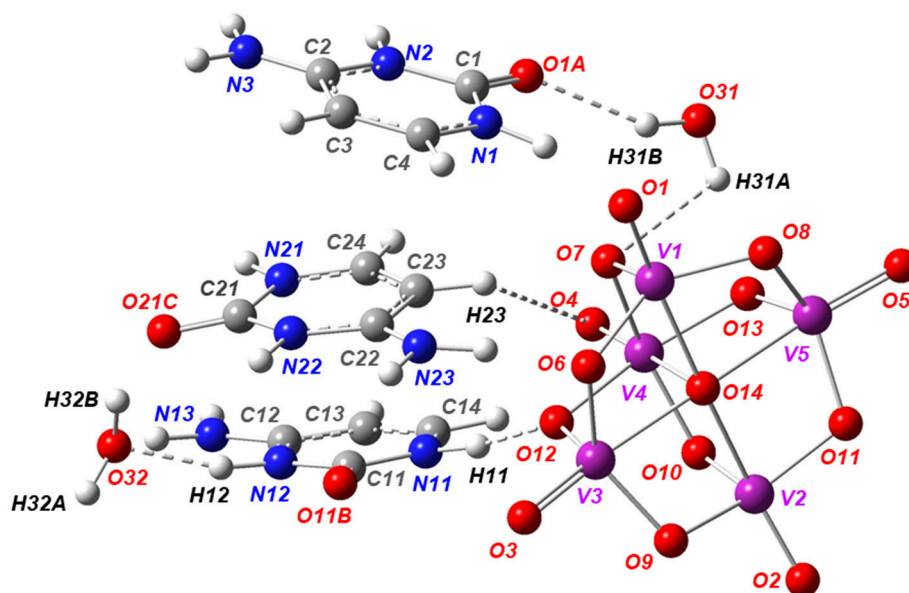


FIGURE 8 | Solution-phase of the optimized structure of the asymmetric unit of Compound **1**, using the B97-D3 functional with the 6-31G(d) basis set for the C, H, O, N, atoms and the LanL2MB basis set for the V atoms.

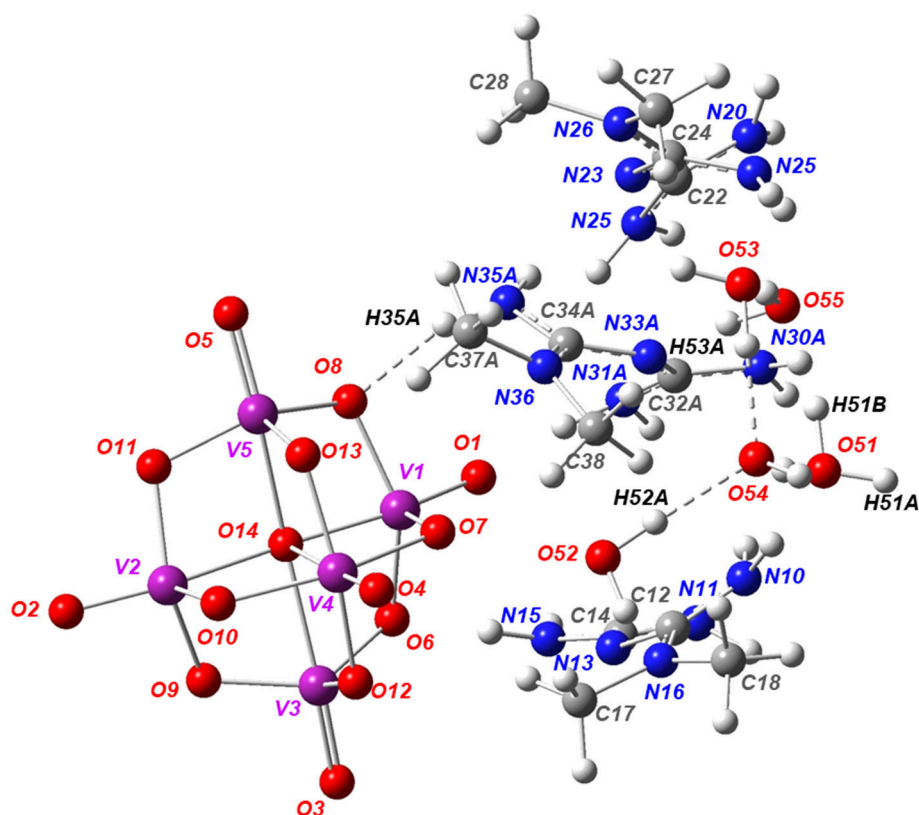


FIGURE 9 | Solution-phase optimized structure of the asymmetric unit of Compound **2** using the B97-D3 functional with the 6-31G(d) basis set for the C, H, O, N, atoms and the LanL2MB basis set for V atoms.

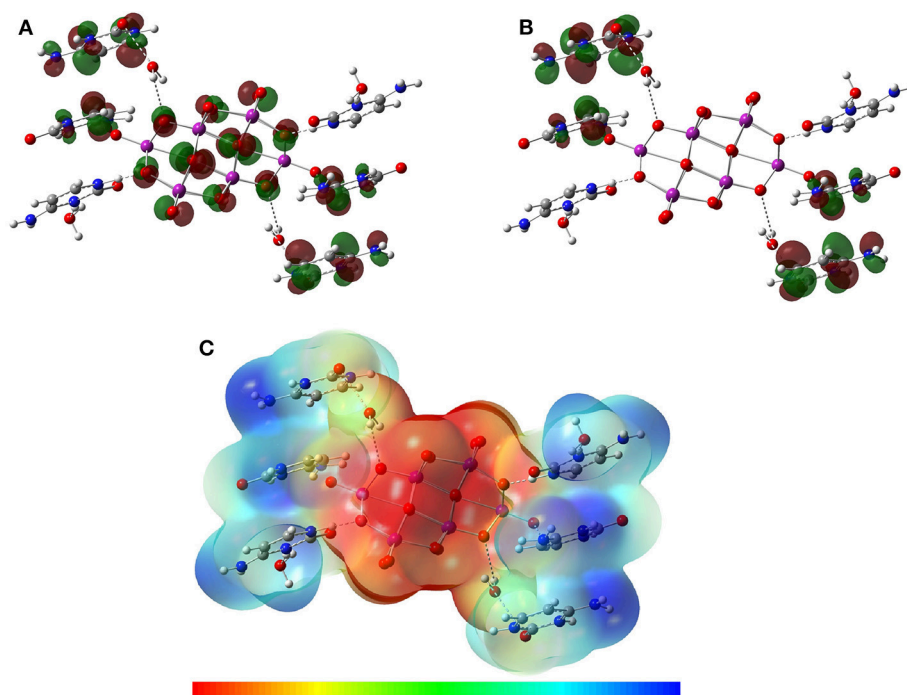


FIGURE 10 | Isosurfaces of frontier molecular orbitals **(A)** HOMO and **(B)** LUMO, and **(C)** MEP of Compound **1** at B97-D3 functional with the 6-31G(d) basis set for C, H, O, N, atoms and LanL2MB basis set for V atoms in solution phase.

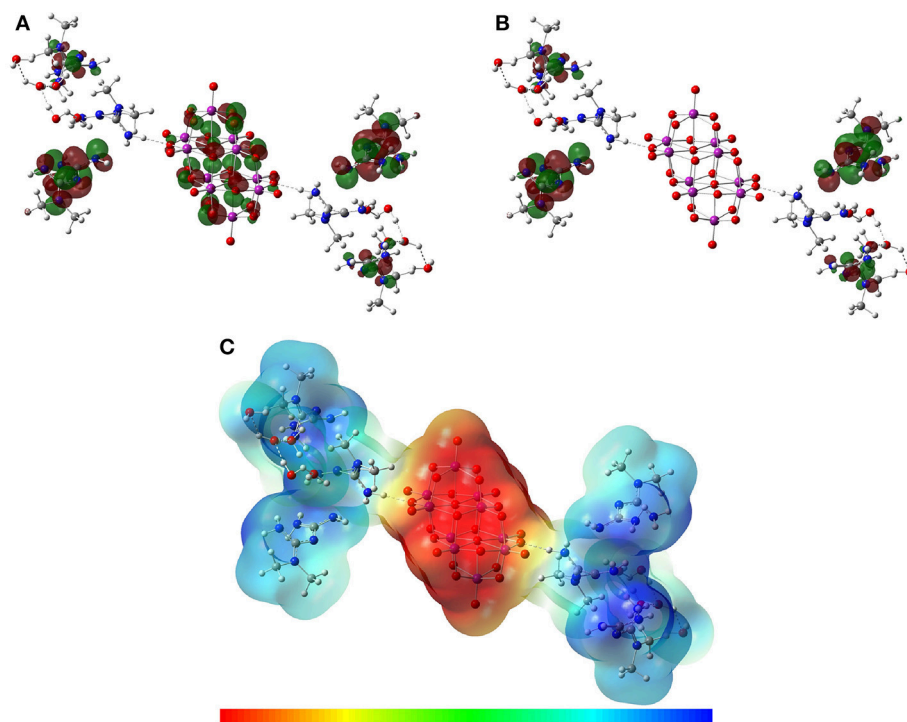


FIGURE 11 | Isosurfaces of frontier molecular orbitals **(A)** HOMO and **(B)** LUMO, and **(C)** MEP of Compound **2** at B97-D3 functional with the 6-31G(d) basis set for C, H, O, N, atoms and LanL2MB basis set for V atoms in solution phase.

of the counterions. The terminal $V=O$ bonds occur in the 900–1,000 cm^{-1} region; bridging $V-O-V$ bonds vibrate in the 500–700 cm^{-1} region as symmetric and asymmetric stretching modes, respectively, while the $V-O$ bending modes occur in the 300–400 cm^{-1} region. The ^{51}V -NMR experiments showed that the equilibrium between decavanadate and vanadate species is progressively displaced toward the formation of V1, V2, and V4 species.

On the other hand, theoretical characterization of optimized structures, frontier molecular orbitals, and the electrostatic potential distribution were obtained. The main non-covalent interactions $N-H \cdots O$ and $O-H \cdots O$ were characterized using DFT-D methods, including dispersion forces that are essential for the treatment of this kind of complexes. The inclusion of solvent effect showed interesting results for correlating the electronic and electrostatic properties with the optimized structures, regardless of those obtained for the crystalline environment.

Currently, further calculations of the theoretical spectroscopic characterization of the IR, Raman, and ^{51}V -NMR spectra, as well as a topological analysis of the complexes, are being carried out. Although the scope of this work is far from a biological analysis, we consider that the reported structures can provide interesting insights into their potential pharmacological effects, due to biological activities of the counterions used. First, Compound **2** combined with Metformin shows higher water solubility, becoming promising candidates for carrying out biological studies. Second, it has been reported that decavanadate has anticancer and antidiabetic properties and Metformin, widely recognized as one of the safest and most effective therapeutic compounds for the treatment of Type 2 *D. mellitus* is currently used in the treatment of different types of cancer. Also, deoxycytidine, cytosine arabinoside, and gemcitabine, which are derivatives of Cytosine are widely used for the treatment of various malignancies. Benchmark drugs are cytarabine for acute myeloid leukemia and gemcitabine for pancreatic and lung cancer (Muggia et al., 2012).

Biological studies are currently under investigation in our laboratory. However, preliminary results in a mouse colon

adenocarcinoma model have shown similar IC_{50} value as CISPLATIN for Cytosinium decavanadate (Sánchez-Lara et al., 2016a). As for the Metforminium decavanadate 3:1, promising results have been obtained in type 1 and 2 murine models of *D. mellitus*. (Treviño et al., 2015, 2016, 2018). The combination of two therapeutic agents opens up a window toward the generation of potential metalopharmaceuticals with new and exciting pharmacological properties. The results of those investigations will be reported elsewhere in due course.

AUTHOR CONTRIBUTIONS

All authors listed have made a substantial, direct and intellectual contribution to the work, and approved it for publication.

ACKNOWLEDGMENTS

ES-L thanks CONACYT (Mexico) for the Ph.D. Scholarship (Support No. 293256). We thank Prof. S. Bernès for the structures solution and refinement, as well as for his comments to the final version of the draft. MEC and FJM-B would like to thank the Laboratorio Nacional de Supercómputo del Sureste de México (LNS-BUAP) of the CONACYT network of national laboratories, for the computer resources and support provided. FT-Raman measurements were carried out by Dra. L. Serrano, Laboratorio Central del Instituto de Física Luis Rivera Terrazas (IFUAP), Benemérita Universidad Autónoma de Puebla. TGA-DTA measurements were carried out by Rubi E. Gonzalez-Campos, UDLAP. The authors wish to thank Vicerrectoria de Investigación y Estudios de Posgrado (VIEP-BUAP) for the financial support obtained through projects 100517029-VIEP2018 and 100256733-VIEP2018.

SUPPLEMENTARY MATERIAL

The Supplementary Material for this article can be found online at: <https://www.frontiersin.org/articles/10.3389/fchem.2018.00402/full#supplementary-material>

REFERENCES

- Aureliano, M. (2011). Recent perspectives into the biochemistry of decavanadate. *World J. Biol. Chem.* 2:215. doi: 10.4331/wjbc.v2.i10.215
- Aureliano, M. (2016). Decavanadate toxicology and Pharmacological Activities: V10 or V1, Both or None? *Oxid. Med. Cell Longev.* 2016:6103457. doi: 10.1155/2016/6103457
- Aureliano, M. (2017). The role of decavanadate in anti-tumor activity. *Glob. J. Cancer Ther.* 3, 12–14. doi: 10.17352/gjct.000015
- Aureliano, M., and Crans, D. C. (2009). Decavanadate (V10O28-) and oxovanadates: oxometalates with many biological activities. *J. Inorg. Biochem.* 103, 536–546. doi: 10.1016/j.jinorgbio.2008.11.010
- Aureliano, M., and Ohlin, C. A. (2014). Decavanadate *in vitro* and *in vivo* effects: facts and opinions. *J. Inorg. Biochem.* 137, 123–130. doi: 10.1016/j.jinorgbio.2014.05.002
- Aureliano, M., Ohlin, C. A., Meira, M. O., Marques, M. P. M., Casey, W. H., and De Carvalho, L. A. B. (2016). Characterization of decavanadate and decaniobate solutions by Raman spectroscopy. *Dalton Trans.* 45, 7391–7399. doi: 10.1039/C5DT04176G
- Ayed, M., Ayed, B., and Haddad, A. (2015). Synthesis and structural characterization of new inorganic-organic hybrid: arsenomolybdate compound with cytosinium cations. *Bull. Mater. Sci.* 38, 13–21. doi: 10.1007/s12034-014-0805-8
- Barone, V., Cossi, M., and Tomasi, J. (1998). Geometry optimization of molecular structures in solution by the polarizable continuum model. *J. Comput. Chem.* 19, 404–417. doi: 10.1002/(SICI)1096-987X(199803)19:4<404::AID-JCC3>3.0.CO;2-W
- Bartošová, L., Padělková, Z., Rakovský, E., and Schwendt, P. (2012). Synthesis and crystal structure of two copper (II) complexes with coordinated decavanadate ion. *Polyhedron* 31, 565–569. doi: 10.1016/j.poly.2011.10.042
- Benmessaoud, I., Koutchoukali, O., Bouhelsa, M., Nouar, A., and Veessler, S. (2016). Solvent screening and crystal habit of metformin hydrochloride. *J. Cryst. Growth.* 451, 42–51. doi: 10.1016/j.jcrysgro.2016.07.001
- Bijelic, A., Aureliano, M., and Rompel, A. (2018). Polyoxometalates as potential next-generation metallodrugs in the combat against cancer. *Angewante Chem. Int Ed.* doi: 10.1002/anie.201803868. [Epub ahead of print].

- Bošnjakovic-Pavlovic, N., Spasojevic-de Biré, A., Tomaz, I., Bouhaida, N., AVECILLA, F., Mioc, U. B., et al. (2009). Electronic properties of a cytosine decavanadate: toward a better understanding of chemical and biological properties of decavanadates. *Inorg. Chem.* 48, 9742–9753. doi: 10.1021/ic9008575
- Cafferty, B. J., Fialho, D. M., Khanam, J., Krishnamurthy, R., and Hud, N. V. (2016). Spontaneous formation and base pairing of plausible prebiotic nucleotides in water. *Nat. Commun.* 7:11328. doi: 10.1038/ncomms11328
- Cantley, L. C. Jr., Josephson, L., Warner, R., Yanagisawa, M., Lechene, C., and Guidotti, G. (1977). Vanadate is a potent (Na,K)-ATPase inhibitor found in ATP derived from muscle. *J. Biol. Chem.* 252, 7421–7423.
- Chatkon, A., Barres, A., Samart, N., Boyle, S. E., Haller, K. J., and Crans, D. C. (2014). Guanyurea metformium double salt of decavanadate, $(\text{HGU}^+)_4(\text{HMet}^+)_2(\text{V}_{10}\text{O}_{28}) \cdot 2\text{H}_2\text{O}$. *Inorg. Chim. Acta* 420, 85–91. doi: 10.1016/j.ica.2013.12.031
- Chatkon, A., Chatterjee, P. B., Sedgwick, M. A., Haller, K. J., and Crans, D. C. (2013). Counterion affects interaction with interfaces: the antidiabetic drugs metformin and decavanadate. *Eur. J. Inorg. Chem.* 2013, 1859–1868. doi: 10.1002/ejic.201201345
- Childs, S. L., Chyall, L. J., Dunlap, J. T., Coates, D. A., Stahly, B. C., and Stahly, G. P. (2004). A metastable polymorph of metformin hydrochloride: isolation and characterization using capillary crystallization and thermal microscopy techniques. *Cryst. Growth Des.* 4, 441–449. doi: 10.1021/cg034243p
- China, E., Dakternieks, D., Duthie, A., Ghilardi, C. A., Gili, P., Mederos, A., et al. (2000). Synthesis and characterization of $(\text{NH}_4)_4[\text{H}_4\text{V}_{10}\text{O}_{28}][\text{NTPH}_2]_2 \cdot 4\text{H}_2\text{O}$ ($\text{NTPH}_3 = \text{N}(\text{CH}_2\text{CH}_2\text{COOH})_3$). *Inorg. Chim. Acta* 298, 172–177. doi: 10.1016/S0020-1693(99)00440-5
- Correia, I., AVECILLA, F., Marcão, S., and Costa-Pessoa, J. (2004). Structural studies of decavanadate compounds with organic molecules and inorganic ions in their crystal packing. *Inorg. Chim. Acta* 357, 4476–4487. doi: 10.1016/j.ica.2004.06.055
- Costa-Pessoa, J., Etcheverry, S., and Gambino, D. (2015). adium compounds in medicine. *Coord. Chem. Rev.* 301, 24–48. doi: 10.1016/j.ccr.2014.12.002
- Crans, D. C. (2000). Chemistry and insulin-like properties of vanadium(IV) and vanadium(V) compounds. *J. Inorg. Biochem.* 80, 123–131. doi: 10.1016/S0162-0134(00)00048-9
- Crans, D. C. (2015). Antidiabetic, chemical, and physical properties of organic vanadates as presumed transition-state inhibitors for phosphatases. *J. Org. Chem.* 80, 11899–11915. doi: 10.1021/acs.joc.5b02229
- Del Carpio, E., Hernández, L., Ciangherotti, C., Villalobos Coa, V., Jiménez, L., Lubes, V., et al. (2018). Vanadium: history, chemistry, interactions with α -amino acids and potential therapeutic applications. *Coord. Chem. Rev.* 372, 117–140. doi: 10.1016/j.ccr.2018.06.002
- Dennington, R. D. II., Keith, T. A., and Millam, J. M. (2016). *Gauss View, Version 6.0.16*. Shawnee Mission: Semichem Inc.
- Dissem, N., Artetxe, B., San Felices, L., Lezama, L., Haddad, A., and Gutierrez-Zorrilla, J. M. (2018). A robust framework based on polymeric octamolybdate anions and copper (ii) complexes of tetradentate N-donor ligands. *Crystals* 8:20. doi: 10.3390/cryst8010020
- Dolomanov, O. V., Bourhis, L. J., Gildea, R. J., Howard, J. A., and Puschmann, H. (2009). OLEX2: a complete structure solution, refinement, and analysis program. *J. Appl. Cryst.* 42, 339–341. doi: 10.1107/S0021889808042726
- Dong, J., Liu, B., and Yang, B. (2015). Crystal structure of bis {2-[amino(iminiumyl) methyl]-1, 1-dimethylguanidine} carbonate methanol disolvate. *Acta Cryst. E* 71, o747–o748. doi: 10.1107/S2056989015016771
- Dorsey, B. M., McLauchlan, C. C., and Jones, M. A. (2018). Evidence that speciation of oxovanadium complexes does not solely account for inhibition of leishmania acid phosphatases. *Front. Chem.* 6:109. doi: 10.3389/fchem.2018.00109
- Elberg, G., He, Z., Li, J., Sekar, N., and Shechter, Y. (1997). Vanadate activates membranous nonreceptor protein tyrosine kinase in rat adipocytes. *Diabetes* 46:16841690.
- El-Mir, M. Y., Nogueira, V., Fontaine, E., Avéret, N., Rigoulet, M., and Leverve, X. (2000). Dimethylbiguanide inhibits cell respiration via an indirect effect targeted on the respiratory chain complex I. *J. Biol. Chem.* 275, 223–228. doi: 10.1074/jbc.275.1.223
- Etter, M. C., MacDonald, J. C., and Bernstein, J. (1990). Graph-set analysis of hydrogen-bond patterns in organic crystals. *Acta Cryst. B* 46, 256–262. doi: 10.1107/S0108768189012929
- Evans, J. M., Donnelly, L. A., Emslie-Smith, A. M., Alessi, D. R., and Morris, A. D. (2005). Metformin and reduced risk of cancer in diabetic patients. *Brit. Med. J.* 330, 1304–1305. doi: 10.1136/bmj.38415.708634.F7
- Frisch, M. J., Trucks, G. W., Schlegel, H. B., Scuseria, G. E., Robb, M. A., Cheeseman, J. R., et al. (2016). *Gaussian 16, Revision B.01*. Wallingford, CT: Gaussian, Inc.
- Frost, R. L., Erickson, K. L., Weier, M. L., and Carmody, O. (2005). Raman and infrared spectroscopy of selected vanadates. *Spectrochim. Acta A* 61, 829–834. doi: 10.1016/j.saa.2004.06.006
- Frost, R. L., and Palmer, S. J. (2011). Raman spectroscopic study of pascoite $\text{Ca}_3\text{V}_{10}\text{O}_{28} \cdot 17\text{H}_2\text{O}$. *Spectrochim. Acta A* 78, 248–252. doi: 10.1016/j.saa.2010.10.002
- Gadape, H. H., and Parikh, K. S. (2011). Quantitative determination and validation of metformin hydrochloride in pharmaceutical using quantitative nuclear magnetic resonance spectroscopy. *J. Chem.* 8, 767–781. doi: 10.1155/2011/461898
- Ghasemi, F., Rezvani, A. R., Ghasemi, K., and Graiff, C. (2018). Glycine and metformin as new counter ions for mono and dinuclear vanadium (V)-dipicolinic acid complexes based on the insulin-enhancing anions: synthesis, spectroscopic characterization, and crystal structure. *J. Mol. Struct.* 1154, 319–326. doi: 10.1016/j.molstruc.2017.10.055
- Grimme, S., Ehrlich, S., and Goerigk, L. (2011). Effect of the damping function in dispersion corrected density functional theory. *J. Comput. Chem.* 32, 1456–1465. doi: 10.1002/jcc.21759
- Groom, C. R., Bruno, I. J., Lightfoot, M. P., and Ward, S. C. (2016). The Cambridge structural database. *Acta Cryst. B* 72, 171–179. doi: 10.1107/S2052520616003954
- Gunasekaran, S., Natarajan, R. K., Renganayaki, V., and Natarajan, S. (2006). *Vibrational Spectra and Thermodynamic Analysis of Metformin*. Available online at: <http://nopr.niscair.res.in/handle/123456789/8327>
- Hay, P. J., and Wadt, W. R. (1985). Ab initio effective core potentials for molecular calculations. Potentials for the transition metal atoms Sc to Hg. *J. Chem. Phys.* 82, 270–283. doi: 10.1063/1.448799
- Hayashi, Y. (2011). Hetero and lacunary polyoxovanadate chemistry: synthesis, reactivity, and structural aspects. *Coord. Chem. Rev.* 255, 2270–2280. doi: 10.1016/j.ccr.2011.02.013
- Hohenberg, P., and Kohn, W. (1964). Inhomogeneous electron gas. *Phys. Rev.* 136:B864. doi: 10.1103/PhysRev.136.B864
- Ibrahim, M. M., Mohamed, M. A., Mersal, G. A., and Al-Juaid, S. (2015). Insulin-like action of novel metformin-containing vanadate as a new antidiabetic drug: synthesis, characterization, and crystal structure of $[\text{Metformin-H}]_2[\text{V}_2\text{O}_6] \cdot \text{H}_2\text{O}$. *J. Mol. Struct.* 1098, 92–100. doi: 10.1016/j.molstruc.2015.05.050
- Iyer, A. K., Roy, S., Haridasan, R., Sarkar, S., and Peter, S. C. (2014). Ligand-mediated valence fluctuation of copper in new hybrid materials constructed from decavanadate and a Cu(1,10-phenanthroline) complex. *Dalton Trans.* 43, 2153–2160. doi: 10.1039/C3DT52484A
- Kaszniak, J., Sliwinski, A., and Drzewoski, J. (2014). Metformin in cancer prevention and therapy. *Ann. Transl. Med.* 2:57. doi: 10.3978/j.issn.2305-5839.2014.06.01
- Kathuria, D., Bankar, A. A., and Bharatam, P. V. (2018). “What’s in a structure?” The story of biguanides. *J. Mol. Struct.* 1152, 61–78. doi: 10.1016/j.molstruc.2017.08.100
- Kioseoglou, E., Gabriel, C., Petanidis, S., Psycharis, V., Raptopoulou, C. P., Terzis, A., et al. (2013). Binary decavanadate-betaine composite materials of potential anticarcinogenic activity. *Z. Anorg. Allg. Chem.* 639, 1407–1416. doi: 10.1002/zaac.201300144
- Kojima, T., Antonio, M. R., and Ozeki, T. (2011). Solvent-driven association and dissociation of the hydrogen-bonded protonated decavanadates. *J. Am. Chem. Soc.* 133, 7248–7251. doi: 10.1021/ja110781f
- Lee, T., and Wang, P. Y. (2010). Screening, manufacturing, photoluminescence, and molecular recognition of co-crystals: cytosine with dicarboxylic

- acids. *Cryst. Growth Des.* 10, 1419–1434. doi: 10.1021/cg901412d
- Lee, U. K., and Joo, H. C. (2003). Potassium–sodium double salt of decavanadate, $K_4Na_2[V_{10}O_{28}] \cdot 10H_2O$. *Acta Cryst. E* 59, i122–i124. doi: 10.1107/S1600536803016453
- Libby, G., Donnelly, L. A., Donnan, P. T., Alessi, D. R., Morris, A. D., and Evans, J. M. (2009). New users of metformin are at low risk of incident cancer: a cohort study among people with type 2 diabetes. *Diabetes care* 32, 1620–1625. doi: 10.2337/dc08-2175
- Macrae, C. F., Bruno, I. J., Chisholm, J. A., Edgington, P. R., McCabe, P., Pidcock, E., et al. (2008). Mercury CSD 2.0 - new features for the visualization and investigation of crystal structures. *J. Appl. Cryst.* 41, 466–470. doi: 10.1107/S0021889807067908
- Madzharova, F., Heiner, Z., Gühlke, M., and Kneipp, J. (2016). Surface-enhanced hyper-Raman spectra of adenine, guanine, cytosine, thymine, and uracil. *J. Phys. Chem.* 120, 15415–15423. doi: 10.1021/acs.jpcc.6b02753
- Mal, S. S., Tröppner, O., Ivanović-Burmazović, I., and Burger, P. (2013). Tetraalkylphosphonium decavanadates: synthesis, structures, and solution properties. *Eur. J. Inorg. Chem.* 2013, 1960–1967. doi: 10.1002/ejic.201201447
- Martín-Caballero, J., San José Wéry, A., Reinoso, S., Artetxe, B., San Felices, L., Bakkali, E. I., et al. (2016). A robust open framework formed by decavanadate clusters and copper(II) complexes of macrocyclic polyamines: permanent microporosity and catalytic oxidation of cycloalkanes. *Inorg. Chem.* 55, 4970–4979. doi: 10.1021/acs.inorgchem.6b00505
- Mathlouthi, M., Seuvre, A. M., and Koenig, J. L. (1986). FT-IR and laser-Raman spectra of cytosine and cytidine. *Carbohydr. Res.* 146, 1–13. doi: 10.1016/0008-6215(86)85019-4
- Muggia, F., Diaz, I., and Peters, G. J. (2012). Nucleoside and nucleobase analogs in cancer treatment: not only sapacitabine but also gemcitabine. *Expert Opin. Investig. Drugs* 21, 403–408. doi: 10.1517/13543784.2012.666236
- Nagazi, I., and Haddad, A. (2014). Synthesis, crystal structure and physicochemical properties of a cytosine selenomolybdate based on strandberg-type $[Se_2Mo_5O_{21}]^{4-}$ polyanion. *J. Cluster Sci.* 25, 627–638. doi: 10.1007/s10876-013-0658-0
- Narla, R. K., Chen, C. L., Dong, Y., and Uckun, F. M. (2001). In vivo antitumor activity of bis(4,7-dimethyl-1,10-phenanthroline) sulfatoxovanadium(IV) (METVAN $[VO(SO_4)(Me_2-Phen)_2]$). *Clin. Cancer Res.* 7, 2124–2133.
- Olar, R., Badea, M., Marinescu, D., Chifriuc, C. M., Bleotu, C., Grecu, M. N., et al. (2010). Prospects for new antimicrobials based on N, N-dimethylbiguanide complexes as effective agents on both planktonic and adhered to microbial strains. *Eur. J. Med. Chem.* 45, 2868–2875. doi: 10.1016/j.ejmech.2010.03.009
- Omri, I., Mhiri, T., and Graia, M. (2015). Novel decavanadate cluster complexes $(Hlmz)_{12}(V_{10}O_{28}) \cdot 2.3H_2O$: synthesis, characterization, crystal structure, optical and thermal properties. *J. Mol. Struct.* 1098, 324–331. doi: 10.1016/j.molstruc.2015.06.011
- Ortoboy, S., Acar, E. T., and Atun, G. (2018). The removal of radioactive strontium ions from aqueous solutions by isotopic exchange using a strontium decavanadate and corresponding mixed oxides. *Chem. Eng. J.* 344, 194–205. doi: 10.1016/j.cej.2018.03.069
- Orvig, C., Caravan, P., Gelmini, L., Glover, N., Herring, F. G., Li, H., et al. (1995). Reaction chemistry of BMOV, bis (maltolato) oxovanadium (IV), a potent insulin mimetic agent. *J. Am. Chem. Soc.* 117, 12759–12770. doi: 10.1021/ja00156a013
- Parker, W. B. (2009). Enzymology of purine and pyrimidine antimetabolites used in the treatment of cancer. *Chem. Rev.* 109, 2880–2893. doi: 10.1021/cr900028p
- Pavliuk, M. V., Makhankova, V. G., Khavryuchenko, O. V., Kokozay, V. N., Omelchenko, I. V., Shishkin, O. V., et al. (2014). Decavanadates decorated with $[Cu(en)_2]^{2+}$: convenient synthetic route, crystal structures and analysis of vibrational spectra. *Polyhedron* 81, 597–606. doi: 10.1016/j.poly.2014.06.044
- Pereira, M. J., Carvalho, E., Eriksson, J. W., Crans, D. C., and Aureliano, M. (2009). Effects of decavanadate and insulin enhancing vanadium compounds on glucose uptake in isolated rat adipocytes. *J. Inorg. Biochem.* 103, 1687–1692. doi: 10.1016/j.jinorgbio.2009.09.015
- Pérez-Fernández, R., Fresno, N., Goya, P., Elguero, J., Menéndez-Taboada, L., García-Granda, S., et al. (2013). Structure and thermodynamical properties of metformin salicylate. *Cryst. Growth Des.* 13, 1780–1785. doi: 10.1021/cg401015f
- Perumalla, S. R., Pedireddi, V. R., and Sun, C. C. (2013). Protonation of cytosine: cytosinium vs. hemicytosinium duplexes. *Cryst. Growth Des.* 13, 429–432. doi: 10.1021/cg3014915
- Rasheed, T., and Ahmad, S. (2010). Approximate solution of the mode-mode coupling integral: application to cytosine and its deuterated derivative. *Spectrochim. Acta A* 77, 446–456. doi: 10.1016/j.saa.2010.06.015
- Rassolov, V. A., Pople, J. A., Ratner, M. A., and Windus, T. L. (1998). 6-31G* basis set for atoms K through Zn. *J. Chem. Phys.* 109, 1223–1229. doi: 10.1063/1.476673
- Rehder, D. (2008). *Bioinorganic Vanadium Chemistry*, Vol. 30. Hoboken, NJ: John Wiley & Sons.
- Rehder, D. (2011). A possible role for extraterrestrial vanadium in the encounter of life. *Coord. Chem. Rev.* 255, 2227–2231. doi: 10.1016/j.ccr.2011.04.015
- Rehder, D. (2012). The potentiality of vanadium in medicinal applications. *Future Med. Chem.* 4, 1823–1837. doi: 10.4155/fmc.12.103
- Rehder, D. (2015a). The (biological) speciation of vanadate (V) as revealed by 51V NMR: a tribute on Lage Pettersson and his work. *J. Inorg. Biochem.* 147, 25–31. doi: 10.1016/j.jinorgbio.2014.12.014
- Rehder, D. (2015b). The role of Vanadium in biology. *Metallomics* 7, 730–742. doi: 10.1039/C4MT00304G
- Rehder, D., Polenova, T., and Bühl, M. (2007). Vanadium-51 NMR. *Annu. Rep. NMR Spectrosc.* 62, 49–114. doi: 10.1016/S0066-4103(07)62002-X
- Repišćak, P., Erhardt, S., Rena, G., and Paterson, M. J. (2014). Biomolecular mode of action of metformin in relation to its copper binding properties. *Biochemistry* 53, 787–795. doi: 10.1021/bi401444n
- Riou, D., Roubeau, O., and Férey, G. (1998). Evidence for the solid state structural transformation of the network-type decavanadate $(NC_7H_{14})_4[H_2V_{10}O_{28}]$ into a lamellar topology $(NC_7H_{14})[V_4O_{10}]$. *Z. Anorg. Allg. Chem.* 624, 1021–1025. doi: 10.1002/(SICI)1521-3749(199806)624:63:0.CO;2-K
- Rozenberg, M., Shoham, G., Reva, I., and Fausto, R. (2004). Low-temperature FTIR spectroscopy and hydrogen bonding in cytosine polycrystals. *Spectrochim. Acta A* 60, 463–470. doi: 10.1016/S1386-1425(03)00251-8
- Sánchez-Lara, E., Pérez-Benítez, A., Treviño, S., Bernés, S., Delgado, R., Sánchez-Mora, E., et al. (2016a). “Metforminium decavanadates as a potential metallodrugs in the treatment of cancer and diabetes,” in *V Latinamerican Meeting on Biological Inorganic Chemistry*. Santiago de Querétaro.
- Sánchez-Lara, E., Pérez-Benítez, A., Treviño, S., Mendoza, A., Meléndez, F. J., Sánchez-Mora, E., et al. (2016b). Synthesis and 3D network architecture of 1- and 16-hydrated salts of 4-dimethylaminopyridinium decavanadate, $(DMAPH)_6[V_{10}O_{28}] \cdot nH_2O$. *Crystals* 6:65. doi: 10.3390/cryst6060065
- Sánchez-Lara, E., Sanchez-Lombardo, I., Pérez-Benítez, A., Mendoza, A., Flores-Alamo, M., and Gonzalez-Vergara, E. (2015). A new dicationic ring $[(Water)_6-(Ammonium)_2]$ acts as a building block for a supramolecular 3D assembly of decavanadate clusters and 4-(N,Ndimethylamino) pyridinium Ions. *J. Cluster Sci.* 26, 901–912. doi: 10.1007/s10876-014-0779-0
- Sánchez-Lombardo, I., Sánchez-Lara, E., Pérez-Benítez, A., Mendoza, Á., Bernés, S., and González-Vergara, E. (2014). Synthesis of metforminium (2+) decavanadates—crystal structures and solid-state characterization. *Eur. J. Inorg. Chem.* 2014, 4581–4588. doi: 10.1002/ejic.201402277
- Selman, M., Rouso, C., Bergeron, A., Son, H. H., Krishnan, R., El-Sayes, N. A., et al. (2018). Multi-modal potentiation of oncolytic virotherapy by vanadium compounds. *Mol. Ther.* 26, 55–69. doi: 10.1016/j.ymthe.2017.10.014
- Serb, M. D., Kalf, I., and Englert, U. (2014). Biguanide and squaric acid as pH-dependent building blocks in crystal engineering. *Cryst. Eng. Comm.* 16, 10631–10639. doi: 10.1039/C4CE01643B
- Sheela, N. R., Muthu, S., and Krishnan, S. S. (2010). FTIR, FT Raman and UV-visible spectroscopic analysis on metformin hydrochloride. *Asian J. Chem.* 22, 5049–5056.
- Sheldrick, G. M. (2015). Crystal structure refinement with SHELXL. *Acta Cryst. C* 71, 3–8. doi: 10.1107/S2053229614024218
- Soares, S. S., Martins, H., Duarte, R. O., Moura, J. J., Coucelo, J., Gutiérrez-Merino, C., et al. (2007). Vanadium distribution, lipid peroxidation and oxidative stress markers upon decavanadate in vivo administration. *J. Inorg. Biochem.* 101, 80–88. doi: 10.1016/j.jinorgbio.2005.02.023
- Sridhar, B., Nanubolu, J. B., and Ravikumar, K. (2012). Competition between the two-point and three-point synthon in cytosine–carboxylic acid complexes. *Cryst. Eng. Comm.* 14, 7065–7074. doi: 10.1039/c2ce26076j

- Steens, N., Ramadan, A. M., Absillis, G., and Parac-Vogt, T. N. (2010). Hydrolytic cleavage of DNA-model substrates promoted by polyoxovanadates. *Dalton Trans.* 14, 585–592. doi: 10.1039/b913471a
- Swallow, A. G., and Barnes, W. H. (1964). The structure of the decavanadate Ion. *J. Am. Chem. Soc.* 86, 4209–4210. doi: 10.1021/ja01073a070
- Thompson, H. J., Chasteen, D. N., and Neeker, L. (1984). Dietary vanadyl (IV) sulfate inhibits chemically-induced mammary carcinogenesis. *Carcinogenesis* 5, 849–851. doi: 10.1093/carcin/5.6.849
- Treviño, S., Díaz, A., Sánchez-Lara, E., Sarmiento-Ortega, V. E., Flores-Hernandez, J. A., Brambila, E., et al. (2018). Pharmacological and toxicological threshold of bisammonium tetrakis 4-(N,N-Dimethylamino) pyridinium decavanadate in a rat model of metabolic syndrome and insulin resistance. *Bioinorganic Chem. Appl.* 2018:2151079. doi: 10.1155/2018/2151079
- Treviño, S., Velázquez-Vázquez, D., Sánchez-Lara, E., Díaz-Fonseca, A., Flores-Hernandez, J. A., Pérez-Benítez, A., et al. (2016). Metforminium decavanadate as a potential metallopharmaceutical drug for the treatment of *Diabetes mellitus*. *Oxid. Med. Cell. Longev.* 2016:6058705. doi: 10.1155/2016/6058705
- Treviño, S., Sánchez-Lara, E., Sarmiento-Ortega, V. E., Sánchez Lombardo, I., Flores-Hernández, J. A., Pérez-Benítez, A. et al. (2015). Hypoglycemic, lipid-lowering and metabolic regulation activities of metforminium decavanadate $(\text{H}_2\text{Metf})_3 [\text{V}_{10}\text{O}_{28}] \cdot 8\text{H}_2\text{O}$ using hypercaloric-induced carbohydrate and lipid deregulation in wistar rats as biological model. *J. Inorg. Biochem.* 147, 85–92. doi: 10.1016/j.jinorgbio.2015.04.002
- UK Prospective Diabetes Study (UKPDS) Group. (1998). Effect of intensive blood-glucose control with metformin on complications in overweight patients with type 2 diabetes (UKPDS 34). *Lancet* 352, 854–865.
- Vermes, A., Guchelaar, H. J., and Dankert, J. (2000). Flucytosine: a review of its pharmacology, clinical indications, pharmacokinetics, toxicity and drug interactions. *J. Antimicrob. Chemother.* 46, 171–179. doi: 10.1093/jac/46.2.171
- Vilter, H. (1984). Peroxidase from Phaeophyceae A Vanadium(V)-dependent peroxidase from *Ascophyllum nodosum*. *Phytochemistry* 23, 1387–1390. doi: 10.1016/S0031-9422(00)80471-9
- Weng, J., Hong, M., Liang, Y., Shi, Q., and Cao, R. (2002). A nucleobase-inorganic hybrid polymer consisting of copper bis (phosphopentamolybdate) and cytosine. *J. Chem. Soc. Dalton Trans.* 3, 289–290. doi: 10.1039/b111457n
- Winkler, P. A., Huang, Y., Sun, W., Du, J., and Lü, W. (2017). Electron cryo microscopy structure of a human TRPM4 channel. *Nature* 552, 200–204. doi: 10.1038/nature24674
- Yraola, F., García-Vicente, S., Martí, L., Albericio, F., Zorzano, A., and Royo, M. (2007). Understanding the mechanism of action of the novel SSAO substrate $(\text{C}_7\text{NH}_{10})_6(\text{V}_{10}\text{O}_{28}) \cdot 2\text{H}_2\text{O}$, a prodrug of peroxovanadate insulin mimetics. *Chem. Biol. Drug. Des.* 69, 423–428. doi: 10.1111/j.1747-0285.2007.00516.x
- Zhu, M., Lu, L., and Yang, P. (2003). N, N-dimethylbiguanidium nitrate. *Acta Cryst E* 59, o586–o588. doi: 10.1107/S1600536803006639
- Zhu, M., Lu, L., Yang, P., and Jin, X. (2002). Bis (1, 1-dimethylbiguanido) nickel (II). *Acta Cryst. E* 58, m272–m274. doi: 10.1107/S1600536802007869
- Zorzano, A., Palacín, M., Martí, L., and García-Vicente, S. (2009). Arylalkylamine vanadium salts as new anti-diabetic compounds. *J. Inorg. Biochem.* 103, 559–566. doi: 10.1016/j.jinorgbio.2009.01.015

Conflict of Interest Statement: The authors declare that the research was conducted in the absence of any commercial or financial relationships that could be construed as a potential conflict of interest.

Copyright © 2018 Sánchez-Lara, Treviño, Sánchez-Gaytán, Sánchez-Mora, Castro, Meléndez-Bustamante, Méndez-Rojas and González-Vergara. This is an open-access article distributed under the terms of the Creative Commons Attribution License (CC BY). The use, distribution or reproduction in other forums is permitted, provided the original author(s) and the copyright owner(s) are credited and that the original publication in this journal is cited, in accordance with accepted academic practice. No use, distribution or reproduction is permitted which does not comply with these terms.



Selective Targeting of Proteins by Hybrid Polyoxometalates: Interaction Between a Bis-Biotinylated Hybrid Conjugate and Avidin

Valeria A. Zamolo¹, Gloria Modugno¹, Elisa Lubian¹, Alessandro Cazzolaro¹, Fabrizio Mancin¹, Livia Giotta², Disma Mastrogiacomo², Ludovico Valli², Alessandra Saccani³, Silke Krol^{3,4}, Marcella Bonchio^{1*} and Mauro Carraro^{1*}

¹ Department of Chemical Sciences, University of Padova and ITM-CNR, Padova, Italy, ² Department of Biological and Environmental Sciences and Technologies – DiSTeBA, University of Salento, Lecce, Italy, ³ NanoMed Lab, Fondazione IRCCS Institute of Neurology “Carlo Besta,” Milan, Italy, ⁴ Laboratory of Translational Nanotechnology, IRCCS Oncologic Institute “Giovanni Paolo II,” Bari, Italy

OPEN ACCESS

Edited by:

Tatjana N. Parac-Vogt,
KU Leuven, Belgium

Reviewed by:

Alexander Anyushin,
KU Leuven, Belgium
Scott George Mitchell,
Consejo Superior de Investigaciones
Científicas (CSIC), Spain

*Correspondence:

Marcella Bonchio
marcella.bonchio@unipd.it
Mauro Carraro
mauro.carraro@unipd.it

Specialty section:

This article was submitted to
Inorganic Chemistry,
a section of the journal
Frontiers in Chemistry

Received: 30 April 2018

Accepted: 20 June 2018

Published: 11 July 2018

Citation:

Zamolo VA, Modugno G, Lubian E, Cazzolaro A, Mancin F, Giotta L, Mastrogiacomo D, Valli L, Saccani A, Krol S, Bonchio M and Carraro M (2018) Selective Targeting of Proteins by Hybrid Polyoxometalates: Interaction Between a Bis-biotinylated Hybrid Conjugate and Avidin. *Front. Chem.* 6:278. doi: 10.3389/fchem.2018.00278

The Keggin-type polyoxometalate $[\gamma\text{-SiW}_{10}\text{O}_{36}]^{8-}$ was covalently modified to obtain a bis-biotinylated conjugate able to bind avidin. Spectroscopic studies such as UV-vis, fluorimetry, circular dichroism, coupled to surface plasmon resonance technique were used to highlight the unique interplay of supramolecular interactions between the homotetrameric protein and the bis-functionalized polyanion. In particular, the dual recognition mechanism of the avidin encompasses (i) a complementary electrostatic association between the anionic surface of the polyoxotungstate and each positively charged avidin subunit and (ii) specific host-guest interactions between each biotinylated arm and a corresponding pocket on the tetramer subunits. The assembly exhibits peroxidase-like reactivity and it was used in aqueous solution for L-methionine methyl ester oxidation by H_2O_2 . The recognition phenomenon was then exploited for the preparation of layer-by-layer films, whose structural evolution was monitored *in situ* by ATR-FTIR spectroscopy. Finally, cell tracking studies were performed by exploiting the specific interactions with a labeled streptavidin.

Keywords: biotin, avidin, polyoxometalates, recognition, surface plasmon resonance, bio-hybrids, oxidation catalysis

INTRODUCTION

The preparation of bio-inorganic conjugates is currently investigated for the preparation of biosensors, metal-based antibiotics, radiopharmaceuticals, anti-cancer drugs, and imaging contrast agents (Orvig and Abrams, 1999; Barry and Sadler, 2013; Albada and Metzler-Nolte, 2016; Liu et al., 2016). In addition, bio-hybrid nanostructures are emerging as innovative functional materials (Wortmann et al., 2014; Liu et al., 2016). Among inorganic nanodrug candidates, polyoxometalates (POMs) are multi-metallic and polyanionic oxides which have shown interesting potential applications as antibacterial, antiviral, antitumoral agents (Rhule et al., 1998; Hasenknopf, 2005; Bijelic et al., 2018). Such biological activity mainly derives from their redox behavior, their biomimetic activity, or from their capability to interact with biological macromolecules through

electrostatic interactions (Prudent et al., 2008; Li et al., 2016). Due to their nanosized dimension and polyanionic charge, indeed, POMs can easily interact with positively charged domains of peptides and proteins, affecting their secondary/tertiary structure and altering their functionalities (Wu et al., 2005; Zhang et al., 2008; Geng et al., 2011). On the other hand, the competition with electron rich natural substrates, such as DNA and ATP, can also lead to the inhibition of enzymatic processes (Judd et al., 2001; Prudent et al., 2010; Iqbal et al., 2013; Stephan et al., 2013). To control this behavior, POMs can be engineered to tune their polarity, redox potential, shape, acidity and surface charge distribution (Rhule et al., 1998; Hasenknopf, 2005; Bijelic et al., 2018). However, since inorganic POMs present low hydrolytic stability at physiologically relevant pH values, leading to cytotoxic derivatives, many efforts have been made to modify their structure and composition, in order to obtain compounds with low toxicity, higher stability and selectivity (Wang et al., 2003). In particular, the covalent functionalization of POMs with organic pendants (Dolbecq et al., 2010; Proust et al., 2012) imparts higher stability under physiological conditions, and offers an appealing strategy for improving their bio-distribution (Dong et al., 2011; Flötsch et al., 2011; Yang et al., 2013; Fu et al., 2015; Karimian et al., 2017; Linnenberg et al., 2017). There is a definite potential of hybrid, organic-inorganic, POMs to trigger the recognition of cellular receptors and of biological matter, although with few cases (Li et al., 2013; Ventura et al., 2018). In this direction, we have designed a tweezer-like (Carraro et al., 2012a; Modugno et al., 2014) biotinylated POM (Prudent et al., 2008; Linnenberg et al., 2017) in order to exploit the well-known avidin-biotin complex (ABC).

The affinity between biotin (vitamin H) and the homotetrameric avidin is known as one of the strongest non-covalent interactions in nature, with a dissociation constant $K_D = 10^{-15}$ M. Avidin is the natural transport protein of biotin and the biotin-avidin association is routinely exploited in several biochemical assays. In addition, since avidin can expose a diffuse positive charge (with an isoelectric point, pI, of about 10.5), the complementary electrostatic interaction with the negative POM surface can be a further assembly drive. We show herein that a bis-functionalized decatungstosilicate complex with formula $(^{\text{Bu}}\text{Bu}_4\text{N})_3\text{H}[\gamma\text{-SiW}_{10}\text{O}_{36}\{(\text{C}_5\text{H}_7\text{N}_2\text{OS})(\text{CH}_2)_4\text{CONH}(\text{CH}_2)_3\text{Si}\}_2\text{O}]$ (**TBA-POM-biot₂**) interacts with the avidin target by an interplay of electrostatic and host-guest binding interactions, which set the basis for novel supramolecular bio-conjugates with applications in drug delivery, catalysis and material sciences. In particular, surface plasmon resonance (SPR), UV-vis, circular dichroism (CD), fluorescence spectroscopy and attenuated total reflectance Fourier transform infrared spectroscopy (ATR-FTIR) evidences are compared and contrasted vis-à-vis the association properties of biotin-free POMs, as well as considering the stoichiometry/geometry of the resulting bio-hybrid adduct.

Our results include catalytic tests in the presence of H_2O_2 as co-factor, which highlight the functional response of the POM surface as artificial peroxidase, and a preliminary investigation on cell internalization (Dong et al., 2011; Flötsch et al., 2011; Yang

et al., 2013; Fu et al., 2015; Karimian et al., 2017; Linnenberg et al., 2017) of the biotinylated POM by means of labeled streptavidin.

EXPERIMENTAL SECTION

$\text{K}_8[\gamma\text{-SiW}_{10}\text{O}_{36}]$ (**K-POM**), (Canny et al., 1986) $(^{\text{Bu}}\text{Bu}_4\text{N})_4[\gamma\text{-SiW}_{10}\text{O}_{36}(\text{H}_2\text{O})_2]$ (**TBA-POM**) (Kamata et al., 2003) $(^{\text{Bu}}\text{Bu}_4\text{N})_4[\gamma\text{-SiW}_{10}\text{O}_{36}\{\text{NH}_2(\text{CH}_2)_3\text{Si}\}_2\text{O}]$ (**TBA-POM-NH₂**) (Carraro et al., 2006, 2012a; Modugno et al., 2014) were prepared as described in the literature.

Phosphate saline buffer (PBS) was prepared dissolving sodium phosphate 0.01 M, sodium chloride 0.14 M, potassium chloride 0.03 M in deionized water and used in all experiments.

Synthesis of $(^{\text{Bu}}\text{Bu}_4\text{N})_3\text{H}[\gamma\text{-SiW}_{10}\text{O}_{36}\{(\text{C}_5\text{H}_7\text{N}_2\text{OS})(\text{CH}_2)_4\text{CONH}(\text{CH}_2)_3\text{Si}\}_2\text{O}]$ (TBA-POM-biot₂**):** Biotin (37 mg, 151 μm) was introduced in a well dried Schlenk with magnetic stirring, under N_2 atmosphere. Anhydrous DMF (0.5 mL) and CH_3CN (1 mL), $\text{N,N}'$ -dicyclohexylcarbodiimide DCC (33 mg, 160 μm) and N -hydroxysuccinimide NHS (19 mg, 164 μm) were then added. The reaction mixture, vigorously stirred, was allowed to react for one night at 50°C , under nitrogen. Then, **TBA-POM-NH₂** (200 mg, 59.4 μm) and TEA (21.3 μL , 149 μm) were dissolved in 2 mL of anhydrous CH_3CN and added to the reaction mixture. The mixture was stirred for 1 day at room temperature. Finally, the reaction mixture was centrifuged to remove insoluble reagents and byproducts. The volume of the solution was reduced to 1 mL, upon evaporation under vacuum, then water was added to precipitate the product. The solid was washed with water (3 times) and diethyl ether (3 times) on a fritted funnel under vacuum. 154 mg of product were obtained (68% yield).

FT-IR (KBr, cm^{-1}): 2961 (m), 2,934 (m), 2,873 (m), 1,662 (m), 1,469 (m), 1,387 (w), 1,099 (w), 948 (m), 901 (s), 820 (s), 734 (s), 544 (w); ^1H NMR (300 MHz, CD_3CN , δ): 0.55 (4 H, m), 0.99 (48 H, m), 1.39 (32 H, m), 1.64 (32 H, m), 2.63 (2 H, m), 3.15 (32 H, m), 4.33 (2 H, m), 4.49 (2 H, m), 5.09 (2 H, s, br), 5.85 (2 H, s, br), 6.89 (2 H, s, br); ^{13}C NMR (75.5 MHz, CD_3CN , 301 K, δ): 14.08 (32 C), 20.42 (32 C), 21.96 (2 C), 24.47 (32 C), 25.92 (2 C), 26.67 (2 C), 29.21 (2 C), 36.77 (2 C), 41.89 (2 C), 42.90 (2 C), 56.56 (2 C), 61.24 (2 C), 62.77 (2 C), 164.69 (2 C), 174.18 (2 C); ^{29}Si NMR ($\text{CH}_3\text{CN}/\text{CD}_3\text{CN}$, 301 K, δ): -62.01 (2 Si, s), -88.43 (1 Si, s); ^{183}W NMR (16.67 MHz, $\text{CH}_3\text{CN}/\text{CD}_3\text{CN}$, 301 K, δ): -107.55 (4 W, s), -136.09 (2 W, s), -142.08 (4 W, s); ESI-MS (-), CH_3CN , m/z : calcd for $[\text{C}_{26}\text{H}_{44}\text{N}_6\text{O}_{41}\text{S}_2\text{Si}_3\text{W}_{10}]^{4-}$ 770.9; found, 768.2, Anal. calcd. for $\text{C}_{74}\text{H}_{153}\text{N}_9\text{O}_{41}\text{S}_2\text{Si}_3\text{W}_{10}$ C 23.3; H 4.1; N 3.3; S 1.7; found: C 23.1; H 4.2; N 2.7; S 0.9.

Synthesis of hybrid POMs as sodium salts: $\text{Na}_4[\gamma\text{-SiW}_{10}\text{O}_{36}\{(\text{C}_5\text{H}_7\text{N}_2\text{OS})(\text{CH}_2)_4\text{CONH}(\text{CH}_2)_3\text{Si}\}_2\text{O}]$ (**Na-POM-biot₂**) and $\text{Na}_4[\gamma\text{-SiW}_{10}\text{O}_{36}\{\text{NH}_2(\text{CH}_2)_3\text{Si}\}_2\text{O}]$ (**Na-POM-NH₂**): In around-bottomed flask, 100 mg of **TBA-POM-Biot₂** or **TBA-POM-NH₂** (24.7 μmol) were dissolved in 3 mL of acetonitrile. Then 26.7 mg of tetramethylammonium bromide (173 μmol), dissolved in 2 mL of water, were added. The reaction mixture was stirred at room temperature for one night. The solution obtained was then poured into EtOH (15 mL). The white precipitate

obtained was filtered, dried under vacuum and, finally, eluted in a chromatography column (3 cm diameter, 40 cm length) partially filled (ca. 100 cm³ volume) with a cation exchange resin (Amberlyst 15) pre-loaded with sodium ions (1M NaCl overnight), using ca. 50 mL of water/acetonitrile mixtures with variable composition (from 50:50 to 100:0) as eluent. Finally, the solution was lyophilized to remove water. The Na-POMs were collected with ca. 40% yield. FT-IR of **Na-POM-biot₂** (KBr, cm⁻¹): 3,464 (s,b), 2,928 (w), 2,870 (w), 1,684 (s), 1,635 (s), 1,558 (m), 1,541 (m), 1,458 (s), 1,270 (s), 1,039 (m), 958 (m), 883 (s), 824 (m), 753 (s), 528 (w). FT-IR of **Na-POM-NH₂** (KBr, cm⁻¹): 997 (w), 862 (m), 901 (s), 797 (s), 744 (m), 517 (m).

SPR Measurements

SPR analysis was performed on a BIACORE 100 system. CM5 chips from BIACORE (Uppsala, Sweden) were used for all the experiments. Avidin was anchored to the chip via EDC-NHS activation of the surface. To this aim, a dextrane-coated gold chip (CM5) was activated by flowing a 1:1 mixture of 0.2 M N-ethyl-N-(3-dimethylaminopropyl) carbodiimide (EDC) and 0.05 M N-hydroxysuccinimide (NHS) in water. Avidin (50 µg/mL) in 10 mM sodium acetate (pH 5) was immobilized on the activated chip surfaces at a flow rate of 10 µL/min. Excess of activated carboxylic groups on the chip was blocked with ethanolamine. HBS-EP buffer (0.01 M HEPES pH 7.4, 0.15 M NaCl, 3 mM EDTA, 0.005% v/v Surfactant P20) was used as running buffer to dilute avidin and water soluble POM solutions and for avidin immobilization. HBS-EP buffer with 5% DMSO was used to dilute all the other POMs solution and as running buffer in the corresponding experiments. All the solutions were filtered on a 0.22 µm membrane prior to use. All the experiments were conducted at 25°C with constant flux of 10 µL/min. Association and dissociation phases were 200 s and 100 s long, respectively. After each experiment, the surface was regenerated using 1 M NaCl in 50 mM NaOH. The recovery of the initial RU count was controlled before considering chip reutilization. The kinetic parameters were calculated using the BIACORE evaluation software on a personal computer. Analysis and fitting were performed using the bridging ligand model.

ATR-FTIR Monitoring of LbL Self-Assembly

ATR-FTIR spectra were acquired with a Perkin Elmer Spectrum One spectrometer equipped with an ATR horizontal sampling apparatus. The internal reflection element (IRE) was a three bounce 4 mm diameter diamond microprism (Smith Detection, USA, former SensIR technologies). The spectral resolution used for all measurements was 4 cm⁻¹. Before each experiment, the diamond crystal was polished with an aqueous 0.05 µm Al₂O₃ slurry and then rinsed with deionized water and ethanol. The deposition of alternate layers of **Na-POM-biot₂** and avidin onto the diamond surface was achieved in a flow-based “layer by layer” manner by means of a cylindrical flow cell clamped onto the ATR plate and sealed via a Parafilm gasket, with an internal volume of 150 µL. Spectra were acquired while **Na-POM-biot₂** or avidin solutions were flowed across the surface of the IRE at a flow rate of 2.2 mL min⁻¹ using a peristaltic pump. Both

POM and avidin were dissolved in PBS buffer at pH 7.0. Final POM and avidin concentrations were 0.13 and 0.4 g/L (40 and 6.3 µM) respectively. A positively charged protein as cytochrome *c* (*pI* = 10.0–10.5, close to that of avidin) can be easily bound to **Na-POM-biot₂** layers, while a negatively charged protein as GOx (*pI* = 4.05) suffers from a strong repulsion with the polyanion, which is completely rinsed from the surface.

Cell Culture and Imaging

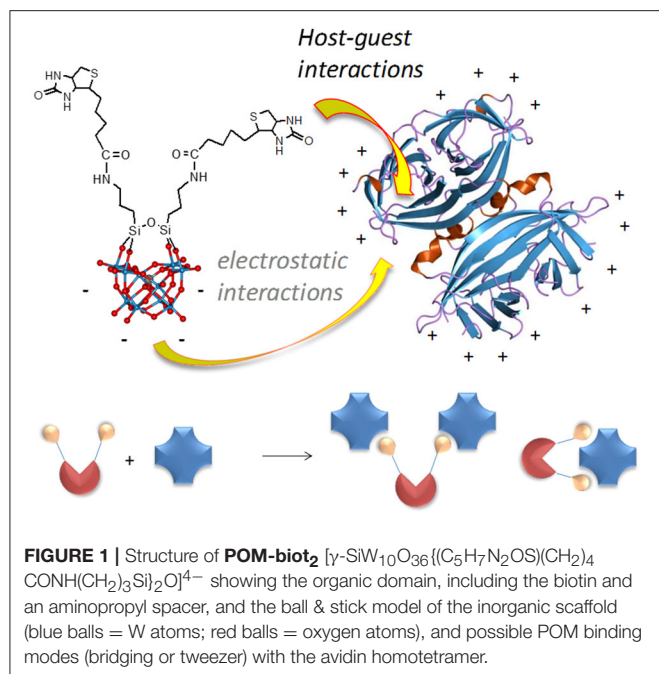
Human cervical carcinoma cells (HeLa) were grown in a standard culture media at 37°C and in 5% CO₂ atmosphere. Cells were seeded in a µ-Slide 8-well ibidi plate (Martinsried, Germany) at a density of 5 × 10⁴ cells per well (1.0 cm²) and were allowed to adhere overnight. Before cell incubation with POMs, the medium was changed. Cells were then incubated with 0.2 or 0.4 mg/ml of **Na-POM-NH₂** or **Na-POM-biot₂** for 24 h at 37°C. After incubation the cells were washed 3 times with PBS, fixed with paraformaldehyde, permeabilized by Triton and then stained with Atto 633-Streptavidin (Sigma #00336). Nuclei were counterstained with Hoechst 33342 (Invitrogen, Oregon, USA), according to manufacturer's instructions. Cellular uptake and internalization of biotin labeled POMs was visualized and evaluated with an inverted confocal laser scanning microscope (CLSM; Carl Zeiss LSM 510) equipped with a 63×/1.3 oil DIC objective, using excitation lines at 405 (Hoechst 33342) and 633 nm (Atto 633-Streptavidin 638/658). ImageJ software was used for image analysis. PI staining and FACS (Fluorescence-activated cell sorting) signals were analyzed accordingly to a literature protocol (Riccardi and Nicoletti, 2006).

RESULTS AND DISCUSSION

Synthesis

The bis-biotinylated POM has been obtained starting from the divacant decatungstosilicate K₈[γ-SiW₁₀O₃₆] K-POM, which has been initially treated with aminopropyl triethoxysilane (APTES) and tetrabutylammonium bromide to yield the doubly functionalized amino-derivative (“Bu₄N”)₃H[γ-SiW₁₀O₃₆{NH₂(CH₂)₃Si}₂O}] TBA-POM-NH₂ (Scheme S1) (Carraro et al., 2006).

The addition of dicyclohexylcarbodiimide (DCC) to a CH₃CN/DMF solution of **POM-NH₂**, biotin and N,N-diisopropylethylamine at 0°C, results in the formation of the biotinylated conjugate (“Bu₄N”)₃H[γ-SiW₁₀O₃₆{(C₅H₇N₂OS)(CH₂)₄CONH(CH₂)₃Si}₂O}] (**TBA-POM-biot₂**) (68% yield, **Figure 1**). **TBA-POM-biot₂** has been characterized by ¹H, ¹³C, ²⁹Si, ¹⁸³W NMR (CD₃CN), FT-IR, ESI-MS (Figures S1–S6) and elemental analysis. ¹H and ¹³C NMR signals confirm the presence of biotin signals (among diagnostic peaks, three broad NHCO signals at 5.1, 5.9, 6.9 ppm and the two C=O signals at 164.7 and 174.2 ppm, Figures S1, S2), while heteronuclear (²⁹Si and ¹⁸³W, Figures S3, S4) NMR yield the typical signal patterns expected for a divacant Keggin structure decorated with a R-Si-O-Si-R tweezer-like motif,¹¹ thus confirming the integrity of the POM scaffold after the post-functionalization with biotin. ESI-MS (negative mode, CH₃CN, Figure S5) shows a peak at *m/z* = 768.2, due to the tetra-anionic species ([C₂₆H₄₄N₆O₄₁S₂Si₃W₁₀]⁴⁻,



calcd. $m/z = 770.9$). The corresponding water soluble salt (**Na-POM-biot₂**) was obtained by replacing TBA counterions with Na⁺ on an ion-exchange resin (Figure S7).

Study of the Avidin/POM-Biot₂ Host-Guest Binding Interaction

The interaction between avidin and **TBA-POM-biot₂** was investigated including a direct comparison with the biotin free precursors **TBA-POM-NH₂** (Carraro et al., 2006, 2012a; Modugno et al., 2014) and **(ⁿBu₄N)₄[γ -SiW₁₀O₃₄(H₂O)₂]** **TBA-POM**, (Kamata et al., 2003) their corresponding alkali metal salts **Na-POM-biot₂**, **Na-POM-NH₂**, **K-POM**, as well as the POM-free biotin (**Biot**). This approach is aimed at dissecting the diverse contribution of the POM components (anionic charge, satellite counterions, organic spacer and biotin-tweezer) that could play a role with respect to the avidin binding.

A first investigation on the interaction between avidin and **TBA-POM-biot₂** was performed by monitoring circular dichroism (CD, Figures S8–S11). Avidin, in the region 220–235 nm, shows a positive Cotton effect ($\lambda_{\text{max}} = 227$ nm), (Verdoliva et al., 2010) which is only slightly affected (15% decrease) by **Biot** guest, with a maximum decrease after addition of 4 guest equivalents (Figure S8). Addition of POMs has a stronger impact, with an abatement of the dichroic signal ranging from 50% (for **K-POM**) to 60% (for **POM-Biot₂**), after addition of about one POM equivalent per avidin subunit. This evidence suggests that the POM scaffold by itself induces a modification of the protein structure, likely ascribed to electrostatic or hydrogen bond interactions between the inorganic POM surface and the protein residues Wu et al., 2005; Zhang et al., 2008; Geng et al., 2011; Li et al., 2013; Ventura et al., 2018).

Fluorescence quenching is generally used to monitor the ABC host-guest interaction, that leads to the rearrangement of two

or three tryptophan (Trp) residues shifting into an internal, more hydrophobic protein environment. These phenomena are responsible for a typical blue-shifted fluorescence quenching (Kurzbán et al., 1989). This is indeed the case of avidin titrated with **Biot** or **TBA-POM-biot₂** (Figure 2, Figures S12, S13), which both give a partial quenching of the emission, with a wavelength shift from 338 to 331 nm. Monitoring of the fluorescence intensity ratio, $(I_0/I)-1$, at 338 nm upon addition of **TBA-POM-biot₂** (Figure 2, Figure S13), yields an initially upward curvature, suggesting the involvement of both static and dynamic quenching, followed by a different regime after the addition of 1 biotin equivalent per avidin subunit (corresponding to two POM equivalents per tetrameric avidin, 1×10^{-6} M). The lower slope of the second region is in agreement with a decreased affinity for additional POM units.

No fluorescence shift is observed with the biotin-free POMs (Figures S14–S16), that are instead responsible for a continuous static quenching, as reported in literature for other proteins, with Stern-Volmer constant $K_{\text{SV}} = 10^4$ – 10^6 M⁻¹ (Zhang et al., 2007; Goovaerts et al., 2013). From the initial points of the Stern-Volmer plots (Figure 2, Figures S12–S16), it is indeed possible to compare the quenching efficiency of all samples, being >3 times higher for **TBA-POM-biot₂** ($K_{\text{SV}} = 9.6 \times 10^5$ M⁻¹) than those obtained for the other samples (K_{SV} in the range 1 – 3×10^5 M⁻¹). This result highlights the dual role of both the biotin pendant and of the POM scaffold interacting with avidin.

To gain further insight on the binding nature, the affinity of all synthesized POMs toward avidin was investigated via UV-vis by means of the HABA (4'-hydroxyazobenzene-2-carboxylic acid, a molecule with lower affinity for avidin with respect to biotin) competitive titration probe (Figure 2, Figures S17–S20) (Skander et al., 2004). When the commercially available HABA-avidin adduct (K_D (HABA-avidin) = 10^{-6} M) is titrated with biotin, a progressive decrease of the 500 nm absorption peak, due to bound HABA, is observed. In this way, the number of the effective hosting sites can be monitored from the number of released HABA equivalents. Four biotin equivalents are required to displace all HABA molecules. In our case, 2 equivalents of **TBA-POM-biot₂** are indeed enough to replace HABA, thus confirming the retention of the guest-specificity of both biotins installed on POM surface. As expected, the biotin-free POMs have no effect on HABA displacement (Figure 2, Figures S19, S20).

Concerning the binding geometry, **POM-biot₂** can adopt two possible arrangements: either one avidin serves as a di-topic receptor for the **POM-biot₂** tweezer, or **POM-biot₂** bridges two distinct avidins (Figure 1). Considering the steric hindrance of the POM scaffold, the latter binding mode is the most likely (Green et al., 1971; Geninatti Crich et al., 2005). The POM-bridging model was further inspected through a modified HABA-substitution titration. HABA-avidin was first titrated with 3 equivalents of biotin, in order to generally leave only one binding site occupied by HABA per protein (Figure S21). When 0.5 equivalents of **TBA-POM-biot₂** were added to the solution, they displaced all the remaining avidin-bound HABA, suggesting that each conjugate may easily arrange in a bridging conformation where two avidins are simultaneously bound.

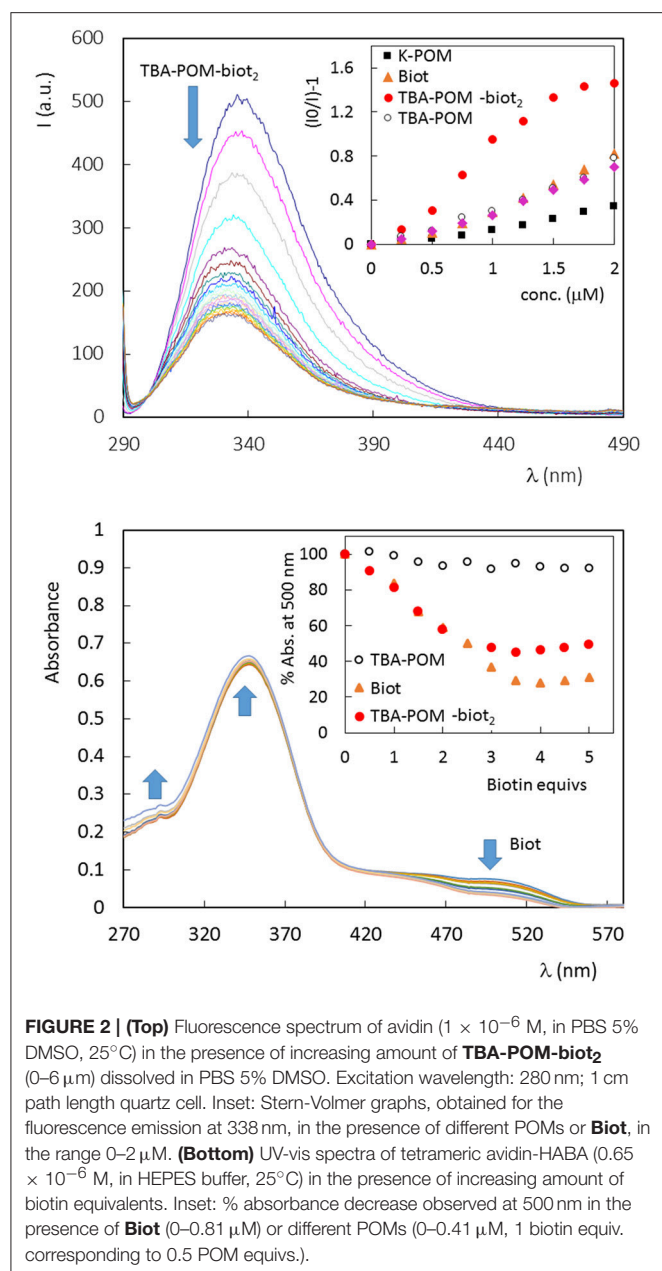


FIGURE 2 | (Top) Fluorescence spectrum of avidin (1×10^{-6} M, in PBS 5% DMSO, 25°C) in the presence of increasing amount of **TBA-POM-biot₂** (0–6 μM) dissolved in PBS 5% DMSO. Excitation wavelength: 280 nm; 1 cm path length quartz cell. Inset: Stern-Volmer graphs, obtained for the fluorescence emission at 338 nm, in the presence of different POMs or **Biot**, in the range 0–2 μM. **(Bottom)** UV-vis spectra of tetrameric avidin-HABA (0.65×10^{-6} M, in HEPES buffer, 25°C) in the presence of increasing amount of biotin equivalents. Inset: % absorbance decrease observed at 500 nm in the presence of **Biot** (0–0.81 μM) or different POMs (0–0.41 μM, 1 biotin equiv. corresponding to 0.5 POM equiv.).

The strength of the interaction between the guests and avidin was then investigated by using the SPR (Surface Plasmon Resonance) technique. To this aim, avidin was immobilized on a dextran-coated gold chip via amide coupling (about 2–4 ng/mm²) and exposed to an increasing amount of **TBA-POM-biot₂** in HBS-ES buffer containing 5% DMSO, producing the corresponding sensorgram (Figure 3, top). Each injection of **TBA-POM-biot₂** produces a clear increase of signal, measured in resonance units (RU), indicating the binding of the compound to the chip surface. After the injections, the flow of the buffered solutions induces a partial dissociation of **TBA-POM-biot₂** from the surface but, after four additions, a substantial amount of **TBA-POM-biot₂** (250 RU,

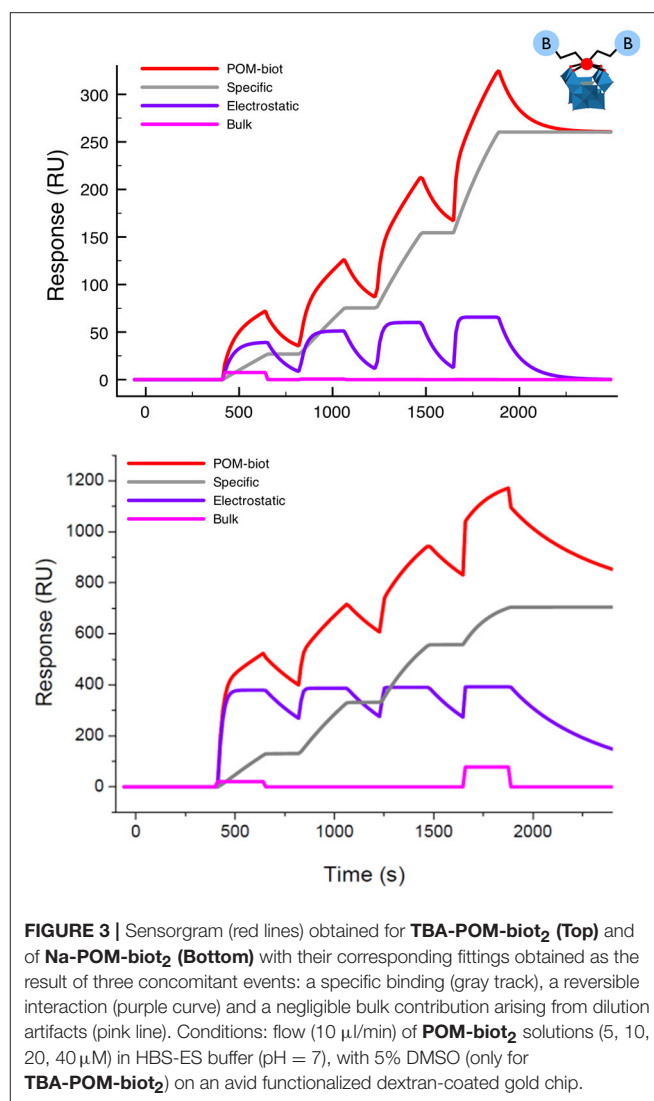


FIGURE 3 | Sensorgram (red lines) obtained for **TBA-POM-biot₂** (Top) and of **Na-POM-biot₂** (Bottom) with their corresponding fittings obtained as the result of three concomitant events: a specific binding (gray track), a reversible interaction (purple curve) and a negligible bulk contribution arising from dilution artifacts (pink line). Conditions: flow (10 μl/min) of **POM-biot₂** solutions (5, 10, 20, 40 μM) in HBS-ES buffer (pH = 7), with 5% DMSO (only for **TBA-POM-biot₂**) on an avidin functionalized dextran-coated gold chip.

corresponding to 0.25 ng/mm²) remains strongly anchored on the surface.

The sensorgram in Figure 3 is the result of two different binding contributions, featuring different strength and specificity. Indeed, the sensorgram could be successfully fitted with a model accounting for two binding modes. The first is characterized by a slow association, followed by a very slow dissociation rate, resulting in irreversible binding that leads to a stable anchorage of the **TBA-POM-biot₂** on the avidin-modified chip.

This behavior is typical of the specific ABC formation, yielding the dissociation constant $K_D = 2 \times 10^{-14}$ M, which is in the expected range of the avidin-biotin interactions. The second binding mode, which is likely related to unspecific electrostatic interactions, features quite fast association and dissociation rates, resulting in a calculated $K_D = 4 \times 10^{-6}$ M. Owing to its reversible character, it does not contribute to the final RU counts, i.e., to the amount of **TBA-POM-biot₂** that remains irreversibly bound to the avidin-modified chip.

Similar results were obtained for **Na-POM-biot₂** (Figure 3, bottom) whereby, taking into account the different loading and the different solvent buffer composition (HBS-ES buffer with no DMSO), the only relevant difference is a lower dissociation constant for the unspecific electrostatic binding ($K_D = 5 \times 10^{-8}$) M, that is likely ascribed to an easier cationic exchange, in aqueous environment, between the tetracationic avidin subunits and Na^+ .

To evaluate the contribution of the organic groups and of the anionic surface of the POM in the affinity toward avidin, the behavior of other POMs was then screened (Figures S23, S24). Both **TBA-POM-NH₂** and **TBA-POM** revealed an unusually high affinity toward avidin, corresponding respectively to a K_D of 10^{-9} M and 10^{-8} M, in addition to a reversible contribution with value $K_D = 10^{-6}$ M.

The fluorescence quenching profiles and the SPR results indicate that the presence of organic residues, on the POM surface, promotes a stable association with avidin, since both **TBA-POM-NH₂** and **TBA-POM** display an improved affinity and on-chip adhesion with respect to totally inorganic species (cfr. **K-POM** in Figure S25). This behavior can be ascribed to a preferential interaction of POM hybrids with the apolar binding site of avidin, thus reinforcing the association (Mock et al., 1988; Rosano et al., 1999).

To highlight the cross-linking potential of the **TBA-POM-biot₂**, for the organization of multi-avidin networks, we have explored the modification of the SPR response upon alternate addition cycles of the avidin host and of the biotinylated POM guest (Taylor et al., 1991)¹. Interestingly, addition of further avidin on the chip irreversibly loaded with POM-based ABC in the first experiment cycle, shows a significant increase of the RU values, confirming the additional scavenging of avidin by the **TBA-POM-biot₂** (Figure S22), and the occurrence of the bridging binding mode (Figure 1). Moreover, fitting of the SPR curves, yields a K_D of ca. 10^{-14} M for the second binding event, that points to an independent behavior of the two biotinylated arms anchored on the POM surface.

This POM-directed biotinylated bridge is expected to enable the formation of polymeric structures². The cross-linked interaction between the biotinylated POM and avidin can be carefully controlled by means of a layer-by-layer (LbL) approach (Ariga et al., 2007). ATR-FTIR spectroscopy was thus employed for *in-situ* monitoring of the sequential deposition of alternate **POM-biot₂**/avidin layers on diamond micro prism which served as internal reflection element and as solid support for the deposited layers (in this case, the sodium salt was used to fully exploit the two binding contributions, while avoiding the competing hydrophobic interactions, see text above). By means of a simple physisorption process, avidin proved to adhere

irreversibly onto the bare ATR crystal forming the first protein layer. The intensity of infrared absorption bands, arising from subsequent deposition of alternate POM/avidin layers, reveals that the amount of immobilized avidin increases in presence of a **Na-POM-biot₂** layer, according to the deposition process sketched in Figure 4 (steps A-D). The bridging action of **Na-POM-biot₂**, indeed, promotes the deposition of multiple avidin layers and strengthen the bio-hybrid architecture.

Moreover, *in situ* ATR-FTIR spectroscopy monitoring under flow conditions, shows that the **Na-POM-biot₂** adhesion occurs by a strong irreversible host-guest interaction but also via a much weaker binding mode that appears reversible upon rinsing.

The total loading of avidin in the second deposition cycle (step D) is consistent with ca. 3 fold infrared signal enhancement, which is indicative of multiple cross-links directed by the biotinylated POM (Figure 4).

On the other hand, spectra recorded upon addition of **Na-POM-biot₂** over a biotin-saturated avidin layer show signal intensities 3 times lower than those obtained with the free avidin, highlighting the role of host-guest interaction in promoting an efficient protein/POM association (Figure S27). A further evidence in this direction has been collected by using streptavidin, another target protein of biotin, which is characterized by a negative surface at neutral pH ($pI = 5$, Dittmer et al., 1989). In this case, a smaller (25% lower) ATR-FTIR signal can be detected, as a result of the repulsion between the negative charge densities on both surfaces, which hampers the formation of a dense protein layer onto the physisorbed **Na-POM-biot₂** layer (Figure S28).

The possibility to access POM based bio-hybrid films is relevant for the design of functional materials with application in sensor technology, electronics, catalysis and nanomedicine (Volatron et al., 2015).

Catalytic Behavior of the POM/Avidin Assembly

The highly specific interaction resulting from the association of biotin with avidin is commonly exploited for the design of novel semi-synthetic metalloenzymes, whereby the natural protein, functionalized with a biotinylated metal complex, provides a biostructured environment for the catalytic core (Steinreiber and Ward, 2008). Owing to the capability of vacant POMs to activate hydrogen peroxide (Carraro et al., 2006, 2012b; Sartorel et al., 2007), the **Na-POM-biot₂/avidin (2:1)** assembly has been evaluated as potential POM-based bio-hybrid catalyst for the oxygen transfer to a hydrosoluble organic sulfide. The two-step oxidation of L-methionine methyl ester to its corresponding sulfone has thus been considered as model reaction to demonstrate the retention of catalytic properties of the assembled POM (Carraro et al., 2011). The reaction smoothly occurs in buffered aqueous solution [pH 7, at $T = 28^\circ\text{C}$, i.e., under non-denaturing conditions (Thomas et al., 2005; Pordea et al., 2009)] where it was monitored by FT-IR, see Figure S29). Owing to its polymeric nature, **Na-POM-biot₂/avidin** acts as dispersed heterogeneous peroxidase. While the conversion of the L-methionine methyl ester to its sulfoxide is very fast

¹The amount of loaded POM, after a first measurement corresponds to about 10% of the maximum hosting capability by the avidin, meaning that biotin equivalents are in stoichiometric defect.

²Transmission electron microscopy (TEM) images obtained for **Na-POM-Biot₂** and avidin (2:1) assembled in aqueous environment show the occurrence of entangled amorphous aggregates with cross section > 50 nm (Figure S26)

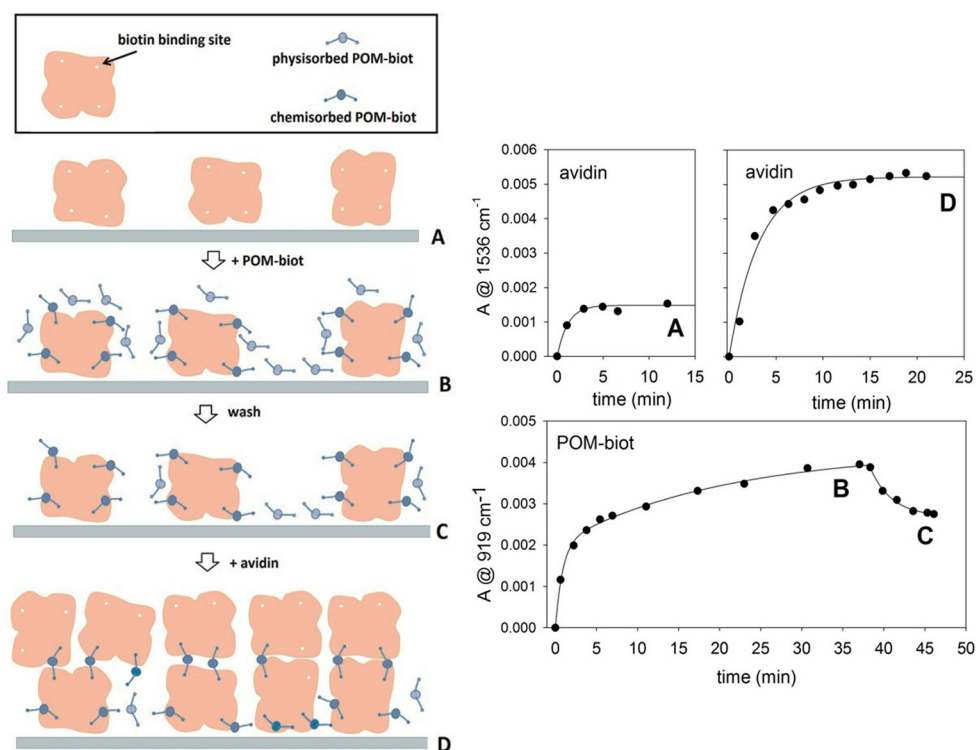


FIGURE 4 | Layer by Layer deposition of alternating avidin/**Na-POM-biot₂** layers. The deposition model proposed (left) is in agreement with adsorption kinetics of both components (right). The letters A, B, C, D allow to relate the steady infrared signals with the molecular architecture of the films. Marker bands for avidin and POM are at 1,536 and 919 cm^{-1} respectively. Each kinetic curve was obtained in difference mode, thus following the deposition of the last fluxed component.

(quantitative conversion was observed in ca. 10 min), further oxidation to sulfone was achieved in ca 24 h, with $t_{1/2} = 5.1$ h (Figure S29). The isolated **Na-POM-biot₂** displays a similar catalytic activity ($t_{1/2} = 4.1$ h) thus indicating that the avidin ligation is not precluding the access of both substrate and H_2O_2 to the POM active sites³.

POM Delivery and Tracking Into HeLa Cells

The control of the interaction between POMs and protein can be also exploited to design new delivery strategies. The cell delivery of metal-cores as bio-hybrid conjugates often represents a challenging task, while offering a promising strategy for advanced theranostic and anti-oxidant defense (Orvig and Abrams, 1999; Barry and Sadler, 2013; Albada and Metzler-Nolte, 2016; Liu et al., 2016). The negatively charged surface of the cells, indeed, represents an obstacle to internalization of POMs, that can be considered the molecular analogs of metal-oxide nanoparticles, showing a prominent peroxidase-activity. In addition, tracking of the polyanions often requires

disruptive methods, which involves metal detection by X-ray-based spectroscopies. Recently, detection of labeled POMs (Geisberger et al., 2013; Carraro et al., 2014) or encapsulation onto labeled carriers (Geisberger et al., 2011; del Mercato et al., 2014) have been proposed as methods to track hybrid POMs by fluorescence microscopy. We show herein a novel approach, based on a Labeled Streptavidin Biotin (LSAB) complex strategy. POM tracking has thus been investigated by incubating HeLa cells with 0.4 mg/mL of water soluble **Na-POM-biot₂** or **Na-POM-NH₂**, followed by treatment of the pre-incubated cells with Atto 633-labeled Streptavidin, used as a staining agent. As expected, the internalization of the **Na-POM-biot₂**, that binds strongly to the streptavidin staining agent, is tracked by means of confocal microscopy, thanks to the red-fluorescent streptavidin probe. Vice-versa, because of the weak binding to the biotin-free POM, the labeled streptavidin is readily washed off in the control experiment with **Na-POM-NH₂**.

Indeed, the **Na-POM-biot₂** incubated cells show well defined red spots in the cytoplasm region (Figure 5 shows nuclei-stained HeLa cells). These defined spots correspond to the intracellular localization of biotin, detected as Labeled Streptavidin Biotin (LSAB) complex. Although this increased biotin content (Dakshinamurti and Chalifour, 1981) is likely ascribed to the biotinylated POM, whose amphiphilic nature promotes the formation of vesicles or aggregates in the physiological cell

³Considering the biotin-POM spacer (valeric acid side chain, ca. 13.5 Å) and the POM molecular volume [$>600 \text{ Å}^3$, calculated for Keggin structures, see López et al. (2006)]. The avidin binding pocket [9 Å below the surface of the avidin molecule, with a molecular volume of 293 Å³, see Rosano et al. (1999)] is not expected to encapsulate the POM scaffold, which explains the lack of stereo control registered for the methionine methyl ester sulfoxidation by the bio-hybrid catalyst.

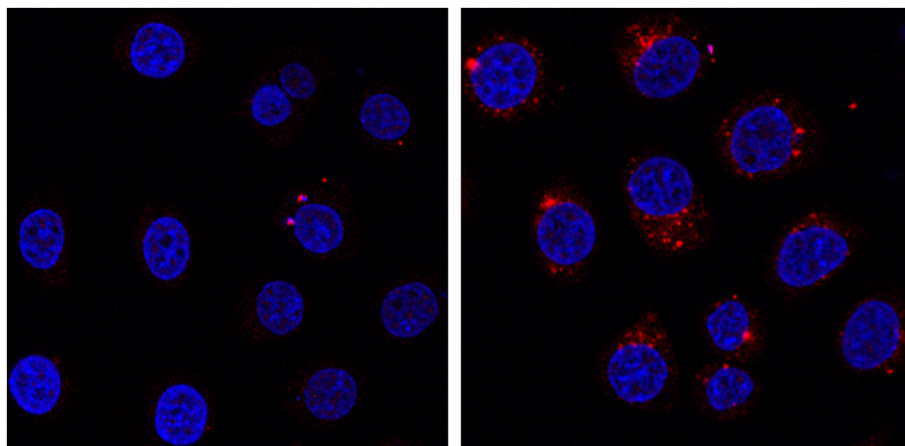


FIGURE 5 | HeLa cells incubated at 37°C for 24 h in presence of 0.4 mg/mL of **Na-POM-NH₂** (Left) **Na-POM-biot₂** (Right), and stained with Atto 633-Streptavidin (red fluorescent signal). Nucleus stained by Hoechst 33342 (blue). Images acquired by a confocal light scanning microscope (CLSM). A similar signal was seen with a concentration of 0.2 mg/ml POM.

environment (Geisberger et al., 2013; Fu et al., 2015), further experiments will be required to assess both POM content and its internalization mechanism.

The cytotoxicity of these POMs was determined by flow cytometry, after staining non-viable HeLa cell with propidium iodide (PI), after 24 and 48 h incubation with 60–500 µg/mL of POMs (Figures S30, S31). The experiments showed no decrease of viability and no pro-apoptotic events, suggesting a low cytotoxicity of hybrid POMs even at high doses (Riccardi and Nicoletti, 2006).

CONCLUSIONS

In summary, we have presented for the first time a POM-based bio-conjugate for specific targeting of proteins. The selectivity of **POM-biot₂** for avidin was confirmed by CD, fluorimetry, UV-vis titrations, SPR and ATR-FTIR of LbL self-assembly. Among the explored samples, **Na-POM-biot₂** displays the highest affinity toward avidin, arising from two distinct binding contributions, i.e., a host-guest specific interaction, strengthened by an unspecific electrostatic interaction, and it allows the cross-linking of proteins to obtain a 2D bio-hybrid network.

This approach provides an efficient engineering of bioactive nano-inorganics and paves the way to a tailored functionalization of the POM surface for bio-recognition, biomimetic catalysis and cell internalization.

REFERENCES

- Albada, B., and Metzler-Nolte, N. (2016). Organometallic-peptide bioconjugates: synthetic strategies and medicinal applications. *Chem. Rev.* 116, 11797–11839. doi: 10.1021/acs.chemrev.6b00166
- Ariga, K., Hill, J. P., and Ji, Q. (2007). Layer-by-layer assembly as a versatile bottom-up nanofabrication technique for exploratory research and realistic application. *Phys. Chem. Chem. Phys.* 9, 2319–2340. doi: 10.1039/b700410a

AUTHOR CONTRIBUTIONS

VZ: synthesis, characterization and binding studies of biotinylated POMs. GM: synthesis and characterization of biotinylated POMs. EL: binding studies by SPR. AC: synthesis and characterization of biotinylated POMs as sodium salts. FM: design of binding studies by SPR. LG: LbL approaches, synthesis and characterization of the layers. DM: catalytic studies by FT-IR. LV: design of the LbL approaches. AS and SK: *in vitro* studies with streptavidin. MB and MC: design of the POMs, planning of the experiments, manuscript writing.

ACKNOWLEDGMENTS

Financial support from MIUR (PRIN 2010N3T9M4, FIRB RBAP11ETKA) University of Padova (PRAT CPDA158234), Fondazione Cariparo (Starting Grant AMYCORES) is gratefully acknowledged. We also acknowledge the participation in the ESF COST CM1203 Polyoxometalate chemistry for molecular nanoscience (PoCheMoN).

SUPPLEMENTARY MATERIAL

The Supplementary Material for this article can be found online at: <https://www.frontiersin.org/articles/10.3389/fchem.2018.00278/full#supplementary-material>

- Barry, N. P. E., and Sadler, P. J. (2013). Exploration of the medical periodic table: towards new targets. *Chem. Commun.* 49, 5106–5131. doi: 10.1039/c3cc41143e
- Bijelic, A., Aureliano, M., and Rompel, A. (2018). The antibacterial activity of polyoxometalates: structures, antibiotic effects and future perspectives. *Chem. Commun.* 54, 1153–1169. doi: 10.1039/C7CC07549A
- Canny, J., Tézé A., Thouvenot, R., and Hervé G. (1986). Disubstituted tungstosilicates. 1. synthesis, stability, and structure of the lacunary precursor

- polyanion of a tungstosilicate gamma-SiW₁₀O₃₆⁸⁻. *Inorg. Chem.* 25, 2114–2119. doi: 10.1021/ic00233a003
- Carraro, M., Modugno, G., Fiorani, G., Maccato, C., Sartorel, A., and Bonchio, M. (2012a). Organic-inorganic molecular nano-sensors: a bis-dansylated tweezer-like fluoroionophore integrating a polyoxometalate core. *Eur. J. Org. Chem.* 2012, 281–289. doi: 10.1002/ejoc.201101122
- Carraro, M., Modugno, G., Zamolo, V., Bonchio, M., and Fabbretti, E. (2014). Polyoxometalate-based conjugates for biological targeting. *J. Biol. Inorg. Chem.* 19, S406–S406.
- Carraro, M., Mognon L., Caneva, F., Gardan, M., Maccato, C., and Bonchio, M. (2012b). Hybrid polyoxotungstates as functional comonomers in new cross-linked catalytic polymers for sustainable oxidation with hydrogen peroxide. *Chem. Eur. J.* 18, 13195–13202. doi: 10.1002/chem.201201849
- Carraro, M., Nsouli, N. H., Oelrich, H., Sartorel, A., Sorarù A., Mal, S. S., et al. (2011). Reactive ZrIV and HfIV butterfly peroxides on polyoxometalate surfaces: bridging the gap between homogeneous and heterogeneous catalysis. *Chem. Eur. J.* 17, 8371–8378. doi: 10.1002/chem.201003103
- Carraro, M., Sandei, L., Sartorel, A., Scorrano, G., and Bonchio, M. (2006). Hybrid polyoxotungstates as second-generation POM-based catalysts for microwave-assisted H₂O₂ activation. *Org. Lett.* 8, 3671–3674. doi: 10.1021/ol061197o
- Dakshinamurti, K., and Chalifour, L. E. (1981). The biotin requirement of HeLa cells. *J. Cell. Physiol.* 107, 427–438. doi: 10.1002/jcp.1041070314
- del Mercato, L. L., Carraro, M., Zizzari, A., Bianco, M., Miglietta, R., Arima, V., et al. (2014). Catalytic self-propulsion of supramolecular capsules powered by polyoxometalate cargos. *Chem. Eur. J.* 20, 10910–10914. doi: 10.1002/chem.201403171
- Dittmer, J., Dittmer, A., Delia Bruna, R., and Kasche, V. (1989). A native, affinity-based protein blot for the analysis of streptavidin heterogeneity: consequences for the specificity of streptavidin mediated binding assay. *Electrophoresis* 10, 762–765. doi: 10.1002/elps.1150101106
- Dolbecq, A., Dumas, E., Mayer, C. R., and Mialane, P. (2010). Hybrid organic-inorganic polyoxometalate compounds: from structural diversity to applications. *Chem. Rev.* 110, 6009–6048. doi: 10.1021/cr1000578
- Dong, Z. X., Tan, R. K., Cao, J., Yang, Y., Kong, C. F., Du, J., et al. (2011). Discovery of polyoxometalate-based HDAC inhibitors with profound anticancer activity *in vitro* and *in vivo*. *Eur. J. Med. Chem.* 46, 2477–2484. doi: 10.1016/j.ejmech.2011.03.036
- Flütsch, A., Schroeder, T., Grütter, M. G., and Patzke, G. R. (2011). HIV-1 protease inhibition potential of functionalized polyoxometalates. *Bioorg. Med. Chem. Lett.* 21, 1162–1166. doi: 10.1016/j.bmcl.2010.12.103
- Fu, L., Gao, H., Yan, M., Li, S., Li, X., Dai, Z., et al. (2015). Polyoxometalate-based organic-inorganic hybrids as antitumor drugs. *Small* 11, 2938–2945. doi: 10.1002/smll.201500232
- Geisberger, G., Gyenge, E. B., Hinger, D., Bösiger, P., Maake, C., and Patzke, G. R. (2013). Synthesis, characterization and bioimaging of fluorescent labeled polyoxometalates. *Dalton Trans.* 42, 9914–9920. doi: 10.1039/c3dt50414j
- Geisberger, G., Paulus, S., Besic Gyenge, E., Maake, C., Patzke, G. R. (2011). Targeted Delivery of Polyoxometalate Nanocomposites. *Small* 7, 2808–2814. doi: 10.1002/smll.201101264
- Geng, J., Li, M., Ren, J., Wang, E., and Qu, X. (2011). Polyoxometalates as inhibitors of the aggregation of amyloid β peptides associated with Alzheimer's disease. *Angew. Chem. Int. Ed.* 50, 4184–4188. doi: 10.1002/anie.201007067
- Geninatti Crich, S., Barge, A., Battistini, E., Cabella, C., Coluccia, S., Longo, D., et al. (2005). Magnetic resonance imaging visualization of targeted cells by the internalization of supramolecular adducts formed between avidin and biotinylated Gd³⁺ chelates. *J. Biol. Inorg. Chem.* 10, 78–86. doi: 10.1007/s00775-004-0616-2
- Goovaerts, V., Stroobants, K., Absillis, G., and Parac-Vogt, T. N. (2013). Molecular interactions between serum albumin proteins and Keggin type polyoxometalates studied using luminescence spectroscopy. *Phys. Chem. Chem. Phys.* 15, 18378–18387. doi: 10.1039/c3cp52848k
- Hasenknopf, B. (2005). Polyoxometalates: introduction to a class of inorganic compounds and their biomedical applications. *Front. Biosci.* 10, 275–287. doi: 10.2741/1527
- Iqbal, J., Barsukova-Stuckart, M., Ibrahim, M., Ali, S. U., Khan, A. A., and Kortz, U. (2013). Polyoxometalates as potent inhibitors for acetyl and butyrylcholinesterases and as potential drugs for the treatment of Alzheimer's disease. *Med. Chem. Res.* 22, 1224–1228. doi: 10.1007/s00044-012-0125-8
- Judd, D. A., Nettles, J. H., Nevins, N., Snyder, J. P., Liotta, D. C., Tang, J., et al. (2001). Polyoxometalate HIV-1 protease inhibitors. a new mode of protease inhibition. *J. Am. Chem. Soc.* 123, 886–897. doi: 10.1021/ja001809e
- Kamata, K., Yonehara, K., Sumida, Y., Yamaguchi, K., Hikichi, S., and Mizuno, N. (2003). Efficient epoxidation of olefins with $\geq 99\%$ selectivity and use of hydrogen peroxide. *Science* 300, 964–966. doi: 10.1126/science.1083176
- Karimian, D., Yadollahi, B., and Mirkhani, V. (2017). Dual functional hybrid-polyoxometalate as a new approach for multidrug delivery Microporous Mesoporous. *Mater* 247, 23–30. doi: 10.1016/j.micromeso.2017.03.048
- Kurzban, G. P., Gitlin, G., Bayer, E. A., Wilchek, M., and Horowitz, P. M. (1989). Shielding of tryptophan residues of avidin by the binding of biotin. *Biochemistry* 28, 8537–8542. doi: 10.1021/bi00447a040
- Li, J., Chen, Z., Zhou, M., Jing, J., Li, W., Wang, Y., et al. (2016). Polyoxometalate-driven self-assembly of short peptides into multivalent nanofibers with enhanced antibacterial activity. *Chem. Int. Ed.* 55, 2592–2595. doi: 10.1002/anie.201511276
- Li, M., Xu, C., Wu, L., Ren, J., Wang, E., and Qu, X. (2013). Self-assembled peptide-polyoxometalate hybrid nanospheres: two in one enhances targeted inhibition of amyloid β -peptide aggregation associated with Alzheimer's disease. *Small* 9, 3455–3461. doi: 10.1002/smll.201202612
- Linnenberg, O., Kondinski, A., Stöcker, C., and Monakhov, K. Y. (2017). The Cu(I)-catalysed Huisgen 1,3-dipolar cycloaddition route to (bio-) organic functionalisation of polyoxovanadates. *Dalton Trans.* 46, 15636–15640. doi: 10.1039/C7DT03376A
- Liu, F., Xue, L., Yuan, Y., Pan, J., Zhang, C., Wang, H., et al. (2016). Multifunctional nanoparticle-protein conjugates with controllable bioactivity and pH responsiveness. *Nanoscale* 8, 4387–4394. doi: 10.1039/C5NR07436C
- López, X., Fernandez, J. A., and Poblet, J. M. (2006). Redox properties of polyoxometalates: new insights on the anion charge effect. *Dalton Trans.* 1162–1167. doi: 10.1039/B507599H
- Mock, D. M., Lankford, G., and Horowitz, P. (1988). A study of the interaction of avidin with 2-anilinonaphthalene-6-sulfonic acid as a probe of the biotin binding site. *Biochim. Biophys. Acta Proteins Struct. Molec. Enzym.* 956, 23–29. doi: 10.1016/0167-4838(88)90293-2
- Modugno, G., Syrgiannis, Z., Bonasera, A., Carraro, M., Giancane, G., Valli, L., et al. (2014). The supramolecular design of low-dimensional carbon nano-hybrids encoding a polyoxometalate-bis-pyrene tweezer. *Chem. Commun.* 50, 4881–4883. doi: 10.1039/C3CC49725A
- Green, L., Konieczny, E. J., Toms, R., and Valentine, C. (1971). The use of bifunctional biotinyl compounds to determine the arrangement of subunits in avidin. *Biochem. J.* 125, 781–791. doi: 10.1042/bj1250781
- Orvig, C., and Abrams, M. J. (1999). Medicinal inorganic chemistry: introduction. *Chem. Rev.* 99, 2201–2204. doi: 10.1021/cr980419w
- Pordea, A., Mathis, D., and Ward, T. R. (2009). Incorporation of biotinylated manganese-salen complexes into streptavidin: new artificial metalloenzymes for enantioselective sulfoxidation. *J. Organomet. Chem.* 694, 930–936. doi: 10.1016/j.jorganchem.2008.11.023
- Proust, A., Matt, B., Villanneau, R., Guillemot, G., Gouzerh, P., and Izzet, G. (2012). Functionalization and post-functionalization: a step towards polyoxometalate-based materials. *Chem. Soc. Rev.* 41, 7605–7622. doi: 10.1039/c2cs35119f
- Prudent, R., Moucadel, V., Laudet, B., Barette, C., Lafanechere, L., Hasenknopf, B., et al. (2008). Identification of polyoxometalates as nanomolar noncompetitive inhibitors of protein kinase CK2. *Chem. Biol.* 15, 683–692. doi: 10.1016/j.chembiol.2008.05.018
- Prudent, R., Sautel, C. F., and Cochet, C. (2010). Structure-based discovery of small molecules targeting different surfaces of protein-kinase CK2. *Biochim. Biophys. Acta* 1804, 493–498. doi: 10.1016/j.bbapap.2009.09.003
- Rhule, J. T., Hill, C. L., Judd, D. A., and Schinazi, R. F. (1998). Polyoxometalates in Medicine. *Chem. Rev.* 98, 327–357. doi: 10.1021/cr960396q
- Riccardi, C., and Nicoletti, I. (2006). Analysis of apoptosis by propidium iodide staining and flow cytometry. *Nat. Prot.* 1, 1458–1461. doi: 10.1038/nprot.2006.238
- Rosano, C., Arosio, P., and Bolognesi, M. (1999). The X-ray three-dimensional structure of avidin. *Biomol. Eng.* 16, 5–12. doi: 10.1016/S1050-3862(99)00047-9
- Sartorel, A., Carraro, M., Bagno, A., Scorrano, G., and Bonchio, M. (2007). Asymmetric tetra-protonation of γ -[(SiO₄)W₁₀O₃₂]⁸⁻ triggers a catalytic epoxidation reaction: perspectives in the assignment of the active catalytic. *Angew. Chem. Int. Ed.* 46, 3255–3258. doi: 10.1002/anie.200605120

- Skander, M., Humbert, N., Collot, J., Gradinaru, J., Klein, G., Loosli, A., et al. (2004). Artificial metalloenzymes: (Strept)avidin as host for enantioselective hydrogenation by achiral biotinylated rhodium–diphosphine complexes. *J. Am. Chem. Soc.* 126, 14411–14418. doi: 10.1021/ja0476718
- Steinreiber, J., and Ward, T. R. (2008). Artificial metalloenzymes as selective catalysts in aqueous media. *Coord. Chem. Rev.* 252, 751–766. doi: 10.1016/j.ccr.2007.09.016
- Stephan, H., Kubeil, M., Emmerling, F., and Muller, C. E. (2013). Polyoxometalates as versatile enzyme inhibitors. *Eur. J. Inorg. Chem.* 2013, 1585–1594. doi: 10.1002/ejic.201201224
- Taylor, D. M., Morgan, H., and Silva, C. D'. (1991). Characterization of chemisorbed monolayers by surface potential measurements. *J. Phys. D Appl. Phys.* 24, 1443–1450. doi: 10.1088/0022-3727/24/8/032
- Thomas, C. M., Letondor, C., Humbert, N., and Ward, T. R. (2005). Aqueous oxidation of alcohols catalyzed by artificial metalloenzymes based on the biotin–avidin technology. *J. Organomet. Chem.* 690, 4488–4491. doi: 10.1016/j.jorganchem.2005.02.001
- Ventura, D., Calderan, A., Honisch, C., Krol, S., Serrati, S., Bonchio, M., et al. (2018). Synthesis and biological activity of an Anderson polyoxometalate bis-functionalized with a Bombesin-analog peptide. *Peptide Sci.* 100:e24047. doi: 10.1002/pep2.24047
- Verdoliva, A., Bellofiore, P., Riviaccio, V., Catello, S., Colombo, M., Albertoni, C., et al. (2010). Biochemical and biological characterization of a new oxidized avidin with enhanced tissue binding properties. *J. Biol. Chem.* 285, 9090–9099. doi: 10.1074/jbc.M109.080457
- Volatron, F., Noël, J. M., Rinfrey, C., Decorse, P., Combella, C., Kanoufi, F., et al. (2015). Electron transfer properties of a monolayer of hybrid polyoxometalates on silicon. *J. Mater. Chem. C* 3, 6266–6275. doi: 10.1039/C5TC00074B
- Wang, X., Liu, J., Li, J., Yang, Y., Liu, J., Pope, M. T., et al. (2003). Synthesis and antitumor activity of cyclopentadienyltitanium substituted polyoxotungstate $[\text{CoW}_{11}\text{O}_{39}(\text{CpTi})]^{7-}$ ($\text{Cp}=\text{eta}^5\text{-C}_5\text{H}_5$). *J. Inorg. Biochem.* 94, 279–284. doi: 10.1016/S0162-0134(02)00631-1
- Wortmann, L., Ilyas, S., Niznansky, D., Valldor, M., Arroub, K., Berger, N., et al. (2014). Bioconjugated iron oxide nanocubes: synthesis, functionalization, and vectorization. *ACS Appl. Mater. Interfaces* 6, 16631–16642. doi: 10.1021/am503068r
- Wu, Q., Wang, J., Zhang, L., Hong, A., and Ren, J. (2005). Molecular recognition of basic fibroblast growth factor by polyoxometalates. *Angew. Chem. Int. Ed.* 44, 4048–4052. doi: 10.1002/anie.200500108
- Yang, H., Cheng, Y., Su, M., Xiao, Y., Hu, M., Wang, W., et al. (2013). Polyoxometalate-biomolecule conjugates: a new approach to create hybrid drugs for cancer therapeutics. *Bioorg. Med. Chem. Lett.* 23, 1462–1466. doi: 10.1016/j.bmcl.2012.12.081
- Zhang, G., Keita, B., Brochon, J. C., de Oliveira, P., Nadjio, L., Craescu, C. T., et al. (2007). Molecular interaction and energy transfer between human serum albumin and polyoxometalates. *J. Phys. Chem. B* 111, 1809–1814. doi: 10.1021/jp063758z
- Zhang, G., Keita, B., Craescu, C. T., Miron, S., de Oliveira, P., and Nadjio, L. (2008). Molecular interactions between wells–dawson type polyoxometalates and human serum albumin. *Biomacromolecules* 9, 812–817. doi: 10.1021/bm701120j

Conflict of Interest Statement: The authors declare that the research was conducted in the absence of any commercial or financial relationships that could be construed as a potential conflict of interest.

The reviewer AA and handling Editor declared their shared affiliation.

Copyright © 2018 Zamolo, Modugno, Lubian, Cazzolaro, Mancin, Giotta, Mastrogiacomo, Valli, Saccani, Krol, Bonchio and Carraro. This is an open-access article distributed under the terms of the Creative Commons Attribution License (CC BY). The use, distribution or reproduction in other forums is permitted, provided the original author(s) and the copyright owner(s) are credited and that the original publication in this journal is cited, in accordance with accepted academic practice. No use, distribution or reproduction is permitted which does not comply with these terms.



Effective *in Vitro* Photokilling by Cell-Adhesive Gold Nanorods

Álvaro Artiga^{1†}, Sonia García-Embid^{1†}, Laura De Matteis^{2*}, Scott G. Mitchell^{1*} and Jesús M. de la Fuente¹

¹ Instituto de Ciencia de Materiales de Aragón, Consejo Superior de Investigaciones Científicas, Universidad de Zaragoza and CIBER-BBN, Zaragoza, Spain, ² Instituto de Nanociencia de Aragón, Universidad de Zaragoza and CIBER-BBN, Zaragoza, Spain

OPEN ACCESS

Edited by:

Soumyajit Roy,
Indian Institute of Science Education
and Research Kolkata, India

Reviewed by:

Luca Conti,
Università degli Studi di Firenze, Italy
Tatjana N. Parac-Vogt,
KU Leuven, Belgium

*Correspondence:

Laura De Matteis
lauradem@unizar.es
Scott G. Mitchell
scott@unizar.es

[†]These authors have contributed
equally to this work.

Specialty section:

This article was submitted to
Inorganic Chemistry,
a section of the journal
Frontiers in Chemistry

Received: 27 April 2018

Accepted: 01 June 2018

Published: 22 June 2018

Citation:

Artiga Á, García-Embid S,
De Matteis L, Mitchell SG and
de la Fuente JM (2018) Effective *in Vitro* Photokilling by Cell-Adhesive Gold Nanorods. *Front. Chem.* 6:234.
doi: 10.3389/fchem.2018.00234

Upon excitation of their localized surface plasmon resonance (LSPR) band, gold nanorods (AuNRs) show a characteristic light-to-heat transduction, a useful and versatile property for a range of biomedical applications such as photothermal therapy, drug delivery, optoacoustic imaging and biosensing, among others. Nanoparticle (NP)-mediated photothermal therapy (PTT) rests on the ability of nanomaterials to convert light energy into heat and can currently be considered as a promising method for selectively destroying tumor cells by (photo)-thermoablation. One inherent limitation to NP-mediated PTT is that the nanoparticles must arrive at the site of action to exert their function and this typically involves cellular internalization. Here we report the use of the Keggin-type polyoxometalate (POM) phosphotungstic acid (PTA) as an inorganic gelling agent for the encapsulation of plasmonic gold nanorods (AuNRs) inside a biocompatible and cell-adhesive chitosan hydrogel matrix. These functional sub-micrometric containers are non-cytotoxic and present the ability to adhere to the cytoplasmic membranes of cells avoiding any need for cellular internalization, rendering them as highly efficient thermoablating agents of eukaryotic cells *in vitro*.

Keywords: polyoxometalate, gold nanorod, chitosan hydrogel, encapsulation, photothermal therapy, near infra-red

INTRODUCTION

Plasmonic nanoparticles undergo efficient light-to-heat transduction through excitation of their surface plasmon resonance (SPR) band (Abadeer and Murphy, 2016), a characteristic and versatile property that is applied to a range of biomedical applications: for photothermal therapy (Kharlamov et al., 2015), drug delivery (Yin et al., 2015), optoacoustic imaging (Bao et al., 2013), and biosensing (Parolo et al., 2013) among others. The medical field views nanoparticle (NP)-mediated photothermal therapy (PTT) (based on the ability of nanomaterials to convert light energy into heat) as a promising method for selectively destroying tumor cells (thermoablation). Consequently, NP-mediated PTT can be used as a synergic anticancer therapy to weaken tumor cells (when applied in low doses) by making cells more susceptible to other treatments or permitting a reduction in the effective dose of other aggressive therapies such as radio- (Cooper et al., 2014) and chemo-therapies (Dreaden et al., 2011; Liu et al., 2015). Furthermore, PTT is also used as a highly effective tool to improve the applicability of photodynamic therapy (PDT) by reducing side effects and reducing acquired resistance to drugs (Bucharskaya et al., 2016). The local cellular destructive effect of increased temperature corresponds to damage of sub-cellular components, mainly lysosomes, which then release their contents and biomarkers, which initiate the cascade

of events that lead to cell death (Pérez-Hernández et al., 2015). Anisotropic gold nanoparticles (AuNPs) are particularly interesting for PTT therapy because they present an efficient absorption of light at near infrared (NIR) wavelengths; while the absorption of biological tissues and cells at these wavelengths is highly decreased (Huang et al., 2009).

One inherent limitation to NP-mediated PTT is that the particles must arrive at the site of action to exert their function and this typically involves internalization inside the cell. For some applications, the functionalization of nanomaterials with biomolecules for targeted therapeutic and diagnostic applications is especially interesting (Conde et al., 2014; Fratila et al., 2014).

Gold nanorods (AuNRs) possess potent hyperthermia properties, however their efficacy is unsatisfactory because of low cellular internalization (Alfranca et al., 2016). Literature clearly shows how post-synthetic functionalization of the particles is almost always required (Fan et al., 2016; Liu et al., 2016). This can in turn result in issues with particle stability, aggregation in cell culture media and so forth; not to mention problems with reproducibility and elevated synthesis costs. In recent years investigators have highlighted the need for reducing the complexity of nanotherapeutics to allow for clinical translation but maintaining their therapeutic effect (Barz, 2015)—a concept which has framed the research presented herein.

Embedding the active photothermal element (in this case the AuNR) in a polymeric cell-adhesive hydrogel would improve the efficacy of the thermal treatment required to destroy cells without the need for cellular internalization. Recent studies have shown how AuNP entrapment in implantable macroscopic hydrogels have shown promising results as efficient photothermal antitumor treatments in mice (Conde et al., 2016).

The naturally occurring polymer chitosan has been selected in this work for the entrapment of AuNR. Chitosan is a mucopolysaccharide obtained by deacetylation of chitin, a polymer extracted from the exoskeletons of crustacean, insects and the cellular wall of fungi. This polymer has low toxicity and immunogenicity and it is biocompatible, biodegradable and bioadhesive (Younes and Rinaudo, 2015). Besides, as chitin is one of the most abundant polymers in nature, chitosan is readily available and cheap. The mucoadhesive properties of chitosan are due to the fact that it is one of the richest natural polymers in amino groups. These groups pose a keen interest in the fabrication of matrices as they are available for their interaction with other molecules (Yi et al., 2005). One of the most important characteristics of chitosan is its capacity to form hydrogels in the presence of salts, which has been widely used in the pharmaceutical industry for drug release, gene therapy or vaccines administration (Nagpal et al., 2010; Younes and Rinaudo, 2015). Chitosan has been used for coating AuNPs for subsequent application in gene delivery (Yang et al., 2015), photothermal ablation (Duan et al., 2014), and non-invasive imaging (Charan et al., 2012). Besides, it has also been employed for the synthesis of nanospheres containing AuNPs and anticancer drugs, to obtain nanocomposites for photothermal-chemotherapies (Chen et al., 2013; Zhang et al., 2016). Since chitosan possesses mucoadhesive properties, there is significant potential in exploring the use of chitosan-based

nanomaterials as novel therapies for diseases related with gastrointestinal tract, for example in colorectal cancer (Kang et al., 2017).

In the present work, we have used the ionotropic gelation method for the synthesis of a hybrid organic-inorganic sub-micrometric container based on a chitosan hydrogel. One of the advantages of this method is that it avoids the use of organic solvents; allowing for AuNR entrapment entirely in aqueous solution. The easy and rapid synthesis is based on the interaction of the positively charged amino groups of chitosan with an appropriate anion that acts as an electrostatic crosslinker. In this work polyoxometalates (POMs) were used as anionic gelling agents. POMs represent an extremely diverse group of anionic molecular metal-oxides with promising application to a range of sub-fields of materials science, catalysis, and medicine. They have demonstrated important antibacterial (Bijelic et al., 2018), antiviral and anticancer characteristics (Hasenknopf, 2005; Yamase, 2005). Recently, POM-based chitosan materials have been reported as potent anti-cancer agents (Menon et al., 2011; Shah et al., 2015) and antibacterial materials (Fiorani et al., 2014). Our own research has shown how POMs can act as gelling agents and provide structural stability to hybrid chitosan hydrogels with antibacterial activity (De Matteis et al., 2014). Furthermore, as part of our research we pay particular attention to how nanoparticles interact with cells and tissues in both *in vitro* and *in vivo* environments (Moros et al., 2013). In recent years we have carried out in depth investigations on the photothermal properties of plasmonic nanoparticles for biosensing (Polo et al., 2013), and optoacoustic imaging (Han et al., 2016).

The aim of this work was to use polyoxometalates (POMs) as inorganic gelation agents for the encapsulation of plasmonic nanoparticles (NPs) inside a mucoadhesive hydrogel for optical hyperthermia applications. Here we report the synthesis of a hybrid organic-inorganic sub-micrometric container of phosphotungstic acid (PTA) and gold nanorods (AuNRs) inside a chitosan hydrogel matrix. The resulting functional container is a highly efficient heat mediator that has been used for the photothermoablation of eukaryotic cells *in vitro*.

MATERIALS AND METHODS

Materials

Silver nitrate (AgNO_3) was purchased from Panreac® (Barcelona, Spain). Chitosan (medium molecular weight), hydrogen tetrachloroaurate (III) hydrate, phosphotungstic acid (PTA), sodium borohydride, sodium hydroxide, and hexadecyltrimethylammonium bromide (CTAB) were purchased from Sigma-Aldrich (MI, USA). Complete Dulbecco's modified Eagle's medium (DMEM), phosphate buffered saline (PBS) and Dulbecco's Phosphate Buffered Saline (DPBS) supplemented with Ca^{2+} and Mg^{2+} were purchased from Lonza® (Basel, Switzerland). Hydroquinone was purchased from Alfa Aesar® (MA, USA). DMEM was supplemented with 2 mM glutamine, 100 U/mL penicillin/streptomycin, and 10% fetal bovine serum (FBS) for their use in cell culture. LIVE/DEAD® Viability/Cytotoxicity Kit was purchased from Invitrogen™ (CA, USA). For the cell viability assays, MTT

(3-(4,5-dimethylthiazol-2-yl)-2,5-diphenyltetrazolium bromide) was purchased from Invitrogen™ (CA, USA). Nanorod suspensions were sterilized with 0.22 μm Low Protein Binding Durapore® (PVDF) MilliPore® (MA, USA) filters prior addition to cell cultures and prior chitosan entrapment. Prior to use, all glassware was cleaned with *aqua regia* and washed thoroughly with Milli-Q water from Millipore Q-POD® system.

UV-Vis spectra were acquired employing a Cary 50 Probe® spectrophotometer from Varian (TO, Italy). The composition of the hydrogel and its components was analyzed by Fourier Transform Infrared Spectroscopy analysis in a JASCO FT/IR-4100 Fourier transform infrared spectrometer (Madrid, Spain) in a frequency range of 600–4,000 cm^{-1} with a resolution of 2 cm^{-1} and a scanning number of 32. SEM images were collected using a field emission SEM Inspect F50 with an EDX system INCA PentaFETx3 (FEI Company, Eindhoven, The Netherlands) in an energy range between 10 and 15 keV. Nanomaterials and cells were irradiated using a 3 W Laser Quantum Ventus laser (1,064 nm) (Cheshire, UK) operating at a power output of 1,100 mW, which corresponds with a power per surface of *ca.* 3.3 W cm^{-2} at the sample position. Both bright-field and fluorescence images of the cells were acquired with a Nikon Eclipse Ti (Tokyo, Japan) with PFS system equipped with a phase contrast system and $472 \pm 30/520 \pm 35 \text{ nm}$ (GFP) and $531 \pm 46/593 \pm 40 \text{ nm}$ (TRITC) cube filter connected to NIS-Elements Microscope Imaging Software. The temperature reached by the nanomaterials suspensions under near infrared (NIR) irradiation was monitored using a software program developed by The University of Zaragoza using a Fiber Optic Temperature Sensor TPT-62 (Fiso Technologies Inc., Quebec, Canada). Optical absorbance of the samples at 96-well plate was recorded using a plate reader [ELx800TM, Biotek (Thermo Scientific Multiskan GO UV/Vis microplate spectrophotometer), VT, USA]. For elemental analysis, samples were evaluated by ICP-AES using an Optima 8300 (Perkin Elmer®). Samples were freeze-dried in a Telstar cryodos freeze-dryer (Spain) with an Agilent technologies DS 102 vacuum pump. Dynamic Light Scattering and Electrophoretic mobility (Zeta Potential) of the hybrid matrixes were evaluated using a Brookhaven 90Plus DLS instrument (NY, USA) at a concentration of 0.05 mg/mL in water or KCl 1 mM, respectively.

Gold Nanorod (AuNR) Entrapment on Chitosan Hydrogel (AuNR@CS)

Polyethylene glycol-stabilized gold nanorods (AuNR) were synthesized according to previously reported literature procedure (Alfranca et al., 2016), which in turn was adapted from a synthetic route first reported by Zubarev and co-workers (Vigderman and Zubarev, 2013). For the AuNR entrapment in chitosan hydrogel, 1 mL of a 2 mg/mL (measured by dry weight) aqueous AuNR solution was transferred to a glass vial. Under ultrasonication, 0.5 μmol of PTA (144 μL of a 10 mg/mL) was slowly pipetted into the AuNR solution. 2 mL of 5 mg/mL chitosan in 1% v/v acetic acid was then pipetted into the PTA/AuNR suspension and mixed for 2 min under sonication. This mixture was then added to a separate tube containing 5 mL 50 mM Na_2SO_4 solution, under

sonication for 2 min. The reaction suspension was centrifuged at 6,700 g for 3 min. The supernatant was discarded and the product was resuspended and centrifuged once more at 4,300 g for 3 min. The precipitate was resuspended in water. All the experiments for AuNR entrapment were performed under sterile conditions in a laminar flow hood (Telstar PV-30/70). The concentration of the sub-micrometric containers in water suspension was obtained by measuring the weight of 0.5 mL of sample after freeze-drying.

Elemental Analysis by Inductively Coupled Plasma Atomic Emission Spectroscopy (ICP-AES)

The gold content of the AuNR@CS hydrogel and AuNR starting material was quantified by inductively coupled plasma atomic emission spectroscopy (ICP-AES). One hundred microliters of the samples were previously digested by addition of 100 μL of a 3:1 sulfuric acid (96%)/hydrogen peroxide (33%) solution and incubated 15 min at room temperature. After that, 300 μL of a 1:3 nitric acid (65%)/hydrochloric acid (37%) solution were added. Samples were incubated for 2 h at room temperature and at 60°C for 15 min and they were finally diluted with Milli-Q water up to 20 mL. All samples were prepared and analyzed in duplicate.

Fixation for Scanning Electron Microscopy Imaging of AuNRs Entrapped in Chitosan Hydrogel (AuNR@CS)

AuNR@CS samples were covalently crosslinked with glutaraldehyde prior to electron microscopy imaging to fix their supramolecular structure. One milligram of the AuNR@CS hydrogel was incubated for 1 h in a 1.5% glutaraldehyde solution in PBS. The nanomaterials were then washed with Milli-Q water *via* three successive centrifugation cycles (5,500 g for 5 min per cycle).

Heating Profiles of AuNRs and AuNR@Cs

The heating curves were measured using a homogeneous laser beam adjusted to the bottom area of one single well on each irradiation (96-well-plates). All samples were irradiated at 1,100 mW for 10 min registering the temperature every 5 s and measurements were performed in triplicate. To avoid pre-heating adjacent samples by heat diffusion and/or diffraction of the beam, one empty well was located between sample rows. The temperature probe was rinsed and cooled in Milli-Q water before collecting new data.

Each concentrated stock of nanomaterials was diluted in Milli-Q water to a final volume of 200 μL per well, giving a final concentration of 0, 5, 15, 30, and 60 μg of gold/mL of AuNRs or AuNR@CS. These heating curves were also used to calculate the heating potency and efficiency of both nanomaterials at the studied concentrations. For this purpose, a linear regression of the heating curves during the first 60 s of irradiation was calculated in order to obtain the temperature increase per second. The specific heat and density values of the suspensions were approximated to those of water and the heat needed to produce this temperature increase

in each well was determined. The heating efficiency was calculated using these heat values and the laser power of 1,100 mW.

In Vitro Studies

All *in vitro* studies were performed using Vero cell line (kidney epithelial cells from African green monkey), acquired from the American Type Culture Collection (ATCC: CCL-81). Cells were cultured at 37°C in a 5% CO₂ atmosphere in Dulbecco's modified Eagle's medium (DMEM) supplemented with 10% fetal bovine serum (FBS), 2 mM glutamine, and 100 U/mL penicillin/streptomycin.

MTT Cell Viability Assays

Vero cells were seeded at a density of 5×10^3 cells per well in a 96-multiwell plate and incubated with the nanomaterials for 24 h, as previously described. At this point, cells were irradiated with the NIR laser and incubated for 5 h under cell culture conditions. Thereafter, medium was removed and cells were incubated with 200 μ L of DMEM containing 10 μ L of 5 mg/mL MTT in the dark, under culture conditions, for 90 min. Finally, the plate was centrifuged at 1,250 g for 30 min using an Eppendorf centrifuge 5810R with an A-4-62 rotor, the supernatant was removed and the formazan crystals were solubilised with 100 μ L of dimethyl sulfoxide (DMSO). After mixing, the optical density at 555 nm was recorded using a plate reader. Experiments were performed in quintuplet to determine the standard deviations. Experiments were reproduced in triplicate to verify the reproducibility of the results.

Thermoablation Conditions

Vero cells were seeded at a density of 5×10^3 cells per well in a 96-multiwell plate and incubated under cell culture standard conditions. After 24 h the medium was replaced for fresh DMEM with the desired concentrations of each nanomaterial (ranging from 0 to 60 μ g of gold/mL with a final water concentration of 10%) and incubated for another 24 h under culture standard conditions. Thereafter, the cells were washed twice with DPBS to remove any excess of remaining particles or dead cells and fresh phenol red-free DMEM was added. Samples were performed in triplicate and irradiated under working laser configuration for 10 min, with temperature control set at 37°C. Non-irradiated samples of cells with and without nanomaterials and irradiated cells (without nanomaterials) were used as controls. Representative images were collected 5 h post-irradiation.

Live/Dead Cell Viability Assays

LIVE/DEADTM Viability/Cytotoxicity Kit tests were performed according to the instructions of the supplier. Briefly, DMEM of irradiated samples and their respective controls was removed after 5 h under standard culture conditions. Thereafter, cells were incubated for 30 min at room temperature (protected from light) with 100 μ L of DPBS containing calcein (2,000 times diluted from the stock solution) and Ethidium Bromide homodimer (500 times diluted from stock solution). Finally, bright field and fluorescent images of the cells were acquired

using the microscope previously described employing $472 \pm 30/520 \pm 35$ nm (GFP) and $531 \pm 46/593 \pm 40$ nm (TRITC) cube filters. Images of all studied conditions were acquired employing identical optical parameters in the microscopy in order to be comparable.

RESULTS AND DISCUSSION

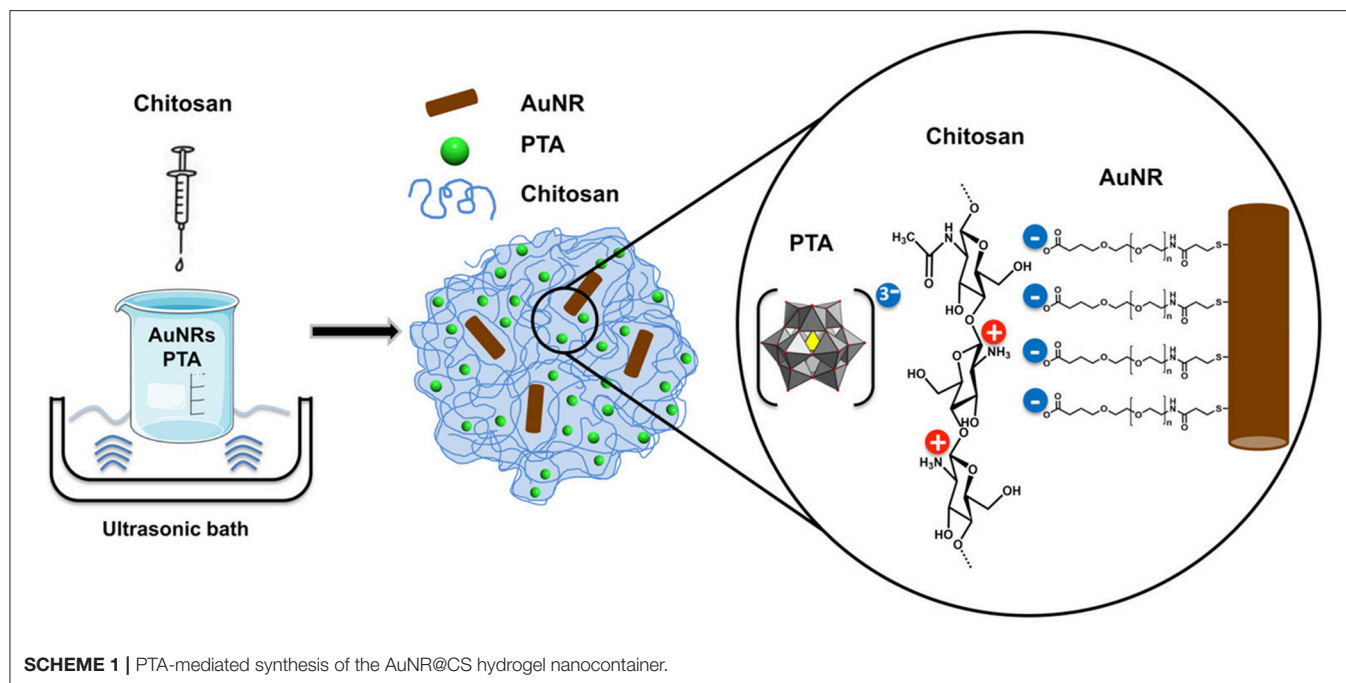
AuNR Entrapment in a Chitosan Hydrogel and Characterisation

The synthesis of high aspect ratio AuNRs was performed following our previously reported seed mediated growth process (Alfranca et al., 2016). AuNRs with a LSPR at 1,040 nm, close to the 1,064 nm wavelength of the laser used in the photothermal therapy and well within the NIR biological window were obtained. This is of great importance because at this wavelength the absorption of light by tissues and cells is highly decreased, meaning that heating will only be produced in the presence of AuNRs and so reducing damage to cells that are not interacting with AuNRs.

The overall aim of entrapping this photothermal agent in the cell-adhesive chitosan was to enhance the AuNR interaction with cells. It has been proven that chitosan possesses excellent mucoadhesive properties enhancing the retention in mucosal tissues (Ways et al., 2018). To take advantage of this property, our hybrid material was synthesized by an ionotropic gelation method, in which the polymer matrix is formed by interaction of the positively charged amino groups in chitosan with a negatively charged gelling agent (See **Scheme 1**). In this case, the gelling agent of choice was the Keggin-type polyoxometalate (POM) phosphotungstic acid (PTA), which gives structural stability to the hydrogel matrix. PTA was chosen based on previous studies illustrating its ability to form spherical and biocompatible nanocapsules (De Matteis et al., 2014).

One of the key advantages of this synthesis method is that it is performed in aqueous solution, making it compatible with all the components involved in the hybrid hydrogel (CS, PTA, and AuNR). The synthesized hydrogel was fully characterized to investigate the chemical composition, structure, and morphology, as well as to confirm the presence of AuNRs in the hydrogel matrix and the suitability of the developed system for its application in photothermal therapy.

FTIR spectroscopy was used to determine the composition of hybrid organic-inorganic matrix. FTIR data in **Figure 1** show the most important vibrational peaks of chitosan: 1,630 (primary amide), 1,414 (–CH₂), 1,375 (–CH₃), and 1,150 cm^{–1} (C–O–C skeletal vibrations). Protonated amino group appears at 1,530 cm^{–1} only for the AuNR@CS, probably due to the fact that in the case of AuNR@CS amino groups are electrostatically interacting with negative charges of PTA and/or PEG in the surface of AuNRs. The presence of the POM is largely masked by the chitosan stretches, but can be confirmed by the appearance of small peaks in the AuNR@CS spectrum below 1,000 cm^{–1}, corresponding to P–O and W=O stretches.



AuNR peaks cannot be observed in the AuNR@CS, because their intensity is too low in comparison with other spectral bands.

The AuNRs possess a distinctive LSPR band at a wavelength of 1,040 nm, which is highly appropriate for PTT using a 1,064 nm NIR laser. Confirmation of the presence of AuNR in the polymer matrix was performed by UV-vis spectrophotometry. This technique shows that the characteristic LSPR peak at 1,040 nm of free AuNR is still present in AuNR@CS, supporting the fact that the plasmonic properties of AuNRs were maintained after their entrapment and that they were not affected by their close proximity within the hydrogel matrix. Both spectra also show an absorbance peak at 505 nm, corresponding to transversal absorbance band of AuNRs.

The amount of gold from AuNR entrapped in the hydrogel was precisely quantified using ICP-AES. Correlating the Au concentration obtained from ICP-AES analysis of the hybrid matrix with the initial amount of Au added in the synthesis, we obtained an encapsulation efficiency (mg of encapsulated AuNR/mg of AuNR initially added $\times 100$) of 61%. Moreover, an AuNR loading (mg of encapsulated AuNR/mg of hydrogel $\times 100$) of 28 % was obtained in the final material.

SEM was used to study the morphology of the hybrid matrix and to confirm the presence of the AuNRs inside the chitosan hydrogel (**Figure 2**). SEM images of the AuNR@CS nanocontainers were obtained by fixing the hydrogel by glutaraldehyde covalent crosslinking. Glutaraldehyde acts as a crosslinker between the amino groups in chitosan polymer chains, rigidifying the hydrogel structure and helping to maintain it under electron microscopy conditions. Using this method sub-micron containers ranging from 200 to 500 nm in diameter were observed, all of them containing AuNRs embedded in their structure (**Figures 2B,C**). From **Figures 2B,C**

it is possible to observe how the polymeric structure was affected by the microscope conditions (high vacuum) even after glutaraldehyde crosslinking. However, in both images polymer residues are clearly observed surrounding the AuNRs. This sub-micrometric size of the hydrogel structure was confirmed by DLS analysis by means of photocorrelation spectroscopy in which a mean hydrodynamic diameter of 475 nm was obtained. The electrophoretic mobility of the container was also evaluated. In this case, a Zeta Potential of +24.4 mV was obtained, which is in agreement with the composition of the hydrogel, whereby protonated amino groups in the chitosan polymer structure confer a positive potential to the material.

Cytotoxicity of AuNR@CS

The cytotoxicity of the hydrogel nanocontainers was assessed prior to further testing and analysis. Increasing concentrations of sterile nanocontainers, from 0, 10, 50, 100 to 200 μg of capsules/mL (measured by dry weight), were incubated with Vero cells for 24 h, washed and the viability of the cells was evaluated by MTT cell viability assay (Supplementary Figure 2). In this assay, NAD(P)H-dependent cellular oxidoreductase enzymes reduce MTT reagent to its purple colored product showing both differences in the number of remained viable cells and their metabolic activity. The lack of any cytotoxicity from AuNR@CS at the highest tested concentration of 200 μg of capsules/mL serves as a first indication of their safety as photothermal agents for future *in vivo* studies.

Heating Profiles

In order to evaluate if the entrapment of AuNR as part of the chitosan hydrogel affected their capability to convert light into heat, identical Au concentrations of AuNR and AuNR@CS diluted in Milli-Q water were compared. Their heating capability

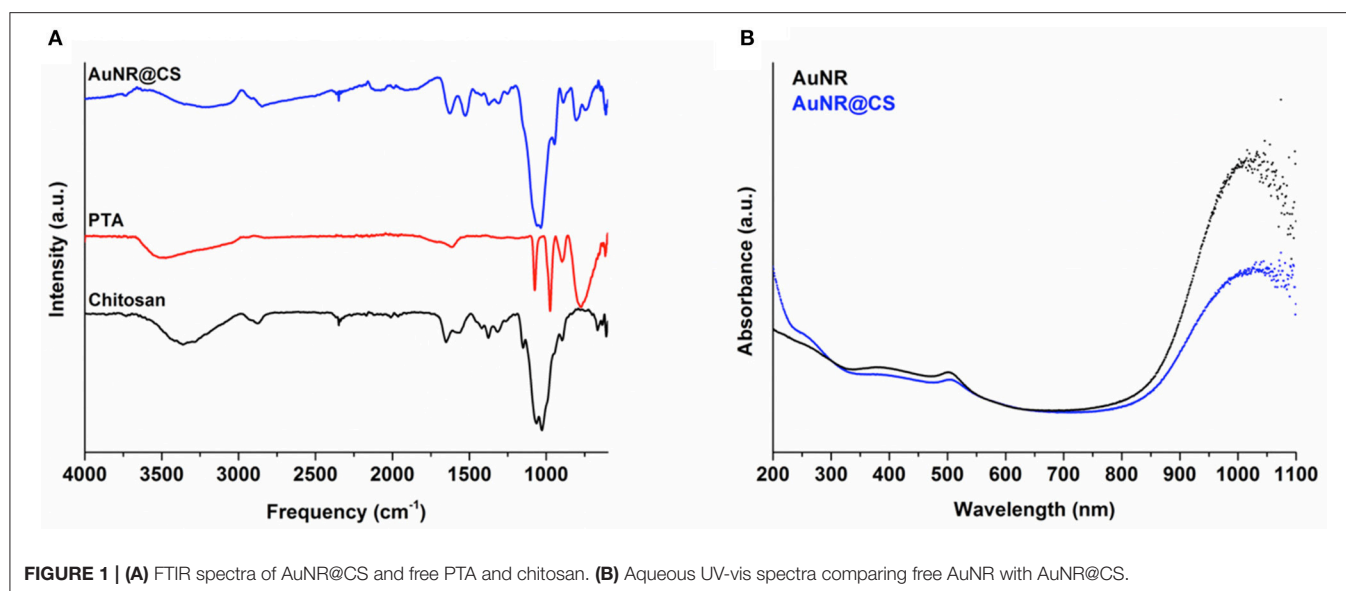


FIGURE 1 | (A) FTIR spectra of AuNR@CS and free PTA and chitosan. (B) Aqueous UV-vis spectra comparing free AuNR with AuNR@CS.

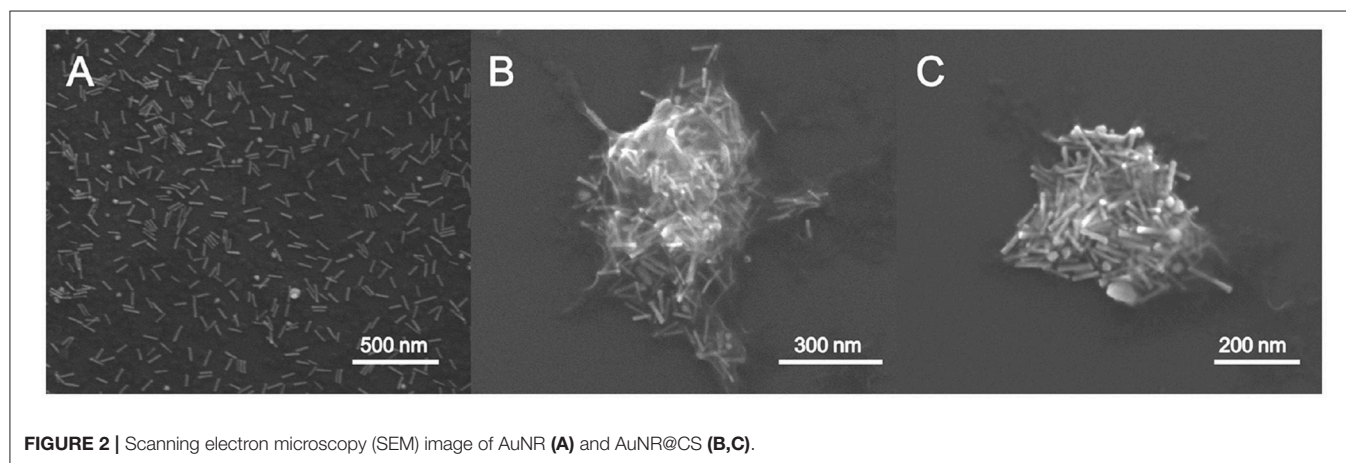


FIGURE 2 | Scanning electron microscopy (SEM) image of AuNR (A) and AuNR@CS (B,C).

was investigated over a 10 min period of irradiation using a 1,064 nm NIR laser operating at 1,100 mW. Compared with the free AuNR, there was only a minor reduction in the initial temperature increase of AuNR@CS (3–7°C/min) as can be seen in **Figure 3**. We attribute this reduction in temperature increase to a combination of thermal insulation caused by the hydrogel and weak interactions between the LSPR bands of other nearby AuNRs. In any case, the final global temperatures following 10 min of irradiation were highly increased both in the case of AuNR and AuNR@CS at all concentrations studied (see **Figure 3B**), compared to water control that only reached $43.4 \pm 1.3^\circ\text{C}$. These results suggested that irradiation at tested conditions should be harmless for cells and biological tissues without nanoparticles and they also demonstrated the suitability of these nanomaterials for photothermal treatment.

The heating power and the heating efficiency (see Materials and Methods section) for each of the tested concentrations were quantified by calculating the initial heating increase per second (See SI, Supplementary Figure 1). As a result, the heating efficiency of AuNRs ranged from 13 to 31% depending on

the concentration studied and from 10 to 27% in the case of AuNR@CS as described in the **Figure 3**.

Improving *in Vitro* Photothermal Therapy of AuNR via Chitosan Entrapment

In previous work we have shown how AuNRs possessed a high potential for photothermal applications due their efficacy as light-to-heat transducers; however, this potential was affected by the fact that AuNR suffer from very poor cellular internalization when compared with other gold nanoparticles (Alfranca et al., 2016). The entrapment of AuNRs in a cationic chitosan hydrogel matrix using an anionic POM as gelling agent allowed us to overcome this limitation for the use of AuNRs in photothermal applications—while simultaneously avoiding the use of complex AuNR surface functionalization strategies. Optical microscopy images taken during the MTT assays illustrated how the AuNR@CS showed a cell-adhesive behavior and confirmed that the AuNR@CS were still interacting with the surface of the cells even after several washing steps, as can be seen in **Figure 4D**.

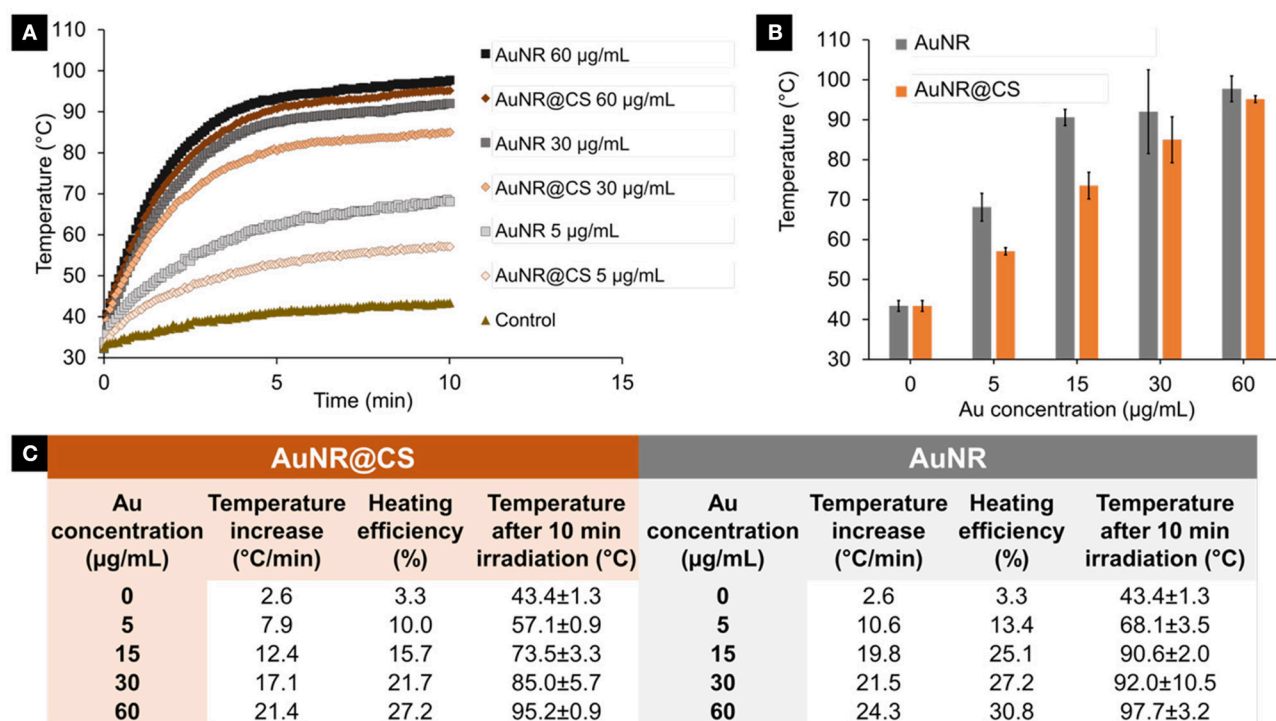


FIGURE 3 | (A) Temperature increase during 10 min irradiation of different concentrations (5–60 µg/ml) of AuNR and AuNR@CS. **(B)** Final temperature after 10 min irradiation of different concentrations of AuNR and AuNR@CS. **(C)** General data table of all tested samples, including concentrations, initial temperature increase, heating efficiency, and final temperature after 10 min irradiation.

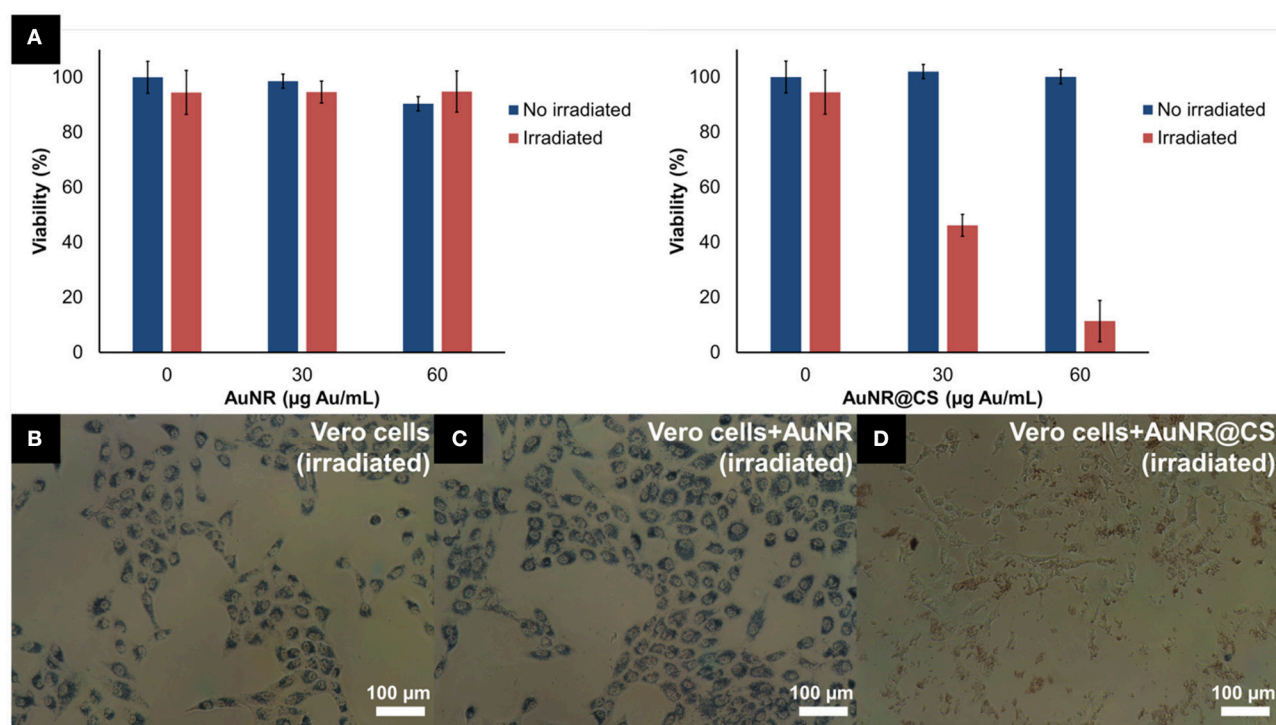


FIGURE 4 | (A) MTT cell viability of Vero cells incubated with different concentrations of AuNR or AuNR@CS 5 h after laser irradiation. **(B–D)** Phase contrast microscopy images of cells during MTT incubation, after irradiation: untreated cells **(B)**, 60 µg/mL of AuNR **(C)**, or 60 µg/mL of AuNR@CS **(D)**.

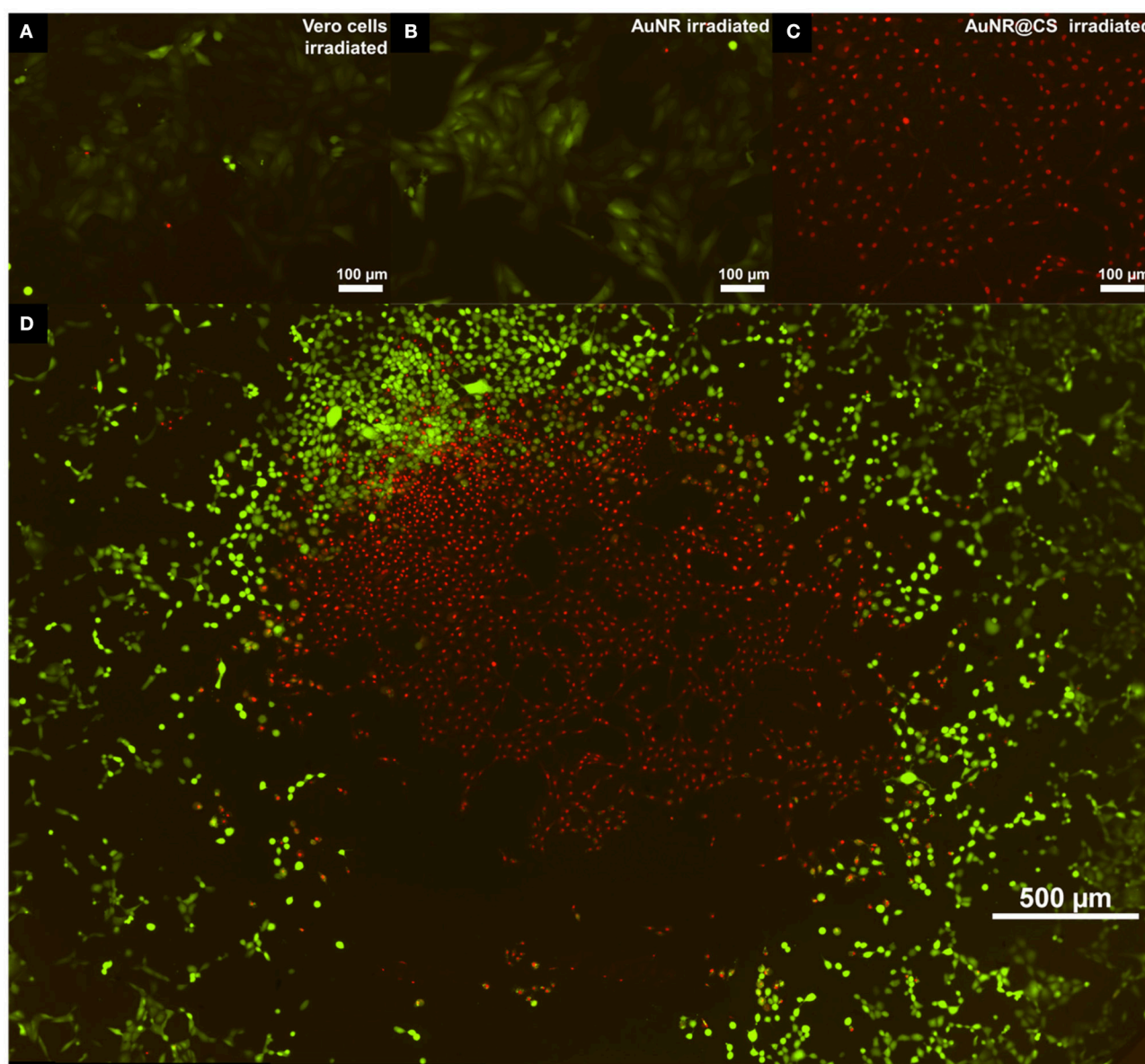


FIGURE 5 | Fluorescent microscopy images of live/dead test 5 h post irradiation of untreated cells (A); treated with 60 µg/mL of AuNR (B); or with 60 µg/mL of AuNR@CS (C). Image (D) shows an entire 96-well irradiation of 60 µg/mL AuNR@CS with the laser adjusted to irradiate only the central part of the well.

The low cytotoxicity combined with cell-adhesive nature of the AuNR@CS make them promising candidates for improving photothermal therapy. The excess of material that was not interacting with cells was removed with PBS before irradiating the cells for 10 min using a 1,064 nm NIR laser operating at 1,100 mW. This allowed a very localized delivery of heat in cells that contained AuNR, or in which AuNRs were interacting with their surfaces. Five hours after irradiation, morphological changes could be clearly seen in the case of cells incubated with AuNR@CS (Supplementary Figure 3); while no morphological changes were observed in the case of irradiated control cells and irradiated cells incubated with AuNR.

MTT cell viability assay was used to quantify the photothermal behavior of AuNR@CS 5 h after irradiation. This study was carried out 5 h after irradiation because at this time the effects of apoptosis or secondary necrosis were observed in previous PTT studies (Pérez-Hernández et al., 2015). The results of these experiments confirmed that there was no associated toxicity of both AuNR and AuNR@CS in non-irradiated cells. The absence of cell death derived from the laser and the AuNR was demonstrated using laser-irradiated control cells (without nanorods) and cells incubated with AuNR, respectively. In contrast, for irradiated cells treated with AuNR@CS the cell viability showed a marked decrease to $46.1 \pm 7.5\%$ at a

concentration of Au entrapped in the hydrogel of 30 $\mu\text{g/mL}$ and a more dramatic decrease ($11.4 \pm 1.7\%$ of unaffected cells) at 60 $\mu\text{g/mL}$ of entrapped Au (corresponding to a dry weight of matrices of 200 $\mu\text{g/mL}$; **Figure 4A**). It should be noted that irradiated cells incubated with AuNR@CS at 60 $\mu\text{g/mL}$ of gold failed to reduce the MTT reagent, indicating severe cellular damage, as observed in **Figure 4**.

To confirm the results and observations from the MTT assay and to study how irradiation of the cells in the presence of the nanomaterials affects the integrity of cell membranes, a commercial LIVE/DEADTM test was carried out 5 h after irradiation (See SI, Supplementary Figure 4). In this test, the intracellular esterase activity of live cells transform calcein AM to the green fluorescent calcein; while ethidium homodimer only enters into dead cells with damaged plasma membranes, increasing its red fluorescence when it interacts with nucleic acids. Irradiated control cells and cells incubated with AuNR displayed only live cells (**Figures 5A,B**, respectively); however, in the case of cells incubated with AuNR@CS the majority of irradiated cells were red stained, indicating cell death (**Figure 5C**). In addition, when the laser was adjusted to irradiate only the central part of the well of cells incubated with AuNR@CS, hyperthermia affected only cells in the irradiated area, while the remaining cells in the well remained alive (**Figure 5D**). These results confirmed that by entrapping the AuNRs in the cell-adhesive chitosan hydrogel we could dramatically increase their efficiency as photothermal agents *in vitro*, thereby turning ineffective free AuNRs into highly applicable nanomaterials. These promising *in vitro* results provide the first lines of evidence that the AuNR@CS nanocontainers present potential application for the treatment of certain tumors. Further, the hybrid composite would be of particular use in intratumoural administration or after surgical removal of tumors, similar to other recent applications of hybrid gold nanoparticle materials (Conde et al., 2016). In addition, these AuNR@CS could be employed for gastrointestinal tumor treatment, as other chitosan hybrid nanomaterials have demonstrated to be able to effectively cross the intestinal epithelia and displayed tumor reduction with longer survival rates *in vivo* (Kang et al., 2017).

CONCLUSIONS

This work describes the development of a simple strategy to significantly increase the efficacy of AuNRs for photothermal therapy applications *in vitro*. Although AuNRs are important class of photothermal nanoparticles, their cellular internalization

is limited and must be increased using complex and time-consuming surface-functionalization techniques. As an alternative strategy, we have entrapped AuNRs in chitosan-based sub-micrometric hydrogels (AuNR@CS) that showed cell-adhesive properties. Importantly, an anionic polyoxometalate (POM) was employed as a gelling agent to control the sub-micrometric size of the hydrogel matrix. In addition, the anionic POM completes the ionic interaction with cationic chitosan to capture the AuNRs as part of the hydrogel. The AuNR@CS showed no cytotoxicity, even at high concentrations; however, laser irradiation of cells treated with AuNR@CS displayed clear signs of necrosis. In contrast, cells treated with free AuNR were completely unaffected, showing almost 100% viability. Consequently, our hydrogel entrapment strategy has increased the *in vitro* efficiency of AuNRs for photothermal therapy applications and could potentially be employed in intratumoural administration, resection of tumors zones after surgery or for oral delivery to treat tumors located in the digestive tract.

AUTHOR CONTRIBUTIONS

ÁA and SG-E performed all the experimental research under the supervision and guidance of LD, SM, and JdIF. All authors were involved in writing the manuscript.

ACKNOWLEDGMENTS

Financial support by the Fundación General CSIC (SM, Programa ComFuturo), Fondo Social Europeo-Gobierno de Aragón and Ministerio de Educación, Cultura y Deportes (ÁA for FPU grant FPU014/06249 and SG-E for FPU grant FPU15/04482) is gratefully acknowledged. The Advanced Microscopy Laboratory of the Universidad de Zaragoza is acknowledged for its technical support. The authors wish to thank J. C. Raposo of the Servicio Central de Análisis de Bizkaia from SGIker of Universidad del País Vasco (EHU) for the ICP-AES technical support.

SUPPLEMENTARY MATERIAL

The Supplementary Material for this article can be found online at: <https://www.frontiersin.org/articles/10.3389/fchem.2018.00234/full#supplementary-material>

Heating profiles of laser irradiated nanomaterials, MTT cell viability assays, phase contrast microscopy, and fluorescence microscopy images of cells treated with AuNRs@CS.

REFERENCES

- Abadeer, N. S., and Murphy, C. J. (2016). Recent progress in cancer thermal therapy using gold nanoparticles. *J. Phys. Chem. C* 120, 4691–4716. doi: 10.1021/acs.jpcc.5b11232
- Alfranca, G., Artiga, Á., Stepien, G., Moros, M., Mitchell, S. G., and de la Fuente, J. M. (2016). Gold nanoprism – nanorod face off : comparing the heating efficiency, cellular internalization and thermoablation capacity. *Nanomedicine* 11, 2903–2916. doi: 10.2217/nnm-2016-0257
- Bao, C., Beziere, N., del Pino, P., Pelaz, B., Estrada, G., Tian, F., et al. (2013). Gold nanoprisms as optoacoustic signal nanoamplifiers for *in vivo* bioimaging of gastrointestinal cancers. *Small* 9, 68–74. doi: 10.1002/sml.201779
- Barz, M. (2015). Complexity and simplification in the development of nanomedicines. *Nanomedicine* 10, 3093–3097. doi: 10.2217/nnm.15.146
- Bijelic, A., Aureliano, M., and Rompel, A. (2018). The antibacterial activity of polyoxometalates: structures, antibiotic effects and future perspectives. *Chem. Commun.* 54, 1153–1169. doi: 10.1039/C7CC07549A

- Bucharskaya, A., Maslyakova, G., Terentyuk, G., Yakunin, A., Avetisyan, Y., Bibikova, O., et al. (2016). Towards effective photothermal/photodynamic treatment using plasmonic gold nanoparticles. *Int. J. Mol. Sci.* 17, 1–26. doi: 10.3390/ijms17081295
- Charan, S., Sanjiv, K., Singh, N., Chien, F.-C., Chen, Y.-F., Nergui, N. N., et al. (2012). Development of chitosan oligosaccharide-modified gold nanorods for *in vivo* targeted delivery and noninvasive imaging by NIR irradiation. *Bioconjug. Chem.* 23, 2173–2182. doi: 10.1021/bc3001276
- Chen, R., Zheng, X., Qian, H., Wang, X., Wang, J., and Jiang, X. (2013). Combined near-IR photothermal therapy and chemotherapy using gold-nanorod/chitosan hybrid nanospheres to enhance the antitumor effect. *Biomater. Sci.* 1, 285–293. doi: 10.1039/C2BM00138A
- Conde, J., Dias, J. T., Grazú, V., Moros, M., Baptista, P. V., and de la Fuente, J. M. (2014). Revisiting 30 years of biofunctionalization and surface chemistry of inorganic nanoparticles for nanomedicine. *Front. Chem.* 2:48. doi: 10.3389/fchem.2014.00048
- Conde, J., Oliva, N., Zhang, Y., and Artzi, N. (2016). Local triple-combination therapy results in tumour regression and prevents recurrence in a colon cancer model. *Nat. Mater.* 15, 1128–1138. doi: 10.1038/nmat4707
- Cooper, D. R., Bekah, D., and Nadeau, J. L. (2014). Gold nanoparticles and their alternatives for radiation therapy enhancement. *Front. Chem.* 2:86. doi: 10.3389/fchem.2014.00086
- De Matteis, L., Mitchell, S. G., and de la Fuente, J. M. (2014). Supramolecular antimicrobial capsules assembled from polyoxometalates and chitosan. *J. Mater. Chem. B* 2, 7114–7117. doi: 10.1039/C4TB01460J
- Dreaden, E. C., Mackey, M. A., Huang, X., Kang, B., and El-Sayed, M. A. (2011). Beating cancer in multiple ways using nanogold. *Chem. Soc. Rev.* 40, 3391–3404. doi: 10.1039/c0cs00180e
- Duan, R., Zhou, Z., Su, G., Liu, L., Guan, M., Du, B., et al. (2014). Chitosan-coated gold nanorods for cancer therapy combining chemical and photothermal effects. *Macromol. Biosci.* 14, 1160–1169. doi: 10.1002/mabi.201300563
- Fan, L., Zhang, Y., Wang, F., Yang, Q., Tan, J., Grifantini, R., et al. (2016). Multifunctional all-in-one drug delivery systems for tumor targeting and sequential release of three different anti-tumor drugs. *Biomaterials* 76, 399–407. doi: 10.1016/j.biomaterials.2016.11.002
- Fiorani, G., Saoncella, O., Kaner, P., Altinkaya, S. A., Figoli, A., Bonchio, M., et al. (2014). Chitosan-polyoxometalate nanocomposites: synthesis, characterization and application as antimicrobial agents. *J. Clust. Sci.* 25, 839–854. doi: 10.1007/s10876-013-0685-x
- Fratila, R. M., Mitchell, S. G., del Pino, P., Grazu, V., and De La Fuente, J. M. (2014). Strategies for the biofunctionalization of gold and iron oxide nanoparticles. *Langmuir* 30, 15057–15071. doi: 10.1021/la5015658
- Han, J., Zhang, J., Yang, M., Cui, D., and de la Fuente, J. M. (2016). Glucose-functionalized Au nanoprisms for optoacoustic imaging and near-infrared photothermal therapy. *Nanoscale* 8, 492–499. doi: 10.1039/C5NR06261F
- Hasenknopf, B. (2005). Polyoxometalates: introduction to a class of inorganic compounds and their biomedical applications. *Front. Biosci.* 10:275. doi: 10.2741/1527
- Huang, Y., Chen, A. C., and Hamblin, M. (2009). Low-level laser therapy: an emerging clinical paradigm. *SPIE Newsroom* 9, 1–3. doi: 10.1117/2.1200906.1669
- Kang, S. H., Revuri, V., Lee, S. J., Cho, S., Park, I. K., Cho, K. J., et al. (2017). Oral siRNA delivery to treat colorectal liver metastases. *ACS Nano* 11, 10417–10429. doi: 10.1021/acsnano.7b05547
- Kharlamov, A. N., Tyurnina, A. E., Veselova, V. S., Kovtun, O. P., Shur, V. Y., and Gabinsky, J. L. (2015). Silica-gold nanoparticles for atheroprotective management of plaques: results of the NANOM-FIM trial. *Nanoscale* 7, 8003–8015. doi: 10.1039/c5nr01050k
- Liu, Y., Yang, M., Zhang, J., Zhi, X., Li, C., Zhang, C., et al. (2016). Human induced pluripotent stem cells for tumor targeted delivery of gold nanorods and enhanced photothermal therapy. *ACS Nano* 10, 2375–2385. doi: 10.1021/acsnano.5b07172
- Liu, Y., Yuan, H., Fales, A. M., Register, J. K., and Vo-Dinh, T. (2015). Multifunctional gold nanostars for molecular imaging and cancer therapy. *Front. Chem.* 3:51. doi: 10.3389/fchem.2015.00051
- Menon, D., Thomas, R. T., Narayanan, S., Maya, S., Jayakumar, R., Hussain, F., et al. (2011). A novel chitosan/polyoxometalate nano-complex for anti-cancer applications. *Carbohydr. Polym.* 84, 887–893. doi: 10.1016/j.carbpol.2010.12.030
- Moros, M., Mitchell, S. G., Grazú, V., and De la Fuente, J. M. (2013). The fate of nanocarriers as nanomedicines *in vivo*: important considerations and biological barriers to overcome. *Curr. Med. Chem.* 20, 2759–2778. doi: 10.2174/0929867311320220003
- Nagpal, K., Singh, S. K., and Mishra, D. N. (2010). Chitosan nanoparticles : a promising system in novel drug delivery. *Chem. Pharm. Bull.* 58, 1423–1430. doi: 10.1248/cpb.58.1423
- Parolo, C., de La Escosura-Muñiz, A., Polo, E., Grazú, V., De La Fuente, J. M., and Merkoçi, A. (2013). Design, preparation, and evaluation of a fixed-orientation antibody/gold-nanoparticle conjugate as an immunosensing label. *ACS Appl. Mater. Interface* 5, 10753–10759. doi: 10.1021/am4029153
- Pérez-Hernández, M., Del Pino, P., Mitchell, S. G., Moros, M., Stepien, G., Pelaz, B., et al. (2015). Dissecting the molecular mechanism of apoptosis during photothermal therapy using gold nanoprisms. *ACS Nano* 9, 52–61. doi: 10.1021/nn505468v
- Polo, E., del Pino, P., Pelaz, B., Grazu, V., and de la Fuente, J. M. (2013). Plasmonic-driven thermal sensing: ultralow detection of cancer markers. *Chem. Commun.* 49, 3676–3678. doi: 10.1039/c3cc39112d
- Shah, H. S., Joshi, S. A., Haider, A., Kortz, U., ur-Rehman, N., and Iqbal, J. (2015). Synthesis of chitosan-coated polyoxometalate nanoparticles against cancer and its metastasis. *RSC Adv.* 5, 93234–93242. doi: 10.1039/C5RA18489D
- Vigderman, L., and Zubarev, E. R. (2013). High-yield synthesis of gold nanorods with longitudinal SPR peak greater than 1200 nm using hydroquinone as a reducing agent. *Chem. Mater.* 25, 1450–1457. doi: 10.1021/cm303661d
- Ways, T. M. M., Lau, W. M., and Khutoryanskiy, V. V. (2018). Chitosan and its derivatives for application in mucoadhesive drug delivery systems. *Polymers* 10:267. doi: 10.3390/polym10030267
- Yamase, T. (2005). Anti-tumor, -viral, and -bacterial activities of polyoxometalates for realizing an inorganic drug. *J. Mater. Chem.* 15:4773. doi: 10.1039/b504585a
- Yang, Z., Liu, T., Xie, Y., Sun, Z., Liu, H., Lin, J., et al. (2015). Chitosan layered gold nanorods as synergistic therapeutics for photothermal ablation and gene silencing in triple-negative breast cancer. *Acta Biomater.* 25, 194–204. doi: 10.1016/j.actbio.2015.07.026
- Yi, H., Wu, L. Q., Bentley, W. E., Ghodssi, R., Rubloff, G. W., Culver, J. N., et al. (2005). Biofabrication with Chitosan. *Biomacromolecules* 6, 2881–2894. doi: 10.1021/bm050410l
- Yin, F., Yang, C., Wang, Q., Zeng, S., Hu, R., Lin, G., et al. (2015). A light-driven therapy of pancreatic adenocarcinoma using gold nanorods-based nanocarriers for co-delivery of doxorubicin and siRNA. *Theranostics* 5, 818–833. doi: 10.7150/thno.11335
- Younes, I., and Rinaudo, M. (2015). Chitin and chitosan preparation from marine sources. Structure, properties and applications. *Mar. Drugs* 13, 1133–1174. doi: 10.3390/md13031133
- Zhang, N., Xu, X., Zhang, X., Qu, D., Xue, L., Mo, R., et al. (2016). Nanocomposite hydrogel incorporating gold nanorods and paclitaxel-loaded chitosan micelles for combination photothermal-chemotherapy. *Int. J. Pharm.* 497, 210–221. doi: 10.1016/j.ijpharm.2015.11.032

Conflict of Interest Statement: The authors declare that the research was conducted in the absence of any commercial or financial relationships that could be construed as a potential conflict of interest.

The handling Editor and reviewer TP declared their involvement as co-editors in the Research Topic, and confirm the absence of any other collaboration.

Copyright © 2018 Artiga, García-Embida, De Matteis, Mitchell and de la Fuente. This is an open-access article distributed under the terms of the Creative Commons Attribution License (CC BY). The use, distribution or reproduction in other forums is permitted, provided the original author(s) and the copyright owner are credited and that the original publication in this journal is cited, in accordance with accepted academic practice. No use, distribution or reproduction is permitted which does not comply with these terms.



Evidence That Speciation of Oxovanadium Complexes Does Not Solely Account for Inhibition of *Leishmania* Acid Phosphatases

Benjamin M. Dorsey, Craig C. McLauchlan* and Marjorie A. Jones*

Department of Chemistry, Illinois State University, Normal, IL, United States

OPEN ACCESS

Edited by:

Soumyajit Roy,
Indian Institute of Science Education
and Research Kolkata, India

Reviewed by:

Alexey Nazarov,
Moscow State University, Russia
Julia Lorenzo,
Universidad Autónoma de Barcelona,
Spain

*Correspondence:

Craig C. McLauchlan
ccmclau@ilstu.edu
Marjorie A. Jones
majone3@ilstu.edu

Specialty section:

This article was submitted to
Inorganic Chemistry,
a section of the journal
Frontiers in Chemistry

Received: 02 February 2018

Accepted: 26 March 2018

Published: 12 April 2018

Citation:

Dorsey BM, McLauchlan CC and
Jones MA (2018) Evidence That
Speciation of Oxovanadium
Complexes Does Not Solely Account
for Inhibition of *Leishmania* Acid
Phosphatases. *Front. Chem.* 6:109.
doi: 10.3389/fchem.2018.00109

Leishmaniasis is an endemic disease affecting a diverse spectra of populations, with 1.6 million new cases reported each year. Current treatment options are costly and have harsh side effects. New therapeutic options that have been previously identified, but still underappreciated as potential pharmaceutical targets, are *Leishmania* secreted acid phosphatases (SAP). These acid phosphatases, which are reported to play a role in the survival of the parasite in the sand fly vector, and in homing to the host macrophage, are inhibited by orthovanadate and decavanadate. Here, we use *L. tarentolae* to further evaluate these inhibitors. Using enzyme assays, and UV-visible spectroscopy, we investigate which oxovanadium starting material (orthovanadate or decavanadate) is a better inhibitor of *L. tarentolae* secreted acid phosphatase activity *in vitro* at the same total moles of vanadium. Considering speciation and total vanadium concentration, decavanadate is a consistently better inhibitor of SAP in our conditions, especially at low substrate:inhibitor ratios.

Keywords: oxovanadium, decavanadate, phosphatase inhibition, *Leishmania*, acid phosphatase, enzyme studies

INTRODUCTION

Leishmania, Leishmaniasis, and Current Treatment Options

Leishmaniasis is defined by the Center for Disease Control and Prevention as a neglected tropical disease carried by the sand fly vector. It affects populations in Asia, India, the Middle East, Africa, Central and South America, and southern Europe. This disease is caused by any of 20 species of the parasitic protozoan *Leishmania* (CCDC, 2013b). Leishmaniasis presents clinically in three forms: visceral, cutaneous, and mucocutaneous (CCDC, 2013b). Over 1.6 million new cases of leishmaniasis are reported yearly (CCDC, 2013b), and current treatment options include: pentavalent antimony salts, amphotericin B, liposomal amphotericin B, ketoconazole, itraconazole, and fluconazole (CCDC, 2013a). Treatments can cost from \$ 20 to \$252 USD per day, and treatments can last from 20 days to 4 months or longer depending on how long it takes for the lesion to heal (Monzote, 2009; CCDC, 2013b). *Leishmania* diseases are becoming more wide spread, and there are few good drug therapies, thus new directions of treatments should be explored.

Polyoxometalates

Polyoxometalates (POM) have been known for many years (Wu, 1920; Dawson, 1953; Pope, 1976; Acerete et al., 1979a,b) with a range of interesting uses (Pope and Müller, 1991). Their use in medicine has also been investigated (Hill et al., 1990a,b; Rhule et al., 1998) and the interaction

with proteins, amino acids, and DNA have been examined (Steens et al., 2010; Goovaerts et al., 2013; Arefian et al., 2017). Of particular interest to this manuscript (*vide infra*), is decavanadate (V_{10} , $V_{10}O_{28}^{6-}$), which has gained recent interest for its biological activity (Aureliano and Gândara, 2005; Aureliano and Crans, 2009; Turner et al., 2012; Aureliano, 2016).

Phosphatases

Phosphatases are hydrolytic enzymes (EC 3.1) that are responsible for the hydrolysis of phosphoesters from substrate producing a phosphate and an alcohol (Bairoch, 2000). Classically, there are three general types of phosphatases; acid phosphatases, neutral phosphatases, and alkaline phosphatases (Vincent et al., 1992; Gani and Wilkie, 1997). These phosphatases are categorized based upon their pH optimum, although alternative classification systems do exist. Most relevant to this work are acid phosphatases. Acid phosphatases (AP) are located, in humans, in the cellular components of bone, spleen, kidney, liver, intestine, and are also found in the blood (Henneberry et al., 1979; Anand and Srivastava, 2012). *Leishmania* have been reported by a number of other laboratories to contain two different genes for secreted acid phosphatases (SAP) (Gottlieb and Dwyer, 1982; Ilg et al., 1994; Fernandes et al., 2013). The pathogenesis of *Leishmania* changes during the life cycle from the amastigote form to the promastigote form of the parasite (CCDC, 2013b). *In vitro* parasites in the stationary phase of their growth curve are more infective to macrophages than are parasites in the logarithmic phase (Mojtahedi et al., 2008; Navabi and Soleimanifard, 2015). It has also been reported that the kinetic parameters of SAP isolated from the *in vitro* stationary phase of *Leishmania major* change, such that the enzymes have a larger V_{max} and a smaller K_m compared to the logarithmic phase enzyme (Fernandes et al., 2013). *Leishmania* SAP are established to play several roles during the life cycle of the parasite, including: aiding in the survival of the parasite in the sand fly alternative host (Baghaei and Mesripour, 2003; Fernandes et al., 2013), and formation of the parasitophorous vacuole, thus preventing macrophages from forming hydrogen peroxide (Baghaei and Mesripour, 2003). Thus, *Leishmania* SAP are of interest as potential pharmaceutical targets for the treatment of leishmaniasis.

L. Tarentolae Secreted Acid Phosphatase Enzymes

Leishmania tarentolae serves as a good model system for the investigation of the two *Leishmania* SAP for several reasons. First, *L. tarentolae* are easy to grow, and their growth in culture is easily assessed (Morgenthaler et al., 2008). *L. tarentolae* do not infect humans, thus lowering the risk for investigators. *L. tarentolae* have utility in the macrophage model system used to assess infectivity. Finally, *L. tarentolae* are sensitive to current treatment options, thus therapeutics that are effective in this model system may also be potentially effective for work the human parasite, *L. major* (Taylor et al., 2010).

Using acid phosphatase amino acid sequence alignment from rat (*Rattus norvegicus* EC3.1.3.2, PDB 1rpt) as a comparative model to *Leishmania* SAP, it can be seen that there is overlap

between the reported vanadate binding residues in the *R. norvegicus* and the *L. mexicana* acid phosphatases (SAP1L.mex gene accession number Z46969.1 and SAP2L.mex gene accession number Z46970.1) as shown in **Figure 1**. The gray and purple highlights are the amino acids reported to be in the active site of these acid phosphatases. Gray highlights indicate different, but similar, amino acids between species. Purple highlights indicate identical amino acids between species. Using the amino acid numbering from *R. norvegicus*, the following residues (Arg11, His12, Arg15, Arg79, His257, and Asp258) is also sometimes indicated; Lindqvist et al., 1994) are responsible for coordinating vanadate, and are highlighted in blue in **Figure 1**. In the structure of AP from *R. norvegicus* (Lindqvist et al., 1994), His12 directly coordinates to vanadium, whereas the other residues indicated are all involved in secondary interactions.

Vanadium Background, Vanadium Human Exposure, Vanadium Chemistry, and Speciation

The typical total amount of vanadium in humans is about 1 mg (Rehder, 2013). Vanadium is a very versatile element and has five common oxidation states available, with the vanadium (V) oxidation state being the overwhelmingly dominant species in aqueous solution under typical pH and reduction potential conditions (Baes and Mesmer, 1976; Crans et al., 2004). Vanadium forms covalent adducts with oxygen, which produce numerous different species of vanadium in its (V) oxidation state as a function of pH (**Figure 2**), including a broad variety of polyoxometalates (POMs; Baes and Mesmer, 1976). This speciation is of critical importance when examining aqueous vanadium solutions (Levina et al., 2017).

Speciation of vanadium, specifically decavanadate speciation in acidic media, has been investigated (**Figures 2, 3**; Baes and Mesmer, 1976). It is clear that under acidic conditions, protonation status changes either by deprotonation or cation exchange with the medium, and vanadium speciation is a function of vanadium concentration, solution pH, and ionic strength of the solution (Rossotti and Rossotti, 1956; Corigliano and Di Pasquale, 1975; Baes and Mesmer, 1976; Crans et al., 2004). Because of this, vanadium speciation, degree of protonation, and degree of proton displacement by cations in solution are likely different for solutions of different composition. Therefore, when using decavanadate or orthovanadate as inhibitors of phosphatases under assay conditions (often involving various buffers and cell growth media), it is not always clear what species are present, or what species are responsible for inhibition of the enzyme being assayed.

Vanadium Is a Potential Medicinal Agent as a Phosphatase Inhibitor

It is well known that oxovanadium species act as phosphatase inhibitors with varying efficacy (Van Etten et al., 1974; Abbott et al., 1979; Knowles, 1980; Gresser et al., 1987; Gordon, 1991; Li et al., 2008; Crans, 2015; McLauchlan et al., 2015). How vanadium acts as a phosphatase inhibitor is thought to be through the action of a vanadium (V) monomeric oxyanion,

SAP1L.mex	1	MASRLVRVLAAAMLVAAAVSVDARFVVRMVQVVHRRHGARSALIDDNTTEICGTLYP--CG
SAP2L.mex	1	MASRLVRVLAAAMLVAAAVSVDARFVVRMVQVVHRRHGARSALIDDNTTEICGTLYP--CG
APR.norvegicus	1	-----KELKFVTLVFRHGD RGPIETFPNDPIKES SWPQGF G
SAP1L.mex	59	ELTGEGVEMVRAIGEFARSRYNNLSLVESPLFPSTRYNSSVVHTRSTHTQRTIQSATAFL
SAP2L.mex	59	ELTGEGVEMVRAIGEFARSRYNNLSLVESPLFPSTRYNSSVVHTRSTHTQRTIQSATAFL
APR.norvegicus	37	QLTKWGMGQHYELGSYIRRRYGR-----FLNNSYKHDQVYIRSTD VD RTIMSAMTNL
SAP1L.mex	275	SPSYNMFQYSAHDTT VT PLAVTFGDQGETTMRPPFAVTIFVELLQDTADASGWYVRLIRG
SAP2L.mex	275	SPSYNMFQYSAHDTT VT PLAVTFGDQGETTMRPPFAVTIFVELLQDTADASGWYVRLIRG
APR.norvegicus	246	QKARKLIMYSAHDTT VS GLQMALDVYNG--LLPPYASCHIMELYQDNG---GHFVEM---

FIGURE 1 | Multiple sequence alignment of three acid phosphatases. This sequence alignment was completed using Kalign (Lassmann and Sonnhammer, 2005) and the BoxShade Server (Hoffmann and Baron, 2014). Gray highlights indicate different, but similar, amino acids between species. Purple highlights indicate identical amino acids between species. Blue text indicates likely residues for coordinating vanadate.

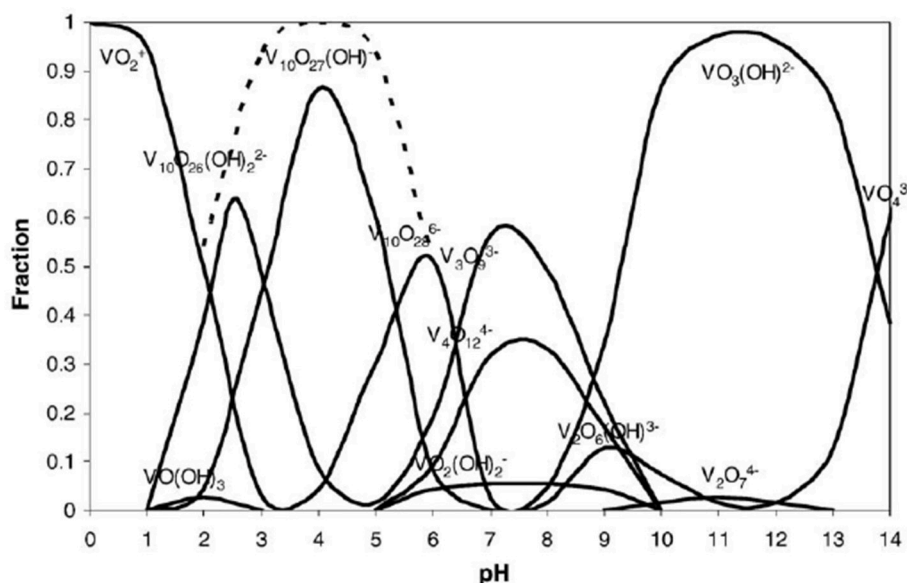


FIGURE 2 | Vanadium (V) speciation as a mole fraction of total vanadium present at a given pH, over the typical pH scale (0–14). This speciation diagram is for a 0.1 molal vanadium solution. Reproduced from Baes and Mesmer (1976) with permission from Wiley and Sons.

vanadate, mimicking a five-coordinate high energy intermediate of the transition state phosphate, therefore behaving as a competitive inhibitor (Van Etten et al., 1974; Abbott et al., 1979; Knowles, 1980; Gresser et al., 1987; Gordon, 1991; Li et al., 2008; Crans, 2015; McLauchlan et al., 2015). There are numerous crystal structures of phosphatases, with nitrogen-containing, oxygen containing, or sulfur-containing active site amino acids deposited in the Protein Data Bank (Berman et al., 2000), that have been recently reviewed (Crans, 2015; McLauchlan et al., 2015). These phosphatases function to hydrolyze esters, phosphoesters, and phosphoanhydrides. These crystal structures had been determined from crystals soaked with vanadium complexes; the majority of experiments using orthovanadate, at pH values ranging from 5.40 to 8.00. The overwhelming majority of these phosphatases, regardless of the type of active

site amino acid residues (O-, N-, or S-containing), have a monomeric form of vanadium (VO_3^{1-} or VO_4^{3-}) present in the phosphatase active site upon solving the crystal structure. It should be noted at the employed concentrations of vanadium and in this pH range, that di-, tri-, and tetrameric vanadium species V_2 , V_3 , and V_4 (Figure 3), respectively, are predicted (Baes and Mesmer, 1976; Rigden et al., 2003; Crans, 2015; McLauchlan et al., 2015) to be the major forms of vanadium present, and not the monomeric form(s) that are reported in the enzyme's active site. Thus, there is a discrepancy between what one might hypothesize about the species responsible for inhibition (the major species present may be responsible for the inhibition), and what one actually finds (a minor species present may be responsible for the inhibition). There may also be speciation ambiguities under experimental conditions using

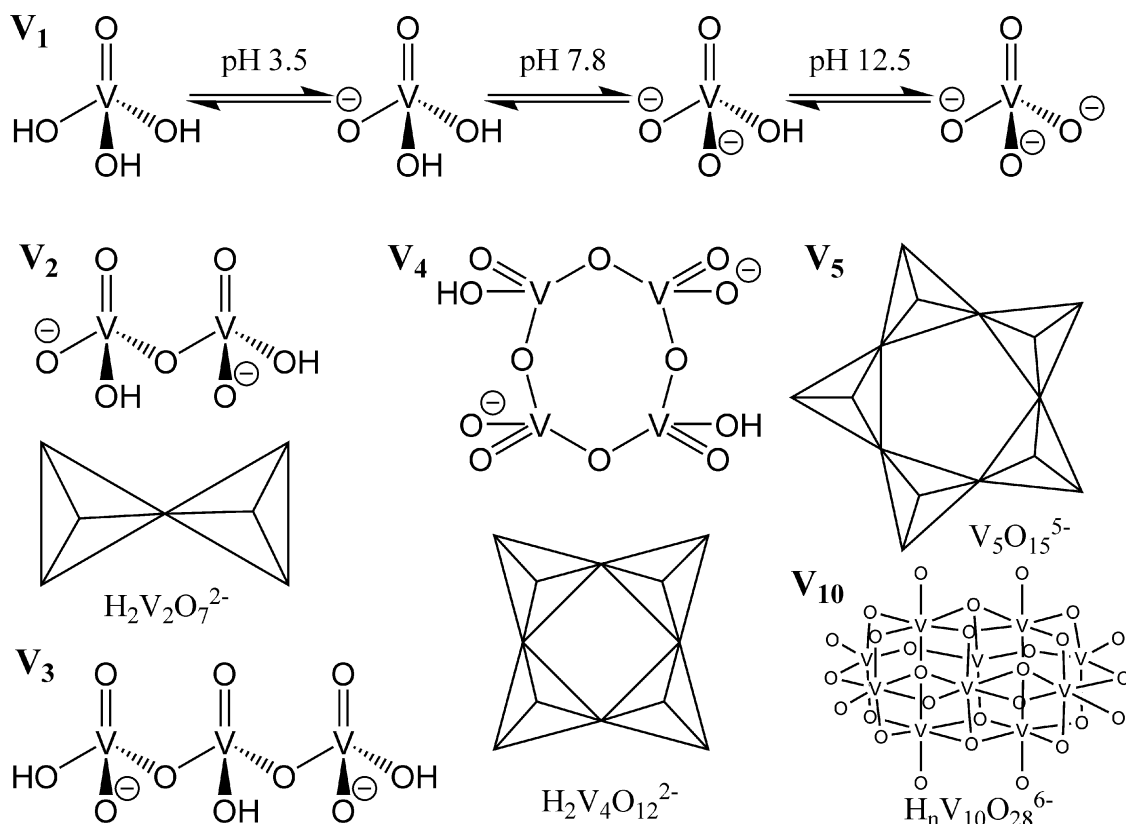


FIGURE 3 | Representation of common vanadium polyoxometalates in aqueous solution. Reproduced with permission from McLauchlan et al. (2015) with permission from Elsevier.

solutions of a complex nature that are not easily resolved by current predictors of vanadium speciation. Regardless, it is thought that these monomeric species are likely responsible for phosphatase inhibition. There is, however, a likely discrepancy between solid state speciation of vanadium that occurs under soaking conditions, and aqueous speciation of vanadium that occurs in enzymatic assays because crystal dynamic conditions are likely to be different than those of the more flexible protein under enzymatic assay conditions in terms of pH, ionic strength, and vanadium concentration. Therefore, the species of vanadium present in enzymatic assays cannot necessarily be assumed to be the same as the species present after crystal soaking experiments. To further stress the importance of speciation, crystallographic soaking studies that used metavanadate (50 mM) starting material, under acidic conditions (pH 5.0) produced protein crystals of *Bacillus stearothermophilus* phosphatase with trivanadate, $V_3O_8^{2-}$ (V_3), located in the putative active site, when the authors had expected to find orthovanadate, VO_4^{3-} (PDB ID 1h2f.) (Rigden et al., 2003).

We have previously reported that a number of vanadium compounds (including orthovanadate, decavanadate, and complexes with picolinate or imidazolyl-carboxylate as ligands) negatively affect *L. tarentolae* viability as well as secreted acid phosphatase activity *in vitro* (Turner et al., 2012; Mendez et al., 2014). However, in those studies we did not address the potential

problem of speciation. To further investigate the ambiguities of vanadium speciation and phosphatase inhibition, we used a previously published model (Baumhardt et al., 2015) involving plotting the log of substrate divided by inhibitor effects on product formation; this model was demonstrated to be useful for comparing competitive enzyme inhibitors. Thus, here we use the model to compare decavanadate ($V_{10}O_{28}^{6-}$, V_{10}) and orthovanadate (VO_4^{3-} , V_1) as *in vitro* inhibitors of *L. tarentolae* SAP. Several studies of anti-trypanosomal (Urquiola et al., 2006; Benítez et al., 2009; Gambino, 2011; Demoro et al., 2012; Fernández et al., 2013) and anti-leishmanial (Turner et al., 2012; Adiazola et al., 2014; Mendez et al., 2014; Machado et al., 2015; Christensen et al., 2016) activity of vanadium complexes have been reported. The current studies can give insight into the clinical use of these and other vanadate complexes as anti-*Leishmania* therapies.

EXPERIMENTAL

Materials and Methods

Cell Culture of *L. tarentolae* and Assessment of Cell Viability by the MTT Viability Assay

L. tarentolae (ATCC 30143) promastigote cells were sterilely grown in brain heart infusion medium (BHI; 37.0 g/L) supplemented with hemin (10 μ M), penicillin (10,000 units/mL),

and streptomycin (10 mg/mL) following the methods of Morgenthaler et al. (2008). *L. tarentolae* cell viability was assessed by the 3-(4,5-dimethylthiazol-2-yl)-2,5-diphenyltetrazolium bromide (MTT) viability assay (Mosmann, 1983). The MTT assay serves as a quantitative measure (A595 nm) of cell mitochondrial activity, and therefore indirectly monitors cell viability. Sample absorbance at A595 nm was determined with an iMark microplate reader (BioRad Laboratories, Hercules, CA). The BHI growth medium alone was considered as a blank value subtracted from the sample absorbance (BHI and cells). Results are reported as corrected absorbance (A595 nm/Hr incubation with MTT reagent, or A595 nm/Hr incubation with medium only) mean \pm standard deviation (SD) for $n = 4$ replicates. In this work, the parasites were grown at room temperature in 25 cm² canted flasks (Corning, Inc.; Product number 430372). Samples for assessment by MTT assay were collected daily using sterile technique.

Preparation of the *L. tarentolae* Acid Phosphatase Enzyme Source

A sample of *L. tarentolae* from each stage of the growth curve (lag, log, stationary, and senescence) was collected and centrifuged (2,000 \times g, 10°C, 10 min). The supernatant was collected and stored on ice until it was used for acid phosphatase enzyme assays.

Secreted Acid Phosphatase Enzyme Assay

SAP activity was evaluated using *para*-nitrophenyl phosphate (pNPP, Sigma Aldrich) as substrate following the method of Mendez et al. (2014). This assay at room temperature was performed in 1.5 mL polypropylene tubes in a total reaction volume of 0.9 mL. Sodium acetate buffer (500 μ L, 0.5 M, pH 4.5) was used. The enzyme source was *L. tarentolae* cell supernatant from the log phase of the growth curve (300 μ L). Then 100 μ L substrate (5 mg pNPP/1 mL buffer; 20 mM), made in sodium acetate buffer (0.5 M, pH 4.5) was added to start the reaction. After room temperature incubation for 23 h (under apparent first order conditions), the reaction was stopped with addition of 100 μ L of 10 M sodium hydroxide, and samples were vortexed. Product formation was measured by spectroscopy at A405 nm. BHI was used to replace enzyme source for spectrophotometric blanks. Data are reported as corrected absorbance (A405 nm) per day in culture. Product (*para*-nitrophenolate) was calculated from corrected A405 nm/23 h by dividing by molar absorptivity (18,000 cm⁻¹ M⁻¹) and reported as μ M/ 23 hr.

Secreted Acid Phosphatase Enzyme Inhibition Assay

To determine which form of vanadium is a better inhibitor, decavanadate, or orthovanadate, of *L. tarentolae* secreted acid phosphatase enzyme activity the method of Baumhardt et al. (2015) was used. Using the previously determined K_M substrate concentration of 391 μ M (Mendez et al., 2014), the log ratio of substrate to total vanadium concentration in the assay was calculated for either orthovanadate or decavanadate (as shown in Table 1).

Table 1 indicates the relationship between the log of substrate to inhibitor ratio to the total moles of vanadium, or the total

TABLE 1 | The concentrations of vanadium (I) used as either total vanadium, or orthovanadate, or decavanadate in each sample.

Sample	log[S]/[I]	[Total Vanadium] μ M	[Decavanadate] μ M	[Orthovanadate] μ M
1	-2.0	39,100	3,910	39,100
2	-1.5	12,400	1,240	12,400
3	-1.0	3,910	391	3,910
4	-0.5	1,240	124	1,240
5	0.0	391	39.1	391
6	0.5	124	12.4	124
7	1.0	39.1	3.91	39.1
8	1.5	12.4	1.24	12.4
9	2.0	3.91	0.391	3.91

Substrate was constant at 391 μ M in all assays.

moles of decavanadate, or the total moles of orthovanadate in the assay. It should be noted that for every mole of orthovanadate, there is one mole of vanadium. For every mole of decavanadate, there are 10 moles of vanadium. Thus, orthovanadate was used at 10 times the molar concentration of decavanadate, but the total moles of vanadium from either compound, in the assay, was the same as listed in Table 1.

The order of addition of material to the assay was as follows: Sodium acetate buffer (0.5 M, pH 4.5 from Fisher Scientific), vanadium as either sodium orthovanadate (Acros Organics) or ammonium decavanadate (as synthesized by Turner et al., 2012) freshly prepared in assay buffer, and enzyme source (300 μ L of log phase *L. tarentolae* cell supernatant) were added to the assay and allowed to preincubate at room temperature for 10 min. Following substrate addition, assays were incubated at room temperature for 23 h. To stop the reaction, sodium hydroxide (100 μ L, 10 M) was added and the samples were vortexed. Product was evaluated by spectroscopy at A405 nm. Spectrophotometric blanks were prepared using the same volumes of assay buffer, vanadium as either orthovanadate or decavanadate, and substrate as experimental samples. The enzyme source was replaced with brain heart infusion, the same medium the enzyme was in for kinetic and inhibition assays. Data are reported as mean \pm standard deviation for $n = 4$ replicates.

UV-Visible Comparison of Decavanadate to Orthovanadate

To assess if samples containing starting material decavanadate or starting material orthovanadate (same total vanadium concentration between samples being compared) are different by electronic absorption (UV-Visible) spectroscopy, samples were prepared ($n = 3$ replicates). The sample contents were identical to those used in the Baumhardt et al. (2015) inhibition studies (Table 1). However, enzyme source was replaced with BHI medium, and substrate was replaced with an equal volume of assay buffer. Samples were prepared, allowed to rest for 23 h, and then samples were evaluated by spectroscopy. Local maxima that were consistently present, but whose amplitude changed with changes in total vanadium concentration, between all samples were identified and used to compare samples containing the same

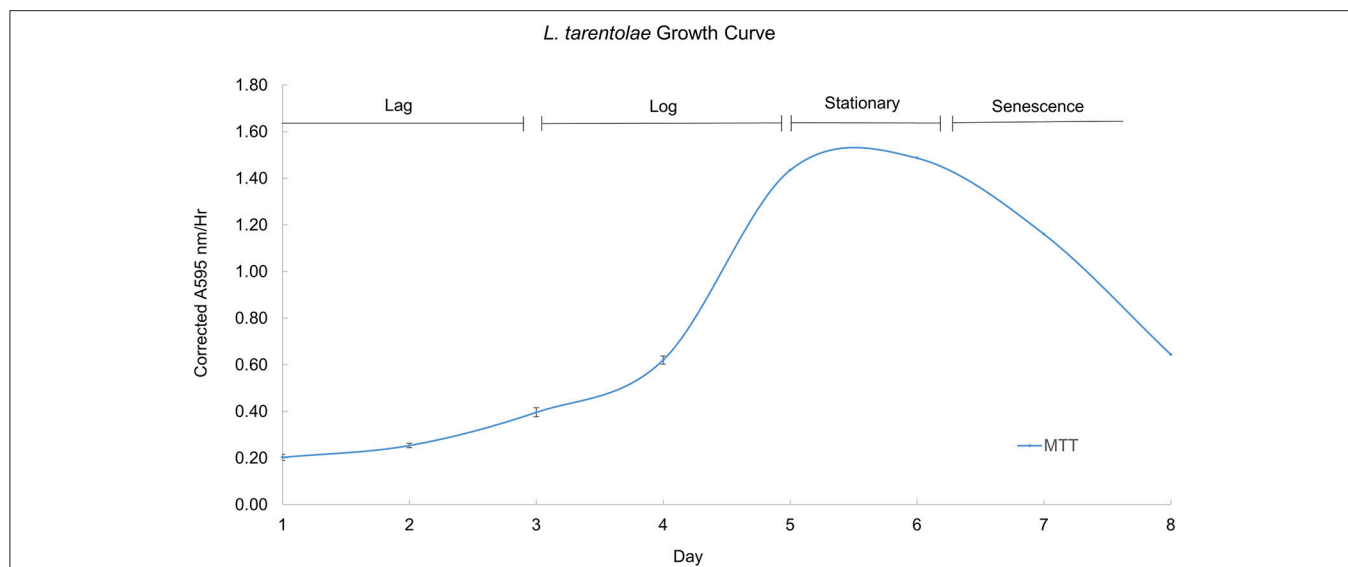


FIGURE 4 | A typical growth curve for *L. tarentolae* with the corrected MTT response plotted on the Y-axis and the day in culture plotted on the X-axis. The lag phase occurs on days 1–3. The log phase occurs on days 4–5. The stationary phase occurs between days 5 and 6. The senescence phase occurs on days 6–8. Each point is the mean \pm standard deviation of $n = 4$ replicates.

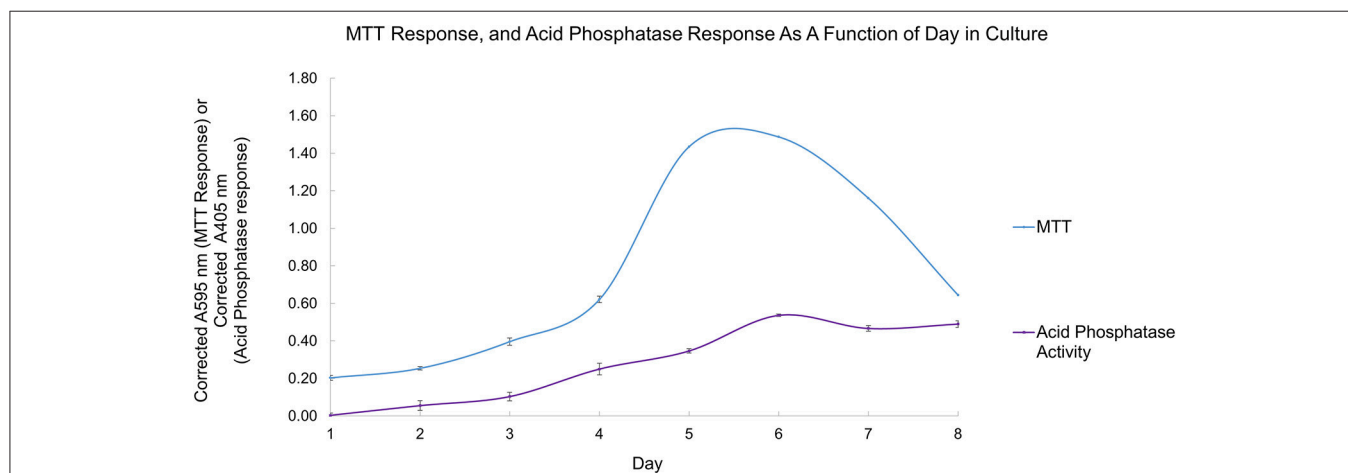


FIGURE 5 | Secreted acid phosphatase activity detected as a function of day in culture (purple curve). The typical *L. tarentolae* growth curve evaluated by MTT response (blue curve). Each point is the mean \pm standard deviation of $n = 3$ replicates (secreted acid phosphatase assay) or $n = 4$ (MTT response).

total vanadium concentration either as decavanadate starting material or orthovanadate starting material.

RESULTS AND DISCUSSION

Cell Culture of *L. tarentolae* and Assessment of Cell Viability by the MTT Viability Assay

During their growth curve, *L. tarentolae* respond in a predictable manner to the MTT reagent. This predictable and repeatable response is useful as a metric because it gives a context for normal *L. tarentolae* behavior, and serves a reference point from which enzyme pools, whole cells or cell supernatant, are collected.

Furthermore, knowing what phase of the growth curve cells are in is useful because it allows more accurate interpretation of an effective potential treatment. **Figure 4** shows a typical growth curve with the four characteristic phases of *in vitro* cell growth exhibited by *L. tarentolae*.

Secreted Acid Phosphatase Enzyme Assay

Using the growth curve as a reference point, detectable secreted acid phosphatase activity tracks with the MTT response up to day 6, as shown in **Figure 5**. When the cells' response to the MTT reagent decreases, the detectable secreted acid phosphatase activity plateaus (days 6–8). Secreted acid phosphatase activity for *L. tarentolae* supernatant is detectable on all 8 days of a typical

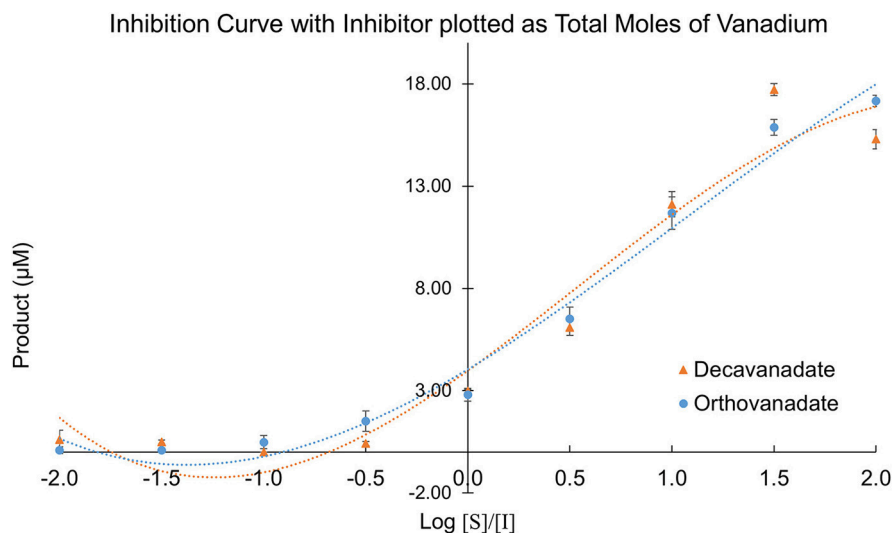


FIGURE 6 | *L. tarentolae* secreted acid phosphatase enzyme activity (Y-axis) when incubated with decavanadate (orange curves) or orthovanadate (blue curves) plotted as a function of $\log [S]/[I]$ (X-axis). $[I]$ is total molarity of vanadium. This plot assumes complete speciation of decavanadate to orthovanadate.

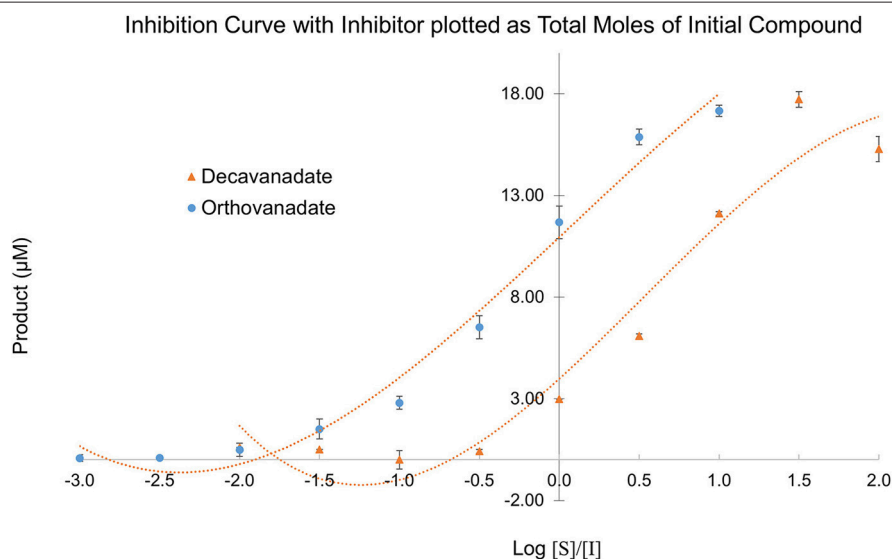


FIGURE 7 | *L. tarentolae* secreted acid phosphatase enzyme activity (Y-axis) when incubated with decavanadate (orange curves) or orthovanadate (blue curves) plotted as a function of $\log [S]/[I]$ (X-axis). $[I]$ is molarity of starting compound. This plot assumes no speciation of either decavanadate or orthovanadate occurs.

L. tarentolae growth curve. Because the log phase is likely the most relevant phase to the *Leishmania* infection cycle, log phase supernatant was used for the inhibition and spectroscopic studies in this work.

Secreted Acid Phosphatase Enzyme Inhibition Assays

Owing to the complexity of the enzyme pool, the relative amounts of mono-, di-, tri-, tetra-, penta-, or deca-nuclear vanadium present in assay are not known. Standard speciation diagrams would indicate that under our secreted acid phosphatase assay conditions ($\text{pH} = 4.5$), the main form of vanadium

present is decavanadate (Figure 2; Baes and Mesmer, 1976), whereas computational models typically indicate that V1 is the main species present at total vanadium concentrations in the single micromolar range. When plotting *L. tarentolae* secreted acid phosphatase enzyme activity (Y-axis) incubated with decavanadate (orange curves) or orthovanadate (blue curves) as a function of $\log [S]/[I]$ as X-axis, where $[I]$ is either total moles of decavanadate or orthovanadate, there are three conditions where decavanadate or orthovanadate resulted in different effects from control and each other (Figure 6). These conditions are statistically significant ($\alpha = 0.05$ in a paired, two-tailed *t*-test). These conditions occur when the

TABLE 2 | Electronic absorption (UV-Visible) results at 375 nm after 24 h of incubation.

Total vanadium (μM)	Molarity of starting material	Mean corrected A ₃₇₅ nm	p-value	Statistically different?
39,100	3,910 39,100	1.423 1.440	0.038	Yes
12,400	1,240 12,400	0.713 0.719	0.210	No
3,910	391 3,910	0.465 0.261	0.001	Yes
1,240	124 1,240	0.380 0.071	0.384	No
391	391 391	0.019 0.019	1.000	No
124	1.24 124	0.005 0.015	0.109	No
39.1	3.91 39.1	0.000 0.000	N/A	N/A
12.4	1.24 12.4	0.001 0.003	0.742	No
3.91	0.391 3.91	0.000 0.002	0.423	No

Total vanadium concentration used in spectroscopic assays, the starting amount of either decavanadate (orange shading) or orthovanadate (no shading), the corrected mean absorbance value at a single wavelength, and the calculated p-value. The statistical threshold ($\alpha = 0.05$) is used in regards to the comparison between the samples containing decavanadate starting material as compared to the samples containing orthovanadate starting material.

TABLE 3 | Electronic absorption (UV-Visible) results at 405 nm after 24 h of incubation.

Total vanadium (μM)	Molarity of starting material	Mean Corrected A ₄₀₅ nm	p-value	Statistically different?
39,100	3,910 39,100	1.577 1.603	0.094	No
12,400	1,240 12,400	0.791 0.801	0.023	Yes
3,910	391 3,910	0.368 0.180	0.001	Yes
1,240	124 1,240	0.078 0.052	0.014	Yes
391	391 391	0.015 0.015	0.742	No
124	1.24 124	0.006 0.019	0.160	No
39.1	3.91 39.1	0.000 0.004	0.187	No
12.4	1.24 12.4	0.004 0.007	0.524	No
3.91	0.391 3.91	0.000 0.000	0.155	No

Total vanadium concentration used in spectroscopic assays, the starting amount of either decavanadate (orange shading) or orthovanadate (no shading), the corrected mean absorbance value at a single wavelength, and the calculated p-value. The statistical threshold ($\alpha = 0.05$) is used in regards to the comparison between the samples containing decavanadate starting material as compared to the samples containing orthovanadate starting material.

$\log[S]/[I]$ ratio is equal to -0.5 , 1.5 , or 2.0 . Orthovanadate is a better inhibitor in two of these conditions ($\log[S]/[I] = -0.5$ or 2.0), and the polyoxometalate decavanadate is a better inhibitor in one condition ($\log[S]/[I] = 1.5$). Plotting the $\log[S]/[I]$ as X-axis in this manner treats decavanadate as if it undergoes complete speciation to orthovanadate. When plotting *L. tarentolae* secreted acid phosphatase enzyme activity as Y-axis, incubated with decavanadate (orange curves) or orthovanadate (blue curves), as a function of $\log[S]/[I]$ (X-axis), where $[I]$ is total moles of starting compound, there are six conditions where decavanadate or orthovanadate resulted in different effects from control and each other (Figure 7). These conditions are statistically significant ($\alpha = 0.05$ in a paired, two-tailed *t*-test). These conditions occur when the $\log[S]/[I]$ ratio is equal to -1.5 , -1.0 , -0.5 , 0.0 , 0.5 , or 1.0 . It should be noted that at $\log[S]/[I] = -3.0$ and -2.5 , there were no decavanadate values for product formation to compare to the orthovanadate samples, and at $\log[S]/[I] = 1.5$ and 2.0 , there are no orthovanadate values to compare to the decavanadate values.

Despite the complex equilibrium dynamics of vanadium in aqueous solutions which might lead one to predict different speciation depending on the starting conditions, it is predicted

that at micromolar concentrations, decavanadate will undergo speciation completely to orthovanadate (Rehder, 2008). In such a case, we should expect to see identical experimental results for sufficiently low total concentrations of vanadium, independent of the choice of either orthovanadate or decavanadate starting material. Even with identical total moles of vanadium, though, we see differing values depending on the starting species. Decavanadate is a better inhibitor in all six of these experimental conditions. Plotting the data in this manner treats decavanadate and orthovanadate as if neither compound undergoes any speciation. Under this assumption, decavanadate is consistently better at inhibiting *L. tarentolae* secreted acid phosphatase activity on a mole of compound basis.

These plots represent the extremes of speciation: complete speciation of vanadium to overwhelmingly one form (Figure 6) or no speciation of vanadium (Figure 7), leaving either decavanadate or orthovanadate completely intact. We recognize that the accurate description of what occurs to these vanadium complexes under SAP assay conditions likely lies in between the extremes depicted. As mentioned previously, multiple factors affect oxovanadium speciation. The interpretation of these data to answer the question, which oxovanadium complex is best

TABLE 4 | Electronic absorption (UV-Visible) results at 415 nm after 24 h of incubation.

Total vanadium (μM)	Molarity of starting material	Mean corrected $A_{415\text{ nm}}$	p-value	Statistically different?
39,100	3,910 39,100	1.690 1.720	0.000	Yes
12,400	1,240 12,400	0.841 0.856	0.033	Yes
3,910	391 3,910	0.330 0.155	0.001	Yes
1,240	124 1,240	0.069 0.046	0.029	Yes
391	391 391	0.013 0.013	0.742	No
124	1.24 124	0.003 0.018	0.702	No
39.1	3.91 39.1	0.000 0.007	0.423	No
12.4	1.24 12.4	0.004 0.003	0.957	No
3.91	0.391 3.91	0.000 0.004	0.423	No

Total vanadium concentration used in spectroscopic assays, the starting amount of either decavanadate (orange shading) or orthovanadate (no shading), the corrected mean absorbance value at a single wavelength, and the calculated p-value. The statistical threshold ($\alpha = 0.05$) is used in regards to the comparison between the samples containing decavanadate starting material as compared to the samples containing orthovanadate starting material.

at inhibiting *L. tarentolae* SAP activity, is largely a function of being able to solve the speciation dilemma under our assay conditions. Currently, it is reported that decavanadate is thermodynamically unstable at micromolar concentrations and undergoes speciation almost entirely to orthovanadate (Rehder, 2008). Therefore, orthovanadate was used at 10 times the molar concentration as decavanadate as a control to see the difference in impact of V_1 vs. V_{10} . The equilibria expressions describing the speciation of decavanadate to orthovanadate, however, are non-linear. Thus, it does not suffice to use orthovanadate at 10 times the concentration of decavanadate. When using orthovanadate at 10 times the molar concentration as decavanadate, and comparing samples with the same total moles of vanadium, our UV-Visible spectroscopic data indicate that at multiple local maxima (A375 nm, A405 nm, A415 nm) and millimolar vanadium concentrations, the samples are different (as shown in Tables 2–4). We are not able to report that the samples containing single or double digit micromolar concentrations of total vanadium were different. This is largely due to our inability to detect sample absorbance values above background at these low concentrations given the nature of the milieu.

CONCLUSIONS

The UV-Visible study shows that sample types containing the same total moles of vanadium, but starting with either orthovanadate starting material or decavanadate starting material do not result in the same spectroscopic data after 24 h of incubation under assay conditions ($\alpha = 0.05$, in a paired, two-tailed *t*-test). We interpret these differences as implying different amounts of the oxovanadium species responsible for the absorbance measurements at A375, A405, and A415 nm are present. Data collected at A375 nm show that samples containing 39.1 or 3.91 mM total vanadium, but using decavanadate or orthovanadate starting material, are different (Table 2). Data collected at A405 nm show that samples containing 12.4, 3.91, or 1.24 mM total vanadium, but using decavanadate or orthovanadate starting material, are different (Table 3). Data collected at A415 nm show that samples containing 39.1, 12.4, 3.91, or 1.24 mM total vanadium, but using decavanadate or orthovanadate starting material, are different (Table 4). It is interesting to note that regardless of how one assumes the X-axis should be interpreted, i.e., how one defends “solving” the speciation problem under assay conditions, both orthovanadate and decavanadate starting material are excellent inhibitors of *L. tarentolae* secreted acid phosphatase at total vanadium concentrations of 39.1, 12.4, 3.91, and 1.24 mM. It is at these concentrations of total vanadium and pH that decavanadate is reported to be the major form of vanadium present (Rossotti and Rossotti, 1956; Baes and Mesmer, 1976). It is also at these total vanadium concentrations that the UV-visible data are statistically different. Therefore, we report that decavanadate is also an inhibitor of *L. tarentolae* secreted acid phosphatase activity. This work supports the results that other vanadium speciation studies imply, that in a complex biochemical environment, speciation must be experimentally addressed and should not be assumed. Vanadium speciation is a known source of variability, and potentially significantly important for its impact on medical efficacy and patient risk. We strongly recommend investigating vanadium speciation as part of the standard methods of assessing vanadium compounds capable of speciation as therapeutics. Even so, it seems practical from a clinical perspective, that a topical formulation using easily-synthesized decavanadate may be a robust short-term treatment option for cutaneous leishmaniasis. This treatment option is robust because the pH of the skin is acidic with an average pH of 4.7 (Lambers et al., 2006), thus a pH in which decavanadate is stable.

AUTHOR CONTRIBUTIONS

The initial manuscript draft was prepared by BD as part of his M.S. thesis and revised by CM and MJ. Figures were prepared by BD, except as noted. All the authors had final approval of the submitted version of the paper.

ACKNOWLEDGMENTS

We would like to thank the Chemistry Department at Illinois State University, and the Kurz Fellowship (to BD) for partial funding of this research.

REFERENCES

- Abbott, S. J., Jones, S. R., Weinman, S. A., Bockhoff, F. M., McLafferty, F. W., and Knowles, J. R. (1979). Chiral O-16,O-17,O-18 phosphate monoesters – asymmetric synthesis and stereochemical analysis of 1(R)-O-16,O-17,O-18 phospho-(S)-propane-1,2-diol. *J. Am. Chem. Soc.* 101, 4323–4332. doi: 10.1021/ja00509a046
- Acerete, R., Hammer, C. F., and Baker, L. C. W. (1979a). Direct tungsten-183 nuclear magnetic resonance: a powerful new structural tool for heteropoly- and isopolytungstate chemistry. *J. Am. Chem. Soc.* 101, 267–269.
- Acerete, R., Harmalkar, S., Hammer, C. F., Pope, M. T., and Baker, L. C. W. (1979b). Concerning isomerisms and interconversions of 2: 18 and 2: 17 heteropoly complexes and their derivatives. *J. Chem. Soc. Chem. Commun.* 777–779.
- Adriazola, I. O., Amaral, A. E., Amorim, J. C., Correia, B. L., Petkowicz, C. L., Mercê, A. L., et al. (2014). Macrophage activation and leishmanicidal activity by galactomannan and its oxovanadium (IV/V) complex *in vitro*. *J. Inorg. Biochem.* 132, 45–51. doi: 10.1016/j.jinorgbio.2013.09.017
- Anand, A., and Srivastava, P. K. (2012). A molecular description of acid phosphatase. *Appl. Biochem. Biotechnol.* 167, 2174–2197. doi: 10.1007/s12010-012-9694-8
- Arefian, M., Mirzaei, M., Eshtiaq-Hosseini, H., and Frontera, A. (2017). A survey of the different roles of polyoxometalates in their interaction with amino acids, peptides and proteins. *Dalton Trans.* 46, 6812–6829. doi: 10.1039/C7DT00894E
- Aureliano, M. (2016). Decavanadate toxicology and pharmacological activities: V₁₀ or V₁, both or none? *Oxid. Med. Cell. Longev.* 2016:8. doi: 10.1155/2016/6103457
- Aureliano, M., and Crans, D. C. (2009). Decavanadate (V₁₀O₂₈⁶⁻) and oxovanadates: oxometalates with many biological activities. *J. Inorg. Biochem.* 103, 536–546. doi: 10.1016/j.jinorgbio.2008.11.010
- Aureliano, M., and Gândara, R. M. C. (2005). Decavanadate effects in biological systems. *J. Inorg. Biochem.* 99, 979–985. doi: 10.1016/j.jinorgbio.2005.02.024
- Baer, Jr. C. F., and Mesmer, R. E. (eds.). (1976). “The first transition series vanadium,” in *The Hydrolysis of Cations*, (New York, NY: John Wiley and Sons), 193–210.
- Baghaei, M., and Mesripour, M. (2003). Characterization of acid phosphatase in the promastigotes of three isolates of *Leishmania major*. *Iran. J. Med. Sci.* 28, 1–8. Available online at: <http://ijms.sums.ac.ir/index.php/IJMS/article/view/2418>
- Bairoch, A. (2000). The ENZYME database in 2000. *Nucleic Acids Res.* 28, 304–305. doi: 10.1093/nar/28.1.304
- Baumhardt, J. M., Dorsey, B. M., McLauchlan, C. C., and Jones, M. A. (2015). An additional method for analyzing the reversible inhibition of an enzyme using acid phosphatase as a model. *Curr. Enzym. Inhib.* 11, 140–146. doi: 10.2174/1573408011666150605223952
- Benítez, J., Guggeri, L., Tomaz, I., Arrambide, G., Navarro, M., Costa Pessoa, J., et al. (2009). Design of vanadium mixed-ligand complexes as potential anti-protozoa agents. *J. Inorg. Biochem.* 103, 609–616. doi: 10.1016/j.jinorgbio.2008.10.018
- Berman, H. M., Westbrook, J., Feng, Z., Gilliland, G., Bhat, T. N., Weissig, H., et al. (2000). The protein data bank. *Nucleic Acids Res.* 28, 235–242.
- CCDC (2013a). *Leishmaniasis Professionals* [Online]. Center for Disease Control and Prevention. Available online at: https://www.cdc.gov/parasites/leishmaniasis/health_professionals/index.html (Accessed January 4, 2018).
- CCDC (2013b). *Parasites-Leishmaniasis* [Online]. Center for Disease Control and Prevention. Available online at: <http://www.cdc.gov/parasites/leishmaniasis/> (Accessed January 4, 2018).
- Christensen, A. T., McLauchlan, C. C., Dolbecq, A., Mialane, P., and Jones, M. A. (2016). Studies of the effectiveness of bisphosphonate and vanadium-bisphosphonate compounds *in vitro* against axenic *Leishmania tarentolae*. *Oxid. Med. Cell Longev.* 2016, 1–12. doi: 10.1155/2016/9025627
- Corigliano, F., and Di Pasquale, S. (1975). Decavanadate protonation degrees in aqueous solution. *Inorg. Chim. Acta* 12, 102–104. doi: 10.1016/S0020-1693(00)89843-6
- Crans, D. C. (2015). Antidiabetic, chemical, and physical properties of organic vanadates as presumed transition-state inhibitors for phosphatases. *J. Org. Chem.* 80, 11899–11915. doi: 10.1021/acs.joc.5b02229
- Crans, D. C., Smee, J. J., Gaidamauskas, E., and Yang, L. (2004). The chemistry and biochemistry of vanadium and the biological activities exerted by vanadium compounds. *Chem. Rev.* 104, 849–902. doi: 10.1021/cr020607t
- Dawson, B. (1953). The structure of the 9(18)-heteropoly anion in potassium 9(18)-tungstophosphate, K₆(P₂W₁₈O₆₂).14H₂O. *Acta Crystallogr.* 6, 113–126. doi: 10.1107/S0365110X53000466
- Demoro, B., Caruso, F., Rossi, M., Benítez, D., González, M., Cerecetto, H., et al. (2012). Bisphosphonate metal complexes as selective inhibitors of *Trypanosoma cruzi* farnesyl diphosphate synthase. *Dalton Trans.* 41, 6468–6476. doi: 10.1039/c2dt12179d
- Fernandes, A. C., Soares, D. C., Saraiva, E. M., Meyer-Fernandes, J. R., and Souto-Grado, T. (2013). Different secreted phosphatase activities in *Leishmania amazonensis*. *FEMS Microbiol. Lett.* 340, 117–128. doi: 10.1111/1574-6968.12080
- Fernández, M., Becco, L., Correia, I., Benítez, J., Piro, O. E., Echeverría, G. A., et al. (2013). Oxidovanadium(IV) and dioxidovanadium(V) complexes of tridentate salicylaldehyde semicarbazones: searching for prospective antitrypanosomal agents. *J. Inorg. Biochem.* 127, 150–160. doi: 10.1016/j.jinorgbio.2013.02.010
- Gambino, D. (2011). Potentiality of vanadium compounds as anti-parasitic agents. *Coord. Chem. Rev.* 255, 2193–2203. doi: 10.1016/j.ccr.2010.12.028
- Gani, D., and Wilkie, J. (1997). “Metal ions in the mechanism of enzyme-catalysed phosphate monoester hydrolyses,” in *Metal Sites in Proteins and Models*, eds H. A. O. Hill, P. J. Sadler, and A. J. Thomson (Berlin; Heidelberg: Springer), 133–175.
- Gottlieb, M., and Dwyer, D. W. (1982). Identification and partial characterization of an extracellular acid phosphatase activity of *Leishmania donovani* promastigotes. *Mol. Cell. Biol.* 2, 76–81. doi: 10.1128/MCB.2.1.76
- Goovaerts, V., Stroobants, K., Absillis, G., and Parac-Vogt, T. N. (2013). Molecular interactions between serum albumin proteins and Keggin type polyoxometalates studied using luminescence spectroscopy. *Phys. Chem. Chem. Phys.* 15, 18378–18387. doi: 10.1039/c3cp52848k
- Gordon, J. A. (1991). “Use of vanadate as protein-phosphotyrosine phosphatase inhibitor,” in *Methods Enzymol.*, eds B. M. S. Tony Hunter (Cambridge, MA: Academic Press), 477–482.
- Gresser, M. J., Tracey, A. S., and Stankiewicz, P. J. (1987). “The interaction of vanadate with tyrosine kinases and phosphatases,” in *Advances in Protein Phosphatases*, eds W. Merlevede and J. DiSalvo (Leuven; Belgium: Leuven University Press), 35–57.
- Henneberry, M. O., Engel, G., and Grayhack, J. T. (1979). Acid phosphatase. *Urol. Clin. North Am.* 6, 629–641.
- Hill, C. L., Hartnup, M., Faraj, M., Weeks, M., Prosser-McCarthy, C. M. Jr., Brown, R. B., et al. (1990a). “Polyoxometalates as inorganic anti-HIV-1 compounds. Structure-activity relationships,” in *Advances in Chemotherapy of AIDS*, eds R. B. Diasio and J.-P. Sommadossi (New York, NY: Pergamon Press), 33–41.
- Hill, C. L., Weeks, M. S., and Schinazi, R. F. (1990b). Anti-HIV-1 activity, toxicity, and stability studies of representative structural families of polyoxometalates. *J. Med. Chem.* 33, 2767–2772.
- Hoffmann, K., and Baron, M. (2014). *BoxShade. 3.0 Edn*. Available online at: <http://sourceforge.net/projects/boxshade> (Accessed January 31, 2018).
- Ilg, T., Overath, P., Ferguson, M. A. J., Rutherford, T., Campbell, D. G., and McConville, M. J. (1994). O- and N-glycosylation of the *Leishmania mexicana*-secreted acid phosphatase. Characterization of a new class of phosphoserine-linked glycans. *J. Biol. Chem.* 269, 24073–24081.
- Knowles, J. R. (1980). Enzyme-catalyzed phosphoryl transfer reactions. *Annu. Rev. Biochem.* 49, 877–919. doi: 10.1146/annurev.bi.49.070180.004305
- Labbers, H., Piessens, S., Bloem, A., Pronk, H., and Finkel, P. (2006). Natural skin surface pH is on average below 5, which is beneficial for its resident flora. *Int. J. Cosmet. Sci.* 28, 359–370. doi: 10.1111/j.1467-2494.2006.00344.x
- Lassmann, T., and Sonnhammer, E. L. (2005). Kalign – an accurate and fast multiple sequence alignment algorithm. *BMC Bioinformatics* 6:298. doi: 10.1186/1471-2105-6-298
- Levina, A., Crans, D. C., and Lay, P. A. (2017). Speciation of metal drugs, supplements and toxins in media and bodily fluids controls *in vitro* activities. *Coord. Chem. Rev.* 352(Suppl. C), 473–498. doi: 10.1016/j.ccr.2017.01.002
- Li, M., Ding, W., Baruah, B., Crans, D. C., and Wang, R. (2008). Inhibition of protein tyrosine phosphatase 1B and alkaline phosphatase by bis(maltolato)oxovanadium (IV). *J. Inorg. Biochem.* 102, 1846–1853. doi: 10.1016/j.jinorgbio.2008.06.007

- Lindqvist, Y., Schneider, G., and Vihko, P. (1994). Crystal structures of rat acid phosphatase complexed with the transition-state analogs vanadate and molybdate. *Eur. J. Biochem.* 221, 139–142. doi: 10.1111/j.1432-1033.1994.tb18722.x
- Machado, P. de A., Mota, V. Z., Cavalli, A. C., de Carvalho, G. S., Da Silva, A. D., Gameiro, J., et al. (2015). High selective antileishmanial activity of vanadium complex with stilbene derivative. *Acta Trop.* 148, 120–127. doi: 10.1016/j.actatropica.2015.04.018
- McLauchlan, C. C., Peters, B. J., Willsky, G. R., and Crans, D. C. (2015). Vanadium–phosphatase complexes: phosphatase inhibitors favor the trigonal bipyramidal transition state geometries. *Coord. Chem. Rev.* 301–302, 163–199. doi: 10.1016/j.ccr.2014.12.012
- Mendez, R. S., Dorsey, B. M., McLauchlan, C. C., Beio, M., Turner, T. L., Nguyen, V. H., et al. (2014). Vanadium complexes are *in vitro* inhibitors of *Leishmania* secreted acid phosphatases. *Int. J. Chem.* 6, 35–49. doi: 10.5539/ijc.v6n1p35
- Mojtahedi, Z., Clos, J., and Kamali-Sarvestani, E. (2008). *Leishmania major*: identification of developmentally regulated proteins in procyclic and metacyclic promastigotes. *Exp. Parasitol.* 119, 422–429. doi: 10.1016/j.exppara.2008.04.008
- Monzote, L. (2009). Current treatment of leishmaniasis: a review. *Open Antimicrob. Agents. J.* 1, 9–19. Available online at: <https://benthamopen.com/ABSTRACT/TOANTIMJ-1-9>
- Morgenthaler, J. B., Peters, S. J., Cedeño, D. L., Constantino, M. H., Edwards, K. A., Kamowski, E. M., et al. (2008). Carbaporphyrin ketals as potential agents for a new photodynamic therapy treatment of leishmaniasis. *Bioorg. Med. Chem.* 16, 7033–7038. doi: 10.1016/j.bmc.2008.05.037
- Mosmann, T. (1983). Rapid colorimetric assay for cellular growth and survival: application to proliferation and cytotoxicity assays. *J. Immunol. Methods* 65, 55–63. doi: 10.1016/0022-1759(83)90303-4
- Navabi, A., and Soleimanifard, S. (2015). Enzymatic characterization of acid phosphatase in the logarithmic and stationary phase of *Leishmania major* promastigotes. *Shiraz E Med. J.* 16:e26246. doi: 10.17795/semj.26246
- Pope, M. T. (1976). Structural isomers of 1:12 and 2:18 heteropoly anions. Novel and unexpected chirality. *Inorg. Chem.* 15, 2008–2010.
- Pope, M. T., and Müller, A. (1991). Polyoxometalate chemistry: an old field with new dimensions in several disciplines. *Angew. Chem. Int. Ed. Engl.* 30, 34–48. doi: 10.1002/anie.199100341
- Rehder, D. (ed.). (2008). “Inorganic and coordination compounds of vanadium,” in *Bioinorganic Vanadium Chemistry* (West Sussex: John Wiley and Sons, Ltd), 13–51.
- Rehder, D. (2013). “Vanadium. Its role for humans,” in *Interrelations Between Essential Metal Ions and Human Diseases*, eds A. Sigel, H. Sigel, and R. K. O. Sigel (Dordrecht: Springer Netherlands), 139–169. doi: 10.1007/978-94-007-7500-8_5
- Rhule, J. T., Hill, C. L., Judd, D. A., and Schinazi, R. F. (1998). Polyoxometalates in medicine. *Chem. Rev.* 98, 327–358. doi: 10.1021/cr960396q
- Rigden, D. J., Littlejohn, J. E., Henderson, K., and Jedrzejewski, M. J. (2003). Structures of phosphate and triphosphate complexes of *Bacillus stearothermophilus* phosphatase phoe: structural and functional analysis in the cofactor-dependent phosphoglycerate mutase superfamily. *J. Mol. Biol.* 325, 411–420. doi: 10.1016/S0022-2836(02)01229-9
- Rossotti, F. J. C., and Rossotti, H. (1956). Equilibrium studies of polyanions. I. Isopolyvanadates in acidic media. *Acta Chem. Scand.* 10, 957–984. doi: 10.3891/acta.chem.scand.10-0957
- Steens, N., Ramadan, A. M., Absillis, G., and Parac-Vogt, T. N. (2010). Hydrolytic cleavage of DNA-model substrates promoted by polyoxovanadates. *Dalton Trans.* 39, 585–592. doi: 10.1039/B913471A
- Taylor, V. M., Muñoz, D. L., Cedeño, D. L., Vélez, I. D., Jones, M. A., and Robledo, S. M. (2010). *Leishmania tarentolae*: utility as an *in vitro* model for screening of antileishmanial agents. *Exp. Parasitol.* 126, 471–475. doi: 10.1016/j.exppara.2010.05.016
- Turner, T. L., Nguyen, V. H., McLauchlan, C. C., Dymon, Z., Dorsey, B. M., Hooker, J. D., et al. (2012). Inhibitory effects of decavanadate on several enzymes and *Leishmania tarentolae* *in vitro*. *J. Inorg. Biochem.* 108, 96–104. doi: 10.1016/j.jinorgbio.2011.09.009
- Urquiola, C., Vieites, M., Aguirre, G., Marín, A., Solano, B., Arrambide, G., et al. (2006). Improving anti-trypanosomal activity of 3-aminoquinoxaline-2-carbonitrile N1,N4-dioxide derivatives by complexation with vanadium. *Bioorg. Med. Chem.* 14, 5503–5509. doi: 10.1016/j.bmc.2006.04.041
- Van Etten, R. L., Waymack, P. P., and Rehkop, D. M. (1974). Transition metal ion inhibition of enzyme-catalyzed phosphate ester displacement reactions. *J. Am. Chem. Soc.* 96, 6782–6785. doi: 10.1021/ja00828a053
- Vincent, J. B., Crowder, M. W., and Averill, B. A. (1992). Hydrolysis of phosphate monoesters: a biological problem with multiple chemical solutions. *Trends Biochem. Sci.* 17, 105–110. doi: 10.1016/0968-0004(92)90246-6
- Wu, H. (1920). Contribution to the chemistry of phosphomolybdic acids, phosphotungstic acids, and allied substances. *J. Biol. Chem.* 43, 189–220.

Conflict of Interest Statement: The authors declare that the research was conducted in the absence of any commercial or financial relationships that could be construed as a potential conflict of interest.

Copyright © 2018 Dorsey, McLauchlan and Jones. This is an open-access article distributed under the terms of the Creative Commons Attribution License (CC BY). The use, distribution or reproduction in other forums is permitted, provided the original author(s) and the copyright owner are credited and that the original publication in this journal is cited, in accordance with accepted academic practice. No use, distribution or reproduction is permitted which does not comply with these terms.



Selectivity and Reactivity of Zr^{IV} and Ce^{IV} Substituted Keggin Type Polyoxometalates Toward Cytochrome c in Surfactant Solutions

Thomas Quanten¹, Tessa De Mayaer¹, Pavletta Shestakova² and Tatjana N. Parac-Vogt^{1*}

¹ Laboratory of Bio-Inorganic Chemistry, Department of Chemistry, KU Leuven, Leuven, Belgium, ² NMR Centre, Institute of Organic Chemistry with Centre of Phytochemistry, Bulgarian Academy of Sciences, Sofia, Bulgaria

OPEN ACCESS

Edited by:

Jun Chen,
University of Wollongong, Australia

Reviewed by:

Tilo Sönnel,
University of Auckland, New Zealand
Guo-Hong Tao,
Sichuan University, China

*Correspondence:

Tatjana N. Parac-Vogt
tatjana.vogt@kuleuven.be

Specialty section:

This article was submitted to
Inorganic Chemistry,
a section of the journal
Frontiers in Chemistry

Received: 02 May 2018

Accepted: 02 August 2018

Published: 28 August 2018

Citation:

Quanten T, De Mayaer T, Shestakova P and Parac-Vogt TN (2018) Selectivity and Reactivity of Zr^{IV} and Ce^{IV} Substituted Keggin Type Polyoxometalates Toward Cytochrome c in Surfactant Solutions. *Front. Chem.* 6:372. doi: 10.3389/fchem.2018.00372

In this paper we investigate the effect of three different types of surfactants, on the hydrolysis of Cytochrome c (Cyt c), a predominantly α helical protein containing a heme group, promoted by [Ce(α PW₁₁O₃₉)₂]¹⁰⁻ (CeK) and [Zr(α PW₁₁O₃₉)₂]¹⁰⁻ (ZrK) polyoxometalates. In the presence of SDS, Zw3 12, or CHAPS surfactants, which are commonly used for solubilizing hydrophobic proteins, the specificity of CeK or ZrK toward hydrolysis of Cyt c does not change. However, the hydrolysis rate of Cyt c by CeK was increased in the presence of SDS, but decreased in the presence of CHAPS, and was nearly inhibited in the presence of Zw3 12. The Circular dichroism and Tryptophan fluorescence spectroscopy have shown that the structural changes in Cyt c caused by surfactants are similar to those caused by POMs, hence the same specificity in the absence or presence of surfactants was observed. The results also indicate that for Cyt c hydrolysis to occur, large unfolding of the protein is needed in order to accommodate the POMs. While SDS readily unfolds Cyt c, the protein remains largely folded in the presence of CHAPS and Zw3 12. Addition of POMs to Cyt c solutions in CHAPS results in unfolding of the structure allowing the interaction with POMs to occur and results in protein hydrolysis. Zw3 12, however, locks Cyt c in a conformation that resists unfolding upon addition of POM, and therefore results in nearly complete inhibition of protein hydrolysis.

Keywords: polyoxometalates, Keggin, protein, hydrolysis, surfactants, cytochrome c

INTRODUCTION

Membrane proteins perform key functions in crucial processes at the interface between the intra- and extracellular environment (Tan et al., 2008). Atypical or dysfunctional behavior of membrane proteins often presents itself in a range of diseases. Identifying these abnormal membrane proteins might result in novel therapeutic targets (Carter et al., 2004). Approximately 60% of known and future drug targets are membrane proteins (Hopkins and Groom, 2002; Overington et al., 2006). Unfortunately, membrane proteins are often underrepresented in proteomic studies (Santoni et al., 2000; Whitelegge et al., 2003; Seddon et al., 2004; Speers and Wu, 2007; Tan et al., 2008; Rabilloud, 2009), even though the predicted number of membrane associated proteins is sizable (Wallin and von Heijne, 1998). Their limited representation is attributed to their low abundance

and their heterogeneous and hydrophobic nature. To solubilize membrane proteins in aqueous solutions, surfactants are often employed. The surfactants form micelles or liposomes that mimic the hydrophobic environment of the cell membrane. Unfortunately, proteolytic enzymes are mostly hydrophilic and tend to denature in the presence of surfactants, resulting in the loss of catalytic activity. Therefore, artificial peptidases that remain active in the presence of surfactants need to be developed.

Proteomics is a field of science that studies the proteome, i.e., the entire population of proteins of a cell, tissue or organism, mostly by means of mass spectrometry (MS) techniques. Intact proteins are often too large to study via MS and are therefore digested in a controlled fashion. Digestion of proteins is achieved by controlled hydrolysis of the peptide bonds that link amino acids in a protein. However, the half-life of peptide bonds under physiological conditions has been estimated to be between 350 and 600 years (Bryant and Hansen, 1996; Radzicka and Wolfenden, 1996; Smith and Hansen, 1998). To accelerate protein digestions, hydrolytic enzymes are employed. A well-known example is trypsin which specifically targets the C-terminal peptide bond of lysine (Lys) and arginine (Arg) residues (Rodriguez et al., 2008). However, the frequency with which these residues occur results in many fragments that are too small (56% of fragments contain ≤ 6 residues) to be confidentially detected and analyzed by MS techniques (Swaney et al., 2010; Tsiatsiani and Heck, 2015). Additionally, most of the currently available hydrolytic enzymes produce fragments between 0.5 and 3 kDa in size. Such short fragments are not compatible with the emerging field of middle-down proteomics that focusses on the analysis of middle-sized fragments which are typically 10–15 kDa.

Most of the chemical agents used for peptide bond hydrolysis reported so far require harsh conditions to achieve efficient cleavage of the targeted peptide bonds. These conditions often chemically modify some amino acids and the native terminal groups. Transition metals and their complexes hold great potential as synthetic enzymes. Numerous examples of metal ion promoted peptide bond hydrolysis in peptides, oligopeptides and proteins in aqueous solutions have been reported (Grant and Kassai, 2006; Wezynfeld et al., 2016). However, the selective hydrolysis of proteins in the presence of surfactants has been largely unexplored and only two examples involving Pt^{II} and Pd^{II} complexes have been reported albeit at very acidic pH conditions (2.5–2.9) (Milovic et al., 2003; Miskevich et al., 2011).

Polyoxometalates or POMs are anionic, oligomeric aggregates of early transition metal ions bridged by oxo ligands with versatile physical and chemical properties (Pope, 1983; Pope and Müller, 1991; Hasenknopf, 2005). Due to their versatile nature POMs are employed in numerous fields such as catalysis, material science and medicine (Rhule et al., 1998; Sadakane and Steckhan, 1998; Kozhevnikov, 2002; Long et al., 2007, 2010; Wang and Yang, 2015). Investigating their activity toward biomolecules and model systems has demonstrated their unprecedented carboxyesterase, phosphoesterase, peptidase, and sialidase activity (Hegg and Burstyn, 1998; Absillis et al., 2008, 2011; Cartuyvels et al., 2008; Lokeren et al., 2008; Steens et al., 2009, 2010; Ho et al., 2011a,b, 2012; Absillis and Parac-Vogt, 2012; Vanhaecht et al., 2012, 2013; Ly et al., 2013a,b, 2015b; Luong

et al., 2014, 2015a,b, 2016, 2017; Stroobants et al., 2014c; Van Rompuy and Parac-Vogt, 2017).

Ce^{IV} and Zr^{IV} substituted POMs were shown to promote selective hydrolysis of a variety of water soluble proteins, ranging from flexible polypeptide such as oxidized insulin chain B (Sap et al., 2015), to larger, globular proteins such as hen egg white lysozyme (Stroobants et al., 2013, 2014d), human serum albumin (HSA) (Goovaerts et al., 2013; Stroobants et al., 2014a,b), horse heart cytochrome c (Cyt c) (Sap et al., 2016) and horse heart myoglobin (Ly et al., 2015a; Ly and Parac-Vogt, 2017). However, the potential of these POMs to act as artificial proteases toward hydrolysis of proteins in the presence of surfactants is still largely unexplored. We have previously investigated the interaction between metal-substituted POMs and different surfactants with the help of ^{31}P and ^1H DOSY NMR spectroscopy and demonstrated that the POM retains its catalytic activity in the presence of surfactants (Quanten et al., 2016). Sap et al. later investigated the effect of the zwitterionic surfactant 3-[(3-Cholamidopropyl)dimethylammonio]-1-propanesulfonate, also known as CHAPS, on the activity and selectivity of $[\text{Zr}(\alpha_2\text{-P}_2\text{W}_{17}\text{O}_{61})_2]^{16-}$ toward the hydrolysis of the HSA (Sap et al., 2017). In the absence of surfactants, HSA was cleaved at four sites (Arg114-Leu115, Ala257-Asp258, Lys313-Asp314, and Cys302-Glu303), while hydrolysis of seven peptide bonds (Cys62-Asp63, Gly71-Asp72, Asp107-Asp108, Lys313-Asp314, His367-Gly368, Ser470-Asp471, and Ala511-Asp512) was observed in the presence of 0.5% CHAPS. Interestingly, most of the POM-targeted peptide bonds were at an aspartic acid or glutamic acid residue, and the POM affinity to cleave at these amide bonds remained the same in the presence of 0.5% CHAPS.

Encouraged by this result, in this paper we investigate the effect of three different types of surfactants on the hydrolysis of Cytochrome c (Cyt c), a predominantly α -helical protein containing a heme group (Bushnell et al., 1990), promoted by $[\text{Ce}(\alpha\text{-PW}_{11}\text{O}_{39})_2]^{10-}$ (**CeK**) and $[\text{Zr}(\alpha\text{-PW}_{11}\text{O}_{39})_2]^{10-}$ (**ZrK**) polyoxometalates. In comparison to HSA, Cyt c is a small globular protein consisting out of 104 amino acids with a net positive charge of +8 at neutral pH and an isoelectric point of almost 10. Due to its smaller size and a net positive charge, the interaction of Cyt c by POM catalysts is likely to be affected by the presence of different surfactants. In order to elucidate the role of surfactants on the catalytic performance of POMs, in this work we study the hydrolysis of Cyt c by **CeK** and **ZrK** (see **Figure 1**) in the presence of surfactants shown in **Figure 2**. Furthermore, a range of spectroscopic techniques was used to gain insight into the molecular interactions between **CeK** and **ZrK** POMs and Cyt c in different surfactant solutions.

RESULTS AND DISCUSSION

Hydrolysis of Cyt c by CeK and ZrK in the Presence of Different Surfactants

Previous research has shown that **CeK** and **ZrK** specifically cleaved Cyt c in aqueous solution, but at different sequences. While **CeK** cleaved Cyt c at Trp60-Lys61 and Gly78-Thr79 peptide bonds at pH 7.4, the **ZrK** splits three peptide bonds:

Asp3-Val4, Asp51-Ala52, and Gly78-Thr79 at pH 4.1 (Sap et al., 2016). These differences in selectivity are likely due to the oxido-reduction processes that occur during protein hydrolysis by CeK, as evidenced by ^{31}P NMR spectroscopy, but are absent during Cyt c hydrolysis by Zr POMs. These oxido-reduction processes can change the folding of Cyt c through a modification of the side-chains of redox-active amino acids and can also change the coordination ability of Ce due to a change in its oxidation state (Ce^{IV} to Ce^{III}). In this work we examine the effect of three different surfactants, which are used in the study of membrane proteins, on the selectivity and the efficiency of the hydrolysis. These surfactants differ in their charge and polarity and are therefore expected to exhibit different interactions with POMs and proteins. Zw3-12 and SDS have the same hydrophobic dodecyl chain, however SDS is anionic while Zw3-12 is zwitterionic in nature. CHAPS has the same zwitterionic head group as Zw3-12, but as a tail it has hydroxyl functionalized steroid skeleton, making it the most hydrophilic surfactant among the examined three (see Figure 2). As can be seen in Figure 3, in the absence of surfactants CeK cleaves Cyt c in two fragments with a molecular weight (Mw) of 7.8 and 3.9

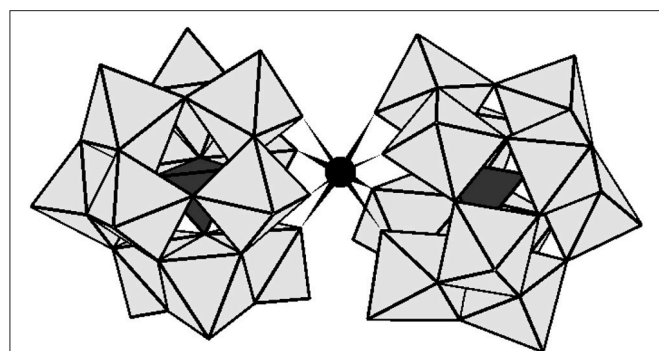


FIGURE 1 | The polyhedral representation of $[\text{Ce}(\alpha\text{-PW}_{11}\text{O}_{39})_2]^{10-}$ and $[\text{Zr}(\alpha\text{-PW}_{11}\text{O}_{39})_2]^{10-}$. The gray octahedral represents WO_6 and the black tetrahedral stand for PO_4 . The black sphere represents Zr^{IV} or Ce^{IV} .

kDa, which are the same as previously observed by Sap et al. When 0.5% CHAPS or 0.5% SDS were added to the incubation mixture, the same fragments were observed, indicating that these surfactants do not alter the specificity of CeK. Interestingly, addition of 0.5% Zw3-12, resulted in complete inhibition of the catalytic activity of CeK as no hydrolysis of Cyt c was observed in the SDS-PAGE.

Figure 4 demonstrates the selective cleavage of Cyt c in the presence of ZrK, which results in three fragments with Mw 10.3, 7.6 and 5.6 kDa at pH 7.4. These fragments have the same Mw

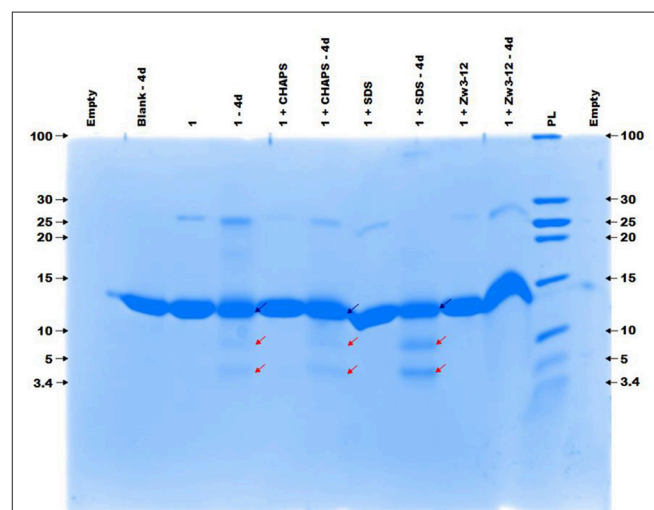


FIGURE 3 | The colloidal Coomassie blue (CCB) stained gel of the hydrolysis of $40\ \mu\text{M}$ Cyt c by $2\ \text{mM}$ of 1 in the absence or presence of different surfactants. Cyt c was incubated for 4 days at 60°C and pH 7.4 ($10\ \text{mM}$ sodium phosphate buffer). The blue and red arrows indicate the intact protein and the generated fragments at 7.8 and 3.9 kDa, respectively. The values at the left and right side of the gel indicate the Mw reference in kDa. An aliquot of each sample was taken after mixing and 4 days (4d) of incubation, except for the blank (Cyt c without 1 or surfactants present) which only shows an aliquot after 4 days. The content of each lane is shown on top of the gel and the concentration of each surfactant was kept at 0.5%. PL stand for protein ladder.

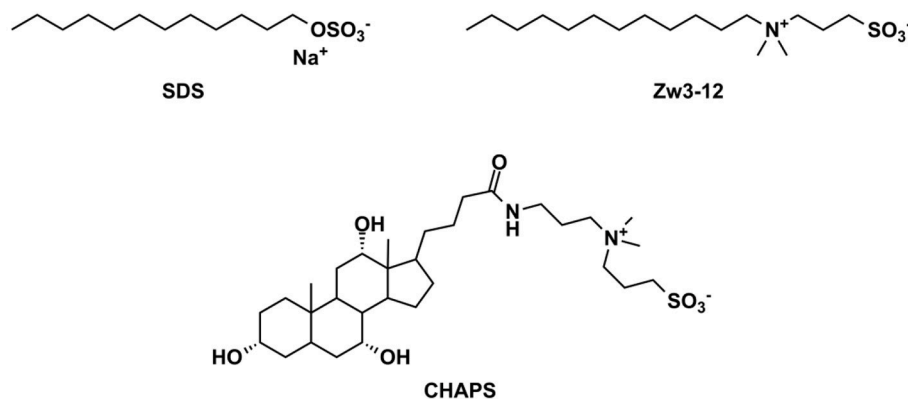
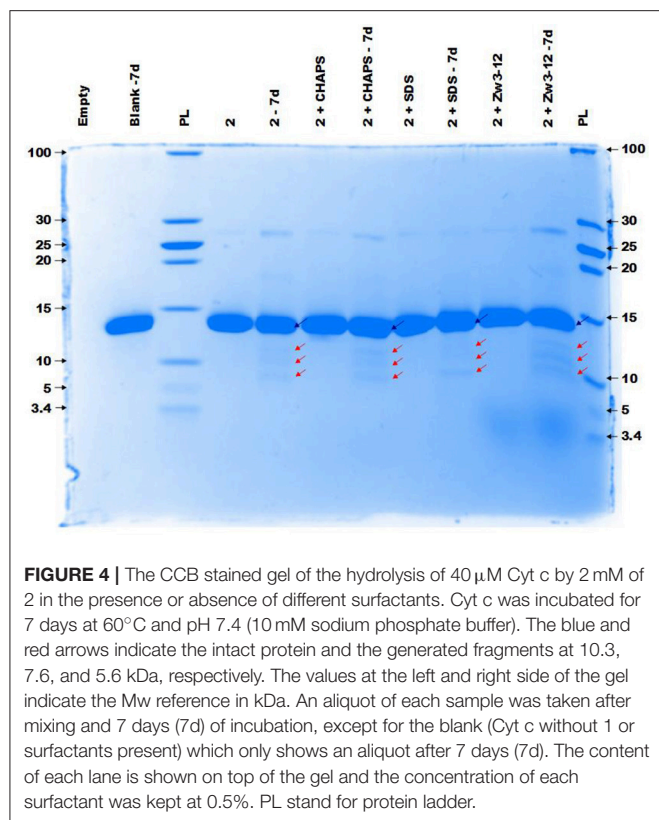


FIGURE 2 | The chemical structures of the surfactants used in this study. SDS, sodium dodecyl sulfate; Zw3-12, dodecyltrimethylammonium-1-propanesulfonate and CHAPS; 3-[(3-cholamidopropyl)dimethylammonio]-1-propanesulfonate.



as those previously observed at pH 4.1 (10 mM acetate buffer) by Sap *et al.* Interestingly, the addition of CHAPS, SDS or Zw3-12 surfactants does not have a significant effect on the specificity of **ZrK**, as the same fragments were observed in the absence or presence of these surfactants.

Comparison of the results shown in **Figures 3, 4** reveals that the most striking difference between **CeK** and **ZrK** is their efficiency as catalyst for the hydrolysis of Cyt c. Where **CeK** was able to selectively hydrolyze most of intact Cyt c after 4 days, hydrolysis of Cyt c by **ZrK** was only noticeable after 7 days of incubation at 60°C. This difference is most likely the result of the different Lewis acidic strength of both metals. Cerium is characterized by a stable 3+ and 4+ oxidation state, while zirconium is only stable in a 4+ state. This difference allows Ce^{IV} to take up more electron density than Zr^{IV} , resulting in a stronger Lewis acidity for Ce^{IV} . Another interesting observation is that the rates of protein hydrolysis were differently influenced by three surfactants. The rate of protein hydrolysis could be assessed by measuring the intensity decrease of the intact protein band upon incubation at 60°C. **Table 1** summarizes the amount of hydrolyzed Cyt c measured in the absence or presence of different surfactants.

Interestingly, in 0.5% SDS solutions of **CeK**, the yield of protein hydrolysis by **CeK** nearly doubled. While only 24% of Cyt c was cleaved in the absence of any surfactants, 44% hydrolysis of Cyt c was observed after 4 days in the presence of 0.5% SDS. In the presence of 0.5% CHAPS 21% of Cyt c was fragmented, which is similar to the hydrolysis rate in the absence of surfactants. In

TABLE 1 | The breakdown of Cyt c by CeK and ZrK after incubation at 60°C and pH 7.4 (10 mM sodium phosphate buffer).

Surfactant (0.5%)	Cyt c breakdown by CeK (%) ^a	Cyt c breakdown by ZrK (%) ^b
–	24	18
SDS	44	4
CHAPS	21	17
Zw3-12	–	9

^aafter 4 days of incubation.

^bafter 7 days of incubation.

the presence of 0.5% Zw3-12, however, no degradation of Cyt c was observed after 4 days.

Compared to **CeK**, **ZrK** is an overall less efficient catalyst. At pH 7.4. Sap *et al.* also observed weak hydrolysis at this pH, but were able to observe more efficient hydrolysis of Cyt c in more acidic solutions (pH 4.1) (Sap *et al.*, 2016). At pH 7.4, **ZrK** was able to degrade 18% of Cyt c in absence of surfactants. CHAPS had very little effect on the hydrolysis yield, but adding 0.5% of SDS or Zw3-12, slightly lowered the Cyt c digestion to 4 and 9%, respectively.

These findings suggest that the nature of the surfactant plays a role in the hydrolytic activity of **CeK** and **ZrK** toward Cyt c. Therefore the molecular interactions between Cyt c and **CeK** and **ZrK** in the absence or presence of the different surfactants were studied with the help of different spectroscopic techniques in order to elucidate the origin of the observed specificity and reactivity of **CeK** and **ZrK** in the absence or presence of different surfactants.

Effect of CeK, ZrK and Surfactants on the Secondary and Tertiary Structure of Cyt c

The structural changes caused in Cyt c by **CeK**, **ZrK** and/or surfactants were studied with circular dichroism (CD) spectroscopy. The conformation of the protein backbone is reflected in the far-UV region of a CD spectrum, making it a useful technique to study the secondary structure of a protein. The far-UV CD spectra of Cyt c recorded in the absence or presence of 0.5% SDS or 0.5% Zw3-12 are shown in **Figure S1** (see Supporting Information). Due to the strong absorption of CHAPS in the far-UV region, it was not possible to use it in the far-UV CD measurements.

As can be seen from **Figure S1** SDS and Zw3-12 have a different influence on the secondary structure of Cyt c. The zwitterionic surfactant Zw3-12 does not change the overall shape of the CD spectrum but increases the intensity of the negative signals at 222 and 210 nm and positive signals at 195 and 185 nm. SDS, however, causes a larger change of the shape of the CD signal, as can be seen by the emergence of a strong negative signal at 208 nm and strong positive signal at 193 nm. Hiramatsu *et al.* have observed a similar effect of SDS on the secondary structure of Cyt c, where the negative signals at 209 and 222 nm disappeared in favor for a new negative trough at 207 nm (Hiramatsu

and Yang, 1983). These observations were rationalized by an altered helicity of Cyt c in the presence of SDS, however the observed structural changes were not quantified. In this work DICHROWEB was employed to estimate the secondary structural content of Cyt c in the absence or presence of different surfactants and/or POMs. The far-UV region of a CD spectrum is the sum of the CD signals from the individual structural components (Sreerama and Woody, 2000; Whitmore and Wallace, 2004, 2008). DICHROWEB exploits this cumulative nature to deconvolute the various contributions of the different secondary structure elements (α -helices, β -sheets and random coils) with the help of protein reference sets and empirical algorithms (Whitmore and Wallace, 2004, 2008; Greenfield, 2006). DICHROWEB could provide calculated secondary structure contents of Cyt c in the presence or absence of surfactants, which are summarized in **Table S1** (see Supporting Information). The calculated secondary structure content of Cyt c in the absence of surfactants is similar to that previously reported in literature (see first entry **Table S1**,

Supporting Information) (Nantes et al., 2001). The calculated content confirms that Zw3-12 has a minor influence on protein structure, increasing the α -helical content by 3% and lowering the β -sheet content by the same amount, while SDS causes a restructuring of Cyt c by enhancing both the α -helical and β -sheet content by 2 and 6%, respectively. Next, the effect of **CeK** and **ZrK** on the structure of Cyt c was investigated in the absence or presence of Zw3-12 or SDS (see **Figure 5** and **Figure S2**, respectively).

In solution, Cyt c assumes a predominantly α -helical structure as demonstrated by the negative signals at 209 and 222 nm and positive signal at 195 nm. Adding **CeK** to Cyt c in the absence of surfactants decreases the intensity of the signals at 209 nm and 222 nm and a new negative signal emerges at 205 nm. Additionally, the two positive signals at 186 and 195 nm disappear in favor for a new positive peak at 189 nm (see **Figure 5I**). After analyzing these CD spectra, it was calculated that the native Cyt c in solution contains 32 and 12% of α -helix and β -sheets, respectively (see **Table S2**). After adding 50 μ M

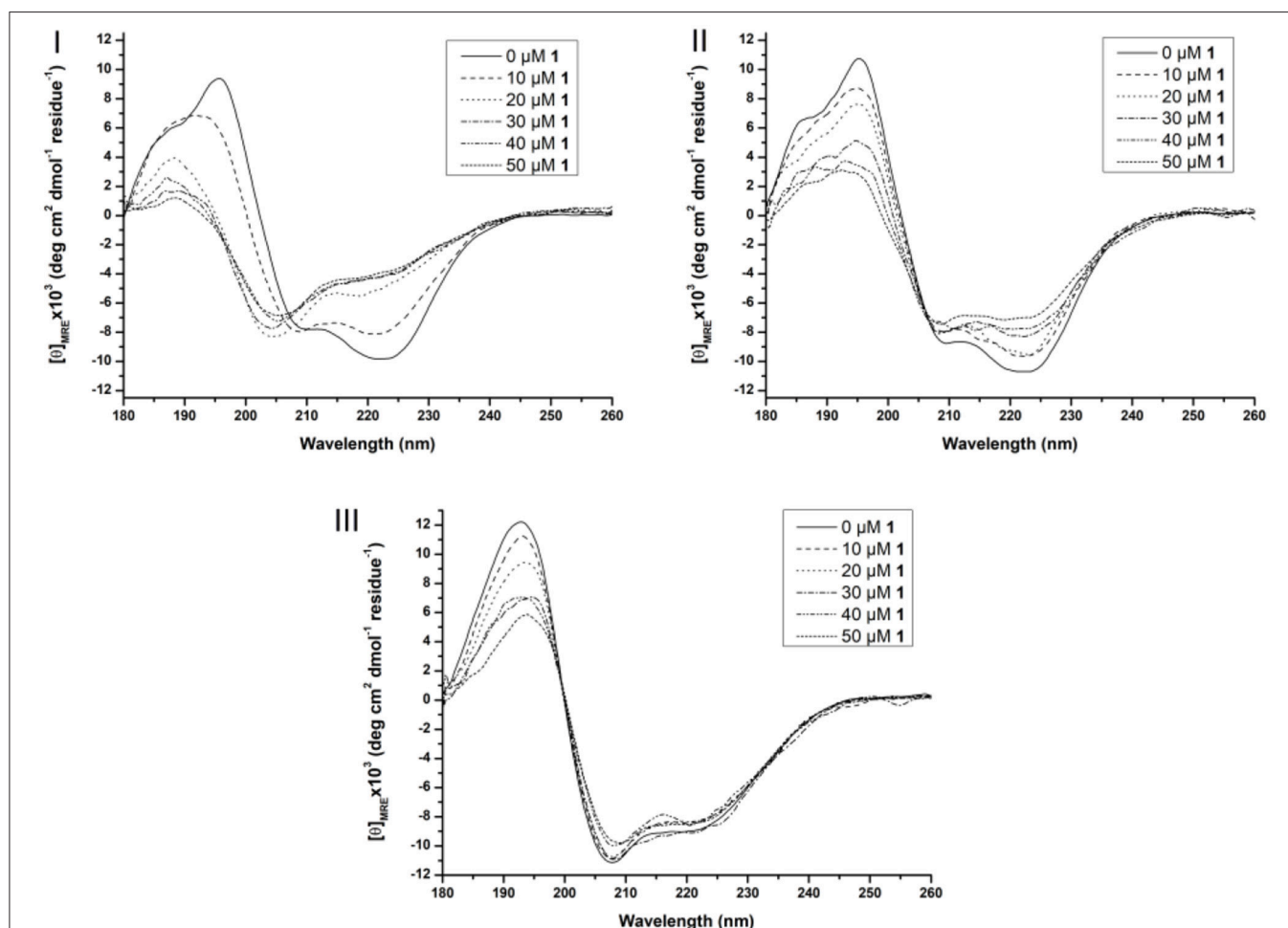


FIGURE 5 | Far-UV CD spectra of 10 μ M Cyt c solutions in presence of increasing concentration of 1 (from 0 to 50 μ M) in the absence of surfactants (I), in the presence of 0.5% Zw3-12 (II) and 0.5% SDS (III). All samples were buffered at pH 7.4 by a 10 mM sodium phosphate buffer and kept at 25 \pm 0.1°C during measurements.

of **CeK** to Cyt c the secondary structure contents changed to 8% α -helix (24% decrease) and 34% β -sheets (23% increase). In the presence of 0.5% SDS or 0.5% Zw3-12 the structural changes are less pronounced (see **Figures 5II, III**). The structure that Cyt c assumes in the presence of Zw3-12, but in the absence of POMs, is similar to its structure in the absence of surfactants and POMs. However, when the concentration of **CeK** is increased, the structural changes are limited, as seen in the gradual decrease of signal intensity in **Figure 5II**. Adding 50 μ M of **CeK** to a Zw3-12/Cyt c solution (0.5% Zw3-12) caused a 16% decrease in α -helix and 19% increase in β -sheet content (see **Table S2**). In the presence of 0.5% SDS, the restructuring effect of **CeK** is even smaller as seen in **Figure 5III**. The calculated structural content is summarized in **Table S2** where it can be seen that change in secondary structure content in the absence or presence of **CeK** is rather limited ($\leq 4\%$). These observations can be explained by competition between **CeK** and the surfactant for binding sites at Cyt c. This competitive model lowers the binding strength between **CeK** and Cyt c, explaining the limited influence of **CeK** on the secondary structure in the presence of surfactants. The strong anionic nature of SDS repels the polyanionic POM stronger than the zwitterionic Zw3-12 resulting in a lower binding strength in the presence of SDS compared to Zw3-12. These observations agree with a competitive model. An alternative explanation involves the surfactant locking Cyt c in a structure, which is only marginally influenced by the binding of **CeK**. Similar observations were made for the Zr^{IV} substituted POM, **ZrK** (see **Figure S2** and **Table S2**), where the strongest influence of **ZrK** on the secondary structure is seen in absence of surfactants and this influence decreases when shifting from Zw3-12 to SDS. This indicates that the POM skeleton, and not the imbedded metal ion, plays the most significant role in altering the structure of Cyt c.

At higher wavelengths (300–500 nm) the CD spectrum of Cyt c is characterized by a Soretbisignate signal with a negative and positive peak at 418 and 404 nm, respectively. This bisignate band is assigned to the heme-polypeptide interactions close to the heme crevice and indicative for a natively folded Cyt c (Myer, 1968a,b; Kaminsky et al., 1972; Santucci and Ascoli, 1997; Thomas et al., 2000; Mugnol et al., 2008; Wei and Danielson, 2011). When Cyt c unfolds the negative signal disappears, while the positive signal becomes more intense (Santucci and Ascoli, 1997; Thomas et al., 2000; Mugnol et al., 2008; Wei and Danielson, 2011). The effect of the surfactants on the tertiary structure can be seen in **Figure S4**. Zw3-12 and CHAPS do not denature Cyt c as evidenced by the unaltered bisignate band around 410 nm in the presence of 1.0% CHAPS or Zw3-12. SDS, however, causes the negative signal at 418 nm to disappear, leaving only the positive signal at 406 nm. This suggests that Cyt c is largely denatured in the presence of 0.25% SDS as a result of its harsh nature. The effect of **CeK** and **ZrK** on the tertiary structure of Cyt c was also determined in the absence or presence of different surfactants (see **Figure 6** and **Figure S3**, respectively).

In the absence of surfactants, large unfolding of Cyt c is observed in the presence of 10 μ M **CeK**, indicated by the

disappearance of the negative signal at 418 nm and appearance of a positive signal at 406 nm. A similar trend was observed in the presence of 0.5% CHAPS. In the presence of 0.5% Zw3-12, however, increasing the concentration of **CeK** caused a more gradual unfolding of Cyt c. The signal at 418 nm gradually disappeared when the amount of **CeK** increased and was completely suppressed at 50 μ M. Simultaneously, the positive signal around 406 nm increased. The observed differences between Zw3-12 and CHAPS can be explained by their hydrophobic moiety. Zw3-12 has a saturated, linear dodecyl chain, while CHAPS has a polar, functionalized steroid skeleton. This makes Zw3-12 a more hydrophobic surfactant, resulting in a stronger interaction with Cyt c, and making it more difficult to be displaced by **CeK**. As a result, **CeK** has a weaker denaturing effect on Cyt c in the presence of Zw3-12 than in the presence of CHAPS. The final surfactant, SDS is known for its harsh denaturing effect on globular proteins. At 0.25%, SDS completely unfolds Cyt c, as evidenced by the loss of the negative part of the bisignate Soret band around 410 nm. The unfolded state of Cyt c in the presence of 0.5% SDS is comparable to its unfolded state in the presence of 50 μ M **CeK** (compare **Figure 6I** with **Figure 6IV**). This might explain why adding 50 μ M of **CeK** to a SDS:Cyt c mixture causes no changes in tertiary structure. The same trends are observed for **ZrK** (see **Figure S3**), proving again that the POM framework is the main determinant in the refolding of Cyt c in the presence of metal substituted Keggin POMs.

The hydrolysis rate of Cyt c by **CeK** is the fastest in the presence of 0.5% SDS, while in the presence of 0.5% CHAPS and in absence of surfactants the rates are comparable. In the presence of 0.5% Zw3-12, however, the hydrolysis is strongly inhibited. The reaction rate appears to be related to the unfolded state of Cyt c under these conditions. In the presence of SDS, Cyt c is largely unfolded and this new conformation closely resembles the structure that Cyt c assumes when binding with **CeK** or **ZrK**. In the absence of surfactants or in the presence of CHAPS these conformations are very similar, and increased POM concentrations result in large unfolding of Cyt c. Zw3-12, however, appears to lock Cyt c in a folded conformation that is rather resistant to unfolding upon addition of POMs. This resistance to denaturing might explain the inhibiting effect of Zw3-12 on Cyt c hydrolysis by POMs. The strong denaturing effect caused by SDS results in acceleration of hydrolysis by exposing the cleavage sites to the POMs. CHAPS does not cause structural changes in Cyt c and therefore, similar interactions with the POM are expected as in the absence of surfactant, which is reflected in the negligible effect of CHAPS on kinetics of Cyt c hydrolysis.

In order to further understand these phenomena on a molecular level, we investigated the effect of surfactants and POMs on the structure of Cyt c with the help of tryptophan fluorescence spectroscopy.

Tryptophan Fluorescence of Cyt c in the Presence of **CeK**, **ZrK**, and Surfactants

Cyt c is a small protein consisting of 104 amino acids with only one tryptophan residue (Trp) and a covalently bound

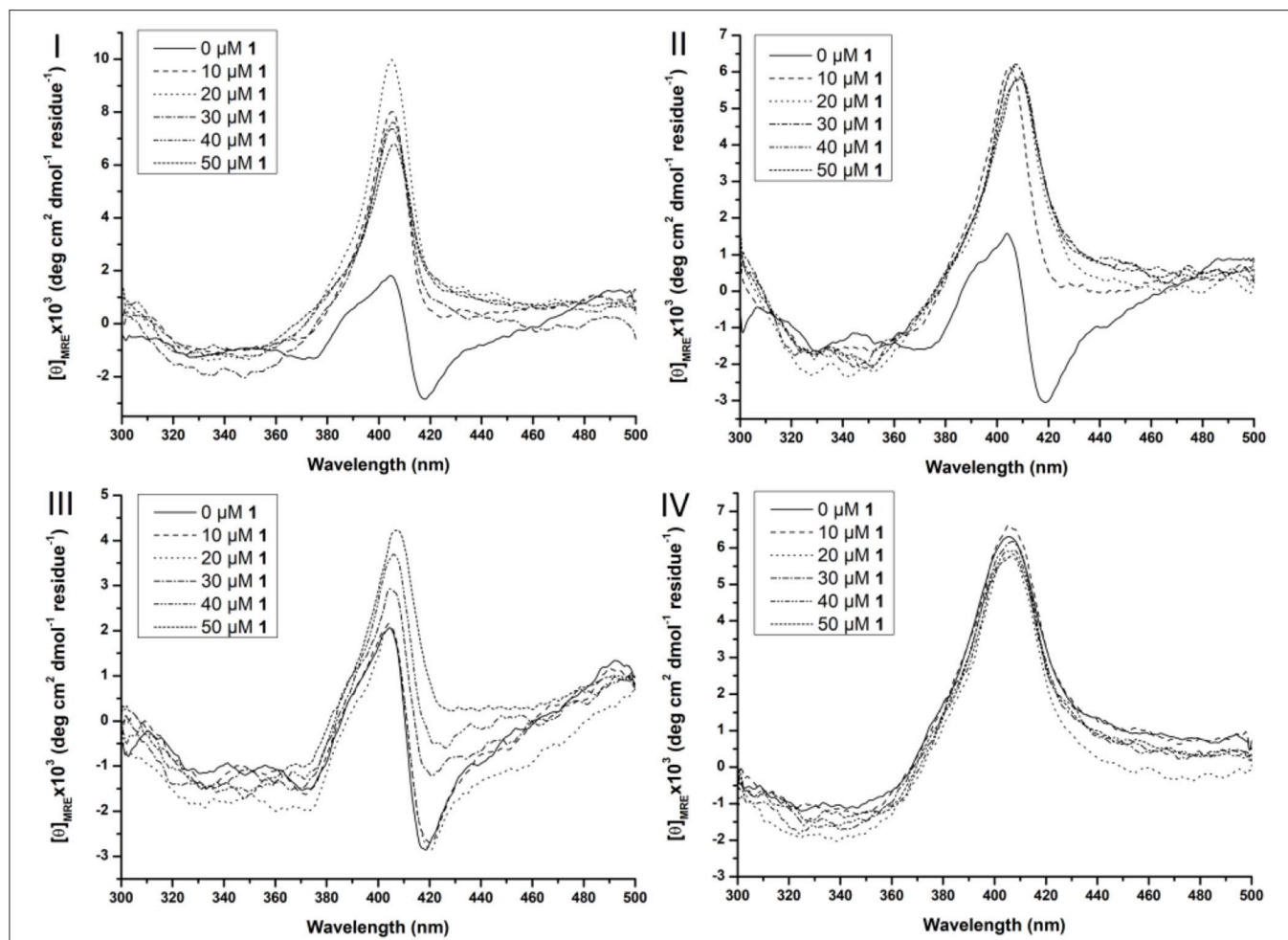


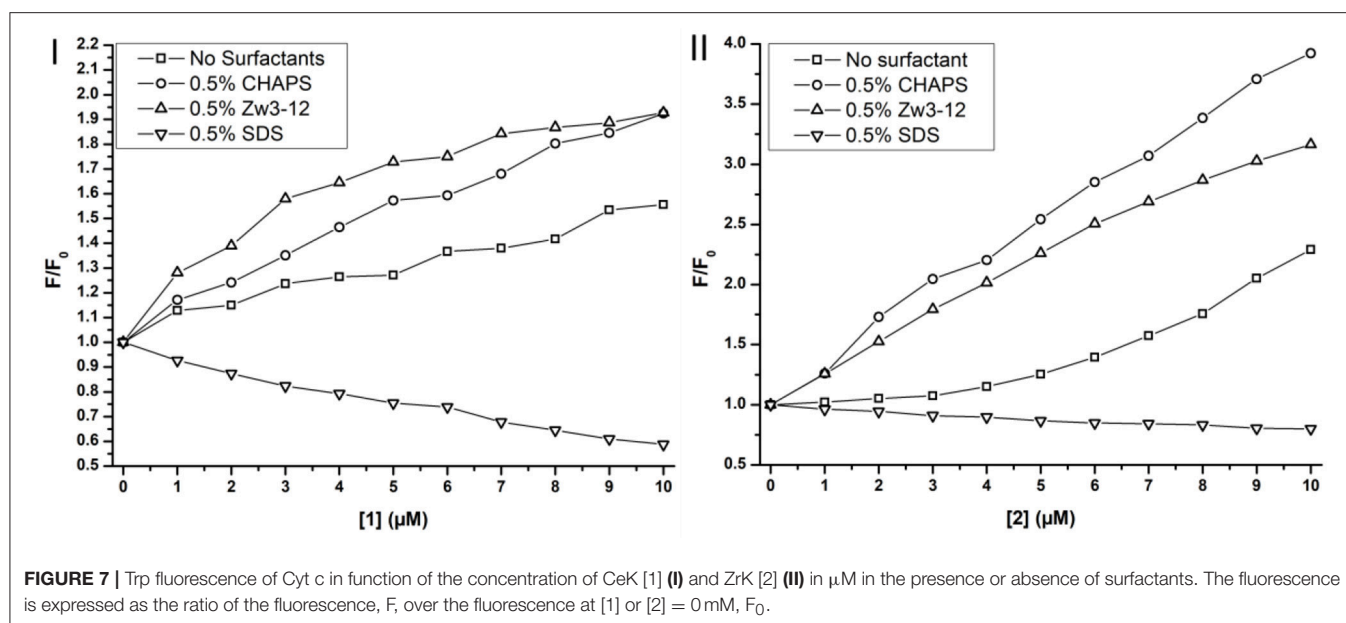
FIGURE 6 | Soret region CD spectra of 10 μ M Cyt c solutions in the presence of increasing concentration of CeK (1) (from 0 to 50 μ M) in the absence of surfactants (I), in the presence of 0.5% CHAPS (II), 0.5% Zw3-12 (III), and 0.5% SDS (IV). All samples were buffered at pH 7.4 by a 10 mM sodium phosphate buffer and kept at $25 \pm 0.1^\circ\text{C}$ during measurements.

heme group. In its native state Trp is hydrogen bonded to a propionate of the heme group. The proximity of the heme causes an intrinsic quenching of Trp fluorescence due to the energy transfer from the excited Trp residue to the heme group. When Cyt c unfolds, the distance between Trp and the heme group increases, which enhances the fluorescence intensity (Myer et al., 1980; Elöve et al., 1992; Bychkova et al., 1996; Kamatari et al., 1996; Konermann and Douglas, 1997; Rodriguez-Cruz et al., 2001; Tsong, 2002). **Figure S5** shows the effect of the surfactants on the Trp fluorescence of Cyt c.

Previously, Soret CD spectroscopy indicated that CHAPS and Zw3-12 did not alter the tertiary structure of Cyt c, while SDS caused severe structural changes of the protein (see **Figure S5**). These observations were confirmed with Trp fluorescence spectroscopy. In the presence of 0.5% Zw3-12 or 0.5% CHAPS the intensity of fluorescence is increased by factor of 3, which implies that these surfactants do not cause severe unfolding of Cyt c. SDS, however, amplified the fluorescence to nearly 62 times at even lower concentrations

(0.2%). Increasing the SDS concentration did not result in further increase of fluorescence, indicating that Cyt c is already completely unfolded in the presence of 0.2% SDS. The effect of adding CeK and ZrK POMs to Cyt c:surfactant mixtures is shown in **Figure 7**.

Adding metal substituted POMs to Cyt c in absence of any surfactants causes a slight increase in fluorescence intensity. The intensity increased approximately 1.5 and 2.2 times upon adding 10 μ M of CeK and ZrK, respectively. This indicates that Cyt c partially unfolds upon binding to these POMs, but the effect of ZrK is slightly more pronounced than the effect of CeK. A partial unfolding of Cyt c was already observed in the presence of Zw3-12 or CHAPS, but adding 10 μ M of CeK resulted in doubling of the emission intensity in the presence of 0.5% CHAPS or 0.5% Zw3-12. ZrK increases the Cyt c fluorescence intensity approximately 3 and 4 times at 10 μ M in the presence of 0.5% CHAPS and Zw3-12, respectively. Both CD and Trp fluorescence spectroscopy demonstrated that SDS completely unfolds Cyt c. Adding CeK or ZrK to a Cyt c/SDS solution



quenched the fluorescence. This quenching appeared to be static in nature and could be fitted to a derived Stern-Volmer equation (see **Figure S6**) (Lakowicz, 2007). The binding constants were determined to be $(3 \pm 1) \times 10^4 \text{ M}^{-1}$ and $(4 \pm 1) \times 10^3 \text{ M}^{-1}$ for **CeK** and **ZrK**, respectively. The order of magnitude difference might be explained by a different counterion present in these POMs. While **CeK** contains potassium cations, **ZrK** has diethylammonium (Et_2NH_2^+). Potassium might compensate the negative charge of SDS by making it appear less anionic to **CeK**. Et_2NH_2^+ however has a positive charge that is partly shielded by the ethyl groups, making it less capable of shielding the negative charge of SDS. Because of this inefficient shielding, SDS will cause a stronger repulsion of the polyanionic POM **ZrK** than it does to POM **CeK**. However, all Trp fluorescence measurements indicate that both **CeK** and **ZrK** bind to Cyt c in the presence or in the absence of surfactants.

Speciation of CeK in the Presence of Surfactants

The Ce^{IV} substituted Keggin POM, **CeK**, is known to undergo reduction during incubation with proteins (Stroobants et al., 2013; Sap et al., 2016). Luckily, the reduction of the POM does not result in oxidative cleavage of peptide bonds (Stroobants et al., 2013; Sap et al., 2016), as the side chains of amino acids that contain aromatic residues (Trp, Tyr, or Thr), thiols (Cys) and thioethers (Met) are the most likely targets of the oxidation by Ce^{IV} . The resulting Ce^{III} substituted POM is thought to be less active as a protease due to the loss in Lewis acidity. The $\text{Ce}^{\text{IV}} \rightarrow \text{Ce}^{\text{III}}$ reduction can be monitored with ^{31}P NMR spectroscopy as both species have a distinctly different chemical shift. The Ce^{IV} substituted Keggin is characterized by a ^{31}P resonance at ca. -13.5 ppm , while the Ce^{III} species shows a peak at -18.6 ppm . Monitoring the reduction of **CeK** in the presence

of the three different surfactants might explain the differences in hydrolysis yields observed above. **Figure 8** shows the progress of the reduction of **CeK** in the presence of Cyt c and 0.5% CHAPS over the course of 48 h.

As can be seen from **Figure 8**, the amount of the Ce^{IV} POM species decreases over time in favor of the Ce^{III} POM. The relative amount of Ce^{IV} after incubation at 60°C in the presence of different surfactants is plotted as function of time in **Figure 9**.

In the presence of 0.5% CHAPS, the reduction of Ce^{IV} is accelerated significantly in comparison to SDS and Zw3-12. After 48 h in the presence of 0.5% CHAPS only 38% of Ce^{IV} POM was present, while 54 and 53% of Ce^{IV} POM was observed in the presence of 0.5% SDS and 0.5% Zw3-12, respectively. This decrease of the active catalyst in the presence of CHAPS might explain the slightly lower hydrolysis yield in the presence of this surfactant. However, the strong inhibition of Zw3-12 on hydrolysis appears to originate from its effect on the Cyt c structure in solution and not on its impact on the reduction of Ce^{IV} POM catalyst.

CONCLUSIONS

This study has shown that in the presence of SDS, Zw3-12 or CHAPS surfactants, which are commonly used for solubilizing hydrophobic proteins, the specificity of **CeK** or **ZrK** toward hydrolysis of Cyt c does not change. Zw3-12 and CHAPS did not have a large effect on the secondary and tertiary structure of Cyt c, and therefore the same selectivity as in the absence of the surfactants was observed. In the presence of SDS unfolding of Cyt c secondary and tertiary structure were observed, indicating a large degree of a denaturation. Similar structural changes were observed in the presence of a $50 \mu\text{M}$ concentration of **CeK** or **ZrK**, indicating that POM binding to Cyt c results in large protein unfolding, both in

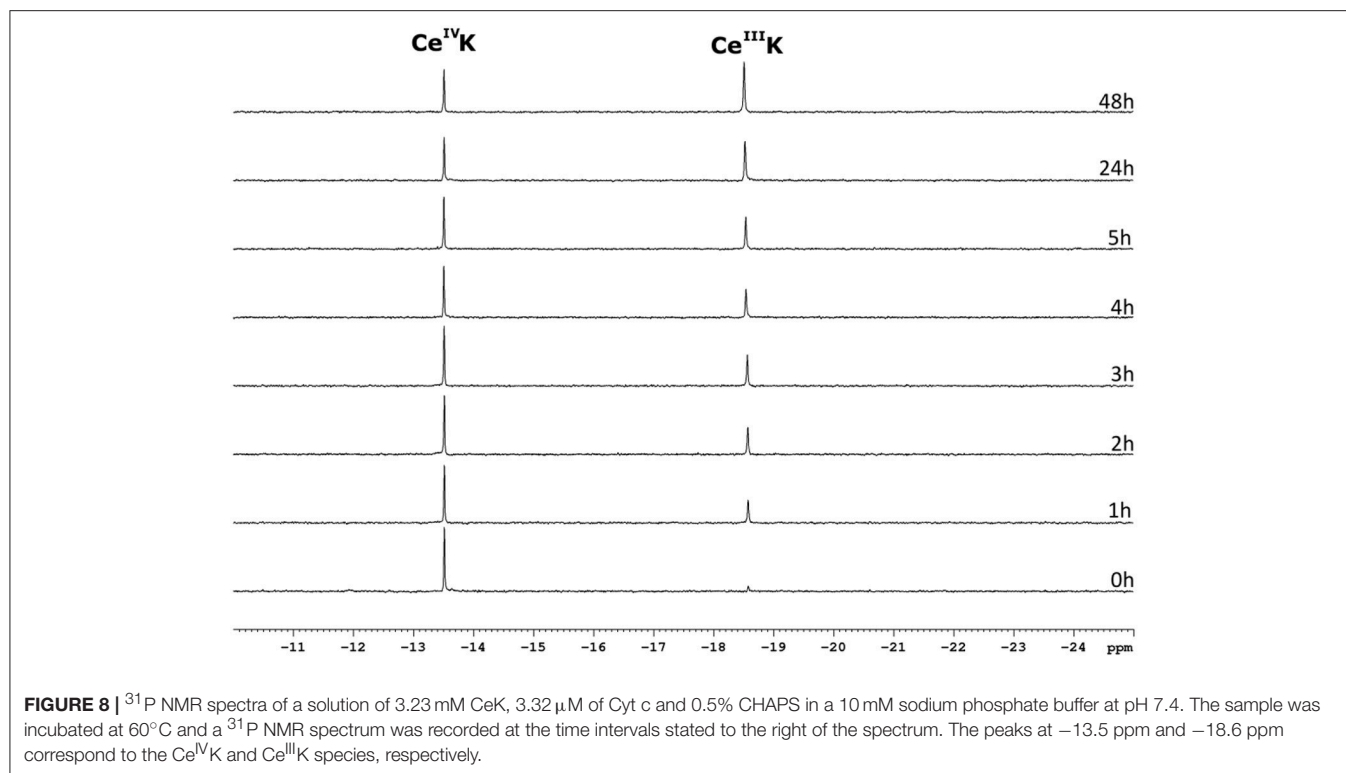


FIGURE 8 | ^{31}P NMR spectra of a solution of 3.23 mM CeK, 3.32 μM of Cyt c and 0.5% CHAPS in a 10 mM sodium phosphate buffer at pH 7.4. The sample was incubated at 60°C and a ^{31}P NMR spectrum was recorded at the time intervals stated to the right of the spectrum. The peaks at -13.5 ppm and -18.6 ppm correspond to the $\text{Ce}^{\text{IV}}\text{K}$ and $\text{Ce}^{\text{III}}\text{K}$ species, respectively.

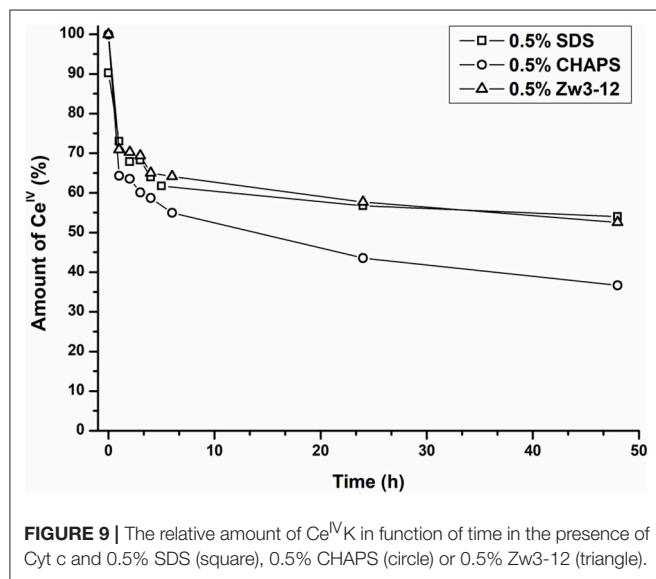


FIGURE 9 | The relative amount of $\text{Ce}^{\text{IV}}\text{K}$ in function of time in the presence of Cyt c and 0.5% SDS (square), 0.5% CHAPS (circle) or 0.5% Zw3-12 (triangle).

the absence or presence of all three surfactants. This finding might explain why surfactants have no noticeable effect on the selectivity of **CeK** and **ZrK**. Recent work has reported on the specificity of $[\text{Zr}(\alpha_2\text{-P}_2\text{W}_{17}\text{O}_{61})_2]^{16-}$ toward HSA in the absence or presence of CHAPS (Sap et al., 2017), in which 7 distinct cleavage sites were observed in the presence of 0.5% CHAPS whereas 4 were determined in the absence of any surfactant. This was explained by the fact that the partial unfolding of HSA in the presence of CHAPS allowed the POM access to

peptide bonds, which were previously buried in the native structure of the protein. This different effect of the surfactants on the hydrolysis of HSA and Cyt c is probably due to different size of these proteins. While HSA is a large protein of 66.4 kDa (609 amino acids), Cyt c is a relatively small protein consisting of 12.4 kDa (104 amino acids). In their native state, larger proteins can accommodate POMs without causing drastic structural changes (Goovaerts et al., 2013, 2015; Stroobants et al., 2014a), whereas the smaller proteins undergo significant structural changes when binding with POMs (Stroobants et al., 2013). This work shows that the structural changes in Cyt c caused by surfactants are similar to those caused by POMs, hence the same specificity in the absence or presence of surfactants was observed.

The hydrolysis of Cyt c by **CeK** was increased in the presence of SDS, but decreased in the presence of CHAPS, and was nearly inhibited in the presence of Zw3-12. The tertiary structure of Cyt c in the presence of SDS closely resembles the structure in the presence of 50 μM **CeK**, but the structure in the presence of CHAPS and Zw3-12 is closely related to the native structure. These findings indicate that for Cyt c hydrolysis to occur, large unfolding of the protein is needed in order to accommodate the POMs. While SDS readily unfolds Cyt c, the protein remains largely folded in the presence of CHAPS and Zw3-12. Addition of POMs to Cyt c solutions in CHAPS results in unfolding of the structure allowing the interaction with POMs to occur and results in protein hydrolysis. Zw3-12, however, locks Cyt c in a conformation that resists unfolding upon addition of POM, and therefore results in nearly complete inhibition of protein hydrolysis.

These findings, which reveal the effect of different surfactants on the reactivity of POMs, may be an important step forward in developing metal-substituted POMs as a potential class of metalloproteases for the hydrolysis of hydrophobic and membrane proteins.

EXPERIMENTAL

Materials

Deuteriumoxide (D₂O), N,N,N',N'-tetramethylethylenediamine (TEMED), ammonium persulphate (APS), phosphotungstic acid hydrate (H₃[PW₁₂O₄₀].xH₂O), glycine, disodium phosphate (Na₂HPO₄), sodium dodecyl sulfate (SDS), horse heart cytochrome c (Cyt c) and bromophenol blue were bought from Sigma-Aldrich. Zirconium oxychloride octahydrate and diethyl ether were purchased from ChemLab. Aqueous hydrochloric acid (37%), potassium hydrogen carbonate and ammonium cerium^{IV} nitrate (CAN) were obtained from Acros organics. Ethanol, sodium hydrogen carbonate, aqueous *ortho*-phosphoric acid (85%), diethylaminehydrochloride and protein ladders were acquired from Thermo Fisher Scientific. Methanol and monosodiumphosphate (NaH₂PO₄) were purchased from VWR. Potassium chloride, tris(hydroxymethyl)aminomethane (TRIS) and acrylamide:bisacrylamide (29:1) solution (30%) were procured from Applchem. [Ce(α-PW₁₁O₃₉)₂]¹⁰⁻ (**CeK**) was synthesized according to (Griffith et al., 2000) [Zr(α-PW₁₁O₃₉)₂]¹⁰⁻ (**ZrK**) was synthesized following a slightly altered procedure from (Sokolov et al., 2007).

Methods

Circular Dichroism Spectroscopy

Solution containing 10 μM Cyt c neat or in the presence of 0.5% SDS or 0.5% Zw3-12 were prepared in a 10 mM sodium phosphate buffer at pH 7.4. The concentration of **CeK** and **ZrK** was increased incremental from 0 to 50 μM in 10 μM steps. The samples were kept at a constant temperature of 25 ± 0.1°C during the recording of all spectra. The CD spectra were recorded with a JASCO-1500 spectrometer directly after the samples were prepared. The far-UV (180–260 nm) and Soret (300–500 nm) CD spectra were recorded with a 1 mm and 10 mm quartz cuvette, respectively. The resulting spectra are averaged over 3 accumulations with bandwidth of 1 nm. All spectra were corrected for background effects by subtracting the spectra of the respective buffer solutions. The machine response (θ in mdeg) was converted to mean residue ellipticity ([θ]_{MRE}) according to Equation (1): (Wallace and Janes, 2009).

$$[\theta]_{MRE} = \frac{\theta \times 0.1 \times \langle M \rangle}{c_g \times l_{cm}} = \frac{\theta}{c_M \times n \times l_{mm}} \quad (1)$$

Where <M> is the mean residue molar weight (equal to Mw/(n-1)); c_g and c_M the protein concentration in g/L and mol/L, respectively; l_{cm} and l_{mm} the optical path length in cm and mm, respectively and n the number of peptide bonds in the protein (equal to the total number of amino acids minus one).

The secondary structural content was calculated using the web service DICHROWEB (Whitmore and Wallace, 2004, 2008) with the CDSSTR algorithm and protein reference set 3 (optimized for the spectral region from 185 to 240 nm) (Sreerama and Woody, 2000).

Fluorescence Spectroscopy

Samples containing 10 μM Cyt c neat or in the presence of 0.5% SDS, CHAPS or Zw3-12 were prepared in a 10 mM sodium phosphate buffer at pH 7.4. The concentration of **CeK** and **ZrK** was increased from 0 to 10 in 1 μM steps. The samples were kept at ambient temperature during the recording of the spectra. A 10.0 mm quartz cuvette was used to record emission spectra using an Edinburgh Instruments FLS-980 spectrometer. The samples were excited at 295 nm and emission was observed from 300 to 450 nm with a maximum at approximately 333 nm.

Hydrolysis Experiments

Solutions containing 30 μM Cyt c and 50 equivalents of **CeK** or **ZrK** in the presence or absence of the different surfactants (0.5% CHAPS, SDS or Zw3-12) were prepared in 10 mM sodium phosphate buffer at pH 7.4. The samples were incubated for several days at 60°C and aliquots were taken at several time intervals. SDS-PAGE was used to monitor the progress of the hydrolysis (6% stacking gels and 18% running in 0.1 M Tris-Tricine, 0.1% SDS running buffer).

Samples were mixed in a 2 to 1 ratio with a 3x sample buffer (250 mM DTT, 50% glycerol, 5% SDS, 0.05% bromophenol blue, 225 mM Tris-HCl buffer, pH 6.8) and incubated at 95°C for 5 min. After 3 min of centrifuging, 10 μM of the final sample solution was loaded on an 18% gel. The PageRuler™ Unstained Low Range Protein Ladder of Thermo scientific was used as Mw reference. The gels were run at 300 V and 30 mA/gel current using an OmniPage electrophoretic cell combined with an EV243 power supply. The gels were developed with Coomassie blue or silver staining and analyzed using a GelDoc EZ set-up with the Image Lab software (Bio-Rad, Hercules, CA).

³¹P NMR Spectroscopy

Samples containing 32.2 μM Cyt c and 3.23 mM **CeK** neat or in the presence of 0.5% CHAPS, Zw3-12 or SDS were prepared in a 10 mM sodium phosphate buffer at pH 7.4. The samples contained 10% D₂O and were incubated at 60°C and measured at different time points. The spectra were recorded on a 400 MHz Avance III+ spectrometer (Bruker) with a sweep width of 100 ppm, 256 scans, relaxation delay of 2.5 s and the center of the spectrum at 0 ppm. A 25% H₃PO₄ solution was used as an external reference to calibrate all spectra.

AUTHOR CONTRIBUTIONS

All experimental work and data analysis was performed by TQ and TD under guidance of TQ. The manuscript was written by TQ with valuable contributions and corrections of TP-V and PS.

FUNDING

TQ thanks Science Foundation Flanders (FWO) for FWO-SB doctoral fellowship. TP-V thanks Science Foundation Flanders (FWO) and KU Leuven for the funding.

REFERENCES

- Absillis, G., Cartuyvels, E., Van Deun, R., and Parac-Vogt, T. N. (2008). Hydrolytic cleavage of an RNA-model phosphodiester catalyzed by a highly negatively charged polyoxomolybdate $[\text{Mo}_7\text{O}_{24}]^{6-}$ cluster. *J. Am. Chem. Soc.* 130, 17400–17408. doi: 10.1021/ja804823g
- Absillis, G., and Parac-Vogt, T. N. (2012). Peptide bond hydrolysis catalyzed by the Wells-Dawson $\text{Zr}(\alpha_2\text{-P}_2\text{W}_{17}\text{O}_{61})_2$ polyoxometalate. *Inorg. Chem.* 51, 9902–9910. doi: 10.1021/ic301364n
- Absillis, G., Van Deun, R., and Parac-Vogt, T. N. (2011). Polyoxomolybdate promoted hydrolysis of a DNA-model phosphoester studied by NMR and EXAFS spectroscopy. *Inorg. Chem.* 50, 11552–11560. doi: 10.1021/ic201498u
- Bryant, R. A. R., and Hansen, D. E. (1996). Direct measurement of the uncatalyzed rate of hydrolysis of a peptide bond. *J. Am. Chem. Soc.* 118, 5498–5499. doi: 10.1021/ja953137b
- Bushnell, G. W., Louie, G. V., and Brayer, G. D. (1990). High-resolution three-dimensional structure of horse heart cytochrome c. *J. Mol. Biol.* 214, 585–595. doi: 10.1016/0022-2836(90)90200-6
- Bychkova, V. E., Dujsekina, A. E., Klenin, S. I., Tiktopulo, E. I., Uversky, V. N., and Ptitsyn, O. B. (1996). Molten globule-like state of cytochrome c under conditions simulating those near the membrane surface. *Biochemistry* 35, 6058–6063. doi: 10.1021/bi9522460
- Carter, P., Smith, L., and Ryan, M. (2004). Identification and validation of cell surface antigens for antibody targeting in oncology. *Endocr. Relat. Cancer* 11, 659–687. doi: 10.1677/erc.1.00766
- Cartuyvels, E., Absillis, G., and Parac-Vogt, T. N. (2008). Questioning the paradigm of metal complex promoted phosphodiester hydrolysis: $[\text{Mo}_7\text{O}_{24}]^{6-}$ -polyoxometalate cluster as an unlikely catalyst for the hydrolysis of a DNA model substrate. *Chem. Commun.* 1, 85–87. doi: 10.1039/B714860G
- Elöve, G. A., Chaffotte, A. F., Roder, H., and Goldberg, M. E. (1992). Early steps in cytochrome c folding probed by time-resolved circular dichroism and fluorescence spectroscopy. *Biochemistry* 31, 6876–6883. doi: 10.1021/bi00145a003
- Goovaerts, V., Stroobants, K., Absillis, G., and Parac-Vogt, T. (2015). Understanding the regioselective hydrolysis of human serum albumin by $\text{Zr}(\text{IV})$ -substituted polyoxotungstates using tryptophan fluorescence spectroscopy. *Inorganics* 3, 230–245. doi: 10.3390/inorganics3020230
- Goovaerts, V., Stroobants, K., Absillis, G., and Parac-Vogt, T. N. (2013). Molecular interactions between serum albumin proteins and Keggin type polyoxometalates studied using luminescence spectroscopy. *Phys. Chem. Chem. Phys.* 15, 18378–18387. doi: 10.1039/c3cp52848k
- Grant, K., and Kassai, M. (2006). Major advances in the hydrolysis of peptides and proteins by metal ions and complexes. *Curr. Org. Chem.* 10, 1035–1049. doi: 10.2174/13852720677435535
- Greenfield, N. J. (2006). Using circular dichroism spectra to estimate protein secondary structure. *Nat. Protoc.* 1, 2876–2890. doi: 10.1038/nprot.2006.202
- Griffith, W. P., Morley-Smith, N., Nogueira, H. I. S., Shoaib, A. G. F., Suriaatmaja, M., White, A. J. P., et al. (2000). Studies on polyoxo and polyperoxo-metalates. *J. Organomet. Chem.* 607, 146–155. doi: 10.1016/S0022-328X(00)00308-9
- Hasenknopf, B. (2005). Polyoxometalates: introduction to a class of inorganic compounds and their biomedical applications. *Front. Biosci.* 10, 275–287. doi: 10.2741/1527
- Hegg, E. L., and Burstyn, J. N. (1998). Toward the development of metal-based synthetic nucleases and peptidases: a rationale and progress report in applying the principles of coordination chemistry. *Coord. Chem. Rev.* 173, 133–165. doi: 10.1016/S0010-8545(98)00157-X
- Hiramatsu, K., and Yang, J. T. (1983). Cooperative binding of hexadecyltrimethylammonium chloride and sodium dodecyl sulfate to cytochrome c and the resultant change in protein conformation. *Biochim. Biophys. Acta* 743, 106–114. doi: 10.1016/0167-4838(83)90423-5
- Ho, P. H., Breynaert, E., Kirschhock, C. E., and Parac-Vogt, T. N. (2011a). Hydrolysis of carboxyesters promoted by vanadium(V) oxyanions. *Dalton Trans.* 40, 295–300. doi: 10.1039/C0DT00744G
- Ho, P. H., Mihaylov, T., Pierloot, K., and Parac-Vogt, T. N. (2012). Hydrolytic activity of vanadate toward serine-containing peptides studied by kinetic experiments and DFT theory. *Inorg. Chem.* 51, 8848–8859. doi: 10.1021/ic300761g
- Ho, P. H., Stroobants, K., and Parac-Vogt, T. N. (2011b). Hydrolysis of serine-containing peptides at neutral pH promoted by $[\text{MoO}_4]^{2-}$ oxyanion. *Inorg. Chem.* 50, 12025–12033. doi: 10.1021/ic2015034
- Hopkins, A. L., and Groom, C. R. (2002). The druggable genome. *Nat. Rev. Drug Discov.* 1, 727–730. doi: 10.1038/nrd892
- Kamatari, Y. O., Konno, T., Kataoka, M., and Akasaka, K. (1996). The methanol-induced globular and expanded denatured states of cytochrome c: a study by CD fluorescence, NMR and small-angle X-ray scattering. *J. Mol. Biol.* 259, 512–523. doi: 10.1006/jmbi.1996.0336
- Kaminsky, L. S., Yong, F. C., and King, T. E. (1972). Circular dichroism studies of the perturbations of cytochrome c by alcohols. *J. Biol. Chem.* 247, 1354–1359.
- Konermann, L., and Douglas, D. J. (1997). Acid-induced unfolding of cytochrome c at different methanol concentrations: electrospray ionization mass spectrometry specifically monitors changes in the tertiary structure. *Biochemistry* 36, 12296–12302. doi: 10.1021/bi971266u
- Kozhevnikov, I. (2002). *Catalysts for Fine Chemical Synthesis, Catalysis by Polyoxometalates*. Chichester: Wiley.
- Lakowicz, J. R. (2007). *Principles of Fluorescence Spectroscopy*. New York, NY: Springer.
- Lokeren, L. V., Cartuyvels, E., Absillis, G., Willem, R., and Parac-Vogt, T. N. (2008). Phosphoesterase activity of polyoxomolybdates: diffusion ordered NMR spectroscopy as a tool for obtaining insights into the reactivity of polyoxometalate clusters. *Chem. Commun.* 28, 2774–2776. doi: 10.1039/b802671h
- Long, D. L., Burkholder, E., and Cronin, L. (2007). Polyoxometalate clusters, nanostructures and materials: from self assembly to designer materials and devices. *Chem. Soc. Rev.* 36, 105–121. doi: 10.1039/B502666K
- Long, D. L., Tsunashima, R., and Cronin, L. (2010). Polyoxometalates: building blocks for functional nanoscale systems. *Angew. Chem. Int. Edn. Engl.* 49, 1736–1758. doi: 10.1002/anie.200902483
- Luong, T. K., Absillis, G., Shestakova, P., and Parac-Vogt, T. N. (2015a). Hydrolysis of the RNA model substrate catalyzed by a binuclear Zr^{IV} -substituted Keggin polyoxometalate. *Dalton Trans.* 44, 15690–15696. doi: 10.1039/C5DT02077H
- Luong, T. K., Govaerts, I., Robben, J., Shestakova, P., and Parac-Vogt, T. N. (2017). Polyoxometalates as artificial nucleases: hydrolytic cleavage of DNA promoted by a highly negatively charged $\text{Zr}(\text{IV})$ -substituted Keggin polyanion. *Chem. Commun.* 53, 617–620. doi: 10.1039/C6CC08555E
- Luong, T. K., Shestakova, P., Absillis, G., and Parac-Vogt, T. N. (2016). Detailed mechanism of phosphoanhydride bond hydrolysis promoted by a binuclear $\text{Zr}(\text{IV})$ -substituted keggin polyoxometalate elucidated by a combination of (31)P, (31)P DOSY, and (31)P EXSY NMR spectroscopy. *Inorg. Chem.* 55, 4864–4873. doi: 10.1021/acs.inorgchem.6b00385
- Luong, T. K., Shestakova, P., Mihaylov, T. T., Absillis, G., Pierloot, K., and Parac-Vogt, T. N. (2015b). Multinuclear diffusion NMR spectroscopy and DFT modeling: a powerful combination for unraveling the mechanism of phosphoester bond hydrolysis catalyzed by metal-substituted polyoxometalates. *Chem. Eur. J.* 21, 4428–4439. doi: 10.1002/chem.201405810
- Luong, T. K. N., Absillis, G., Shestakova, P., and Parac-Vogt, T. N. (2014). Solution speciation of the dinuclear Zr^{IV} -substituted keggin polyoxometalate

SUPPLEMENTARY MATERIAL

The Supplementary Material for this article can be found online at: <https://www.frontiersin.org/articles/10.3389/fchem.2018.00372/full#supplementary-material>

- [α -PW₁₁O₃₉Zr(μ -OH)(H₂O)₂]⁸⁻ and its reactivity towards DNA-model phosphodiester hydrolysis. *Eur. J. Inorg. Chem.* 2014, 5276–5284. doi: 10.1002/ejic.201402735
- Ly, H. G., Absillis, G., Janssens, R., Proost, P., and Parac-Vogt, T. N. (2015a). Highly amino acid selective hydrolysis of myoglobin at aspartate residues as promoted by zirconium(IV)-substituted polyoxometalates. *Angew. Chem. Int. Ed Engl.* 54, 7391–7394. doi: 10.1002/anie.201502006
- Ly, H. G., Absillis, G., and Parac-Vogt, T. N. (2013a). Amide bond hydrolysis in peptides and cyclic peptides catalyzed by a dimeric Zr(IV)-substituted Keggin type polyoxometalate. *Dalton Trans.* 42, 10929–10938. doi: 10.1039/c3dt50705j
- Ly, H. G. T., Absillis, G., Bajpe, S. R., Martens, J. A., and Parac-Vogt, T. N. (2013b). Hydrolysis of dipeptides catalyzed by a zirconium(IV)-substituted lindqvist type polyoxometalate. *Eur. J. Inorg. Chem.* 2013, 4601–4611. doi: 10.1002/ejic.201300270
- Ly, H. G. T., Absillis, G., and Parac-Vogt, T. N. (2015b). Comparative study of the reactivity of zirconium(IV)-substituted polyoxometalates towards the hydrolysis of oligopeptides. *Eur. J. Inorg. Chem.* 2015, 2206–2215. doi: 10.1002/ejic.201500161
- Ly, H. G. T., and Parac-Vogt, T. N. (2017). Spectroscopic study of the interaction between horse heart myoglobin and zirconium^{IV}-substituted polyoxometalates as artificial proteases. *Chem. Phys. Chem.* 18, 2451–2458. doi: 10.1002/cphc.201700680
- Milovic, N. M., Dutca, L. M., and Kostic, N. M. (2003). Transition-metal complexes as enzyme-like reagents for protein cleavage: complex cis-[Pt(en)(H₂O)₂]²⁺ as a new methionine-specific protease. *Chem. Eur. J.* 9, 5097–5106. doi: 10.1002/chem.200304772
- Miskevich, F., Davis, A., Leepapawong, P., Giganti, V., Kostic, N. M., and Angel, L. A. (2011). Metal complexes as artificial proteases in proteomics: a palladium(II) complex cleaves various proteins in solutions containing detergents. *J. Inorg. Biochem.* 105, 675–683. doi: 10.1016/j.jinorgbio.2011.01.010
- Mugnol, K. C., Ando, R. A., Nagayasu, R. Y., Faljoni-Alario, A., Brochsztain, S., Santos, P. S., et al. (2008). Spectroscopic, structural, and functional characterization of the alternative low-spin state of horse heart cytochrome C. *Biophys. J.* 94, 4066–4077. doi: 10.1529/biophysj.107.116483
- Myer, Y. P. (1968a). Conformation of cytochromes. III. Effect of urea, temperature, extrinsic ligands, and pH variation on the conformation of horse heart ferricytochrome c. *Biochemistry* 7, 765–776. doi: 10.1021/bi00842a035
- Myer, Y. P. (1968b). Far ultraviolet circular dichroism spectra of cytochrome c. *Biochim. Biophys. Acta Protein Struct.* 154, 84–90. doi: 10.1016/0005-2795(68)90261-4
- Myer, Y. P., Macdonald, L. H., Verma, B. C., and Pande, A. (1980). Urea denaturation of horse heart ferricytochrome c. Equilibrium studies and characterization of intermediate forms. *Biochemistry* 19, 199–207. doi: 10.1021/bi00542a030
- Nantes, I. L., Zucchi, M. R., Nascimento, O. R., and Faljoni-Alario, A. (2001). Effect of heme iron valence state on the conformation of cytochrome c and its association with membrane interfaces. A CD and EPR investigation. *J. Biol. Chem.* 276, 153–158. doi: 10.1074/jbc.M006338200
- Overington, J. P., Al-Lazikani, B., and Hopkins, A. L. (2006). How many drug targets are there? *FEBS J.* 5, 993–996. doi: 10.1038/nrd2199
- Pope, M. T. (1983). *Heteropoly and Isopoly Oxometalates*. Berlin; Heidelberg: Springer-Verlag.
- Pope, M. T., and Müller, A. (1991). Polyoxometalate chemistry: an old field with new dimensions in several disciplines. *Angew. Chem. Int. Edn. Engl.* 30, 34–48. doi: 10.1002/anie.199100341
- Quanten, T., Shestakova, P., Van Den Bulck, D., Kirschhock, C., and Parac-Vogt, T. N. (2016). Interaction study and reactivity of Zr(IV)-substituted wells-dawson polyoxometalate towards hydrolysis of peptide bonds in surfactant solutions. *Chem. Eur. J.* 22, 3775–3784. doi: 10.1002/chem.201503976
- Rabilloud, T. (2009). Membrane proteins and proteomics: love is possible, but so difficult. *Electrophoresis* 30(Suppl. 1), S174–S180. doi: 10.1002/elps.200900050
- Radzicka, A., and Wolfenden, R. (1996). Rates of uncatalyzed peptide bond hydrolysis in neutral solution and the transition state affinities of proteases. *J. Am. Chem. Soc.* 118, 6105–6109. doi: 10.1021/ja954077c
- Rhule, J. T., Hill, C. L., Judd, D. A., and Schinazi, R. F. (1998). Polyoxometalates in medicine. *Chem. Rev.* 98, 327–358. doi: 10.1021/cr960396q
- Rodriguez, J., Gupta, N., Smith, R. D., and Pevzner, P. A. (2008). Does trypsin cut before proline? *J. Proteome Res.* 7, 300–305. doi: 10.1021/pr0705035
- Rodriguez-Cruz, S. E., Khoury, J. T., and Parks, J. H. (2001). Protein fluorescence measurements within electrospray droplets. *J. Am. Soc. Mass Spectrom.* 12, 716–725. doi: 10.1016/S1044-0305(01)00241-0
- Sadakane, M., and Steckhan, E. (1998). Electrochemical properties of polyoxometalates as electrocatalysts. *Chem. Rev.* 98, 219–238. doi: 10.1021/cr960403a
- Santoni, V., Molloy, M., and Rabilloud, T. (2000). Membrane proteins and proteomics: un amour impossible? *Electrophoresis* 21, 1054–1070. doi: 10.1002/(SICI)1522-2683(20000401)21:6<1054::AID-ELPS1054>3.0.CO;2-8
- Santucci, R., and Ascoli, F. (1997). The solet circular dichroism spectrum as a probe for the heme Fe(III)-Met(80) axial bond in horse cytochrome c. *J. Inorg. Biochem.* 68, 211–214. doi: 10.1016/S0162-0134(97)00100-1
- Sap, A., Absillis, G., and Parac-Vogt, T. N. (2015). Selective hydrolysis of oxidized insulin chain B by a Zr(IV)-substituted Wells-Dawson polyoxometalate. *Dalton Trans.* 44, 1539–1548. doi: 10.1039/C4DT01477D
- Sap, A., Van Tichelen, L., Mortier, A., Proost, P., and Parac-Vogt, T. N. (2016). Tuning the selectivity and reactivity of metal-substituted polyoxometalates as artificial proteases by varying the nature of the embedded lewis acid metal ion. *Eur. J. Inorg. Chem.* 2016, 5098–5105. doi: 10.1002/ejic.201601098
- Sap, A., Vandebroek, L., Goovaerts, V., Martens, E., Proost, P., and Parac-Vogt, T. N. (2017). Highly selective and tunable protein hydrolysis by a polyoxometalate complex in surfactant solutions: a step toward the development of artificial metalloproteases for membrane proteins. *ACS Omega* 2, 2026–2033. doi: 10.1021/acsomega.7b00168
- Seddon, A. M., Curnow, P., and Booth, P. J. (2004). Membrane proteins, lipids and detergents: not just a soap opera. *Biochim. Biophys. Acta* 1666, 105–117. doi: 10.1016/j.bbame.2004.04.011
- Smith, R. M., and Hansen, D. E. (1998). The pH-rate profile for the hydrolysis of a peptide bond. *J. Am. Chem. Soc.* 120, 8910–8913. doi: 10.1021/ja9804565
- Sokolov, M. N., Chubarova, E. V., Peresyphkina, E. V., Virovets, A. V., and Fedin, V. P. (2007). Complexes of ZrIV and HfIV with monolacunary Keggin-and Dawson-type anions. *Russ. Chem. Bull.* 56, 220–224. doi: 10.1007/s11172-007-0036-x
- Speers, A. E., and Wu, C. C. (2007). Proteomics of integral membrane proteins—theory and application. *Chem. Rev.* 107, 3687–3714. doi: 10.1021/cr068286z
- Sreerama, N., and Woody, R. W. (2000). Estimation of protein secondary structure from circular dichroism spectra: comparison of CONTIN, SELCON, and CDSSTR methods with an expanded reference set. *Anal. Biochem.* 287, 252–260. doi: 10.1006/abio.2000.4880
- Steens, N., Ramadan, A. M., Absillis, G., and Parac-Vogt, T. N. (2010). Hydrolytic cleavage of DNA-model substrates promoted by polyoxovanadates. *Dalton Trans.* 39, 585–592. doi: 10.1039/B913471A
- Steens, N., Ramadan, A. M., and Parac-Vogt, T. N. (2009). When structural and electronic analogy leads to reactivity: the unprecedented phosphodiesterase activity of vanadates. *Chem. Commun.* 28, 965–967. doi: 10.1039/B816785K
- Stroobants, K., Absillis, G., Moelants, E., Proost, P., and Parac-Vogt, T. N. (2014a). Regioselective hydrolysis of human serum albumin by Zr^{IV}-substituted polyoxotungstates at the interface of positively charged protein surface patches and negatively charged amino acid residues. *Chem. Eur. J.* 20, 3894–3897. doi: 10.1002/chem.201303622
- Stroobants, K., Goovaerts, V., Absillis, G., Bruylants, G., Moelants, E., Proost, P., et al. (2014b). Molecular origin of the hydrolytic activity and fixed regioselectivity of a Zr(IV)-substituted polyoxotungstate as artificial protease. *Chem. Eur. J.* 20, 9567–9577. doi: 10.1002/chem.201402683
- Stroobants, K., Ho, P. H., Moelants, E., Proost, P., and Parac-Vogt, T. N. (2014c). Selective hydrolysis of hen egg white lysozyme at Asp-X peptide bonds promoted by oxomolybdate. *J. Inorg. Biochem.* 136, 73–80. doi: 10.1016/j.jinorgbio.2014.03.006
- Stroobants, K., Moelants, E., Ly, H. G., Proost, P., Bartik, K., and Parac-Vogt, T. N. (2013). Polyoxometalates as a novel class of artificial proteases: selective hydrolysis of lysozyme under physiological pH and temperature promoted by a cerium(IV) Keggin-type polyoxometalate. *Chem. Eur. J.* 19, 2848–2858. doi: 10.1002/chem.201203020
- Stroobants, K., Saadallah, D., Bruylants, G., and Parac-Vogt, T. N. (2014d). Thermodynamic study of the interaction between hen egg white lysozyme and

- Ce(IV)-Keggin polyoxotungstate as artificial protease. *Phys. Chem. Chem. Phys.* 16, 21778–21787. doi: 10.1039/C4CP03183K
- Swaney, D. L., Wenger, C. D., and Coon, J. J. (2010). Value of using multiple proteases for large-scale mass spectrometry-based proteomics. *J. Proteome Res.* 9, 1323–1329. doi: 10.1021/pr900863u
- Tan, S., Tan, H. T., and Chung, M. C. (2008). Membrane proteins and membrane proteomics. *Proteomics* 8, 3924–3932. doi: 10.1002/pmic.200800597
- Thomas, Y. G., Goldbeck, R. A., and Kliger, D. S. (2000). Characterization of equilibrium intermediates in denaturant-induced unfolding of ferrous and ferric cytochromes using magnetic circular dichroism, circular dichroism, and optical absorption spectroscopies. *Biopolymers* 57, 29–36. doi: 10.1002/(SICI)1097-0282(2000)57:1<29::AID-BIP5>3.0.CO;2-V
- Tsiatsiani, L., and Heck, A. J. (2015). Proteomics beyond trypsin. *FEBS J.* 282, 2612–2626. doi: 10.1111/febs.13287
- Tsong, T. Y. (2002). Ferricytochrome c chain folding measured by the energy transfer of tryptophan 59 to the heme group. *Biochemistry* 15, 5467–5473. doi: 10.1021/bi00670a007
- Van Rompuy, L. S., and Parac-Vogt, T. N. (2017). Polyoxometalates as sialidase mimics: selective and non-destructive removal of sialic acid from a glycoprotein promoted by phosphotungstic acid. *Chem. Commun.* 53, 10600–10603. doi: 10.1039/C7CC05888H
- Vanhaecht, S., Absillis, G., and Parac-Vogt, T. N. (2012). Hydrolysis of DNA model substrates catalyzed by metal-substituted Wells-Dawson polyoxometalates. *Dalton Trans.* 41, 10028–10034. doi: 10.1039/c2dt30588g
- Vanhaecht, S., Absillis, G., and Parac-Vogt, T. N. (2013). Amino acid side chain induced selectivity in the hydrolysis of peptides catalyzed by a Zr(IV)-substituted Wells-Dawson type polyoxometalate. *Dalton Trans.* 42, 15437–15446. doi: 10.1039/c3dt51893k
- Wallace, B. A., and Janes, R. W. (eds.). (2009). “An introduction to circular dichroism and synchrotron radiation circular dichroism spectroscopy,” in *Modern Techniques for Circular Dichroism and Synchrotron Radiation Circular Dichroism Spectroscopy*, (Amsterdam: IOS Press), 1–18.
- Wallin, E., and von Heijne, G. (1998). Genome-wide analysis of integral membrane proteins from eubacterial, archaean, and eukaryotic organisms. *Protein Sci.* 7, 1029–1038. doi: 10.1002/pro.5560070420
- Wang, S. S., and Yang, G. Y. (2015). Recent advances in polyoxometalate-catalyzed reactions. *Chem. Rev.* 115, 4893–4962. doi: 10.1021/cr500390v
- Wei, W., and Danielson, N. D. (2011). Fluorescence and circular dichroism spectroscopy of cytochrome c in alkylammonium formate ionic liquids. *Biomacromolecules* 12, 290–297. doi: 10.1021/bm1008052
- Wezynfeld, N. E., Fraczyk, T., and Bal, W. (2016). Metal assisted peptide bond hydrolysis: chemistry, biotechnology and toxicological implications. *Coord. Chem. Rev.* 327–328, 166–187. doi: 10.1016/j.ccr.2016.02.009
- Whitelegge, J. P., Gomez, S. M., and Faull, K. F. (2003). Proteomics of membrane proteins. *Adv. Protein. Chem.* 65, 271–307.
- Whitmore, L., and Wallace, B. A. (2004). DICHROWEB, an online server for protein secondary structure analyses from circular dichroism spectroscopic data. *Nucleic Acids Res.* 32, W668–W673. doi: 10.1093/nar/gkh371
- Whitmore, L., and Wallace, B. A. (2008). Protein secondary structure analyses from circular dichroism spectroscopy: methods and reference databases. *Biopolymers* 89, 392–400. doi: 10.1002/bip.20853

Conflict of Interest Statement: The authors declare that the research was conducted in the absence of any commercial or financial relationships that could be construed as a potential conflict of interest.

Copyright © 2018 Quanten, De Mayaer, Shestakova and Parac-Vogt. This is an open-access article distributed under the terms of the Creative Commons Attribution License (CC BY). The use, distribution or reproduction in other forums is permitted, provided the original author(s) and the copyright owner(s) are credited and that the original publication in this journal is cited, in accordance with accepted academic practice. No use, distribution or reproduction is permitted which does not comply with these terms.



A Molecular CO₂ Reduction Catalyst Based on Giant Polyoxometalate {Mo₃₆₈}

Santu Das^{1,2}, Tuniki Balaraju^{1,2}, Soumitra Barman^{1,2}, S. S. Sreejith^{1,2},
Ramudu Pochamoni^{1,2} and Soumyajit Roy^{1,2*}

¹ Eco-Friendly Applied Materials Laboratory, College of Chemistry, Central China Normal University, Wuhan, China,

² Eco-Friendly Applied Materials Laboratory, Department of Chemical Sciences, Materials Science Centre, Mohanpur, Indian Institute of Science Education & Research, Kolkata, India

OPEN ACCESS

Edited by:

Rajesh Ramanathan,
RMIT University, Australia

Reviewed by:

Tatsuki Morimoto,
Tokyo University of Technology, Japan
Etienne Derat,
Université Pierre et Marie Curie,
France

*Correspondence:

Soumyajit Roy
s.roy@mail.ccnu.edu.cn;
s.roy@iiserkol.ac.in;
roy.soumyajit@gmail.com

Specialty section:

This article was submitted to
Inorganic Chemistry,
a section of the journal
Frontiers in Chemistry

Received: 15 January 2018

Accepted: 05 October 2018

Published: 02 November 2018

Citation:

Das S, Balaraju T, Barman S,
Sreejith SS, Pochamoni R and Roy S
(2018) A Molecular CO₂ Reduction
Catalyst Based on Giant
Polyoxometalate {Mo₃₆₈}.
Front. Chem. 6:514.
doi: 10.3389/fchem.2018.00514

Photocatalytic CO₂ reduction in water is one of the most attractive research pursuits of our time. In this article we report a giant polyoxometalate {Mo₃₆₈} based homogeneous catalytic system, which efficiently reduces CO₂ to formic acid with a maximum turnover number (TON) of 27,666, turnover frequency (TOF) of 4,611 h⁻¹ and external quantum efficiency of the reaction is 0.6%. The catalytic system oxidizes water and releases electrons, and these electrons are further utilized for the reduction of CO₂ to formic acid. A maximum of 8.3 mmol of formic acid was observed with the loading of 0.3 μmol of the catalyst. Our catalyst material is also stable throughout the reaction. The starting materials for this experiment are CO₂ and H₂O and the end products are HCOOH and O₂. The formic acid formed in this reaction is an important H₂ gas carrier and thus significant in renewable energy research.

Keywords: CO₂ reduction, polyoxometalate, homogeneous catalysis, water oxidation, photochemistry

INTRODUCTION

The CO₂ concentration in environment is ever increasing. Thus, to find out a suitable pathway to recycle CO₂ to an energy rich material is a crucial challenge nowadays (Hoffert et al., 2002; Crabtree and Lewis, 2007; Meinshausen et al., 2009; Mikkelsen et al., 2010; Garai et al., 2012; Bandeira et al., 2015; Twidell and Weir, 2015). The depletion of fossil fuel during production of energy increases the CO₂ level in the environment (Hoel and Kverndokk, 1996; Höök and Tang, 2013). It is also known that abundance of fossil fuel is limited. Thus, it is necessary to find out a new pathway which can produce energy without hampering the environment and burning fossil fuels. With this end in view if we convert a greenhouse gas like CO₂ to energy rich material it would be very interesting and helpful for a sustainable environment and economy (Khenkin et al., 2010; Rankin and Cummins, 2010; Wang W. et al., 2011; Bontemps et al., 2012; Kuhl et al., 2012; Ohtsu and Tanaka, 2012; Wesselbaum et al., 2012; Xi et al., 2012; Arai et al., 2013; Costentin et al., 2013; Asadi et al., 2014; Blondiaux et al., 2014; Herrero et al., 2014; Kim et al., 2014; Kou et al., 2014; Lu et al., 2014; Studt et al., 2014; Zhang et al., 2014; Gao et al., 2015; Kornienko et al., 2015; Liu et al., 2015; Marszewski et al., 2015; Matlachowski and Schwalbe, 2015; Roberts et al., 2015; Sypaseuth et al., 2015; Iwase et al., 2016; Kuriki et al., 2017). However, the challenge is as CO₂ is a very stable oxide of carbon at its stable oxidation state, a large amount of energy is required to activate CO₂. Activation of CO₂ is a challenge. Here this challenge is addressed via photochemical reduction of CO₂ to HCOOH using an unusually large giant POM cluster, first synthesized by Müller group in Bielefeld

{Mo₃₆₈} (Müller et al., 2002, 2004; Müller and Roy, 2003). The TON (27,666) and TOF (4,611 h⁻¹) of this conversion is quite high as compared to other reported molecular catalysts (Tamaki et al., 2015). In photosynthesis, nature continuously activates CO₂ with ease where CO₂ from environment is converted into carbohydrates through photosensitization using sun as the source of light. The process happens in nature such that first water gets oxidized and releases electrons which further reduce CO₂ to carbohydrate in a long catalytic cycle (Hatch, 1976). Drawing inspiration from this process, use of a proper catalytic system can lead to the conversion of CO₂ to different high energy carbon material under light. Many potential catalytic systems have been developed over the last few decades for the synthesis of different fuel and organic materials from CO₂. Some of the catalysts initially bind with CO₂ and further reduce it to different reduced materials (Castro-Rodriguez and Meyer, 2005; Laitar et al., 2005; Sakakura et al., 2007; Sadique et al., 2008; Cokoja et al., 2011; Langer et al., 2011; Mandal and Roesky, 2011; Sato et al., 2011; Schmeier et al., 2011). Some catalysts convert CO₂ following electrochemical methods (Amatore and Saveant, 1981; Hori et al., 1989; Whipple and Kenis, 2010; Agarwal et al., 2011; Finn et al., 2012; Kuhl et al., 2012; Sullivan et al., 2012; Costentin et al., 2013; Zhang et al., 2014; Kornienko et al., 2015; Lin et al., 2015). Electrochemically CO₂ can be reduced to different alkane, ethylene, CO, and HCOOH. The major problem associated with this process is the selectivity in the reduction of CO₂ to different reduced products. Recently Yaghi group showed that electrochemically CO₂ can be reduced to CO selectively using Co-porphyrin based COF and MOF catalysts in water (Kornienko et al., 2015; Lin et al., 2015). Imminent challenge lies in the photochemical reduction of CO₂ (Matsuoka et al., 1993; Daniel and Astruc, 2004; Schwartzberg and Zhang, 2008; Takeda et al., 2008; Li and Zhang, 2009; Morris et al., 2009; Dhakshinamoorthy et al., 2012; Tornow et al., 2012; Sato et al., 2013; Sekizawa et al., 2013; Zhu et al., 2013; Wang et al., 2014; Kim et al., 2015; Li et al., 2015; Low et al., 2015). Among various proposed technologies, photocatalytic CO₂ reduction has been known as one of the most important strategies for solving both global energy and environmental problems due to its low cost, cleanliness, and environmental friendliness (Maginn, 2010; Iizuka et al., 2011; Sato et al., 2011; Yu et al., 2014). Lehn (Hawecker et al., 1984) and Sauvage (Beley et al., 1984) started photochemical and photoelectrochemical CO₂ reduction in 1980 using different rhenium, ruthenium, nickel, and cobalt complexes of different macrocycles as catalysts (Fisher and Eisenberg, 1980; Beley et al., 1984). Many hybrid nano materials are potential catalysts for this purpose. Also, some ruthenium and rhenium-based metal complexes can reduce CO₂ in presence of light. Photo-electrochemical method is another important tool in this regard (Halmann, 1978; Barton et al., 2008). The major problem associated with photochemical CO₂ reduction is the use of a sacrificial electron donor, an organic amine, which cannot be recovered from the reaction (Takeda et al., 2008; Morris et al., 2009). One of the interesting solution of this problem is using water as a sacrificial electron donor (Wang C. et al., 2011; Kim et al., 2014). However, all such avenues for CO₂ reduction suffers from low yield of the reduced product. Moreover, the

catalyst materials are also expensive. Thus, it is necessary to develop a catalyst which is inexpensive, easy to synthesize and can reduce CO₂ in water with promising yield. Till date the photo catalyst materials used for CO₂ reduction in water are majorly heterogeneous (Barton et al., 2008; Xi et al., 2012; Kuriki et al., 2016). Homogeneous photochemical CO₂ reduction in water is also reported (Nakada et al., 2016).

A wide variety of catalysts both homogenous and heterogenous have been reported for the reduction of CO₂ to formic acid ranging from macrocycles (Chen et al., 2015; Ikeyama and Amao, 2018), hybrid materials (Yadav et al., 2012; Sekizawa et al., 2013; Yoshitomi et al., 2015), ionic liquids (Lu et al., 2017), nanoparticles (Kortlever et al., 2015), B doped nanodiamonds (Ikemiya et al., 2018) to alloys (Bai et al., 2017) with some of them reaching selectivity as high as 100%. On the other hand, reports on photochemical CO₂ reduction to HCOOH using molecular catalysts mainly employs Ru based complexes as the active catalyst (Boston et al., 2013). Use of bipyridine based Ru(II) complexes with an external light sensitizer have been reported for the selective reduction of CO₂ to formic acid (80%) with a TON = 526 (Rosas-Hernández et al., 2015). By employing Ru based supramolecular photocatalysts which acts as both light sensitizer and catalyst, Ishitani *et al.* have showed selective reduction of CO₂ to formic acid in the presence of an external reductant (Tamaki et al., 2012). Further they have tuned the catalytic activity of Ru(II)-Ru(II) supramolecular photocatalyst [Ru₂-Ru(CO)] by employing a suitable reductant to increase formic acid selectivity (87%) and TON_{HCOOH} = 2,766 (Tamaki et al., 2015). Here a synergistic interaction between the reductant employed and the photocatalyst is dictating the outcome of the reaction. These catalysts have an advantage of visible light absorption but require a need for an external electron donor, which was either added externally or added as a part of the solvent. Also, a similar RuReCl photocatalyst was investigated in aqueous solution but the efficiency of formic acid production was low due to the degradation of photocatalyst owing to the back-electron transfer from one electron reduced species to the photosensitizer unit (Nakada et al., 2015). In contrast, in this work a giant {Mo₃₆₈} POM based homogenous photocatalyst system is used to achieve higher selectivity and TON toward formic acid production by employing water solvent as the electron donor.

Recently our group has reported molybdenum based heterogeneous Soft-Oxometalate materials as efficient catalysts for CO₂ reduction reaction (Das et al., 2016). To achieve the same in homogenous realm, an oxo-molybdate based catalyst material which is completely soluble in water is chosen. In this work a molecular catalyst based on giant molybdenum polyoxometalate {Mo₃₆₈} is synthesized, which can reduce CO₂ to formic acid in water with a good yield. The mixed valent molybdenum based giant polyoxometalate {Mo₃₆₈} is synthesized following the literature procedure (Müller et al., 2002). Due to the presence of Mo^V and Mo^{VI} centers in the cluster, intra-valance charge transfer bands are observed in the polyoxometalate. This band imparts deep blue color to the solution. The cluster, a member of molybdenum blue family, is also photoactive and thus there is no need of an addition of any photosensitizer (Das et al., 2016a).

Photoactivity of polyoxometalates is known and has been used by us as a catalyst in photo-polymerization (Chen et al., 2013; Das and Roy, 2015, 2016), as well as in photochemical water oxidation reaction (Roy et al., 2007a,b, 2008; Das et al., 2016b; Barman et al., 2018) without addition of any sensitizer and other reactions (Roy et al., 2013). The cluster {Mo₃₆₈} is extremely efficient as a catalyst and 8.3 mmol of formic acid is obtained with a loading of 0.3 μmol of catalyst. Here the catalyst acts with a maximum turnover number (TON) of 27,666 and turnover frequency (TOF) of 4,611 h⁻¹.

MATERIALS AND METHODS

All the materials and reagents were purchased from commercially available source and used without further purification. Only water is used as a solvent which was distilled twice before starting any reaction. Before use, all the glass apparatus were first boiled in acid bath then cleaned first with tap water then with double distilled water and finally rinsed with acetone and dried in hot air oven overnight, the temperature of which was set at 90°C. A Luzchem UV photoreactor operating at a power of 64 W (8 × 8 W) with UVA lamp is used for photochemical CO₂ reduction reaction in water.

Synthesis of

Na₄₈[H_xMo₃₆₈O₁₀₃₂(H₂O)₂₄₀(SO₄)₄₈]. ca. 1,000H₂O

{Mo₃₆₈} is synthesized by following literature procedure. To a solution of Na₂MoO₄·2H₂O (3 g, 12.4 mmol) in water Na₂S₂O₄ (0.15 g, 0.86 mmol) is added as a reducing agent. The reaction mixture is acidified with 0.5 M H₂SO₄ (35 mL; immediate color change to blue). The solution is then stored in a closed flask for 2 weeks and after 2 weeks the precipitated deep-blue crystals of {Mo₃₆₈} are obtained by filtration, Yield: 135 mg.

General Reaction Procedure for Photo Catalytic CO₂ Reduction

Photo catalytic carbon dioxide reduction reactions are carried out as follows. Desired amount of {Mo₃₆₈} is taken in 10 ml of oxygen free double distilled deionized water. The reaction mixture is closed in a two neck round bottom flask and CO₂ gas is purged for 2.5 h. Then the reaction mixture is kept in the photo reactor under UV-light (eight 8 W lamps, λ = 373 nm) for different intervals of time. 20 μL of reaction mixture is taken out and further diluted with 10 ml HPLC grade water, which is used for carrying out MALDI-MS experiment. For MALDI-MS experiments the reaction mixture is co-crystallized with HCCA matrix and then the mass spectrum was recorded. Mass spectrum gives a molecular ion peak of formic acid (m/z = 46; **Figure S1**). Further to detect formic acid, HPLC measurement was performed by injecting the diluted reaction mixture in carbohydrate column with an external standard, 0.1 M formic acid solution. and all the quantitative measurements of formic acid is done by using HPLC experiments. CV measurements with the reaction mixture are done using 0.1 M KCl as an electrolyte, in a potential range of +0 to -2 V with respect to saturated

Ag/AgCl reference electrode in a standard 3-electrode system and a peak around -0.59 V in cyclic voltammogram further confirms the formation of formic acid from carbon dioxide in our reaction mixture. To further prove formic acid is formed in our reaction mixture, a coupling reaction is performed with our reaction solution using the following method. A solution of aniline (100 μL) in 2 ml acetonitrile along with 20 mg HATU is added to the reaction mixture as a coupling reagent. The reaction mixture is stirred for 2 h at room temperature. The N-phenylformamide is formed in the reaction mixture. Organic components are extracted with EtOAc (3 × 15 ml) and the EtOAc is evaporated in vacuum. The extracted organic component is dissolved in acetonitrile to perform GC-MS and MALDIMS analysis by following above mentioned procedures. Also we have taken the proton NMR spectrum of amide in CDCl₃ solution to further confirm the formation of amide (**Figure S1**).

Determination of Oxygen Using YSI Dissolve Oxygen Meter

Oxygen formed in the reaction is detected by YSI dissolved oxygen meter. YSI dissolved oxygen meter is first calibrated by degassed water. For that purpose, Nitrogen gas is first bubbled through double distilled water for an hour and then put YSI dissolved oxygen meter into this water and recorded the amount of oxygen present. Next, dissolved oxygen meter is dipped into the reaction system i.e., photo illuminated sample and amount of oxygen present in the reaction system is recorded. Now from the difference of oxygen reading in YSI dissolved oxygen meter the total oxygen formed in the reaction is calculated.

pH Dependent Reaction

These experiments are performed by following the previous procedure using different buffer solutions in the range of pH 5 to 9. Measurement of the formic acid is carried out by similar methods as mentioned above.

Characterization Techniques

Fourier Transform Infra-Red Spectroscopy (FT-IR)

FTIR spectrum of {Mo₃₆₈} is performed by KBr pallet technique. Initially a pellet is prepared from the mixture of KBr and {Mo₃₆₈}. FTIR spectrum is recorded by using Perkin Elmer Spectrum RX1 spectrophotometer with FTTR facility in the range 2,000–450 cm⁻¹.

Electronic Absorption Spectroscopy (EAS)

A stable solution of {Mo₃₆₈} is taken in a quartz cuvette and the electronic absorption spectrum is recorded on U-4100 Spectrophotometer (Liquid).

Cyclic Voltammetry

PAR model 273 potentiostat is used for CV experiment. A platinum wire auxiliary electrode, a glassy carbon working electrode with surface area of 0.002826 cm² and an aqueous Ag/Ag⁺ reference electrode which is filled with saturated KCl solution, is used in a three-electrode configuration. All the measurements were performed at 298 K in an inert atmosphere.

Raman Spectroscopy

A LABRAM HR800 Raman spectrometer is employed using a He-Ne ion laser ($\lambda = 1,024$ nm) as the excitation source to analyse the sample.

HPLC

All reaction samples were monitored by HITACHI- HPLC system equipped with binary 2,130 pumps, a manual sampler, and 2,490 refractive index detector, maintained at 50°C. The products were separated in sugar ion-exclusion column (250 × 4.8 mm), maintained at 60°C using water as mobile phase with 0.8 mL/min flow rate. The HPLC system is controlled and processed by InKarp software. Standard Formic acid and Formaldehyde solution were prepared and calibrated. Each time the product obtained is diluted with a known volume of milliQ water before analysis to prevent the overloading of the column. All experiments were done in triplicates and the average values were reported within the standard deviations of <2.0%.

Gas Chromatography-Mass Spectrometry (GC-MS)

The products were identified and analyzed using a GCMS-QP-2010 Ultra (M/s. Shimadzu Instruments, Japan) with a HB-5 capillary column (20 m × 0.18 mm) supplied by M/s. J&W Scientific, USA and Trace 1300 GC and ISQ qd single quadrupole Mass spectrometer with a TG-5MS capillary column (30 m × 0.32 mm × 0.25 μ m) supplied by Thermo Fisher Scientific, India. Gas samples were detected by Molecular sieve 5Å packed column. Thermal Conductivity Detector (TCD) was used for gas samples and Mass Detector (MSD) was used for formic acid measurement.

NMR

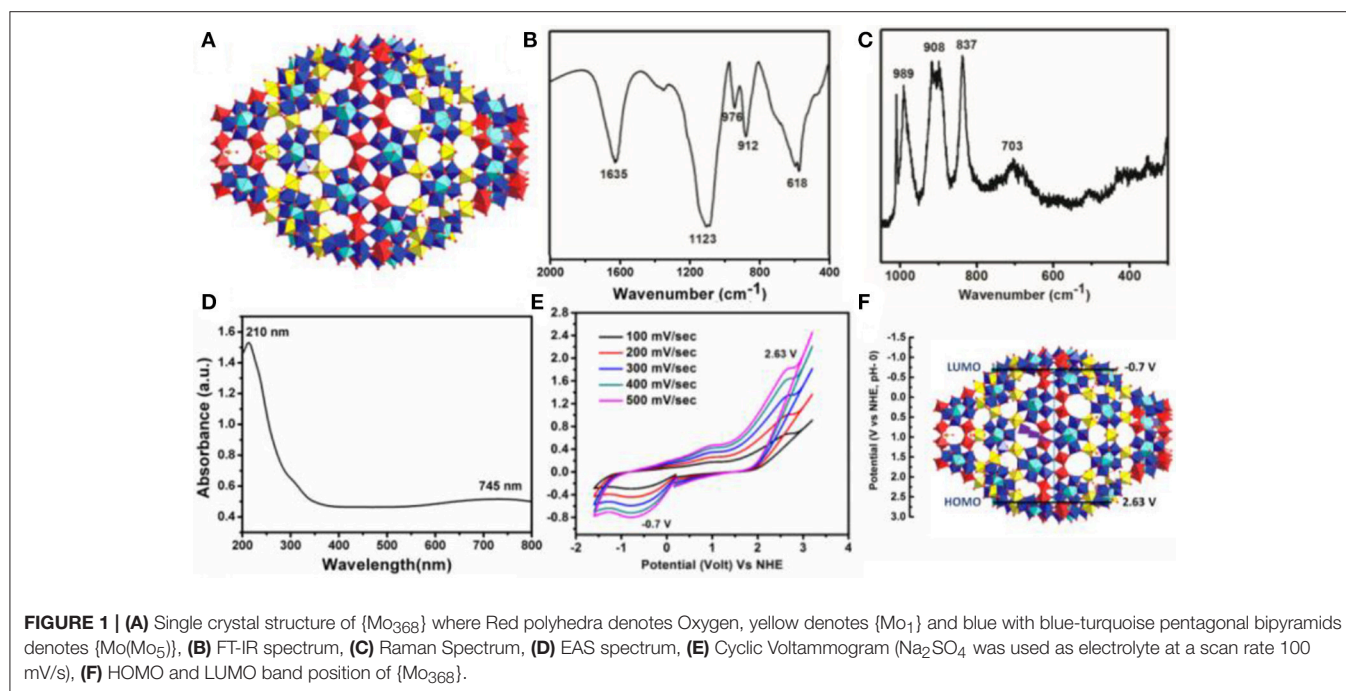
¹H NMR and ¹³C NMR spectrum is recorded on 500 MHz Bruker and 400 MHz Jeol NMR machine. For detection of formic acid by ¹H NMR, solvent suppression (water) method is used.

Matrix Assisted Laser Desorption Ionization Mass Spectroscopy (MALDI-MS)

All samples were prepared in HPLC grade acetonitrile, by dissolving very minute amount of sample on 2 ml acetonitrile, and then filtering the sample using 0.2 micron syringe filter. Then the sample is cocrystallized with HCCA matrix.

RESULT AND DISCUSSION

Deep blue crystals of {Mo₃₆₈} with *I*4mm space group are isolated from the mother liquor in a week by following the literature procedure (Müller et al., 2002). The structure was first determined by A. Müller group using single crystal X-ray diffraction. In the structure, the unit cell contains two hedgehogs like anions which possess D₄ symmetry (Figure 1A). The complete cluster contains a central ball shaped unit {Mo₂₈₈O₇₈₄(H₂O)₁₉₂(SO₄)₃₂} and two other capping units {Mo₄₀O₁₂₄(H₂O)₂₄(SO₄)₈}. These two units also possess local symmetry, D_{8d}, and C_{4v}, respectively. The molecule has large cavity in which 400 water molecules can be encapsulated. Further this structure can be considered as a hybrid of ring shaped {Mo₁₇₆} structure and ball shaped {Mo₁₀₂} structure. The cluster shows typical peaks in the FTIR spectrum which are as follows (Figure 1B), 1,635 ($\delta_{\text{H}_2\text{O}}$), 1,123 ($\nu_{\text{as}}\text{SO}_4^{2-}$), 976 ($\nu_{\text{Mo}} = \text{Ot}$), 912, 618 cm⁻¹, respectively. Raman spectrum ($\lambda = 1,024$ nm) shows peak at 989, 908 (broad peak), 837, and 703 cm⁻¹, respectively (Figure 1C). Electronic absorption spectrum shows



maximum absorbance at 747 nm which is observed due to the IVCT transition between Mo^V to Mo^{VI} which is characteristic for molybdenum blue species (**Figure 1D**). From the above all characterization details, it confirms that {Mo₃₆₈} is formed in our reaction. Further cyclic voltammogram of {Mo₃₆₈} under Ar atmosphere is recorded at different scan rates (**Figure 1E**), which gave three peaks at −0.7, 1.01, and 2.663 V, respectively vs. NHE. From the cyclic voltammogram of the material the position of HOMO and LUMO of the catalyst material was calculated. From the data, the position of HOMO is 2.63 V vs. NHE and the position of LUMO is −0.7 V vs. NHE (**Figure 1F**). The band gap of the catalyst material is 3.33 eV. Thus, from the band position it can be proposed that {Mo₃₆₈} is able to reduce CO₂ as well as oxidize water simultaneously under UV-light source of 373 nm (**Figure S3**). The external quantum efficiency (EQE) of the system is measured by irradiating monochromatic LED light source of wavelength 365 nm ($I = 67 \text{ mW/cm}^2$) and 745 nm ($I = 32 \text{ mW/cm}^2$) where we find the EQE of 0.6 and $1.54 \times 10^{-3}\%$, respectively (SI).

To describe the detailed catalytic process of CO₂ reduction in water, CO₂ reduction under UV-light without addition of any photosensitizer as well as any organic sacrificial electron donor is performed. The reaction is carried out in an air tight quartz tube which is first purged with nitrogen to remove trace amount of oxygen from the reaction system. Later CO₂ is purged for 3 h. The quartz tube is sealed and kept in a photo reactor for different intervals of time. CO₂ undergoes reduction under aforementioned reaction condition, the reduced product is characterized first by GC-MS and further confirmed from ¹H-NMR by solvent suppression method (water peak suppression; **Figure 2A**). These above results confirm that formic acid is

formed from CO₂ in our reaction condition. Further formic acid is characterized and quantified by HPLC against a standard 0.1 M formic acid solution. A peak at −0.6 V in cyclic voltammogram is also observed using saturated Ag/AgCl as a reference electrode (**Figure 3A**), which further confirms the formation of formic acid in the reaction mixture. Besides formic acid, trace amount of formaldehyde which is characterized by HPLC against 0.1 M formaldehyde solution is also found. To further check whether any gaseous reduced product is formed in the reaction, GC-MS is performed by injecting the gases from the reaction chamber and no CO, CH₄, or any other reduced gaseous product is observed from the reaction mixture. Thus, in our present reaction we get formic acid selectively over other reduced product obtained from the reduction of CO₂. Formic acid is formed from CO₂ only and not from any other carbon impurity. To further prove the source of carbon in formic acid, same reaction is performed using ¹³CO₂ as a reactant yielding H¹³COOH. The product is characterized by ¹³C-NMR (**Figure 2B**) taken before and after reaction and Raman spectroscopy (**Figure S4**). Prior to UV-light irradiation ¹³C-NMR gave strong signal at 125.5 ppm corresponding to ¹³CO₂. After the completion of 6 h of photoreduction, ¹³CO₂ signal is found to decrease and a new peak at 166.6 ppm corresponding to H¹³COOH is obtained (Tamaki et al., 2015). We also performed ¹H-NMR after reducing ¹³CO₂ enriched solution where a doublet (¹J_{CH} = 216 Hz) is found at 7.9 ppm which coupled with ¹³C atom (**Figure 2D**). These results indicate that formic acid is formed from CO₂ and not from any other carbon source. This can be proved in a control experiment by recording HPLC of the light illuminated sample without purging of CO₂. In that case, no trace of formic acid or formaldehyde is found in the reaction mixture. This indicates that formic

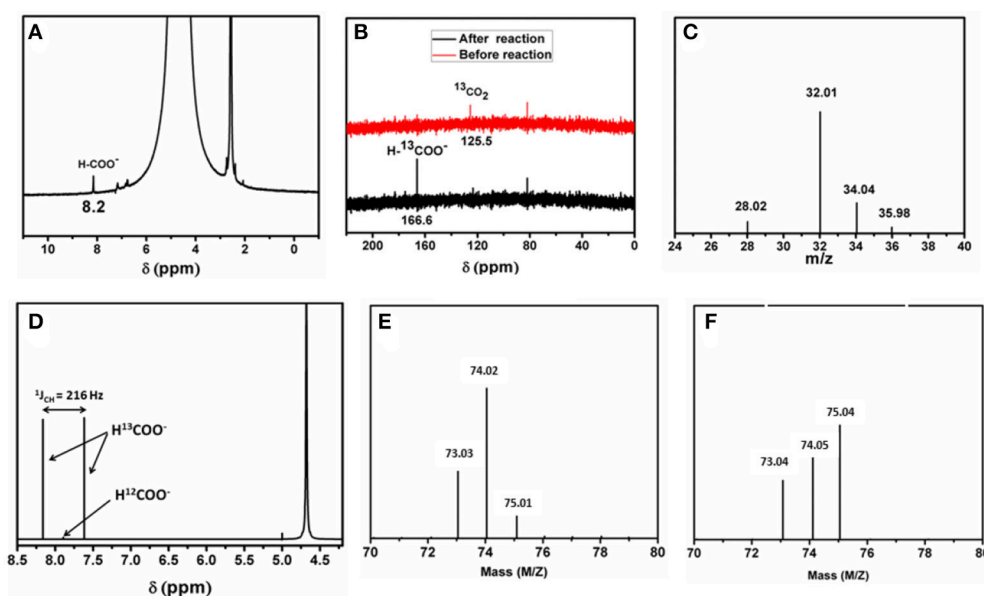


FIGURE 2 | (A) Representative ¹H-NMR of the product from photochemical CO₂ reduction. **(B)** ¹³C-NMR spectrum of the reaction mixture before (red) and after (black) the reaction. **(C)** Full mass spectrum representing all the isotopes of the gaseous products (O₂, ¹⁶O¹⁸O, ¹⁸O¹⁸O and N₂). **(D)** ¹H-NMR spectrum of the reaction mixture using ¹³CO₂. **(E)** Mass of ethylformate (molecular peak) after reaction with H₂O and **(F)** with D₂O and H₂O mixture.

acid and formaldehyde is obtained from CO₂ only. During the photo catalytic CO₂ reduction water also gets oxidized to oxygen simultaneously. Formation of oxygen is characterized by the YSI dissolved oxygen meter and GC-MS. The experiment is further repeated using mixture of H₂¹⁸O (isotopic purity = 97%) and H₂¹⁶O (1:8) where we found the corresponding masses at *m/z* = 32.01, 34.04 and 35.98. The mass *ca.* 32 corresponds to ¹⁶O¹⁶O whereas *m/z* = 34 and 36 resemble to ¹⁶O¹⁸O and ¹⁸O¹⁸O, respectively (Figure 2C) which confirms that oxygen is produced from oxidation of solvent water molecule. Besides, deuterium-labeling experiment was conducted using D₂O (isotopic purity = 99.9%) and H₂O as a solvent (3:2). We found that the deuterium was incorporated into formate moiety (*m/z* = 75), which was confirmed from mass spectrometry (Figures 2E,F). As exchangeable D is found in the reaction medium, it got incorporated during the formation of formic acid and later deuterium incorporated ethylformate is obtained after reaction with ethanol.

Further time dependent study reveals, 6 h is needed to complete the reduction of CO₂ to formic acid. The TOF of the reaction is quite high 4,611 h⁻¹ in water. The yield of the formic acid initially increases rapidly with time (Figure 3B). It increases almost linearly with time. After certain time of reaction, the rate of the increment of the formic acid formation with time decreases and reaction yield does not increase further after 6 h of the reaction. This indicates that the CO₂ reduction reaction is complete within 6 h and same trend can be observed for oxygen evolution too (Figure 3B). Both the processes i.e., CO₂ reduction and water oxidation are coupled which can be confirmed from Figure 3A where current increase occurs at 0.9 V vs. Ag/AgCl only after photoreduction. Furthermore, loading of the catalyst is varied in photochemical CO₂ reduction in a controlled fashion (Figure 3D). Here, initially the yield of the

formic acid increases almost linearly with the increasing loading of the catalyst and further after certain range of the loading of the catalyst the reaction yield becomes independent of the catalyst loading (Figure 3D). We have observed a maximum yield of 8.3 mmol of formic acid with a loading of 0.3 μmol of the catalyst with maximum turnover number of 27,666 (Figure 3F). This clearly indicates high reactivity of the {Mo₃₆₈} unit. Other than formic acid, 37 μmol of formaldehyde is also obtained at the same loading of the catalyst under the same reaction condition. The selectivity of the formation of the formic acid with respect to the total CO₂ reduced product is around 95.73% for formic acid and 4.27% for formaldehyde (Figure 3C). To see the effect of the proton concentration in the photo catalytic CO₂ reduction reaction, pH is varied in the range from 5 to 9 in the course of the reaction. To do so, different buffer solutions are used (Acetate buffer was used to regulate the pH). pH dependent study reveals that the yield of formic acid is maximum at pH 7 (Figure 3E). The yield of the reaction is almost identical on moving toward acidic pH. But when we move toward the basic pH the yield of the reaction decreases drastically. This is due to the dissociation of {Mo₃₆₈} in basic medium. Also, this may be due to the fact that CO₂ reduction is a proton coupled electron transfer (PCET) reaction, the reaction in basic pH, protons are quenched from the reaction medium therefore the yield of the reaction also decreases.

For carbon dioxide reduction reaction two major constituents, i.e., electrons and protons are required. As no sacrificial proton donor or electron donor is used in this case, there is a possibility that water acts as a source of both protons as well as electron in the reaction. To prove this observation, different sets of experiment were performed. Initially, when the same reaction was performed in dry DMF, due to lack of availability of protons, no trace of formic acid was detected indicating that water is

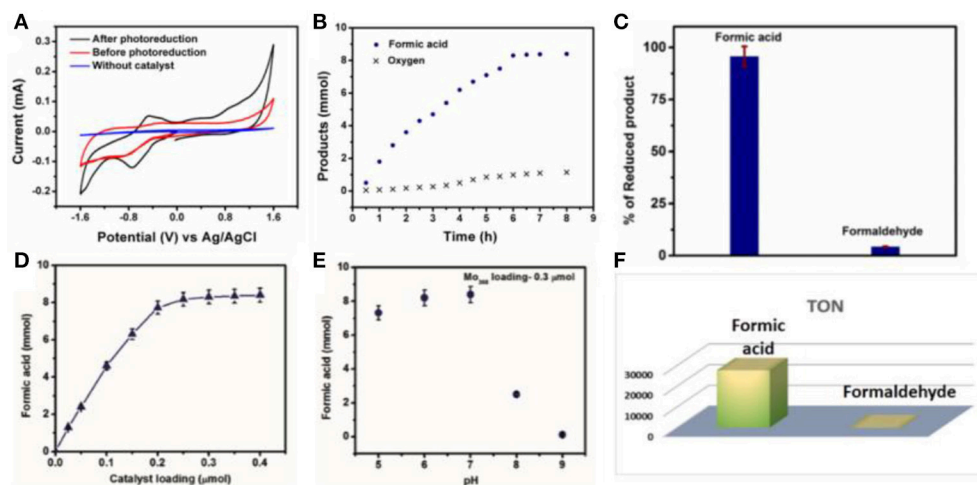
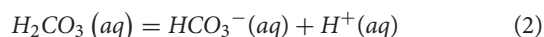
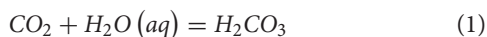


FIGURE 3 | (A) Cyclic voltammogram of the reaction mixture, blue line corresponds to blank where there is neither CO₂ nor catalyst, red line corresponds to CO₂ addition without UV light illumination and black line corresponds to photo CO₂ reduction in water using {Mo₃₆₈} as a catalyst. **(B)** Time dependent formic acid and oxygen formation by photochemical carbon dioxide reduction using {Mo₃₆₈} as a catalyst. **(C)** Formation of different reduced product using {Mo₃₆₈}, and their respective percentage yield in total CO₂ reduced product. **(D)** Effect of variation of {Mo₃₆₈} loading on formation of formic acid. **(E)** pH dependent formic acid formation using {Mo₃₆₈} as a catalyst. **(F)** TON of the formic acid and formaldehyde [Amount of product formed (mol)/amount of catalyst taken (mol)].

playing a crucial role in carbon dioxide reduction reaction under the prevalent reaction conditions (**Figure 4A**). Further to prove the role of the water in the photo catalytic condition, different set of reactions with varying ratio of water and DMF in the reaction mixture was carried out keeping the total volume of the reaction mixture constant (**Figure 4A**). From the experimental result it can be concluded that with increasing loading of water in the reaction the yield of formic acid increases linearly, which supports the role of water as proton donor.



The dependency of water on CO₂ reduction reaction is further obtained from pH dependent study. As, carbon dioxide reduction is proton dependent process (Equation 3), the yield of the reaction should increase on increasing the proton concentration in the reaction medium. But in our present case we observe a decrease in reduced product concentration upon going from neutral pH to acidic pH. This result indicates that another component of CO₂ reduction reaction equilibrium i.e., electron concentration may vary with the change in the pH of the reaction. There are generally two electron sources present in reaction system: one is the catalyst material itself and another is the water. Now if the cluster were to act as electron donor in the reaction then it would degrade in the solution. If it were the situation then a decrease in the absorbance of the catalyst with increasing time of illumination may be observed. But the absorption spectrum of cluster remains unchanged throughout the reaction (**Figure 4B**). Moreover, in all pH variation reactions the same amount of catalyst was used resulting in a constant electronic concentration in the reaction. On the other hand, if the reaction equilibrium totally depended on proton concentration of the reaction system then the yield should have increased at lower pH. However, this does not happen in our reaction system. Hence from the above two

observations it can be concluded that the catalyst material does not act as a source of electrons in the photo chemical CO₂ reduction reaction and water must act as an electron source in the reaction.

As already discussed, oxygen formation was detected in the system during CO₂ reduction which proves that the oxidation of water releases electrons into the system. As it is known that the water oxidation reaction depends on the pH of the medium and it increases with increasing pH of the reaction i.e., ongoing from the acidic to basic pH water oxidation increases. As water oxidation increases at higher pH electron concentration also increases which will facilitate the reduction process. Thus, CO₂ reduction should increase at higher pH. It is also observed in our present reaction system that CO₂ reduction increases with increasing pH (Up to pH 7, as at basic pH the catalyst dissociates). Thus, from the above two observations we can conclude that water only acts as a sacrificial electron donor in the reaction and photo chemical CO₂ reduction depends on photo-chemical water oxidation reaction which also takes place parallelly in the reaction system. Thus, a maximum yield of formic acid is obtained in neutral pH as compared to acidic pH.

To investigate the active catalyst species in the reaction, the reaction is repeated with the precursor of {Mo₃₆₈} i.e., with sodium molybdate and no reduced product is found in the reaction. Thus, from this result, it can be concluded that the giant cluster {Mo₃₆₈} is only responsible for CO₂ reduction reaction and not a single molybdenum unit. Cluster cage thus plays a crucial role for the reaction. It is already mentioned that {Mo₃₆₈} is a photoactive material and it absorbs UV-light of 373 nm wave length to generate holes (h⁺) and electrons (e⁻) in the system. These holes can oxidize water to generate electrons, protons and oxygen in the medium. The electrons and protons so generated reduce CO₂ to formic acid and formaldehyde. This also explains the high photo catalytic activity of {Mo₃₆₈}. {Mo₃₆₈} comprises of different small molybdenum based units i.e., {Mo^{VI}(Mo₅^{VI})}, {Mo₂^V}, {Mo₁^V}, respectively. We believe that upon photo excitation, {Mo^{VI}(Mo₅^{VI})} goes to excited state and forms {Mo^{VI}(Mo₅^{VI})}*. This species has potential to oxidize water to liberate oxygen and release protons and electrons. On the other hand, the {Mo₂} unit and {Mo₁}

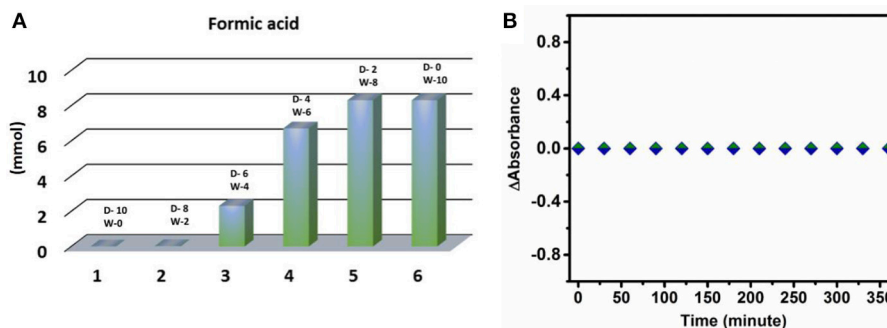


FIGURE 4 | (A) Variation of DMF and water content in reaction mixture (D-DMF, W-water, all values given in ml unit). **(B)** Plot of change of absorbance of {Mo₃₆₈} with time vs. reaction time.

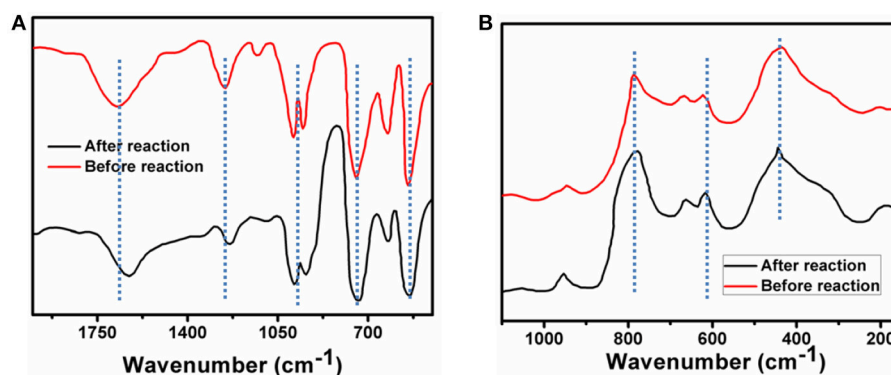


FIGURE 5 | (A) FT-IR spectrum of {Mo₃₆₈}, black line corresponds to FT-IR spectrum of before reaction and brown line corresponds to FT-IR spectrum of after reaction. **(B)** Raman spectrum of {Mo₃₆₈}, black line corresponds to Raman spectrum of before reaction and brown line corresponds to Raman spectrum of after reaction.

unit plays a crucial role for photochemical CO₂ reduction. It has been already shown by Müller group that CO₂ can coordinate with {Mo₂} units of the giant molybdenum based polyoxometalates (Garai et al., 2012; Bandeira et al., 2015). Thus, in our present case it is also reasonable to postulate that CO₂ can co-ordinate with {Mo₂} unit. It is also observed that there is change in cyclic voltammogram of {Mo₃₆₈} upon purging of CO₂ in {Mo₃₆₈} solution (**Figure S2**). Further this coordinated CO₂ unit can be reduced by electrons and protons present in the reaction medium. Possibly CO₂ also can coordinate with {Mo₁} unit and reduction of coordinated CO₂ takes place in a synergistic fashion. We believe that adsorbed CO₂ converted to CO₂^{•-}. The activation barrier of this reduction is lowered by the cluster. Later this species accept proton to generate carboxyhydroxyl intermediate species which participates in PCET process to form formic acid. Due to direct attachment, a large number of CO₂ molecules are reduced for every molecule of {Mo₃₆₈}, and hence the cluster shows such high photocatalytic activity.

The stability of the catalyst is discussed under prevalent photocatalytic conditions. After reaction the catalyst is recovered by slow evaporation of solvent. In this present case it is shown that the {Mo₃₆₈} is stable under the photocatalytic condition using different techniques. FT-IR spectrum of {Mo₃₆₈} after completion of the reaction shows peaks at 1632, 1124, 985, 916, 615 cm⁻¹, respectively which are almost similar to that of the solid catalyst. This indicates that the cluster is stable under the reaction conditions (**Figure 5A**). Moreover, the IVCT bands responsible for the Mo(V)→Mo(VI) transitions do not change with the reaction and it further indicates that there is no change in the catalyst composition and that the catalyst is stable under the reaction conditions. Similar result is also observed from Raman spectrum of catalyst which also shows the catalyst remains intact after the photochemical CO₂ reduction (**Figure 5B**). Also note that no presence of particulate matter is detected from DLS in this system during catalysis which indicates that the catalyst is homogeneous. Hence our catalyst is a stable homogeneous catalyst which reduces CO₂ to formic acid in water.

CONCLUSION

Photochemical reduction of CO₂ to formic acid in water using molybdenum based giant polyoxometalate {Mo₃₆₈} molecular catalyst is reported. The photocatalytic system shows excellent selectivity for formic acid production (95.73%) with high TON (27,666) and TOF (4,419 h⁻¹); which is quite high in its class. The presence of different Mo based sub units in the cluster is responsible for the exceptional activity of the catalyst. As the system is photoactive, no external photosensitizer is added and water solvent acts as electron donor making the whole process environmentally benign and self-sustained. We believe that this work can lead to the development of a class of highly efficient homogeneous CO₂ reduction catalysts based on water soluble polyoxometalates.

AUTHOR CONTRIBUTIONS

SD, TB and SB contributed equally. SD, TB and SB performed the experiments. SS assisted in those experiments. RP carried out GC-MS and HPLC experiments. SR designed the project, analyzed the results and wrote the paper with inputs from all other co-authors.

ACKNOWLEDGMENTS

The authors thank Prof. Dr. Abhishek Dey, of IACS Kolkata, for his help with ¹³CO₂ experiments. SR gratefully acknowledges the start-up grant and FIRE and PRIS grant from IISER Kolkata, India, and grants from CCNU, and NSFC, P. R. China. TB acknowledges IISER Kolkata for his fellowship. SS thanks SERB for financial assistance (PDF/2017/000676) and SB acknowledges UGC for fellowship.

SUPPLEMENTARY MATERIAL

The Supplementary Material for this article can be found online at: <https://www.frontiersin.org/articles/10.3389/fchem.2018.00514/full#supplementary-material>

REFERENCES

- Agarwal, A. S., Zhai, Y., Hill, D., and Sridhar, N. (2011). The electrochemical reduction of carbon dioxide to formate/formic acid: engineering and economic feasibility. *ChemSusChem* 4, 1301–1310. doi: 10.1002/cssc.201100220
- Amatore, C., and Saveant, J. M. (1981). Mechanism and kinetic characteristics of the electrochemical reduction of carbon dioxide in media of low proton availability. *J. Am. Chem. Soc.* 103, 5021–5023. doi: 10.1021/ja00407a008
- Arai, T., Sato, S., Kajino, T., and Morikawa, T. (2013). Solar CO₂ reduction using H₂O by a semiconductor/metal-complex hybrid photocatalyst: enhanced efficiency and demonstration of a wireless system using SrTiO₃ photoanodes. *Energy Environ. Sci.* 6, 1274–1282. doi: 10.1039/c3ee24317f
- Asadi, M., Kumar, B., Behranginia, A., Rosen, B. A., Baskin, A., Repnin, N., et al. (2014). Robust carbon dioxide reduction on molybdenum disulfide edges. *Nat. Commun.* 5, 4470. doi: 10.1038/ncomms5470
- Bai, X., Chen, W., Zhao, C., Li, S., Song, Y., Ge, R., et al. (2017). Exclusive formation of formic acid from CO₂ electroreduction by tunable Pd-Sn alloy. *Angew. Chem.* 129, 12387–12391. doi: 10.1002/ange.201707098
- Bandeira, N. A., Garai, S., Müller, A., and Bo, C. (2015). The mechanism of CO₂ hydration: a porous metal oxide nanocapsule catalyst can mimic the biological carbonic anhydrase role. *Chem. Commun.* 51, 15596–15599. doi: 10.1039/C5CC06423F
- Barman, S., Das, S., Sreejith, S., Garai, S., Pochamoni, R., and Roy, S. (2018). Selective light driven reduction of CO₂ to HCOOH in water using a [MoV₉]_n (n = 1332–3600) based soft-oxometalate (SOM). *Chem. Commun.* 54, 2369–2372. doi: 10.1039/C7CC09520A
- Barton, E. E., Rampulla, D. M., and Bocarsly, A. B. (2008). Selective solar-driven reduction of CO₂ to methanol using a catalyzed p-GaP based photoelectrochemical cell. *J. Am. Chem. Soc.* 130, 6342–6344. doi: 10.1021/ja0776327
- Beley, M., Collin, J.-P., Ruppert, R., and Sauvage, J.-P. (1984). Nickel (II)-cyclam: an extremely selective electrocatalyst for reduction of CO₂ in water. *J. Chem. Soc. Chem. Commun.* 1315–1316. doi: 10.1039/c39840001315
- Blondiaux, E., Pouessel, J., and Cantat, T. (2014). Carbon dioxide reduction to methylamines under metal-free conditions. *Angew. Chem. Int. Ed.* 53, 12186–12190. doi: 10.1002/anie.201407357
- Bontemps, S., Vendier, L., and Sabo-Etienne, S. (2012). Borane-mediated carbon dioxide reduction at ruthenium: formation of C1 and C2 Compounds. *Angew. Chem.* 124, 1703–1706. doi: 10.1002/ange.201107352
- Boston, D. J., Xu, C., Armstrong, D. W., and MacDonnell, F. M. (2013). Photochemical reduction of carbon dioxide to methanol and formate in a homogeneous system with pyridinium catalysts. *J. Am. Chem. Soc.* 135, 16252–16255. doi: 10.1021/ja406074w
- Castro-Rodriguez, I., and Meyer, K. (2005). Carbon dioxide reduction and carbon monoxide activation employing a reactive uranium (III) complex. *J. Am. Chem. Soc.* 127, 11242–11243. doi: 10.1021/ja053497r
- Chen, D., Sahasrabudhe, A., Wang, P., Dasgupta, A., Yuan, R., and Roy, S. (2013). Synthesis and properties of a novel quaternized imidazolium [α-PW₁₂O₄₀]³⁻ salt as a recoverable photo-polymerization catalyst. *Dalton Trans.* 42, 10587–10596. doi: 10.1039/c3dt32916j
- Chen, L., Guo, Z., Wei, X.-G., Gallenkamp, C., Bonin, J., Anxolabéhère-Mallart, E. et al. (2015). Molecular catalysis of the electrochemical and photochemical reduction of CO₂ with earth-abundant metal complexes. Selective production of CO vs HCOOH by switching of the metal center. *J. Am. Chem. Soc.* 137, 10918–10921. doi: 10.1021/jacs.5b06535
- Cokoja, M., Bruckmeier, C., Rieger, B., Herrmann, W. A., and Kühn, F. E. (2011). Transformation of carbon dioxide with homogeneous transition-metal catalysts: a molecular solution to a global challenge? *Angew. Chem. Int. Ed.* 50, 8510–8537. doi: 10.1002/anie.201102010
- Costentin, C., Robert, M., and Savéant, J.-M. (2013). Catalysis of the electrochemical reduction of carbon dioxide. *Chem. Soc. Rev.* 42, 2423–2436. doi: 10.1039/C2CS35360A
- Crabtree, G. W., and Lewis, N. S. (2007). Solar energy conversion. *Phys. Today* 60, 37–42. doi: 10.1063/1.2718755
- Daniel, M. C., and Astruc, D. (2004). Gold nanoparticles: assembly, supramolecular chemistry, quantum-size-related properties, and applications toward biology, catalysis, and nanotechnology. *Chem. Rev.* 104, 293–346. doi: 10.1021/cr030698+
- Das, K., and Roy, S. (2015). Direct synthesis of controlled-size nanospheres inside nanocavities of self-organized photopolymerizing soft oxometalates [PW₁₂O₄₀]_n (n = 1100–7500). *Chem. Asian J.* 10, 1884–1891. doi: 10.1002/asia.201500336
- Das, S., Biswas, S., Balaraju, T., Barman, S., Pochamoni, R., and Roy, S. (2016). Photochemical reduction of carbon dioxide coupled with water oxidation using various soft-oxometalate (SOM) based catalytic systems. *J. Mater. Chem. A* 4, 8875–8887. doi: 10.1039/C6TA02825J
- Das, S., Lai, D., Mallick, A., and Roy, S. (2016a). Photo redox mediated inexpensive one-pot synthesis of 1,4-diphenyl substituted butane-1,4-dione from styrene using polyoxometalate as a catalyst. *ChemistrySelect* 1, 691–695. doi: 10.1002/slct.201500052
- Das, S., Misra, A., and Roy, S. (2016b). Enhancement of photochemical heterogeneous water oxidation by a manganese based soft oxometalate immobilized on a graphene oxide matrix. *New J. Chem.* 40, 994–1003. doi: 10.1039/C5NJ01099C
- Das, S., and Roy, S. (2016). A newly designed softoxometalate [Bmim][2][Dmim][α-PW₁₂O₄₀]@hydrocalumite that controls the chain length of polyacrylic acid in presence of light. *RSC Adv.* 6, 37586–37590. doi: 10.1039/C6RA02685K
- Dhakshinamoorthy, A., Navalon, S., Corma, A., and Garcia, H. (2012). Photocatalytic CO₂ reduction by TiO₂ and related titanium containing solids. *Energy Environ. Sci.* 5, 9217–9233. doi: 10.1039/c2ee21948d
- Finn, C., Schnittger, S., Yellowlees, L. J., and Love, J. B. (2012). Molecular approaches to the electrochemical reduction of carbon dioxide. *Chem. Commun.* 48, 1392–1399. doi: 10.1039/C1CC15393E
- Fisher, B. J., and Eisenberg, R. (1980). Electrocatalytic reduction of carbon dioxide by using macrocycles of nickel and cobalt. *J. Am. Chem. Soc.* 102, 7361–7363. doi: 10.1021/ja00544a035
- Gao, D., Zhou, H., Wang, J., Miao, S., Yang, F., Wang, G., et al. (2015). Size-dependent electrocatalytic reduction of CO₂ over Pd nanoparticles. *J. Am. Chem. Soc.* 137, 4288–4291. doi: 10.1021/jacs.5b00046
- Garai, S., Haupt, E. T., Bögge, H., Merca, A., and Müller, A. (2012). Picking up 30 CO₂ molecules by a porous metal oxide capsule based on the same number of receptors. *Angew. Chem.* 124, 10680–10683. doi: 10.1002/ange.201204089
- Halmann, M. (1978). Photoelectrochemical reduction of aqueous carbon dioxide on p-type gallium phosphide in liquid junction solar cells. *Nature* 275, 115–116.
- Hatch, M. D. (1976). *The C4 Pathway of Photosynthesis: Mechanism and Function*. Baltimore, MD: University Park Press.
- Hawecker, J., Lehn, J.-M., and Ziessel, R. (1984). Electrocatalytic reduction of carbon dioxide mediated by Re (bipy)(CO)₃Cl (bipy= 2,2'-bipyridine). *J. Chem. Soc. Chem. Commun.* 328–330. doi: 10.1039/C39840000328
- Herrero, C., Quaranta, A., El Ghachtouli, S., Vauzeilles, B., Leibl, W., and Aukauloo, A. (2014). Carbon dioxide reduction via light activation of a ruthenium-Ni (cyclam) complex. *PCCP* 16, 12067–12072. doi: 10.1039/c3cp54946a
- Hoel, M., and Kverndokk, S. (1996). Depletion of fossil fuels and the impacts of global warming. *Res. Energy Econ.* 18, 115–136. doi: 10.1016/0928-7655(96)00005-X
- Hoffert, M. I., Caldeira, K., Benford, G., Criswell, D. R., Green, C., Herzog, H., et al. (2002). Advanced technology paths to global climate stability: energy for a greenhouse planet. *Science* 298, 981–987. doi: 10.1126/science.1072357
- Höök, M., and Tang, X. (2013). Depletion of fossil fuels and anthropogenic climate change—a review. *Energy Policy* 52, 797–809. doi: 10.1016/j.enpol.2012.10.046
- Hori, Y., Murata, A., and Takahashi, R. (1989). Formation of hydrocarbons in the electrochemical reduction of carbon dioxide at a copper electrode in aqueous solution. *J. Chem. Soc. Faraday Trans. 1* 85, 2309–2326. doi: 10.1039/f19898502309
- Iizuka, K., Wato, T., Miseki, Y., Saito, K., and Kudo, A. (2011). Photocatalytic reduction of carbon dioxide over Ag cocatalyst-loaded ALa₄Ti₄O₁₅ (A = Ca, Sr, and Ba) using water as a reducing reagent. *J. Am. Chem. Soc.* 133, 20863–20868. doi: 10.1021/ja207586e
- Ikemiya, N., Natsui, K., Nakata, K., and Einaga, Y. (2018). Long-term continuous conversion of CO₂ to formic acid using boron-doped diamond electrodes. *ACS Sustain. Chem. Eng.* 6, 8108–8112. doi: 10.1021/acssuschemeng.8b00793.
- Ikeyama, S., and Amao, Y. (2018). The effect of the functional ionic group of the viologen derivative on visible-light driven CO₂ reduction to formic acid with the system consisting of water-soluble zinc porphyrin

- and formate dehydrogenase. *Photochem. Photobiol. Sci.* 17, 60–68. doi: 10.1039/C7PP00277G
- Iwase, A., Yoshino, S., Takayama, T., Ng, Y. H., Amal, R., and Kudo, A. (2016). Water splitting and CO₂ reduction under visible light irradiation using Z-scheme systems consisting of metal sulfides, CoO_x-Loaded BiVO₄, and a reduced graphene oxide electron mediator. *J. Am. Chem. Soc.* 138, 10260–10264. doi: 10.1021/jacs.6b05304
- Khenkin, A. M., Efremenko, I., Weiner, L., Martin, J. M., and Neumann, R. (2010). Photochemical reduction of carbon dioxide catalyzed by a ruthenium-substituted polyoxometalate. *Chem. Eur. J.* 16, 1356–1364. doi: 10.1002/chem.200901673
- Kim, C., Jeon, H. S., Eom, T., Jee, M. S., Kim, H., Friend, C. M., et al. (2015). Achieving selective and efficient electrocatalytic activity for CO₂ reduction using immobilized silver nanoparticles. *J. Am. Chem. Soc.* 137, 13844–13850. doi: 10.1021/jacs.5b06568
- Kim, W., Yuan, G., McClure, B. A., and Frei, H. (2014). Light induced carbon dioxide reduction by water at binuclear ZrOCo(II) unit coupled to Ir oxide nanocluster catalyst. *J. Am. Chem. Soc.* 136, 11034–11042. doi: 10.1021/ja504753g
- Kornienko, N., Zhao, Y., Kley, C. S., Zhu, C., Kim, D., Lin, S., et al. (2015). Metal-organic frameworks for electrocatalytic reduction of carbon dioxide. *J. Am. Chem. Soc.* 137, 14129–14135. doi: 10.1021/jacs.5b08212
- Kortlever, R., Peters, I., Koper, S., and Koper, M. T. (2015). Electrochemical CO₂ reduction to formic acid at low overpotential and with high faradaic efficiency on carbon-supported bimetallic Pd–Pt nanoparticles. *ACS Catal.* 5, 3916–3923. doi: 10.1021/acscatal.5b00602
- Kou, Y., Nabetani, Y., Masui, D., Shimada, T., Takagi, S., Tachibana, H., et al. (2014). Direct detection of key reaction intermediates in photochemical CO₂ reduction sensitized by a rhenium bipyridine complex. *J. Am. Chem. Soc.* 136, 6021–6030. doi: 10.1021/ja500403e
- Kuhl, K. P., Cave, E. R., Abram, D. N., and Jaramillo, T. F. (2012). New insights into the electrochemical reduction of carbon dioxide on metallic copper surfaces. *Energy Environ. Sci.* 5, 7050–7059. doi: 10.1039/c2ee21234j
- Kuriki, R., Matsunaga, H., Nakashima, T., Wada, K., Yamakata, A., Ishitani, O., et al. (2016). Nature-inspired, highly durable CO₂ reduction system consisting of a binuclear ruthenium (II) complex and an organic semiconductor using visible light. *J. Am. Chem. Soc.* 138, 5159–5170. doi: 10.1021/jacs.6b01997
- Kuriki, R., Yamamoto, M., Higuchi, K., Yamamoto, Y., Akatsuka, M., Lu, D., et al. (2017). Robust binding between carbon nitride nanosheets and a binuclear ruthenium (II) complex enabling durable, selective CO₂ reduction under visible light in aqueous solution. *Angew. Chem. Int. Ed.* 56, 4867–4871. doi: 10.1002/anie.201701627
- Laitar, D. S., Müller, P., and Sadighi, J. P. (2005). Efficient homogeneous catalysis in the reduction of CO₂ to CO. *J. Am. Chem. Soc.* 127, 17196–17197. doi: 10.1021/ja0566679
- Langer, R., Diskin-Posner, Y., Leitun, G., Shimon, L. J., Ben-David, Y., and Milstein, D. (2011). Low-pressure hydrogenation of carbon dioxide catalyzed by an iron pincer complex exhibiting noble metal activity. *Angew. Chem. Int. Ed.* 50, 9948–9952. doi: 10.1002/anie.201104542
- Li, F., Zhao, S.-F., Chen, L., Khan, A., MacFarlane, D. R., and Zhang, J. (2015). Polyethylenimine promoted electrocatalytic reduction of CO₂ to CO in aqueous medium by graphene-supported amorphous molybdenum sulphide. *Energy Environ. Sci.* 9, 216–223. doi: 10.1039/C5EE02879E
- Li, J., and Zhang, J. Z. (2009). Optical properties and applications of hybrid semiconductor nanomaterials. *Coord. Chem. Rev.* 253, 3015–3041. doi: 10.1016/j.ccr.2009.07.017
- Lin, S., Diercks, C. S., Zhang, Y.-B., Kornienko, N., Nichols, E. M., Zhao, Y., et al. (2015). Covalent organic frameworks comprising cobalt porphyrins for catalytic CO₂ reduction in water. *Science* 349, 1208–1213. doi: 10.1126/science.1258343
- Liu, S., Xia, J., and Yu, J. (2015). Amine-functionalized titanate nanosheet-assembled yolk@ shell microspheres for efficient cocatalyst-free visible-light photocatalytic CO₂ reduction. *ACS Appl. Mater. Interfaces* 7, 8166–8175. doi: 10.1021/acsami.5b00982
- Low, J., Yu, J., and Ho, W. (2015). Graphene-based photocatalyst for CO₂ reduction to solar fuel. *J. Phys. Chem. Lett.* 6, 4244–4251. doi: 10.1021/acs.jpclett.5b01610
- Lu, Q., Rosen, J., Zhou, Y., Hutchings, G. S., Kimmel, Y. C., Chen, J. G., et al. (2014). A selective and efficient electrocatalyst for carbon dioxide reduction. *Nat. Commun.* 5, 3242. doi: 10.1038/ncomms4242
- Lu, W., Jia, B., Cui, B., Zhang, Y., Yao, K., Zhao, Y., et al. (2017). Efficient photoelectrochemical reduction of CO₂ to formic acid with functionalized ionic liquid as absorbent and electrolyte. *Angew. Chem. Int. Ed.* 129, 12013–12016. doi: 10.1002/ange.201703977
- Maginn, E. J. (2010). What to do with CO₂. *J. Phys. Chem. Lett.* 1, 3478–3479. doi: 10.1021/jz101582c
- Mandal, S. K., and Roesky, H. W. (2011). Group 14 hydrides with low valent elements for activation of small molecules. *Acc. Chem. Res.* 45, 298–307. doi: 10.1021/ar2001759
- Marszewski, M., Cao, S., Yu, J., and Jaroniec, M. (2015). Semiconductor-based photocatalytic CO₂ conversion. *Mater. Horiz.* 2, 261–278. doi: 10.1039/C4MH00176A
- Matlachowski, C., and Schwalbe, M. (2015). Photochemical CO₂-reduction catalyzed by mono-and dinuclear phenanthroline-extended tetramesityl porphyrin complexes. *Dalton Trans.* 44, 6480–6489. doi: 10.1039/C4DT03846K
- Matsuoka, S., Yamamoto, K., Ogata, T., Kusaba, M., Nakashima, N., Fujita, E., et al. (1993). Efficient and selective electron mediation of cobalt complexes with cyclam and related macrocycles in the p-terphenyl-catalyzed photoreduction of carbon dioxide. *J. Am. Chem. Soc.* 115, 601–609. doi: 10.1021/ja00055a032
- Meinshausen, M., Meinshausen, N., Hare, W., Raper, S. C., Frieler, K., Knutti, R., et al. (2009). Greenhouse-gas emission targets for limiting global warming to 2°C. *Nature* 458, 1158–1162. doi: 10.1038/nature08017
- Mikkelsen, M., Jørgensen, M., and Krebs, F. C. (2010). The teraton challenge. A review of fixation and transformation of carbon dioxide. *Energy Environ. Sci.* 3, 43–81. doi: 10.1039/B912904A
- Morris, A. J., Meyer, G. J., and Fujita, E. (2009). Molecular approaches to the photocatalytic reduction of carbon dioxide for solar fuels. *Acc. Chem. Res.* 42, 1983–1994. doi: 10.1021/ar9001679
- Müller, A., Beckmann, E., Bögge, H., Schmidtmann, M., and Dress, A. (2002). Inorganic chemistry goes protein size: a Mo368 nano-hedgehog initiating nanotechnology by symmetry breaking. *Angew. Chem. Int. Ed.* 41, 1162–1167. doi: 10.1002/1521-3773(20020402)41:7<1162::AID-ANIE1162>3.0.CO;2-8
- Müller, A., Rehder, D., Haupt, E. T., Merca, A., Bögge, H., Schmidtmann, M., et al. (2004). Artificial cells: temperature-dependent, reversible Li⁺-ion uptake/release equilibrium at metal oxide nanocontainer pores. *Angew. Chem. Int. Ed.* 43, 4466–4470. doi: 10.1002/anie.200453762
- Müller, A., and Roy, S. (2003). En route from the mystery of molybdenum blue via related manipulatable building blocks to aspects of materials science. *Coord. Chem. Rev.* 245, 153–166. doi: 10.1016/S0010-8545(03)00110-3
- Nakada, A., Koike, K., Maeda, K., and Ishitani, O. (2016). Highly efficient visible-light-driven CO₂ reduction to CO using a Ru (ii)–Re (i) supramolecular photocatalyst in an aqueous solution. *Green Chem.* 18, 139–143. doi: 10.1039/C5GC01720C
- Nakada, A., Koike, K., Nakashima, T., Morimoto, T., and Ishitani, O. (2015). Photocatalytic CO₂ reduction to formic acid using a Ru (II)–Re (I) supramolecular complex in an aqueous solution. *Inorg. Chem.* 54, 1800–1807. doi: 10.1021/ic502707t
- Ohtsu, H., and Tanaka, K. (2012). An organic hydride transfer reaction of a ruthenium NAD model complex leading to carbon dioxide reduction. *Angew. Chem. Int. Ed.* 51, 9792–9795. doi: 10.1002/anie.201204348
- Rankin, M. A., and Cummins, C. C. (2010). Carbon dioxide reduction by terminal tantalum hydrides: formation and isolation of bridging methylene diolate complexes. *J. Am. Chem. Soc.* 132, 10021–10023. doi: 10.1021/ja104761n
- Roberts, F. S., Kuhl, K. P., and Nilsson, A. (2015). High selectivity for ethylene from carbon dioxide reduction over copper nanocube electrocatalysts. *Angew. Chem.* 127, 5268–5271. doi: 10.1002/ange.201412214
- Rosas-Hernández, A., Junge, H., and Beller, M. (2015). Photochemical reduction of carbon dioxide to formic acid using ruthenium (II)-based catalysts and visible light. *ChemCatChem* 7, 3316–3321. doi: 10.1002/cctc.201500494
- Roy, B., Arya, M., Thomas, P., Jürgschat, J. K., Venkata Rao, K., Banerjee, A., et al. (2013). Self-assembly of mesoscopic materials to form controlled and continuous patterns by thermo-optically manipulated laser induced microbubbles. *Langmuir* 29, 14733–14742. doi: 10.1021/la402777e

- Roy, S., Bossers, L. C., Meeldijk, H. J., Kuipers, B. W., and Kegel, W. K. (2008). Directed synthesis of stable large polyoxomolybdate spheres. *Langmuir* 24, 666–669. doi: 10.1021/la703467d
- Roy, S., Mourad, M. C., and Rijnveld-Ockers, M. T. (2007b). Synthesis and characterization of large surface hexagonal polyoxometalate platelets. *Langmuir* 23, 399–401. doi: 10.1021/la062831+
- Roy, S., Rijnveld-Ockers, M. T., Groenewold, J., Kuipers, B. W., Meeldijk, H., and Kegel, W. K. (2007a). Spontaneous formation of micrometer-size inorganic peapods. *Langmuir* 23, 5292–5295. doi: 10.1021/la700373h
- Sadique, A. R., Brennessel, W. W., and Holland, P. L. (2008). Reduction of CO₂ to CO using low-coordinate iron: formation of a four-coordinate iron dicarbonyl complex and a bridging carbonate complex. *Inorg. Chem.* 47, 784–786. doi: 10.1021/ic701914m
- Sakakura, T., Choi, J.-C., and Yasuda, H. (2007). Transformation of carbon dioxide. *Chem. Rev.* 107, 2365–2387. doi: 10.1021/cr068357u
- Sato, S., Arai, T., Morikawa, T., Uemura, K., Suzuki, T. M., Tanaka, H., et al. (2011). Selective CO₂ conversion to formate conjugated with H₂O oxidation utilizing semiconductor/complex hybrid photocatalysts. *J. Am. Chem. Soc.* 133, 15240–15243. doi: 10.1021/ja204881d
- Sato, S., Morikawa, T., Kajino, T., and Ishitani, O. (2013). A highly efficient mononuclear iridium complex photocatalyst for CO₂ reduction under visible light. *Angew. Chem.* 125, 1022–1026. doi: 10.1002/ange.201206137
- Schmeier, T. J., Dobereiner, G. E., Crabtree, R. H., and Hazari, N. (2011). Secondary coordination sphere interactions facilitate the insertion step in an iridium (III) CO₂ reduction catalyst. *J. Am. Chem. Soc.* 133, 9274–9277. doi: 10.1021/ja2035514
- Schwartzberg, A. M., and Zhang, J. Z. (2008). Novel optical properties and emerging applications of metal nanostructures. *J. Phys. Chem. C* 112, 10323–10337. doi: 10.1021/jp801770w
- Sekizawa, K., Maeda, K., Domen, K., Koike, K., and Ishitani, O. (2013). Artificial Z-scheme constructed with a supramolecular metal complex and semiconductor for the photocatalytic reduction of CO₂. *J. Am. Chem. Soc.* 135, 4596–4599. doi: 10.1021/ja311541a
- Studt, F., Sharafutdinov, I., Abild-Pedersen, F., Elkjær, C. F., Hummelshøj, J. S., Dahl, S., et al. (2014). Discovery of a Ni-Ga catalyst for carbon dioxide reduction to methanol. *Nat. Chem.* 6, 320–324. doi: 10.1038/nchem.1873
- Sullivan, B. P., Krist, K., and Guard, H. (2012). *Electrochemical and Electrocatalytic Reactions of Carbon Dioxide*. Amsterdam: Elsevier.
- Sypaseuth, F. D., Matlachowski, C., Weber, M., Schwalbe, M., and Tzschucke, C. C. (2015). Electrocatalytic carbon dioxide reduction by using cationic pentamethylcyclopentadienyl-iridium complexes with unsymmetrically substituted bipyridine ligands. *Chem. Eur. J.* 21, 6564–6571. doi: 10.1002/chem.201404367
- Takeda, H., Koike, K., Inoue, H., and Ishitani, O. (2008). Development of an efficient photocatalytic system for CO₂ reduction using rhenium (I) complexes based on mechanistic studies. *J. Am. Chem. Soc.* 130, 2023–2031. doi: 10.1021/ja077752e
- Tamaki, Y., Koike, K., and Ishitani, O. (2015). Highly efficient, selective, and durable photocatalytic system for CO₂ reduction to formic acid. *Chem. Sci.* 6, 7213–7221. doi: 10.1039/C5SC02018B
- Tamaki, Y., Morimoto, T., Koike, K., and Ishitani, O. (2012). Photocatalytic CO₂ reduction with high turnover frequency and selectivity of formic acid formation using Ru (II) multinuclear complexes. *Proc. Natl. Acad. Sci. U.S.A.* 109, 15673–15678. doi: 10.1073/pnas.1118336109
- Tornow, C. E., Thorson, M. R., Ma, S., Gewirth, A. A., and Kenis, P. J. (2012). Nitrogen-based catalysts for the electrochemical reduction of CO₂ to CO. *J. Am. Chem. Soc.* 134, 19520–19523. doi: 10.1021/ja308217w
- Twidell, J., and Weir, T. (2015). *Renewable Energy Resources*. Abingdon: Routledge.
- Wang, C., Xie, Z., deKrafft, K. E., and Lin, W. (2011). Doping metal-organic frameworks for water oxidation, carbon dioxide reduction, and organic photocatalysis. *J. Am. Chem. Soc.* 133, 13445–13454. doi: 10.1021/ja203564w
- Wang, W., Wang, S., Ma, X., and Gong, J. (2011). Recent advances in catalytic hydrogenation of carbon dioxide. *Chem. Soc. Rev.* 40, 3703–3727. doi: 10.1039/c1cs15008a
- Wang, Y., Wang, F., Chen, Y., Zhang, D., Li, B., Kang, S., et al. (2014). Enhanced photocatalytic performance of ordered mesoporous Fe-doped CeO₂ catalysts for the reduction of CO₂ with H₂O under simulated solar irradiation. *Appl. Catal. B* 147, 602–609. doi: 10.1016/j.apcatb.2013.09.036
- Wesselbaum, S., vom Stein, T., Klankermayer, J., and Leitner, W. (2012). Hydrogenation of carbon dioxide to methanol by using a homogeneous ruthenium-phosphine catalyst. *Angew. Chem.* 124, 7617–7620. doi: 10.1002/ange.201202320
- Whipple, D. T., and Kenis, P. J. (2010). Prospects of CO₂ utilization via direct heterogeneous electrochemical reduction. *J. Phys. Chem. Lett.* 1, 3451–3458. doi: 10.1021/jz1012627
- Xi, G., Ouyang, S., Li, P., Ye, J., Ma, Q., Su, N., et al. (2012). Ultrathin W₁₈O₄₉ Nanowires with Diameters below 1 nm: synthesis, near-infrared absorption, photoluminescence, and photochemical reduction of carbon dioxide. *Angew. Chem. Int. Ed.* 51, 2395–2399. doi: 10.1002/anie.201107681
- Yadav, R. K., Baeg, J.-O., Oh, G. H., Park, N.-J., Kong, K.-J., Kim, J., et al. (2012). A photocatalyst-enzyme coupled artificial photosynthesis system for solar energy in production of formic acid from CO₂. *J. Am. Chem. Soc.* 134, 11455–11461. doi: 10.1021/ja3009902
- Yoshitomi, F., Sekizawa, K., Maeda, K., and Ishitani, O. (2015). Selective formic acid production via CO₂ reduction with visible light using a hybrid of a perovskite tantalum oxynitride and a binuclear ruthenium (II) complex. *ACS Appl. Mater. Interfaces* 7, 13092–13097. doi: 10.1021/acsami.503509
- Yu, J., Low, J., Xiao, W., Zhou, P., and Jaroniec, M. (2014). Enhanced photocatalytic CO₂-reduction activity of anatase TiO₂ by coexposed {001} and {101} facets. *J. Am. Chem. Soc.* 136, 8839–8842. doi: 10.1021/ja5044787
- Zhang, S., Kang, P., and Meyer, T. J. (2014). Nanostructured tin catalysts for selective electrochemical reduction of carbon dioxide to formate. *J. Am. Chem. Soc.* 136, 1734–1737. doi: 10.1021/ja4113885
- Zhu, W., Michalsky, R., Metin, Ö., Lv, H., Guo, S., Wright, C. J., et al. (2013). Monodisperse Au nanoparticles for selective electrocatalytic reduction of CO₂ to CO. *J. Am. Chem. Soc.* 135, 16833–16836. doi: 10.1021/ja409445p

Conflict of Interest Statement: The authors declare that the research was conducted in the absence of any commercial or financial relationships that could be construed as a potential conflict of interest.

Copyright © 2018 Das, Balaraju, Barman, Sreejith, Pochamoni and Roy. This is an open-access article distributed under the terms of the Creative Commons Attribution License (CC BY). The use, distribution or reproduction in other forums is permitted, provided the original author(s) and the copyright owner(s) are credited and that the original publication in this journal is cited, in accordance with accepted academic practice. No use, distribution or reproduction is permitted which does not comply with these terms.



Large Magnetic Polyoxometalates Containing the Cobalt Cubane $[\text{Co}^{\text{III}}\text{Co}_3^{\text{II}}(\text{OH})_3(\text{H}_2\text{O})_{6-m}(\text{PW}_9\text{O}_{34})]^{3-}$ ($m = 3$ or 5) as a Subunit

Yan Duan, Juan M. Clemente-Juan, Carlos Giménez-Saiz* and Eugenio Coronado*

Instituto de Ciencia Molecular, Universidad de Valencia, Valencia, Spain

OPEN ACCESS

Edited by:

Tatjana N. Parac-Vogt,
KU Leuven, Belgium

Reviewed by:

Haralampos N. Miras,
University of Glasgow,
United Kingdom

Tilo Söhnle,

University of Auckland, New Zealand

*Correspondence:

Carlos Giménez-Saiz
carlos.gimenez@uv.es
Eugenio Coronado
eugenio.coronado@uv.es

Specialty section:

This article was submitted to
Inorganic Chemistry,
a section of the journal
Frontiers in Chemistry

Received: 23 April 2018

Accepted: 31 May 2018

Published: 19 June 2018

Citation:

Duan Y, Clemente-Juan JM,
Giménez-Saiz C and Coronado E
(2018) Large Magnetic
Polyoxometalates Containing the
Cobalt Cubane
 $[\text{Co}^{\text{III}}\text{Co}_3^{\text{II}}(\text{OH})_3(\text{H}_2\text{O})_{6-m}(\text{PW}_9\text{O}_{34})]^{3-}$
($m = 3$ or 5) as a Subunit.
Front. Chem. 6:231.
doi: 10.3389/fchem.2018.00231

A synthetic procedure is presented to construct new magnetic polyoxometalates (POMs) containing one or two subunits of $[\text{Co}^{\text{III}}\text{Co}_3^{\text{II}}(\text{OH})_3(\text{H}_2\text{O})_{6-m}(\text{PW}_9\text{O}_{34})]^{3-}$ ($m = 3$ or 5). The substitution of the water ligands present in these subunits by oxo or hydroxo ligands belonging to other POM fragments, gives rise to four, larger POM anions: $[\text{Co}_7(\text{OH})_6(\text{H}_2\text{O})_6(\text{PW}_9\text{O}_{34})_2]^{9-}$ (**2**), $[\text{Co}_7(\text{OH})_6(\text{H}_2\text{O})_4(\text{PW}_9\text{O}_{34})_2]^{9n-}$ (**2'**), $[\text{Co}_{11}(\text{OH})_5(\text{H}_2\text{O})_5(\text{W}_6\text{O}_{24})(\text{PW}_9\text{O}_{34})_3]^{22-}$ (**3**) and $[\{\text{Co}_4(\text{OH})_3(\text{H}_2\text{O})(\text{PW}_9\text{O}_{34})\}_2\{\text{K}(\text{H}_2\text{W}_{12}\text{O}_{41})_2\}\{\text{Co}(\text{H}_2\text{O})_4\}_2]^{17-}$ (**4**). The crystal structures, magnetic characterization and stabilities in aqueous solutions of these POM derivatives are also presented.

Keywords: polyoxometalate, magnetism, cubane cluster, cobalt, crystal structure

INTRODUCTION

Polyoxometalates (POMs) are molecular metal-oxo clusters containing W, Mo, or V (as constituent metals) in their highest oxidation states (Pope, 1983; Pope and Müller, 1991). They can incorporate almost any kind of metals or non-metals giving rise to a large chemical and structural richness that explains their importance in many areas and applications, such as catalysis, photochemistry, magnetism, etc. (Kozik and Baker, 1994; Hill and Prosser-McCartha, 1995; Coronado and Gómez-García, 1998; Hill, 1998; Neumann, 1998; Clemente-Juan and Coronado, 1999; Pope and Müller, 2001; Yamase and Pope, 2002, 2004; Coronado et al., 2005; Kortz, 2009; Kortz et al., 2009; Dolbecq et al., 2010; López et al., 2012; Miras et al., 2012; Song and Tsunashima, 2012; Zheng and Yang, 2012; Sartorel et al., 2013). For more than 25 years our group has been interested in the synthesis and study of substituted POMs containing magnetic metal ions (both *d*-transition metals and lanthanides). These inorganic complexes have shown to provide ideal examples of magnetic molecules of interest in molecular magnetism (magnetic clusters with new topologies, single-molecule magnets, molecular spin qubits, etc.) (Clemente-Juan and Coronado, 1999; Clemente-Juan et al., 2012). Typically, two main synthetic strategies have been followed to obtain transition metal substituted POMs with new topologies: (i) reacting preformed lacunary POM species with transition metal ions and/or additional oxoanions (step-by-step approach) and (ii) direct self-assembly of tungstate (or molybdate, vanadate, etc.) anions, transition metal ions and/or additional oxoanions (one-pot approach). Both strategies require strict control of the key synthetic parameters, such as pH, temperature, concentration of reagents, etc. While the first approach is more directed toward the preparation of a specific POM species, the second one is prone to generate multiple POM products in solution which could need to be separated in the workup or by crystallization/recrystallization steps (Miras et al., 2012).

In the last years, some POM compounds containing cubane $\{\text{Co}_4\text{O}_4\}$ clusters have attracted great attention because they possess single-molecule magnet (SMM) behavior or can act as water oxidation catalysts (Ibrahim et al., 2011, 2014; Lydon et al., 2012; Han et al., 2014). Recently, we also reported a series of POM compounds containing isolated cubane $\{\text{Co}_4\text{O}_4\}$ or dicubane $\{\text{Co}_7\text{O}_8\}$ cobalt clusters and $[\text{B}-\alpha\text{-PW}_9\text{O}_{34}]^{9-}$ or $[\alpha\text{-P}_2\text{W}_{15}\text{O}_{56}]^{9-}$ trilacunary ligands (Duan et al., 2016b). The cubane containing POM, formulated as $[\text{Co}_4^{\text{II}}(\text{OH})_3(\text{H}_2\text{O})_6(\text{PW}_9\text{O}_{34})]^{4-}$ (**1**), has three water molecules coordinated to the apical cobalt atom (in the following ‘apical water’), and three more to each of the three basal cobalt atoms, (in the following ‘basal water’), see **Figures 1A,B**. Since D. E. Katsoulis and M. T. Pope first demonstrated that the water molecules coordinated to 3d metal ions could be substituted by other organic or inorganic ligands (Katsoulis and Pope, 1984), numerous examples of hybrid POMs have been reported in the literature (Lisnard et al., 2007; Al-Oweini et al., 2014). These water molecules can also be substituted by oxo ligands belonging to other polyoxoanions giving rise to larger POM species, which are usually polymeric, such as: $[\text{PMnW}_{11}\text{O}_{39}]^{5n-}$ (Galán-Mascarós et al., 1995), $[\text{XCo}^{\text{II}}\text{W}_{11}\text{O}_{39}]_n^{5n-}$ ($\text{X} = \text{P}^{\text{V}}$ or As^{V}) (Evans et al., 1996), $[\alpha\text{-XCuW}_{11}\text{O}_{39}]_n^{6n-}$ ($\text{X} = \text{Si}^{\text{IV}}$ or Ge^{IV}) (Yan et al., 2001), and $[\alpha\text{-PCuW}_{11}\text{O}_{39}]_{2n}^{10n-}$ (Zhao et al., 2008). In these examples, one water molecule acting as ligand of each 3d metal has been replaced by an oxo group of a similar POM species, giving rise to infinite linear chains.

In the case of **1**, the three apical water molecules lie in an almost equilateral triangle of side length 2.6–2.8 Å and so, they are in an ideal position to be replaced by three oxo (or hydroxo) ligands belonging to an edge-shared $\{\text{W}_3\text{O}_{13}\}$ group of any other POM (see green dashed lines in **Figure 1B**). In addition, the basal water molecules can also be substituted by oxo (or hydroxo) ligands to afford polymeric POM species. Therefore, the six water molecules in **1** provide the possibility to build larger POMs with new topologies by replacing some of them with oxo (or hydroxo) ligands belonging to other POMs.

Here we develop a one-pot synthetic approach to construct new magnetic polyoxometalates (POMs) containing one or two subunits of $[\text{Co}^{\text{III}}\text{Co}_3^{\text{II}}(\text{OH})_3(\text{H}_2\text{O})_{6-m}(\text{PW}_9\text{O}_{34})]^{3-}$ ($m = 3$ or 5). In these subunits some water ligands have been substituted by oxo or hydroxo ligands belonging to other POM fragments, giving rise to four POM anions: $[\text{Co}_7(\text{OH})_6(\text{H}_2\text{O})_6(\text{PW}_9\text{O}_{34})_2]^{9-}$ (**2**), $[\text{Co}_7(\text{OH})_6(\text{H}_2\text{O})_4(\text{PW}_9\text{O}_{34})_2]_n^{9n-}$ (**2'**), $[\text{Co}_{11}(\text{OH})_5(\text{H}_2\text{O})_5(\text{W}_6\text{O}_{24})(\text{PW}_9\text{O}_{34})_3]^{22-}$ (**3**) and $[\{\text{Co}_4(\text{OH})_3(\text{H}_2\text{O})(\text{PW}_9\text{O}_{34})\}_2\{\text{K}(\text{H}_2\text{W}_{12}\text{O}_{41})_2\}\{\text{Co}(\text{H}_2\text{O})_4\}_2]^{17-}$ (**4**), see **Figures 1C–E**.

EXPERIMENTAL SECTION

General Methods and Materials

All reagents were of high purity grade quality, obtained from commercial sources, and used without further purification. The preparation and characterization of the POM salts $\text{Na}_{1.5}\text{Cs}_{2.5}[\text{Co}_4(\text{OH})_3(\text{H}_2\text{O})_6(\text{PW}_9\text{O}_{34})]\cdot 9\text{H}_2\text{O}$ (**Q-1**) and $\text{K}_5\text{Na}_2[\text{Co}_7(\text{OH})_6(\text{H}_2\text{O})_4(\text{PW}_9\text{O}_{34})_2]\{\text{Co}(\text{H}_2\text{O})_2\}\cdot 20\text{H}_2\text{O}$

(**Q-2'**) have been previously described by us (Duan et al., 2016b). Pure water ($\rho > 18 \text{ M}\Omega\cdot\text{cm}$) was used throughout. It was obtained using an Elix-3/Millipore-Q Academic water purification system. IR spectra were recorded with KBr pellets on a Thermo NICOLET-5700 FT-IR spectrophotometer. Elemental analysis was performed by inductively-coupled-plasma optical-emission-spectroscopy (ICP-OES) on solutions prepared by treating the compounds in a hydrofluoric acid/hydrochloric acid mixture of ratio 1:8 and diluted with water to a known volume. Thermogravimetric analysis was performed on a Mettler Toledo TGA/SDTA851e analyzer. The UV-vis spectra of the relevant POMs (10^{-5} M) were recorded on an Agilent 8453 UV-vis spectrophotometer from 190 to 400 nm using 10-mm-optical-path quartz cuvettes in buffer solutions of 0.5 M sodium acetate (pH 4.8).

Preparation of the Starting Solution

5.40 g (16.4 mmol) of $\text{Na}_2\text{WO}_4\cdot 2\text{H}_2\text{O}$ and 0.21 g (1.48 mmol) of Na_2HPO_4 were dissolved in 15 mL of water and the pH of the solution was adjusted to 5.4 using glacial acetic acid. Another aqueous solution containing 1.29 g (5.18 mmol) of $\text{Co}(\text{CH}_3\text{COO})_2\cdot 4\text{H}_2\text{O}$ in 20 mL of water was added dropwise to the first solution, giving rise to a solution with pH = 5.5.

Synthesis of

$\text{K}_{4.2}\text{Na}_{2.8}[\text{Co}(\text{H}_2\text{O})_6][\text{Co}_7(\text{OH})_6(\text{H}_2\text{O})_6(\text{PW}_9\text{O}_{34})_2]\cdot 19\text{H}_2\text{O}$ (**Q-2**)

The starting solution was refluxed for 2 h and hot filtered. To the warm filtrate, 2.24 g (22.8 mmol) of potassium acetate and 0.11 g (0.41 mmol) of potassium persulfate were successively added in small portions. After the addition, the dark solution was allowed to stand at room temperature in an open beaker (pH = 6.0). A big amount of orange precipitate appeared overnight, which was filtered and recrystallized in 15 mL of water. After 1 week, orange plate shaped crystals were formed (yield: 0.352 g, 6.6% based on W). Anal. Calcd (Found) for **Q-2**: Na 1.1 (0.82); K 2.8 (3.2); Co 8.1 (7.3); P 1.1 (0.9); W 56.9 (57.2). IR (2% KBr pellet 1,100–400 cm^{-1}) (Figure S1): 1056(m), 1033(s), 982(m, sh), 953(sh), 938(s), 883(s), 792(w), 715(m, sh), 588(w), 540(m), 479(m, sh), 415(s). The TGA curve of **Q-2** (Figure S2) shows a total weight loss of 11.36% in the range 25–800°C, which agrees with the loss of 31 water molecules and 6 hydroxyls in the structure (calcd 11.29%).

Synthesis of

$\text{K}_5\text{Na}_2[\text{Co}_7(\text{OH})_6(\text{H}_2\text{O})_4(\text{PW}_9\text{O}_{34})_2]\{\text{Co}(\text{H}_2\text{O})_2\}\cdot 20\text{H}_2\text{O}$ (**Q-2'**)

The synthesis and characterization of this salt have been previously reported by us (Duan et al., 2016b). We describe the procedure here again in order to show that the synthetic method used follows the same strategy as for the rest of compounds (**2–4**). The starting solution was refluxed for 2 h and hot filtered. To the hot filtrate, 2.24 g (22.8 mmol) of potassium acetate and 0.11 g (0.41 mmol) of potassium persulfate were successively added in small portions. After the addition of the solids, the solution was concentrated at 80°C until a final volume of 25 mL was attained. Then, the solution was allowed to cool to room temperature

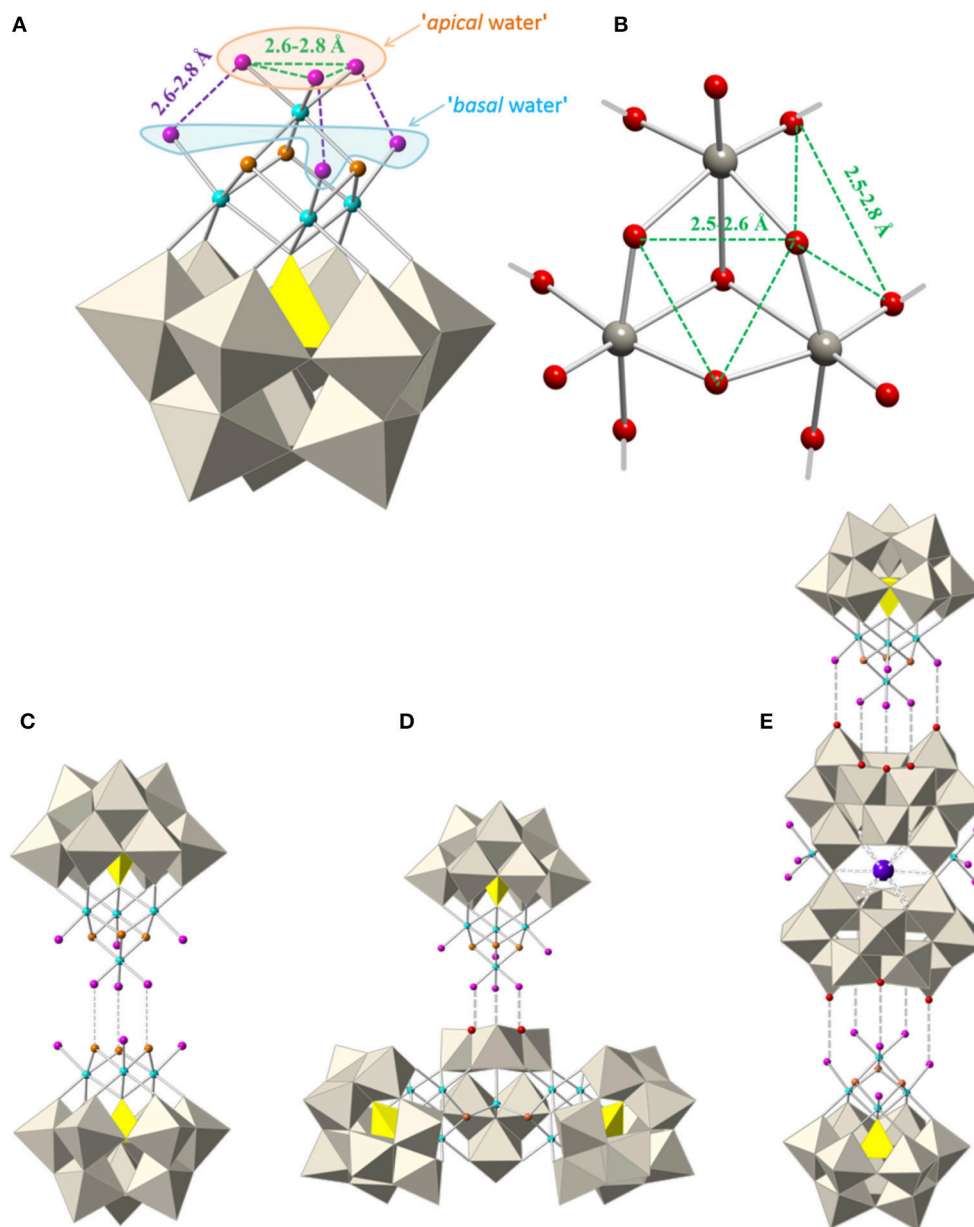


FIGURE 1 | (A) Polyhedral and ball-and-stick representation of the polyoxoanion $[\text{Co}_4^{\text{II}}(\text{OH})_3(\text{H}_2\text{O})_6(\text{PW}_9\text{O}_{34})]^{4-}$ (**1**) in which some mean distances between water molecules (pink spheres) have been indicated. **(B)** Ball-and-stick representation of an edge-shared $\{\text{W}_3\text{O}_{13}\}$ group, with indication of some O...O distances to illustrate the possibilities of water substitution in **1**. Polyhedral and ball-and-stick representations of the assembling of polyoxoanions **(C)** $[\text{Co}_7(\text{OH})_6(\text{H}_2\text{O})_6(\text{PW}_9\text{O}_{34})_2]^{9-}$ (**2**); **(D)** $[\text{Co}_{11}(\text{OH})_5(\text{H}_2\text{O})_5(\text{W}_6\text{O}_{24})(\text{PW}_9\text{O}_{34})_3]^{22-}$ (**3**) and **(E)** $[\{\text{Co}_4(\text{OH})_3(\text{H}_2\text{O})(\text{PW}_9\text{O}_{34})\}_2\{\text{K}(\text{H}_2\text{W}_{12}\text{O}_{41})_2\}\{\text{Co}(\text{H}_2\text{O})_4\}_2]^{17-}$ (**4**). POM **2'** (not shown) is a polymeric chain made of units of **2**. (Grey octahedra, $\{\text{WO}_6\}$; yellow tetrahedra, $\{\text{PO}_4\}$; gray spheres, W; cyan spheres, Co^{II} ; blue spheres, Co^{III} ; red spheres, O; orange spheres, OH; pink spheres, H_2O ; violet sphere, K).

and a large amount of a black precipitate, (identified as $\text{K}_{10.5}\text{Na}_{0.3}\{\text{Co}_{0.6}(\text{H}_2\text{O})_{3.6}\}[\text{Co}_4(\text{H}_2\text{O})_2(\text{CoW}_9\text{O}_{34})(\text{PW}_9\text{O}_{34})] \cdot 19.4\text{H}_2\text{O}$) (Duan et al., 2016a) was formed and filtered out. The filtrate (pH = 5.9) was allowed to stand at room temperature in an open container and, after 1 day, a brown precipitate was formed which was filtered and recrystallized in water to afford orange-brown, plate-like crystals.

Synthesis of $\text{K}_{12}\text{Na}_4\text{H}_3\{\text{Co}_{1.5}(\text{H}_2\text{O})_{5.5}\}[\text{Co}_{11}(\text{OH})_5(\text{H}_2\text{O})_5(\text{W}_6\text{O}_{24})(\text{PW}_9\text{O}_{34})_3] \cdot 37.5\text{H}_2\text{O}$ (Q-3)

The pH of the starting solution was readjusted to 5.4 with glacial acetic acid (0.27 mL were used). Then, the solution was refluxed for 2 h and hot filtered. To the hot filtrate, 2.24 g (22.8 mmol) of potassium acetate and 0.11 g (0.41 mmol) of

potassium persulfate were successively added in small portions. After the addition of the solids, the solution was concentrated at 100°C until a final volume of 20 mL was attained. Then, the solution was allowed to cool to room temperature and a large amount of black precipitate, (identified as $K_{10.5}Na_{0.3}\{Co_{0.6}(H_2O)_{3.6}[Co_4(H_2O)_2(CoW_9O_{34})(PW_9O_{34})]\cdot 19.4H_2O\}$ (Duan et al., 2016a) was formed and filtered out. The filtrate (pH = 5.8) was allowed to stand at room temperature in an open beaker and, after 1 week, blue needle shaped crystals were formed (yield: 0.128 g, 2.7% based on W). Anal. Calcd (Found) for **Q-3**: Na 0.88 (0.75); K 4.5 (4.6); Co 7.1 (6.9); P, 0.89 (0.85); W 58.2 (58.1). IR (2% KBr pellet 1100–400 cm^{-1}) (Figure S1): 1068(m), 1048(w), 1030(s), 954(m, sh), 937(s), 883(s), 803(w), 727(m, sh), 587(w), 511(m), 484(m, sh), 415(s). The TGA curve of **Q-3** (Figure S3) shows a total weight loss of 9.10% in the range 25–800°C, which agrees with the loss of 48 water molecules and 5 hydroxyls in the structure (calcd 9.02%).

Synthesis of

$K_{12}NaCo_2(H_2O)_{10}\{[Co_4(OH)_3(H_2O)(PW_9O_{34})]_2[KC(H_2W_{12}O_{41})_2][Co(H_2O)_4]_2\}\cdot 71H_2O$ (**Q-4**)

The starting solution was refluxed for 2 h and, then, 2.24 g (22.8 mmol) of potassium acetate and 0.11 g (0.41 mmol) of potassium persulfate were successively added to the hot solution. After the addition of the solids, the solution was filtered and kept in an open beaker. A black precipitate appeared overnight which was filtered and identified as $K_{10.5}Na_{0.3}\{Co_{0.6}(H_2O)_{3.6}[Co_4(H_2O)_2(CoW_9O_{34})(PW_9O_{34})]\cdot 19.4H_2O\}$ (Duan et al., 2016a). The filtrate (pH 5.5) was allowed to evaporate at room temperature in an open beaker until the volume of the reaction mixture reached approximately 20 mL and a large amount of orange precipitate appeared. This solid was filtered and recrystallized in boiling water. After 1 week, orange block shaped crystals were formed, filtered and washed with a small amount of cold water (yield: 0.180 g, <0.1% based on W). Anal. Calcd (Found) for **Q-4**: Na 0.17 (0.21); K 3.9 (3.9); Co 5.3 (5.4); P 0.47 (0.71); W 58.7 (58.0). IR (2% KBr pellet 1,100–400 cm^{-1}) (Figure S1): 1064(m), 1033(s), 954(m, sh), 938(s), 882(s), 786(w), 715(m, sh), 627(w), 510(m), 410(m, sh). The TGA curve of **Q-4** (Figure S4) shows a total weight loss of 13.65% in the range 25–800°C, which agrees with the loss of 91 water molecules and 10 hydroxyls in the structure (calcd 13.74%).

X-Ray Crystallography

The crystal structures of salts **Q-1** and **Q-2'** were previously reported (Duan et al., 2016b). Suitable crystals of salts **Q-2**, **Q-3**, and **Q-4** were coated with Paratone N oil, suspended on small fiber loops, and placed in a stream of cooled nitrogen (120 K) on an Oxford Diffraction Supernova diffractometer equipped with a graphite-monochromated Enhance (Mo) X-ray Source ($\lambda = 0.71073$ Å). The data collection routines, unit cell refinements, and data processing were carried out using the CrysAlis software package (Agilent Technologies, 2011) and structure solution and refinement were carried out using SHELXS-97 and SHELXL-2016/4 (Sheldrick, 2008).

All atoms were refined anisotropically in the four crystal structures except some disordered counter cations and water molecules of solvation having partial occupancies. Analytical absorption corrections were performed for all compounds based on face indexations of the single crystals. Hydrogen atoms of water molecules and hydroxo anions were not included in the models.

The structure of salt **Q-4** contains channels parallel to the crystallographic *c* axis, containing disordered water molecules that could not be modeled as discrete atomic sites. We employed PLATON SQUEEZE (Spek, 2009) to calculate the contribution to the diffraction from the solvent/cation region and thereby produced a set of solvent-free diffraction intensities. According to the TGA, 44 water molecules per POM reside in these channels in accordance with the volume of the void and electron count found by SQUEEZE. These additional water molecules were added to the final formula of **Q-4**.

In the case of salt **Q-3**, 31 solvation water molecules were found in Fourier maps and included in the structural model. The TGA indicated the presence of 6.5 additional water molecules of solvation, which were included in the final formula of **Q-3**. In this case, the SQUEEZE procedure was considered to be unnecessary.

CSD reference numbers: 432446 (for **Q-2**, **Q-3** and **Q-4**) and 430365 (for the previously reported **Q-1** and **Q-2'**). CCDC reference numbers: 1538253 (for **Q-2**), 1538254 (for **Q-3**) and 1538255 (for **Q-4**). A summary of the crystallographic data for all compounds is given in Table 1.

Magnetic Measurements

Samples of **Q-3** and **Q-4** were prepared by compacted powder molded from ground crystalline samples. Each sample was covered with the minimum amount of liquid eicosane (40 °C) in order to prevent crystallite torquering. Variable-temperature susceptibility measurements were carried out in the temperature range 2–300 K on a magnetometer equipped with a SQUID sensor (Quantum Design MPMS-XL-5). The data were corrected for diamagnetic contribution from eicosane and for the diamagnetic contributions of the polyanions as deduced by using the Pascal's constant tables. Isothermal magnetization measurements at low temperature (2 K and 5 K) were performed up to a field of 5 T in the same apparatus.

RESULTS AND DISCUSSION

Synthetic Approach

The synthesis of **1** was previously reported. It was obtained by reaction of the trilacunary anion $[B-\alpha-PW_9O_{34}]^{9-}$ with Co^{2+} ions at pH 6.6 (Duan et al., 2016b). In contrast, the synthesis of **Q-2** to **Q-4** was accomplished by the self-assembly of WO_4^{2-} , Co^{2+} and PO_4^{3-} ions in the presence of $S_2O_8^{2-}$ as oxidant (see Scheme 1).

The occurrence of a cubane $\{Co^{III}Co_3^{II}O_4\}$ cluster in all compounds is likely to be related to the use of $S_2O_8^{2-}$ as oxidant and, therefore, to the presence of Co^{3+} in the reaction medium. In all compounds, Co^{3+} ions are located in the apical position of

TABLE 1 | Crystallographic data for $K_{4.2}Na_{2.8}[Co(H_2O)_6][Co_7(OH)_6(H_2O)_6(PW_9O_{34})_2] \cdot 19H_2O$ (**Q-2**), $K_{12}Na_4H_3[Co_{1.5}(H_2O)_{5.5}][Co_{11}(OH)_5(H_2O)_5(W_6O_{24})(PW_9O_{34})_3] \cdot 37.5H_2O$ (**Q-3**) and $K_{12}NaCo_2(H_2O)_{10}[(Co_4(OH)_3(H_2O)(PW_9O_{34}))_2]K_2(H_2W_{12}O_{41})_2[Co(H_2O)_4]_2 \cdot 71H_2O$ (**Q-4**).

Compound	Q-2	Q-3	Q-4
empirical formula	$Co_8H_{68}K_{4.20}Na_{2.80}O_{105}P_2W_{18}$	$Co_{12.5}H_{104}K_{12}Na_4O_{179}P_3W_{33}$	$Co_{12}H_{192}K_{13}Na_{247}P_2W_{42}$
formula weight	5819.82	10426.58	13167.63
space group	$P\bar{1}$	$P\bar{1}$	$Pmmn$
$a/\text{\AA}$	11.5505(3)	12.30440(12)	46.3907(3)
$b/\text{\AA}$	12.4263(3)	24.7192(2)	19.63375(16)
$c/\text{\AA}$	20.3358(8)	27.2759(2)	12.80597(7)
$\alpha/^\circ$	75.365(3)	85.7259(7)	90
$\beta/^\circ$	76.876(3)	86.8164(7)	90
$\gamma/^\circ$	68.308(2)	89.0860(8)	90
$V/\text{\AA}^3$	2594.94(14)	8259.68(12)	11663.98(14)
Z	1	2	2
T/K	120.00(10)	120.00(10)	120.00(10)
$\lambda/\text{\AA}$	0.71073	0.71073	0.71073
$\rho_{\text{calcd}}/\text{g cm}^{-3}$	3.724	4.192	3.749
μ/mm^{-1}	21.422	24.555	21.883
$R[F_o^2 > 2\sigma(F_o^2)]^a$	0.0571	0.0473	0.0627
$R_w[F_o^2 > 2\sigma(F_o^2)]^b$	0.1425 ^c	0.1052 ^d	0.1554 ^e

The crystallographic data for **Q-1** and **Q-2'** were previously reported (Duan et al., 2016b).

^a $R = \Sigma(|F_o| - |F_c|)/\Sigma|F_o|$

^b $R_w = \{\Sigma[w(F_o^2 - F_c^2)^2]/\Sigma[w(F_o^2)^2]\}^{1/2}$. $w = 1/[\sigma^2(F_o^2) + (AP)^2 + BP]$, where $P = (F_o^2 + 2F_c^2)/3$

^c $A = 0.0441$, $B = 271.6505$

^d $A = 0.0381$, $B = 405.0507$

^e $A = 0.0506$, $B = 1340.3177$.

the $\{Co^{III}Co_3^{II}O_4\}$ cubane clusters, in which they are coordinated by six hydroxo ligands in **2** and **2'**, or three hydroxo and three oxo ligands in **3** and **4**. In both cases, the apical position is particularly suitable to accommodate Co^{3+} ions (specially in **2** and **2'**) because hydroxo ligands stabilize Co^{3+} in comparison with water ligands, as evidenced by the E° values of the Co^{3+}/Co^{2+} redox couple¹. In contrast, in the cubane cobalt cluster of **1**, the apical cobalt is coordinated by three hydroxo and three water ligands, favouring the stabilization of Co^{2+} . If the synthesis of POMs containing cubane clusters is performed in the presence of an oxidant, the three apical water molecules will likely be substituted by oxo or hydroxo ligands in order to accommodate a Co^{3+} ion.

The synthesis of all these compounds involves the preparation of a starting solution in which the experimental conditions favor the formation of the trivacant polyanion $[B-\alpha-PW_9O_{34}]^{9-}$ in the presence of Co^{2+} ions (see experimental section). The W:P ratio used in this starting solution (11:1) is higher than the necessary to obtain the trivacant POM ligand. Therefore, the formation of additional polyoxoanions coexisting in solution can be expected. This explains the formation of POMs **2**, **2'**, **3**, and **4**, which consist of the assembly of one or more subunits of **1** with different polyoxoanion fragments. The isolation of each compound requires the implementation of different

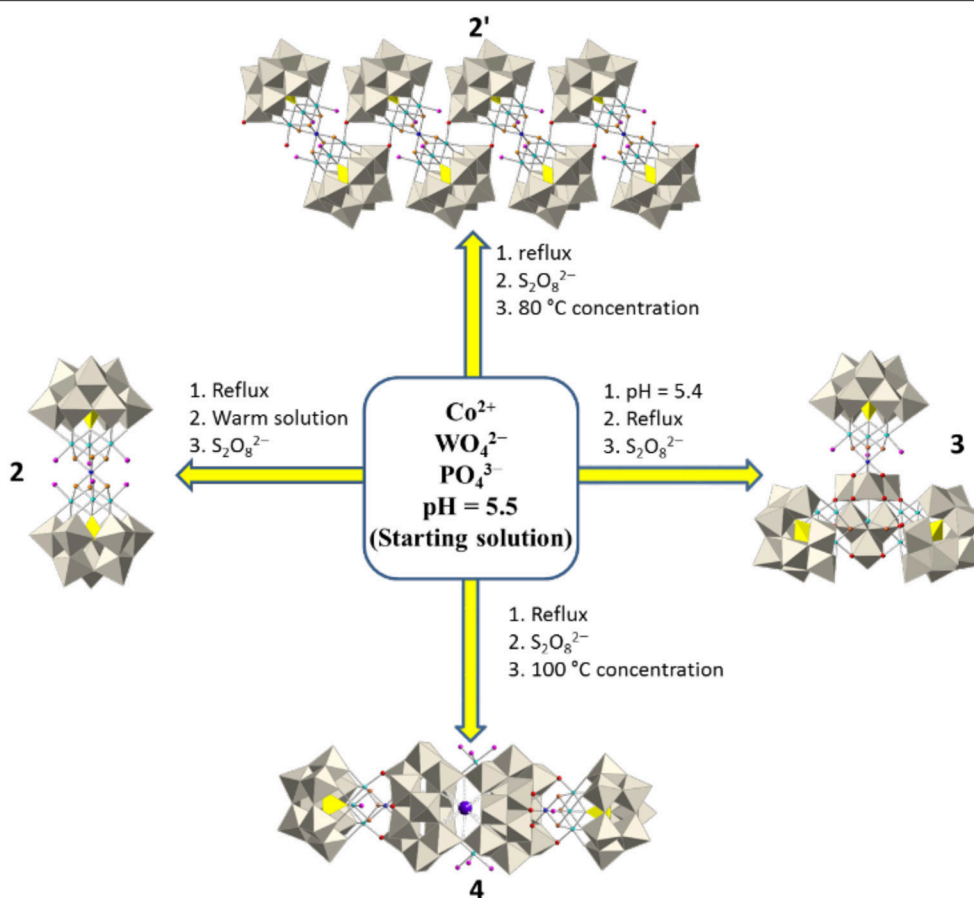
experimental conditions to the starting solution. For example, the preparation of **2** and **2'** requires a pH value of 5.5, while for **3** pH = 5.4 (Additional 0.27 mL of glacial acetic acid were added in the synthesis of **3**). Such a difference seems to be sufficient to favor the coordination of the apical Co^{3+} by six hydroxo ligands in **2** and **2'**. The reason for which **2** is an isolated POM while **2'** is a polymeric chain lies in the concentration of the solutions (**2** crystallizes from a more diluted solution than **2'**).

In the synthesis of **3** and **4** the addition of the oxidant (potassium persulfate) was performed under boiling conditions, favoring the formation of the previously reported asymmetric sandwich POM $[Co_4^{II}(H_2O)_2(Co^{III}W_9O_{34})(PW_9O_{34})]^{12-}$, which contains Co^{3+} in tetrahedral coordination (Duan et al., 2016a). This asymmetric sandwich POM precipitates as a black solid which was filtered out. The main differences in the synthesis of **3** and **4** lie again in the pH values (5.4 and 5.5, respectively) and the concentration processes, carried out at boiling conditions for **3** and at room temperature for **4**.

Apart from all these compounds, we were able to obtain another POM following the same synthetic approach described in this section, i.e., applying a slight modification to the same starting solution used for the synthesis of all compounds. However, due to a lack of reproducibility and very low yield, the synthesis and characterization of this compound are not included in this manuscript but can be found in the Supporting Information section to demonstrate that the synthetic strategy presented here is not limited to the preparation of the four

¹ $[Co(H_2O)_6]^{3+} + e^- \rightarrow [Co(H_2O)_6]^{2+}$ $E^\circ = 1.92$ V

$Co(OH)_3 + e^- \rightarrow Co(OH)_2 + OH^-$ $E^\circ = 0.17$ V



SCHEME 1 | Synthetic scheme for compounds **2–4**. Color code: Gray octahedra, $\{WO_6\}$, yellow tetrahedral; $\{PO_4\}$, cyan spheres; Co^{II} , blue spheres; Co^{III} , red spheres; O, orange spheres; OH, pink spheres; H_2O , violet sphere, K.

POM compounds reported in this work. All attempts to obtain these compounds using $[PW_9O_{34}]^{9-}$ as precursor have been unsuccessful.

Crystal Structure of Q-1

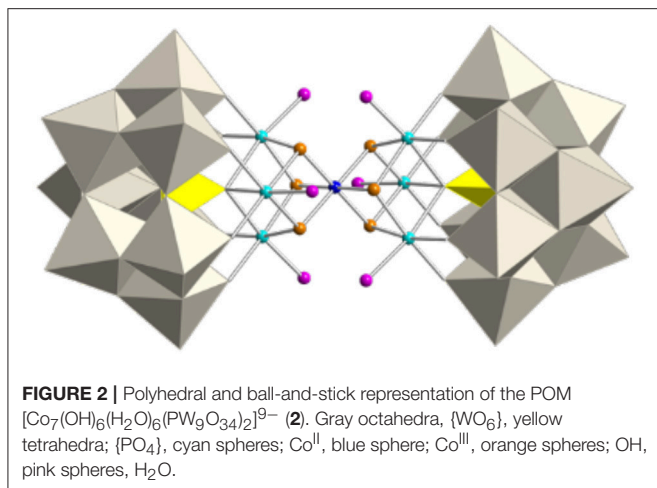
The salt containing the polyoxoanion $[Co_4^{II}(OH)_3(H_2O)_6(PW_9O_{34})]^{4-}$ (**1**) has been recently reported by us (Duan et al., 2016b). The nickel derivative was previously reported by Kortz et al. (Kortz et al., 1999). Basically, polyoxoanion **1** consists of one heptadentate $[B-\alpha-PW_9O_{34}]^{9-}$ ligand which incorporates a $\{Co_4^{II}O_4\}$ cubane unit arising from the tetrahedral arrangement of four edge-shared $\{CoO_6\}$ octahedra (see **Figure 1A**), giving rise to an idealized C_{3v} symmetry for **1**. The three μ_3 -bridging oxygen atoms of the cubane unit correspond to hydroxo groups. The apical cobalt atom is coordinated by three water ligands, while each of the three basal cobalt atoms is coordinated by only one water ligand. **1** can be considered as a common structural subunit of **2**, **2'**, **3**, and **4** (except that the oxidation state of the apical cobalt atom is different), in which the water molecules coordinated to the apical cobalt have been replaced by oxo or hydroxo ligands belonging

to other POM units, giving rise to the crystal structures described below.

Crystal Structures of Q-2 and Q-2'

The salt containing polyoxoanion **2** crystallizes in the triclinic $P\bar{1}$ space group and can be considered to be constructed from one subunit of **1** in which the three apical water molecules have been replaced by three hydroxo ligands from a unit formulated as $[Co_3^{II}(OH)_3(H_2O)_3(PW_9O_{34})]^{6-}$. As a result, a heptanuclear $\{Co^{III}Co_6^{II}O_8\}$ cluster is encapsulated by two heptadentate $[B-\alpha-PW_9O_{34}]^{9-}$ ligands (**Figure 2**). The topology of this dicubane cluster has also been found encapsulated between two trilacunary Dawson ligands ($[\alpha-P_2W_{15}O_{56}]^{9-}$) for cobalt, nickel, and manganese (Fang et al., 2012; Bassil et al., 2016; Duan et al., 2016b).

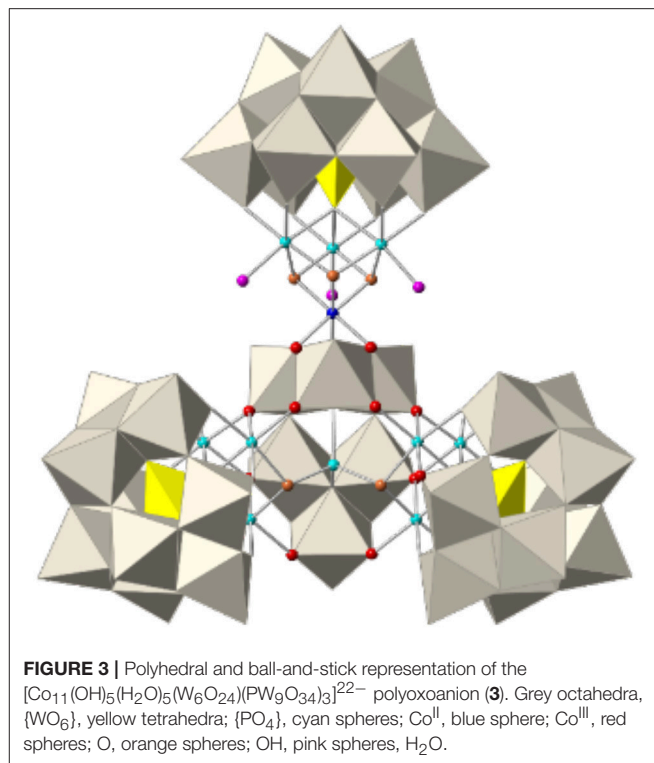
The central cobalt atom of this cluster exhibits an oxidation state of +3, while the other six cobalt atoms are divalent. According to BVS calculations (Figure S5), the six μ_3 -O ligands coordinated to the central cobalt atom correspond to hydroxo groups. The packing of **2** is formed by layers parallel to the crystallographic ab plane which are separated by external $[Co(H_2O)_6]^{2+}$ cations. The long axis of the POMs forms an angle



of 69.7° with the packing plane and keeps parallel in adjacent layers, giving rise to a $\cdots\text{AA}\cdots$ layer packing mode. **2** could also be obtained by a step-by-step approach as a mixed cesium/sodium salt which crystallizes in the monoclinic space group $P2_1/c$ and does not contain any external Co^{2+} acting as counterion of the POM (Duan et al., 2016b). The cesium/sodium salt is made of layers perpendicular to the b axis, in which the POMs are parallel and form an angle of 79.6° with the packing plane. POMs in the adjacent layers form the same angle but in the opposite direction (see Figures S11a,c), giving rise to a $\cdots\text{ABAB}\cdots$ layer packing mode. In contrast, the structure of **2'** is made of units of **2**, in which one of the basal water molecules is replaced by a terminal oxo ligand of an adjacent POM (see Figure S11b and Scheme 1) giving rise to one-dimensional polymeric chains running along the crystallographic a -axis.

Crystal Structure of Q-3

The novel polyoxoanion $[\text{Co}_{11}(\text{OH})_5(\text{H}_2\text{O})_5(\text{W}_6\text{O}_{24})(\text{PW}_9\text{O}_{34})_3]^{22-}$ (**3**) can be considered to be formed by one subunit of **1** and one heptameric cobalt fragment formulated as $\{[\text{Co}_3^{\text{II}}(\text{H}_2\text{O})]_2[\text{Co}^{\text{II}}(\text{OH})_2\text{W}_6\text{O}_{24}](\text{PW}_9\text{O}_{34})_2\}^{18-}$, giving rise to a C_s symmetry for the whole assembly. This fragment replaces the three apical water molecules in **1** by three oxo ligands (see Figure 3) and can be constructed from the previously reported POM $\{[\text{Co}_3^{\text{II}}(\text{H}_2\text{O})]_2[\text{Co}^{\text{II}}(\text{OH})_2\text{W}_7\text{O}_{26}](\text{PW}_9\text{O}_{34})_2\}^{16-}$ by removal of one $\{\text{WO}_2\}$ group from the central $[\text{Co}^{\text{II}}(\text{OH})_2\text{W}_7\text{O}_{26}]^{10-}$ unit (Clemente-Juan et al., 2004). In addition, it is topologically similar to the previously reported series formulated as $\{[\text{M}_3(\text{H}_2\text{O})]_2[\text{XW}_6\text{O}_{26}](\text{X}'\text{W}_9\text{O}_{34})_2\}^{n-}$ [$\text{X} = \text{X}' = \text{P}^{\text{V}}$ and $\text{M} = \text{Co}^{\text{II}}$, Mn^{II} , Ni^{II} (Ritorto et al., 2004; Yang et al., 2012); $\text{X} = \text{X}' = \text{V}^{\text{V}}$ and $\text{M} = \text{Co}^{\text{II}}$ (Lv et al., 2013); $\text{X} = \text{X}' = \text{As}^{\text{V}}$ and $\text{M} = \text{Co}^{\text{II}}$, Mn^{II} , and Zn^{II} (Fukaya and Yamase, 2007); and $\text{X} = \text{X}' = \text{Ge}^{\text{IV}}$ and $\text{M} = \text{Fe}^{\text{III}}$; (Wang et al., 2014)]. Two analogous POMs built with Dawson trilaunary ligands have also been reported recently (Martin-Sabi et al., 2016). Therefore, the corresponding fragment in **3** represents the first example in which $\text{X} \neq \text{X}'$ and $\text{X} = \text{M} = \text{Co}^{\text{II}}$. The salt of this POM crystallizes in the triclinic space group $P\bar{1}$ (Table 1) and contains chains of **3** (running along the a -axis) linked by one



external Co^{2+} disordered in two close positions (see Figure S12). BVS calculations confirm that the apical cobalt atom exhibits an oxidation state of +3, while all other cobalt atoms are divalent (see Figure S6). From the magnetic point of view, both the heptameric and tetrameric cobalt cores are expected to be isolated from each other and from the external Co^{2+} ions by the diamagnetic polyoxotungstate framework.

Crystal Structure of Q-4

The novel elongated-shaped polyoxoanion $[\{\text{Co}_4(\text{OH})_3(\text{H}_2\text{O})(\text{PW}_9\text{O}_{34})\}_2\{\text{K}(\text{H}_2\text{W}_{12}\text{O}_{41})_2\}\{\text{Co}(\text{H}_2\text{O})_4\}_2]^{17-}$ (**4**) consists of a central fragment formulated as $[\text{K}(\text{H}_2\text{W}_{12}\text{O}_{41})_2\{\text{Co}(\text{H}_2\text{O})_4\}_2]^{11-}$, bi-capped by two subunits of **1** (see Figure 4). This central fragment is made by condensation of two paratungstate-B anions $[\text{H}_2\text{W}_{12}\text{O}_{42}]^{10-}$ associated through two common oxygen atoms which were terminal in the parent paratungstate-B anions. The two paratungstate-B subunits are connected in an open arrangement in such a way that they leave an internal cavity occupied by a K^+ cation. The K^+ cation is coordinated by ten $\mu_2\text{-O}$ atoms from corner-shared $\{\text{WO}_6\}$ octahedra, with $\text{K}\cdots\text{O}$ distances ranging between 2.77 and 2.97 Å. In addition, the open configuration of the central fragment delimits two coordination sites for two extra Co^{2+} cations, which are *cis*-chelated by two terminal oxygen atoms belonging to different paratungstate-B subunits.

The subunits of **1** are linked to the central fragment through substitution of five water ligands. The three apical water molecules of subunit **1** are substituted by three $\mu_2\text{-O}$ atoms (from two corner-shared and one edge-shared $\{\text{WO}_6\}$ octahedra), while two basal water molecules are substituted by two terminal oxygen

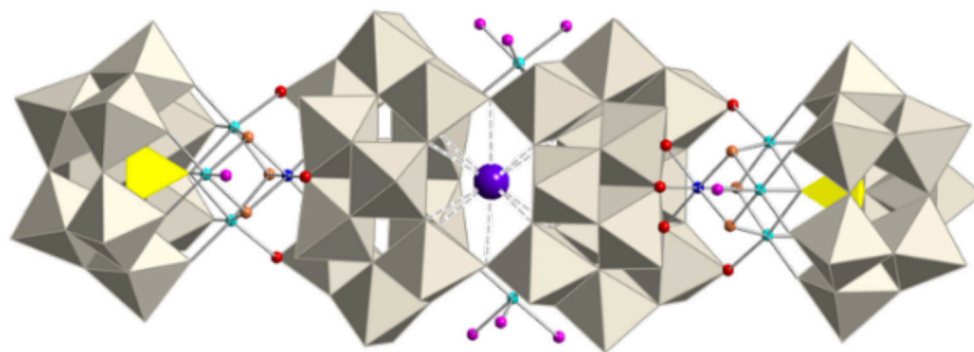


FIGURE 4 | Polyhedral and ball-and-stick representation of the $[[Co_4(OH)_3(H_2O)(PW_9O_{34})_2]\{K_4(H_2W_{12}O_{41})_2\}[Co(H_2O)_4]_2]^{17-}$ polyoxoanion (**4**). Grey octahedra, $\{WO_6\}$, yellow tetrahedra; $\{PO_4\}$, cyan spheres; Co^{II} , blue spheres; Co^{III} , red spheres; O, orange spheres; OH, pink spheres; H_2O , violet sphere, K.

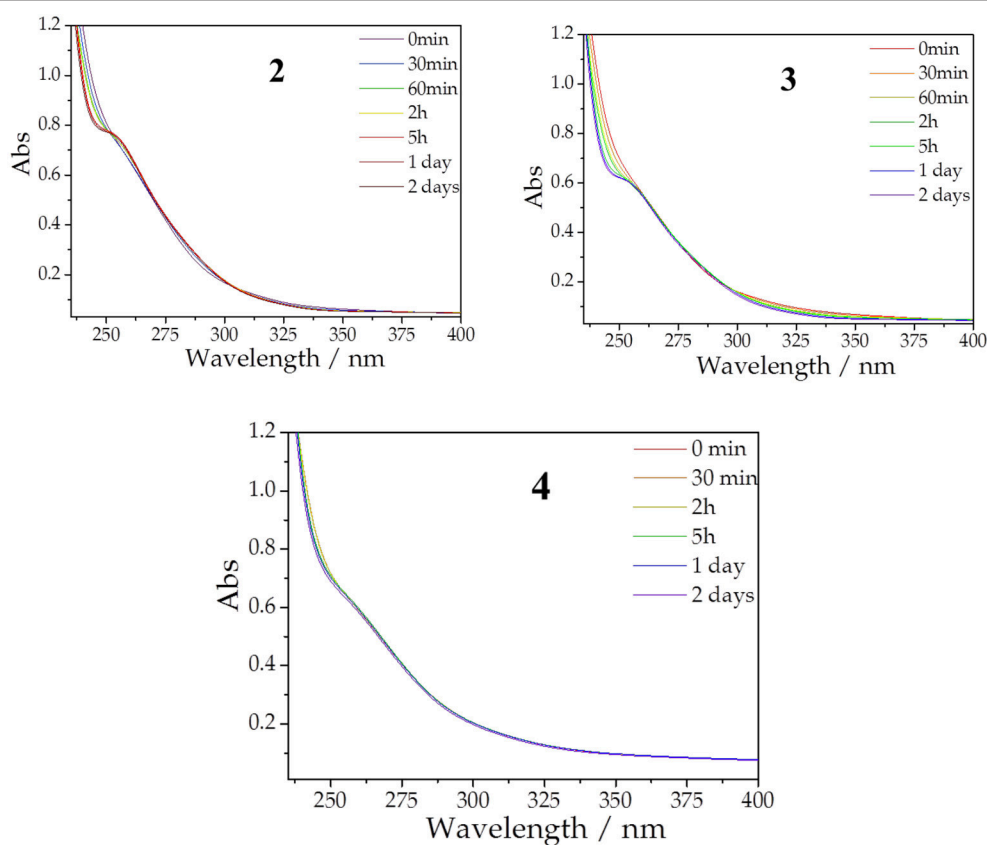


FIGURE 5 | Evolution of UV spectra of solutions of **2**, **3**, and **4** at concentration of 10^{-5} M with time, recorded in a buffer solution of 0.5 M sodium acetate (pH 4.8).

atoms from each paratungstate-B subunit. The arrangement of all fragments leads to an overall C_{2v} symmetry for polyanion **4**. BVS calculations yield the same results as in **2**, **2'**, and **3** concerning the oxidation state of the cobalt atoms, i.e., the apical cobalt atom bears an oxidation state of +3, while the basal cobalt atoms are divalent (see Figure S7). Salt **Q-4** crystallizes in the orthorhombic space group $Pmmn$, forming columns of eclipsed POMs in which the long axis of **4** is perpendicular to the stacking c direction

(see Figure S13). Each stack is surrounded by other four stacks, creating channels along the c direction in which water molecules of crystallization reside.

Stabilities in Aqueous Solution

Given the interest of Co-based POMs in catalysis, the stabilities in solution of the discrete species were studied using UV-vis spectroscopy. The aqueous solution stability of **1** was previously

studied by UV-vis spectroscopy and cyclic voltammetry (Duan et al., 2016b). It was concluded that aqueous solutions of **1** decompose mainly into the mono-substituted POM $[\text{PCo}(\text{H}_2\text{O})\text{W}_{11}\text{O}_{39}]^{5-}$, as evidenced by the appearance of a characteristic peak in the UV-vis spectrum at 252 nm within 24 h of standing. We have also investigated the stability of aqueous solutions of POMs **2**, **3**, and **4** in 0.5 M NaOAc/HOAc buffer solution at pH 4.8 at room temperature (see Figure 5). The evolution of the UV-vis spectra of **2** and **3** clearly indicate that, similarly to **1**, a new peak develops in all cases within 24 h at 252 nm, suggesting that these POMs decompose also producing the mono-substituted $[\text{PCo}(\text{H}_2\text{O})\text{W}_{11}\text{O}_{39}]^{5-}$ as the major product (Jabbour et al., 2004; Holclajtner-Antunović et al., 2008). By comparison with the decomposition of **1**, these mono-substituted species should come from the decomposition of the corresponding subunit in **2** and **3**, which is topologically identical to **1**. In contrast, the UV-vis spectra of **4** remains almost unchanged during the first 48 h of standing, suggesting that this POM is stable in aqueous solution at pH 4.8 during this period. We have also checked that **4** is stable at pH values 4.3 and 3.8 (see Figure S15). In fact, **4** can be recrystallized from hot water (80 °C) and recovered from solution after 1 week in high yield, in accordance with the UV-vis spectra results. Compared to **1-3**, the higher stability of **4** is likely due to the fact that five water molecules from subunit **1** (three apical and two basal) have been substituted by oxo ligands from the central fragment of **4**, providing rigidity to the cubane cluster $\{\text{Co}^{\text{III}}\text{Co}_3^{\text{II}}\text{O}_4\}$ and, therefore, hindering its decomposition.

Magnetic Properties

The magnetic studies of the salts **Q-1**, **Q-2**, and **Q-2'** were previously reported by us (Duan et al., 2016b). Here, we report the magnetic properties of **Q-3** and **Q-4** (Figure 6 and Figure S14). For **Q-3** the $\chi_m T$ vs. T curve shows a smooth decrease from room temperature ($\chi_m T = 37.5 \text{ emu K mol}^{-1}$) down to 50 K ($\chi_m T = 32.0 \text{ emu K mol}^{-1}$). Below this temperature, a sharp peak is observed with a maximum at 5.0 K ($\chi_m T = 52 \text{ emu K mol}^{-1}$), which clearly depends on the magnetic field: as it increases, the maximum decreases, shifts to higher temperatures and becomes broader. In the case of **Q-4**, the $\chi_m T$ vs. T curve exhibits a smooth and continuous decrease from room temperature ($\chi_m T = 35.0 \text{ emu K mol}^{-1}$) down to 15 K. Below this temperature, a sharp decrease is observed.

To analyse the results it is necessary to take into account the contributions of the different cobalt ions. Octahedral Co^{2+} ions are described by a high-spin ground electronic term 4T_1 with first-order spin-orbit coupling. This ground state is split into six anisotropic Kramers doublets (Ginsberg, 1971; Lines, 1971). At low temperature, only the lowest anisotropic Kramers doublet is populated. The apical cobalt atom in the cubane unit bears an oxidation state of +3 and is diamagnetic due to the strong field associated with the hydroxyl groups, having no net contribution to the magnetic properties.

We discuss first the magnetic behavior of **Q-4** because it contains two identical cubane cobalt clusters, while **Q-3** contains one of such cubane clusters and one additional, independent, heptameric cluster. The magnetic behavior of **Q-4** can be

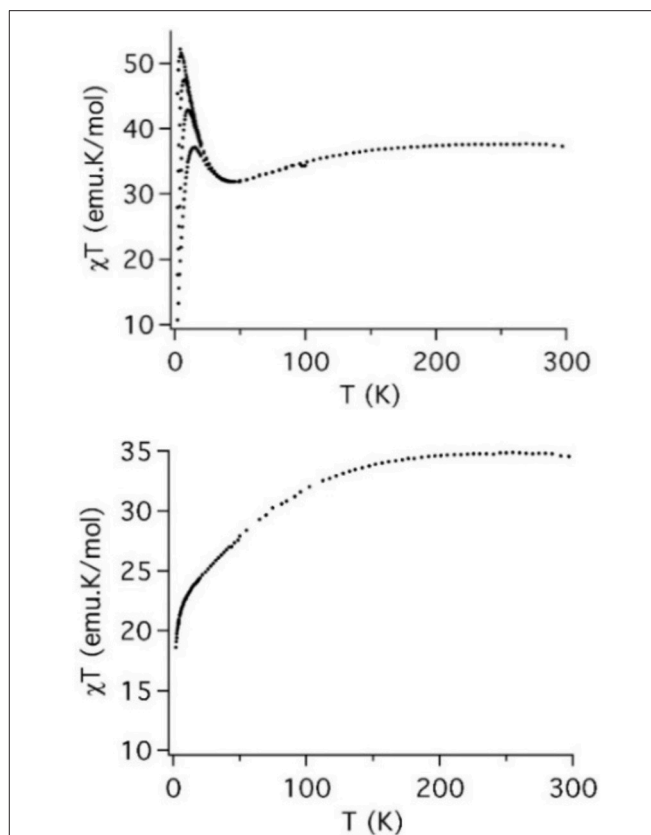


FIGURE 6 | Thermal dependence of $\chi_m T$ for **Q-3** (left) and **Q-4** (right) at different fields (0.1, 0.5, 1 and 2 T for **Q-3**; 0.1 T for **Q-4**) in the range 2–300 K.

explained by the superposition of two different contributions: the two cubane units present in the POM, and four isolated Co^{2+} (two of them are bridging the two central paratungstate units and the remaining two are external cobalt atoms acting as counteranions). Due to the diamagnetic behavior of the apical cobalt, the magnetic exchange scheme of **Q-4** can be described as an equilateral triangle of Co^{2+} ions coupled with a single anisotropic interaction.

We have recently studied several POMs containing similar triangular units, which present ferromagnetic interactions (Clemente-Juan et al., 2002, 2005; Bassil et al., 2005; Lisnard et al., 2007). In these triangular units, the ferromagnetic sign of the exchange parameter was explained by the orthogonality of the magnetic orbitals in the edge-sharing $\{\text{CoO}_6\}$ octahedra (Co-O-Co angles close to 90°). All these systems present a sharp maximum at low temperature due to the ferromagnetic interaction between the lowest Kramers doublets of each Co^{2+} atom. The height of this maximum depends greatly on the position of the anisotropy axes of the cobalt atoms involved in the triangular unit. However, for **Q-4**, no maximum is observed and only a change in the slope of the curve is observed upon cooling from room temperature to 8 K, where a sudden drop occurs. This may be due to the presence in the salt of a large number (four) of monomeric external cobalt ions, which dominate the magnetic behavior, masking the behavior of the triangular cobalt units.

In contrast to **Q-4**, **Q-3** exhibits the characteristic maximum in $\chi_m T$ at low temperature, which clearly indicates the presence of dominant ferromagnetic interactions. To explain this behavior, it is necessary to take into account the three different contributions present in this system: the first arises from a cobalt cubane unit (similar to that found in **Q-4**), the second from a heptameric cobalt unit, and the third from some external and isolated Co^{2+} ions. An identical heptameric unit was reported in the POM $[\{\text{Co}_3^{\text{II}}(\text{H}_2\text{O})_2\}[\text{Co}^{\text{II}}(\text{OH})_2\text{W}_7\text{O}_{26}](\text{PW}_9\text{O}_{34})_2]^{16-}$ (Clemente-Juan et al., 2004). In this case the $\chi_m T$ curve exhibited a maximum in the same temperature region. This heptameric unit exhibits ferrimagnetic behavior, with ferromagnetic interaction between the cobalt atoms of each triangular unit, and antiferromagnetic interaction between the central cobalt atom and the outer cobalt trimers. The cubane unit, together with the outer Co^{2+} ions, should show similar behavior as in **Q-4**. Thus, the experimental behavior may result from the sum of the three different contributions, with a dominant contribution at low temperature coming from the heptameric ferrimagnetic unit. Unfortunately, the large overparameterization and the existence of external Co^{2+} ions make a quantitative analysis of the data impossible in this case.

CONCLUSIONS

We have reported a one-pot synthetic approach which gives rise to four cobalt-containing POMs (**2**, **2'**, **3**, and **4**) by carrying out slight and subtle variations to a common starting solution containing WO_4^{2-} , PO_4^{3-} , and Co^{2+} at pH 5.5. Each synthetic procedure includes the addition of persulfate, which causes the oxidation of some cobalt ions and promotes the formation of the $\{\text{Co}^{\text{III}}\text{Co}_3^{\text{II}}\text{O}_4\}$ -cubane-containing fragment $[\{\text{Co}^{\text{III}}\text{Co}_3^{\text{II}}(\text{OH})_3(\text{H}_2\text{O})_{6-m}(\text{PW}_9\text{O}_{34})\}]^{3-m-}$ ($m = 3$ or 5) which acts as a common subunit of POMs **2**, **2'**, **3**, and **4** (Figures 1C–E). This subunit is topologically similar to the previously reported $\{\text{Co}_4^{\text{II}}\text{O}_4\}$ -cubane-containing POM $[\text{Co}_4^{\text{II}}(\text{OH})_3(\text{H}_2\text{O})_3(\text{PW}_9\text{O}_{34})]^{4-}$ (**1**) which exists as an individual entity (Duan et al., 2016b).

The use of persulfate as oxidant is responsible for the oxidation of the apical cobalt in the cubane cluster. This Co^{3+} ion is stabilized by the substitution of the three apical water molecules in **1** by oxo or hydroxo groups of other POM fragments present in the solution, giving rise to larger POM entities. Thus, an heptacobalt-containing POM $[\text{Co}_7(\text{OH})_6(\text{H}_2\text{O})_6(\text{PW}_9\text{O}_{34})_2]^{9-}$ (**2**) is formed by substitution of the three apical water molecules in a subunit of **1** by the fragment $\{\text{Co}_3^{\text{II}}(\text{OH})_3(\text{H}_2\text{O})_3(\text{PW}_9\text{O}_{34})\}^{6-}$ (see Figure 1C). The additional substitution of one basal water molecule in the subunit of **1** gives rise to an infinite polymeric chain formulated as $[\text{Co}_7(\text{OH})_6(\text{H}_2\text{O})_4(\text{PW}_9\text{O}_{34})_2]_n^{9n-}$ (**2'**). On the other hand, if all three apical water molecules are replaced by the heptanuclear fragment $\{[\{\text{Co}_3^{\text{II}}(\text{H}_2\text{O})_2\}[\text{Co}^{\text{II}}(\text{OH})_2\text{W}_6\text{O}_{24}](\text{PW}_9\text{O}_{34})_2]^{18-}\}$, a novel undecacobalt-containing POM $[\text{Co}_{11}(\text{OH})_5(\text{H}_2\text{O})_5(\text{W}_6\text{O}_{24})(\text{PW}_9\text{O}_{34})_3]^{22-}$ (**3**) is obtained (see Figure 1D). Finally, a new decacobalt-containing POM $[\{\text{Co}_4(\text{OH})_3(\text{H}_2\text{O})(\text{PW}_9\text{O}_{34})\}_2\{\text{KC}(\text{H}_2\text{W}_{12}\text{O}_{41})_2\}\{\text{Co}(\text{H}_2\text{O})_4\}_2]$

¹⁷⁻ (**4**) is formed by the substitution of the three apical water molecules and two basal water molecules of two subunits of **1** by bridging the di-paratungstate fragment $[\{\text{KC}(\text{H}_2\text{W}_{12}\text{O}_{41})_2\}\{\text{Co}(\text{H}_2\text{O})_4\}_2]^{11-}$ (see Figure 1E).

As far as the stability of these POMs is concerned, we have observed that **4** is stable in aqueous solutions for at least 48 h, as confirmed by UV-vis spectroscopy, while **2** and **3** slowly decompose forming the mono-substituted Keggin anion $[\text{PCo}(\text{H}_2\text{O})\text{W}_{11}\text{O}_{39}]^{5-}$ as the major product. Concerning the magnetic properties, we have focused on the new POMs (**3** and **4**). In the corresponding salts, the presence of several isolated octahedrally coordinated Co^{2+} ions acting as counterions have made impossible to carry out a quantitative analysis. Nonetheless, the magnetic properties of **3** can be understood qualitatively from the known magnetic interactions existing in previously reported cobalt clusters encapsulated in POMs. In fact, the magnetic behavior of this large POM (formed by the fusion of a heptanuclear Co^{2+} cluster with the $\{\text{Co}^{\text{III}}\text{Co}_3^{\text{II}}\text{O}_4\}$ cubane unit) is dominated at low temperatures by the ferrimagnetic coupling within the heptanuclear cluster.

Finally, it has to be noted that the synthetic strategy reported in this work can be further exploited to obtain other new POMs with larger nuclearities made from the linkage of subunits of **1** with other polyoxoanion fragments, by substitution of the water ligands coordinated to the cobalt atoms of the cubane cluster.

AUTHOR CONTRIBUTIONS

All authors listed have made a substantial, direct and intellectual contribution to the work, and approved it for publication.

FUNDING

The present work has been funded by the EU (ERC Advanced Grant SPINMOL and COST Action CM1203 Polyoxometalate Chemistry for molecular Nanoscience, PoCheMon), the Spanish MINECO (grants CTQ2014-52758-P and MAT2014-56143-R), the Generalitat Valenciana (Prometeo and ISIC Programmes of excellence), and the María de Maeztu Project (MDM-2015-0538).

ACKNOWLEDGMENTS

We thank José M^a Martínez-Agudo and Gloria Agustí-López for performing some physical measurements.

SUPPLEMENTARY MATERIAL

The Supplementary Material for this article can be found online at: <https://www.frontiersin.org/articles/10.3389/fchem.2018.00231/full#supplementary-material>

Crystallographic data in from the Inorganic Crystal Structure Database (ICSD) for **Q-2**, **Q-3** and **Q-4** (CSD CIF format can be obtained No. 432446) or the

Cambridge Structural Database (CCDC) for **Q-2**, **Q-3** and **Q-4** (CCDC 1538253-1538255). FT-IR spectra. Thermograms. Bond valence sum calculations. X-ray

powder diffraction. Magnetic properties of **Q-3** and **Q-4**. Stability of **Q-4**. Synthesis and characterization of **Q-5**.

REFERENCES

- Agilent Technologies (2011). *CrysAlis PRO Software system*, version. 1.171.35.15, Oxford, UK: Agilent Technologies UK Ltd.
- Al-Oweini, R., Sartorel, A., Bassil, B. S., Natali, M., Berardi, S., Scandola, F., et al. (2014). Photocatalytic water oxidation by a mixed-valent ($\text{Mn}^{\text{III}}\text{Mn}^{\text{IV}}\text{O}_3$) manganese oxo core that mimics the natural oxygen-evolving center. *Angew. Chem. Int. Ed. Engl.* 53, 11182–11185. doi: 10.1002/anie.201404664
- Bassil, B. S., Kortz, U., Tigan, A. S., Clemente-Juan, J. M., Keita, B., de Oliveira, P., et al. (2005). Cobalt-containing silico-tungstate sandwich dimer $[\{\text{Co}_3(\text{B}-\beta\text{-SiW}_9\text{O}_{33}(\text{OH}))(\text{B}-\beta\text{-SiW}_8\text{O}_{29}(\text{OH}))_2\}]^{22-}$. *Inorg. Chem.* 44, 9360–9368. doi: 10.1021/ic0515554
- Bassil, B. S., Xiang, Y., Haider, A., Hurtado, J., Novitchi, G., Powell, A. K., et al. (2016). Heptanickel(II) double-cubane core in wells-dawson heteropolytungstate, $[\text{Ni}_7(\text{OH})_6(\text{H}_2\text{O})_6(\text{P}_2\text{W}_{15}\text{O}_{56})_2]^{16-}$. *Chem. Commun.* 52, 2601–2604. doi: 10.1039/C5CC09823H
- Clemente-Juan, J., and Coronado, E. (1999). Magnetic clusters from polyoxometalate complexes. *Coord. Chem. Rev.* 193–5, 361–394. doi: 10.1016/S0010-8545(99)00170-8
- Clemente-Juan, J. M., Coronado, E., Forment-Aliaga, A., Galán-Mascarós, J. R., Giménez-Saiz, C., and Gómez-García, C. J. (2004). A new heptanuclear cobalt(II) cluster encapsulated in a novel heteropolyoxometalate topology: synthesis, structure, and magnetic properties of $[\text{Co}_7(\text{H}_2\text{O})_2(\text{OH})_2\text{P}_2\text{W}_{25}\text{O}_{94}]^{16-}$. *Inorg. Chem.* 43, 2689–2694. doi: 10.1021/ic0354872
- Clemente-Juan, J. M., Coronado, E., and Gaita-Ariño, A. (2012). Magnetic polyoxometalates: from molecular magnetism to molecular spintronics and quantum computing. *Chem. Soc. Rev.* 41, 7464–7478. doi: 10.1039/c2cs35205b
- Clemente-Juan, J. M., Coronado, E., Gaita-Ariño, A., Giménez-Saiz, C., Chaboussant, G., Güdel, H. U., et al. (2002). Magnetism in polyoxometalates: anisotropic exchange interactions in the Co_3^{II} moiety of $[\text{Co}_3\text{W}(\text{D}_2\text{O})_2(\text{ZnW}_9\text{O}_{34})_2]^{12-}$ —A magnetic and inelastic neutron scattering study. *Chem. Eur. J.* 8, 5701–5708. doi: 10.1002/1521-3765(20021216)8:24<5701::AID-CHEM5701>3.0.CO;2-T
- Clemente-Juan, J. M., Coronado, E., Gaita-Ariño, A., Giménez-Saiz, C., Güdel, H. U., Sieber, A., et al. (2005). Magnetic polyoxometalates: anisotropic exchange interactions in the Co_3^{II} moiety of $[(\text{NaOH})_2\text{Co}_3(\text{H}_2\text{O})(\text{P}_2\text{W}_{15}\text{O}_{56})_2]^{17-}$. *Inorg. Chem.* 44, 3389–3395. doi: 10.1021/ic048552w
- Coronado, E., Giménez-Saiz, C., and Gómez-García, C. J. (2005). Recent advances in polyoxometalate-containing molecular conductors. *Coord. Chem. Rev.* 249, 1776–1796. doi: 10.1016/j.ccr.2005.02.017
- Coronado, E., and Gómez-García, C. J. (1998). Polyoxometalate-based molecular materials. *Chem. Rev.* 98, 273–296. doi: 10.1021/cr970471c
- Dolbecq, A., Dumas, E., Mayer, C. R., and Mialane, P. (2010). Hybrid organic-inorganic polyoxometalate compounds: from structural diversity to applications. *Chem. Rev.* 110, 6009–6048. doi: 10.1021/cr1000578
- Duan, Y., Clemente-Juan, J. M., Fierro, J. L., Giménez-Saiz, C., and Coronado, E. (2016a). A decacobalt(II) cluster with triple-sandwich structure obtained by partial reductive hydrolysis of a pentacobalt(II/III) Weakley-type polyoxometalate. *Chem. Commun.* 52, 13245–13248. doi: 10.1039/C6CC05485D
- Duan, Y., Clemente-Juan, J. M., Giménez-Saiz, C., and Coronado, E. (2016b). Cobalt clusters with cubane-type topologies based on trivacant polyoxometalate ligands. *Inorg. Chem.* 55, 925–938. doi: 10.1021/acs.inorgchem.5b02532
- Evans, H. T., Weakley, T. J. R., and Jameson, G. B. (1996). Crystal structures of $[\text{NEt}_3\text{H}]_5[\text{XCo}^{\text{II}}\text{W}_{11}\text{O}_{39}]\cdot 3\text{H}_2\text{O}$ ($\text{X} = \text{P}$ or As). *J. Chem. Soc. Dalton Trans.* 2537–2540. doi: 10.1039/DT9960002537
- Fang, X., Kögerler, P., Speldrich, M., Schilder, H., and Luban, M. (2012). A polyoxometalate-based single-molecule magnet with an $S=21/2$ ground state. *Chem. Commun.* 48, 1218–1220. doi: 10.1039/C1CC15520B
- Fukaya, K., and Yamase, T. (2007). V-shaped polyoxotungstoarsenates incorporating a prism-like hexa transition-metals center: $[\text{M}_6(\text{H}_2\text{O})_2(\text{AsW}_9\text{O}_{34})_2(\text{AsW}_6\text{O}_{26})]^{17-}$ ($\text{M}^{2+} = \text{Mn}^{2+}, \text{Co}^{2+}, \text{Zn}^{2+}$). *Bull. Chem. Soc. Jpn.* 80, 178–182. doi: 10.1246/bcsj.80.178
- Galán-Mascarós, J. R., Giménez-Saiz, C., Triki, S., Gómez-García, C. J., Coronado, E., and Ouahab, L. (1995). A novel chainlike heteropolyanion formed by Keggin units: synthesis and structure of $(\text{ET})_8[\text{PMnW}_{11}\text{O}_{39}]_n\cdot 2n\text{H}_2\text{O}$. *Angew. Chem. Int. Ed. Engl.* 34, 1460–1462. doi: 10.1002/anie.199514601
- Ginsberg, A. P. (1971). Magnetic exchange in transition metal complexes vi: aspects of exchange coupling in magnetic cluster complexes. *Inorg. Chim. Acta Rev.* 5, 45–68. doi: 10.1016/0073-8085(71)80012-8
- Han, X. B., Zhang, Z. M., Zhang, T., Li, Y. G., Lin, W., You, W., et al. (2014). Polyoxometalate-based cobalt-phosphate molecular catalysts for visible light-driven water oxidation. *J. Am. Chem. Soc.* 136, 5359–5366. doi: 10.1021/ja412886e
- Hill, C. L. (ed.). (1998). Special thematic issue on polyoxometalates. *Chem. Rev.* 98, 1–389. doi: 10.1021/cr960395y
- Hill, C. L., and Prosser-McCarthy, C. M. (1995). Homogeneous catalysis by transition-metal oxygen anion clusters. *Coord. Chem. Rev.* 143, 407–455. doi: 10.1016/0010-8545(95)01141-B
- Holclajtner-Antunović, I., Bajuk-Bogdanović, D., Todorović, M. B., Mioč, U., Zakrzewska, J., and Uskoković-Marković, S. (2008). Spectroscopic study of stability and molecular species of 12-tungstophosphoric acid in aqueous solution. *Can. J. Chem.* 86, 996–1004. doi: 10.1139/v08-138
- Ibrahim, M., Haider, A., Lan, Y., Bassil, B. S., Carey, A. M., Liu, R., et al. (2014). Multinuclear Cobalt(II)-containing heteropolytungstates: structure, magnetism, and electrochemistry. *Inorg. Chem.* 53, 5179–5188. doi: 10.1021/ic500298u
- Ibrahim, M., Lan, Y., Bassil, B. S., Xiang, Y., Suchopar, A., Powell, A. K., et al. (2011). Hexadecacobalt(II)-containing polyoxometalate-based single-molecule magnet. *Angew. Chem. Int. Ed.* 50, 4708–4711. doi: 10.1002/anie.201100280
- Jabbour, D., Keita, B., Mbomekallé, I. M., Nadjo, L., and Kortz, U. (2004). Investigation of multi-nickel-substituted tungstophosphates and their stability and electrocatalytic properties in aqueous media. *Eur. J. Inorg. Chem.* 10, 2036–2044. doi: 10.1002/ejic.200300830
- Katsoulis, D. E., and Pope, M. T. (1984). New Chemistry for heteropolyanions in anhydrous nonpolar-solvents-coordinative unsaturation of surface atoms-polyanion oxygen carriers. *J. Am. Chem. Soc.* 106, 2737–2738. doi: 10.1021/ja00321a064
- Kortz, U. (2009). Issue dedicated to polyoxometalates. *Eur. J. Inorg. Chem.* 2009, 5056. doi: 10.1002/ejic.200990096
- Kortz, U., Müller, A., van Slageren, J., Schnack, J., Dalal, N. S., and Dressel, M. (2009). Polyoxometalates: fascinating structures, unique magnetic properties. *Coord. Chem. Rev.* 253, 2315–2327. doi: 10.1016/j.ccr.2009.01.014
- Kortz, U., Tézé, A., and Hervé, G. (1999). A cubane-substituted polyoxoanion: structure and magnetic properties of $\text{Cs}_2[\text{H}_2\text{PW}_9\text{Ni}_4\text{O}_{34}(\text{OH})_3(\text{H}_2\text{O})_6]\cdot 5\text{H}_2\text{O}$. *Inorg. Chem.* 38, 2038–2042. doi: 10.1021/ic981138+
- Kozik, M., and Baker, L. C. W. (1994). *Polyoxometalates: From Platonic Solids to Antiretroviral Activity*. eds M. T. Pope and A. Müller (Dordrecht: Kluwer Academic Publishers), 191.
- Lines, M. E. (1971). Orbital angular momentum in theory of paramagnetic clusters. *J. Chem. Phys.* 55, 2977–2984. doi: 10.1063/1.1676524
- Lisnard, L., Mialane, P., Dolbecq, A., Marrot, J., Clemente-Juan, J. M., Coronado, E., et al. (2007). Effect of cyanato, azido, carboxylato, and carbonato ligands on the formation of cobalt(II) polyoxometalates: characterization, magnetic, and electrochemical studies of multinuclear

- cobalt clusters. *Chem. Eur. J.* 13, 3525–3536. doi: 10.1002/chem.200601252
- López, X., Carbo, J. J., Bo, C., and Poblet, J. M. (2012). Structure, properties and reactivity of polyoxometalates: a theoretical perspective. *Chem. Soc. Rev.* 41, 7537–7571. doi: 10.1039/c2cs35168d
- Lv, H., Song, J., Geletii, Y. V., Guo, W., Bacs, J., and Hill, C. L. (2013). A hexanuclear Cobalt(II) cluster incorporated in a banana-shaped tungstovanadate: $[(\text{Co}(\text{OH}_2)\text{Co}_2\text{VW}_9\text{O}_{34})_2(\text{VW}_6\text{O}_{26})]^{17-}$. *Eur. J. Inorg. Chem.* 2013, 1720–1725. doi: 10.1002/ejic.201201130
- Lydon, C., Sabi, M. M., Symes, M. D., Long, D., Murrie, M., Yoshii, S., et al. (2012). Directed assembly of nanoscale Co(II)-substituted $\{\text{Co}_9[\text{P}_2\text{W}_{15}]_3\}$ and $\{\text{Co}_{14}[\text{P}_2\text{W}_{15}]_4\}$ polyoxometalates. *Chem. Commun.* 48, 9819–9821. doi: 10.1039/c2cc34865a
- Martin-Sabi, M., Winter, R. S., Lydon, C., Cameron, J. M., Long, D., and Cronin, L. (2016). Rearrangement of $\{\alpha\text{-P}_2\text{W}_{15}\}$ to $\{\text{PW}_6\}$ moieties during the assembly of transition-metal-linked polyoxometalate clusters. *Chem. Commun.* 52, 919–921. doi: 10.1039/C5CC08486E
- Miras, H. N., Yan, J., Long, D., and Cronin, L. (2012). Engineering polyoxometalates with emergent properties. *Chem. Soc. Rev.* 41, 7403–7430. doi: 10.1039/c2cs35190k
- Neumann, R. (1998). Polyoxometalate complexes in organic oxidation chemistry. *Prog. Inorg. Chem.* 47, 317–370.
- Pope, M. T. (1983). *Heteropoly and Isopoly Oxometalates*. Heidelberg: Springer-Verlag Berlin.
- Pope, M., and Müller, T. A. (2001). *Polyoxometalate Chemistry: From Topology via Self-Assembly to Applications*. Dordrecht: Kluwer.
- Pope, M. T., and Müller, A. (1991). Polyoxometalate chemistry: an old field with new dimensions in several disciplines. *Angew. Chem. Int. Ed Engl.* 30, 34–48. doi: 10.1002/anie.199100341
- Ritorto, M. D., Anderson, T. M., Neiwert, W. A., and Hill, C. L. (2004). Decomposition of A-type sandwiches. Synthesis and characterization of new polyoxometalates incorporating multiple d-electron-centered units. *Inorg. Chem.* 43, 44–49. doi: 10.1021/ic035115t
- Sartorel, A., Bonchio, M., Campagna, S., and Scandola, F. (2013). Tetrametallic molecular catalysts for photochemical water oxidation. *Chem. Soc. Rev.* 42, 2262–2280. doi: 10.1039/C2CS35287G
- Sheldrick, G. M. (2008). A short history of SHELX. *Acta Crystallogr. Sect. A* 64, 112–122. doi: 10.1107/S0108767307043930
- Song, Y., and Tsunashima, R. (2012). Recent advances on polyoxometalate-based molecular and composite materials. *Chem. Soc. Rev.* 41, 7384–7402. doi: 10.1039/c2cs35143a
- Spek, A. L. (2009). Structure validation in chemical crystallography. *Acta Crystallogr. Sect. D Biol. Crystallogr.* 65, 148–155. doi: 10.1107/S090744490804362X
- Wang, J., Zhao, J., Zhao, H., Yang, B., He, H., and Yang, G. (2014). Syntheses, structures and properties of two multi-iron-samarium/multi-iron substituted germanotungstates. *Cryst. Eng. Comm.* 16, 252–259. doi: 10.1039/C3CE42023J
- Yamase, T., and Pope, M. T. (eds.). (2002). *Polyoxometalate Chemistry for Nanocomposite Design*. Dordrecht: Kluwer.
- Yamase, T., and Pope, M. T. (eds.). (2004). *Polyoxometalate Molecular Science*. Dordrecht: Kluwer.
- Yan, B. B., Xu, Y., Bu, X. H., Goh, N. K., Chia, L. S., and Stucky, G. D. (2001). Hydrothermal syntheses and structures of three one-dimensional heteropolytungstates formed by Dawson or Keggin cluster units. *J. Chem. Soc. Dalton Trans.* 2009–2014. doi: 10.1039/b103024h
- Yang, L., Zhao, J., Zhao, J., and Niu, J. (2012). Syntheses, crystal structures, and magnetic properties of the banana-shaped tungstophosphates: $[\text{M}_6(\text{H}_2\text{O})_2(\text{PW}_9\text{O}_{34})_2(\text{PW}_6\text{O}_{26})]^{17-}$ ($\text{M}^{\text{II}} = \text{Ni}^{\text{II}}, \text{Co}^{\text{II}}$). *J. Coord. Chem.* 65, 3363–3371. doi: 10.1080/00958972.2012.715344
- Zhao, J., Zheng, S., and Yang, G. (2008). 0-D and 1-D inorganic-organic composite polyoxotungstates constructed from in-situ generated monocopper(II)-substituted Keggin polyoxoanions and copper(II)-organoamine complexes. *J. Solid State Chem.* 181, 2205–2216. doi: 10.1016/j.jssc.2008.04.042
- Zheng, S. T., and Yang, G. (2012). Recent advances in paramagnetic-TM-substituted polyoxometalates (TM = Mn, Fe, Co, Ni, Cu). *Chem. Soc. Rev.* 41, 7623–7646. doi: 10.1039/c2cs35133a

Conflict of Interest Statement: The authors declare that the research was conducted in the absence of any commercial or financial relationships that could be construed as a potential conflict of interest.

Copyright © 2018 Duan, Clemente-Juan, Giménez-Saiz and Coronado. This is an open-access article distributed under the terms of the Creative Commons Attribution License (CC BY). The use, distribution or reproduction in other forums is permitted, provided the original author(s) and the copyright owner are credited and that the original publication in this journal is cited, in accordance with accepted academic practice. No use, distribution or reproduction is permitted which does not comply with these terms.



Strategic Isolation of a Polyoxocation Mimicking Vanadium(V) Oxide Layered-Structure by Stacking of $[\text{H}_2\text{V}_2\text{O}_8]^{4-}$ Anions Bridged by (1,4,7-Triazacyclononane)Co(III) Complexes

Sugiarto, Keisuke Kawamoto and Yoshihito Hayashi*

Department of Chemistry, Kanazawa University, Kanazawa, Japan

OPEN ACCESS

Edited by:

Debbie C. Crans,
Colorado State University,
United States

Reviewed by:

Fernando Novio,
Instituto Catalán de Nanociencia y
Nanotecnología (CIN2), Spain
Annette Rompel,
Universität Wien, Austria

*Correspondence:

Yoshihito Hayashi
hayashi@se.kanazawa-u.ac.jp

Specialty section:

This article was submitted to
Inorganic Chemistry,
a section of the journal
Frontiers in Chemistry

Received: 01 May 2018

Accepted: 03 August 2018

Published: 28 August 2018

Citation:

Sugiarto, Kawamoto K and Hayashi Y
(2018) Strategic Isolation of a
Polyoxocation Mimicking Vanadium(V)
Oxide Layered-Structure by Stacking
of $[\text{H}_2\text{V}_2\text{O}_8]^{4-}$ Anions Bridged by
(1,4,7-Triazacyclononane)Co(III)
Complexes. *Front. Chem.* 6:375.
doi: 10.3389/fchem.2018.00375

An isolation of a vanadium(V) oxide cluster mimicking V_2O_5 layered structure was achieved formulated as $[\{\text{Co}(\text{tacn})\}_4\text{V}_4\text{O}_{12}(\text{OH})_4]^{4+}$ (**1**) (tacn = 1,4,7-triazacyclononane). From the ^{51}V NMR spectra of the reaction mixtures, we optimized the reaction condition in terms of a molar ratio of VO_4^{3-} and $[\text{Co}(\text{tacn})(\text{H}_2\text{O})_3]^{3+}$ as well as a pH value. Cluster **1** is stable in a wide range of pH values from 1.5 to 8.0, and the presence of multiple hydrogen bondings in the structure is a unique feature. In the X-ray analysis of cluster **1**, the $\text{V}\cdots\text{V}$ distances are classified into two groups of relatively shorter distances (2.978(1) Å) and longer interactions (3.554(1) Å), and it is a good model of the substructure of V_2O_5 bulk material. As far as we know, this is a first example of an isolation of mixed-metal cluster including a unit of V_2O_5 structure by a stack of two layers of $[\text{H}_2\text{V}_2\text{O}_8]^{4-}$, although cubic V_4O_4 cubane-type clusters are well known. The solid sample of compound **1-Cl** and **1-Br** shows reversible thermochromic behavior accompanied by crystal to amorphous transformation upon hydration-dehydration process.

Keywords: cationic oxide cluster, protecting group, hydrogen bonding, **1**, **4**, **7**-triazacyclononane (= tacn), divanadate anion, Cobalt(III)

INTRODUCTION

Metal oxide clusters have attracted much attention because of their relevance to water splitting catalysts with their interesting properties such as redox, magnetism, and reactivity (Pope, 1983; Sessoli et al., 1993; Saha et al., 2011; Ye et al., 2018). To study structure-property relationships, a precise structural control of the oxide cluster is necessary, for example, to survey the interaction between substrates and active sites on metal oxide surfaces (Isobe and Yagasaki, 1993). As one of the important metal oxides, vanadium(V) oxides, V_2O_5 , has been attracted much attention in terms of oxidation catalysts and biological activities on the oxide surfaces (Al-Qatati et al., 2013). Various vanadium(V) oxide clusters such as polyoxovanadates as mimics of their oxide surfaces also have significance for a construction of better practical materials, because the screening of the model complexes based on the proposed mechanism are possible. To realize their oxide surface structures as model clusters, a synthetic chemistry of anionic oxide clusters of polyoxomolybdate, polyoxotungstate, or polyoxovanadate have been developed in the past decade. Some of the

attempts to control oxide cluster structures have been achieved using organometallic capping ligand to prevent the formation of infinitely condensed oxide precipitates and the capping ligands restrict an unlimited condensation and facilitate a formation of an oligometric oxide core (Hayashi et al., 1988; Do et al., 1991; Proust et al., 1993; Takara et al., 1997; Artero et al., 2000, 2001; Villanneau et al., 2003; Boujday et al., 2007).

Another approach to control the structure of oxide clusters is utilizing hydrogen bondings for the stabilization of a cluster unit. Hydrogen bonding interactions in inorganic metal complexes have been receiving attention because they have a potential to induce very interesting properties such as spin flipping (Matheu et al., 2015), proton coupled electron transfer (PCET) (Yikilmaz et al., 2002), low overpotential for essential redox catalysts (Matheu et al., 2017), and oxygen activation in bioinorganic chemistry (Shook and Borovik, 2008). Recently, the importance of intermolecular hydrogen bondings to enable multi-electron-multi-proton transfer in artificial Co_4O_4 cluster system was demonstrated for a water-splitting reaction (Olshansky et al., 2018).

Our focus is a development of a new synthetic method for metal oxide complexes by using inert coordination complexes as a protecting group for the termination of a polyoxoanion growth

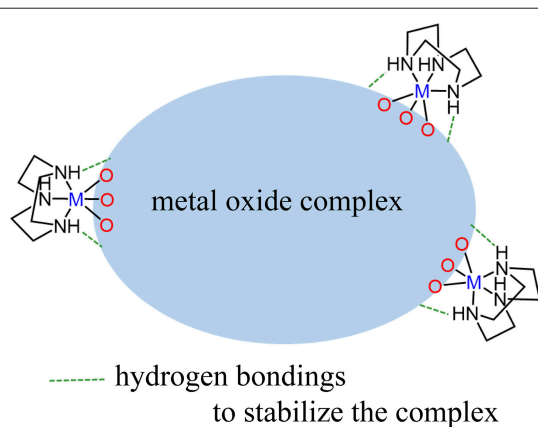
as well as gaining solubility in water (**Scheme 1**). Our strategy is using coordination chemistry of $\text{fac}\{-\text{Co}(\text{tacn})\}^{3+}$ ($\text{tacn} = 1,4,7\text{-triazacyclononane}$) (Chaudhuri and Wiegardt, 2011) to induce a following two-fold synergistic effect: (1) the inert $\text{fac}\{-\text{Co}(\text{tacn})\}^{3+}$ units have a role to terminate the cluster core by capping the ends of oxide units, and (2) NH groups on tacn ligands offer intramolecular hydrogen bondings to stabilize the cluster structures while attaining solubility in water.

Based on the strategy as shown in **Scheme 1**, we have studied successful stabilization of oxide clusters of molybdenum(VI), vanadium(V), and other various transition metal ions by using $\text{fac}\{-\text{Co}(\text{tacn})\}^{3+}$ capping units. Regarding to the molybdenum(VI) cluster chemistry protected by the capping unit, we have reported a neutral species of $[\{\text{Co}(\text{tacn})\}_2\text{Mo}_3\text{O}_{12}]$ and two cationic species of $[\{\text{Co}(\text{tacn})\}_4\text{H}_2\text{Mo}_7\text{O}_{27}]^{2+}$ and $[\{\text{Co}(\text{tacn})\}_4\text{H}_3\text{Mo}_4\text{O}_{17}]^{5+}$ (Sugiarto et al., 2018). All these clusters have a common structural building block of $[\{\text{Co}(\text{tacn})\}_2\text{Mo}_3\text{O}_{13}]$, and the structural similarity allows us to figure out the method to achieve the controlled structural transformations among them by adjusting the pH conditions for the syntheses. In this paper, we report a synthesis of a distorted cubane-like V_4O_4 oxide cluster capped by four $\text{fac}\{-\text{Co}(\text{tacn})\}^{3+}$ units, in the formula of $[\{\text{Co}(\text{tacn})\}_4\text{V}_4\text{O}_{12}(\text{OH})_4]^{4+}$ (**1**) (**Figure 1**). By the reaction of $\text{fac}\{-\text{Co}(\text{tacn})(\text{H}_2\text{O})_3\}^{3+}$ and vanadate anion in water, we demonstrated a rare example of the synthesis of cationic oxide cluster from vanadate anionic core (Šimuneková et al., 2013), although some neutral clusters bearing vanadium(V) oxide moiety have been previously reported using $4,4'\text{-}^t\text{Bu-bpy}$ as organic neutral capping groups (Kodama et al., 2016). Cluster **1** possesses intramolecular hydrogen bondings to stabilize the cluster core based on NH groups from tacn ligands. Multinuclear NMR measurements reveal cluster **1** is stable in a wide range of pH values. In addition, cluster **1** exhibits reversible thermochromic behavior accompanied by crystal to amorphous transformation upon hydration-dehydration process.

EXPERIMENTAL

Materials and Methods

Tacn and $[\text{Co}(\text{tacn})(\text{H}_2\text{O})_3](\text{CF}_3\text{SO}_3)_3 \cdot \text{H}_2\text{O}$ were prepared according to the reported procedures (Wiegardt et al., 1979;



SCHEME 1 | Schematic scheme to stabilize metal oxide complexes protected by tacn complexes with a hydrogen bonding wrapping.

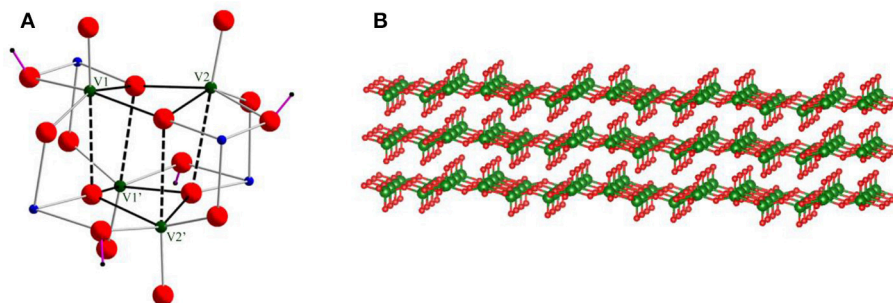


FIGURE 1 | (A) Skeletal structure of cationic cluster **1**. Green, blue, and red balls show vanadium, cobalt, and oxygen atoms, respectively. Purple lines are OH bonds. The tacn ligands on Co(III) centers are omitted for clarity. (B) V_2O_5 layered structure.

TABLE 1 | Crystallographic data for **1-Cl**, **1-Br**, and **1-ClO₄**.

	1-Cl	1-Br	1-ClO₄
Formula	C ₁₂ H ₃₂ Cl ₂ Co ₂ N ₆ O ₁₃ V ₂	C ₁₂ H ₃₂ Br ₂ Co ₂ N ₆ O ₁₃ V ₂	C ₁₂ H ₃₀ Cl ₂ Co ₂ N ₆ O ₁₈ V ₂
fw	759.07	848.00	837.06
Crystal system	Tetragonal	Tetragonal	Monoclinic
Space group	<i>P</i> 4 ₂ <i>c</i>	<i>P</i> 4 ₂ <i>c</i>	<i>P</i> 2 ₁ / <i>n</i> (#14)
<i>a</i> , Å	14.5508(4)	14.7055(3)	15.2827 (8)
<i>b</i> , Å	14.5508(4)	14.7055(3)	14.9893 (8)
<i>c</i> , Å	12.4185(4)	12.4952(3)	25.1980 (13)
α , deg	90	90	90
β , deg	90	90	106.744 (3)
γ , deg	90	90	90
<i>V</i> , Å ³	2629.32 (17)	2702.11 (13)	5527.5 (5)
<i>Z</i>	4	4	8
<i>R</i> ; <i>wR</i> ₂ (all data)	0.0278; 0.0725	0.0278; 0.0671	0.1074; 0.2904
<i>R</i> ₁	0.0258	0.0260	0.0951

Galsbøl et al., 1996). The other chemicals were purchased and used as received. NMR spectra were recorded using a JEOL Spectrometer (400 MHz). FT-IR spectra were recorded using Jasco FT/IR-4100 in KBr pellets. UV-Vis solution absorption and solid state reflectance spectra were recorded using a Hitachi U-3500 spectrometer. CHN elemental analysis was performed by the Research Institute for Instrumental Analysis at Kanazawa University. X-ray powder diffraction (XRD) pattern was recorded using D8 ADVANCE eco.

Syntheses

[Co₄V₄O₁₂(OH)₄(tacn)₄](CF₃SO₃)₄ (**1-OTf**). Na₃VO₄ (24.0 mg, 0.13 mmol) and [Co(tacn)(H₂O)₃](CF₃SO₃)₃·H₂O (80.0 mg, 0.11 mmol) were mixed in water (2.0 mL). The mixture was acidified by 0.22 M of triflic acid adjusted to pH 7.0. The crystals formed were harvested after 2 days. Yield: 30.5 mg (65% based on Co). Anal. Calcd., for [Co₄V₄O₁₂(OH)₄(C₆H₁₅N₃)₄](CF₃SO₃)₄·4H₂O: C, 17.84; H, 3.86; N, 8.92. Found: C, 17.76; H, 3.68; N, 8.95%. ¹H NMR (D₂O, δ): 4.06 (m, 4H), 3.48 (m, 4H), 3.26 (m, 4H), 3.00–2.65 (m, 24H), 2.52 (m, 4H), 2.40 (m, 4H), 2.26 (m, 4H) ppm. ⁵¹V NMR (D₂O, δ): –380 ppm. ⁵⁹Co NMR (D₂O, δ): 9550 ppm. UV-Vis λ_{MAX} / nm (ϵ / M^{–1} cm^{–1}) (H₂O): 529.5 (754), 401.0 (4086).

The bromide (**1-Br**), chloride (**1-Cl**), and perchlorate (**1-ClO₄**) salts were also obtained by adding four equivalents of potassium bromide, sodium chloride, and sodium perchlorate to the reaction mixture, respectively. From IR and NMR spectra of the products, the cluster integrity in the solution was confirmed (Figure S1).

X-Ray Crystallography

X-ray analyses of **1-ClO₄**, **1-Br**, and **1-Cl** were performed. The crystallographic parameters are shown in Table 1. All measurements were performed at 90K by using a Bruker D8 VENTURE diffractometer with graphite monochromated Cu-K α radiation (λ = 1.54178 Å). The data reduction and absorption

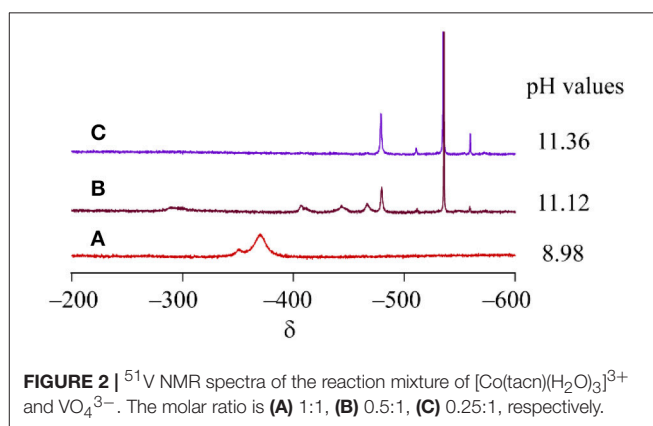


FIGURE 2 | ⁵¹V NMR spectra of the reaction mixture of [Co(tacn)(H₂O)₃]³⁺ and VO₄^{3–}. The molar ratio is (A) 1:1, (B) 0.5:1, (C) 0.25:1, respectively.

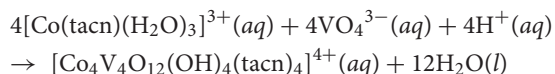
correction were performed on APEX3 program (Bruker, 2016). The structural analyses were performed on APEX3 and shelxle software (Hübschle et al., 2011). The structures were solved by SHELXT (Sheldrick, 2015b), and the refinements were performed using SHELXL-2014 program (Sheldrick, 2015a). In the refinement of **1-ClO₄**, the twin law (–1 0 0 0–1 0 1 0 1) was used to reduce *R*₁ value from 11.15 to 9.51. CCDC reference numbers 1835286–1835288.

RESULTS AND DISCUSSION

Synthesis

Cluster **1** was synthesized by the reaction of VO₄^{3–} and [Co(tacn)(H₂O)₃]³⁺ in water with a 1:1 molar ratio. To monitor the formation of cluster **1**, ⁵¹V NMR spectra of the reaction mixtures were measured at different molar ratios of the starting materials. When 0.25 or 0.50 equivalence of [Co(tacn)(H₂O)₃]³⁺ to VO₄^{3–} was added to the reaction mixture, a signal for cluster **1** was not found and only a strong peak from VO₄^{3–} at –535 ppm was observed, but there are unidentified peaks that was presumed to be an intermediate species (Figure 2). After adding

1.00 equivalence of $[\text{Co}(\text{tacn})(\text{H}_2\text{O})_3]^{3+}$ to VO_4^{3-} , the strong peak from cluster **1** at -370 ppm was observed and the peak from the starting material was disappeared (**Figure 2**). Reaction of $[\text{Co}(\text{tacn})(\text{H}_2\text{O})_3]^{3+}$ and VO_4^{3-} with a 1.5:1 molar ratio leads to a rapid crystallization of cluster **1**. This observation suggests that formation of cluster **1** is kinetically favored. The variation of the molar ratio of the starting material also affected the pH value of the solution. Formation of cationic cluster **1** can be expressed as:



From the above equation, the addition of acids is necessary. In fact, we optimized the best synthetic condition for the synthesis of cluster **1** with 1:1 molar ratio at pH 7 by addition of trifluoromethanesulfonic acid.

Structure Description

The chloride salt of **1** crystallizes in a tetragonal crystal system. The crystallographic parameters are shown in **Table 1**. The structural feature of **1-Cl** is similar to that of **1-Br** and **1-ClO₄**. Therefore, we describe the structural features of V_4O_4 unit based on the structure of **1-Cl** in this section.

Figure 1A shows the skeletal structure of cationic cluster **1**. Cluster **1** is composed of a $\text{V}_4\text{O}_{12}(\text{OH})_4^{8-}$ core capped by four $\{\text{Co}(\text{tacn})\}^{3+}$ complexes. Bond valence sum calculations indicated that the four cobalt and vanadium centers are assigned to III and V oxidation states, respectively. It also reveals protonations on four doubly bridged oxygen ligands between Co(III) and V(V) centers, i.e. the ligands are hydroxyl groups. The hydroxyl bridging ligands play an important role to construct intramolecular hydrogen bonding interactions. Four Co(III) centers are six-coordination-mode, and the bond distance of Co(III) and N donors of tacn ligands is in a range from 1.932(3) Å to 1.953(3) Å and it is consistent to the previous reported values (Berseth et al., 2000). For the geometry of V(V) centers, if the weak interactions at the trans-position of $\text{V}=\text{O}$ [2.564(3) Å] are ignored, four V(V) centers can be regarded as a five-coordination-mode with one terminal oxygen ligand ($\text{V}=\text{O}$) and four bridged ligands. Thus, the geometry around V(V) centers can be regarded as a distorted square pyramid and it is also indicated by its geometry index τ of 0.06 (τ is defined as $(\alpha - \beta)/60^\circ$, where α = the largest angle and β = the second largest angle. ($\tau = 0.0$ for an ideal square pyramidal. $\tau = 1.0$ for an ideal trigonal bipyramidal.)) (Addison et al., 1984).

Although the tetranuclear $\text{V}_4\text{O}_{12}(\text{OH})_4^{8-}$ unit has a cubane-like arrangement, the long distances between $[\text{H}_2\text{V}_2\text{O}_8]^{4-}$ units suggest that the structure is better described as a stack of two $[\text{H}_2\text{V}_2\text{O}_8]^{4-}$ dimers. The $\text{V} \cdots \text{V}$ distances are classified into two groups of relatively shorter distances (2.978(1) Å) and longer interactions (3.554(1) Å). From the layered structure, we postulated that the structure of cluster **1** can be regarded as a model species which represents a unit of the layered structure of V_2O_5 (**Figure 1B**). Although a cubane type structure of V_4O_4 has been previously reported in literature, our structure is quite different from the previous reported cases. In one

of the precedented cases, the cubane type cluster was capped by phosphate bridging ligands (Shi et al., 2004). Although the phosphate ligand bridges the V centers in tetrahedral coordination mode, the Co(III) centers on Co(tacn) moieties have octahedral one. As a result, the cluster core geometry protected by the phosphate ligand is totally different to that of **1-Cl**. Dey et al. also described the phosphate ligand coordinated V_4O_4 structure linked by two copper(II) 1,10-phenanthroline complexes (Dey et al., 2012). This V_4O_4 structure is similar to that of **1-Cl**, but the cubane structure is more tightly packed and the intra-layer distance is much more shorter ca. 3.4 Å (**Table 2**). Our $[\text{H}_2\text{V}_2\text{O}_8]^{4-}$ layered structure is representing the V_2O_5 stacked structure by the influence of a bridging metalloligand of $\{\text{Co}(\text{tacn})\}^{3+}$ which enable to keep the layered structure in the cluster by forming hydrogen bondings from NH groups.

There are two types intramolecular hydrogen bonding interactions. One is between NH group and terminal oxygen ligand with a donor-acceptor distance of 3.431(5) Å, another is an interaction between NH group and bridged hydroxo ligand as a donor-acceptor distance of 2.878(5) Å (**Figure 3**). All hydrogen bonding interactions are orienting to form the structure of a windmill-shaped geometry with S_4 symmetry. In crystal packing, counter chloride anions are stabilized by hydrogen bondings with NH groups as well as three crystallization water molecular chains. Regarding to their crystallization water molecules, one water molecule directly interacts with the hydroxido ligands bridged between vanadium(V) and cobalt(III). The packing water molecule allows the linkage between the cluster units by hydrogen bondings at hydroxido group on the cluster. In addition, the water molecule interacted to the hydroxido bridging ligand also binds counter chloride anion via hydrogen bonding. Finally, another water molecule bridges between the counter chloride anion and terminal oxygen ligand on vanadium(V). This crystal packing implies that the alternation of the hydrogen bonding patterns with the crystallization water molecules may relate to the thermochromic behavior. In fact, the desorption of water molecules from the crystal leads to manifest an interesting thermochromism behavior (vide infra).

TABLE 2 | Distances (Å) between vanadium centers. The serial numbers of vanadium centers are shown in **Figure 1**.

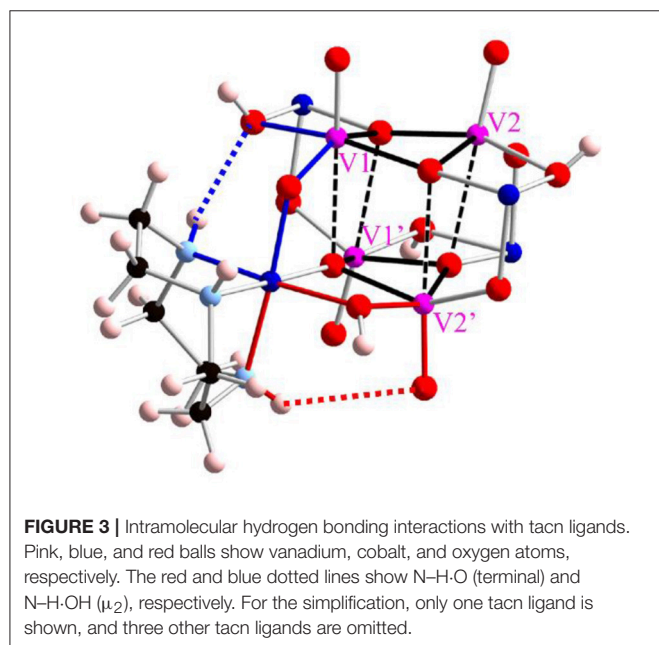
	V1–V2	V1 ... V1' (V2 ... V2')
1-Cl	2.978 (1)	3.554 (1)
1-Br	2.992 (2)	3.563 (2)
1-ClO ₄	2.998 (2)	3.442 (2)
	2.994(2)	3.431 (2)
		3.427 (2)
		3.425 (2)
Dey et al., 2012	2.7618 (9)	3.311 (1)
Shi et al., 2004	2.762 (1)	3.302 (1)
	2.816 (1)	3.332 (1)
		3.354 (2)
		3.362 (2)

NMR Spectroscopy

Cluster **1** has four Co(III) and four V(V) centers which are diamagnetic transition metal ions. Therefore, the synthetic procedure of cluster **1** was optimized by monitoring NMR spectra (described in above), and the stability of cluster **1** was also evaluated using NMR technique. **Figure 4** shows ^{51}V and ^{59}Co NMR spectra of cluster **1** at pH = 6.5. In the measurements of ^{51}V and ^{59}Co nuclei, only one signal in each spectrum was observed at -380 ppm and $9,650$ ppm, respectively, implying that the structure of cluster **1** as described in the above section is maintained even in solution, because the chemical environments of each metal atom is equivalent. In addition, the NMR signals of cluster **1** suggest the structural integrity is maintained in the pH range from pH = 1.5 to pH = 9 (**Figure S2**).

The tacn ligand is a good indicator to monitor the symmetry of the cluster in solution because ^1H NMR signals on tacn give stereo-specific signals according to the symmetry of the structure. Concerning the methylene proton signals in ^1H NMR spectrum in D_2O , six well-separated signals were observed at 4.06, 3.48, 3.26, 2.52, 2.40, and 2.26 ppm, whereas the rest of signals corresponding to six protons are overlapped between 3.00 and 2.65 ppm. The signal intensities are 1:1:1:1:1:6. Thus, all twelve protons of a tacn moiety were observed independently, indicating that the capping of $\{\text{Co}(\text{tacn})\}^{3+}$ to $\text{V}_4\text{O}_{12}(\text{OH})_4^{8-}$ core are maintained even in solution.

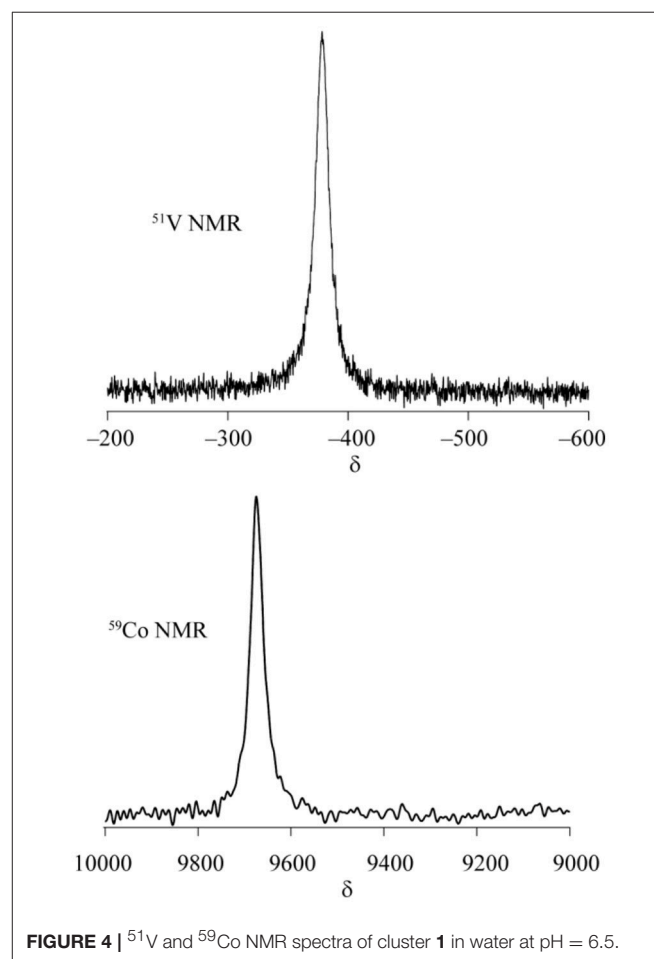
The important feature to bind the layered structure is the formation of hydrogen bondings. Two NH protons on tacn ligand are loosely linked to terminal oxygen ligand or crystallization water molecule by hydrogen bonding, whereas another NH proton is strongly interacted with hydroxo bridging ligand. As a consequence, the observation of hydrogen-deuterium (H/D) exchange reactions allows us to investigate difference of the strength of the hydrogen bondings. The ^1H

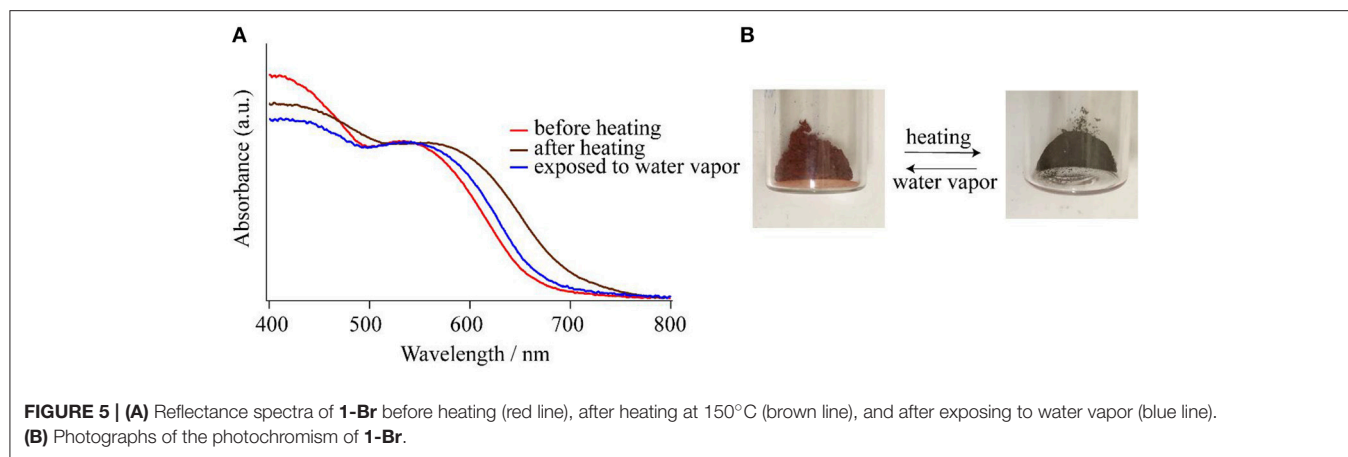


NMR signals from OH and NH protons show an important information due to its H/D exchange reactions. To obtain H/D exchange reaction profile, ^1H NMR spectrum of cluster **1** was measured in $\text{DMSO}-d_6$ as an aprotic solvent (**Figure S3**). There are four kinds of hydrogen bondings: three types of NH protons (7.29, 6.15, 5.69 ppm) arose from independent tacn environment and the fourth type of proton from OH protons (3.69 ppm). After adding D_2O to the $\text{DMSO}-d_6$ solution of cluster **1**, the intensities of the signals for NH and OH at 7.29 and 6.15 ppm are rapidly decreased while the signal at 5.69 ppm is slowly decreased (**Figure S4**). It is noteworthy that the observation suggests the inner core hydrogen bondings are slower to exchange and they are utilized to firmly support the cluster frameworks.

Chromism Behavior

As shown in the section of *Structure description*, the counter anions of Cl^- and Br^- in **1-Cl** and **1-Br** are interacted through hydrogen bonding networks with NH groups and crystallization water molecules, respectively. The crystal packings of **1-Cl** and **1-Br** are identical, because they are isomorphous (**Table 1**). Therefore, it is expected that these species should show similar behaviors in crystalline phases. In fact, compounds **1-Cl** and **1-Br** show similar thermochromic behaviors by heating at 150°C . In



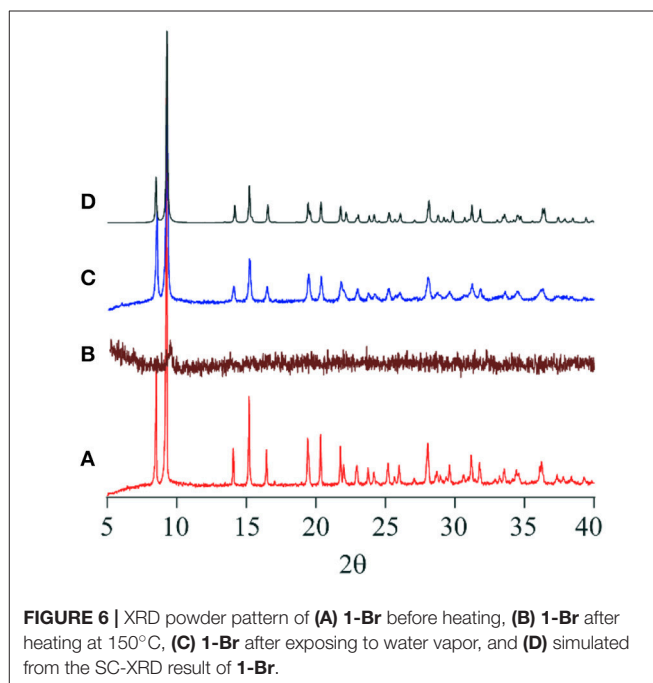


this section, the thermochromic behavior of **1-Br** is described. Compound **1-Br** shows red color, and the solid state reflectance spectrum exhibits an absorption around 550 nm assigned to Co(III) d-d transition, and the feature is identical to solution state absorption spectrum. After heating **1-Br**, the color shift was observed from red to greenish brown with bathochromic shift of the reflectance spectra (**Figure 5**). Exposure of the greenish brown powder to water vapor retrieves the red **1-Br** salt. It is noteworthy that the color changings by heating and exposing water vapor occur repeatedly with phase transitions between crystal and amorphous state. Powder X-ray diffraction (PXRD) pattern of **1-Br** is identical to the simulated result from the single-crystal X-ray analysis (**Figure 6**). After changing the color from red to greenish brown by heating, the crystallinity of the sample was lost, resulting the loss of Bragg peaks in PXRD (**Figure 6**). The peaks of **1-Br** were appeared again when the amorphous sample was exposed to water vapor (**Figure 6**). These reversible thermochromism is an interesting feature of these clusters and we suggest the presence of hydrogen bondings in the cluster unit is reflected to the reversible change on the alternation of the coordination environment of Co(III) centers.

Interestingly, no thermochromic behavior was observed in the case of **1-OTf**. Although a single crystal X-ray analysis of **1-OTf** was not successful, the crystal system is expected to be different from **1-Cl** and **1-Br** because of the difference of the anion shape. Thus, the absence of the behavior is due to the different hydrogen bonding interactions among the cluster, the counter anions, and the crystallization water molecules in **1-OTf**. We did not examine the property in the case of **1-CIO₄**, due to the risk of the explosion for perchlorate sample without crystallization water molecules.

CONCLUSIONS

A V_4O_4 oxide cluster in the formula of $[Co(tacn)_4V_4O_{12}(OH)_4]^{4+}$ (**1**) was synthesized utilizing the following synergetic effects: (1) termination of vanadium(V) oxide cluster by Co(tacn) protecting groups, and (2) hydrogen bonding interactions from NH groups on tacn ligands. The V_4O_4 core can be regarded as a stacking of $[H_2V_2O_8]^{4-}$ cluster units, mimicking a substructure of V_2O_5 oxide. The stacking



geometry of cluster **1** is maintained by Co(tacn) termination as well as hydrogen bondings within the cluster units.

Our strategy of a termination of polyoxo-anions by coordination complexes enhances the possibility to isolate a substructure of metal oxido species and take a snapshot of interesting intermediate species in aqueous solution. This study opens the new way to isolate versatile mixed-metal clusters that have an intermediate structure with water solubility by the utilization of hydrogen bonding stabilization and termination by the capping groups. The synthetic strategy defines here is applicable to a wide range of mixed-metal clusters because there are unlimited combination of potential capping groups and oxide cluster cores. Unique feature of this study is that by adding the cationic protecting group, anionic polyoxometalates come to gain exceeding

positive charges from the cationic complexes, and the change from polyoxoanions to polyoxocations allows to study a reactivity change from the well-established catalytic ability of polyoxoanions. The further reactivity study for these clusters is in progress.

AUTHOR CONTRIBUTIONS

The initial manuscript draft and figures were prepared by S for his PhD research and revised by KK and YH. All the authors had final approval of the submitted version of the paper.

REFERENCES

- Addison, A. W., Rao, T. N., Reedijk, J., van Rijn, J., and Verschoor, G. C. (1984). Synthesis, structure, and spectroscopic properties of copper(II) compounds containing nitrogen-sulphur donor ligands; the crystal and molecular structure of aqua[1,7-bis(N-methylbenzimidazol-2'-yl)-2,6-dithiaheptane]copper(II) perchlorate. *J. Chem. Soc. Dalton Trans.* 1349–1356. doi: 10.1039/DT9840001349
- Al-Qatati, A., Fontes, F. L., Barisais, B. G., Zhang, D., Roess, D. A., and Crans, D. C. (2013). Raft localization of Type I Fcε receptor and degranulation of RBL-2H3 cells exposed to decavanadate, a structural model for V₂O₅. *Dalton Trans.* 42, 11912. doi: 10.1039/c3dt50398d
- Artero, V., Proust, A., Herson, P., and Gouzerh, P. (2001). Interplay of Cubic Building Blocks in (η⁶-arene)Ruthenium-Containing Tungsten and Molybdenum Oxides. *Chem. Eur. J.* 7, 3901–3910. doi: 10.1002/1521-3765(20010917)7:18<3901::AID-CHEM3901>3.0.CO;2-3
- Artero, V., Proust, A., Herson, P., Thouvenot, R., and Gouzerh, P. (2000). (η⁶-Arene)ruthenium oxomolybdenum and oxotungsten clusters. Stereochemical non-rigidity of [{Ru(η⁶-p-MeC₆H₄Pr^t)₄MoO₁₆] and crystal structure of [{Ru(η⁶-p-MeC₆H₄Pr^t)₄W₂O₁₀}. *Chem. Commun.* 18, 883–884. doi: 10.1039/b000782j
- Berseth, P. A., Sokol, J. J., Shores, M. P., Heinrich, J. L., and Long, J. R. (2000). High-nuclearity metal-cyanide clusters: assembly of a Cr₈Ni₆(CN)₂₄ cage with a face-centered cubic geometry. *J. Am. Chem. Soc.* 122, 9655–9662. doi: 10.1021/ja001991j
- Boujday, S., Blanchard, J., Villanneau, R., Krafft, J.-M., Geantet, C., Louis, C., et al. (2007). Polyoxomolybdate-Stabilized Ru⁰ nanoparticles deposited on mesoporous silica as catalysts for aromatic hydrogenation. *ChemPhysChem* 8, 2636–2642. doi: 10.1002/cphc.200700533
- Brucker (2016). APEX3. APEX3; SAINT; Bruker AXS Inc. Madison, WI.
- Chaudhuri, P., and Wieghardt, K. (2011). “The chemistry of 1,4,7-triazacyclononane and related tridentate macrocyclic compounds,” in *Progress in Inorganic Chemistry*, ed K. D. Karlin Hoboken (New York, NY: John Wiley & Sons, Inc), 329–436.
- Dey, C., Das, R., Poddar, P., and Banerjee, R. (2012). Solid phase morphological diversity of a rare vanadium cubane (V₄O₁₆) based metal organic framework. *Cryst. Growth Des.* 12, 12–17. doi: 10.1021/cg201030u
- Do, Y., You, X. Z., Zhang, C., Ozawa, Y., and Isobe, K. (1991). Trishomocubane-type methoxide cluster as a novel mediator in the extension of cube size in organometallic oxide clusters: synthesis and structures of [(RhCp*)₂Mo₃O₉(OMe)₄]-MeOH and a linear quadruple cubane-type cluster [(RhCp*)₄Mo₆O₂₂]-4CH₂Cl₂. *J. Am. Chem. Soc.* 113, 5892–5893. doi: 10.1021/ja00015a070
- Galsbøl, F., Petersen, C. H., and Simonsen, K. (1996). Preparation and characterization of *fac*-[Rh(tacn)Cl₃], *fac*-[Rh(tacn)(H₂O)₃](CF₃SO₃)₃, [Rh(tacn)₂]Br₃·2.8H₂O and *fac*-[Co(tacn)(H₂O)₃](CF₃SO₃)₃·H₂O. The acid dissociation constants of *fac*-[M(tacn)(H₂O)₃]³⁺ (M = Cr^{III}, Co^{III}, Rh^{III} and Ir^{III}; tacn = 1,4,7-triazacyclononane). *Acta Chem. Scand.* 50, 567–570. doi: 10.3891/acta.chem.scand.50-0567
- Hayashi, Y., Toriumi, K., and Isobe, K. (1988). Novel triple-cubane type organometallic oxide clusters: [MCp*MoO₄]₄·nH₂O (M = Rh and Ir; Cp* = C₅Me₅; n = 2 for Rh and 0 for Ir). *J. Am. Chem. Soc.* 110, 3666–3668. doi: 10.1021/ja00219a056
- Hübschle, C. B., Sheldrick, G. M., and Dittrich, B. (2011). ShelXle: A Qt graphical user interface for SHELXL. *J. Appl. Crystallogr.* 44, 1281–1284. doi: 10.1107/S0021889811043202
- Isobe, K., and Yagasaki, A. (1993). Cubane-type clusters as potential models for inorganic solid surfaces. *Acc. Chem. Res.* 26, 524–529. doi: 10.1021/ar00034a002
- Kodama, S., Taya, N., Inoue, Y., and Ishii, Y. (2016). Synthesis and Interconversion of V₄, V₇, and V₈ Oxide Clusters: Unexpected Formation of Neutral Heptanuclear Oxido(alkoxido)vanadium(V) Clusters [V₇O₁₇(OR)(4,4'-t-Bu₂p₂)₃] (R = Et, MeOC₂H₄). *Inorg. Chem.* 55, 6712–6718. doi: 10.1021/acs.inorgchem.6b00963
- Matheu, R., Ertem, M. Z., Benet-Buchholz, J., Coronado, E., Batista, V. S., Sala, X., et al. (2015). Intramolecular proton transfer boosts water oxidation catalyzed by a Ru Complex. *J. Am. Chem. Soc.* 137, 10786–10795. doi: 10.1021/jacs.5b06541
- Matheu, R., Ertem, M. Z., Gimbert-Suriñach, C., Benet-Buchholz, J., Sala, X., and Llobet, A. (2017). Hydrogen bonding rescues overpotential in seven-coordinated Ru water oxidation catalysts. *ACS Catal.* 7, 6525–6532. doi: 10.1021/acscatal.7b01860
- Olshansky, L., Huerta-Lavorie, R., Nguyen, A. I., Vallapurackal, J., Furst, A., Tilley, T. D., et al. (2018). Artificial metalloproteins containing Co₄O₄ cubane active sites. *J. Am. Chem. Soc.* 140, 2739–2742. doi: 10.1021/jacs.7b13052
- Pope, M. T. (1983). *Heteropoly and Isopoly Oxometalates*. Heidelberg: Springer-Verlag Berlin.
- Proust, A., Gouzerh, P., and Robert, F. (1993). Organometallic Oxides: lacunary lindqvist-type polyanion-supported cyclopentadienylrhodium complex fragments. *Angew. Chem. Int. Ed. Engl.* 32, 115–116. doi: 10.1002/anie.199301151
- Saha, A., Thompson, M., Abboud, K. A., Wernsdorfer, W., and Christou, G. (2011). Family of double-cubane Mn₄Ln₂ (Ln = Gd, Tb, Dy, Ho) and Mn₄Y₂ complexes: a new Mn₄Tb₂ single-molecule magnet. *Inorg. Chem.* 50, 10476–10485. doi: 10.1021/ic201683p
- Sessoli, R., Gatteschi, D., Caneschi, A., and Novak, M. A. (1993). Magnetic bistability in a metal-ion cluster. *Nature* 365, 141–143. doi: 10.1038/365141a0
- Sheldrick, G. M. (2015a). Crystal structure refinement with SHELXL. *Acta Cryst.* C71, 3–8. doi: 10.1107/S2053229614024218
- Sheldrick, G. M. (2015b). SHELXT - Integrated space-group and crystal-structure determination. *Acta Cryst.* A71, 3–8. doi: 10.1107/S2053273314026370
- Shi, F.-N., Paz, F. A. A., Rocha, J., Klinowski, J., and Trindade, T. (2004). Novel phosphovanadate layered structure assembled from a tetrametallic cubane-like V^V Cluster. *Eur. J. Inorg. Chem.* 3031–3037. doi: 10.1002/ajic.200400249
- Shook, R. L., and Borovik, A. S. (2008). The effects of hydrogen bonds on metal-mediated O₂ activation and related processes. *Chem. Commun.* 6095. doi: 10.1039/b810957e
- Šimuneková, M., Prodius, D., Mereacre, V., Schwendt, P., Turta, C., Bettinelli, M., et al. (2013). Tetradecanuclear lanthanide-vanadium “nanochocolates”: catalytically-active cationic heteropolyoxovanadium clusters. *RSC Adv.* 3, 6299–6304. doi: 10.1039/c3ra40385h

ACKNOWLEDGMENTS

KK would like to thank grants from TEPCO Memorial Foundation. Ms. Taeko Kanamori is acknowledged for her contribution in the initial synthesis of the title complex.

SUPPLEMENTARY MATERIAL

The Supplementary Material for this article can be found online at: <https://www.frontiersin.org/articles/10.3389/fchem.2018.00375/full#supplementary-material>

- Sugiarto, Tagami, T., Kawamoto, K., and Hayashi, Y. (2018). Synthesis of cationic molybdenum-cobalt heterometallic clusters protected against hydrolysis by macrocyclic triazacyclononane complexes. *Dalton Trans.* 47, 9657–9664. doi: 10.1039/c8dt01226a
- Takara, S., Nishioka, T., Kinoshita, I., and Isobe, K. (1997). A novel organometallic oxide cluster with multi-valley sites: synthesis and structure of $[\text{NBu}_4]_2[\{(\eta^5\text{-C}_5\text{Me}_5)\text{Rh}\}_2\text{Mo}_6\text{O}_{20}(\text{OMe})_2]$ and its framework transformations. *Chem. Commun.* 20, 891–892. doi: 10.1039/a701618b
- Villanneau, R., Artero, V., Laurencin, D., Herson, P., Proust, A., and Gouzerh, P. (2003). Organometallic polyoxometalates: synthesis and structural analysis of $(\eta^6\text{-arene})$ ruthenium-containing polyoxomolybdates. *J. Mol. Struct.* 656, 67–77. doi: 10.1016/S0022-2860(03)00356-9
- Wiegardt, K., Schmidt, W., Nuber, B., and Weiss, J. (1979). Neue μ -Hydroxo-Übergangsmetallkomplexe, I. Darstellung und Struktur destrans-Diaqua-di- μ -hydroxo-bis[(1,4,7-triazacyclononan)cobalt(III)]-Kations; Kinetik und Mechanismus seiner Bildung. *Chem. Ber.* 112, 2220–2230. doi: 10.1002/cber.19791120629
- Ye, S., Ding, C., Chen, R., Fan, F., Fu, P., Yin, H., et al. (2018). Mimicking the key functions of photosystem II in artificial photosynthesis for photoelectrocatalytic water splitting. *J. Am. Chem. Soc.* 140, 3250–3256. doi: 10.1021/jacs.7b10662
- Yikilmaz, E., Xie, J., Brunold, T. C., and Miller, A. F. (2002). Hydrogen-bond-mediated tuning of the redox potential of the non-heme Fe site of superoxide dismutase. *J. Am. Chem. Soc.* 124, 3482–3483. doi: 10.1021/ja011220v

Conflict of Interest Statement: The authors declare that the research was conducted in the absence of any commercial or financial relationships that could be construed as a potential conflict of interest.

Copyright © 2018 Sugiarto, Kawamoto and Hayashi. This is an open-access article distributed under the terms of the Creative Commons Attribution License (CC BY). The use, distribution or reproduction in other forums is permitted, provided the original author(s) and the copyright owner(s) are credited and that the original publication in this journal is cited, in accordance with accepted academic practice. No use, distribution or reproduction is permitted which does not comply with these terms.



A Versatile Polyoxovanadate in Diverse Cation Matrices: A Supramolecular Perspective

Srinivasa Rao Amanchi and Samar K. Das*

School of Chemistry, University of Hyderabad, Central University, Hyderabad, India

OPEN ACCESS

Edited by:

Debbie C. Crans,
Colorado State University,
United States

Reviewed by:

Akira Odani,
Kanazawa University, Japan
Tilo Söhnle,
University of Auckland, New Zealand
Enrique González-Vergara,
Benemérita Universidad Autónoma de
Puebla, Mexico

*Correspondence:

Samar K. Das
skdas@uohyd.ac.in

Specialty section:

This article was submitted to
Inorganic Chemistry,
a section of the journal
Frontiers in Chemistry

Received: 30 April 2018

Accepted: 18 September 2018

Published: 16 October 2018

Citation:

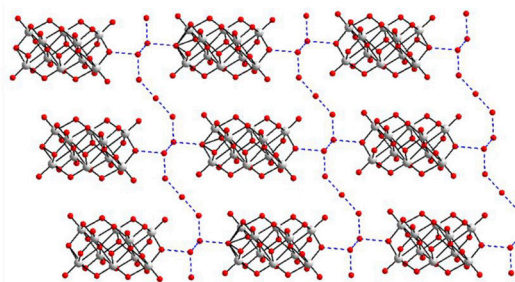
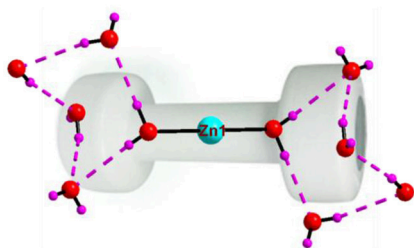
Amanchi SR and Das SK (2018) A
Versatile Polyoxovanadate in Diverse
Cation Matrices: A Supramolecular
Perspective. *Front. Chem.* 6:469.
doi: 10.3389/fchem.2018.00469

A series of decavanadate based compounds, formulated as $[\text{Co}(\text{H}_2\text{O})_6][\{\text{Na}_4(\text{H}_2\text{O})_{14}\}\{\text{V}_{10}\text{O}_{28}\}]\cdot 4\text{H}_2\text{O}$ (**1**), $[\text{Zn}(\text{H}_2\text{O})_6][\text{Na}_3(\text{H}_2\text{O})_{14}][\text{HV}_{10}\text{O}_{28}]\cdot 4\text{H}_2\text{O}$ (**2**), $[\text{HMTAH}]_2[\{\text{Zn}(\text{H}_2\text{O})_4\}_2\{\text{V}_{10}\text{O}_{28}\}]\cdot 2\text{H}_2\text{O}$ (**3**), $[\{\text{Co}(3\text{-amp})(\text{H}_2\text{O})_5\}]_2[3\text{-ampH}]_2[\text{V}_{10}\text{O}_{28}]\cdot 6\text{H}_2\text{O}$ (**4**), $[4\text{-ampH}]_{10}[\{\text{Na}(\text{H}_2\text{O})_6\}][\text{HV}_{10}\text{O}_{28}][\text{V}_{10}\text{O}_{28}]\cdot 15\text{H}_2\text{O}$ (**5**), $[\{4\text{-ampH}\}]_6[\{\text{Co}(\text{H}_2\text{O})_6\}]_3[\text{V}_{10}\text{O}_{28}]_2\cdot 14\text{H}_2\text{O}$ (**6**), and $[\{4\text{-ampH}\}]_{10}[\text{Zn}(\text{H}_2\text{O})_6][\text{V}_{10}\text{O}_{28}]_2\cdot 10\text{H}_2\text{O}$ (**7**), have been synthesized (where HMTAH = mono-protonated hexamethylenetetramine, 3-ampH = protonated 3-amino pyridine and 4-ampH = protonated 4-aminopyridine) from the relevant aqueous sodium-vanadate solution, by varying the pH of the solution and amino pyridine/hexamine derivatives as well as transition metal salts (Co(II)- and Zn(II)-salts). In this series of compounds **1–7**, the polyoxovanadate (POV) cluster $[\text{V}_{10}\text{O}_{28}]^{6-}$ is the common cluster anion, stabilized by diverse cations. The diverse supramolecular patterns around the decavanadate cluster anion in different cationic matrices have been described to understand the microenvironment in the decavanadate-based minerals. All of these compounds have solvent water molecules in their respective crystal lattices. Since water can interact directly with cations and anions, providing an additional stability and structural diversity, we have analyzed supramolecular water structures in all these compounds to comprehend the role of the lattice water in the formation of natural decavanadate containing minerals. Compounds **1–7**, that are isolated at an ambient condition from aqueous solution, are characterized by routine spectral analysis, elemental analyses and finally unambiguously by single crystal X-ray crystallography.

Keywords: decavanadate cluster anion, diverse cations, crystal structures, supramolecular chemistry, decavanadate mineralogy

INTRODUCTION

The modern chemical research on polyoxometalates (POMs)-based solid state materials fascinates synthetic chemists because of their potential applications in diverse research areas, such as, catalysis (Vazlyev et al., 2005; Hill, 2007; Zhou et al., 2014; Lechner et al., 2016; Mukhopadhyay et al., 2018), medicinal chemistry (Pope and Müller, 1991; Liu et al., 2012; Xie et al., 2018), and materials science (Guo et al., 2000; Rao et al., 2011; Kulikov and Meyer, 2013; Omwoma et al., 2015; Walsh et al., 2016). Among these, the area of polyoxovanadate (henceforth, POV) based materials have received special attention due to not only their diverse topologies (Miiller et al., 1990; Klemperer et al., 1992; Chen et al., 2005), structural (Miiller et al., 1987; Koene et al., 1999) and electronic properties (Müller et al., 1997) but also their fascinating versatile industrial applications, e.g., catalysis (Gao and Hua, 2006) and materials applications (Khan et al., 2003; Arumuganathan and Das, 2009; Chen et al., 2018). Among POVs, decavanadate cluster anion $[\text{V}_{10}\text{O}_{28}]^{6-}$ is a versatile POM cluster



GRAPHICAL ABSTRACT | Decavanadate cluster $[V_{10}O_{28}]^{6-}$ is the common anion to synthesize the materials **1–7**, ranging from discrete compounds to coordination polymers. Water clusters, such as, cyclic pentamers are established in some of the crystal structures due to water-water hydrogen bonding (O–H...O) interactions. There are analogies between these synthesized compounds and decavanadate based minerals in terms of the microenvironment around the isopolyanion.

anion, which is constructed by ten edge-shared VO_6 octahedra with D_{2h} symmetry (**Figure 1**). Eight terminals-, fourteen doubly bridged (μ^2)-, four triply bridged (μ^3)- and two hexa bridged (μ^6)-oxygen atoms exist within this $[V_{10}O_{28}]^{6-}$ cluster anion. Numerous decavanadate based compounds are known in literature (Crans et al., 2017; Naslhajian et al., 2017; Yerra and Das, 2017) where the decavanadate cluster anion has been isolated using diverse cations including transition metal- and alkali metal-coordination complex cations; relevant supramolecular chemistry has also been described in the context of POV based materials chemistry (Sánchez-Lombardo et al., 2014; Wang et al., 2016). Choosing a particular cation plays a vital role in tuning the property of the resulting decavanadate cluster containing ion pair compound (Chatkon et al., 2013). The biological role of decavanadate cluster is enormous (Rehder, 2013; Winkler et al., 2017). Aureliano and co-workers described, in a perspective, the biological interactions of decavanadate with ion pump Ca^{2+} -ATPase and compared the mode of action with those of already established ion-pump inhibitors of therapeutic importance (Aureliano et al., 2013). In addition to ion pumps, lipid structures also have been shown to represent biological targets for decavanadate (Aureliano and Crans, 2009). Crans and co-workers reported that rabbit skeletal muscle phosphorylase can be inhibited by decavanadate (Crans et al., 2004). They examined the interactions of decavanadate in an inorganic model system as well as in cells and determined the biological effects of decavanadate on rat basophilic leukemia (RBL-2H3) plasma membrane functions (Al-Qatati et al., 2013). In a recent report, de Carvalho and co-workers have demonstrated that decavanadate can interact with G-actin (multifunctional proteins), activating a protein conformational change and thereby that induces oxidation of the cysteine core residues (Marques et al., 2017). Even though, a good number of reports of the decavanadate cluster anion on diverse aspects of its biological significance is available including its catalytic applications (Kwon et al., 1988; Villa et al., 2001; Derat et al., 2006; Conte and Floris, 2010; Mestiri et al., 2013; Martín-Caballero et al., 2016; Amini et al., 2017; Huang et al., 2018), there are only few reports on decavanadate-based inorganic compounds along with their structural characterizations, that have been used as models to understand the formation of decavanadate-based minerals in

Nature. D. C. Crans and C. C. McLauchlan and their co-workers have recently published an excellent review article covering the mineral-aspects of decavanadate compounds (Crans et al., 2017). There are more than 10 such minerals known, where the negative charges of decavanadate anion are counter-balanced mostly by alkali and alkali-earth metal cations and these minerals are stabilized with a good number of solvent water molecules. In order to comprehend their speciation in Nature, inorganic chemists have to synthesize decavanadate-based compounds with diverse cations from an aqueous solution and to characterize them crystallographically to investigate the micro-environments around decavanadate anion in these diverse cation matrices. This might offer an understanding the formation of decavanadate-based minerals in Nature. Moreover, exploration of the detailed interactions between decavanadate cluster anion and diverse counter cations is not only important for their categorization (da Silva et al., 2003) but also to gain the knowledge of new supramolecular chemistry of decavanadate ion (Crans et al., 1994; Yi et al., 2010; Chatkon et al., 2014). Thus we have synthesized and structurally characterized seven decavanadate based ion-pair compounds $[Co(H_2O)_6]\{[Na_4(H_2O)_{14}]\{V_{10}O_{28}\}} \cdot 4H_2O$ (**1**), $[Zn(H_2O)_6][Na_3(H_2O)_{14}][HV_{10}O_{28}] \cdot 4H_2O$ (**2**), $[HMTAH]_2[Zn(H_2O)_4][V_{10}O_{28}] \cdot 2H_2O$ (**3**), $[Co(3-amp)(H_2O)_5]_2[3-ampH]_2[V_{10}O_{28}] \cdot 6H_2O$ (**4**), $[4-ampH]_{10}\{[Na(H_2O)_6]\{HV_{10}O_{28}\}}[V_{10}O_{28}] \cdot 15H_2O$ (**5**), $[4-ampH]_6[Co(H_2O)_6]_3[V_{10}O_{28}]_2 \cdot 14H_2O$ (**6**), and $[4-ampH]_{10}[Zn(H_2O)_6][V_{10}O_{28}]_2 \cdot 10H_2O$ (**7**). Since in the present work, we are dealing with diverse cations ion-pairing with a common decavanadate polyanion, diverse supramolecular interactions are possible in their respective crystal structures. We have analyzed here the detailed supramolecular chemistry associated with each of these compounds and we have compared the microenvironment of decavanadate anion in these synthesized systems with that in some of the known decavanadate-based natural minerals (**Graphical Abstract**).

EXPERIMENTAL SECTION

Materials

Sodium metavanadate was received from SISCO Laboratory. The distilled water was used throughout the experiments.

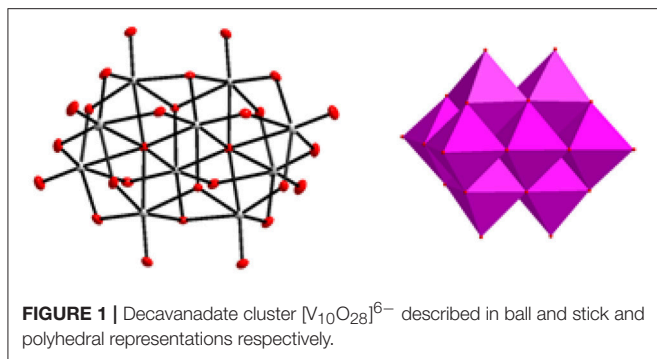


FIGURE 1 | Decavanadate cluster $[V_{10}O_{28}]^{6-}$ described in ball and stick and polyhedral representations respectively.

2-Aminopyridine, 3-aminopyridine, 4-aminopyridine, and hexamine (hexamethylenetetramine) were received from CHEMLABS. $Zn(NO_3)_2 \cdot 6H_2O$ and $Co(NO_3)_2 \cdot 6H_2O$ were used as received from S.D. Fine and FINAR chemicals respectively.

Physical Measurements

Micro analytical (C, H, N) data were obtained with a FLASH EA 1112 Series CHNS Analyzer. Infrared (IR) spectra were recorded on KBr pellets with a JASCO FT/IR-5300 spectrometer in the region of 400–4000 cm^{-1} .

Preparation of Compounds 1–7

Synthesis of

$[Co(H_2O)_6][Na_4(H_2O)_{14}][V_{10}O_{28}] \cdot 4H_2O$ (1)

Sodium metavanadate (1 g, 4.13 mmol) was dissolved in 100 mL of water and its pH was adjusted to 9.0 by dil. HCl. In a separate beaker, the metal salt, $Co(NO_3)_2 \cdot 6H_2O$ (0.5 g, 1.7 mmol) was dissolved in 20 mL of water. This reaction mixture of metal salt was added drop wise to the sodium vanadate solution with stirring. The resulting reaction mixture was stirred for 5 h (during stirring, the formation of precipitate / turbidity was dissolved by heating the reaction mixture at 70–80°C in three to four slots). The reaction mixture was then filtered and kept in open beaker for crystallization without any disturbance at room temperature. After 1 week, orange colored crystals formed, were filtered, washed with plenty of water and finally dried at room temperature. One of the single crystals, suitable for X-ray diffraction study, was selected and characterized structurally. Yield: 1.23 g. Anal. Calcd. (%) for $CoH_{48}Na_4O_{52}V_{10}$: C, 0.00; H, 3.14, N, 0.00. Found: C, 0.03; H, 3.39, N, 0.04. IR (KBr pellet): (ν/cm^{-1}) 3329, 3171, 1658, 1622, 1541, 1475, 1383, 1327, 1244, 1168, 991, 889, 829, 765, 617.

Synthesis of

$[Zn(H_2O)_6][Na_3(H_2O)_{14}][HV_{10}O_{28}] \cdot 4H_2O$ (2)

The reaction procedure is same as the synthesis of compound 1 except $Zn(NO_3)_2 \cdot 6H_2O$ (0.5 g, 1.68 mmol) was taken instead of $Co(NO_3)_2 \cdot 6H_2O$. The resulting reaction mixture was stirred for 5 h (during stirring, the formation of precipitate / turbidity was dissolved by heating the reaction mixture at 70–80°C in three to four slots). The reaction mixture was then filtered and kept in

open beaker for crystallization without any disturbance at room temperature. After 1 week, orange colored crystals formed, were filtered, washed with plenty of water and finally dried at room temperature. One of the single crystals from, suitable for X-ray diffraction study, was selected and characterized structurally. Yield: 0.35 g. Anal. Calcd. (%) for $H_{58}Na_3O_{52}V_{10}Zn$: C, 0.00; H, 3.81; N, 0.00. Found: C, 0.09; H, 3.71; N 0.10. IR (KBr pellet): (ν/cm^{-1}) 3337, 3229, 3057, 2085, 1614, 1560, 1485, 1398, 1327, 1332, 1280, 1072, 922, 885, 829, 679, 584.

Synthesis of

$[HMTAH]_2[Zn(H_2O)_4]_2[V_{10}O_{28}] \cdot 2H_2O$ (3)

Sodium metavanadate (1 g, 4.13 mmol) was dissolved in 100 mL of water and its pH was adjusted to 3.0 by dil. HCl. In a separate beaker, the $Zn(NO_3)_2 \cdot 6H_2O$ and hexamine (0.25 g, 1.68 mmol) were dissolved in 20 mL of water. This reaction mixture was added drop wise to the sodium vanadate solution with stirring. The resulting reaction mixture was stirred for 5 h (during stirring, the formation of precipitate / turbidity was dissolved by heating the reaction mixture at 70–80°C in three to four slots). The reaction mixture was then filtered and kept in open beaker for crystallization without any disturbance at room temperature. After 1 week, orange colored crystals formed, were filtered, washed with water and finally dried at room temperature. Yield: 0.27 g. Anal. Calcd. (%) for $Zn_2V_{10}O_{38}C_{12}N_8H_{46}$: C, 9.29; H, 2.99; N, 7.23. Found: C, 9.11; H, 2.78; N, 7.89. IR (KBr pellet): (ν/cm^{-1}) 3420, 3310, 3190, 3078, 2918, 1647, 1614, 1570, 1464, 1386, 1313, 1230, 1182, 1086, 920, 883, 605.

Synthesis of $[Co(3-amp)(H_2O)_5]_2[3-ampH]_2[V_{10}O_{28}] \cdot 6H_2O$ (4)

Sodium metavanadate (1 g, 4.13 mmol) was dissolved in 100 mL of water and its pH was adjusted to 3.0 by dil. HCl. In a separate beaker, the $Co(NO_3)_2 \cdot 6H_2O$ (0.5 g, 1.7 mmol) and 3-aminopyridine (0.25 g, 1.68) were dissolved in 20 mL of water. This reaction mixture was added drop wise to the sodium vanadate solution with stirring. The resulting reaction mixture was stirred for 5 h (during stirring, the formation of precipitate/turbidity was dissolved by heating the reaction mixture at 70–80°C in three to four slots). The reaction mixture was then filtered and kept in open beaker for crystallization without any disturbance at room temperature. After 1 week, orange colored crystals formed, were filtered, washed with water and finally dried at room temperature. Yield: 0.27 g. Anal. Calcd. (%) for $Co_2V_{10}O_{44}C_{20}N_8H_{58}$: C, 13.79; H, 3.36; N, 6.43. Found: C, 13.21; H, 3.23; N, 6.89. IR (KBr Pellet): (ν/cm^{-1}): 3456, 3322, 3170, 2998, 2978, 1654, 1625, 1567, 1469, 1398, 1267, 1156, 1076, 937, 896, 608.

Synthesis of

$[4-ampH]_{10}[Na(H_2O)_6][HV_{10}O_{28}][V_{10}O_{28}] \cdot 15H_2O$ (5)

Sodium metavanadate (1 g, 4.13 mmol) was dissolved in 100 mL of water and its pH was adjusted to 6.0 by dil. HCl. In a separate beaker, the 4-aminopyridine (0.25 g, 1.70 mmol)

were dissolved in 20 mL of water. 4-aminopyridine solution was added drop wise to the sodium vanadate solution with stirring. The resulting reaction mixture was stirred for 5 h (during stirring, the formation of precipitate / turbidity was dissolved by heating the reaction mixture at 70–80°C in three to four slots). The reaction mixture was then filtered and kept in an open beaker for crystallization without any disturbance at room temperature. After 1 week, orange colored crystals formed, were filtered, washed with good amount of water and finally dried at room temperature. Yield: 0.47 g. Anal. Calcd (%) for $V_{20}NaO_{77}C_{50}N_{20}H_{113}$: C, 18.37; H, 3.48; N, 8.57. Found: C, 18.15; H 3.99; N, 8.55. IR (KBr Pellet): (ν/cm^{-1}): 3467, 3335, 3178, 2929, 1684, 1629, 1547, 1498, 1339, 1235, 1178, 1007, 967, 849, 619.

Synthesis of $[[\{4\text{-ampH}\}_6\{\text{Co}(\text{H}_2\text{O})_6\}_3][\text{V}_{10}\text{O}_{28}]_2 \cdot 14\text{H}_2\text{O}$ (6)
Synthesis of compound **6** is same as that of compound **4** except 4-aminopyridine (0.25 g, 1.68 mmol) was taken (instead of 3-aminopyridine) in the reaction and maintained the same pH as was maintained in the synthesis of compound **4**. The resulting

reaction mixture was stirred for 5 hrs (during stirring, the formation of precipitate / turbidity was dissolved by heating the reaction mixture at 70–80°C in three to four slots). The reaction mixture was then filtered and kept in open beaker for crystallization without any disturbance at room temperature. After 1 week, orange colored crystals formed, were filtered, washed with water and finally dried at room temperature. Yield: 1.87 g. Anal. Calcd. (%) for $V_{20}\text{Co}_3\text{O}_{88}\text{C}_{30}\text{N}_{12}\text{H}_{106}$: C, 11.13; H, 3.30; N, 5.19. Found: C, 11.55; H, 3.79; N, 5.43. IR (KBr pellet) (ν/cm^{-1}): 3427, 3345, 3196, 2822, 1690, 1645, 1556, 1489, 1338, 1268, 1189, 1039, 979, 890, 650.

Synthesis of $[[\{4\text{-ampH}\}_{10}\{\text{Zn}(\text{H}_2\text{O})_6\}][\text{V}_{10}\text{O}_{28}]_2 \cdot 10\text{H}_2\text{O}$ (7)
Synthesis of compound **7** is same as that of compound **4** except $\text{Zn}(\text{NO}_3)_2 \cdot 6\text{H}_2\text{O}$ (0.5 g, 1.7 mmol) and 4-aminopyridine (0.25 g, 2.6 mmol) were taken (instead of $\text{Co}(\text{NO}_3)_2 \cdot 6\text{H}_2\text{O}$ and 3-aminopyridine respectively) in the reaction and maintained the same pH as was maintained in the synthesis of compound **4**. The resulting reaction mixture was stirred for 5 h (during stirring, the formation of precipitate/turbidity was dissolved by heating the reaction mixture at 70–80°C in

TABLE 1 | Crystal data and structure refinement details for compounds **2**, **3**, and **4**.

Entry	2	3	4
Molecular formula	$\text{H}_{10}\text{ZnNa}_3\text{O}_{52}\text{V}_{10}$	$\text{C}_{12}\text{H}_{24}\text{N}_8\text{O}_{38}\text{V}_{10}\text{Zn}_2$	$\text{C}_{20}\text{H}_{38}\text{Co}_2\text{N}_8\text{O}_{44}\text{V}_{10}$
Formula weight	1485.42	1528.53	1721.84
Temperature (K)	298 (2)	298 (2)	298 (2)
Wavelength (Å)	0.71073	0.71073	0.71073
Crystal system	Triclinic	Monoclinic	Triclinic
Space group	$P\bar{1}$	$P2_1/c$	$P\bar{1}$
a (Å)	8.940 (3)	10.5993 (17)	10.5180 (16)
b (Å) 13.877 (4)	16.4355 (18)	11.9208 (18)	
c (Å)	18.360 (5)	13.865 (3)	12.711 (2)
α (deg)	91.766 (4)	90.00	97.818 (2)
β (deg) 91.744 (4)	120.191 (13)	107.937 (2)	
γ (deg)	104.705 (4)	90.00	100.240 (2)
Volume (Å ³) 2200.4 (11)	2087.7 (6)	1460.8 (4)	
Z	2	2	1
ρ (g cm ^{−3})	2.243	2.432	1.957
μ (mm ^{−1}) 2.718		3.378	2.181
F (000)	1438	1492	850
Crystal size (mm ³)	0.24 × 0.18 × 0.14	0.36 × 0.18 × 0.14	0.46 × 0.34 × 0.20
θ range (°)	1.11 to 25.00	2.98 to 25.00	2.20 to 25.09
Reflections collected	18286	9787	13958
Unique reflections	6532	3683	5139
R(int)	0.0238	0.0819	0.0209
Parameters	7714/0/640	3683/0/316	5139/0/455
Goodness of fit on F ²	1.063	1.086	1.537
R ₁ , wR ₂ [$I > 2 \sigma(I)$]	0.0433, 0.1238	0.0885, 0.2660	0.0465, 0.1582
R ₁ , wR ₂ (all data)	0.0511, 0.1300	0.1387, 0.2895	0.0479, 0.1598
Largest diff. Peak and hole (e.Å ^{−3})	0.989/−1.051	1.854, −3.604	2.248, −0.840

three to four slots). The reaction mixture was then filtered and kept in open beaker for crystallization without any disturbance at room temperature. After 1 week, orange colored crystals formed, were filtered, washed thoroughly with water and finally dried at room temperature. One of the single crystals, suitable for X-ray diffraction study, was selected and characterized structurally. The product obtained with Yield of 1.47 g. Anal. Calcd (%) for $V_{20}ZnO_{72}C_{50}N_{20}H_{102}$: C, 18.65; H, 3.19; N, 8.70. Found: C, 18.32; H, 3.45; N, 8.63. IR (KBr pellet) (ν/cm^{-1}): 3445, 3385, 3187, 2842, 1677, 1649, 1537, 1424, 1373, 1229, 1175, 1038, 929, 885, 643.

TABLE 2 | Crystal data and structure refinement details for compounds 5, 6, and 7.

Entry	5	6	7
Molecular formula	$C_{50}H_{100}N_{20}NaO_{72}V_{20}$	$C_{30}H_{88}Co_3N_{12}O_{88}V_{20}$	$C_{50}H_{96}N_{20}O_{72}V_{20}Zn$
Formula weight	3175.29	3220.71	3213.64
Temperature (K)	298 (2)	100 (2)	100 (2)
Wavelength (Å)	0.71073	0.71073	0.71073
Crystal system	Monoclinic	Triclinic	Monoclinic
Space group	$P2_1/c$	$P-1$	$P2_1/c$
a (Å)	13.1158 (10)	10.5396 (12)	13.087 (3)
b (Å)	20.0118 (16)	11.4041 (13)	19.997 (4)
c (Å)	20.1107 (16)	21.068 (2)	20.005 (4)
$\alpha(^{\circ})$	90.000	99.843 (2)	90.000
$\beta(^{\circ})$	95.7520 (10)	91.015 (2)	95.680 (3)
$\gamma(^{\circ})$	90.000	91.547 (2)	90.000
Volume (Å ³)	5251.9 (7)	2493.5 (5)	5209.6 (18)
Z	2	1	2
ρ (g cm ⁻³)	2.008	2.145	2.049
μ (mm ⁻¹)	1.808	2.387	2.043
F (000)	3174	1597	3204
Crystal size (mm ³)	0.36 × 0.24 × 0.18	0.34 × 0.18 × 0.16	0.26 × 0.20 × 0.18
θ range ($^{\circ}$)	1.44 to 26.01	2.20 to 26.00	1.44 to 26.02
Reflections collected	54039	25672	50931
Unique reflections	10321	9682	10234
R(int)	0.0318	0.0230	0.0476
Parameters	10321/0/936	9682/0/898	10234/0/832
GOF on F ²	1.025	1.188	1.147
R_1, wR_2 [$I > 2\sigma(I)$]	0.0355, 0.0962	0.0465, 0.1044	0.0468, 0.1020
R_1, wR_2 (all data)	0.0406, 0.0997	0.0500, 0.1060	0.0549, 0.1056
Largest diff. Peak and hole (e.Å ⁻³)	2.108, -0.417	2.084 and -1.072	0.551, -0.345

TABLE 3 | Decavanadate-based minerals.

Name of minerals	Formulas	Type of decavanadate	References
Huemulite	$Na_4Mg(V_{10}O_{28}) \cdot 24H_2O$	Oxidized	Colombo et al., 2011
Hughesite	$Na_3Al(V_{10}O_{28}) \cdot 22H_2O$	Oxidized	Rakovan et al., 2011
Hummerite	$K_2Mg_2(V_{10}O_{28}) \cdot 16H_2O$	Oxidized	Hughes et al., 2002
Kokinosite	$Na_2Ca_2(V_{10}O_{28}) \cdot 24H_2O$	Oxidized	Kampf et al., 2014
Lasalite	$Na_2Mg_2(V_{10}O_{28}) \cdot 20H_2O$	Oxidized	Hughes et al., 2008
Magnesiopascoite	$MgCa_2(V_{10}O_{28}) \cdot 16H_2O$	Oxidized	Kampf and Steele, 2008
Pascoite	$Ca_3(V_{10}O_{28}) \cdot 17H_2O$	Oxidized	Hughes et al., 2005
Postite	$MgAl_2(V_{10}O_{28})(OH)_2 \cdot 27H_2O$	Oxidized	Kampf et al., 2012
Schindlerite	$Na_2(H_3O)_4(V_{10}O_{28}) \cdot 10H_2O$	Oxidized	Kampf et al., 2013b
Wernerbaurite	$Ca_2(H_3O)_2(V_{10}O_{28}) \cdot 16H_2O$	Oxidized	Kampf et al., 2013b
Gunterite	$Na_4(H_2V_{10}O_{28}) \cdot 22H_2O$	Protonated	Kampf et al., 2011b
Rakovanite	$Na_3(H_3V_{10}O_{28}) \cdot 15H_2O$	Protonated	Kampf et al., 2011a
Nashite	$Na_3Ca_2[(V^IVV^V)_9O_{28}] \cdot 24H_2O$	Mixed valent	Kampf et al., 2013a

X-ray Data Collection and Structure Determination

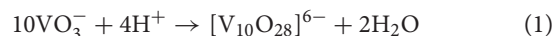
Data were measured on a Bruker SMART APEX CCD area detector system [$\lambda(\text{Mo K}\alpha) = 0.71073 \text{ \AA}$] with a graphite monochromator. 2400 frames were recorded with an ω scan width of 0.3° , each for 8 s keeping a crystal detector distance of 60 mm with a collimator of 0.5 mm. The data were reduced using SAINTPLUS program (software for the CCD detector system, Bruker Analytical X-ray Systems Inc., Madison, WI, 1998); the structures were solved using SHELXS-97 (Sheldrick, 1997) and refined using SHELXL-97 (Sheldrick, 1997). All non hydrogen atoms were refined anisotropically. We tried to locate the hydrogen atom of solvent water molecules for compound **2** through differential Fourier maps, but couldn't succeed. A summary of the crystallographic data and structure determination parameters are described in **Table 1** for compounds **1–2**, in **Table 2** for compounds **3–5** and in **Table 3** for compounds **6** and **7**. Bond lengths and angles for decavanadate anionic cluster for **1** (as it is common cluster for all compounds) are provided in **Table S1** they are in good agreement with those of reported decavanadate cluster anion $[\text{V}_{10}\text{O}_{28}]^{6-}$ (Rao et al., 2011). CCDC- 1840294 (for compound **3**), - 1840295 (for compound **4**), - 1840296 (for compound **5**), - 1840297 (for compound **6**) and - 1840298 (for compound **7**) contain the supplementary crystallographic data for this paper. These data can be obtained free of charge from The Cambridge Crystallographic Data Center via www.ccdc.cam.ac.uk/data_request/cif. CSD-434511 contains the supplementary crystallographic data for carbon free compound **2**; the details of the relevant crystal structure investigation may be obtained from the Fachinformationszentrum, Karlsruhe, D-76344 Eggenstein-Leopoldshafen, Germany (fax: (+49) 7247-808-666;

e-mail: crysdata@fiz-karlsruhe.de) on quoting the depository number CSD-434511. Compound **1** (CSD 418030) is already structurally reported compound.

RESULTS AND DISCUSSION

Synthesis

The synthetic method for the title compounds is simple one pot wet synthesis at a moderate temperature and their isolations are dependent on pH of the concerned solutions. Formation of the decavanadate cluster is feasible in the pH range of 2–9 in the solution, where pH of the solution is maintained by adding dil. HCl acid. Here, we have isolated seven ion pair compounds by altering the various cations and simultaneously pH condition. The formation of decavanadate cluster anion can be explained by protonation of vanadate anion and followed by a series of condensation reactions. The overall chemical reaction for the formation of decavanadate anion is given in equation 1. As expected, IR spectra of all these synthesized compounds reveal the presence of decavanadate anionic cluster as a common anionic component in title compounds. Vanadium-oxygen IR stretching frequencies of the decavanadate cluster anion containing ion pair compound depends on the type of the cation, associated with the anion.



Generally, decavanadate cluster anion decomposes to tetravanadate above pH 7. We still could isolate compounds **1** and **2** at a higher pH value (more than pH 7). We believe that, in our synthesis, although the starting PH is in the range of 9–10, it drops down when the salts are added. That is why, we could isolate decavanadate from the reaction mixture.

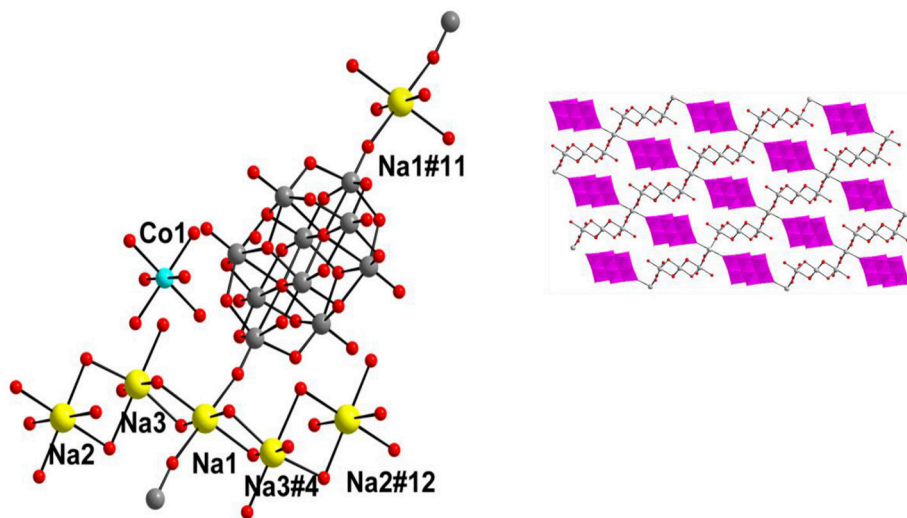


FIGURE 2 | Left: Ball and stick representation of total molecule of the $[\text{Co}(\text{H}_2\text{O})_6][\text{Na}_4(\text{H}_2\text{O})_{14}][\text{V}_{10}\text{O}_{28}]\cdot 4\text{H}_2\text{O}$ (**1**) (Hydrogen atoms and solvent water molecules are omitted for clarity). color codes: Co, cyan; Na, yellow; O, red; V, light grey. **Right:** two-dimensional coordination polymer, formed in the crystal structure of compound **1**. Decavanadate clusters are shown in polyhedral representation (with pink color).

Molecular Structures and Supramolecular Chemistry

Compound $[\text{Co}(\text{H}_2\text{O})_6][\{\text{Na}_4(\text{H}_2\text{O})_{14}\}\{\text{V}_{10}\text{O}_{28}\}]\cdot 4\text{H}_2\text{O}$ (1)

The synthesis and crystal structure of compound **1** has already been reported (Mestiri et al., 2013). Even then, we have described the crystal structure of compound **1** here in terms of supramolecular chemistry. The asymmetric unit of compound **1** reveals the presence of half of the decavanadate cluster, which supports the sodium-aqua-cluster complex cation $\{\text{Na}_2(\text{H}_2\text{O})_7\}^{2+}$ by a coordinate covalent bond and an uncoordinated cobalt tri-aqua complex acting as the cation along with two lattice water molecules. The cationic species $\{\text{Na}_2(\text{H}_2\text{O})_7\}^{2+}$ consists of three crystallographically independent sodium atoms, namely a Na3 (full occupancy), a Na2 (half occupancy) and a Na1 (half occupancy) in the asymmetric unit, which also includes the cobalt atom in the special position. Accordingly the full molecule is formulated as $[\text{Co}(\text{H}_2\text{O})_6][\{\text{Na}_4(\text{H}_2\text{O})_{14}\}\{\text{V}_{10}\text{O}_{28}\}]\cdot 4\text{H}_2\text{O}$ (**1**). Thus, in compound **1**, the negative charges of $\{\text{V}_{10}\text{O}_{28}\}^{6-}$ are counterbalanced by one coordination complex cation $[\text{Co}(\text{H}_2\text{O})_6]^{2+}$ and one alkali metal aqua cluster cation $\{\text{Na}_4(\text{H}_2\text{O})_{14}\}^{4+}$. In the crystal structure, the sodium-aqua cluster cation $\{\text{Na}_4(\text{H}_2\text{O})_{14}\}^{4+}$ is actually combination of $\{\text{Na}_{3.5}(\text{H}_2\text{O})_{12}\}^{3.5+}$ and $\{\text{Na}(\text{H}_2\text{O})_2\}^{0.5+}$, whereby both cationic species are coordinated to the decavanadate cluster anion

by coordinate covalent bonds. Five sodium atoms (two Na3, full occupancy + two Na2, half occupancy + one Na1, half occupancy) form the $\{\text{Na}_{3.5}(\text{H}_2\text{O})_{12}\}^{3.5+}$ cluster cation, coordinating to the decavanadate anion through Na1 cation and the rest sodium atom Na1 (from $\{\text{Na}(\text{H}_2\text{O})_2\}^{0.5+}$ cationic species) coordinates to the same $\{\text{V}_{10}\}$ cluster from opposite side of the cluster anion. All sodium ions are octahedrally coordinated in the crystal structure. The coordination of $\{\text{Na}_4(\text{H}_2\text{O})_{14}\}^{4+}$ cation to the $\{\text{V}_{10}\}$ cluster anion is shown in **Figure 2** (left). We believe that, the pH 9 of the concerned synthesis mixture is important in forming such $[\text{Na}_4(\text{H}_2\text{O})_{14}]^{4+}$ cluster.

In the relevant crystal structure, this sodium aqua cluster cation self assembles to an infinite one-dimensional sodium water chain. These chains are laterally linked by $\{\text{V}_{10}\text{O}_{28}\}^{6-}$ cluster anions through Na1 ion resulting in a two-dimensional pure inorganic coordination polymer as shown in **Figure 2** (right). These two-dimensional sheets are stacked along crystallographic *a* axis as shown from the molecular packing diagram (**Figure 3**). The O–H...O hydrogen bonding situation in the crystal structure of $[\text{Co}(\text{H}_2\text{O})_6][\{\text{Na}_4(\text{H}_2\text{O})_{14}\}\{\text{V}_{10}\text{O}_{28}\}]\cdot 4\text{H}_2\text{O}$ (**1**) has been described in **Supplementary Figure 1** (Supporting Information). The relevant crystallographic data is available in **Table S1** (Supporting Information). **Tables S2, S3** (Supporting Information) have described bond distances along with bond angles and hydrogen bonding parameters respectively.

Compound $[\text{Zn}(\text{H}_2\text{O})_6][\text{Na}_3(\text{H}_2\text{O})_{14}][\text{HV}_{10}\text{O}_{28}]\cdot 4\text{H}_2\text{O}$ (2)

The asymmetric unit in the crystal structure of compound **2** consists of two one-half decavanadate clusters, one tri-sodium aqua-complex $[\text{Na}_3(\text{H}_2\text{O})_{14}]^{3+}$, one zinc hexa-aqua complex $[\text{Zn}(\text{H}_2\text{O})_6]^{2+}$ and four solvent water molecules as shown in **Figure 4**. Thus the full molecule can be formulated as $[\text{Zn}(\text{H}_2\text{O})_6][\text{Na}_3(\text{H}_2\text{O})_{14}][\text{HV}_{10}\text{O}_{28}]\cdot 4\text{H}_2\text{O}$ (**2**), in which decavanadate cluster is singly protonated, and the rest of the charge (−5) is counter-balanced by $[\text{Zn}(\text{H}_2\text{O})_6]^{2+}$ and $[\text{Na}_3(\text{H}_2\text{O})_{14}]^{3+}$ cations. In the crystal structure, along with five lattice water molecules, fourteen water molecules are found to be coordinated with three sodium cations, resulting in the formation of $[\text{Na}_3(\text{H}_2\text{O})_{14}]^{3+}$ cluster cation, in which the coordination of each sodium can be described by an octahedral arrangement of water molecules. The formation of this sodium-aqua cluster can be described by two terminal sodium ions (Na2 and Na3) and one middle sodium ion (Na1) as shown in **Figure 4** (top right).

The middle sodium ion (Na1) is coordinated to four μ_2 -type bridging water molecules (O44, O47, O42, and O52) and two terminal water molecules (O46 and O50). Each of the terminal sodium ions is coordinated to two μ_2 -type bridging water molecules and four terminal water molecules as shown in **Figure 4**. Hydrogen atoms could not be located for all the water molecules in the concerned crystal. By taking O...O separation in the range of 2.779 Å to 3.211 Å, supramolecular chemistry of compound **2** is described. A supramolecular $(\text{H}_2\text{O})_9$ cluster is found to be formed by zinc- and sodium-coordinated water molecules and solvent water molecules. These $(\text{H}_2\text{O})_9$ clusters are further linked by $(\text{H}_2\text{O})_3$ cluster (shown

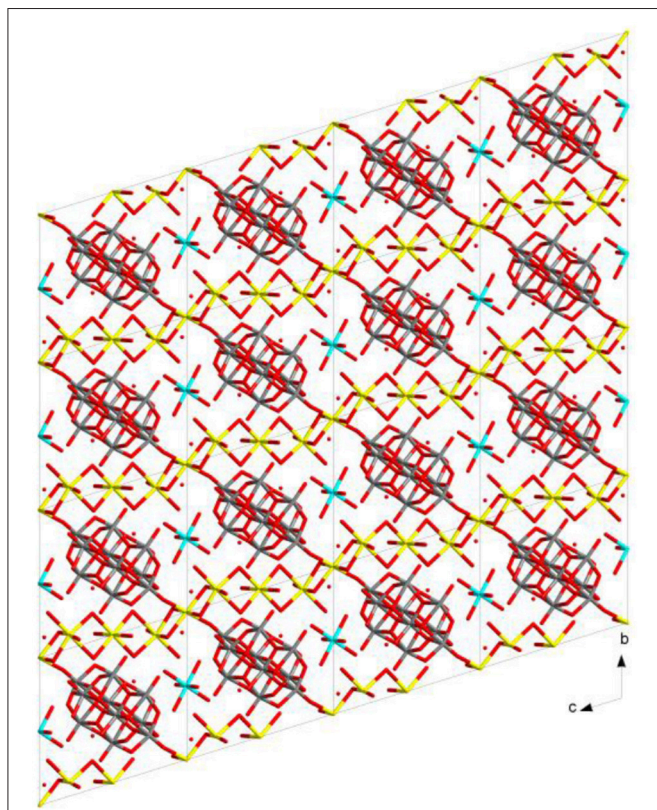


FIGURE 3 | Molecular packing diagram in the crystal structure of compound **1**.

in blue dotted line) resulting in the formation of a chain-like arrangement as shown in **Figure 5**. The supramolecular O...O interactions between decavanadate cluster anions, the water chain and a (lattice) water dimer (O35...O35) lead to the generation of a supramolecular network as shown in **Figure 6**. This situation (**Figure 6**) can be depicted as inclusion of POV clusters in the water chain-network. In other words, it can be described that decavanadate cluster is stabilized in the pool of water.

[HMTAH]₂[[Zn(H₂O)₄]₂{V₁₀O₂₈}]·2H₂O (**3**)

Compound **3**, that has been synthesized starting from sodium metavanadate, zinc nitrate and hexamine at pH 3.0 in a simple wet synthesis, crystallizes in monoclinic system with space group of *P*2₁/*c*. The concerned asymmetric unit consists of half of the decavanadate anion, one HMTAH cation and one zinc aqua complex cation (**Figure 7**). Thus it has been formulated as [HMTAH]₂[[Zn(H₂O)₄]₂{V₁₀O₂₈}]·2H₂O (**3**). In the crystal structure, decavanadate moiety is functionalized

by a Zn(II)-aqua complex, in which Zn1 is coordinated to two terminal oxo groups (O7 and O8) of both sides of decavanadate anion as shown in **Figure 7**. Thus the coordination number of zinc in polyoxovanadate (POV) supported Zn(II)-tetra-aqua coordination complex is six (two terminal oxygen and four water molecules). Two such POV supported Zn(II) coordination complexes form a {Zn₂} dimer through two {μ₂-H₂O} type water bridges. Inter-dimer-decavanadate cluster coordination results in the formation of a 2-dimensional coordination polymer as shown **Figure 8**. Hydrogen bonding environment around HMATAH⁺ moiety due to C-H...O interactions in the crystal structure of compound **3** is shown in **Supplementary Figure 2**. Hydrogen bond distances and angles are presented in **Table S4**.

Compound

[[Co(3-amp)(H₂O)₅]₂{3-ampH}₂][V₁₀O₂₈]·6H₂O (**4**)

A discrete inorganic-organic hybrid material [Co(3-amp)(H₂O)₅]₂{3-ampH}₂[V₁₀O₂₈]·6H₂O (**4**) containing a

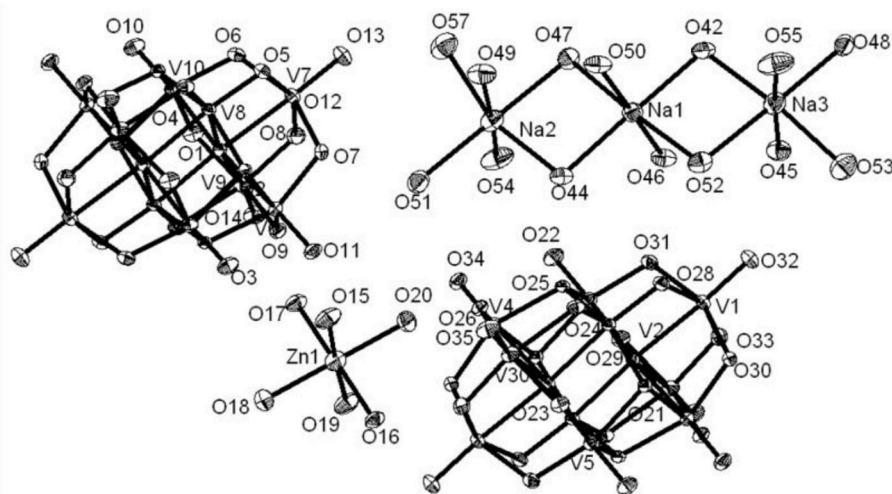


FIGURE 4 | Thermal ellipsoidal diagram of asymmetric part of compound [Zn(H₂O)₆][Na₃(H₂O)₁₄][HV₁₀O₂₈]·4H₂O (**2**) with 30% probability (hydrogen atoms and solvent water molecules are omitted for clarity).

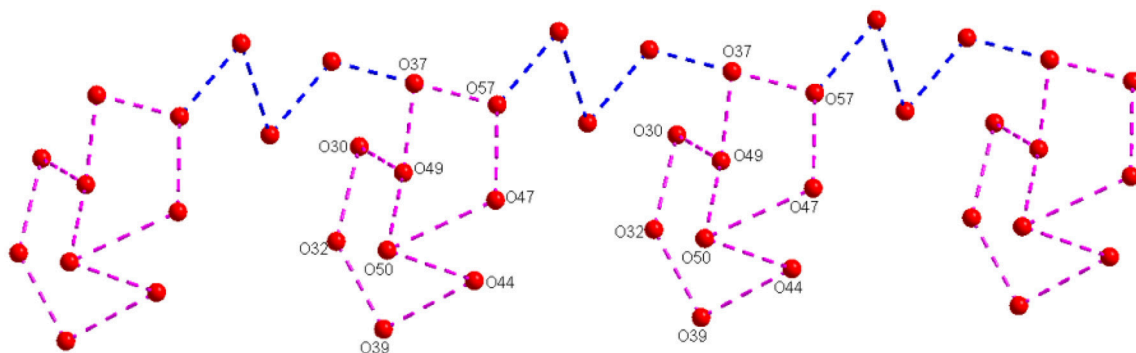


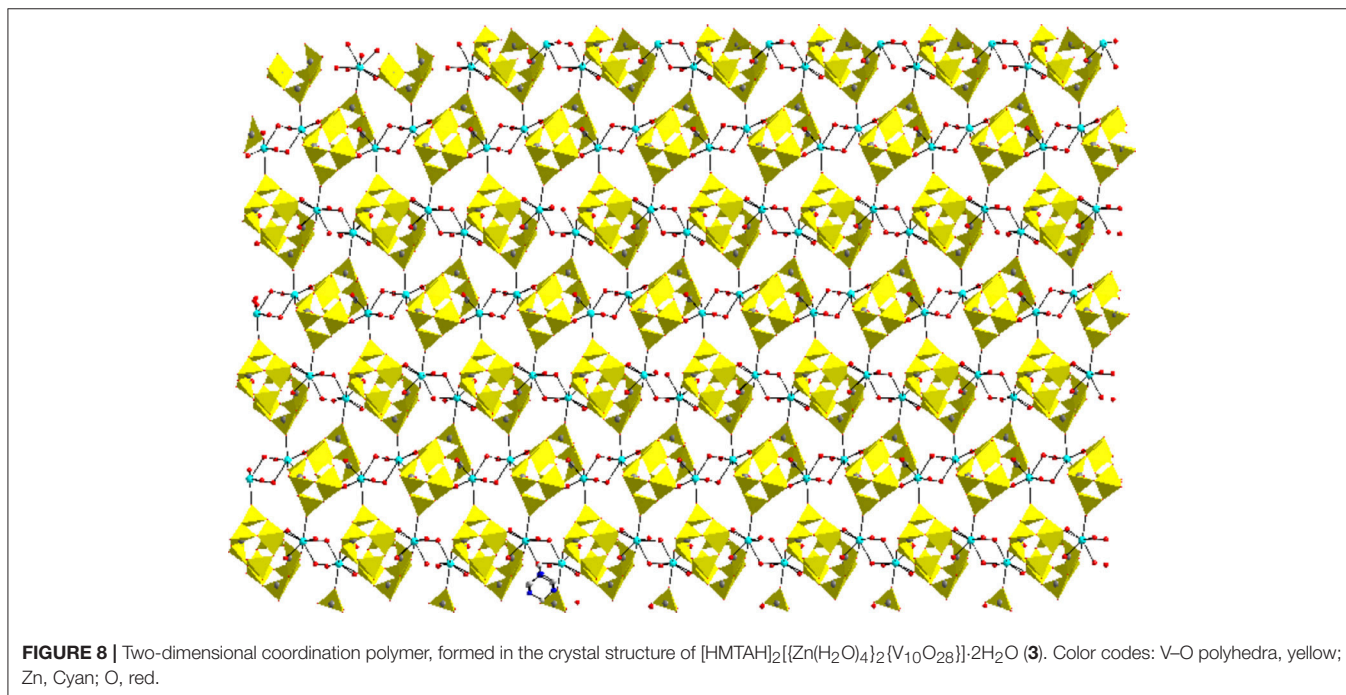
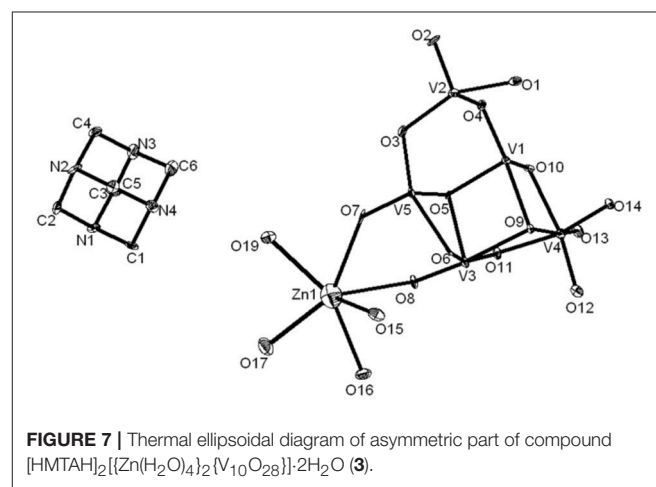
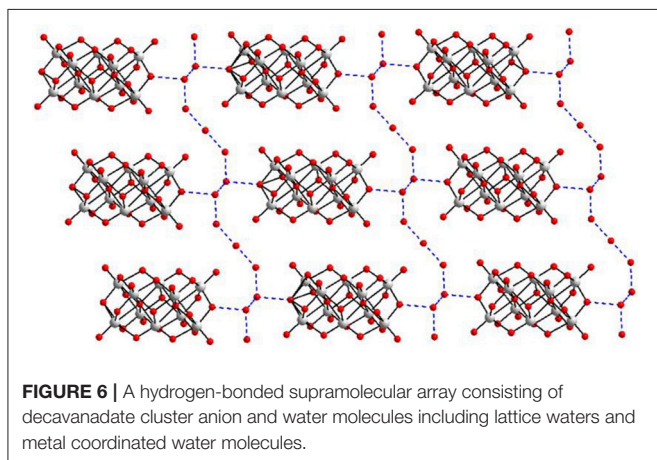
FIGURE 5 | A chainlike water structure, built from water cluster due to O-H...O interactions among the lattice water and zinc and sodium coordinated water molecules in the crystal structure of compound [Zn(H₂O)₆][Na₃(H₂O)₁₄][HV₁₀O₂₈]·4H₂O (**2**).

cobalt complex, a decavanadate cluster anion, aminopyridinium cation and lattice water molecules, has been isolated with 3-aminopyridine in an aqueous medium in an one pot synthesis. Crystal system is confined with triclinic *P*-1 space group. The relevant asymmetric unit, as shown in **Figure 9**, reveals the presence of half of the decavanadate anionic cluster, one molecule of protonated 3-aminopyridine $[3\text{-ampH}]^+$ and a cobalt coordination complex $\{\text{Co}(3\text{-amp})(\text{H}_2\text{O})_5\}^{2+}$. Apart from columbic interaction between cation and anionic species, non-covalent interactions are also responsible for stability of the compound **4**. In the crystal structure, a three-dimensional framework has been built due to C–H...O hydrogen bonding interactions between the cationic part and decavanadate anionic cluster as shown

in **Figure 10**. Hydrogen bonding situation around the 3-aminopyridines (coordinated as well as cation) and water molecule, is shown in **Supplementary Figure 3** and their hydrogen bonding distances and angles are shown in **Table S5** including pertinent symmetry operations. We found weak π - π interactions among the molecules of 3-aminopyridine (see **Supplementary Figure 4**).

Compound $[\text{4-ampH}]_{10}\{\text{Na}(\text{H}_2\text{O})_6\}\{\text{HV}_{10}\text{O}_{28}\}\{\text{V}_{10}\text{O}_{28}\} \cdot 15\text{H}_2\text{O}$ (**5**)

Asymmetric unit of the crystal structure of compound **5** reveals that two independent halves of decavanadate anionic cluster $[\text{V}_{10}\text{O}_{28}]^{6-}$ are assembled with the five cation molecules of 4-ampH $^+$ and a $\text{Na}(\text{H}_2\text{O})_3$ moiety with sodium in special position.



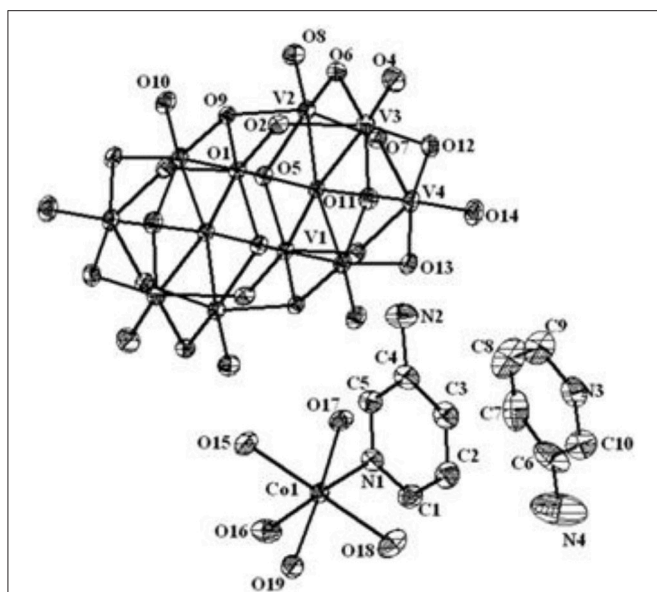


FIGURE 9 | Thermal ellipsoidal diagram of $[(\text{Co}(\text{3-amp})(\text{H}_2\text{O})_5)_2(\text{3-ampH})_2][\text{V}_{10}\text{O}_{28}]\cdot 6\text{H}_2\text{O}$ (**4**) with 30% probability (hydrogen atoms are omitted for clarity).

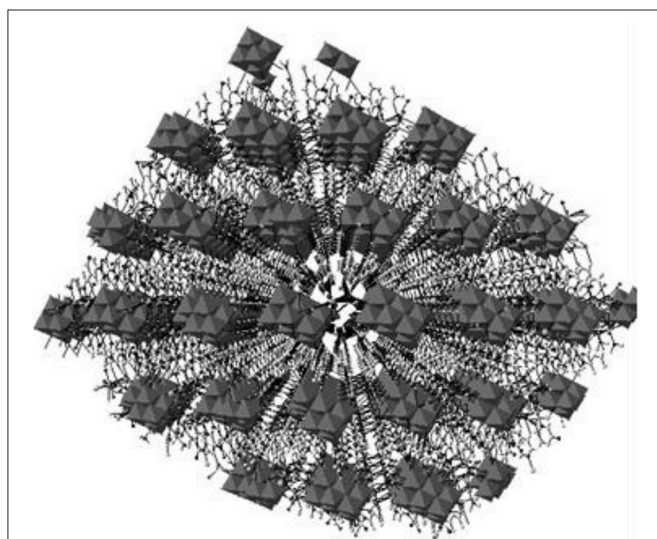


FIGURE 10 | A 3-dimensional framework (a perspective view), generated due to C-H...O hydrogen bonding interactions between cation and decavanadate anion in the crystal of compound $[(\text{Co}(\text{3-amp})(\text{H}_2\text{O})_5)_2(\text{3-ampH})_2][\text{V}_{10}\text{O}_{28}]\cdot 6\text{H}_2\text{O}$ (**4**).

ORTEP diagram of the $[\text{4-ampH}]_{10}[\{\text{Na}(\text{H}_2\text{O})_6\}]\{\text{HV}_{10}\text{O}_{28}\}[\text{V}_{10}\text{O}_{28}]\cdot 15\text{H}_2\text{O}$ (**5**) is shown in the **Figure 11**. We have found ten lattice water molecules in the crystal structure of **5** and a cyclic water pentamer is generated due of the O-H...O hydrogen bonding interactions among the water molecules: O28, O29, O30, O33, and O36 as shown in **Figure 12**, left. Two such water pentamers are connected with a central sodium hexa-aqua complex *via* Na-O-H...O (pentamer)

interactions resulting in the generation of a dumbbell-shaped-supramolecular architecture as presented in **Figure 12**, right. The relevant crystallographic data is provided in **Table 2**. And C-H...O and O-H...O hydrogen bonding interactions around {N1N2}, {N3N4}, {N5N6}, {N7N8}, {N9N10}, and water moieties in the crystal structure of **5** are shown in **Supplementary Figure 5** and pertinent hydrogen bond distances and angles are listed in the **Table S6** including symmetry operations.

Compound $[\{\text{4-ampH}\}_6\{\text{Co}(\text{H}_2\text{O})_6\}_3][\text{V}_{10}\text{O}_{28}]_2\cdot 14\text{H}_2\text{O}$ (**6**)

The asymmetric unit of compound **6** (**Figure 13**) consists of two independent halves of decavanadate $\{\text{V}_{10}\text{O}_{28}\}^{6-}$ cluster anion, 1.5 molecules of $[\text{Co}(\text{H}_2\text{O})_6]^{2+}$, three protonated 4-aminopyridine and seven solvent water molecules. Accordingly, this is formulated as $[\{\text{4-ampH}\}_6\{\text{Co}(\text{H}_2\text{O})_6\}_3][\text{V}_{10}\text{O}_{28}]_2\cdot 14\text{H}_2\text{O}$ (**6**). In the crystal structure, coordinated water molecules and lattice water molecules are non-covalently interacted through hydrogen bonding, generating a water tetramer (O30, O39, O35, O31) with O...H distances of 2.01 Å, 1.842 Å, and 2.077 Å, respectively (**Figure 14**) and each end oxygen atoms of the water tetramer, i.e., O30 and O31, is linked to cobalt center of the cobalt-hexa-aqua complex. Hydrogen bonding situation around {N1N2}, {N3N4}, {N5N6}, {N7N8}, {N9N10}, {Co} and water in the crystal structure of **6** is shown in **Supplementary Figure 6**, which is explained based on C-H...O, O-H...O, and N-H...O interactions. The relevant hydrogen bond distances and angles are listed in the **Table S7** in the section of **Supplementary Material**.

Compound $[\{\text{4-ampH}\}_{10}\{\text{Zn}(\text{H}_2\text{O})_6\}][\text{V}_{10}\text{O}_{28}]_2\cdot 10\text{H}_2\text{O}$ (**7**)

The crystal structure of $[\{\text{4-ampH}\}_{10}\{\text{Zn}(\text{H}_2\text{O})_6\}][\text{V}_{10}\text{O}_{28}]_2\cdot 10\text{H}_2\text{O}$ (**7**) has been characterized with the monoclinic, $P2_1/c$ space group. It consists of two clusters of decavanadate anion $\{\text{V}_{10}\text{O}_{28}\}^{6-}$, ten molecules of protonated 4-aminopyridine and one unit of zinc(II)-hexa-aqua complex $[\text{Zn}(\text{H}_2\text{O})_6]^{2+}$. In addition, ten lattice water molecules are crystallized in the crystal structure of compound **7**. Thermal ellipsoidal diagram of compound **7** is presented in **Figure 15**. In the crystal structure, lattice water molecules (O36, O37, O40, O38), and coordinated water molecule (O16) are non-covalently interacted due to O-H...O hydrogen bonding interactions resulting in the generation of a cyclic water pentamer, that has been represented in **Figure 16**, left. In this supramolecular water pentamer, since the O16 water is the Zn(II)-coordinated water molecule and it is equivalent to another O16 by a symmetry operation coordinated to same Zn(II), it is possible to have two water pentamers connected by a central Zn(II) ion resulting in dumbbell-like construction as shown in **Figure 16**, right (O...H distances lie between 2.007 Å and 2.158 Å). Hydrogen bonding situations around {N1N2}, {N3N4}, {N5N6}, {N7N8}, {N9N10}, {Zn} and water due to C-H...O, N-H...O and O-H...O interactions in the crystal structure of **7** are shown in **Supplementary Figure 7** and relevant hydrogen bond

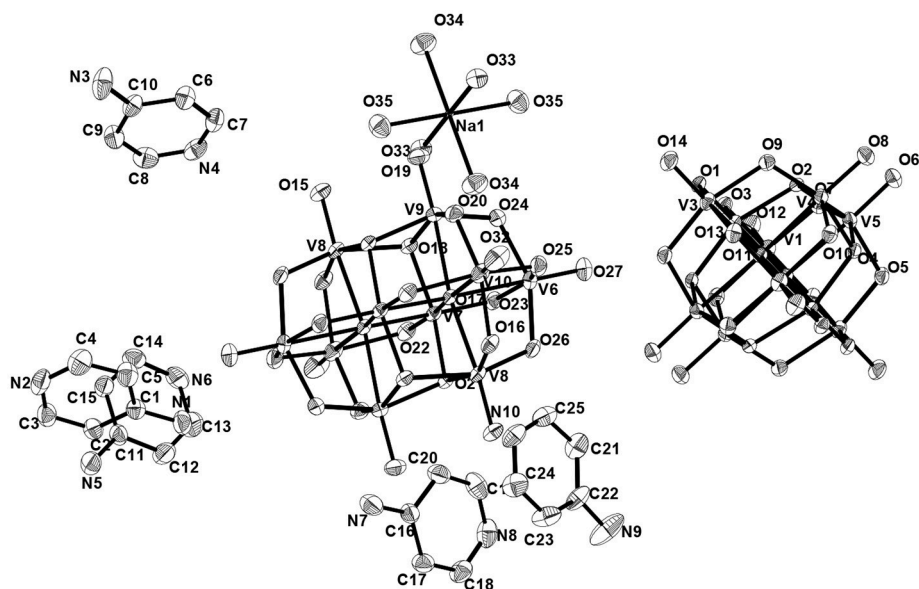


FIGURE 11 | Thermal ellipsoidal Thermal Ellipsoidal diagram of $[4\text{-ampH}]_{10}[\{\text{Na}(\text{H}_2\text{O})_6\} \{\text{HV}_{10}\text{O}_{28}\}] [\text{V}_{10}\text{O}_{28}] \cdot 15\text{H}_2\text{O}$ (**5**) with 30% probability (hydrogen atoms are omitted for clarity).

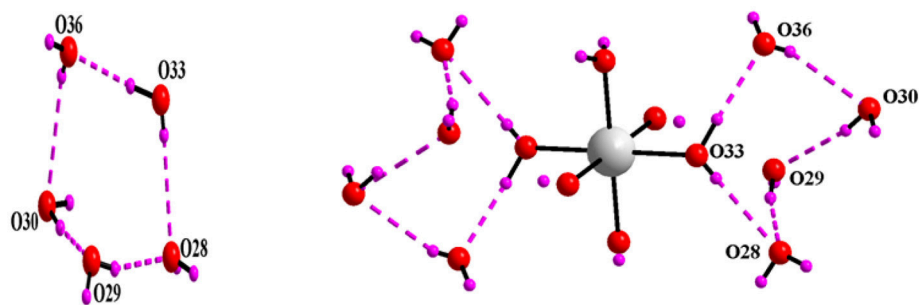


FIGURE 12 | Left: cyclic water pentamer is generated due to O-H...O interactions in $[4\text{-ampH}]_{10}[\{\text{Na}(\text{H}_2\text{O})_6\} \{\text{HV}_{10}\text{O}_{28}\}] [\text{V}_{10}\text{O}_{28}] \cdot 15\text{H}_2\text{O}$ (**5**); right: dumbbell shape diagram due to O-H...O interaction in **6** involving $\{\text{Na}(\text{H}_2\text{O})_6\}$ coordination complex. Color codes: O, red; Na, grey; H, purple.

distances and angles are given in **Table S8** with symmetry codes.

Understanding Decavanadate-Based Mineralogy

Until now, more than 12 decavanadate based minerals have been known (**Table 3**) and interestingly, many of them have been characterized by crystallography. Out of seven described compounds in this work, two compounds $[\text{Co}(\text{H}_2\text{O})_6][\{\text{Na}_4(\text{H}_2\text{O})_{14}\}\{\text{V}_{10}\text{O}_{28}\}] \cdot 4\text{H}_2\text{O}$ (**1**) and $[\text{Zn}(\text{H}_2\text{O})_6][\text{Na}_3(\text{H}_2\text{O})_{14}][\text{HV}_{10}\text{O}_{28}] \cdot 4\text{H}_2\text{O}$ (**2**) have direct relevance to the decavanadate-based mineral. For example, the mineral kokinosite, $\text{Na}_2\text{Ca}_2(\text{V}_{10}\text{O}_{28}) \cdot 24\text{H}_2\text{O}$ (Kampf et al., 2014) and compound $[\text{Co}(\text{H}_2\text{O})_6][\{\text{Na}_4(\text{H}_2\text{O})_{14}\}\{\text{V}_{10}\text{O}_{28}\}] \cdot 4\text{H}_2\text{O}$ (**1**) (the formula of which can also be written as $\text{Na}_4\text{Co}(\text{V}_{10}\text{O}_{28}) \cdot 24\text{H}_2\text{O}$) can be discussed in the context of the microenvironment of

the isopolyanion $[\text{V}_{10}\text{O}_{28}]^{6-}$ in this synthesized compound **1** and in kokinosite. Both compound **1** and the kokinosite mineral have similar / comparable crystal cell parameters and crystallize in the same space group. In the crystal structure of compound **1**, we have found the abundance of $\{\text{Na}_4(\text{H}_2\text{O})_{14}\}^{4+}$ liner-shaped water-bridged cluster (per formula unit), which is coordinated to the decavanadate cluster anion through terminal oxygen of the polyanion. In other words, in the synthesized compound **1**, decavanadate supported sodium-water cluster $\{\text{Na}_4(\text{H}_2\text{O})_{14}\}^{4+}$ exists (**Figure 2**). In the relevant crystal structure, the interlinking of these clusters results in the infinite sodium-water chain. These sodium-water chains are laterally linked by the decavanadate anions to form a two-dimensional coordination polymeric structure; $[\text{Co}(\text{H}_2\text{O})_6]^{2+}$ remains as an isolated discrete coordination complex cation located in the void space (**Figure 3**) to counterbalance the negative charges

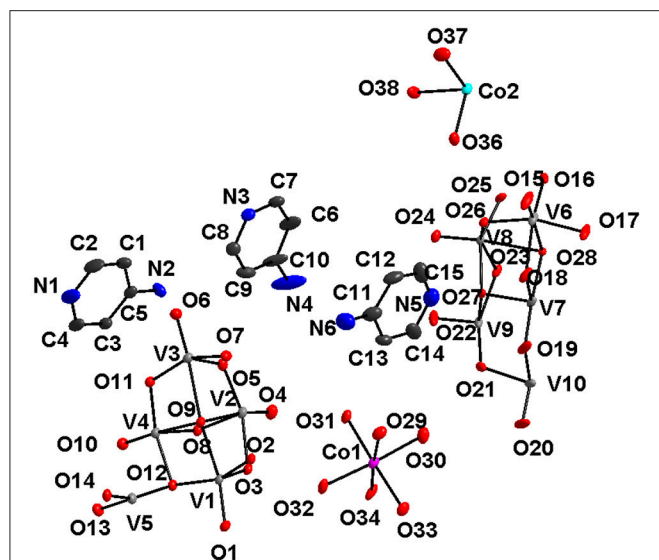


FIGURE 13 | Thermal ellipsoidal plot of the asymmetric unit of compound $[(4\text{-ampH})_6\{\text{Co}(\text{H}_2\text{O})_6\}_3][\text{V}_{10}\text{O}_{28}]_2 \cdot 14\text{H}_2\text{O}$ (**6**) (hydrogen atoms and solvent water molecules are omitted for clarity). Color codes: O, red; V, medium grey; C, dark grey; Co, cyan.

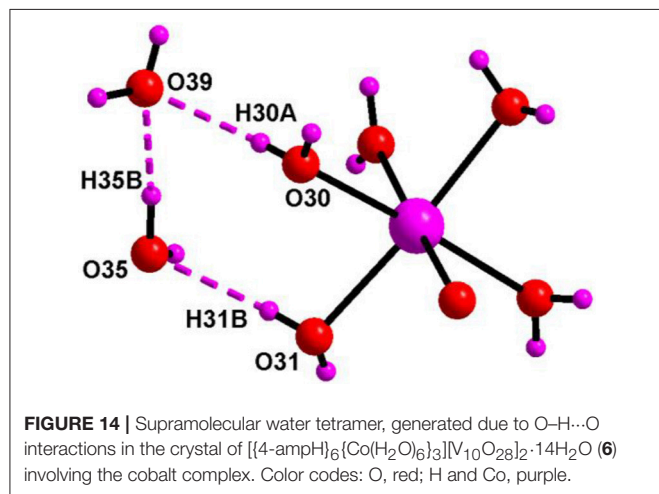


FIGURE 14 | Supramolecular water tetramer, generated due to O-H...O interactions in the crystal of $[(4\text{-ampH})_6\{\text{Co}(\text{H}_2\text{O})_6\}_3][\text{V}_{10}\text{O}_{28}]_2 \cdot 14\text{H}_2\text{O}$ (**6**) involving the cobalt complex. Color codes: O, red; H and Co, purple.

of the decavanadate anion. In the language of decavanadate mineral crystallography, these cations (e.g., sodium and cobalt ions in compound **1**) are called interstitial units (Hughes et al., 2002, 2005, 2008; Colombo et al., 2011; Kampf et al., 2011b, 2013b, 2014). For example, in the crystal structure of the kokinosite mineral (Kampf et al., 2014), the interstitial unit has a composition of $(\text{Na}_2\text{Ca}_2 \cdot 24\text{H}_2\text{O})^{6+}$ and the decavanadate anion $(\text{V}_{10}\text{O}_{28})^{6-}$ forms the structural unit of the mineral. In the relevant crystal structure (kokinosite), the decavanadate cluster anions (structural units) are linked by $\text{Na}(\text{H}_2\text{O})_6$ octahedra (interstitial units) and $\text{Ca}(\text{H}_2\text{O})_8$ polyhedra (interstitial units) that themselves link into infinite chains by edge and corner sharing. So in this case, $\text{Ca}(\text{H}_2\text{O})_8$ is part of the infinite chain (unlike $\text{Co}(\text{H}_2\text{O})_6$ in compound **1**, that remains as a isolated complex cation). Overall, both structures are comparable.

Compound $[\text{Zn}(\text{H}_2\text{O})_6][\text{Na}_3(\text{H}_2\text{O})_{14}][\text{HV}_{10}\text{O}_{28}] \cdot 4\text{H}_2\text{O}$ (**2**), synthesized and characterized in this work, is formulated with a mono-protonated decavanadate cluster anion $[\text{HV}_{10}\text{O}_{28}]^{5-}$. In 2011, Kampf et al. reported diprotonated decavanadate based mineral, gunterite $\text{Na}_4(\text{H}_2\text{V}_{10}\text{O}_{28}) \cdot 22\text{H}_2\text{O}$ (Kampf et al., 2011b). In both the crystal structures, the proton on the decavanadate anion could not be located, but formulated from elemental analyses and crystallographic investigation on the cationic part. In the crystal structure of compound **2**, a sodium trimer-water cluster $[\text{Na}_3(\text{H}_2\text{O})_{14}]^{3+}$ per formula unit is characterized, which unlike compound **1** is not coordinated to decavanadate anion. But in the case of the gunterite mineral, the sodium water cluster is coordinated to the polyanion (Kampf et al., 2011b). In the crystal structure of synthesized compound **2**, the $[\text{Zn}(\text{H}_2\text{O})_6]^{2+}$ moiety remains as an isolated discrete coordination complex cation, counter balancing the residual charge of the decavanadate anion. In most of these mineral structures, solvent waters are found disordered; on the other hand, in most of the synthesized compounds (present work), lattice waters are characterized as forming supramolecular water clusters. So far, no decavanadate based minerals are found, in which the interstitial cation is a transition metal-aqua complex cation, as synthesized in the present work. The present synthesis work predicts that the formation of such transition metal cation associated decavanadate minerals is possible and we expect that transition metal decavanadate minerals will be discovered in future that may feature the presence of discrete hexa-aqua transition metal coordination complex as an interstitial cation, as found in the present model study.

CONCLUSIONS

We have described the synthesis and characterization of seven decavanadate containing compounds $[\text{Co}(\text{H}_2\text{O})_6][\text{Na}_4(\text{H}_2\text{O})_{14}][\text{V}_{10}\text{O}_{28}] \cdot 4\text{H}_2\text{O}$ (**1**), $[\text{Zn}(\text{H}_2\text{O})_6][\text{Na}_3(\text{H}_2\text{O})_{14}][\text{HV}_{10}\text{O}_{28}] \cdot 4\text{H}_2\text{O}$ (**2**), $[\text{HMTAH}]_2[\text{Zn}(\text{H}_2\text{O})_4][\text{V}_{10}\text{O}_{28}] \cdot 2\text{H}_2\text{O}$ (**3**), $[\{\text{Co}(3\text{-amp})(\text{H}_2\text{O})_5\}_2\{3\text{-ampH}\}_2][\text{V}_{10}\text{O}_{28}] \cdot 6\text{H}_2\text{O}$ (**4**), $[4\text{-ampH}]_{10}[\{\text{Na}(\text{H}_2\text{O})_6\}][\text{HV}_{10}\text{O}_{28}][\text{V}_{10}\text{O}_{28}] \cdot 15\text{H}_2\text{O}$ (**5**), $[(4\text{-ampH})_6\{\text{Co}(\text{H}_2\text{O})_6\}_3][\text{V}_{10}\text{O}_{28}]_2 \cdot 14\text{H}_2\text{O}$ (**6**), $[(4\text{-ampH})_{10}\{\text{Zn}(\text{H}_2\text{O})_6\}][\text{V}_{10}\text{O}_{28}]_2 \cdot 10\text{H}_2\text{O}$ (**7**). In this report, we have described detailed supramolecular chemistry of **1–7**. In some of their crystal structures, non-covalent interactions among the lattice water molecules and metal coordinated water molecules lead to the formation of supramolecular water clusters. Thus the microenvironment of the decavanadate cluster anion in diverse cation matrices includes the formation of ordered water structures. We have also observed that, in these decavanadate based systems, the transition metal aqua complexes like to remain as discrete coordination complex cation, whereas the alkali metal aqua complexes like to aggregate to dimer, trimer, tetramer, infinite chain etc. These alkali metal water aggregations mimic the interstitial units of natural minerals of decavanadates. We have discussed the supramolecular chemistry of the synthesized systems comparing the microenvironment of decavanadate cluster anion, found in natural minerals.

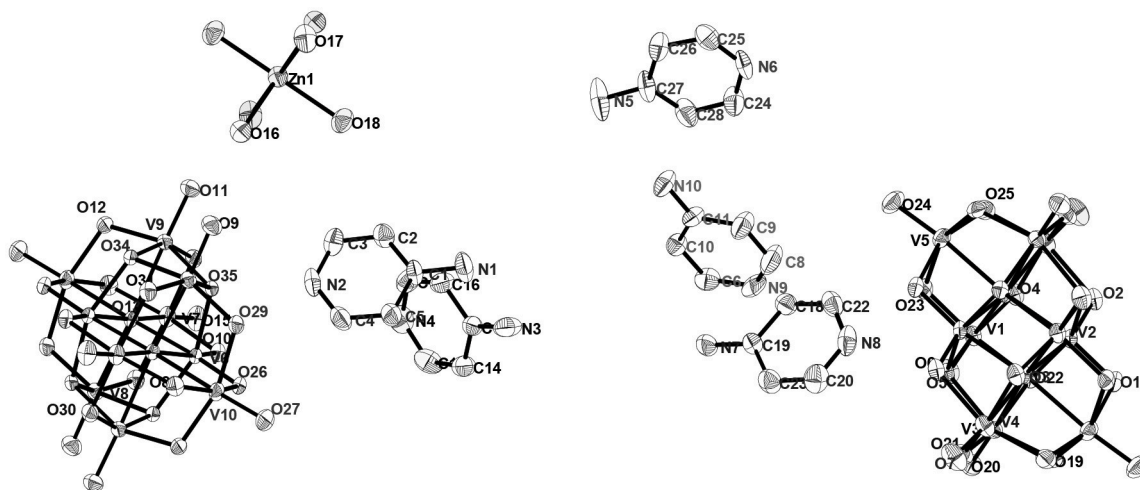


FIGURE 15 | ORTEP diagram in the crystal structure of compound $[[4\text{-ampH}]_{10}\{\text{Zn}(\text{H}_2\text{O})_6\}][\text{V}_{10}\text{O}_{28}]_2 \cdot 10\text{H}_2\text{O}$ (7) with 30% probability (hydrogen atoms and solvent water molecules are omitted for clarity).

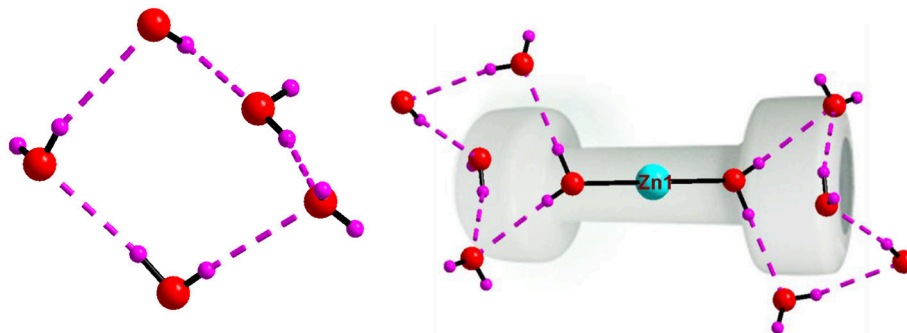


FIGURE 16 | Left: cyclic water pentamer, generated due to O–H...O interactions in compound $[[4\text{-ampH}]_{10}\{\text{Zn}(\text{H}_2\text{O})_6\}][\text{V}_{10}\text{O}_{28}]_2 \cdot 10\text{H}_2\text{O}$ (7); right: dumbbell shape diagram due to O–H...O interactions in 7 involving $\{\text{Zn}(\text{H}_2\text{O})_6\}$ coordination complex and water pentamers. Color codes: O, red; Zn, cyan; H, purple.

AUTHOR CONTRIBUTIONS

SA was Ph.D. student and SD is his Ph.D. supervisor. SA synthesized and characterized the compounds, described in this manuscript under the supervision of SD. Both SA and SD analyzed the data together. This manuscript has been written by SD mainly, but it was shown to SA. SA has agreed with the content of the manuscript.

ACKNOWLEDGMENTS

We thank, SERB, Department of Science and Technology, Government of India, for financial support (Project No.

EMR/2017/002971). We also thank Center for Nano Technology, University of Hyderabad. The National X-ray Diffractometer facility at the University of Hyderabad by the Department of Science and Technology, Government of India, is gratefully acknowledged. SA thank CSIR, Government of India for his fellowship. We acknowledge DST-PURSE, UPE-II, and UGC-CAS.

SUPPLEMENTARY MATERIAL

The Supplementary Material for this article can be found online at: <https://www.frontiersin.org/articles/10.3389/fchem.2018.00469/full#supplementary-material>

REFERENCES

- Al-Qatati, A., Fontes, F. L., Barisas, B. G., Zhang, D., Roessa, D. A., and Debbie, C., et al. (2013). Raft localization of Type I Fcε receptor and degranulation of
- RBL-2H3 cells exposed to decavanadate, a structural model for V_2O_5 . *Dalton Trans.* 42, 11912–11920. doi: 10.1039/c3dt50398d
- Amini, M., Nikkhoo, M., Tekantappeh, S. B., Farnia, S. M. F., Mahmoudi, G., and Büyükgüngör, O. (2017). Synthesis, characterization and catalytic

- properties of a copper complex containing decavanadate nanocluster, $\text{Na}_2[\text{Cu}(\text{H}_2\text{O})_6]_2\{\text{V}_{10}\text{O}_{28}\} \cdot 4\text{H}_2\text{O}$. *Inorg. Chem. Commun.* 77, 72–76. doi: 10.1016/j.inoche.2017.02.001
- Arumuganathan, T., and Das, S. K. (2009). Discrete polyoxovanadate cluster into an organic free metal-oxide-based material: syntheses, crystal structures, and magnetic properties of a new series of lanthanide linked-POV compounds $[\{\text{Ln}(\text{H}_2\text{O})_6\}_2\text{As}_8\text{V}_{14}\text{O}_{42}(\text{SO}_3)] \cdot 8\text{H}_2\text{O}$ (Ln = La³⁺, Sm³⁺, and Ce³⁺). *Inorg. Chem.* 48, 496–507. doi: 10.1021/ic8002383
- Aureliano, M., and Crans, D. C. (2009). Decavanadate ($\text{V}_{10}\text{O}_{28}^{6-}$) and oxovanadates: oxometalates with many biological activities. *J. Inorg. Biochem.* 103, 536–546. doi: 10.1016/j.jinorgbio.2008.11.010
- Aureliano, M., Fraqueza, G., and Ohlin, C. A. (2013). Ion pumps as biological targets for decavanadate. *Dalton Trans.* 42, 11770–11777. doi: 10.1039/c3dt50462j
- Chatkon, A., Barres, A., Samart, N., Boyle, S. E., Haller, K. J., and Crans, D. C. (2014). Guanilylurea metformium double salt of decavanadate, $(\text{HGU}^+)_4(\text{HMet}^+)_2(\text{V}_{10}\text{O}_{28}^{6-}) \cdot 2\text{H}_2\text{O}$. *Inorg. Chem. Acta.* 420, 85–91. doi: 10.1016/j.ica.2013.12.031
- Chatkon, A., Chatterjee, P. B., Sedgwick, M. A., Haller, K. J., and Crans, D. C. (2013). Counterion affects interaction with interfaces: the antidiabetic drugs metformin and decavanadate. *Eur. J. Inorg. Chem.* 2013, 1859–1868. doi: 10.1002/ejic.201201345
- Chen, J.-J., Ye, J.-C., Zhang, X.-G., Symes, M. D., Fan, S.-C., Long, D.-L., et al. (2018). Design and performance of rechargeable sodium ion batteries, and symmetrical Li-ion batteries with supercapacitor-like power density based upon polyoxovanadates. *Adv. Energy Mater.* 8:1701021. doi: 10.1002/aenm.201701021
- Chen, L., Jiang, F., Lin, Z., Zhou, Y., Chengyang Yue, C., and Hong, M. (2005). Basket tetradecavanadate cluster with blue luminescence. *J. Am. Chem. Soc.* 127, 8588–8589. doi: 10.1021/ja0422209
- Colombo, F., Baggio, R., and Kampf, A. R. (2011). The crystal structure of elusive heumulite. *Can. Mineral.* 49, 849–864. doi: 10.3749/canmin.49.3.849
- Conte, V., and Floris, B. (2010). Vanadium catalyzed oxidation with hydrogen peroxide. *Inorg. Chim. Acta* 363, 1935–1946. doi: 10.1016/j.ica.2009.06.056
- Crans, D. C., Mahroof-Tahir, M., Anderson, O. P., and Miller, M. M. (1994). X-ray structure of $(\text{NH}_4)_6(\text{Gly-Gly})_2\text{V}_{10}\text{O}_{28} \cdot 4\text{H}_2\text{O}$ model studies for polyoxometalate–protein interactions. *Inorg. Chem.* 33, 5586–5590.
- Crans, D. C., Peters, B. J., Wu, X., and McLaughlan, C. C. (2017). Does anion-cation organization in Na⁺-containing X-ray crystal structures relate to solution interactions in inhomogeneous nanoscale environments: Sodium-decavanadate in solid state materials, minerals, and microemulsions. *Coordination Chem. Rev.* 344, 115–130. doi: 10.1016/j.ccr.2017.03.016
- Crans, D. C., Smee, J. J., Gaidamauskas, E., and Yang, L. (2004). The chemistry and biochemistry of vanadium and the biological activities exerted by vanadium compounds. *Chem. Rev.* 104, 849–902. doi: 10.1021/cr020607t
- da Silva, J. L. F., da Piedada, M. F. M., and Duarte, M. T. (2003). Decavanadates: a building-block for supramolecular assemblies. *Inorg. Chim. Acta* 356, 222–242. doi: 10.1016/S0020-1693(03)00385-2
- Derat, E., Kumar, D., Neumann, R., and Shaik, S. (2006). Catalysts for monooxygenations made from polyoxometalate: an iron(V)-oxo derivative of the Lindqvist anion. *Inorg. Chem.* 45, 8655–8663. doi: 10.1021/ic0610435
- Gao, F., and Hua, R. (2006). An efficient polyoxovanadate-catalyzed oxidative mineralization of phenols with 30% aqueous H_2O_2 . *Catalysis Commun.* 7, 391–393. doi: 10.1016/j.catcom.2005.12.013
- Guo, Y., Wang, Y., Hu, C., Wang, Y., Wang, E., Zhou, Y., et al. (2000). Microporous polyoxometalates POMs/SiO₂: synthesis and photocatalytic degradation of aqueous organochlorine pesticides. *Chem. Mater.* 12, 3501–3508. doi: 10.1021/cm000074
- Hill, C. L. (2007). Progress and challenges in polyoxometalate-based catalysis and catalytic materials chemistry. *J. Mol. Catalysis A Chem.* 262, 2–6. doi: 10.1016/j.molcata.2006.08.042
- Huang, X., Li, J., Shen, G., Xin, N., Lin, Z., Chi, Y., et al. (2018). Three Pd-decavanadates with a controllable molar ratio of Pd to decavanadate and their heterogeneous aerobic oxidation of benzylic C–H bonds. *Dalton Trans.* 47, 726–733. doi: 10.1039/C7DT03898D
- Hughes, J. M., Schindler, M., and Francies, C. A. (2005). The C2/m disordered structure of pascoite, $\text{Ca}_3(\text{V}_{10}\text{O}_{28}) \cdot 17\text{H}_2\text{O}$. *Can. Mineral.* 43, 1379–1386. doi: 10.2113/gscanmin.43.4.1379
- Hughes, J. M., Schindler, M., Rakovan, J., and Cureton, F. E. (2002). The crystal structure of hummerite. $\text{KMg}(\text{V}_5\text{O}_{14}) \cdot 8\text{H}_2\text{O}$: bonding between the $[\text{V}_{10}\text{O}_{28}]^{6-}$ structural unit and the $\{\text{K}_2\text{Mg}_2(\text{H}_2\text{O})_{16}\}^{6+}$ interstitial complex. *Can. Mineral.* 40, 1429–1435. doi: 10.2113/gscanmin.40.5.1429
- Hughes, J. M., Wise, W. S., Gunter, M. E., Morton, J. P., and Rakovan, J. (2008). A new decavanadate mineral species from the vanadium Queen Mine, La Sal district, Utah: description, atomic arrangement, and relationship to the pascoite group of minerals. *Can. Mineral.* 46, 1365–1372. doi: 10.3749/canmin.46.5.1365
- Kampf, A. R., Hughes, J. M., Marty, J., and Brown, F. H. (2013a). Nashite, $\text{Na}_3\text{Ca}_2([\text{V}_9^{3+}\text{V}_1^{4+}]\text{O}_{28}) \cdot 24\text{H}_2\text{O}$, a new mineral species from the Yellow Cat Mining District, Utah and the slick rock mining district, Colorado: crystal structure and descriptive mineralogy. *Can. Mineral.* 51, 27–37. doi: 10.3749/canmin.51.1.27
- Kampf, A. R., Hughes, J. M., Marty, J., Gunter, M. E., and Nash, B. (2011a). Rakovanite, $\text{Na}_3\{\text{H}_3[\text{V}_{10}\text{O}_{28}]\} \cdot 15\text{H}_2\text{O}$, a new species of the pascoite family with a protonated decavanadate polyanion. *Can. Mineral.* 49, 889–898. doi: 10.3749/canmin.49.2.595
- Kampf, A. R., Hughes, J. M., Marty, J., and Nash, B. (2011b). Gunterite, $\text{Na}_4(\text{H}_2\text{O})_{16}(\text{H}_2\text{V}_{10}\text{O}_{28}) \cdot 6\text{H}_2\text{O}$, a new mineral with a doubly-protonated decavanadate polyanion: crystal structure and descriptive mineralogy. *Can. Mineral.* 49, 1243–1251. doi: 10.3749/canmin.49.5.1243
- Kampf, A. R., Hughes, J. M., Marty, J., and Nash, B. (2012). Postite, $\text{Mg}(\text{H}_2\text{O})_6\text{Al}_2(\text{OH})_2(\text{H}_2\text{O})_8(\text{V}_{10}\text{O}_{28}) \cdot 13\text{H}_2\text{O}$, a new mineral species from the La Sal mining district, Utah: crystal structure and descriptive mineralogy. *Can. Mineral.* 50, 45–53. doi: 10.3749/canmin.50.1.45
- Kampf, A. R., Hughes, J. M., Marty, J., and Nash, B. (2013b). Wernerbaurite, $\{[\text{Ca}(\text{H}_2\text{O})_7]_2(\text{H}_2\text{O})_2(\text{H}_3\text{O})_2\}[\text{V}_{10}\text{O}_{28}]$, and schindlerite, $\{[\text{Na}_2(\text{H}_2\text{O})_{10}](\text{H}_3\text{O})_4\}[\text{V}_{10}\text{O}_{28}]$, the first hydronium-bearing decavanadate minerals. *Can. Mineral.* 51, 297–312. doi: 10.3749/canmin.51.2.297
- Kampf, A. R., Hughes, J. M., Nash, B., and Marty, J. (2014). Kokinosite, $\text{Na}_2\text{Ca}_2(\text{V}_{10}\text{O}_{28}) \cdot 24\text{H}_2\text{O}$, a new decavanadate mineral species from the St. Jude Mine, Colorado: crystal structure and descriptive mineralogy. *Can. Mineral.* 52, 15–25. doi: 10.3749/canmin.52.1.15
- Kampf, A. R., and Steele, I. M. (2008). Magnesio-pascoite, a new member of the pascoite group: description and crystal structure. *Can. Mineral.* 46, 679–686. doi: 10.3749/canmin.46.3.679
- Khan, M. I., Yohannes, E., and Doedens, R. J. (2003). A novel series of materials composed of arrays of vanadium oxide container molecules, $\{\text{V}_{18}\text{O}_{42}(\text{X})\}(\text{X})\text{H}_2\text{O}$, Cl[−], Br[−]: synthesis and characterization of $\text{M}_2(\text{H}_2\text{N}(\text{CH}_2)_2\text{NH}_2)_5\{[\text{M}(\text{H}_2\text{N}(\text{CH}_2)_2\text{NH}_2)_2]_2\text{V}_{18}\text{O}_{42}(\text{X})\} \cdot 9\text{H}_2\text{O}$ (M = Zn, Cd). *Inorg. Chem.* 42, 3125–3129. doi: 10.1021/ic025889u
- Klemperer, W. G., Marquart, T. A., and Yaghi, O. M. (1992). New directions in polyvanadate chemistry: from cages and clusters to baskets, belts, bowls, and barrels. *Angew. Chem.* 31, 49–51. doi: 10.1002/anie.199200491
- Koene, B. E., Taylor, N. J., and Nazar, L. F. (1999). An inorganic tire-tread lattice: hydrothermal synthesis of the layered vanadate $[\text{N}(\text{CH}_3)_4][\text{V}_{18}\text{O}_{46}]$ with a supercell structure. *Angew. Chem. Int. Ed.* 38, 2888–2891. doi: 10.1002/(SICI)1521-3773
- Kulikov, V., and Meyer, G. (2013). A new strategy for the synthetic assembly of inorganic-organic silver(I)-polyoxometalate hybrid structures employing noncovalent interactions between theobromine ligands. *Cryst. Growth Des.* 13, 2916–2927. doi: 10.1021/cg400335y
- Kwon, T., Tsigdinos, G. A., and Pinnavaia, T. J. (1988). Pillaring of layered double hydroxides (LDHs) by polyoxometalate anions. *J. Am. Chem. Soc.* 110, 3653–3654. doi: 10.1021/ja00219a048
- Lechner, M., Güttel, R., and Streb, C. (2016). Challenges in polyoxometalate-mediated aerobic oxidation catalysis: catalyst development meets reactor design. *Dalton Trans.* 45, 16716–16726. doi: 10.1039/c6dt03051c
- Liu, S., Tian, J., Wang, L., Zhang, Y., Luo, Y., Li, H., et al. (2012). Fast and sensitive colorimetric detection of H_2O_2 and glucose: a strategy based on polyoxometalate clusters. *ChemPlusChem* 77, 541–544. doi: 10.1002/cplu.201200051
- Marques, M. P. M., Gianolio, D., Ramos, S., de Carvalho, L. A. E., and Aureliano, M. (2017). An EXAFS approach to the study of polyoxometalate–protein interactions: the case of decavanadate–Actin. *Inorg. Chem.* 56, 10893–10903. doi: 10.1021/acs.inorgchem.7b01018

- Martín-Caballero, J., San José Wéry A., Reinoso, S., Artetxe, B., San Felices, L. E., Bakkali, B. et al. M. (2016). A robust open framework formed by decavanadate clusters and copper(II) complexes of macrocyclic polyamines: permanent microporosity and catalytic oxidation of cycloalkanes. *Inorg. Chem.* 55, 4970–4979. doi: 10.1021/acs.inorgchem.6b00505
- Mestiri, I., Ayed, B., and Haddad, A. (2013). Two novel compounds built up of decavanadate clusters and transition-metal complexes: synthesis and structure. *J. Clust. Sci.* 24, 85–96. doi: 10.1007/s10876-012-0517-4
- Müller, A., Krickemeyer, E., Penk, M., Walberg, H.-J., and Bogge, H. (1987). Spherical mixed-valence $[V_{15}O_{36}]^{5-}$, an example from an unusual cluster family. *Angew. Chem.* 26, 1045–1046. doi: 10.1002/anie.198710451
- Müller, A., Penk, M., Rohljl, R., Krickemeyer, E., and Döring, J. (1990). Topologically interesting cages for negative ions with extremely high “coordination number”: an unusual property of V-O clusters. *Angew. Chem. Int. Ed.* 29, 926–927. doi: 10.1002/anie.199009261
- Mukhopadhyay, S., Debgupta, J., Singh, C., Kar, A., and Das, S. K. (2018). A Keggin polyoxometalate shows water oxidation activity at neutral pH: POM@ZIF-8, an efficient and robust electrocatalyst. *Angew. Chem. Int. Ed.* 57, 1918–1923. doi: 10.1002/anie.201711920
- Müller, A., Sessoli, R., Krickemeyer, E., Böge, H., Meyer, J., Gatteschi, D., et al. (1997). Polyoxovanadates: high-nuclearity spin clusters with interesting host-guest systems and different electron populations. Synthesis, spin organization, magnetochemistry, and spectroscopic studies. *Inorg. Chem.* 36, 5239–5250. doi: 10.1021/ic9703641
- Nashhajian, H., Amini, M., Farnia, S. M. F., Sheykhi, A., Sahin, O., and Okan Zafer Yeşilel, O. Z. (2017). A new decavanadate polyoxovanadate nanocluster: synthesis, characterization and rapid adsorption of methylene blue. *J. Coord. Chem.* 70, 2940–2949. doi: 10.1080/00958972.2017.1383601
- Omwoma, S., Gore, C. T., Ji, Y., Hu, C., and Song, Y.-F. (2015). Environmentally benign polyoxometalate materials. *Coordination Chem. Rev.* 286, 17–29. doi: 10.1016/j.ccr.2014.11.013
- Pope, M. T., and Müller, A. (1991). Polyoxometalate chemistry: an old field with new dimensions in several disciplines. *Angew. Chem. Int. Ed.* 30, 34–38. doi: 10.1002/anie.199100341
- Rakovan, J., Schmidt, G. R., Gunter, M., Nash, B., Kampf, A. R., Marty, J., et al. (2011). Hughesite, $Na_3Al(V_{10}O_{28}) \cdot 22H_2O$, a new member of the pascoite family of minerals from the Sunday mine, San Miguel County, Colorado. *Can. Mineral.* 49, 1253–1265. doi: 10.3749/canmin.49.5.1253
- Rao, A. S., Arumuganathan, T., Shivaiah, V., and Das, S. K. (2011). Polyoxometalates: toward new materials. *J. Chem. Sci.* 123, 229–239. doi: 10.1007/s12039-011-0115-2
- Rehder, D. (2013). The future of/for vanadium. *Dalton Trans.* 42, 11749–11761. doi: 10.1039/c3dt50457c
- Sánchez-Lombardo, I., Sánchez-Lara, E., Pérez-Benítez, A., Mendoza, Á., Bernés, S., and González-Vergara, E. (2014). Synthesis of metforminium(2+) decavanadates—crystal structures and solid-state characterization. *Eur. J. Inorg. Chem.* 2014, 4581–4588. doi: 10.1002/ejic.201402277
- Sheldrick, G. M. (1997). *SHELX-97, Program for Crystal Structure Solution and Refinement*. Göttingen: University of Göttingen.
- Vazylyev, M., Sloboda-Rozner, D., Haimov, A., Maayan, G., and Neumann, R. (2005). Strategies for oxidation catalyzed by polyoxometalates at the interface of homogeneous and heterogeneous catalysis. *Topics Catalysis* 34, 93–99. doi: 10.1007/s11244-005-3793-5
- Villa, A. L., Vos, D. E. D., Verpoort, F., Sels, B. F., and Jacobs, P. A. (2001). A Study of V-pillared layered double hydroxides as catalysts for the epoxidation of terpenic unsaturated alcohols. *J. Catalysis* 198, 223–231. doi: 10.1006/jcat.2000.3104
- Walsh, J. J., I, Bond, A. M., Forster, R. J., and Keyes, T. E. (2016). Hybrid polyoxometalate materials for photo(electro-) chemical applications. *Coordination Chem. Rev.* 306, 217–234. doi: 10.1016/j.ccr.2015.06.016
- Wang, M., Sun, W., Pang, H., Ma, H., Yu, J., Zhang, Z., et al. (2016). Tuning the microstructures of decavanadate-based supramolecular hybrids via regularly changing the spacers of bis(triazole) ligands. *J. Solid State Chem.* 235, 175–182. doi: 10.1016/j.jssc.2015.12.033
- Winkler, P. A., Huang, Y., Sun, W., Juan Du, J., and Lü, W. (2017). Electron cryo-microscopy structure of a human TRPM4 channel. *Nature* 552, 200–204. doi: 10.1038/nature24674
- Xie, F., Ma, F., Cui, S., Shu, G., Zhang, S., Tong Wang, T., et al. (2018). Synthesis and polypyrrole-loading study of antifungal medicine fluconazole functionalized Keggin polyoxotungstates. *J. Coordination Chem.* 71, 78–88. doi:10.1080/00958972.2018.1427234
- Yerra, S., and Das, S. K. (2017). Organic free decavanadate based materials: inorganic linkers to obtain extended structures. *J. Mol. Struct.* 1146, 23–31. doi: 10.1016/j.molstruc.2017.05.097
- Yi, Z., Yu, X., Xia, W., Zhao, L., Yang, C., Chen, Q., et al. (2010). Influence of the steric hindrance of organic amines on the supramolecular network based on polyoxovanadates. *CrystEngComm* 12, 242–249. doi: 10.1039/b916793p
- Zhou, Y., Chen, G., Long, Z., and Wang, J. (2014). Recent advances in polyoxometalate-based heterogeneous catalytic materials for liquid-phase organic transformations. *RSC Adv.* 4, 42092–42113. doi: 10.1039/C4RA05175K

Conflict of Interest Statement: The authors declare that the research was conducted in the absence of any commercial or financial relationships that could be construed as a potential conflict of interest.

Copyright © 2018 Amanchi and Das. This is an open-access article distributed under the terms of the Creative Commons Attribution License (CC BY). The use, distribution or reproduction in other forums is permitted, provided the original author(s) and the copyright owner(s) are credited and that the original publication in this journal is cited, in accordance with accepted academic practice. No use, distribution or reproduction is permitted which does not comply with these terms.



A Multifunctional Dual-Luminescent Polyoxometalate@Metal-Organic Framework EuW₁₀@UiO-67 Composite as Chemical Probe and Temperature Sensor

William Salomon¹, Anne Dolbecq¹, Catherine Roch-Marchal¹, Grégoire Paille^{1,2}, Rémi Dessapt³, Pierre Mialane^{1*} and Hélène Serier-Brault^{3*}

¹ Institut Lavoisier de Versailles, UMR CNRS 8180, Université Paris-Saclay, Université de Versailles Saint-Quentin, Versailles, France, ² Laboratoire de Chimie des Processus Biologiques, UMR CNRS 8229, Collège de France, Université Pierre et Marie Curie, PSL Research University, Paris, France, ³ Institut des Matériaux Jean Rouxel, CNRS, Université de Nantes, Nantes, France

OPEN ACCESS

Edited by:

Tatjana N. Parac-Vogt,
KU Leuven, Belgium

Reviewed by:

David Parker,
Durham University, United Kingdom
Bart Bueken,
KU Leuven, Belgium

*Correspondence:

Pierre Mialane
pierre.mialane@uvsq.fr
Hélène Serier-Brault
helene.brault@cnrs-imn.fr

Specialty section:

This article was submitted to
Inorganic Chemistry,
a section of the journal
Frontiers in Chemistry

Received: 28 June 2018

Accepted: 28 August 2018

Published: 24 September 2018

Citation:

Salomon W, Dolbecq A, Roch-Marchal C, Paille G, Dessapt R, Mialane P and Serier-Brault H (2018) A Multifunctional Dual-Luminescent Polyoxometalate@Metal-Organic Framework EuW₁₀@UiO-67 Composite as Chemical Probe and Temperature Sensor. *Front. Chem.* 6:425. doi: 10.3389/fchem.2018.00425

The luminescent [EuW₁₀O₃₆]⁹⁻ polyoxometalate has been introduced into the cavities of the highly porous zirconium luminescent metal-organic framework UiO-67 via a direct synthesis approach, affording the EuW₁₀@UiO-67 hybrid. Using a combination of techniques (TGA, BET, elemental analysis, EDX mapping,...) this new material has been fully characterized, evidencing that it contains only 0.25% in europium and that the polyoxometalate units are located inside the octahedral cavities and not at the surface of the UiO-67 crystallites. Despite the low amount of europium, it is shown that EuW₁₀@UiO-67 acts as a solid-state luminescent sensor for the detection of amino-acids, the growth of the emission intensity globally following the growth of the amino-acid pKa. In addition, EuW₁₀@UiO-67 acts as a sensor for the detection of metallic cations, with a high sensitivity for Fe³⁺. Noticeably, the recyclability of the reported material has been established. Finally, it is shown that the dual-luminescent EuW₁₀@UiO-67 material behave as a self-calibrated-ratiometric thermometer in the physiological range.

Keywords: polyoxometalate, metal-organic framework, sensor, ratiometric luminescent thermometer, europium

INTRODUCTION

Polyoxometalate (POM)-based photosystems are currently undergoing a remarkable development due to their high relevance in photocatalysis or their ability to act as efficient photoswitches or fluorescent probes (Han et al., 2015; Saad et al., 2015; Holmes-Smith et al., 2016; Chen et al., 2017; Natali et al., 2017). Focusing on this last topic, both materials based on purely inorganic POMs incorporating luminescent metallic centers and hybrid organic-inorganic entities bearing grafted organic optically active moieties have been elaborated. For example, fluorescent microspheres prepared from a Lindqvist POM covalently connected to pyrene groups have been used for the detection of foodborne pathogens (Ju et al., 2016). Inorganic tungsten and/or molybdenum POMs incorporating rare earth (RE) centers have also been shown to act as efficient luminescent probes. For instance, cryogenic optical thermal probes made of polyoxomolybdate building blocks incorporating Eu^{III} and Tb^{III} ions have been recently reported (Kaczmarek et al., 2017). The

luminescence of such RE-incorporating POMs is also very sensitive to the chemical environment. This can be illustrated considering the works devoted to the interaction between proteins and the seminal $[\text{EuW}_{10}\text{O}_{36}]^{9-}$ (EuW_{10}) europium decatungstate characterized by narrow emission bands, a large Stokes shift and a long lifetime (Sugeta and Yamase, 1993). The characteristic emission of the europium decatungstate located at ca. 620 nm is strongly enhanced in presence of bovine or human serum albumin without any alteration of the secondary structure of the protein, showing that such simple molecular oxides could act as biological optical labeling agents (Hungerford et al., 2008; Zheng et al., 2010). Accordingly, Wu et al. showed that hybrid nanospheres made of arginine/lysine-rich peptides and EuW_{10} are characterized by a large Eu^{III} luminescence enhancement. Using a combination of techniques, it was evidenced that the observed phenomenon was due to the exclusion of the hydration water molecules from the secondary coordination sphere of EuW_{10} caused by the strong electrostatic and hydrogen bond interactions between POMs and basic amino-acids (AAs) (Zhang et al., 2015). Inversely, it was found that acidic AAs quench the luminescence while nonpolar AAs do not significantly influence the optical properties of the POM (Zhang et al., 2016). The processing of EuW_{10} by incorporation into films has been achieved, allowing the fabrication of moisture-responsive systems (Clemente-León et al., 2010; Xu et al., 2011; Qiu et al., 2015). Based on all these results, we have undertaken to elaborate a multi-functional hybrid system where the EuW_{10} POM is incorporated in the cavities of a metal-organic framework (MOF). This class of 3D coordination networks represents a unique platform for the development of solid-state luminescent materials due to their crystalline nature, permanent porosity, chemical tunability and robustness (Fernando-Soria et al., 2012; Hu et al., 2014; Lustig et al., 2017). To date, POM@MOF materials have been mainly synthesized for catalytic purposes. Two main synthetic strategies have been considered: (i) a one-pot strategy, where the precursors allowing the formation of the MOF and the POM are mixed all together, the MOF being built around the POM (direct synthesis) and (ii) the pre-formed MOF is impregnated with a solution of the POM (two-step strategy). Such materials have shown their efficiency for catalytic reactions ranging from the oxidation of alkylbenzene (Sun et al., 2016) to the C-H activation of nitrile (Shi et al., 2016) and water oxidation (Mukhopadhyay et al., 2018; Paille et al., 2018). Interestingly, it has also been shown that a single-molecule magnet iron POM isolated in the cavities of a diamagnetic MOF preserves its magnetic properties (Salomon et al., 2016). Besides, while Ln-MOFs and Ln-doped MOFs have been largely studied, the encapsulation of a well-defined inorganic luminescent compound in MOFs for sensing and detection has been rarely described (Cui et al., 2015; Wu et al., 2017). The white water-stable and highly porous zirconium MOF UiO-67 (Cavka et al., 2008) has been selected, and the ability of the EuW_{10} @UiO-67 composite to act as sensor for metallic cations and AAs was investigated. Considering the dual-luminescent properties of EuW_{10} @UiO-67—arising from both the inserted POMs and the 3D host network—its aptitude to act as a self-calibrated temperature sensor has also been explored.

EXPERIMENTAL SECTION

Physical Methods

Infrared (IR) spectra were recorded on a Nicolet 30 ATR 6700 FT spectrometer. Powder X-Ray diffraction data were obtained on a Bruker D5000 diffractometer using Cu radiation (1.54059 Å). C, H, N elemental analyses were performed by the Service de microanalyse of CNRS, 91198 Gif-sur-Yvette Cedex France. EDX measurements were performed on a JEOL JSM 5800 LV apparatus. Thermogravimetry analyses (TGA) were performed on a Mettler Toledo TGA/DSC 1, STARe System apparatus under oxygen flow (50 mL min⁻¹) at a heating rate of 5°C min⁻¹ up to 800°C. N₂ adsorption isotherms were obtained at 77 K using a BELsorp Mini (Bel, Japan). Prior to the analysis, approximately 30 mg of sample were evacuated at 90°C under primary vacuum overnight. Room-temperature and temperature-dependant photoluminescence spectra were recorded on a Jobin-Yvon Fluorolog 3 fluorometer equipped with a CCD camera (excitation source: 450 W Xe arc lamp). The temperature was controlled by a nitrogen-closed cycle cryostat with vacuum system measuring and an Oxford Instrument ITC503S auto-tuning temperature controller with a resistance heater. The temperature can be adjusted from ca. 77 to 300 K with a maximum accuracy of 0.1 K. The sample temperature was fixed to a particular value using the auto-tuning temperature controller; after waiting 5 min to thermalize the sample, five consecutive steady-state emission spectra were measured for each temperature. The luminescence sensing experiments were carried out by introducing EuW_{10} @UiO-67 powder (1.5 mg) into aqueous solutions (3 mL, 10⁻² mol L⁻¹) of MCl_x ($\text{M}^{n+} = \text{Na}^+, \text{K}^+, \text{Ni}^{2+}, \text{Cr}^{3+}, \text{Cu}^{2+}, \text{Al}^{3+}, \text{Mn}^{2+}, \text{and Fe}^{3+}$) or into MES/NaOH (MES = 2-(N-morpholino)ethanesulfonic acid) buffer solutions (pH = 6) of amino-acids (lysine, L-glycine, β-alanine, L-histidine, L-tryptophane, γ-aminobutyric acid, L-arginine) at room temperature. The mixtures were magnetically stirred during 5 min before collecting the luminescence data.

Synthetic Procedures

Chemicals and Reagents

All available chemicals were purchased from major chemical suppliers and used as received. The Lindqvist-type europium decatungstate $\text{Na}_9[\text{EuW}_{10}\text{O}_{36}] \cdot 32\text{H}_2\text{O}$ (EuW_{10}) (Sugeta and Yamase, 1993) and the UiO-67 MOF (Salomon et al., 2015) have been synthesized as previously described.

Synthesis of $\text{DODA}_9[\text{EuW}_{10}\text{O}_{36}] \cdot (\text{DODACl})_2$ ($(\text{DODA})\text{EuW}_{10}$)

The dimethyldioctadecylammonium (DODA) salt of EuW_{10} was synthesized according to a procedure developed by L. Wu. et al. for $(\text{DODA})_{13}\text{H}_2[\text{Eu}(\text{BW}_{11}\text{O}_{39})_2] \cdot 25\text{H}_2\text{O}$ (Li et al., 2008). A stoichiometric amount of DODA.Cl (1 equivalent by charge, 3.281 g, 5.6 mmol) was dissolved in 20 mL of chloroform. The solution was then added dropwise to a 10 mL aqueous solution of $\text{Na}_9[\text{EuW}_{10}\text{O}_{36}] \cdot 32\text{H}_2\text{O}$ (2.082 g, 0.62 mmol) under stirring. The mixture was kept under vigorous stirring for 2 h. The organic phase was separated and dried with MgSO_4 . The solvent was then evaporated with a rotary evaporator to recover

the DODA salt (3.9 g, yield = 72%). Anal. Calc. (found) for (DODA)₉[EuW₁₀O₃₆] \cdot (DODACl)₂ (C₄₁₈H₈₈₀N₁₁EuW₁₀O₃₆Cl₂; M.W.: 8,699 g mol⁻¹): C 57.71 (57.45), H 10.20 (10.51), N 1.77 (1.66). IR (ATR): ν (cm⁻¹) 2,916 (s), 2,849 (s), 1,466 (m), 940 (m), 922 (m), 836 (m), 753 (s), 718 (s). EDX measurements: atomic ratio calc. (exp.): W/Eu 10.0 (11.5).

Synthesis of

[Zr₆O₄(OH)₄][C₁₄H₈O₄]_{5.82}[EuW₁₀O₃₆]_{0.04}·7H₂O (EuW₁₀@UiO-67)

ZrCl₄ (116 mg, 0.5 mmol), biphenyl-dicarboxylic acid (121 mg, 0.5 mmol), (DODA)EuW₁₀ (429 mg, 4.93 \cdot 10⁻⁵ mol) and benzoic acid (1.83 g, 15 mmol) were briefly stirred in 10 mL of dimethylformamide (DMF) inside a 23 mL polytetrafluoroethylene-lined vessel. Hydrochloric acid 37% (83 μ L) was added, and the mixture was heated at 120°C for 24 h. The solid was isolated by filtration of the hot mixture and thoroughly washed with DMF, chloroform, dry acetone and dried in an oven at 120°C overnight (yield: 118 mg, 60% based on Zr, 4% based on POM). Anal. Calc. (found) for [Zr₆O₄(OH)₄][C₁₄H₈O₄]_{5.82}[EuW₁₀O₃₆]_{0.04}·7H₂O (C_{81.2}H_{64.4}O_{39.64}Zr₆W_{0.4}Eu_{0.04}; M.W.: 2,306 g mol⁻¹): C 42.40 (42.50), H 2.82 (3.21). IR (ATR): ν (cm⁻¹) 1,593 (m), 1,545 (m), 1,503 (w), 1,409 (s), 1,180 (w), 770 (m), 754 (w), 736 (m), 704 (m), 669 (s), 455 (s). EDX measurements: atomic ratio calc. (exp.): Zr/W 15.0 (15.6), Eu/W 0.10 (0.13).

RESULTS AND DISCUSSION

Synthesis and Characterization of the EuW₁₀@UiO-67 Material

We recently evidenced that the [PW₁₂O₄₀]³⁻ Keggin (Salomon et al., 2015), the [P₂W₁₈O₆₂]⁶⁻ Dawson (Salomon et al., 2015) as well as the sandwich [(FeW₉O₃₄)₂Fe₄(H₂O)₂]¹⁰⁻ (Salomon et al., 2016) polyanions can be incorporated into the pores of the Zr(IV) biphenyldicarboxylate UiO-67 MOF. Considering the smallest dimensions of these POMs (ca. 12 Å) and the size of the triangular windows of the microporous MOF (ca. 8 Å), no impregnation of the molecular units into the preformed MOF could be envisaged and the POM@UiO-67 materials were obtained *via* a direct synthesis approach (Salomon et al., 2015, 2016). The same approach has been considered here, as the smallest dimension of EuW₁₀ is ca. 9 Å. The title compound (**Figure 1A**) was thus synthesized by heating at 120°C in DMF a mixture of the dimethyldioctadecyl ammonium (DODA) salt of the POM and the precursors of UiO-67, affording EuW₁₀@UiO-67 in good yield (60% based on Zr) as a white crystalline powder.

As observed in **Figure S1**, the experimental powder X-ray diffraction (PXRD) pattern of EuW₁₀@UiO-67 and simulated PXRD pattern of UiO-67 are analogous, showing that the formation of the UiO-67 network can be obtained in the presence of the POM in the synthetic medium. In addition, the experimental PXRD pattern of the as-synthesized EuW₁₀@UiO-67 and of EuW₁₀@UiO-67 stirred for 1 h in water at room

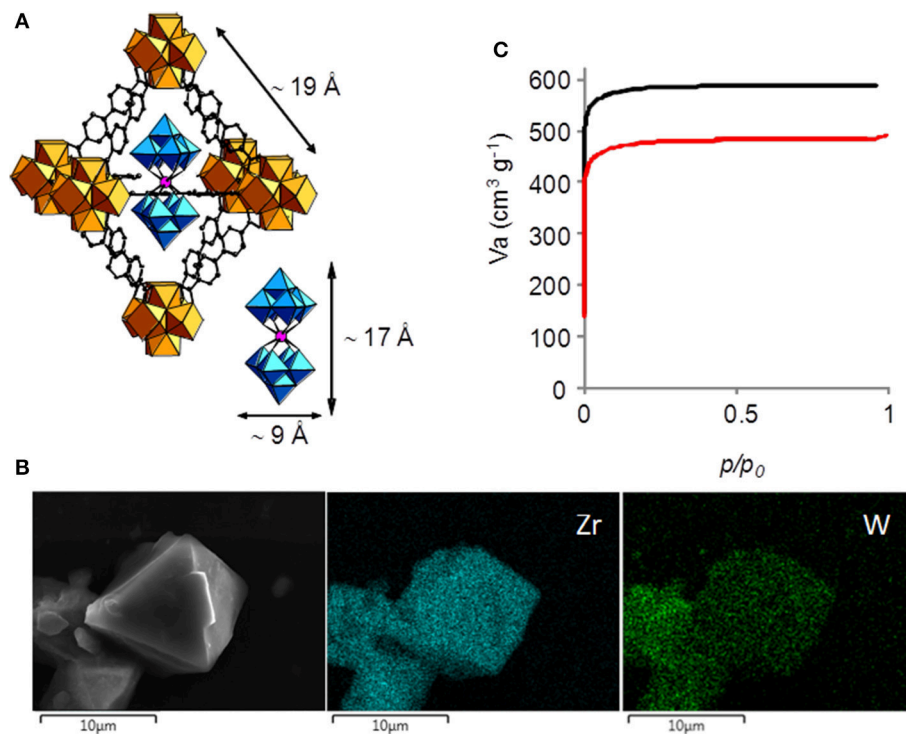


FIGURE 1 | (A) Polyhedral representations of EuW₁₀ and an octahedral cage of EuW₁₀@UiO-67; blue octahedra: WO₆, pink sphere: Eu, orange polyhedra: ZrO₆, black sphere: C, **(B)** SEM image of crystals of EuW₁₀@UiO-67 and EDS mapping for zirconium and tungsten, **(C)** N₂ adsorption/desorption isotherms (77 K, P/P₀ = 1 atm.) of UiO-67 (black) and the EuW₁₀@UiO-67 composite (red).

temperature are similar, showing that the hybrid is stable in such conditions. EDS mapping evidences both the presence of MOF and POM (**Figure 1B**). EDX measurements combined with elemental analysis allowed to propose for EuW₁₀@UiO-67 the formula $[\text{Zr}_6\text{O}_4(\text{OH})_4][\text{C}_{14}\text{H}_8\text{O}_4]_{5.82}[\text{EuW}_{10}\text{O}_{36}]_{0.04} \cdot 7\text{H}_2\text{O}$, indicating that the material only contains ca. 0.25 wt % in europium. The TGA curve (**Figure S2**) reveals steps that are attributed to water removal (weight loss 5.0%, calculated 5.5%), linker decomposition and formation of inorganic oxides (weight loss 58.6%, calculated 60.5%). The IR spectrum (**Figure S3**) confirms that no DODA counterion is present in the MOF, the negative charges introduced by the POMs being compensated by linker deficiencies (Katz et al., 2013). Also, no vibration at ca. $1,680\text{ cm}^{-1}$ is observed, indicating that no free benzoic acid is present in the cavities of the MOF. In addition, it can be deduced from the formula that only 1/25 of the octahedral cavities are occupied by EuW₁₀, this loading being lower than for $[(\text{FeW}_9\text{O}_{34})_2\text{Fe}_4(\text{H}_2\text{O})_2]^{10-}$ (1/10) (Salomon et al., 2016). The N₂ sorption isotherms experiments were conducted for both UiO-67 and EuW₁₀@UiO-67 (**Figure 1C** and **Table S1**). As expected, the surface area is lower for EuW₁₀@UiO-67 ($S_{\text{BET}} = 1,900\text{ m}^2\cdot\text{g}^{-1}$) than for UiO-67 ($S_{\text{BET}} = 2,400\text{ m}^2\cdot\text{g}^{-1}$), since a heavy compound representing 5% of the sample weight has been added. The value of the normalized specific surface area, taking into account the contribution of the mass of UiO-67 in EuW₁₀@UiO-67 ($2,400 \times 0.95 = 2,280\text{ m}^2\cdot\text{g}^{-1}$), is significantly different from the experimental value of EuW₁₀@UiO-67 ($1,900\text{ m}^2\cdot\text{g}^{-1}$), suggesting that EuW₁₀ is located inside the octahedral cavities and not at the surface of the UiO-67 particles (**Table S1**). In addition, it is observed that the porous distribution (**Figure S4**) is not significantly modified, evidencing only one peak since the hexagonal and tetrahedral cavities are connected by the same triangular windows (Barrett et al., 2012).

Photophysical Characterization of EuW₁₀@UiO-67

The photophysical properties of EuW₁₀@UiO-67 were thoroughly investigated at room temperature. Firstly, the solid-state photoluminescence (PL) properties of the pure EuW₁₀ and UiO-67 compounds were studied separately before considering the EuW₁₀@UiO-67 composite. As expected, the excitation spectrum of EuW₁₀ (**Figure S5**) is composed of a broad band centered at 280 nm, corresponding to the O→W ligand-to-metal charge transfer (LMCT) band, and the sharp lines characteristic of the f-f transitions of the Eu³⁺ ion (Yamase and Sugeta, 1993). Under photoexcitation at $\lambda_{\text{exc}} = 280\text{ nm}$, EuW₁₀ shows a red luminescence (**Figures S5 and S6**) associated to the typical $^5\text{D}_0 \rightarrow ^7\text{F}_{0-4}$ transitions of Eu³⁺ ions in the 587–700 nm range, indicating an efficient intramolecular energy transfer from ligand to Eu³⁺. As this latter ion is located in a slightly distorted square antiprismatic site close to D_{4d} point symmetry, the $^5\text{D}_0 \rightarrow ^7\text{F}_2$ electric dipole transition (611–620 nm) gets a very weak intensity compared to that of the $^5\text{D}_0 \rightarrow ^7\text{F}_1$ magnetic dipole transition (Capobianco et al., 1990; Nogami

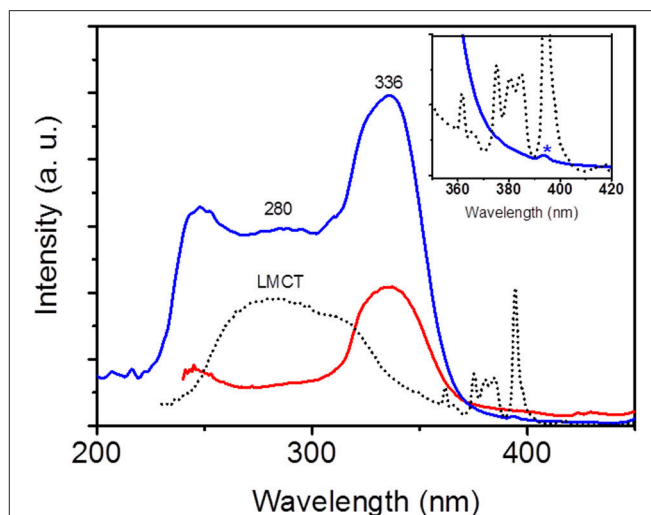


FIGURE 2 | Room-temperature excitation spectra of EuW₁₀@UiO-67 monitored at $\lambda_{\text{em}} = 471\text{ nm}$ (red line) and at $\lambda_{\text{em}} = 700\text{ nm}$ (blue line) and excitation spectrum of EuW₁₀ (black dotted line) monitored at $\lambda_{\text{em}} = 700\text{ nm}$. Inset: the asterisk represents the $^7\text{F}_0 \rightarrow ^5\text{L}_6$ excitation band of the Eu³⁺ ion.

and Abe, 1996). Upon UV excitation at 254 nm, the UiO-67 MOF exhibits a blue emission (**Figure S6**). Its PL spectrum under excitation at 336 nm (**Figure S7**) displays a broad band in the 450–600 nm range, with a maximum wavelength located at 471 nm, attributed to intraligand $\pi \rightarrow \pi^*$ transitions centered on the biphenyldicarboxylate linker. For the EuW₁₀@UiO-67 composite, the excitation spectrum, monitored within the $^5\text{D}_0 \rightarrow ^7\text{F}_4$ (700 nm) Eu³⁺ transition (**Figure 2**), shows the LMCT broad band ($\lambda_{\text{max}} = 280\text{ nm}$) and the weakly intense sharp lines of the Eu³⁺ f-f transitions of EuW₁₀ as well as the excitation bands of UiO-67 ($\lambda_{\text{max}} = 336\text{ nm}$). The presence of the LMCT band is a strong indication of the integrity of EuW₁₀ in the composite, whereas the presence of the excitation bands of UiO-67, within the $^5\text{D}_0 \rightarrow ^7\text{F}_4$ Eu³⁺ transition, quite evidences an intermolecular MOF-to-Eu³⁺ energy transfer. Then, upon UV excitation at 336 nm, the emission spectrum of EuW₁₀@UiO-67 corresponds to the association of the red emission of EuW₁₀ together with the UiO-67 blue one (**Figure 3**), and hence, the composite is a good violet emitter with color coordinates (x, y) equal to $x = 0.356$ and $y = 0.246$. Moreover, the intensity ratio of the $^5\text{D}_0 \rightarrow ^7\text{F}_2$ transition to the $^5\text{D}_0 \rightarrow ^7\text{F}_1$ transition is significantly increased compared to that observed for pure EuW₁₀. In addition, the symmetry-forbidden electric dipole $^5\text{D}_0 \rightarrow ^7\text{F}_0$ transition (580 nm) which does not appear in pure EuW₁₀ is distinguishable in the PL spectrum of EuW₁₀@UiO-67. These results unambiguously reveal that the site symmetry of the Eu³⁺ ion in EuW₁₀ decreases when the POM is introduced into the MOF pores (Sugeta and Yamase, 1993).

EuW₁₀@UiO-67 as Sensor for Metallic Cations and Amino-Acids

The luminescent sensing properties of EuW₁₀@UiO-67 were first investigated for the detection of metal ions (Na^+ , K^+ , Ni^{2+} ,

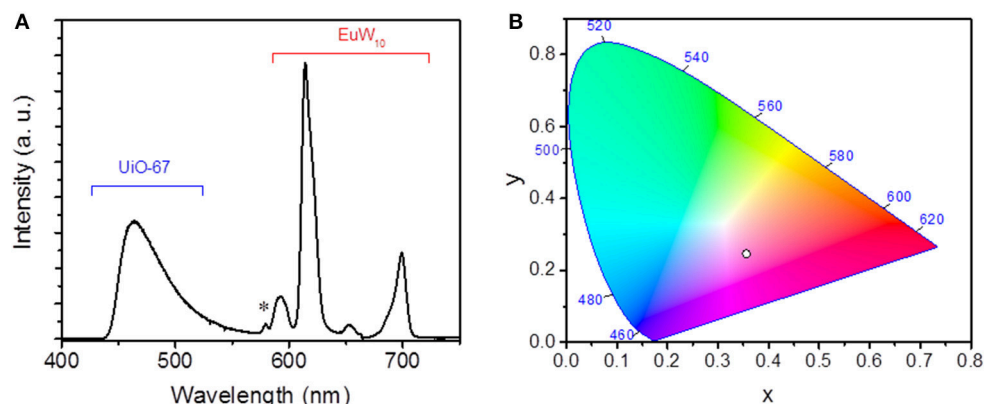


FIGURE 3 | (A) Room-temperature emission spectrum monitored at $\lambda_{\text{exc}} = 336$ nm of $\text{EuW}_{10}@\text{UiO}-67$. The asterisk highlights the $^5\text{D}_0 \rightarrow ^7\text{F}_0$ transition related to the Eu^{3+} ion; **(B)** CIE chromaticity diagram for $\text{EuW}_{10}@\text{UiO}-67$ excited at 336 nm.

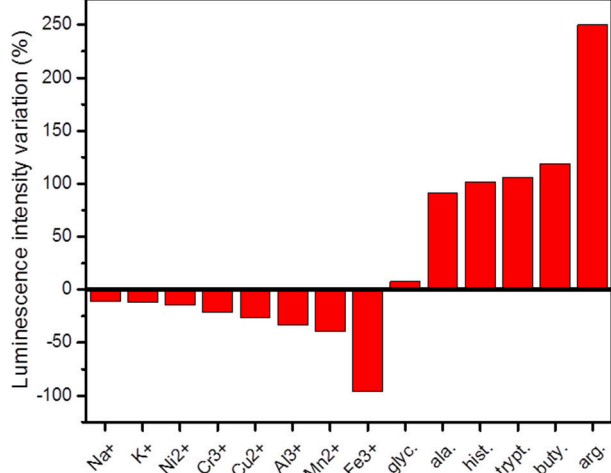


FIGURE 4 | Luminescence intensity variations of the $^5\text{D}_0 \rightarrow ^7\text{F}_2$ transition ($\lambda_{\text{exc}} = 336$ nm) of $\text{EuW}_{10}@\text{UiO}-67$ interacting with amino-acids MES/NaOH buffer solutions (glyc., glycine; ala., β -alanine; hist, L-histidine; trypt., L-tryptophan; buty., γ -aminobutyric acid; arg., L-arginine) and different metal ions aqueous solutions ($C = 10^{-2}$ mol.L $^{-1}$).

Cr^{3+} , Cu^{2+} , Al^{3+} , Mn^{2+} , and Fe^{3+}) present in aqueous solutions (10^{-2} M) as chloride salts. The PL properties of suspensions of $\text{EuW}_{10}@\text{UiO}-67$ into the metallic solutions ($8.5 \mu\text{M}$ in Eu^{3+}) were monitored at $\lambda_{\text{exc}} = 336$ nm and the luminescence intensity variations of the most intense $^5\text{D}_0 \rightarrow ^7\text{F}_2$ Eu^{3+} transition at 611 nm are depicted in **Figure 4** and **Figure S8a**. The presence of all studied metal ions in solution systematically induces a decrease of the luminescence intensity of the Eu^{3+} f-f bands compared to their intensity when $\text{EuW}_{10}@\text{UiO}-67$ is simply immersed in deionized water. The same effect is also observable on the organic ligand emission at 471 nm. Strikingly, Fe^{3+} ions can quench the whole emission of the composite, which becomes non-emissive under UV-light. This high sensitivity regarding Fe^{3+} ions offers an interesting perspective to use $\text{EuW}_{10}@\text{UiO}-67$

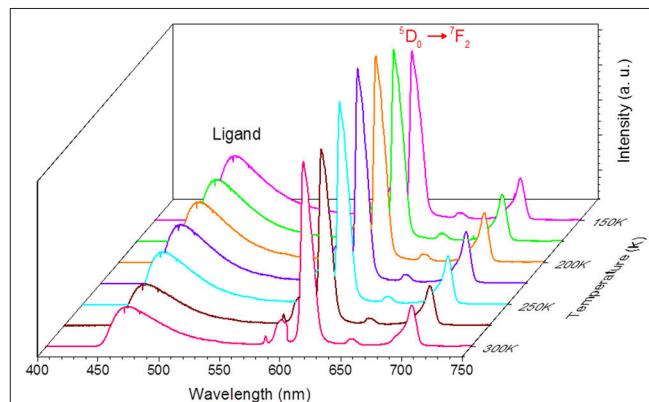


FIGURE 5 | Emission spectra of compound $\text{EuW}_{10}@\text{UiO}-67$ in the range 150–300 K with the excitation fixed at 336 nm.

as an efficient luminescent chemical probe for Fe^{3+} ions which play a relevant role in many biological processes (Xu and Yan, 2015). A study of the dependence of the quenching of the luminescence with the Fe^{3+} concentration was then conducted. The quenching effect can be quantitatively rationalized by the Stern-Volmer equation: $I_0/I = 1 + K_{\text{SV}}[\text{Fe}^{3+}]$, where I_0 and I are the fluorescence intensities of the $^5\text{D}_0 \rightarrow ^7\text{F}_2$ transition of the Eu^{3+} ion in the $\text{EuW}_{10}@\text{UiO}-67$ suspension in the absence or presence of Fe^{3+} , respectively. K_{SV} is the quenching constant, which is calculated as $2,667 \text{ L.mol}^{-1}$ with a very good linear correlation (R) of 0.999, indicating the strong quenching effect from Fe^{3+} (**Figure S9**). The concentration limit for the detection is estimated to be $37 \mu\text{M}$, corresponding to the concentration for which the fluorescence intensity variation is $<10\%$. To assess the robustness of the $\text{EuW}_{10}@\text{UiO}-67$ composite, we have checked its recyclability after immersion into a Fe^{3+} aqueous solution ($C = 10^{-2}$ M). The emission spectrum of the powder was monitored in the same conditions (**Figure S10**) before, directly after immersion, and after being washed several times with ultrapure water, filtered and dried under air. This study

highlights that after washing, the emission of the composite practically recovered its initial intensity, quite evidencing that the EuW₁₀@UiO-67 exhibits a robustness enabling to be reusable to detect Fe³⁺ ions in an aqueous solution. Nevertheless, while the XRD data of EuW₁₀@UiO-67 after immersion in Fe³⁺ aqueous solution are in accordance with the simulated UiO-67 pattern, a certain loss of crystallinity is observed (Figure S11). In short, although the amount of the EuW₁₀ emitter is weak into the MOF, the properties of the composite as a chemical probe is very promising with a recyclability, never investigated in these systems so far.

EuW₁₀@UiO-67 was also tested as chemical probe for basic amino-acids (AAs), such as glycine, β -alanine, L-histidine, L-tryptophan, L-arginine, and γ -aminobutyric acid (Table S2). EuW₁₀@UiO-67 (8.5 μ M in Eu³⁺) was dispersed in MES/NaOH (pH = 6) buffer solutions of AAs (10⁻² M) to further monitor the luminescence properties at $\lambda_{\text{exc}} = 336$ nm. The emission spectra are depicted in Figure S8b. As already noticed for the pure [Eu(SiW₁₀MoO₃₉)₂]¹³⁻ POM in homogeneous aqueous solutions (Li et al., 2014), distinct luminescence enhancements are observed when the EuW₁₀@UiO-67 material is in contact with the various AAs molecules (Figure 4). The arginine, which is the most basic AA of the investigated series, induces more than 2.5-fold enhancement of emission intensity. Moreover, the increase of the emission intensity globally follows the increase of the AA pKa and isoelectric point (Table S2). This is in line with the fact that the luminescence of Eu-based POMs is quenched by the surrounding water molecules, which are displaced in presence of protonated AAs due to electrostatic interactions and C-H...O contacts with the POM surface (Li et al., 2014). The recyclability of the EuW₁₀@UiO-67 composite after exposure to the arginine solution has been also investigated. The emission spectrum of the powder was monitored in the same conditions (Figure S12) before, directly after immersion, and after being washed several times with ultrapure water, filtered and dried under air. This study highlights that after washing, the emission of the composite practically recovered its initial intensity. However, the XRD data of EuW₁₀@UiO-67 after immersion in arginine aqueous solution also reveal a certain loss of crystallinity.

EuW₁₀@UiO-67 as Self-Calibrated-Ratiometric Luminescent Thermometer

As both the biphenyldicarboxylate linker of UiO-67 and EuW₁₀ act as emitters, we further evaluated the capability of EuW₁₀@UiO-67 to be used as a self-calibrated ratiometric luminescent thermometer. For that, the integrated areas of the ligand (I_{Ligand}) and ⁵D₀→⁷F₂ Eu³⁺ (I_{Eu}) emissions were used to define the thermometric parameter $\Delta = I_{\text{Ligand}}/I_{\text{Eu}}$ permitting the conversion of emission intensities into absolute temperature. The temperature dependence of the EuW₁₀@UiO-67 emission is presented in Figure 5 for the 150–300 K range. Five consecutive emission spectra were collected for each temperature and used to determine subsequent average data. The I_{Ligand} and I_{Eu} parameters have been obtained by integrating the emission spectra in the 438–575 nm and 604–630 nm wavelength

intervals, respectively. The temperature dependence of the defined thermometric parameters Δ in the 200–300 K range is presented in Figure S13, where the solid line represents the temperature calibration curve. The parameter Δ decreases with the temperature according to the following empirical linear relationship:

$$\Delta = 1.985 - 0.0029 T$$

with a correlation coefficient R^2 of 0.998. The corresponding relative sensitivity, defined as $s_r = |\partial\Delta/\partial T|/\Delta$, and used as a figure of merit to compare the performance of distinct systems (Brites et al., 2016) is plotted in Figure S14, showing that EuW₁₀@UiO-67 exhibits a maximum relative sensitivity S_m of ca. 0.26% K⁻¹ for the physiological temperature range.

CONCLUSION

In conclusion, we have reported herein an easy to prepare luminescent multifunctional material made of a metal-organic framework incorporating a europium-containing polyoxotungstate. Despite the very low amount of POM inserted in the UiO-67 matrix, it has been shown that EuW₁₀@UiO-67 is able to act as a sensor ([Eu³⁺] = 8.5 μ M) for metallic ions and amino-acids in water and in heterogeneous conditions. Among a series of cationic species, a good sensitivity has been found for Fe³⁺, while an enhancement of the EuW₁₀@UiO-67 luminescence is observed in presence of amino-acids, the enhancement of the emission intensity globally following the increase of the amino-acid pKa. Moreover, the recyclability of EuW₁₀@UiO-67 has been demonstrated, even if a certain loss of crystallinity is observed. In addition, the dual-luminescent properties—arising both from the POM and from the MOF—lead the reported material to behave as a self-calibrated ratiometric luminescent thermometer. Considering the huge number of luminescent POMs and MOFs already available, this first report of a dual-luminescent POM@MOF material thus opens the way to the development of such optical sensors.

AUTHOR CONTRIBUTIONS

WS, AD, CR-M, PM and GP have performed the synthesis and the structural characterizations of the title compound. RD and HS-B have performed the photophysical characterizations. The manuscript was written by PM and HS-B with valuable contributions and corrections of CR-M and RD.

FUNDING

This work was supported by CNRS, UVSQ, University of Nantes and the French National Research Agency (ANR) as part of the Investissements d'Avenir program n°ANR-11-IDEX-0003-02 and CHARMMMAT ANR-11-LABX-0039.

SUPPLEMENTARY MATERIAL

The Supplementary Material for this article can be found online at: <https://www.frontiersin.org/articles/10.3389/fchem.2018.00425/full#supplementary-material>

REFERENCES

- Barrett, S. M., Wang, C., and Lin, W. (2012). Oxygen sensing via phosphorescence quenching of doped metal-organic frameworks. *J. Mater. Chem.* 22, 10329–10334. doi: 10.1039/c2jm15549d
- Brites, C. D. S., Millán, A., and Carlos, L. D. (2016). *Handbook on the Physics and Chemistry of Rare Earths*. eds J. C. Bünzli and V. K. Pecharsky. Amsterdam: Elsevier.
- Capobianco, J. A., Proulx, P. P., Bettinelli, M., and Negrisolo, F. (1990). Absorption and emission spectroscopy of Eu^{3+} in metaphosphate glasses. *Phys. Rev. B* 42, 5936–5944.
- Cavka, J. H., Jakobsen, S., Olsbye, U., Guillou, N., Lamberti, C., Bordiga, S., et al. (2008). A new zirconium inorganic building brick forming metal organic frameworks with exceptional stability. *J. Am. Chem. Soc.* 130, 13850–13851. doi: 10.1021/ja8057953
- Chen, S., Ma, P., Luo, H., Wang, Y., Niu, J., and Wang, J. (2017). A luminescent polyoxoniobate lanthanide derivative $\{\text{Eu}_3(\text{H}_2\text{O})_9[\text{Nb}_{48}\text{O}_{138}(\text{H}_2\text{O})_6]\}^{27-}$. *Chem. Commun.* 53, 3709–3712. doi: 10.1039/C7CC00591A
- Clemente-León, M., Coronado, E., López-Muñoz, A., Repetto, D., Ito, T., Konya, T., et al. (2010). Dual-emissive photoluminescent Langmuir–Blodgett films of decatungstoeuropate and an amphiphilic iridium complex. *Langmuir* 26, 1316–1324. doi: 10.1021/la902513z
- Cui, Y., Song, R., Yu, J., Liu, M., Wang, Z., Wu, C., et al. (2015). Dual-emitting MOF/dye composite for ratiometric temperature sensing. *Adv. Mat.* 27, 1420–1425. doi: 10.1002/adma.201404700
- Fernando-Soria, J., Khajavi, H., Serra-Crespo, P., Gascon, J., Kapteijin, F., Julve, M., et al. (2012). Highly selective chemical sensing in a luminescent nanoporous magnet. *Adv. Mater.* 24, 5625–5629. doi: 10.1002/adma.201201846
- Han, X. B., Li, Y. G., Zhang, Z. M., Tan, H. Q., Lu, Y., and Wang, E. B. (2015). Polyoxometalate-based nickel clusters as visible light-driven water oxidation catalysts. *J. Am. Chem. Soc.* 137, 5486–5493. doi: 10.1021/jacs.5b01329
- Holmes-Smith, A. S., Crisp, J., Hussain, F., Patzke, G. R., and Hungerford, G. (2016). Use of lanthanide-containing polyoxometalates to sensitise the emission of fluorescent labeled serum albumin. *ChemPhysChem* 17, 418–424. doi: 10.1002/cphc.201500954
- Hu, Z., Deibert, B. J., and Li, J. (2014). Luminescent metal-organic frameworks for chemical sensing and explosive detection. *Chem. Soc. Rev.* 43, 5815–5840. doi: 10.1039/C4CS00010B
- Hungerford, G., Suhling, K., and Green, M. (2008). Luminescence enhancement of a europium containing polyoxometalate on interaction with bovine serum albumin. *Photochem. Photobiol. Sci.* 7, 734–737. doi: 10.1039/b802793e
- Ju, W., Song, X., Yan, G., Xu, K., Wang, J., Yin, D., et al. (2016). Layer-by-layer assembly of polyoxometalate-pyrene-decorated fluorescent microspheres for the suspension immunoassay of *Listeria monocytogenes*. *J. Mater. Chem. B*, 4, 4287–4294. doi: 10.1039/C6TB00986G
- Kaczmarek, A. M., Liu, J., Laforce, B., Vincze, L., Van Hecke, K., and Van Deun, R. (2017). Cryogenic luminescent thermometers based on multinuclear $\text{Eu}^{3+}/\text{Tb}^{3+}$ mixed lanthanide polyoxometalates. *Dalton Trans.* 46, 5781–5785. doi: 10.1039/C7DT01058C
- Katz, M. J., Brown, Z. J., Colón, Y. J., Siu, P. W., Scheidt, K. A., Snurr, R. Q., et al. (2013). A facile synthesis of UiO-66, UiO-67 and their derivatives. *Chem. Commun.* 49, 9449–9451. doi: 10.1039/c3cc46105j
- Li, H. W., Wang, Y., Zhang, T., Wu, Y., and Wu, L. (2014). Selective binding of amino acids on europium-substituted polyoxometalates and the interaction-induced luminescent enhancement effect. *ChemPlusChem* 79, 1208–12013. doi: 10.1002/cplu.201402091
- Li, W., Yin, S., Wang, J., and Wu, L. (2008). Tuning mesophase of ammonium amphiphile-encapsulated polyoxometalate complexes through changing component structure. *Chem. Mater.* 20, 514–522. doi: 10.1021/cm702955j
- Lustig, W. P., Mukherjee, S., Rudd, N. D., Desai, A. V., Li, J., and Ghosh, S. K. (2017). Metal-organic frameworks: functional luminescent and photonic materials for sensing applications. *Chem. Soc. Rev.* 46, 3242–3285. doi: 10.1039/C6CS00930A
- Mukhopadhyay, S., Debgupta, J., Singh, C., Kar, A., and Das, S. K. (2018). A Keggin polyoxometalate shows water oxidation activity at neutral pH: POM@ZIF-8, an efficient and Robust electrocatalyst. *Angew. Chem. Int. Ed.* 57, 1918–1923. doi: 10.1002/anie.201711920
- Natali, M., Bazzan, I., Goberna-Ferrón, S., Al-Oweini, R., Ibrahim, M., Bassil, B. S., et al. (2017). Photo-assisted water oxidation by high-nuclearity cobalt-oxo cores: tracing the catalyst fate during oxygen evolution turnover. *Green Chem.* 19, 2416–2426. doi: 10.1039/C7GC00052A
- Nogami, M., and Abe, Y. (1996). Properties of sol–gel-derived Al_2O_3 - SiO_2 glasses using Eu^{3+} ion fluorescence spectra. *J. Non-Cryst. Solid* 197, 73–78.
- Paille, G., Gomez-Mingot, M., Roch-Marchal, C., Lassalle-Kaiser, B., Mialane, P., Fontcave, M., et al. (2018). A fully noble metal-free photosystem based on cobalt-polyoxometalates immobilized in a porphyrinic metal-organic-framework for water oxidation. *J. Am. Chem. Soc.* 140, 3613–3618. doi: 10.1021/jacs.7b11788
- Qiu, Y. F., Liu, H., Zhang, C., Ma, Z., Hu, P. A., and Gao, G. G. (2015). Moisture-responsive films consisting of luminescent polyoxometalates and agarose. *J. Mater. Chem. C* 3, 6322–6328. doi: 10.1039/C5TC00421G
- Saad, A., Oms, O., Dolbecq, A., Menet, C., Dessapt, R., Serier-Brault, H., et al. (2015). A high fatigue resistant, photoswitchable fluorescent spiropyran-polyoxometalate-BODIPY single-molecule. *Chem. Commun.* 51, 16088–16091. doi: 10.1039/C5CC06217A
- Salomon, W., Lan, Y., Rivière, E., Yang, S., Roch-Marchal, C., Dolbecq, A., et al. (2016). Single-molecule magnet behavior of individual polyoxometalate molecules incorporated within biopolymer or metal-organic framework matrices. *Chem. Eur. J.* 22, 6564–6574. doi: 10.1002/chem.201600202
- Salomon, W., Roch-Marchal, C., Mialane, P., Rouschmeyer, P., Serre, C., Haouas, M., et al. (2015). Immobilization of polyoxometalates in the Zr-based metal organic framework UiO-67. *Chem. Commun.* 51, 2972–2975. doi: 10.1039/C4CC09986A
- Shi, D., He, C., Sun, W., Ming, Z., Meng, C., and Duan, C. (2016). A photosensitizing decatungstate-based MOF as heterogeneous photocatalyst for the selective C–H alkylation of aliphatic nitriles. *Chem. Commun.* 52, 4714–4717. doi: 10.1039/C6CC00862C
- Sugeta, M., and Yamase, T. (1993). Crystal structure and luminescence site of $\text{Na}_9[\text{EuW}_{10}\text{O}_{36}]\cdot 32\text{H}_2\text{O}$. *Bull. Chem. Soc. Jpn.* 66, 444–449. doi: 10.1246/bcsj.66.444
- Sun, J. W., Yan, P. F., An, G. H., Sha, J. Q., Li, G. M., and Yang, G. Y. (2016). Immobilization of polyoxometalate in the metal-organic framework rht-MOF-1: towards a highly effective heterogeneous catalyst and dye scavenger. *Sci. Rep.* 6:25595. doi: 10.1038/srep25595
- Wu, M. M., Wang, J. Y., Sun, R., Zhao, C., Zhao, J. P., Che, G. B., et al. (2017). The design of dual-emissive composite material $[\text{Zn}_2(\text{HL})_3]^+ @ \text{MOF-5}$ as self-calibrating luminescent sensors of Al^{3+} ions and monoethanolamine. *Inorg. Chem.* 56, 9555–9562. doi: 10.1021/acs.inorgchem.7b00939
- Xu, J., Zhao, S., Han, Z., Wang, X., and Song, Y. F. (2011). Layer-by-layer assembly of $\text{Na}_9[\text{EuW}_{10}\text{O}_{36}]\cdot 32\text{H}_2\text{O}$ and layered double hydroxides leading to ordered ultra-thin films: cooperative effect and orientation effect. *Chem. Eur. J.* 17, 10365–10371. doi: 10.1002/chem.201101062
- Xu, X. Y., and Yan, B. (2015). Eu(III)-functionalized MIL-124 as fluorescent probe for highly selectively sensing ions and organic small molecules especially for Fe(III) and Fe(II). *ACS Appl. Mater. Interfaces* 7, 721–729. doi: 10.1021/am5070409
- Yamase, T., and Sugeta, M. (1993). Charge-transfer photoluminescence of polyoxotungstates and-molybdates. *J. Chem. Soc. Dalton Trans.* 1993, 759–765. doi: 10.1039/dt9930000759
- Zhang, H., Guo, L., Xie, Z., Xin, X., Sun, D., and Yuan, S. (2016). Tunable aggregation-induced emission of polyoxometalates via

- amino acid-directed self-assembly and their application in detecting dopamine. *Langmuir* 32, 13736–13745. doi: 10.1021/acs.langmuir.6b03709
- Zhang, T., Li, H. W., Wu, Y., Wang, Y., and Wu, L. (2015). Self-assembly of an europium-containing polyoxometalate and the arginine/lysine-rich peptides from human papillomavirus capsid protein L1 in forming luminescence-enhanced hybrid nanoparticles. *J. Phys. Chem. C* 119, 8321–8328. doi: 10.1021/acs.jpcc.5b00032
- Zheng, L., Ma, Y., Zhang, G., Yao, J., Keita, B., and Nadjio, L. (2010). A multitechnique study of europium decatungstate and human serum albumin molecular interaction. *Phys. Chem. Chem. Phys.* 12, 1299–1304. doi: 10.1039/B919952G

Conflict of Interest Statement: The authors declare that the research was conducted in the absence of any commercial or financial relationships that could be construed as a potential conflict of interest.

Copyright © 2018 Salomon, Dolbecq, Roch-Marchal, Paille, Dessapt, Mialane and Serier-Brault. This is an open-access article distributed under the terms of the Creative Commons Attribution License (CC BY). The use, distribution or reproduction in other forums is permitted, provided the original author(s) and the copyright owner(s) are credited and that the original publication in this journal is cited, in accordance with accepted academic practice. No use, distribution or reproduction is permitted which does not comply with these terms.



Photoluminescence Properties of Two Closely Related Isostructural Series Based on Anderson-Evans Cluster Coordinated With Lanthanides

$[\text{Ln}(\text{H}_2\text{O})_7\{\text{X}(\text{OH})_6\text{Mo}_6\text{O}_{18}\}] \cdot y\text{H}_2\text{O}$, $\text{X} = \text{Al}, \text{Cr}$

Shailabh Tewari¹, Mohammad Adnan², Balendra¹, Vineet Kumar¹, Gaurav Jangra¹, Gaddam Vijaya Prakash^{2*} and Arunachalam Ramanan^{1*}

OPEN ACCESS

Edited by:

Tatjana N. Parac-Vogt,
KU Leuven, Belgium

Reviewed by:

Aleksandar Kondinski,
KU Leuven, Belgium
Svetlana V. Eliseeva,
UPR4301 Centre de Biophysique
Moléculaire (CBM), France

*Correspondence:

Gaddam Vijaya Prakash
prakash@physics.iitd.ac.in
Arunachalam Ramanan
aramanan@chemistry.iitd.ac.in

Specialty section:

This article was submitted to
Inorganic Chemistry,
a section of the journal
Frontiers in Chemistry

Received: 08 June 2018

Accepted: 05 December 2018

Published: 07 January 2019

Citation:

Tewari S, Adnan M, Balendra, Kumar
V, Jangra G, Prakash GV and
Ramanan A (2019)
Photoluminescence Properties of Two
Closely Related Isostructural Series
Based on Anderson-Evans Cluster
Coordinated With Lanthanides
 $[\text{Ln}(\text{H}_2\text{O})_7\{\text{X}(\text{OH})_6\text{Mo}_6\text{O}_{18}\}] \cdot y\text{H}_2\text{O}$,
 $\text{X} = \text{Al}, \text{Cr}$. *Front. Chem.* 6:631.
doi: 10.3389/fchem.2018.00631

¹ Department of Chemistry, Indian Institute of Technology Delhi, New Delhi, India, ² Department of Physics, Indian Institute of Technology Delhi, New Delhi, India

The paper describes synthesis and structural characterization of the whole series of two closely related lanthanide coordinated chromium or aluminum hexamolybdates (Anderson-Evans cluster) including twelve new members hitherto unreported: $[\text{Ln}(\text{H}_2\text{O})_7\{\text{X}(\text{OH})_6\text{Mo}_6\text{O}_{18}\}] \cdot 4\text{H}_2\text{O}$ and $[\text{Ln}(\text{H}_2\text{O})_7\{\text{X}(\text{OH})_6\text{Mo}_6\text{O}_{18}\} \text{Ln}(\text{H}_2\text{O})_7\{\text{X}(\text{OH})_6\text{Mo}_6\text{O}_{18}\}] \cdot 16\text{H}_2\text{O}$ where $\text{X} = \text{Al}$ or Cr and $\text{Ln} = \text{La}, \text{Ce}, \text{Pr}, \text{Nd}, \text{Sm}, \text{Eu}, \text{Gd}, \text{Tb}, \text{Dy}, \text{Ho}, \text{Er}, \text{Tm}, \text{Yb}, \text{Lu},$ and Y . Crystal structures of all the solids were established by powder and single crystal X-ray diffraction techniques. The two series are dictated by a different aggregation of the same set of molecular species: Lighter lanthanides favor coordination interaction between lanthanide ions and molybdate cluster forming 1D chains (Series I) while the heavier lanthanides result in the stacking of a cation, a pair of lanthanide hydrates coordinating to the cluster, and an anion, the discrete cluster is further stabilized through a large number of water molecules (Series II). Crystallization with Er^{3+} and Tm^{3+} ions results in a concomitant mixture of Series I and II. Photoluminescence of single crystals of all the chromium molybdates was dominated by a ruby-like emission including those which contain optically active ions $\text{Pr}, \text{Sm}, \text{Eu}, \text{Tb}, \text{Dy},$ and Tm . In contrast, aluminum analogs showed photoluminescence corresponding to characteristic lanthanide emissions. Our results strongly suggest a possible energy transfer from f levels of lanthanide ions to d levels of chromium (III) causing the quenching of lanthanide emission when coordinated with chromium molybdates. Intensity measurements showed that the emission from chromium molybdates are almost two orders of magnitude lower than naturally occurring ruby with broader line widths at room temperature.

Keywords: Anderson-Evans cluster, structural chemistry, lanthanides, chromium molybdate, aluminum molybdate, photoluminescence

INTRODUCTION

Polyoxomolybdates (POM), an important branch in polyoxometalate chemistry, presents an unrivaled structural chemistry and physicochemical properties providing immense opportunities as well as considerable challenges in creating new functional materials (Hill, 1998; Pope, 2002; Li and Xu, 2011; Eldik and Cronin, 2017; Song, 2018). Among the POM anions, a hetero polyoxomolybdate of the composition, $[X^{n+}Mo_6O_{24}H_y]^{(12-n-y)-}$, was found to be a dominant building block in several solids (Blazevic and Rompel, 2016). Its molecular structure, first proposed almost eighty years ago (Anderson, 1937), was established experimentally by refining the X-ray crystallographic data obtained for the tellurium salts, $(NH_4)_6\{TeMo_6O_{24}\} \cdot 7H_2O$ and $K_6\{TeMo_6O_{24}\} \cdot 7H_2O$ (Evans, 1948). Anderson-Evans cluster, as it has been known since, is made of six edge-shared distorted $\{MoO_6\}$ octahedra and the central cavity thus formed is occupied by slightly flattened, $X(OH)_6$, heteroatom octahedron. The cluster assumes a near D_{3d} symmetry with dimensions $\sim 8.6 \times 8.6 \times 2.7$ Å and has been isolated with fifteen different heteroatoms till now [X: **Al** (Lee et al., 1991; Manikumari et al., 2002; Shivaiah et al., 2002; Martin et al., 2004; Shivaiah and Das, 2005; Liu et al., 2006; Dhara et al., 2007; Cao et al., 2008; Zhou et al., 2009), **Cr** (Perloff, 1970; An et al., 2006; Yu et al., 2006; Lee, 2007; Zhou and Yang, 2007; Shi D. et al., 2008; Shi D. M. et al., 2008; Zhang et al., 2008, 2014; Singh et al., 2010b, 2014; Li et al., 2011; Singh and Ramanan, 2011; Kumar et al., 2014a; Joo et al., 2015), **Mn** (He et al., 2012; Oms et al., 2012; Rosnes et al., 2012, 2013; Yan et al., 2012; Zhang et al., 2012, 2015a,b; Hutin et al., 2013; Ai et al., 2014; Yvon et al., 2014), **Fe** (Wu et al., 2001), **Co** (Nolan et al., 1996; Panneerselvam et al., 1996; Lee and Joo, 2000a; Lee et al., 2001; Martin et al., 2004), **Ni** (Lee et al., 2002; Liu et al., 2007; Liu F.-X. et al., 2008), **Cu** (Ito et al., 1989), **Zn** (Allen et al., 1997), **Ga** (Mensingher et al., 2008; Himeno et al., 2009), **Te** (Evans, 1948; Kondo et al., 1980; Robl and Frost, 1993a,b; Lorenzo-Luis et al., 1999; Drewes et al., 2004a,b; Charushnikova et al., 2005; Drewes and Krebs, 2005; Gao et al., 2007; Liu Y. et al., 2008; Yan et al., 2008), **Rh** (Ozawa et al., 1991), **Pd** (Ozawa et al., 1991), **Sb** (Ogawa et al., 1988; Yan et al., 2014), **I** (Kondo et al., 1980; Rosu and Weakley, 2000; An et al., 2005) and **Pt** (Lee and Sasaki, 1984; Lee, 1994; Lee and Joo, 2000b, 2004, 2006a,b, 2007)]. The “disc-shaped” geometry and the nucleophilicity of the twelve terminal oxygens (O_t) render the POM cluster as an attractive ligand to engineer helices (Shivaiah et al., 2003), stacks or multidimensional frameworks (An et al., 2005; Ritchie and Bryant, 2015) through hydrogen bonding as well as metal-oxygen coordination. Furthermore, the structural versatility of this cluster is unique and can be tuned at the molecular level. It can be modified through the substitution of the triply bridged OH groups with fluoride ions (Michailovski et al., 2009), “axle-wheel” type (Schaming et al., 2010; Allain et al., 2013) with appropriate ligands or bent “butterfly” topologies (Zhang et al., 2017) via suitable functionalization (Figure 2). For this reason, a range of applications, from the much studied luminescent (Ohashi et al., 1982; Yamase and Sugeta, 1993; Ito et al., 2006; Kumar et al., 2014a), catalytic (Tanaka et al., 2012; Bayraq et al.,

2013), anti-tumor (Yamase, 1993; Raza et al., 2012; Shah et al., 2014), anti-viral (Inouye et al., 1993), photochromic (Coué et al., 2007; Song et al., 2008; Pardo et al., 2011; Oms et al., 2012; Allain et al., 2013; Hakouk et al., 2014) and magnetic (Leuenberger and Loss, 2001; Lehmann et al., 2007; Kushch et al., 2009; Wu et al., 2009; Feng et al., 2012) to the recently realized macromolecular crystallography (Bijelic et al., 2014; Mauracher et al., 2014a,b; Bijelic and Rompel, 2015) and functional bio-nanomaterials (Massia and Hubbell, 1991; Aota et al., 1994; Song et al., 2009) are envisaged for solids based on it (Figure 1). Synthesis-structure-function correlation is key to recognize the utility of these solids as futuristic materials.

There has been a renewed interest in the synthesis of lanthanide-based coordination solids with multidimensional structures; the trend is to tune the size, shape and dimensionality between nano to micro level to optimize luminescent properties for a desirable purpose (Binnemans, 2009; Armelao et al., 2010; Bünzli and Eliseeva, 2013; de Bettencourt-Dias, 2014). In this context, a few groups have investigated photoluminescence (PL) of lanthanide-Anderson-Evans cluster based solids (Yusov et al., 2002; Cao et al., 2008; Shi D. M. et al., 2008; Yang et al., 2013; Kumar et al., 2014a). The solid $[Eu(H_2O)_7\{Cr(OH)_6Mo_6O_{18}\}] \cdot 4H_2O$ belonging to Series I showed only characteristic emission due to Eu^{3+} ions (Shi D. M. et al., 2008). The solid $[(C_6H_5NO_2)_2Dy(H_2O)_6\{Cr(OH)_6Mo_6O_{18}\}] \cdot 2C_6H_5NO_2 \cdot 6H_2O$ showed characteristic emission due to Dy^{3+} ion (Yang et al., 2013). Dinesh et al. observed that Sm^{3+} and Tb^{3+} members of Series I showed only a red emission (Kumar et al., 2014a) reminiscent of ruby, while the lanthanide ion remained optically silent. Another molecular solid containing no lanthanide ions, $[(Hbipy)_2\{Cr(OH)_6Mo_6O_{17}(OH)\}(bipy)]$ also showed a ruby-like emission (Li et al., 2016). It should be mentioned that Yamase and his group were the first to observe the red emission reminiscent of ruby (Yamase and Sugeta, 1993; Ito et al., 2006) in $Na_3[Cr(OH)_6Mo_6O_{18}] \cdot 8H_2O$ at 4.2 K. It was noted that majority of the chromium hexamolybdate based crystals reported in literature, including the aforementioned solids, appeared pink in color. This suggested the domination of red emission arising from chromium ion. The contradicting photoluminescent behavior raised an obvious question, whether the presence or absence of a coordination linkage between the chromium molybdate cluster and lanthanide ions has any influence on their optical properties. This prompted us to explore the structural landscape of the system $Ln^{3+}_{(aq)} - \{X(OH)_6Mo_6O_{18}\} - H_2O$ ($X = Cr^{3+}$ or Al^{3+}).

A structural analysis of the reported solids with the general composition $[Ln(H_2O)_7\{X(OH)_6Mo_6O_{18}\}] \cdot yH_2O$, in particular, showed the occurrence of two types: (i) Formation of 1D chains between hydrated $\{Ln(H_2O)_n\}$ and the cluster through extended $-Ln-(O_t\text{-cluster-}O_t)-Ln-$ leading to **Series I** (Figure S1) of the composition $[Ln(H_2O)_7\{X(OH)_6Mo_6O_{18}\}] \cdot 4H_2O$ and (ii) occurrence of a molecular solid (0D) resulting from an aggregation between two discrete units, cationic $[Ln(H_2O)_7\{X(OH)_6Mo_6O_{18}\}Ln(H_2O)_7]^{3+}$ and anionic $\{X(OH)_6Mo_6O_{18}\}^{3-}$ crystallizing into **Series II** (Figure S2)

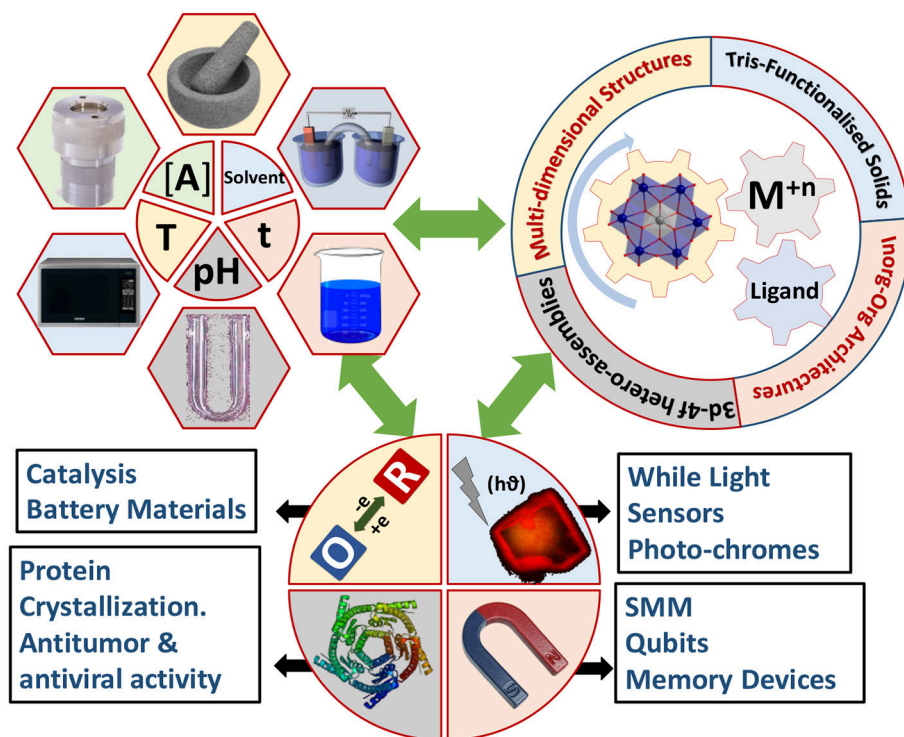


FIGURE 1 | The Synthesis-Structure-Property correlations leading to multiple applications in M^{n+} -Anderson-Evans system.

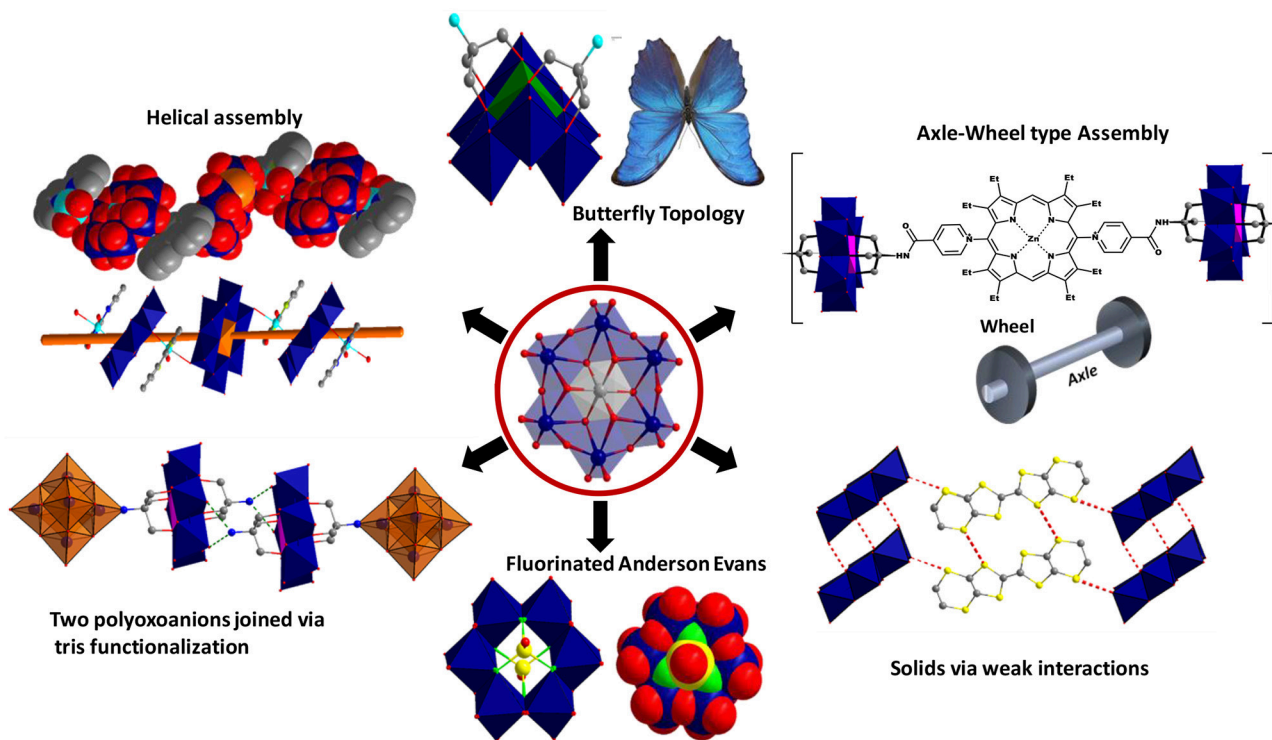


FIGURE 2 | The structural versatility in Anderson-Evans cluster based solids.

of the formula $[\text{Ln}(\text{H}_2\text{O})_7\text{Ln}\{\text{X}(\text{OH})_6\text{Mo}_6\text{O}_{18}\}\text{Ln}(\text{H}_2\text{O})_7]\{\text{X}(\text{OH})_6\text{Mo}_6\text{O}_{18}\}\cdot 16\text{H}_2\text{O}$. The lack of systematic synthetic protocol in literature underlined the need to adopt a uniform procedure to crystallize the complete series of solids $[\text{Ln}(\text{H}_2\text{O})_7\{\text{Cr}(\text{OH})_6\text{Mo}_6\text{O}_{18}\}]\cdot x\text{H}_2\text{O}$ with an objective to understand the crystal structures, the origin of its photophysical properties and establish a structure-property correlation. For comparison, we also synthesized the same series with optically inactive aluminum as heteroatom, though a few members have already been reported. Our study has established the growth of the two structurally related members, Series I and II, with similar composition (except for the number of lattice water) as we go along the period. The decrease in size of the lanthanides favors a coordination change from nine to eight and is thus responsible for triggering a slightly different supramolecular assembly. The paper reports the synthesis, structure and photoluminescence properties of the whole series including twelve new members, to the best of our knowledge, hitherto unreported: $[\text{Ln}(\text{H}_2\text{O})_7\{\text{X}(\text{OH})_6\text{Mo}_6\text{O}_{18}\}]\cdot 4\text{H}_2\text{O}$, $\text{X} = \text{Al}$ and $\text{Ln} = \text{Pr, Nd, Tb, Dy}$ and Ho ; $\text{X} = \text{Cr}$ and $\text{Ln} = \text{Tb, Dy}$ and Ho ; $[\text{Ln}(\text{H}_2\text{O})_7\{\text{X}(\text{OH})_6\text{Mo}_6\text{O}_{18}\}\text{Ln}(\text{H}_2\text{O})_7]\{\text{X}(\text{OH})_6\text{Mo}_6\text{O}_{18}\}\cdot 16\text{H}_2\text{O}$, $\text{X} = \text{Al}$ and $\text{Ln} = \text{Er, Tm}$ and Lu , $\text{X} = \text{Cr}$ and $\text{Ln} = \text{Lu}$.

EXPERIMENTAL

Selected members of the composition $[\text{Ln}(\text{H}_2\text{O})_7\{\text{X}(\text{OH})_6\text{Mo}_6\text{O}_{18}\}]\cdot 4\text{H}_2\text{O}$ and $[\text{Ln}(\text{H}_2\text{O})_7\{\text{X}(\text{OH})_6\text{Mo}_6\text{O}_{18}\}\text{Ln}(\text{H}_2\text{O})_7]\{\text{X}(\text{OH})_6\text{Mo}_6\text{O}_{18}\}\cdot 16\text{H}_2\text{O}$ have been isolated earlier by a few groups and its single crystal structures have been established (Fedoseev et al., 2002; Shivaiah et al., 2002, 2014; Gavrilova and Molchanov, 2005; Zhou and Yang, 2007; Cao et al., 2008; Shi D. et al., 2008; Shi D. M. et al., 2008; Zhang et al., 2008; Zhao et al., 2008; Wang et al., 2011; Kumar et al., 2014a). However, no group has attempted isolation of the whole series of Anderson-Evans cluster based solids containing Al or Cr heteroatoms coordinated to lanthanide cations. Two different approaches have been employed in literature to prepare the compounds: (a) Mixing aqueous solutions of pre-synthesized $\text{Na}_3\text{Cr}(\text{OH})_6\text{Mo}_6\text{O}_{18}\cdot 8\text{H}_2\text{O}$ with aqueous (or methanolic) solutions of lanthanide salts followed by heating or refluxing to 60–80°C for 30 min to 4 h after suitably adjusting pH of the reacting mixture (Zhou and Yang, 2007; Shi D. et al., 2008; Shi D. M. et al., 2008; Zhao et al., 2008; Wang et al., 2011); (b) Reacting aqueous solutions of precursor compounds for the cluster ($\text{Na}_2\text{MoO}_4\cdot 2\text{H}_2\text{O}$ and $\text{CrCl}_3\cdot 6\text{H}_2\text{O}$ or $\text{Cr}(\text{NO}_3)_3\cdot 9\text{H}_2\text{O}/\text{AlCl}_3\cdot 6\text{H}_2\text{O}$) with an acidified solution of lanthanide salts. pH of the reaction mixture was then set before keeping for solvent evaporation. In some cases the reaction mixture was refluxed at 60°C prior to solvent evaporation (Shivaiah et al., 2002, 2014; Cao et al., 2008; Kumar et al., 2014a). Our earlier experience with the synthesis of the chromium molybdate based solids (Singh et al., 2010b, 2014; Pavani et al., 2011; Singh and Ramanan, 2011; Kumar et al., 2014a) showed the quality of crystals and phase homogeneity varied considerably depending on the concentration and pH

of the reacting mixtures and the sequence of the addition of reagents. Although stoichiometry is generally the key to synthesis, in selected cases, excess or control of heteroatom concentration was found to be necessary (Pope, 1983). We also noticed that the procedures employed by other groups were limited leading to low yields and problems associated with the pre-synthesized sodium salt of Anderson-Evans cluster that resulted in competing phases driven by sodium hydrates. In aqueous solution, sodium ions are known to assemble differently with $\{\text{Cr}(\text{OH})_6\text{Mo}_6\text{O}_{18}\}^{3-}$ leading to multiple forms (Perloff, 1970; Yu et al., 2006; Singh et al., 2010b).

This led us to adopt a modified method to prepare new $\{\text{Cr}(\text{OH})_6\text{Mo}_6\text{O}_{18}\}$ based solids coordinated with transition metal ions (Singh et al., 2010b). An extension of this one-pot scheme did yield some success in isolating a few lanthanide-based chromium hexamolybdates (Kumar et al., 2014a). The method, however, was hampered to extend the series with other lanthanide ions due to the appearance of a green colored residue, possibly the formation of the solid $[\{\text{Na}(\text{H}_2\text{O})_6\}\{\text{Cr}(\text{OH})_6\text{Mo}_6\text{O}_{17}(\text{OH})\}]\cdot 24\text{H}_2\text{O}$ (Singh et al., 2010b; Pavani et al., 2011). Furthermore, these crystals started growing when the supernatant solution was left for longer time. Our initial attempts to prepare aluminum analogs led to two types of crystalline solids $[\text{Ln}(\text{H}_2\text{O})_7\{\text{Al}(\text{OH})_6\text{Mo}_6\text{O}_{18}\}]\cdot 4\text{H}_2\text{O}$ (smaller block shaped transparent crystals) and $[\text{Na}_3(\text{H}_2\text{O})_6\{\text{Al}(\text{OH})_6\text{Mo}_6\text{O}_{18}\}]\cdot 2\text{H}_2\text{O}$ (larger block shaped transparent-white crystals). To overcome these issues, we lowered the concentration of $\text{CrCl}_3\cdot 6\text{H}_2\text{O}$ and $\text{AlCl}_3\cdot 6\text{H}_2\text{O}$ and the amount of acetic acid used to adjust pH as per our previous experience. The following modified protocol has enabled us to successfully isolate almost all lanthanide-based chromium and aluminum analogs of Anderson-Evans cluster solids.

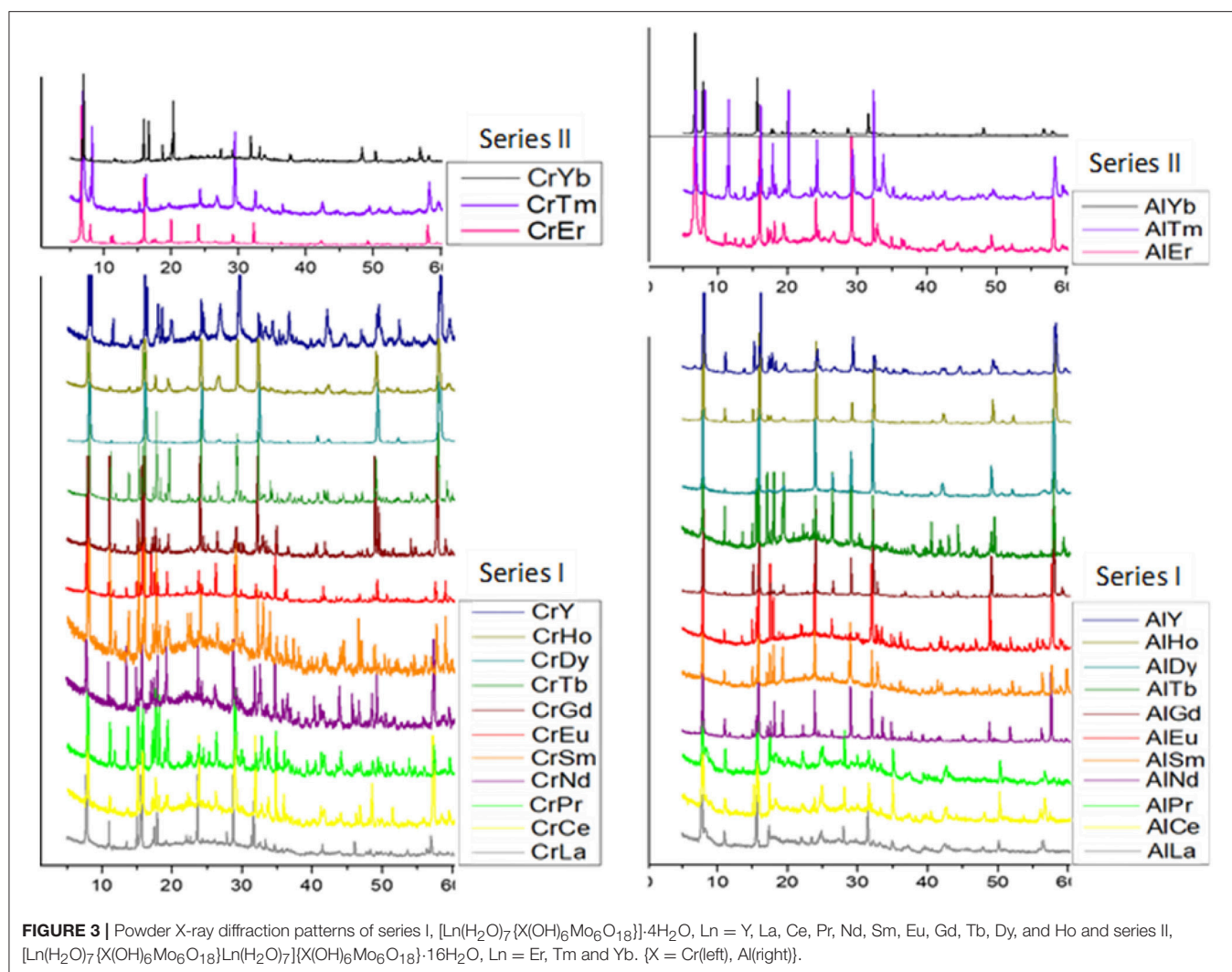
Modified synthetic protocol:

The solid $\text{AlCl}_3\cdot 6\text{H}_2\text{O}$ and all lanthanide salts (99.9% purity, trace metal basis) were purchased from Sigma Aldrich Chemicals Pvt. Ltd. (USA). $\text{Na}_2\text{MoO}_4\cdot 2\text{H}_2\text{O}$ was purchased from TCI Pvt. Ltd. and $\text{CrCl}_3\cdot 6\text{H}_2\text{O}$ was purchased from CDH Pvt. Ltd. All reagents were used without further purification. Initially, two separate solutions were prepared as per our earlier method (Singh and Ramanan, 2011).

Solution A was prepared by dissolving 0.65 mmol of $\text{Na}_2\text{MoO}_4\cdot 2\text{H}_2\text{O}$ and 0.26 mmol $\text{CrCl}_3\cdot 6\text{H}_2\text{O}/\text{AlCl}_3\cdot 6\text{H}_2\text{O}$ in 4 ml distilled water which was further acidified with 1 ml glacial CH_3COOH . **Solution B** was prepared by dissolving 0.65 mmol $\text{LnCl}_3\cdot x\text{H}_2\text{O}$ ($x = 7$ for La and Ce; $x = 6$ for Nd to Er, Yb, Lu and Y) or $\text{Ln}(\text{NO}_3)_3\cdot x\text{H}_2\text{O}$ ($x = 6$ for Pr and $x = 5$ for Tm) in 5 ml distilled water. The contents of solution A and B were mixed with continuous stirring and the resultant solution was kept at room temperature for solvent evaporation. In the case of lanthanum and cerium, crystals grew within 24 h. However, heavier lanthanides took more time to crystallize. Ytterbium crystals appeared after about 10 days.

Crystal Structures

Single crystal (Table 2) and powder X-ray diffraction analysis (Figure 3) revealed that for lighter lanthanides (till $\text{Ln} = \text{Ho}$),



Series I was observed. These solids crystallize in the space group $Pca2_1$; the cell parameters and the intensities of the reflections (Table 1) are comparable and in order with decreasing size of the respective ions. Of these, the compounds TbCr9, DyC10, HoCr11, LuCr29, PrAl18, NdAl19, TbAl23, DyAl24, HoAl25, ErAl26, TmAl27, and LuAl30 are being reported for the first time. The Series II compounds ErAl26 and TmAl27 exhibited different cell parameters when loaded at low temperatures (100K). A similar observation of phase transformation in Series II type solid has been reported in the case of TmCr12 (Zhang et al., 2008). In Series I, the cluster $\{\text{X}(\text{OH})_6\text{Mo}_6\text{O}_{18}\}^{3-}$ with $\text{X} = \text{Al}$ or Cr is the basic building block and coordinates with $\{\text{Ln}(\text{H}_2\text{O})_7\}^{3+}$ to form 1D zig-zag chains (Figure S1A). The solids are further stabilized via nonbonding interactions with lattice water (Figure S1B). The bond lengths and angles are comparable to other members already known (Fedoseev et al., 2002; Shivaiah et al., 2002, 2014; Gavrilova and Molchanov, 2005; Zhou and Yang, 2007; Cao et al., 2008; Shi D. M. et al., 2008; Zhao et al., 2008; Kumar et al., 2014a). An interesting observation is that under our reaction condition yttrium analogs crystallized as Series I (Table 1). It is

not surprising since size of Y^{3+} in 9 CN (1.075 Å) is comparable to 1.083 Å of Dy^{3+} (Shannon, 1976; Lundberg et al., 2010). However, an earlier report had shown yttrium to have crystallized in Series II (Wang et al., 2011). It is clear from Figure 3 that a transition from Series I to II, under our experimental conditions, occurs around Erbium(Er). In the case of Er, reflections clearly indicate the presence of both Series I and II. Tm also shows a concomitant mixture of the two series. However, Yb appears to be predominantly that of Series II. We strongly believe that the presence of a second phase is quite likely in all higher lanthanides and this observation is only reflected in powder XRD (Figure 3).

Crystallization reaction of Anderson-Evans cluster with heavier lanthanides (Er to Yb) led to Series II. These solids crystallized in $P\bar{1}$ space group (Table 2). Though the stoichiometry of lanthanide to the cluster in the crystal structure remained the same as in Series I, the assembly of the molecular solid (0D) was different. Also, the structure contained a larger number of uncoordinated water molecules. In Series II, the cationic cluster $[\text{Ln}(\text{H}_2\text{O})_7\{\text{X}(\text{OH})_6\text{Mo}_6\text{O}_{18}\}]\text{Ln}(\text{H}_2\text{O})_7\{\text{X}(\text{OH})_6\text{Mo}_6\text{O}_{18}\}^{3+}$ derivatised by a pair of lanthanide hydrates involved in

TABLE 1 | Refined cell parameters for solids in series I and series II.

Ln/X	Ionic radius (Ln ³⁺) in 9 and 8 CN (Å)	Series I: [Ln(H ₂ O) ₇ {X(OH) ₆ Mo ₆ O ₁₈ }]·4H ₂ O space group <i>Pca</i> 2 ₁				Volume (Å ³)
		<i>a</i> (Å)	<i>b</i> (Å)	<i>c</i> (Å)		
YCr1#	1.075 ^a	10.889(6)	11.768(8)	22.263(13)		2853(5)
YAl1#	1.019	11.7567(8)	10.8939(7)	22.2145(15)		2845.2(3)
LaCr2	1.216 ^a	11.831(4)	10.968(4)	22.621(8)		2935(3)
LaAl16	1.160	11.844(2)	11.010(2)	22.643(5)		2952.7
CeCr3	1.196 ^a	11.777(6)	10.924(6)	22.549(11)		2901(4)
CeAl17	1.143	11.8255(15)	11.0007(14)	22.556(3)		2934.28
PrCr4	1.179 ^a	11.771(6)	10.925(5)	22.442(12)		2886(4)
PrAl18	1.126	11.8173(6)	10.9707(5)	22.5088(11)		2918.1(2)
NdCr5	1.163 ^a	11.762(5)	10.900(5)	22.425(9)		2875(3)
NdAl19	1.109	11.7659(5)	10.9321(5)	22.4151(10)		2883.2(2)
SmCr6	1.132 ^a	11.759(4)	10.921(4)	22.372(8)		2873(3)
SmAl20	1.079	11.7700(6)	10.9257(6)	22.3586(12)		2875.2(3)
EuCr7	1.120 ^a	11.778(10)	10.961(10)	22.422(19)		2895(4)
EuAl21	1.066	11.732(4)	10.909(3)	22.251(7)		2848(2)
GdCr8	1.107 ^a	11.785(3)	10.926(3)	22.349(6)		2878(2)
GdAl22	1.053	11.716(13)	10.870(12)	22.23(3)		2836(9)
TbCr9	1.095 ^a	11.8213(7)	10.9479(6)	22.3810(13)		2896.5(3)
TbAl23	1.040	11.7860(13)	10.9560(11)	22.333(2)		2883.9(5)
DyCr10	1.083 ^a	11.7813(7)	10.9100(6)	22.2821(13)		2864.0(3)
DyAl24	1.027	11.7385(5)	10.8989(5)	22.2203(10)		2842.8(2)
HoCr11	1.072 ^a	11.7696(10)	10.8829(9)	22.2283(18)		2847.2(4)
HoAl25	1.015	11.7114(11)	10.8538(10)	22.139(2)		2814.2(5)
ErCr12#	1.062 ^a	11.7799(8)	10.8875(7)	22.2105(14)		2848.6(3)
ErAl26#	1.004	11.667(18)	10.846(18)	22.11(4)		2797(8)
TmCr13#	1.052 ^a	11.7665(8)	10.8728(8)	22.2149(16)		2842.1(4)
	0.994					

Ln/X	Series II: [Ln(H ₂ O) ₇ {X(OH) ₆ Mo ₆ O ₁₈ }]Ln(H ₂ O) ₇ {X(OH) ₆ Mo ₆ O ₁₈ }]·16H ₂ O space group <i>P</i> $\bar{1}$						Volume (Å ³)
	<i>a</i> (Å)	<i>b</i> (Å)	<i>c</i> (Å)	α (°)	β (°)	γ (°)	
ErCr12	10.9762(6)	11.6149(7)	13.9397(8)	74.4390(10)	83.8050(10)	89.4570(10)	1701.65(17)
ErAl26	11.038(19)	11.067(3)	14.01(4)	74.67(10)	84.10(8)	89.41(7)	1731(10)
ErAl26*	15.5455(9)	15.8776(9)	16.0412(9)	86.9390(10)	72.4000(10)	64.5440(10)	3394.1(3)
TmCr13	11.0989(13)	11.7203(14)	13.9843(40)	74.993(2)	84.528(2)	89.545(2)	1748.9
TmAl27	10.9836(4)	11.5857(4)	13.9171(5)	74.4310(10)	83.8200(10)	89.4490(10)	1695.75(11)
TmAl27*	15.5445(12)	15.8913(12)	16.0467(12)	86.9470(10)	72.8530(10)	64.5140(10)	3396.1(4)
YbCr14	11.0379(5)	11.6436(5)	13.9044(7)	75.005(1)	84.530(1)	89.466(1)	1718.08(14)
YbAl28	11.011(10)	11.585(12)	13.885(13)	74.895(19)	84.51(2)	89.517(18)	1702(3)
YCr1	11.0492(6)	11.6488(6)	13.9350(8)	75.070(4)	84.551(4)	89.536(4)	1724.94(16)
YAl15	11.052(5)	11.620(5)	13.947(5)	75.006(5)	84.535(5)	89.582(5)	1722.0(12)

^a Ionic radii of Ln³⁺ in coordination number 9. Rest are for coordination number 8. The values are calculated from *r*³ *V* plots.
[#] Represents the solids of series I wherein the solids of series II are also present as a concomitant phase.

complex H-bonding with another discrete anionic cluster {X(OH)₆Mo₆O₁₈}^{3−} (Figure S2). Two groups have crystallized and structurally characterized a few members belonging to Series II (Zhang et al., 2008; Wang et al., 2011). The previous works as well the present one clearly suggest that a few lattice water are disordered in solids belonging to Series II. Bond valence sums conclusively show that lanthanide, chromium/aluminum and molybdenum occur in +3, +3, and +6 oxidation state, respectively.

A close inspection of the structures, however revealed that the crystal packing of the complex cation, and the discrete anion, showed a strong resemblance to Series I (Figures 4A,C).

TABLE 2 | Crystal data and refinement details for all single crystals reported for the first time.

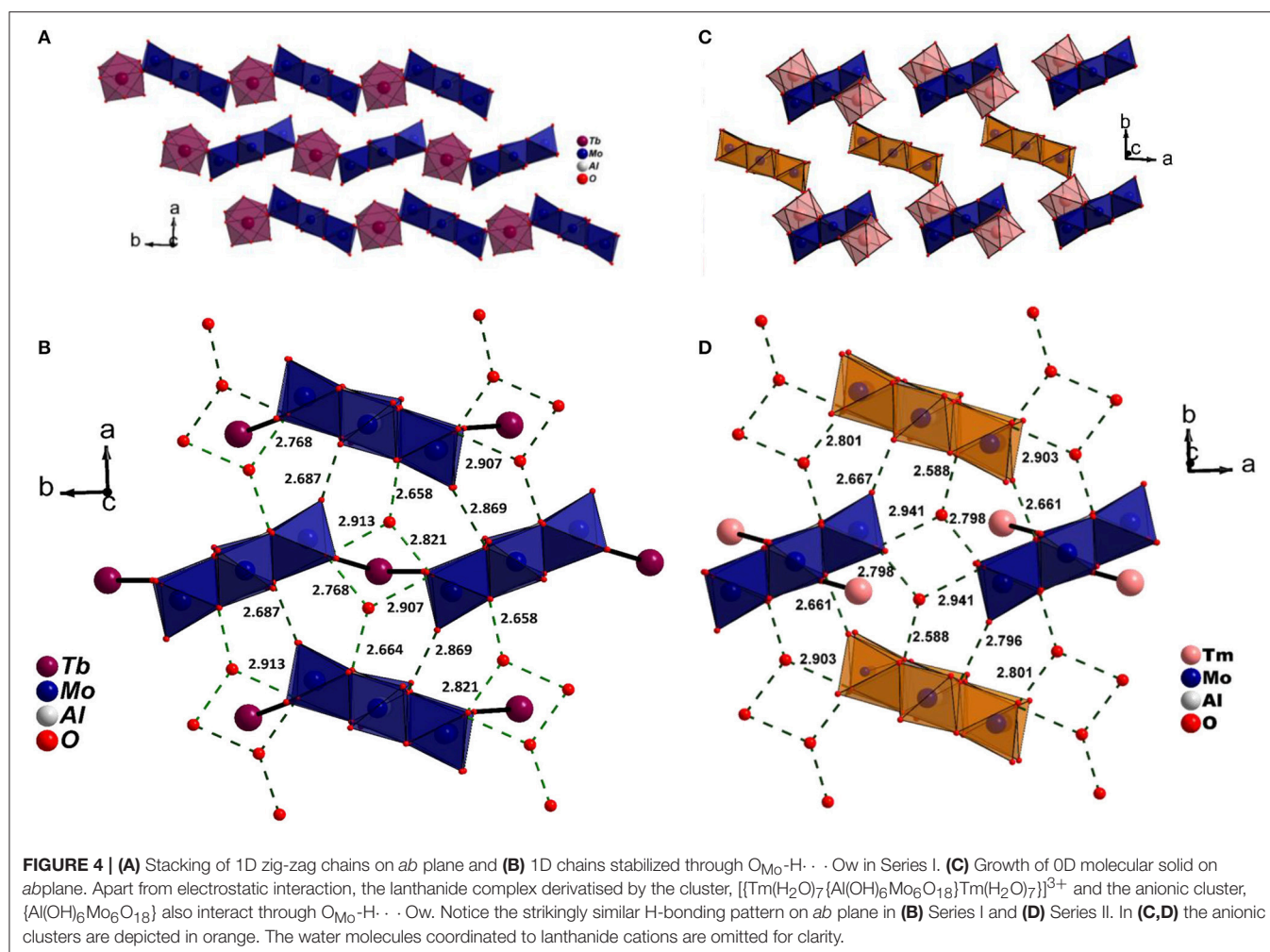
Parameter	TbCr9	DyCr10	HoCr11	ErCr12#	TmCr13#	LuCr29	PrAl18	NdAl19	TbAl23
Formula	Cr ₂ Mo ₁₂ O ₇₀ Tb ₂	Cr ₂ Dy ₂ Mo ₁₂ O ₇₀	Cr ₂ Ho ₂ Mo ₁₂ O ₇₀	Cr ₂ Er ₂ Mo ₁₂ O ₇₀	Cr ₂ Mo ₁₂ O ₇₀ Tm ₂	Cr ₂ Mo ₁₂ O ₇₈ Lu ₂	Al ₂ Mo ₁₂ O ₇₀ Pr ₂	Al ₂ Mo ₁₂ Nd ₂ O ₇₀	Al ₂ Mo ₁₂ O ₇₀ Tb ₂
Formula weight	2,693.14	2,732.28	2,705.14	2,741.80	2,713.14	2,853.22	2,607.06	2,613.72	2,643.10
T (K)	298(2)	100(2)	100(2)	100(2)	100(2)	298(2)	298(2)	100(2)	298(2)
Crystal system	Orthorhombic	Orthorhombic	Orthorhombic	Orthorhombic	Orthorhombic	Triclinic	Orthorhombic	Orthorhombic	Orthorhombic
Space group	<i>Pca</i> 2 ₁	<i>Pca</i> 2 ₁	<i>Pca</i> 2 ₁	<i>Pca</i> 2 ₁	<i>Pca</i> 2 ₁	<i>P</i> $\bar{1}$	<i>Pca</i> 2 ₁	<i>Pca</i> 2 ₁	<i>Pca</i> 2 ₁
<i>a</i> (Å)	11.8213(7)	12.0050(7)	11.8069(12)	11.7799(8)	11.7665(8)	11.0470(2)	11.8173(6)	11.7210(6)	11.7860(13)
<i>b</i> (Å)	10.9479(6)	11.0090(6)	10.9263(11)	10.8875(7)	10.8728(8)	11.6690(2)	10.9707(5)	10.8990(5)	10.9560(11)
<i>c</i> (Å)	22.3810(13)	22.660(13)	22.2930(2)	22.2105(14)	22.2149(16)	13.9150(3)	22.5088(11)	22.3370(11)	22.3330(2)
α (°)	90	90	90	90	90	74.937(4)	90	90	90
β (°)	90	90	90	90	90	11.669(2)	90	90	90
γ (°)	90	90	90	90	90	13.915(3)	90	90	90
<i>V</i> (Å ³)	2,896.5(3)	2,864.0(3)	2,875.9(5)	2,848.6(3)	2,842.1(4)	1,724.0(6)	2,918.1(2)	2,853.2(2)	2,883.9(5)
<i>Z</i>	2	2	2	2	2	1	2	2	2
Dcalc (gcm ^{−3})	3.086	3.006	3.161	3.197	3.170	2.748	2.967	3.042	3.044
$\mu_{\text{MoK}\alpha}$ (cm ^{−1})	5.402	5.320	5.737	5.961	6.139	5.365	4.286	4.494	5.100
Theta range (°)	2.60–31.31	2.50–35.50	2.54–24.57	2.55, 26.44	2.55–28.54	2.51–30.75	2.53–30.44	2.62–31.30	2.54–31.05
<i>R</i> ₁ , <i>wR</i> ₂ [<i>I</i> > 2 σ (<i>I</i>)] ^a	0.0484, 0.1236	0.0744, 0.1985	0.0623, 0.1364	0.0799, 0.1603	0.0695, 0.1964	0.0510, 0.1477	0.0309, 0.0901	0.0442, 0.1051	0.0606, 0.1488
GOF	1.022	1.539	1.064	1.164	1.619	1.275	0.786	0.853	1.088
ICSD no.	1881544	1821829	1881881	1881880	1881833	1881617	1881543	1881610	1881555

Parameter	DyAl24	HoAl25	ErAl26#	ErAl26*	TmAl27	TmAl27*	LuAl30
Formula	Al ₂ Dy ₂ Mo ₁₂ O ₇₀	Al ₂ Ho ₂ Mo ₁₂ O ₇₀	Al ₂ Mo ₁₂ Er ₂ O ₇₀	Al ₂ Er ₂ Mo ₁₂ O ₇₈	Al ₂ Mo ₁₂ O ₇₈ Tm ₂	Al ₂ Mo ₁₂ Tm ₂ O ₇₈	Al ₂ Mo ₁₂ Lu ₂ O ₇₈
Formula weight	2,650.24	2,687.10	2,693.14	2,803.76	2,803.20	2,791.10	2,803.18
T (K)	100(2)	100(2)	100(2)	100(2)	100(2)	100(2)	298(2)
Crystal system	Orthorhombic	Orthorhombic	Orthorhombic	Triclinic	Triclinic	Triclinic	Triclinic
Space group	<i>Pca</i> 2 ₁	<i>Pca</i> 2 ₁	<i>Pca</i> 2 ₁	<i>P</i> $\bar{1}$	<i>P</i> $\bar{1}$	<i>P</i> $\bar{1}$	<i>P</i> $\bar{1}$
<i>a</i> (Å)	11.7385(5)	11.7114(11)	11.667(18)	15.5455(9)	11.0276(7)	15.5445(12)	11.0453(14)
<i>b</i> (Å)	10.8989(5)	10.8538(10)	10.846(18)	15.8776(9)	11.5944(7)	15.8913(12)	11.6203(14)
<i>c</i> (Å)	22.2203(10)	22.1390(2)	22.110(4)	16.0412(9)	13.8969(9)	16.0467(12)	13.8854(17)
α (°)	90	90	90	86.9390(10)	74.981(2)	86.947(1)	74.975(2)
β (°)	90	90	90	72.4000(10)	84.559(2)	72.358(1)	84.571(2)
γ (°)	90	90	90	64.5440(10)	89.539(2)	64.514(1)	89.568(2)
<i>V</i> (Å ³)	2,842.8(2)	2,814.2(4)	2,797.0(8)	3,394.1(3)	1,708.15(19)	3,396.1(4)	1,713.3(4)
<i>Z</i>	2	2	2	2	1	2	1
Dcalc (gcm ^{−3})	3.096	3.133	3.157	2.740	2.725	2.730	2.717
$\mu_{\text{MoK}\alpha}$ (cm ^{−1})	5.314	5.524	5.728	4.738	4.847	4.876	5.124
Theta range (°)	2.55–30.74	2.56–20.92	2.55–27.27	2.28–30.75	2.29–29.09	2.58–30.92	2.51–30.86
<i>R</i> ₁ , <i>wR</i> ₂ [<i>I</i> > 2 σ (<i>I</i>)] ^a	0.0308, 0.0765	0.0571, 0.1415	0.1078, 0.1693	0.0435, 0.1086	0.0557, 0.1000	0.0787, 0.3366	0.0310, 0.1056
GOF	1.020	1.055	1.196	1.027	1.047	2.413	0.861
ICSD no.	1881556	1881882	1881830	1881609	1881832	1881834	1881831

[#]Represents the solids of series I wherein the solids of series II are also present as a concomitant phase.

It is important to point out that the non-bonding interactions of the two series on the *ab* plane are strikingly similar (Figures 4B,D) signifying the small energy difference between the two supramolecular aggregates. However, since higher lanthanides favor a lower coordination number due to smaller size, an extended chain appears to be unfavorable. Interestingly, Ln³⁺ coordinates to terminal oxygen (O_t) of the hexagonal cluster at 1,4 positions (Series II) in contrast to 1,3 found in

Series I (Figures S1, S2). An efficient close packing probably necessitates the formation of a complex cation wherein the cluster is coordinated by a pair of [Ln(H₂O)₇]³⁺ via symmetry equivalent terminal oxygen atoms. As a consequence, the complex cations and anions stack one over the other in a twisted fashion (Figure 5). The packing is further facilitated by non-bonding interactions with additional water molecules that get incorporated into the structure. The present study as well as

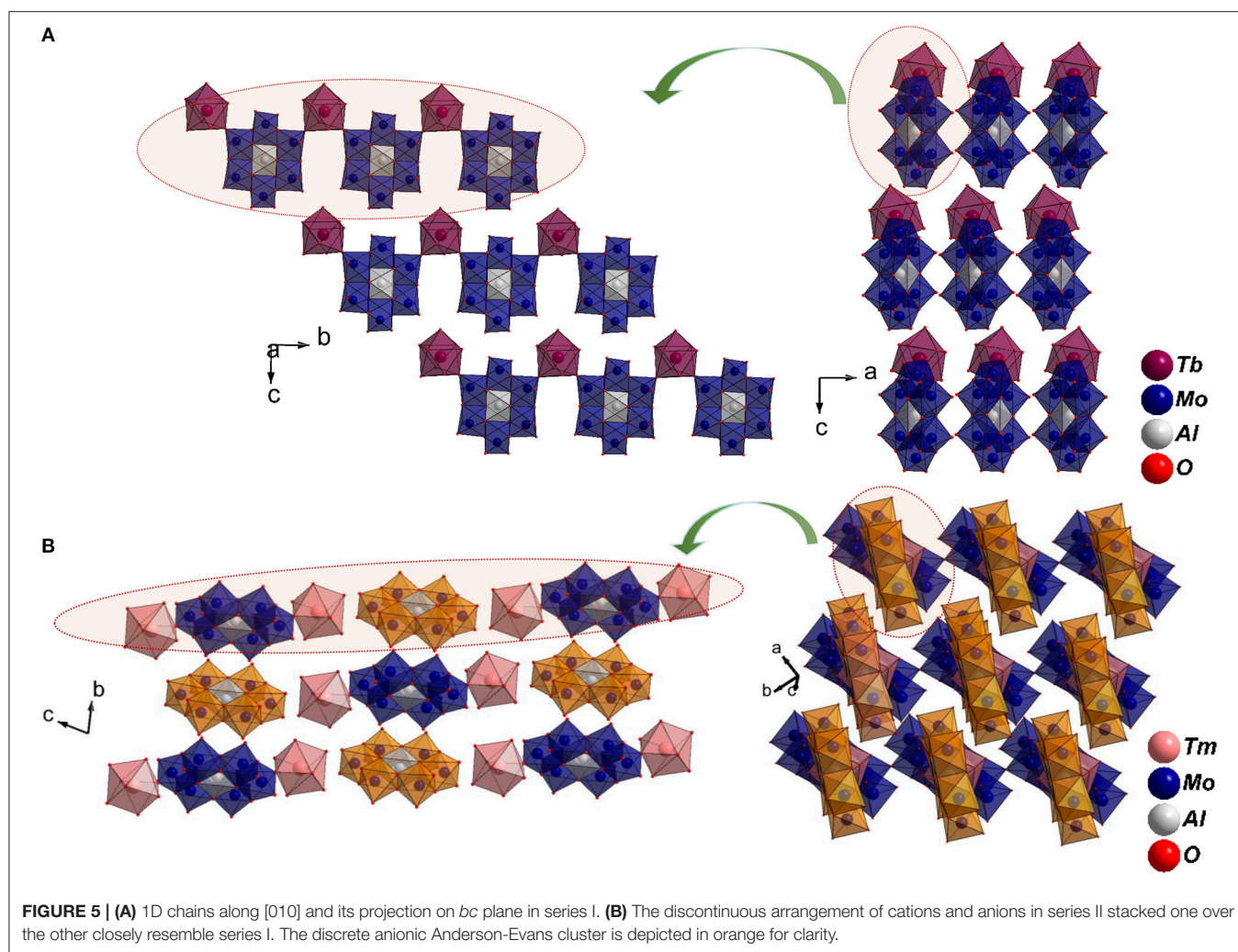


the two literature reports clearly show that the occurrence of a significant disorder among lattice water thus making it difficult to obtain a reliable model.

Crystallization of Lanthanide Coordinated Chromium/Aluminum Molybdates

A molybdenum source dissolved in aqueous medium under varying concentration and *pH* may contain numerous soluble molybdate species (Tkac and Paulenova, 2008). Under our experimental conditions, it is reasonable to assume the occurrence of stable Anderson-Evans cluster (Pavani et al., 2011). Crystallization is a supramolecular reaction (Desiraju, 2007; Singh et al., 2010a; Desiraju et al., 2011; Singh and Ramanan, 2011) and hence a crystal separating from a medium can be considered to occur from the aggregation of appropriate molecular species including solvent molecules. In the context of crystal engineering of lanthanide coordinated with chromium or aluminum molybdate cluster, two species, viz. $\{Ln(H_2O)_n\}^{3+}$ and $\{X(OH)_6Mo_6O_{18}\}^{3-}$ aggregate along with water molecules leading to a stable crystal, belonging to Series I or II (Singh et al., 2010b, 2014; Pavani et al.,

2011; Singh and Ramanan, 2011; Kumar et al., 2014b). In Series I, the cations and anions condense forming extended chains through coordination linkages whereas in Series II, the smaller size of lanthanides results in the formation of a discrete cationic complex wherein the cluster is coordinated by a pair of lanthanide ions. The packing of the cations and the discrete cluster anions are facilitated through nonbonding interactions and hence more water molecules get incorporated into the structure. The two closely related isostructural series represent an intriguing example of crystal engineering of salt hydrates manifested by parsimonious nature to compromise between Kitaigorodskii's close packing principle (Kitaigorodskii, 1965) and non-covalent interactions assembling into a stable crystal under a given condition. The principle appears to be the same operating in a simple salt hydrate crystallizing from a supramolecular assembly of water-mediated $\{Cu(H_2O)_6\}^{2+}$ and SO_4^{2-} leading to 0D (molecular) $CuSO_4 \cdot 7H_2O$ (Boothite), 1D (chain) $CuSO_4 \cdot 5H_2O$ (Chalcantite) and multidimensional $CuSO_4 \cdot 3H_2O$ (Bonattite), $CuSO_4 \cdot H_2O$ (Poitevinte) and $CuSO_4$ (Chalcocyanite) or organic hydrates (Upreti et al., 2007; Singh et al., 2010a).



Excitation and Emission Spectra of Rare-Earth Chromium/Aluminum Molybdates

Till recently there are only five papers that have reported emission (PL) of solids containing lanthanides and chromium molybdate cluster (Yusov et al., 2002; Cao et al., 2008; Shi D. M. et al., 2008; Yang et al., 2013; Kumar et al., 2014a). Generally, polycrystalline samples may be contaminated and are prone to react with air. In this work, we carried out PL studies directly on single crystals. Microscopic PL spectra and images are obtained from a modified microscope. Both excitation (PLE) and emission (PL) studies were conducted on commercial spectrofluorophotometer (see Experimental section). As visible to naked eye, all rare-earth containing chromium molybdate crystals ($\text{Ln} = \text{La}, \text{Ce}, \text{Pr}, \text{Nd}, \text{Sm}, \text{Eu}, \text{Gd}, \text{Tb}, \text{Dy}, \text{Ho}, \text{Er}, \text{Tm}, \text{Yb}, \text{and Y}$) exhibit strong reddish-purple emission. In **Figure 6**, we have shown emission spectra of all the rare-earth containing chromium molybdate solids (refer also **Figure S10**). This is to be noted that only Sm, Eu, Tb, and Dy are known to show strong emission in the visible region. The corresponding aluminum

analog (**Figure 6**) showed only characteristic emission from the respective lanthanide ions. In general, lanthanides are prone to give strong discrete emission due to *f-f* transitions, whereas Cr^{3+} is from *3d* band contribution. The domination of Cr^{3+} emission from the lanthanide containing chromium molybdates still remains an intriguing problem. Europium doped solids (crystalline phosphors and glasses) strongly emitting in orange-red region are known structural probes for identification of symmetry and coordination (Swapna et al., 2014). To analyze further, we recorded PL spectra of EuCr_7 at various excitation levels of both Cr^{3+} and Eu^{3+} transitions (**Figure 7**). For all excitation energies, we observed only signatures of Cr^{3+} ion, occurring at around 692, 709 and 733 nm attributed to Stokes shifted ${}^2\text{T}_1 \rightarrow {}^4\text{A}_2$ (R-lines) and ${}^2\text{E} \rightarrow {}^4\text{A}_2$ transitions. It is widely accepted that Cr^{3+} ion emission is highly dependent on temperature and on the matrix in which the ion is situated. The sharp emission around 703 and 704.4 nm observed for Cr^{3+} in $[\text{Na}_3\{\text{Cr}(\text{OH})_6\text{Mo}_6\text{O}_{18}\} \cdot 8\text{H}_2\text{O}]$ at 4.2 K was assigned to R-lines (Yamase and Sugeta, 1993). Similar to our earlier observation (Kumar et al., 2014a), the room-temperature spectra of all chromium molybdates showed only the dominant red

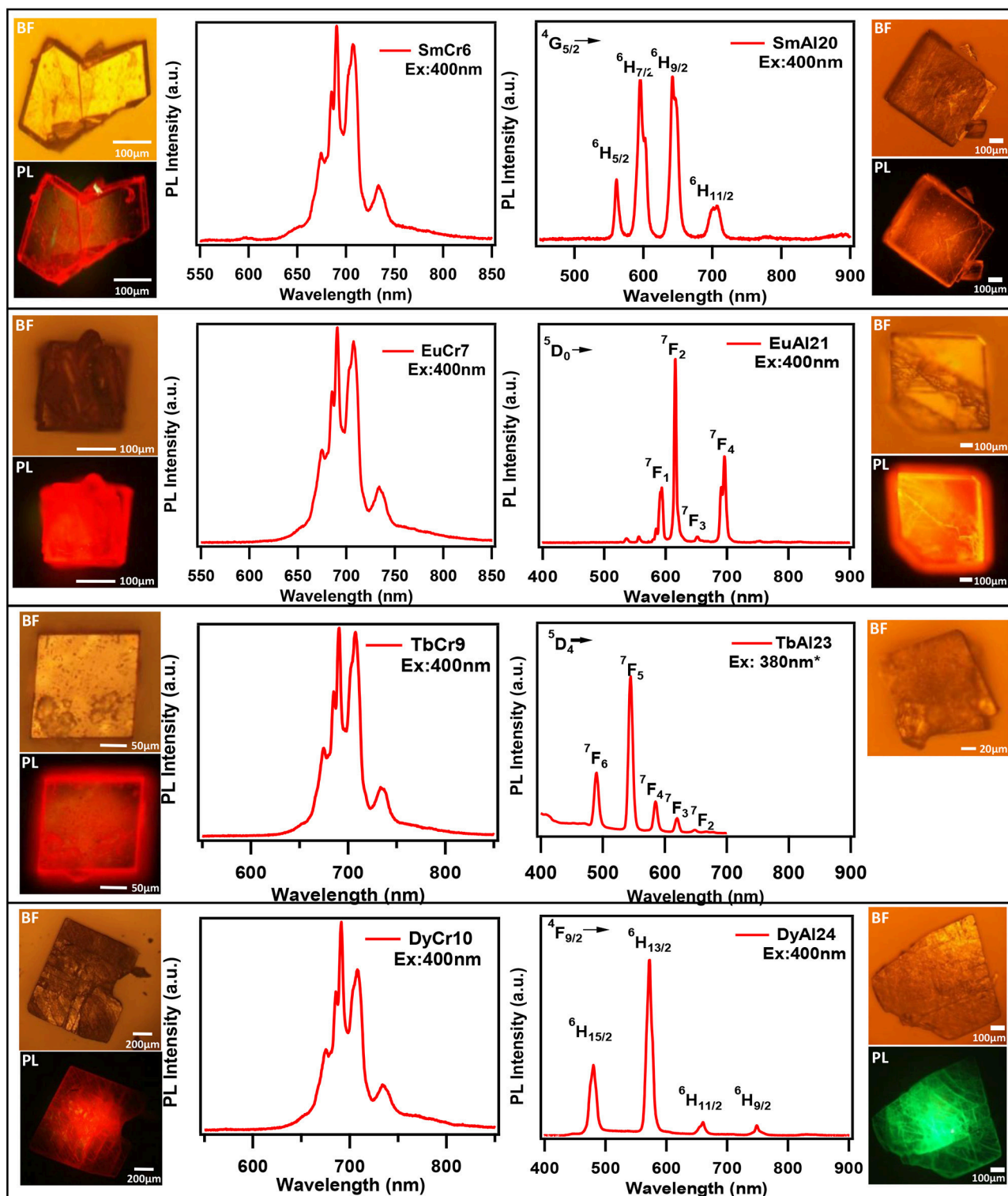


FIGURE 6 | The Emission spectra of single crystals of (A) $\text{Ln}(\text{H}_2\text{O})_7[\text{Cr}(\text{OH})_6\text{Mo}_6\text{O}_{18}]\cdot y\text{H}_2\text{O}$ and (B) $[\text{Ln}(\text{H}_2\text{O})_7[\text{Al}(\text{OH})_6\text{Mo}_6\text{O}_{18}]]\cdot y\text{H}_2\text{O}$. Ln = Sm, Eu, Tb, Dy, and Tm. The Bright field (BF) and PL images (PL) are given at left and right sides for respective crystals. PL spectra and images are recorded using 400 nm laser excitation coupled to a microscope. *Excited by 380 nm of Xe lamp coupled to a monochromator (see text).

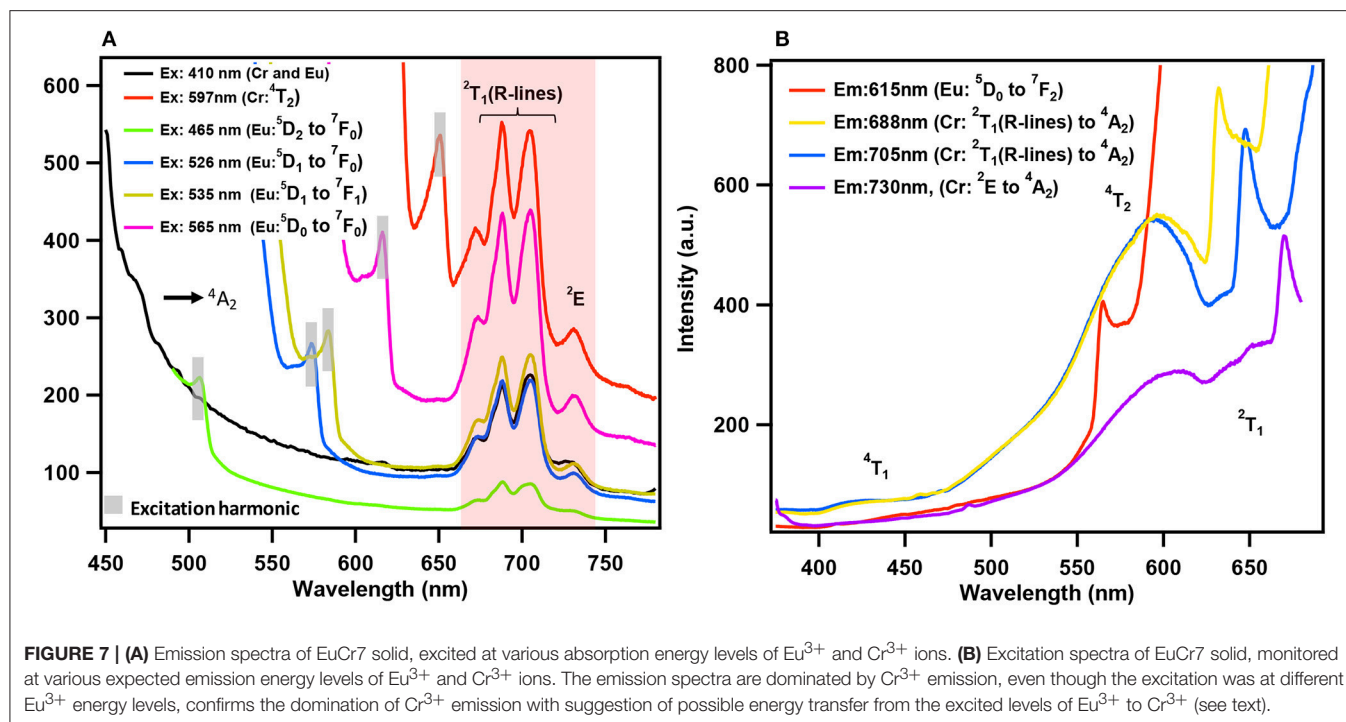


FIGURE 7 | (A) Emission spectra of EuCr7 solid, excited at various absorption energy levels of Eu^{3+} and Cr^{3+} ions. **(B)** Excitation spectra of EuCr7 solid, monitored at various expected emission energy levels of Eu^{3+} and Cr^{3+} ions. The emission spectra are dominated by Cr^{3+} emission, even though the excitation was at different Eu^{3+} energy levels, confirms the domination of Cr^{3+} emission with suggestion of possible energy transfer from the excited levels of Eu^{3+} to Cr^{3+} (see text).

emission (**Figure 6**). The purple color strikingly visible to naked eye suggests that non-radiative processes leading to low emission quantum yield of R-lines is unlikely.

The excitation (PLE) spectra at the prominent emission lines of Cr^{3+} and Eu^{3+} ions (**Figure 7**) observed at 423, 581 and 648 nm correspond to absorption transitions of Cr^{3+} in pseudo-octahedral geometry, $^4\text{A}_2 \rightarrow ^4\text{T}_1$ (F), $^4\text{T}_2$, and $^2\text{T}_1$. Therefore, it is convenient to conclude that the observed emission in EuCr7 and other chromium analogs is essentially from Cr^{3+} without any traces of contribution from the optically active lanthanide ions. PLE and PL spectra shown in **Figure 7**, categorically confirms the domination of Cr^{3+} emission suggesting a possible energy transfer from excited levels of Eu^{3+} to Cr^{3+} . **Figure 8**, shows a comparison of relative emission intensities of EuCr7 and EuAl21 single crystals, along with natural ruby crystal. The experiments are conducted under identical condition (same excitation power densities, integration time etc). The relative PL intensities and profile broadly suggest dominance of Cr^{3+} emission from EuCr7 and characteristic emission of Eu^{3+} from EuAl21. The relative intensities of both solids are about 13% on comparison with the natural ruby. Therefore, in EuCr7 it may be concluded that while excited by 400 nm ($^5\text{D}_3$ level of Eu^{3+}) (or any other transitions of $^5\text{D}_1$ ($J = 0, 1, 2$) levels), the excited densities are completely energy transferred to the equivalent energy bands of $^4\text{T}_1$ and $^4\text{T}_2$, then depopulates radiatively from $^2\text{T}_1$ and ^2E to ground state $^4\text{A}_2$ of Cr^{3+} ion. On the other hand, EuAl21 solid, the excitation to until $^5\text{D}_0$ level, results into the emission from $^5\text{D}_1$ to $^7\text{F}_j$ ($J = 0, 1, 2$) and $^5\text{D}_0$ to $^7\text{F}_j$ ($J = 0, 1, 2, 3, 4$) of Eu^{3+} ion. The schematic energy levels of EuCr7 and EuAl21 are given in **Figure 8**.

It is to be noted that the absence of Eu^{3+} emission and the presence of ruby-like emission (at 77 K) in

$[\text{Eu}(\text{H}_2\text{O})_7\{\text{Cr}(\text{OH})_6\text{Mo}_6\text{O}_{18}\}]$ was also observed previously by another group (Yusov et al., 2002). Surprisingly, two solids reported in the literature have exhibited contrasting results. $[\text{Eu}(\text{H}_2\text{O})_7\{\text{Cr}(\text{OH})_6\text{Mo}_6\text{O}_{18}\}] \cdot 4\text{H}_2\text{O}$ (Shi D. M. et al., 2008) showed only characteristic emission due to Eu^{3+} ions with no trace of Cr^{3+} emission. Similarly, the molecular solid $[(\text{C}_6\text{H}_5\text{NO}_2)_2\{\text{Dy}(\text{H}_2\text{O})_6\}\{\text{Cr}(\text{OH})_6\text{Mo}_6\text{O}_{18}\}] \cdot 2(\text{C}_6\text{H}_5\text{NO}_2) \cdot 6\text{H}_2\text{O}$ also showed characteristic emission only from Dy^{3+} ion (Yang et al., 2013). It can be argued that in the latter solid, there is no direct coordination linkage between the lanthanide and the cluster. However, another molecular solid, $[(\text{Hbipy})_2\{\text{Cr}(\text{OH})_6\text{Mo}_6\text{O}_{17}(\text{OH})\}]$ displayed typical Cr^{3+} emission only (Li et al., 2016). Therefore, having the extensive experimental evidence from the present study, the suppression of lanthanide emission and dominant chromium emission could be attributed to strong absorption cross-section of Cr^{3+} ions and energy transfer (ET) between 4f–4f emission transitions of Ln^{3+} ions to that of Cr^{3+} d-orbital energy levels. While all the compounds showed bright red emission, in the special case of NdCr5, the red emission from Cr^{3+} is considerably quenched. **Figure S8** shows a comparison of the same with EuCr7, recorded under similar condition, along with PL images. It can be speculated that Cr^{3+} emitting energy level ^2E is closer to Nd^{3+} level $^4\text{F}_{3/2}$, therefore the quenching of emission intensity may be possible (Weber, 1973); However, further studies are required to address this issue.

One of the characteristic features of a trivalent lanthanide ion is the strong and sharp 4f shell absorption and emission peaks that cover a wide range of spectral regions, from UV to IR. It is known that the lanthanide 4f–4f transition strengths and positions are sensitive to the local environment within

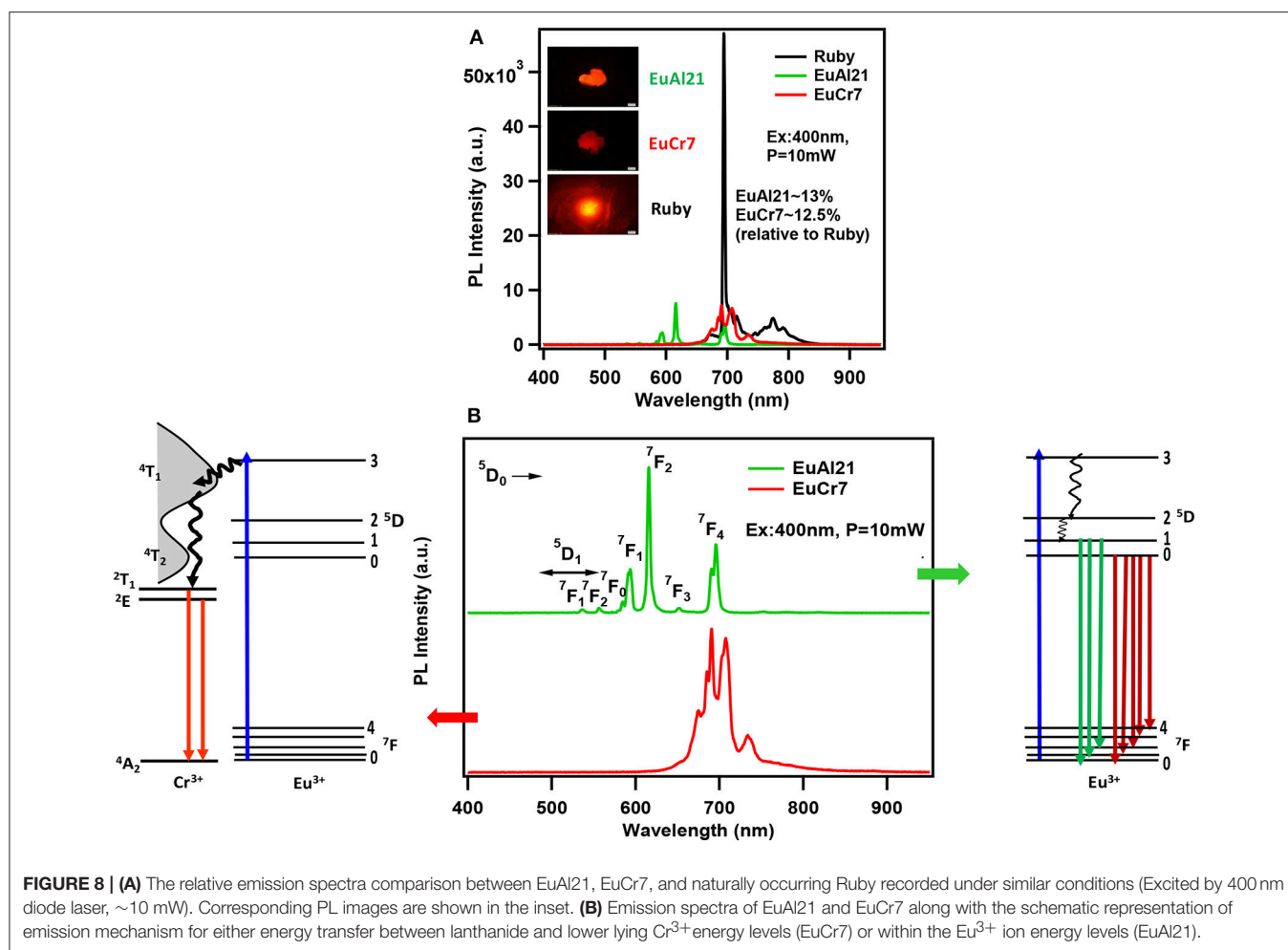


FIGURE 8 | (A) The relative emission spectra comparison between EuAl21, EuCr7, and naturally occurring Ruby recorded under similar conditions (Excited by 400 nm diode laser, ~10 mW). Corresponding PL images are shown in the inset. **(B)** Emission spectra of EuAl21 and EuCr7 along with the schematic representation of emission mechanism for either energy transfer between lanthanide and lower lying Cr³⁺ energy levels (EuCr7) or within the Eu³⁺ ion energy levels (EuAl21).

a crystalline network. PL studies of the aluminum analogs (**Figure 6**) revealed that the solids containing Sm, Eu, and Dy ions exhibited characteristic emission as expected (de Bettencourt-Dias, 2014). In **Table 3**, we have also shown the excitation and emission spectra with corresponding assignments. The visible emitting TbAl23 excitation and emission spectra are given in **Table 3** and **Figure S7**. Since Tb³⁺ does not have any energy level corresponding to the diode laser excitation source (400 nm), the microscopic PL spectra and images could not be obtained in **Figure 6**. The aluminum analogs of Ce³⁺, Pr³⁺, Ho³⁺, and Er³⁺ compounds did not show any appreciable PL in the visible region while excited in the UV-blue region. Another UV-violet low emitting solid TmAl27 and Cr³⁺ emission dominated TmCr13 PL spectra are shown in **Figure S8**.

PHYSICAL MEASUREMENTS

Single-Crystal X-ray Diffraction

Data collections were performed on a Bruker D8-Quest diffractometer with a Turbo X-ray Source (MoK α radiation, $\lambda = 0.71073$ Å) adopting the direct drive rotating anode technique and a PHOTON detector. The data frames were collected using the program APEX3 and processed using the program SAINT

routine in APEX3. The structures were solved by direct methods and refined by the full-matrix least-squares on F^2 using the SHELXTL-2014 program.

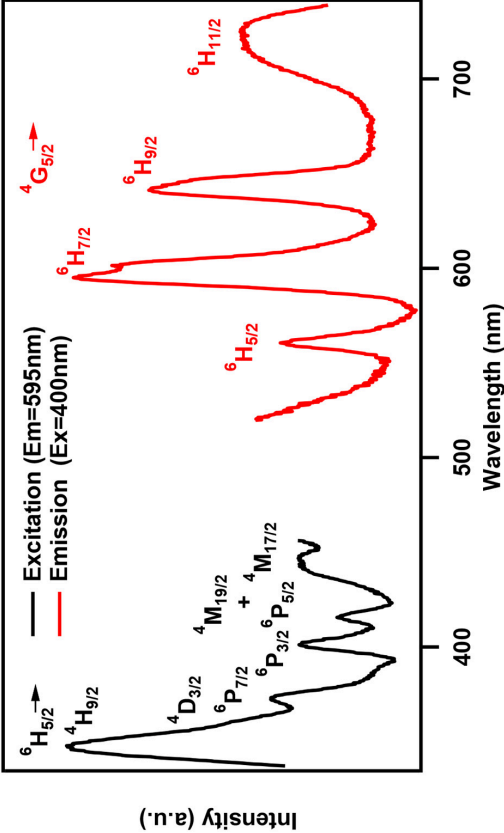
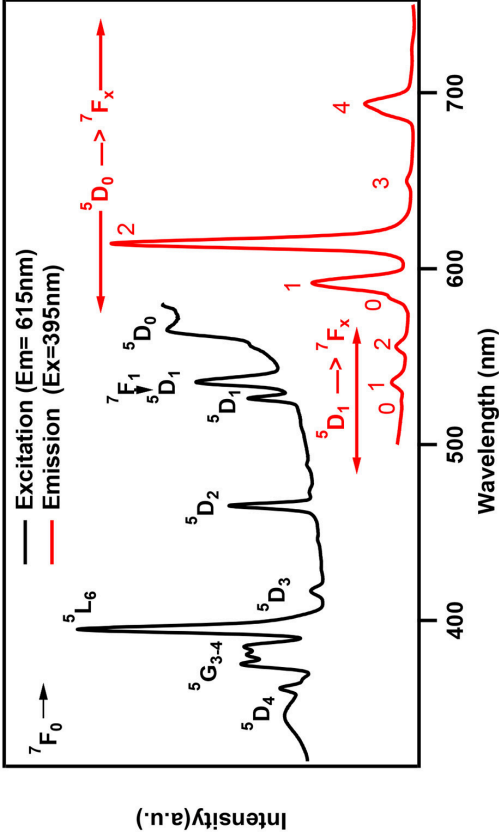
Powder X-ray Diffraction

Room temperature powder X-ray diffraction data (PXRD) were collected on a Bruker D8 Advance diffractometer using Ni-filtered CuK α radiation employing a step size of 0.02 and at count time of 1 s per step over the range $5^\circ < 2\theta < 80^\circ$. Rietveld refinement of powder diffraction data of all polycrystalline samples were carried out using Topas 4.2, Bruker for ensuring homogeneity of the synthesized products (**Table S1**).

Optical Measurements

Visible emission (~400–700 nm) and excitation spectra (300–520 nm) were recorded using a Spectrofluorophotometer (Shimadzu RF-5301PC), where the Xenon lamp is used as light source (**Figure 6** and **Table 3**). The microscopic optical images (Bright field), PL images and visible emission spectra were recorded using a modified confocal high-resolution microscope (Olympus BX-51) (**Figures 6–8**). The modified microscope is equipped with a fiber coupled 400 nm (± 5 nm) diode laser and xenon lamp as sources. The emission spectra and images were

TABLE 3 | Excitation and emission spectra of optically active lanthanides along with corresponding energy levels of Sm, Eu, Tb, and Dy. All the spectra are taken by a spectrofluorophotometer utilizing xenon lamp (see text). All assigned transitions (in parenthesis) are as per the reference (de Bettencourt-Dias, 2014).

Ln ⁺³	Emission transitions			Excitation and emission spectra	
	Experimental (Literature value)				
	Excited state	Ground state	Wavelength (nm)		
Sm	⁴ G _{5/2}	⁶ H _{5/2}	560 (560)		
		⁶ H _{7/2}	595 (595)		
		⁶ H _{9/2}	642 (640)		
		⁶ H _{11/2}	720 (700)		
Eu	⁵ D ₁	⁷ F ₀	525 (525)		
	⁵ D ₀	⁷ F ₁	535 (530)		
		⁷ F ₂	555 (560)		
		⁷ F ₀	583 (583)		
		⁷ F ₁	592 (590)		
		⁷ F ₂	615 (615)		
		⁷ F ₃	650 (650)		
		⁷ F ₄	694 (720)		

(Continued)

TABLE 3 | Continued

Ln ⁺³	Emission transitions Experimental (Literature value)			Excited state	Ground state	Wavelength (nm)	Excitation and emission spectra
Tb	⁵ D ₄	⁷ F ₆				490 (490)	
		⁷ F ₅				545 (540)	
		⁷ F ₄				585 (580)	
		⁷ F ₃				620 (620)	
		⁷ F ₂				648 (650)	
Dy	⁴ F _{9/2}	⁶ H _{15/2}				480 (475)	
		⁶ H _{13/2}				572 (570)	
		⁶ H _{11/2}				658 (660)	
		⁶ H _{9/2}				721 (750)	

collected, respectively by a fiber optic spectrometer (Ocean Optics, Maya 2000Pro) and a camera (Olympus, DP26) through a 425 nm long-pass filter (Pradeesh et al., 2009; Optics Express) in specular reflection mode.

Vibrational Spectroscopy

FT-IR was recorded on a Nicolet 5DX spectrophotometer with pressed KBr pellets in the range of 4,000–400 cm^{-1} . All the peaks are consistent with literature reports (Fedoseev et al., 2002; Bridgeman, 2006; Kumar et al., 2014a) (**Figures S2A–X, S3A–D**). The broad peaks at 3,500–3,200 cm^{-1} correspond to the O–H bond stretch. Due to differently bound water molecules, there is an observable splitting of these bands. The peaks at 1,630–1,620 cm^{-1} are characteristic of the deformation vibrations of H–O–H owing to the presence of coordinated and lattice water molecules. A peak at about 1,400 cm^{-1} in the case of Pr is observed, which has been reported by another group, which could not be explained adequately (Fedoseev et al., 2002). The low wavenumber peaks (960–400 cm^{-1}) are alike and are characteristic of the Anderson-Evans cluster. The bands at 950–890 cm^{-1} correspond to the symmetric stretching frequencies of the Mo–O_t bonds. The shape and intensity of the peaks are not sensitive to the nature of both the lanthanide and the cluster. The bands due to the vibrations of the bridging Mo–O–Mo bonds of different types are observed in the 700–400 cm^{-1} region. The replacement of the larger Cr³⁺ ion by Al³⁺ results in a noticeable shift of the vibrations of Mo–O–Mo from ~460–440 in case of Al to ~410–420 cm^{-1} in case of Cr.

Thermal Studies

Thermogravimetric analysis for selected solids were carried out using a Perkin-Elmer TGA7 system on well ground samples under a flowing nitrogen atmosphere with a heating rate of 10°C min⁻¹ in the range 40–800°C. The weight loss is almost consistent throughout the scan making it difficult to assign loss in steps. The presence of concomitant phases in the heavier lanthanides (Er and Tm) also makes it difficult to assign weight loss appropriately (**Figures S3A–H**).

As expected, thermal behavior of the two series (I and II) of solids were slightly different. For series I, the first weight loss (11–13%) occurred in the range of 40–120°C corresponding to the four lattice and two coordinated water. The slope of the curve clearly suggests the instability of an expected intermediate phase, [Ln(H₂O)₇{X(OH)₆Mo₆O₁₈}]· γ H₂O. The second weight loss of about 5–6% in the range of 150–330°C possibly corresponds to the loss of remaining coordinated water molecules. The total weight loss ~18–20% till ~500°C was in good agreement with complete decomposition of the solids to the respective oxides including the loss of hydroxyl groups attached to the cluster. For series II, the first weight loss (40–170°C) of about 10–11% corresponds to the loss of sixteen water molecules while the second one (170–320°C) about 9–10% correspond to the loss of fourteen coordinated water molecules. It is to be noted that for Er and Tm, the total weight loss showed significant deviation. This can be ascribed to the presence of a mixture of series I and II. Our TGA results are comparable to the earlier reports (Cao et al., 2008; Shi D. M. et al., 2008; Zhang et al., 2008; Wang et al., 2011).

CONCLUSIONS

Our strategy to assemble Anderson-Evans cluster and lanthanide hydrate through a one-pot synthesis led to two closely related structures of the composition [Ln(H₂O)₇{X(OH)₆Mo₆O₁₈}]· γ H₂O (X = Cr or Al). The lighter lanthanide ions (till Ho³⁺) favored extended lanthanide cluster coordination interaction forming 1D chains, while the heavier ones (Er and above) resulted in a stacking of a cation, Anderson-Evans cluster derivatised by a pair of lanthanide hydrates and an anion, a discrete Anderson-Evans clusters through H-bonding (0D). In both series, lattice water provides further stability to the structure. Observation of purple color in all chromium molybdate cluster based solids reported here as well as in literature is attributed to the domination of Cr³⁺ emission. Quenching of lanthanide emission in rare-earth coordinated chromium based Anderson-Evans cluster can be ascribed to energy transfer from 4f levels of Ln³⁺ ions to that of Cr³⁺ d-orbital energy levels. Further theoretical calculations are required to quantify the same. A future problem is to extend our methodology to assemble aluminum based cluster anion with two or more emitting lanthanide ions, i.e., possible solid solutions to realize white light materials. The paper highlights that structure-property evaluation of a POM system is more meaningful toward the design of functional materials if one adopts a crystal engineering approach to rationalize the fundamental chemistry.

AUTHOR CONTRIBUTIONS

AR conceived the idea as he has been working in this field for over 20 years. ST has the lead role in designing the synthesis and characterization. B and VK helped in the refinement crystal structures and supported in data collection and analysis. GJ supported in synthesis and data collection. MA carried out the photoluminescence experiments and related tasks. GVP carried out the photoluminescence studies and related tasks.

FUNDING

ST and AR acknowledge SERB (EMR/2016/004021) for a research fellowship and financial support. AR acknowledges DST: SR/FST/CSII-07/2014) for funding the single crystal diffractometer to the Chemistry Department, IIT Delhi.

ACKNOWLEDGMENTS

We thank both reviewers for their critical comments and suggestions to improve the manuscript. We thank Professor J. J. Vittal (NUS, Singapore) and Dr. B. Sridhar (IICT, Hyderabad) for their help in modeling the disordered water molecules of Series II. We are thankful to Mr. Sami Makki, M/s. Matrix India for gifting native ruby crystals. We also thank Ms. Manisha Jadon and Ms. Bharti Singh for help with various measurements.

SUPPLEMENTARY MATERIAL

The Supplementary Material for this article can be found online at: <https://www.frontiersin.org/articles/10.3389/fchem.2018.00631/full#supplementary-material>

In Supplementary Material, **Table 1** contains crystallographic information files (CIF) for all unreported solids, their Rietveld refinement plots (**Figure S3**), IR plots for all the synthesized solids (**Figures S4, S5**), Thermal Analysis plots for selected solids (**Figure S6**), Emission spectra of TbAl23 from commercial spectrofluorophotometer (**Figure S7**), the emission spectra for TmCr13 and TmAl27 is given in **Figure S8**. Figure S9 shows the emission comparison of EuCr7 and NdCr5. The emission spectra of other Cr-based solids and their corresponding Bright Field and

Photoluminescence images are shown in **Figure S10**. Rietveld refined parameters of all unreported solids (**Table S1**). **Table S2** has crystal structure and refinement parameters of reported solids that were resynthesized. IR frequencies (**Table S3**). Bond Valance Sum calculations for TbAl23 and TmAl27 (**Table S4**). **Table S5** contains the yields for all solids synthesized and **Table S6** reports selected bond distances and angles for all unreported solids. Optical data for all solids (**Figures 4, S10**). **Image 1** contains the **Graphical Abstract** which shows pictures of all the solids prepared for this study taken from Nikon D3300 DSLR camera (middle) and Nikon SMZ-745T microscope (top and bottom). A clear pink color is visible to eye can be seen in chromium analogs whereas in aluminum analogs, the typical color of corresponding lanthanides can be seen.

REFERENCES

- Ai, H., Wang, Y., Li, B., and Wu, L. (2014). Synthesis and characterization of single-side organically grafted Anderson-type polyoxometalates. *Eur. J. Inorg. Chem.* 2014, 2766–2772. doi: 10.1002/ejic.201301596
- Allain, C., Schaming, D., Karakostas, N., Erard, M., Gisselbrecht, J. P., Sorgues, S., et al. (2013). Synthesis, electrochemical and photophysical properties of covalently linked porphyrin-polyoxometalates. *Dalt. Trans.* 42, 2745–2754. doi: 10.1039/c2dt31415k
- Allen, C. C., Burns, R. C., Lawrance, G. A., Turner, P., and Hambley, T. W. (1997). Tetraammonium hexahydrogen-hexamolybdozincate(II) hexahydrate. *Acta Crystallogr. Sect. C Cryst. Struct. Commun.* 53(pt 1), 7–9. doi: 10.1107/S0108270196011043
- An, H., Li, Y., Xiao, D., Wang, E., and Sun, C. (2006). Self-assembly of extended high-dimensional architectures from Anderson-type polyoxometalate clusters. *Cryst. Growth Des.* 6, 1107–1112. doi: 10.1021/cg050326p
- An, H., Wang, E., Xiao, D., Li, Y., and Xu, L. (2005). Self-assembly of a novel 3D open framework from Anderson-type polyoxoanions. *Inorg. Chem. Commun.* 8, 267–270. doi: 10.1016/j.inoche.2004.12.024
- Anderson, J. S. (1937). Constitution of the polyacids. *Nature* 140:850. doi: 10.1038/140850a0
- Aota, S., Nomizu, M., and Yamada, K. M. (1994). The short amino acid sequence Pro-His-Ser-Arg-Asn in human fibronectin enhances cell-adhesive function. *J. Biol. Chem.* 269, 24756–24761.
- Armelo, L., Quici, S., Barigelletti, F., Accorsi, G., Bottaro, G., Cavazzini, M., et al. (2010). Design of luminescent lanthanide complexes: From molecules to highly efficient photo-emitting materials. *Coord. Chem. Rev.* 254, 487–505. doi: 10.1016/j.ccr.2009.07.025
- Bayraq, S. S., Nikseresh, A., and Khosravi, I. (2013). $(\text{NH}_4)_6\text{Mo}_7\text{O}_{34} \cdot 4\text{H}_2\text{O}$ as an efficient, selective, and reusable catalyst for the oxidation of thiols to disulfides using potassium bromate. *Phosphorus Sulfur Silicon Relat. Elem.* 188, 1236–1243. doi: 10.1080/10426507.2012.745076
- Bijelic, A., Molitor, C., Mauracher, S. G., Al-Oweini, R., Kortz, U., and Rompel, A. (2014). Hen egg-white lysozyme crystallisation: protein stacking and structure stability enhanced by a tellurium(VI)-centred polyoxotungstate. *ChemBioChem* 16, 233–241. doi: 10.1002/cbic.201402597
- Bijelic, A., and Rompel, A. (2015). The use of polyoxometalates in protein crystallography—an attempt to widen a well-known bottleneck. *Coord. Chem. Rev.* 299, 22–38. doi: 10.1016/j.ccr.2015.03.018
- Binnemans, K. (2009). Lanthanide-based luminescent hybrid materials. *Chem. Rev.* 109, 4283–4374. doi: 10.1021/cr8003983
- Blazevic, A., and Rompel, A. (2016). The Anderson-Evans polyoxometalate: from inorganic building blocks via hybrid organic-inorganic structures to tomorrow's 'Bio-POM'. *Coord. Chem. Rev.* 307, 42–64. doi: 10.1016/j.ccr.2015.07.001
- Bridgeman, A. J. (2006). Computational study of solvent effects and the vibrational spectra of the Anderson Polyoxometalates. *Chem. Eur. J.* 12, 2094–2102. doi: 10.1002/chem.200500802
- Bünzli, J. C. G., and Eliseeva, S. V. (2013). Intriguing aspects of lanthanide luminescence. *Chem. Sci.* 4, 1939–1949. doi: 10.1039/c3sc22126a
- Cao, R., Liu, S., Xie, L., Pan, Y., Cao, J., and Liu, Y. (2008). Influence of different site symmetries of Eu^{3+} centers on the luminescence properties of Anderson-based compounds. *Inorg. Chim. Acta* 361, 2013–2018. doi: 10.1016/j.ica.2007.10.015
- Charushnikova, I. A., Fedoseev, A. M., Yusov, A. B., and Den, A. C. (2005). Crystal structure of a new neodymium hexamolybdotellurate, $\text{Nd}_2\text{TeMo}_6\text{O}_{24} \cdot 19\text{H}_2\text{O}$. *Crystallogr. Reports* 50, 191–193. doi: 10.1134/1.1887892
- Coué, V., Dessapt, R., Bujoli-Doeuff, M., Evain, M., and Jobic, S. (2007). Synthesis, characterization, and photochromic properties of hybrid organic-inorganic materials based on molybdate, DABCO, and piperazine. *Inorg. Chem.* 46, 2824–2835. doi: 10.1021/ic0621502
- de Bettencourt-Dias, A. (ed.). (2014). *Luminescence of Lanthanide Ions in Coordination Compounds and Nanomaterials*. John Wiley and Sons, Ltd. doi: 10.1002/9781118682760
- Desiraju, G. R. (2007). Crystal engineering: a holistic view. *Angew. Chemie. Int. Ed.* 46, 8342–8356. doi: 10.1002/anie.200700534
- Desiraju, G. R., Vittal, J. J., and Ramanan, A. (2011). *Crystal Engineering: A Textbook*. World Scientific Publishing Co. Pvt. Ltd.
- Dhara, S., Dey, S., Basu, S., Drew, M. G. B., and Chattopadhyay, P. (2007). Separation of Ba-137m from Cs-137 using new ion exchanger $[\text{Na}_2(\text{H}_2\text{O}_4)_3[\text{Al}(\text{OH})_6\text{Mo}_6\text{O}_{18}]]$. *Radiochim. Acta* 95, 297–301. doi: 10.1524/ract.2007.95.5.297
- Drewes, D., and Krebs, B. (2005). Synthesis and structure of a novel type of polyoxomolybdate lanthanide complex: $[(\text{Ln}(\text{H}_2\text{O})_6)_2(\text{TeMo}_6\text{O}_{24})]$ (Ln = Ho, Yb). *Zeitschrift für Anorg. und Allg. Chemie* 631, 2591–2594. doi: 10.1002/zaac.200500089
- Drewes, D., Limanski, E. M., and Krebs, B. (2004a). A series of novel lanthanide polyoxometalates: Condensation of building blocks dependent on the nature of rare earth cations. *Dalt. Trans.* 0, 2087–2091. doi: 10.1039/b404237a
- Drewes, D., Limanski, E. M., and Krebs, B. (2004b). The Anderson-type anion $(\text{TeMo}_6\text{O}_{24})^{6-}$ —a multidentate ligand for trivalent rare earth cations. *Eur. J. Inorg. Chem.* 2, 4849–4853. doi: 10.1002/ejic.200400525
- Eldik, R., and Cronin, L. (Eds.) (2017). *Advances in Inorganic Chemistry: Polyoxometalate Chemistry*, Vol. 69. Academic Press; Springer.
- Evans, H. T. (1948). The crystal structures of ammonium and potassium molybdotellurates. *J. Am. Chem. Soc.* 70, 1291–1292. doi: 10.1021/ja01183a521
- Fedoseev, A. M., Budantseva, N. A., Andreev, G. B., Yusov, A. B., and Shirokova, I. B. (2002). Hexamolybdoaluminates and hexamolybdochromates of some trivalent lanthanides and americium. *Russ. J. Coord. Chem. Khimiya* 28, 279–284. doi: 10.1023/A:1015276121718
- Feng, X., Zhou, W., Li, Y., Ke, H., Tang, J., Clérac, R., et al. (2012). Polyoxometalate-supported 3d-4f heterometallic single-molecule magnets. *Inorg. Chem.* 51, 2722–2724. doi: 10.1021/ic202418y
- Gao, B., Liu, S. X., Zhang, C. D., Xie, L. H., Sun, C. Y., and Yu, M. (2007). Hydrothermal assembly of pyrite-related framework: $(\text{NH}_4)_2\{[\text{Ni}(\text{H}_2\text{O})_3]_2[\text{TeW}_6\text{O}_{24}]\} \cdot \text{H}_2\text{O}$. *J. Coord. Chem.* 60, 911–918. doi: 10.1080/00958970600986075
- Gavrilova, L. O., and Molchanov, V. N. (2005). Heteropoly Complexes $\text{Na}_{0.5}\text{Cs}_{2-x}[\text{H}_{0.5-x}\text{M}^{\text{II}}\text{X}^{\text{III}}(\text{OH})_6\text{Mo}_6\text{O}_{18}] \cdot 7-8\text{H}_2\text{O}$ ($\text{M}^{\text{II}} = \text{Fe, Mn}$; $\text{X}^{\text{III}} = \text{Cr, Al}$). *Russ. J. Coord. Chem.* 31, 627–640. doi: 10.1007/s11173-005-0147-6

- Hakouk, K., Oms, O., Dolbecq, A., Marrot, J., Saad, A., Mialane, P., et al. (2014). New photoresponsive charge-transfer spiropyran/polyoxometalate assemblies with highly tunable optical properties. *J. Mater. Chem. C* 2, 1628–1641. doi: 10.1039/c3tc31992j
- He, Z., Yan, Y., Li, B., Ai, H., Wang, H., Li, H., et al. (2012). Thermal-induced dynamic self-assembly of adenine-grafted polyoxometalate complexes. *Dalt. Trans.* 41, 10043–10051. doi: 10.1039/c2dt30421j
- Hill, C. L. (1998). Introduction: polyoxometalates multicomponent molecular vehicles to probe fundamental issues and practical problems. *Chem. Rev.* 98, 1–2. doi: 10.1021/cr960395y
- Himeno, S., Murata, S., and Eda, K. (2009). A route to a Keggin-Type α -[X(III)O₄Mo₁₂O₃₅(OH)]⁴⁻ anion through an Anderson-type [X(III)(OH)₆Mo₆O₁₈]³⁻ anion: X = Ga. *Dalt. Trans.* 35, 6114. doi: 10.1039/b902794g
- Hutin, M., Yvon, C., Yan, J., Macdonell, A., Long, D. L., and Cronin, L. (2013). Programming the assembly of carboxylic acid-functionalised hybrid polyoxometalates. *CrystEngComm* 15, 4422–4430. doi: 10.1039/c3ce26816k
- Inouye, Y., Tokutake, Y., Yoshida, T., Seto, Y., Hujita, H., Dan, K., et al. (1993). *In vitro* antiviral activity of polyoxomolybdates. Mechanism of inhibitory effect of PM-104 on human immunodeficiency virus type 1. *Antiviral Res.* 20, 317–331. doi: 10.1016/0166-3542(93)90075-T
- Ito, F., Ozeki, T., Ichida, H., Miyamae, H., and Sasaki, Y. (1989). Structure of tetraammonium hexahydrogenhexamolybdocuprate(II) tetrahydrate. *Acta Crystallogr. Sect. C* 45, 946–947. doi: 10.1107/S0108270188014544
- Ito, T., Yashiro, H., and Yamase, T. (2006). Regular two-dimensional molecular array of photoluminescent anderson-type polyoxometalate constructed by langmuir-blodgett technique. *Langmuir* 22, 2806–2810. doi: 10.1021/la052972w
- Joo, H. C., Park, K. M., Lee, U., and Brown, I. D. (2015). Crystal structure of the Anderson-type hetero-polyoxometalate; K₂[H₇Cr(III)Mo₆O₂₄]·8H₂O: A redetermination revealing the position of the extra H atom in the polyanion. *Acta Crystallogr. Sect. E Struct. Reports Online* 71, 157–160. doi: 10.1107/S2056989015000390
- Kitaigorodskii, A. I. (1965). The principle of close packing and the condition of thermodynamic stability of organic crystals. *Acta Crystallogr.* 18, 585–590. doi: 10.1107/S0365110X65001391
- Kondo, H., Kobayashi, A., and Sasaki, Y. (1980). The hexamolybdo-periodate anion in its potassium salt. *Acta Crystallogr. Sect. B* 36, 661–664. doi: 10.1107/S0567740880004037
- Kumar, D., Ahmad, S., Prakash, G. V., Ramanujachary, K. V., and Ramanan, A. (2014a). Photoluminescent chromium molybdate cluster coordinated with rare earth cations: synthesis, structure, optical and magnetic properties. *CrystEngComm* 16, 7097–7105. doi: 10.1039/c4ce00865k
- Kumar, D., Kumar, V., Upreti, S., and Ramanan, A. (2014b). Crystallization of hybrid molybdates based on organic bases. *Zeitschr. Anorg. Allg. Chem.* 640, 1190–1194. doi: 10.1002/zaac.201300687
- Kushch, L. A., Emel'yanov, V. A., Golhen, S., Cador, O., Schaniel, D., Woike, T., et al. (2009). The photochromic paramagnet derived from polyoxometalate [Cr(OH)₆Mo₆O₁₈]³⁻ and ruthenium mononitrosyl complex [RuNO(en)₂Cl]²⁺. *Inorg. Chim. Acta* 362, 2279–2282. doi: 10.1016/j.ica.2008.10.007
- Lee, H. Y., Park, K. M., Lee, U., and Ichida, H. (1991). Structure of tripotassium hexahydrogenhexamolybdoaluminate(III) heptahydrate. *Acta Crystallogr. Sect. C Cryst. Struct. Commun.* 47, 1959–1961. doi: 10.1107/S0108270191002159
- Lee, U. (1994). Dipotassium hexahydrogen- α -hexamolybdoplatinate(IV) pentahydrate, K₂[H₆ α -PtMo₆O₂₄]·5H₂O. *Acta Crystallogr. Sect. C Cryst. Struct. Commun.* 50, 1657–1659. doi: 10.1107/S0108270194001484
- Lee, U. (2007). Dipotassium heptahydrogenhexamolybdochromate(III) octahydrate, the first heptaprotonated Anderson-type polyoxometalate. *Acta Crystallogr. Sect. E Struct. Reports Online* 63, 7–9. doi: 10.1107/S1600536806052883
- Lee, U., and Joo, H. (2006a). Monopotassium monosodium hexahydrogen α -hexamolybdoplatinate(IV) hexahydrate. *Acta Cryst.* (2006). E62, i231–i233. doi: 10.1107/S1600536806043157
- Lee, U., and Joo, H. (2007). Hemiheptapotassium heminonahydrogen α -hexamolybdoplatinate(IV) 5.5-hydrate. *Acta Cryst.* (2007). E63, i11–i13. doi: 10.1107/S1600536806054055
- Lee, U., and Joo, H.-C. (2004). La₂[H₂PtMo₆O₂₄]·16H₂O. *Acta Cryst. E60*, i61–i63. doi: 10.1107/S1600536804007445
- Lee, U., Joo, H.-C., and Kwon, J.-S. (2002). Tetraammonium hexahydrogen hexamolybdonickelate(II) tetrahydrate, (NH₄)₄[H₆NiMo₆O₂₄]·4H₂O. *Acta Crystallogr. Sect. E Struct. Rep.* 58, i6–i8. doi: 10.1107/S1600536801021109
- Lee, U., Joo, H.-C., Kwon, J.-S., and Cho, M.-A. (2001). Tripotassium hexahydrogen hexamolybdocobaltate(III) heptahydrate, K₃[H₆CoMo₆O₂₄]·7H₂O. *Acta Crystallogr. Sect. E Struct. Rep.* 57, i112–i114. doi: 10.1107/S1600536801019365
- Lee, U., and Joo, H. C. (2000a). Tripotassium hexahydrogenhexamolybdocobaltate (III) potassium nitrate tetrahydrate, K₃[H₆CoMo₆O₂₄]·KNO₃·4H₂O. *Acta Crystallogr. Sect. C* 6–8. doi: 10.1107/S0108270100012154
- Lee, U., and Joo, H. C. (2000b). Dineodymium dihydrogen α -hexamolybdoplatinate(IV) tetradecahydrate, Nd₂[(H₂O)₂PtMo₆O₂₄]·14H₂O. *Acta Cryst* c56, e311–e312. doi: 10.1107/S0108270100009689
- Lee, U., and Joo, H. C. (2006b). Dipotassium hexahydrogen hexamolybdo-platinate(IV) hexahydrate. *Acta Crystallogr. Sect. E Struct. Rep.* 62, 241–243. doi: 10.1107/S1600536806046125
- Lee, U., and Sasaki, Y. (1984). Isomerism of the hexamolybdo-platinate(IV) polyanion. Crystal structures of K_{3.5}[α -H_{4.5}PtMo₆O₂₄]·3H₂O and (NH₄)₄[β -H₄PtMo₆O₂₄]·1.5H₂O. *Chem. Lett.* 13, 1297–1300. doi: 10.1246/cl.1984.1297
- Lehmann, J., Gaita-Arino, A., Coronado, E., and Loss, D. (2007). Spin qubits with electrically gated polyoxometalate molecules. *Nat. Nanotechnol.* 2, 312–317. doi: 10.1038/nnano.2007.110
- Leuenberger, M. N., and Loss, D. (2001). Quantum computing in molecular magnets. *Nature* 410, 789–793. doi: 10.1038/35071024
- Li, B., Ye, L., and Wu, L.-X. (2011). [Al(H₂O)₆][Cr(OH)₆Mo₆O₁₈]·10H₂O. *Acta Crystallogr. Sect. E Struct. Rep.* 67, i8–i8. doi: 10.1107/S1600536810053936
- Li, F., and Xu, L. (2011). Coordination assemblies of polyoxomolybdate cluster framework: from labile building blocks to stable functional materials. *Dalt. Trans.* 40, 4024. doi: 10.1039/c0dt00691b
- Li, X. M., Guo, Y., Shi, T., and Chen, Y. G. (2016). Crystal structures and photoluminescence of two inorganic-organic hybrids of anderson anions. *J. Clust. Sci.* 27, 1913–1922. doi: 10.1007/s10876-016-1072-1
- Liu, B., Feng, L., Zhou, S., Li, C. B., and Zhou, W. (2007). Poly[diammonium diaqua-hexahydroxyoctadeca-oxodisodiohexamolybdonickelate(II)]. *Acta Crystallogr. Sect. E Struct. Rep.* 63, 14–15. doi: 10.1107/S1600536806053761
- Liu, B., Zhou, S., Li, C. B., and Zhang, H. G. (2006). Poly[bis(imidazolium) hexahydroxyoctadeca-oxodisodiohexamolybdonickelate dihydrate]. *Acta Crystallogr. Sect. E Struct. Rep.* 62, 3188–3190. doi: 10.1107/S1600536806045168
- Liu, F.-X., Marchal-Roch, C., Dambournet, D., Acker, A., Marrot, J., and Sécheresse, F. (2008). From molecular to two-dimensional anderson polyoxomolybdate: synthesis, crystal structure, and thermal behavior of [Ni(H₂O)₄]₂[Ni(OH)₆Mo₆O₁₈]·4H₂O and [Ni(H₂O)₆][Ag₂[Ni(OH)₆Mo₆O₁₈]]·8H₂O. *Eur. J. Inorg. Chem.* 2008, 2191–2198. doi: 10.1002/ejic.200701288
- Liu, Y., Liu, S. X., Cao, R. G., Ji, H. M., Zhang, S. W., and Ren, Y. H. (2008). Hydrothermal assembly and luminescence property of lanthanide-containing Anderson polyoxometalates. *J. Solid State Chem.* 181, 2237–2242. doi: 10.1016/j.jssc.2008.05.023
- Lorenzo-Luis, P., Gili, P., Sánchez, A., Rodríguez-Castellón, E., Jiménez-Jiménez, J., Ruiz-Pérez, C., et al. (1999). Tungstotellurates of the imidazolium and 4-methylimidazolium cations. *Transit. Met. Chem.* 24, 686–692. doi: 10.1023/A1006987412453
- Lundberg, D., Persson, I., Eriksson, L., D'Angelo, P., and Panfili, S. De. (2010). Structural study of the N,N'-dimethylpropyleneurea solvated lanthanoid(III) ions in solution and solid state with an analysis of the ionic radii of lanthanoid(III) ions. *Inorg. Chem.* 49, 4420–4432. doi: 10.1021/ic100034q
- Manikumar, S., Shivaiah, V., and Das, S. K. (2002). Identification of a near-linear supramolecular water dimer, (H₂O)₂, in the channel of an inorganic framework material. *Inorg. Chem.* 41, 6953–6955. doi: 10.1021/ic025803x
- Martin, C., Lamontier, C., Fournier, M., Mentré, O., Harlé, V., Guillaume, D., et al. (2004). Preparation and characterization of 6-molybdocobaltate and 6-molybdoaluminate cobalt salts. Evidence of a new heteropolymolybdate structure. *Inorg. Chem.* 43, 4636–4644. doi: 10.1021/ic0354365
- Massia, S. P., and Hubbell, J. A. (1991). An RGD spacing of 440 nm is sufficient for integrin α -V- β -3-mediated fibroblast spreading and 140 nm for

- focal contact and stress fiber formation. *J. Cell Biol.* 114, 1089–1100. doi: 10.1083/jcb.114.5.1089
- Mauracher, S. G., Molitor, C., Al-Oweini, R., Kortz, U., and Rempel, A. (2014a). Latent and active abPPO4 mushroom tyrosinase cocrystallized with hexatungstotellurate(VI) in a single crystal. *Acta Crystallogr. Sect. D Biol. Crystallogr.* 70, 2301–2315. doi: 10.1107/S1399004714013777
- Mauracher, S. G., Molitor, C., Al-Oweini, R., Kortz, U., and Rempel, A. (2014b). Crystallization and preliminary X-ray crystallographic analysis of latent isoform PPO4 mushroom (*Agaricus bisporus*) tyrosinase. *Acta Crystallogr. Sect. F Struct. Biol. Commun.* 70, 263–266. doi: 10.1107/S2053230X14000582
- Mensinger, Z. L., Zakharov, L. N., and Johnson, D. W. (2008). Triammonium hexahydroxidooctadeca-oxido-hexamolybdo-gallate(III) hepta-hydrate. *Acta Crystallogr. Sect. E Struct. Rep.* 64, i8–i9. doi: 10.1107/S1600536807068067
- Michailovski, A., Hussain, F., and Spingler, B. (2009). Hydrothermal strategies towards polyoxofluoromolybdates (VI). *Cryst. Growth Des.* 9, 755–765. doi: 10.1021/cg800265q
- Nolan, A. L., Burns, R. C., and Lawrance, G. A. (1996). Reaction kinetics and mechanism of formation of $[H_4Co_2Mo_{10}O_{38}]^{6-}$ by peroxomonosulphate oxidation of Co(II) in the presence of molybdate. *J. Chem. Soc. Dalt. Trans.* 20, 2629–2636. doi: 10.1039/DT9850002629
- Ogawa, A., Yamato, H., Lee, U., Ichida, H., Kobayashi, A., and Sasaki, Y. (1988). Structure of pentapotassium dihydrogenhexamolybdoantimonate heptahydrate. *Acta Crystallogr. Sect. C Cryst. Struct. Commun.* 44, 1879–1881. doi: 10.1107/S0108270188007073
- Ohashi, K., Yanagi, K., Sasada, Y., and Yamase, T. (1982). Crystal Structure and Photochemistry of Isopolymolybdates. I. The crystal structures of hexakis(propylammonium)heptamolybdate(VI) trihydrate and hexakis(isopropylammonium)heptamolybdate(VI) trihydrate. *Bull. Chem. Soc. Jpn.* 55, 1254–1260. doi: 10.1246/bcsj.55.1254
- Oms, O., Hakouk, K., Dessapt, R., Deniard, P., Jobic, S., Dolbecq, A., et al. (2012). Photo- and electrochromic properties of covalently connected symmetrical and unsymmetrical spiropyran-polyoxometalate dyads. *Chem. Commun.* 48, 12103–12105. doi: 10.1039/c2cc35376h
- Ozawa, Y., Hayashi, Y., and Isobe, K. (1991). Structure of triammonium hexahydrogenhexamolybdo-rhodate(III) hexahydrate. *Acta Crystallogr. Sect. C* 47, 637–638. doi: 10.1107/S0108270190009763
- Panneerselvam, K., Soriano-García, M., Holguin-Quinones, S., and Holt, E. M. (1996). Hexa-aqua-gallium hexahydrogenhexamolybdocobaltate(III) decahydrate. *Acta Crystallogr. Sect. C Cryst. Struct. Commun.* 52, 1605–1607. doi: 10.1107/S0108270195017161
- Pardo, R., Zayat, M., and Levy, D. (2011). Photochromic organic-inorganic hybrid materials. *Chem. Soc. Rev.* 40, 672–687. doi: 10.1039/c0cs00065e
- Pavani, K., Singh, M., and Ramanan, A. (2011). Oxalate bridged copper pyrazole complex templated Anderson-Evans cluster based solids. *Aust. J. Chem.* 64, 68–76. doi: 10.1071/CH10276
- Perloff, A. (1970). The crystal structure of sodium hexamolybdochromate(III) Octahydrate, $Na_3(CrMo_6O_{24}H_6) \cdot 8H_2O$. *Inorg. Chem.* 9, 2228–2239. doi: 10.1021/ic50092a006
- Pope, M. T. (1983). *Heteropoly and Isopoly Oxometalates*. Berlin; Heidelberg: Springer-Verlag.
- Pope, M. T. (2002). *Polyoxometalate Chemistry From Topology via Self-Assembly to Applications*. Kluwer Academic Publishers.
- Pradeesh, K., Baumberg, J. J., and Prakash, G. V. (2009). Strong exciton-photon coupling in inorganic-organic multiple quantum wells embedded low-Q microcavity. *Opt. Express* 17:22171. doi: 10.1364/OE.17.022171
- Raza, R., Matin, A., Sarwar, S., Barsukova-Stuckart, M., Ibrahim, M., Kortz, U., et al. (2012). Polyoxometalates as potent and selective inhibitors of alkaline phosphatases with profound anticancer and amoebicidal activities. *Dalt. Trans.* 41, 14329–14336. doi: 10.1039/c2dt31784b
- Ritchie, C., and Bryant, G. (2015). Microwave assisted synthesis of a mono organoimido functionalized Anderson polyoxometalate. *Dalt. Trans.* 44, 20826–20829. doi: 10.1039/c5dt04000k
- Robl, C., and Frost, M. (1993a). $Na_6[TeMo_6O_{24}] \cdot 22H_2O$ —a layered heteropoly compound with the chain-like polycation $[Na_3(H_2O)_{11}]^{3n+}$. *Z. Naturforsch.* 48b, 404–408. doi: 10.1515/znB-1993-0402
- Robl, C., and Frost, M. (1993b). Alkalimolybdo-tellurate: Darstellung und Kristallstruktur von $Rb_6[TeMo_6O_{24}] \cdot 10H_2O$ und $Rb_6[TeMo_6O_{24}] \cdot Te(OH)_6 \cdot 6H_2O$. *Z. Anorg. Allg. Chem.* 619, 1834–1840. doi: 10.1002/zaac.19936191105
- Rosnes, M., Ali, H., Yvon, C., Long, D.-L., and Cronin, L. (2012). Mapping the synthesis of low nuclearity polyoxometalates from octamolybdates to Mn-Anderson cluster. *Dalt. Trans.* 41, 10071–10079. doi: 10.1039/c2dt31008b
- Rosnes, M. H., Musumeci, C., Yvon, C., Macdonell, A., Pradeep, C. P., Sartorio, C., et al. (2013). Exploring the interplay between ligand derivatisation and cation type in the assembly of hybrid polyoxometalate Mn-andersons. *Small* 9, 2316–2324. doi: 10.1002/smll.201202510
- Rosu, C., and Weakley, T. J. R. (2000). Disodium chromium(III) hexamolybdoiodate(VII) 24-hydrate, $Na_2Cr[IMo_6O_{24}] \cdot 24H_2O$. *Acta Crystallogr. Sect. C*, C56, e170–e171.
- Schaming, D., Allain, C., Farha, R., Goldmann, M., Lobstein, S., Giraudeau, A., et al. (2010). Synthesis and photocatalytic properties of mixed polyoxometalate-porphyrin copolymers obtained from anderson-type polyoxomolybdates. *Langmuir* 26, 5101–5109. doi: 10.1021/la903564d
- Shah, H. S., Al-Oweini, R., Haider, A., Kortz, U., and Iqbal, J. (2014). Cytotoxicity and enzyme inhibition studies of polyoxometalates and their chitosan nanoassemblies. *Toxicol. Rep.* 1, 341–352. doi: 10.1016/j.toxrep.2014.06.001
- Shannon, R. D. (1976). Revised effective ionic radii and systematic studies of interatomic distances in halides and chalcogenides. *Acta Crystallogr.* A32, 751–767. doi: 10.1107/S0567739476001551
- Shi, D., Hu, M., Zhang, C., Li, J., and Chen, Y. (2008). Synthesis and structure of a novel polyoxomolybdate lanthanide complex: $[Er_2(H_2O)_{14}Cr(OH)_6Mo_6O_{18}][Cr(OH)_6Mo_6O_{18}] \cdot 14H_2O$. *J. Chem. Crystallogr.* 38, 695–700. doi: 10.1007/s10870-008-9378-y
- Shi, D. M., Ma, F. X., Zhang, C. J., Lu, S., and Chen, Y. G. (2008). Self-assembly of polyoxometalate-supported Ln-H hydroxo/oxo clusters with 1D extended structure: $[LnIII(H_2O)_7Cr(OH)_6Mo_6O_{18}]_n \cdot 4nH_2O$ (Ln = Ce, Sm, Eu). *Zeitschr. Anorg. und Allg. Chemie* 634, 758–763. doi: 10.1002/zaac.200700498
- Shivaiah, V., Chatterjee, T., and Das, S. K. (2014). Coordination of lanthanide cation to an Anderson type polyoxometalate anion leads to isomorphous metal-oxide based one-dimensional inorganic solids: synthesis, crystal structure and spectroscopy. *J. Chem. Sci.* 126, 1525–1533. doi: 10.1007/s12039-014-0688-7
- Shivaiah, V., and Das, S. K. (2005). Supramolecular assembly based on a heteropolyanion: synthesis and crystal structure of $Na_3(H_2O)_6[Al(OH)_6Mo_6O_{18}] \cdot 2H_2O$. *J. Chem. Sci.* 117, 227–233. doi: 10.1007/BF02709291
- Shivaiah, V., Nagaraju, M., and Das, S. K. (2003). Formation of a spiral-shaped inorganic-organic hybrid chain, $[Cu(II)(2,2'-bipy)(H_2O)_2Al(OH)_6Mo_6O_{18}]$: Influence of intra- and interchain supramolecular interactions. *Inorg. Chem.* 42, 6604–6606. doi: 10.1021/ic034581f
- Shivaiah, V., Narasimha Reddy, P. V., Cronin, L., and Das, S. K. (2002). A novel polyoxometalate chain formed from heteropolyanion building blocks and rare earth metal ion linkers: $[La(H_2O)_7Al(OH)_6Mo_6O_{18}]_n \cdot 4nH_2O$. *J. Chem. Soc. Dalt. Trans.* 1, 3781–3782. doi: 10.1039/B207149E
- Singh, M., Kumar, D., and Ramanan, A. (2014). Crystal engineering of Anderson-Evans cluster based salts through N-H...O interactions. *Proc. Natl. Acad. Sci. India Sect. A Phys. Sci.* 84, 305–314. doi: 10.1007/s40010-014-0144-6
- Singh, M., Kumar, D., Thomas, J., and Ramanan, A. (2010a). Crystallization of copper(II) sulfate based minerals and MOF from solution: chemical insights into the supramolecular interactions. *J. Chem. Sci.* 122, 757–769. doi: 10.1007/s12039-010-0064-1
- Singh, M., Lofland, S. E., Ramanujachary, K. V., and Ramanan, A. (2010b). Crystallization of Anderson-Evans type chromium molybdate solids incorporated with a metal pyrazine complex or coordination polymer. *Cryst. Growth Des.* 10, 5105–5112. doi: 10.1021/cg100754k
- Singh, M., and Ramanan, A. (2011). Crystal engineering of polyoxomolybdates based metal-organic solids: the case of chromium molybdate cluster based metal complexes and coordination polymers. *Cryst. Growth Des.* 11, 3381–3394. doi: 10.1021/cg101695w
- Song, P. Y.-F. (2018). *Polyoxometalate-Based Assemblies and Functional Materials*. Springer International Publishing.
- Song, Y. F., McMillan, N., Long, D. L., Kane, S., Malm, J., Riehle, M. O., et al. (2009). Micropatterned surfaces with covalently grafted unsymmetrical polyoxometalate-hybrid clusters lead to selective cell adhesion. *J. Am. Chem. Soc.* 131, 1340–1341. doi: 10.1021/ja807091v

- Song, Y. F., McMillan, N., Long, D. L., Thiel, J., Ding, Y., Chen, H., et al. (2008). Design of hydrophobic polyoxometalate hybrid assemblies beyond surfactant encapsulation. *Chem. A Eur. J.* 14, 2349–2354. doi: 10.1002/chem.200701629
- Swapna, K., Mahamuda, S., Rao, A. S., Sasikala, T., Packiyaraj, P., Moorthy, L. R., et al. (2014). Luminescence characterization of Eu^{3+} doped zinc alumino bismuth borate glasses for visible red emission applications. *J. Lumin.* 156, 80–86. doi: 10.1016/j.jlumin.2014.07.022
- Tanaka, S., Annaka, M., and Sakai, K. (2012). Visible light-induced water oxidation catalyzed by molybdenum-based polyoxometalates with mono- and dicobalt(III) cores as oxygen-evolving centers. *Chem. Commun.* 48, 1653–1655. doi: 10.1039/c2cc16821a
- Tkac, P., and Paulenova, A. (2008). Speciation of molybdenum (VI) in aqueous and organic phases of selected extraction systems. *Sep. Sci. Technol.* 43, 2641–2657. doi: 10.1080/01496390802122261
- Upreti, S., Datta, A., and Ramanan, A. (2007). Role of nonbonding interactions in the crystal growth of phenazinediamine tetrahydrate: new insights into the occurrence of 2D water layers in crystal hydrates. *Cryst. Growth Des.* 7, 966–971. doi: 10.1021/cg060958r
- Wang, H. Y., Zhang, C. J., Zhang, C. H., Tang, Q., and Chen, Y. G. (2011). Synthesis, structure, and magnetism of four polyoxomolybdate compounds containing yttrium and ytterbium. *J. Coord. Chem.* 64, 1481–1490. doi: 10.1080/00958972.2011.573847
- Weber, M. J. (1973). Chromium—rare-earth energy transfer in YAlO_3 . *J. Appl. Phys.* 44, 4058–4064. doi: 10.1063/1.1662895
- Wu, C., Lin, X., Yu, R., Yang, W., Lu, C., and Zhuang, H. (2001). $[\text{Na}_4(\text{H}_2\text{O})_7][\text{Fe}(\text{OH})_6\text{Mo}_6\text{O}_{18}]$: A new [12] metallocrown-6 structure with an octahedrally coordinated iron at the center. *Sci. China Ser. B Chem.* 44, 49–54. doi: 10.1007/BF02879735
- Wu, Q., Li, Y. G., Wang, Y. H., Clérac, R., Lu, Y., and Wang, E. B. (2009). Polyoxometalate-based $\{\text{Mn}^{\text{III}}_2\}$ -Schiff base composite materials exhibiting single-molecule magnet behaviour. *Chem. Commun.* 38, 5743–5745. doi: 10.1039/b909246c
- Yamase, T. (1993). Polyoxometalates for molecular devices: antitumor activity and luminescence. *Mol. Eng.* 3, 241–262. doi: 10.1007/BF00999636
- Yamase, T., and Sugeta, M. (1993). Charge-transfer photoluminescence of polyoxo-tungstates and -molybdates. *J. Chem. Soc. Dalton Trans.* 0, 759–765. doi: 10.1039/DT9930000759
- Yan, J., Gong, K., Xue, X., He, X., Zhao, C., Han, Z., et al. (2014). Two layerlike supramolecular assemblies based on B-Anderson-type polyanionic clusters and their adsorption property. *Eur. J. Inorg. Chem.* 2014, 5969–5976. doi: 10.1002/ejic.201402654
- Yan, X., Mo, S., Ju, Z., Wu, J., and Yao, K. (2008). Synthesis and structure of a series of Anderson-Evans type heteropolymolybdates: $[\text{Ln}(\text{H}_2\text{O})_n]_2[\text{TeMo}_6\text{O}_{24}] \cdot 6\text{H}_2\text{O}$. *Synth. React. Inorg. Met. Nano-Metal Chem.* 38, 529–533. doi: 10.1080/15533170802265459
- Yan, Y., Li, B., He, Q., He, Z., Ai, H., Wang, H., et al. (2012). Synthesis and redox-responsive self-assembly of ferrocene grafted Anderson-type polyoxometalate hybrid complexes. *Soft Matter* 8, 1593–1600. doi: 10.1039/c1sm06610b
- Yang, L., Zhou, Z., Ma, P.-T., Zhang, X.-F., Wang, J.-P., and Niu, J.-Y. (2013). Three organic-inorganic hybrid B-Anderson polyoxoanions as building blocks: syntheses, structures, and characterization of $[(\text{C}_6\text{H}_5\text{NO}_2)_2\text{Ln}(\text{H}_2\text{O})_6](\text{CrMo}_6\text{O}_{24}\text{H}_6) \cdot 2\text{C}_6\text{H}_5\text{NO}_2 \cdot 6\text{H}_2\text{O}$ ($\text{Ln} = \text{Sm}, \text{Dy}, \text{Er}$). *J. Coord. Chem.* 66, 1058–1067. doi: 10.1080/00958972.2013.775429
- Yu, L., Li, S.-Z., and Wang, J.-P. (2006). $[\text{Na}_3(\text{H}_2\text{O})_{11}][\text{CrMo}_6\text{O}_{24}\text{H}_6] \cdot 2\text{H}_2\text{O}$, with an Anderson B-type heteropolyoxoanion. *Acta Crystallogr. Sect. E Struct. Rep.* 62, i190–i192. doi: 10.1107/S1600536806032910
- Yusov, A. B., Yin, M., Fedosseev, A. M., Andreev, G. B., Shirokova, I. B., and Krupa, J.-C. (2002). Luminescence study of new Ln(III) compounds formed from Anderson's heteropoly anions $\{\text{Al}(\text{OH})_6\text{Mo}_6\text{O}_{18}\}^{3-}$ and $\{\text{Cr}(\text{OH})_6\text{Mo}_6\text{O}_{18}\}^{3-}$. *J. Alloys Compd.* 344, 289–292. doi: 10.1016.S0925-8388(02)00371-7
- Yvon, C., Surman, A. J., Hutin, M., Alex, J., Smith, B. O., Long, D. L., et al. (2014). Polyoxometalate clusters integrated into peptide chains and as inorganic amino acids: Solution- and solid-phase approaches. *Angew. Chem. Int. Ed.* 53, 3336–3341. doi: 10.1002/anie.201311135
- Zhang, J., Huang, Y., Hao, J., and Wei, Y. (2017). β - $\{\text{Cr}[\text{RC}(\text{CH}_2\text{O})_3]_2\text{Mo}_6\text{O}_{18}\}^{3-}$: The first organically-functionalized β isomer of Anderson-type polyoxometalates. *Inorg. Chem. Front.* 4, 1215–1218. doi: 10.1039/c7qi00199a
- Zhang, J., Liu, Z., Huang, Y., Zhang, J., Hao, J., and Wei, Y. (2015a). Unprecedented χ isomers of single-side triol-functionalized Anderson polyoxometalates and their proton-controlled isomer transformation. *Chem. Commun.* 51, 9097–9100. doi: 10.1039/c5cc02947c
- Zhang, J., Luo, J., Wang, P., Ding, B., Huang, Y., Zhao, Z., et al. (2015b). Step-by-step strategy from achiral precursors to polyoxometalates-based chiral organic-inorganic hybrids. *Inorg. Chem.* 54, 2551–2559. doi: 10.1021/ic502622k
- Zhang, J., Yin, P., Hao, J., Xiao, F., Chen, L., and Wei, Y. (2012). Synthesis and assembly of a difunctional core POM cluster with two appended POM cluster caps. *Chem. A Eur. J.* 18, 13596–13599. doi: 10.1002/chem.201201098
- Zhang, J., Zhao, Z., Zhang, J., She, S., Huang, Y., and Wei, Y. (2014). Spontaneous resolution of polyoxometalate-based inorganic-organic hybrids driven by solvent and common ion. *Dalt. Trans.* 43, 17296–17302. doi: 10.1039/c4dt01954g
- Zhang, L. Z., Gu, W., Dong, Z. L., Liu, X., and Li, B. (2008). Phase transformation of a rare-earth Anderson polyoxometalate at low temperature. *Crystengcomm* 10, 1318–1320. doi: 10.1039/b808085b
- Zhao, L., Shen, S., and Yu, H. (2008). Synthesis, crystal structure and characterization of a 1D polyoxometalate-based compound: $\{[\text{Pr}(\text{H}_2\text{O})_7][\text{CrMo}_6\text{H}_6\text{O}_{24}]\} \cdot 4\text{H}_2\text{O}$. *Z. Naturforsch.* 63b, 799–803. doi: 10.1515/znbn-2008-0702
- Zhou, D. P., and Yang, D. (2007). A new chain-like polyoxometallate based on B-Anderson-type building blocks and rare earth metal ion linkers. *Acta Crystallogr. Sect. E Struct. Rep.* 63, 113–115. doi: 10.1107/S1600536807007787
- Zhou, Y. H., Zhao, M., Sun, H., Mao, Z. W., and Ji, L. N. (2009). Effect of cyclodextrin dimers with bipyridyl and biphenyl linking groups on carboxyl ester hydrolysis catalyzed by zinc complex. *J. Mol. Catal. A Chem.* 308, 61–67. doi: 10.1016/j.molcata.2009.03.026

Conflict of Interest Statement: The authors declare that the research was conducted in the absence of any commercial or financial relationships that could be construed as a potential conflict of interest.

Copyright © 2019 Tewari, Adnan, Balendra, Kumar, Jangra, Prakash and Ramanan. This is an open-access article distributed under the terms of the Creative Commons Attribution License (CC BY). The use, distribution or reproduction in other forums is permitted, provided the original author(s) and the copyright owner(s) are credited and that the original publication in this journal is cited, in accordance with accepted academic practice. No use, distribution or reproduction is permitted which does not comply with these terms.



Redox Reaction Triggered Nanomotors Based on Soft-Oxometalates With High and Sustained Motility

Apabrita Mallick^{1,2}, Abhrajit Laskar³, R. Adhikari^{3,4*} and Soumyajit Roy^{1,2*}

¹ Eco-Friendly Applied Materials Laboratory, College of Chemistry, Central China Normal University, Wuhan, China,

² Eco-Friendly Applied Materials Laboratory, Department of Chemistry, Materials Science Centre, Indian Institute of Science Education and Research, Kolkata, India, ³ The Institute of Mathematical Sciences, Chennai Institute of Technology, Chennai, India, ⁴ Department of Applied Mathematics and Theoretical Physics (DAMTP), Centre for Mathematical Sciences, University of Cambridge, Cambridge, United Kingdom

OPEN ACCESS

Edited by:

Federico Cesano,
Università degli Studi di Torino, Italy

Reviewed by:

Tilo Söhnle,
University of Auckland, New Zealand
Sukhendu Mandal,
Indian Institute of Science Education
and Research, Thiruvananthapuram,
India

*Correspondence:

R. Adhikari
rjoy@imsc.res.in
Soumyajit Roy
s.roy@iiserkol.ac.in

Specialty section:

This article was submitted to
Inorganic Chemistry,
a section of the journal
Frontiers in Chemistry

Received: 15 January 2018

Accepted: 17 April 2018

Published: 04 May 2018

Citation:

Mallick A, Laskar A, Adhikari R and
Roy S (2018) Redox Reaction
Triggered Nanomotors Based on
Soft-Oxometalates With High and
Sustained Motility.
Front. Chem. 6:152.
doi: 10.3389/fchem.2018.00152

The recent interest in self-propulsion raises an immediate challenge in facile and single-step synthesis of active particles. Here, we address this challenge and synthesize soft oxometalate nanomotors that translate ballistically in water using the energy released in a redox reaction of hydrazine fuel with the soft-oxometalates. Our motors reach a maximum speed of 370 body lengths per second and remain motile over a period of approximately 3 days. We report measurements of the speed of a single motor as a function of the concentration of hydrazine. It is also possible to induce a transition from single-particle translation to collective motility with biomimetic bands simply by tuning the loading of the fuel. We rationalize the results from a physicochemical hydrodynamic theory. Our nanomotors may also be used for transport of catalytic materials in harsh chemical environments that would otherwise passivate the active catalyst.

Keywords: nanomotors, soft-oxometalates (SOMs), redox process, autonomous motion, chemically powered

INTRODUCTION

An immediate challenge in the field of soft active matter (Ghose and Adhikari, 2014; Kim et al., 2014; Li et al., 2014a; Sengupta et al., 2014) is to synthesize self-propelling (Ma et al., 2016; Soto et al., 2016; Teo and Pumera, 2016; Teo et al., 2016; Minh et al., 2017; Zhou et al., 2017) in a manner that is facile, preferably single step and that affords a rational control of motility. All such attributes can be built into colloidal charged metal oxide based soft-oxometalates (SOMs) (Roy, 2011, 2014) due to the presence of redox sites on their diffuse interface. Here we trigger SOMs to move by inducing a simple redox reaction on the surface. (Mallick and Roy, 2016, 2018; Mallick et al., 2016).

Autonomously moving micrometer sized particles were first developed in 2002 by Ismagilov et al. (2002) Following the seminal work (Paxton et al., 2004; Kline et al., 2005; Ibele et al., 2009; Duan et al., 2012; Wang et al., 2013) of Sen and Mallouk on catalytic nanomotors (Paxton et al., 2004; Kline et al., 2005; Jurado-Sánchez et al., 2016) many physical mechanisms for rendering particles motile have been explored. These include chemical (Laoharoensuk et al., 2008; Zacharia et al., 2009; Mirkovic et al., 2010; Sattayasamitsathit et al., 2010; Lu et al., 2016), magnetic (Ghosh and Fischer, 2009; Zhang et al., 2010; Gao et al., 2012a; Tottori et al., 2012; Morozov and Leshansky, 2014), electrical (Chang et al., 2008; Calvo-Marzal et al., 2010; Loget and Kuhn, 2010), optical

(Eelkema et al., 2006; Roy et al., 2014; Zhang et al., 2017), and ultrasound (Garcia-Gradilla et al., 2013; Esteban-Fernández de Ávila et al., 2016) mechanisms. Of these, the mechanism of chemical propulsion is simplest and most robust but remains limited due to toxicity of the fuel and motility that is limited by lifetime of both the motor and the fuel. Therefore, there is a need to direct the design of chemically powered (Sengupta et al., 2012) nanomotors in a direction that reduces fuel toxicity and increases motility lifetimes. In the present paper, we present a design of a soft-oxometalate (SOM) based nanomotor that is facile, single step, uses relatively non-toxic hydrazine as fuel and has a long motile lifetime of approximately 3 days. Metal oxides like manganese dioxide have been extensively used as nanomotors previously (Safdar et al., 2015, 2016). To enhance the efficiency of the nanomotors we have synthesized self-assembly of molybdenum oxides which provide increased surface area and multi-metal centres for redox reaction.

The phenomenon of collective motility (Ismagilov et al., 2002) of nanomotors is of considerable significance in the field of nanotechnology as they can perform intended tasks like transport as well as chemical sensing. Sen et al. and Ren et al. reported collective behavior of AgCl (Ibele et al., 2009) and SiO₂-Pt (Zhang et al., 2015) micromotors respectively in presence of UV light. Our nanomotors also show dynamic schooling behavior in response to high concentration of the fuel which makes them potential devices for transport of catalytic materials.

Chemical propulsion (Paxton et al., 2006; Gao et al., 2012b; Orozco et al., 2013) relies on the conversion of chemical energy to mechanical work performed on the ambient fluid. Typically, chemical reactions on the surface (Ismagilov et al., 2002) induce osmotic flows (Chang et al., 2008; Palacci et al., 2013) in a thin boundary layer surrounding the particle. This osmotic slip flow sets the bulk fluid immediately exterior to the boundary layer into motion. The conservation of mass and momentum, requires a reciprocal motion of the particle in the opposite direction. This chemiosmophoretic mechanism can be realized in a variety of substrates and chemical reactions. The principal requirement for such chemomechanical (Laskar et al., 2013; Sengupta et al., 2013) energy transduction is a reaction that is confined to the motor surface and which produces tangential (Zheng et al., 2013; Brown and Poon, 2014) osmotic stresses that are of sufficient strength and asymmetry to produce macroscopic directional (Patra et al., 2013) fluid flow. The surface of soft-oxometalate (SOM) particles produces osmotic stresses that impart rapid and sustained motility to the particles. Here we show that the redox reaction of hydrazine on the surface of soft-oxometalate (SOM) particles produces osmotic stresses that impart rapid and sustained motility to the particles.

MATERIALS AND METHODS

Materials and Reagents

The reagents were purchased from commercial sources (Merck) and used without further purification. All glassware was cleaned in an acid bath, base bath and rinsed with isopropanol followed by acetone and kept in an oven for 48 h prior use.

Synthesis of Heptamolybdate {Mo₇} Based Soft-Oxometalates (SOMs)

Ammonium heptamolybdate tetrahydrate (1,500 mg, 1.213 mmol) was dispersed in HPLC grade water (4 mL) and heated until simmering hot (140°C). A clear dispersion of ammonium heptamolybdate formed, which was then stored in a refrigerator for 10 min. The dispersion was brought to room temperature which scattered light from laser. This aqueous dispersion is at equilibrium between the homogeneous and heterogeneous phases of heptamolybdate. To remove the homogeneous part diethyl ether was added to the dispersion. White precipitate was observed which was separated out by ultra-centrifugation at 3,500 rpm for 15 min. This was washed three times with cold water and ethanol and dried in air. The white solid was re-dispersed in water and was characterized using scanning electron microscopy (SEM), transmission electron microscopy (TEM) and dynamic light scattering (DLS). This dispersion was used for further experiments.

Preparation of Hydrazine Sulfate Solutions

The solubility of hydrazine sulfate at room temperature was 3.056 mol in 10 mL of water. Calculated amount of hydrazine sulfate was dissolved in 10 mL of distilled water separately to prepare 0.0007, 0.0038, 0.0076, 0.0382, 0.0764, 0.0999, 0.1146, 0.1300, 0.1375, 0.1528, 0.1910, 0.2292, 0.2674, and 0.3056 mol L⁻¹ hydrazine sulfate solutions.

Characterization Using Dynamic Light Scattering (DLS) Measurement

0.5 mL of heptamolybdate SOM dispersion was diluted with 10 mL of deionised water. This dispersion was irradiated with a hand held laser pointer of wavelength 635 nm which resulted in the scattering of a single well-defined line. The resulting dispersion was then subject to DLS experiment using Malvern Zetasizer. This was repeated for all dispersions of SOM and SiO₂ with addition of hydrazine as well.

Characterization Using Transmission Electron Microscopy (TEM)

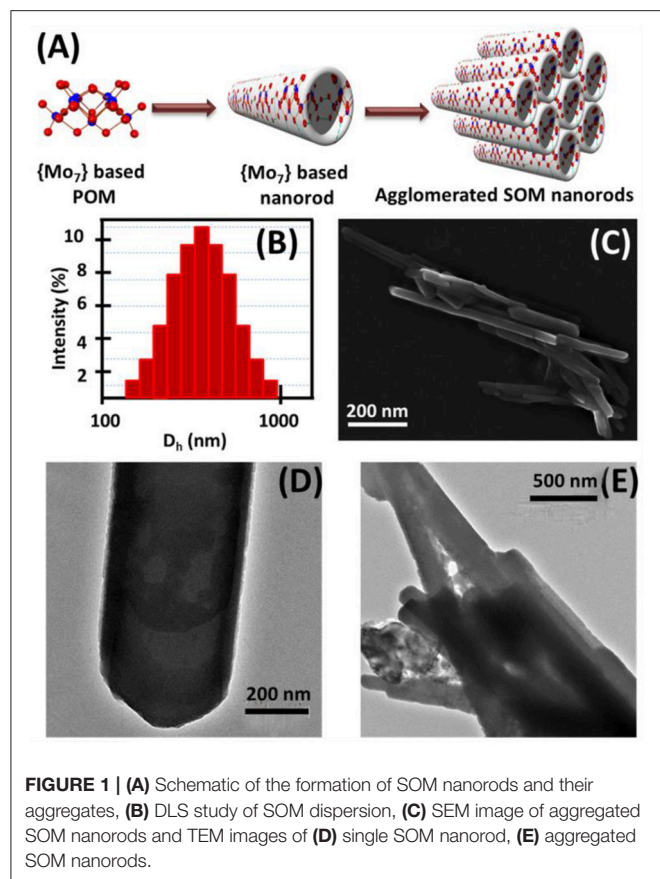
The characterization of isolated SOM and collective SOMs were primarily done by the use of a Tecnai 20 transmission electron microscope (FEI Company) operated at an accelerating voltage of 200 kV. The TEM micrographs were processed using SIS software (Soft Imaging System). The TEM images are illustrated in Figure 1.

Characterization Using Scanning Electron Microscopy (SEM)

The characterization of SOMs was done using SUPRA 55 VP-41-32 instrument with the SmartSEM version 5.05 Zeiss software. The SEM image is shown in Figure 1.

Study of Surface Kinetics by Electron Absorption Spectrophotometry (EAS)

EAS spectra were recorded using Shimadzu UV spectrophotometer (UV 1,800). 100 µL of hydrazine sulfate



solution of known concentration was added to 100 μ L of ammonium heptamolybdate SOM dispersion in a UV cuvette, diluted with distilled water to 3 mL, the kinetics mode was activated in UVProbe 2.5 and the kinetics study was carried out directly in the spectrophotometer for a time period of 5 h. The kinetics study was repeated for all the concentrations of hydrazine sulfate solution following the same procedure.

Microscopy Using Inverted Fluorescence Microscope

An Olympus IX81epi fluorescence microscope with a motorized stage was used for recording videos. 75 \times 25 \times 1.45 mm micro concavity slides with polished spherical concavities of 15 mm diameter \times 0.5 mm depth and a 22 \times 40 mm cover glass were cleaned with methanol and dried to remove any unwanted adsorbed material. The SOM dispersion (100 μ L) was placed in the cavity of the slide. 100 μ L of hydrazine (known concentration, freshly prepared) was added to the SOM dispersion using a 100 μ L micropipette. The cavity was then sealed with the cover slip in order to prevent any air convection current. The whole set-up was then placed on the microscope scanning stage and the stage was controlled using a joystick. The dispersion which was initially colorless gradually turned blue after addition of hydrazine sulfate solution. The microscope was focused at 40X objective and the

videos were recorded using DSIC camera at a rate of 10 frames per second.

Analysis Using ImageJ and TrackPy

The raw image sequence in TIFF format was converted to AVI form using ImageJ. ImageJ (Rasband, 2011; Schneider et al., 2012) is a Java based image processing and analysis software (original name, NIH image) which is available in public domain and allows analysis of multiple images sharing a single window (video). From these videos each frame was separately taken and the SOM particles in that frame were analyzed manually. That is, the co-ordinates of position of a SOM particle was measured over three frames, the body length of that particular SOM was taken into account (as SOMs are of varying size), time gap between the frames was noted and using these velocity of each SOM was calculated. This procedure was repeated for a number of SOMs in each video corresponding to a particular hydrazine concentration. The velocities were found to be coherent. However, the average of these velocities was considered as the velocity of the SOM at that particular hydrazine concentration. The same procedure was carried out for all hydrazine concentrations. The velocities of SOM were plotted against concentration of hydrazine (Figure 2).

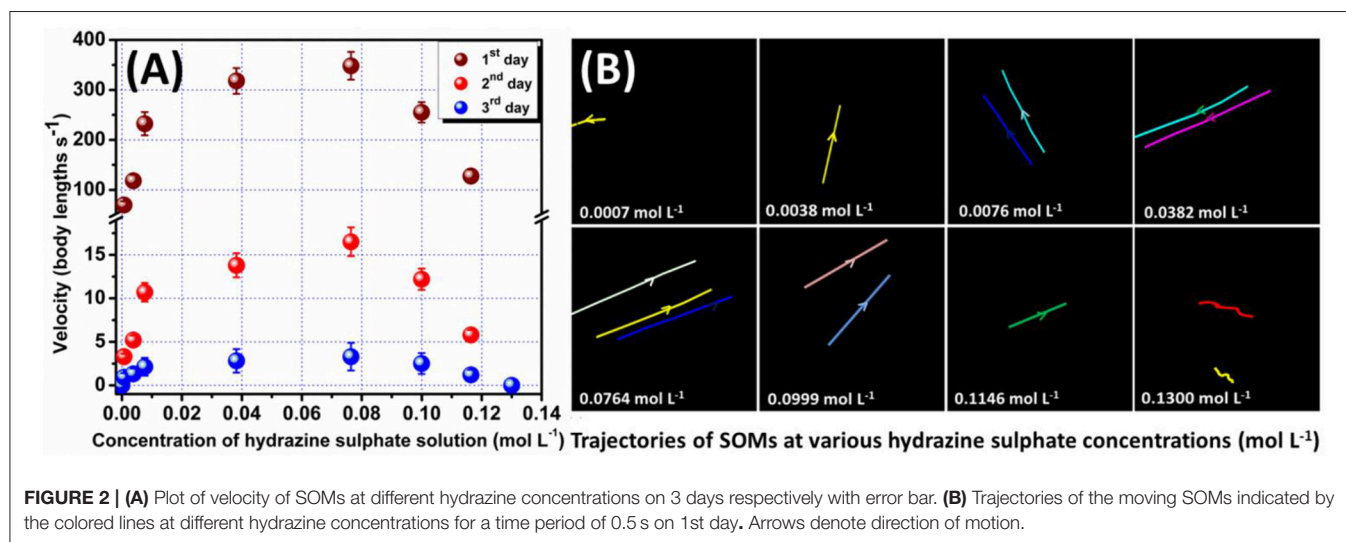
Trackpy is a python packaging tool used for particle tracking. Using this code each video was analyzed and trajectories of SOM were obtained. Trackpy first identified SOM particles in each frame with selective filters in it and then connected the frames in which a SOM particle was present to obtain the particle trajectories which were found to be similar to that obtained with ImageJ (Figure 2, given later).

RESULTS AND DISCUSSION

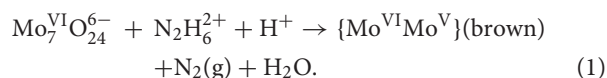
Surface Reaction Chemistry

We now describe the details of the surface reaction chemistry we use to obtain particle motility. We disperse ammonium heptamolybdate tetrahydrate in water and heat it for few min till boiling followed by cooling. Linear {Mo₇} building blocks self-assemble due to charge-regulation (Verhoeff et al., 2007), counter-ion mediated attraction as well as water-bridged hydrogen bonding (Yin et al., 2012) in aqueous solution and form soft-oxometalate nanorods which are shown schematically in Figure 1A. SEM and TEM images reveal that thin and well-defined SOM nanorods of {Mo₇} (Figures 1C,D and Supplementary Figure 1) are formed. The size of the nanorods is approximately 200 \pm 80 nm from SEM and TEM images which is in consistency with the hydrodynamic diameter (approximately 500 nm) from the DLS experiments (Figure 1B). The increase in particle size may be due to surrounding solvent molecules or agglomeration amongst themselves. In aqueous solution counter-ions directly bind covalently to these anionic rods which results in inter-rod attractions (Ryu et al., 2008) and these tubes coalesce to form divergent bundles with a conical apex as revealed from SEM and TEM images in Figures 1C,E respectively.

These particles of soft-oxometalate can be rendered motile through a redox reaction on their surface fuelled by aqueous solution of hydrazine sulfate (N₂H₆SO₄). In heptamolybdate



SOMs the oxidation state of Mo center is +VI. When hydrazine is added to the dispersion of SOMs, it gets oxidized to nitrogen (N₂) which has been confirmed from GC-MS (Supplementary Figure 6) and some Mo (VI) centers of SOM readily get reduced to Mo (V) through the following reaction (Muller et al., 2004):



Owing to micro-environmental effect, the acidity at the vicinity of the {Mo₇} SOMs is higher than the bulk fluid. Thus, these SOMs are inherently greener which leads us to avoid addition of any mineral acids externally, though we still get the efficiency of acidic pH. Brown coloration has been observed in the reaction medium after due to Mo (V) Mo (VI) inter valence charge transfer (IVCT) which has been analyzed with EAS later. The enhanced concentration of nitrogen near the SOM surface produces a gradient of chemical potential which must lead to an osmotic slip flow tangential to the SOM surface. The standard chemiosmophoretic mechanism, then, propels the particle in a direction opposite to the osmotic slip flow. The completion of the above reaction from SOM nanotubes to brown amorphous powder of Mo takes approximately 4–5 days, thereby rendering the motor with a motile life of at least 3 days though with much less velocity (Figure 2A and Supplementary Table 1). The brown powder has been characterized with EAS and FT-IR (Supplementary Figure 3). They are found to be similar but the absence of acetate cannot be confirmed from these spectra because the band at 1,400 cm⁻¹ arises from δ_{as}(NH₄⁺) and according to literature the bands from acetate (δ_{CH3} and γ_{COO}) if present, will be masked. From EAS (Supplementary Figure 3A), a band is observed at 450 nm which implies the brown color formed due to intervalence charge transfer (IVCT) between Mo(V) and Mo(VI) centers. Cyclic voltammetry experiments (Supplementary Figure 4) show a reduction peak at -0.57 V and

an oxidation peak at -0.4 V due to Mo(V)/Mo(VI) (Clemente-León et al., 2007). Further to count the number of Mo(V) centers in the product we have performed cerimetric titrations the results of which have been provided in details in the Supporting Information (Supplementary Figure 5). The results show 8.4 mL of Ce(IV) is required to oxidize the Mo(V) centers to Mo(VI) which corresponds to 2.52 × 10¹⁹ electrons. So in 45 mg of the brown product 2.52 × 10¹⁹ Mo(V) centers are present.

Control of Motility

The possibility of air convection current affecting the motion of the nanomotors has been eliminated by performing the microscopy in a sealed chamber which has been described in the experimental section. Also, to confirm that the motion of SOMs is not an artifact of fluid convection current we have performed control experiments replacing SOMs with silica particles without altering other experimental conditions (Supplementary Videos). Silica particles do not show any directional motion unlike the SOM particles. This is also supported from the dynamic light scattering (DLS) experiments where a clear shift of hydrodynamic diameter is seen for SOMs in presence of hydrazine but for SiO₂ particles the hydrodynamic diameter remains almost same in different concentrations of hydrazine (Figure 3). The speed of isolated nanomotors can be tuned through the loading of hydrazine. We compute the nanomotor speed from particle tracking of trajectories using TrackPy (Allan et al., 2014). Our nanomotors reach a maximum speed of (348 ± 22) body lengths per second as the hydrazine concentration reaches approximately 0.0764 mol L⁻¹, as shown in Figure 2. In comparison, Au-Pt nanorods (Paxton et al., 2004) move at 10 body lengths per second, catalytic Ir/SiO₂ micromotors (Gao et al., 2014) move at 20 body lengths per second, hydrogen bubble propelled PANI/Zn microrockets (Gao et al., 2011) move at 100 body lengths per second while PEDOT/Pt microbots (Gao et al., 2012c) move at 480 body lengths per second. Our motors,

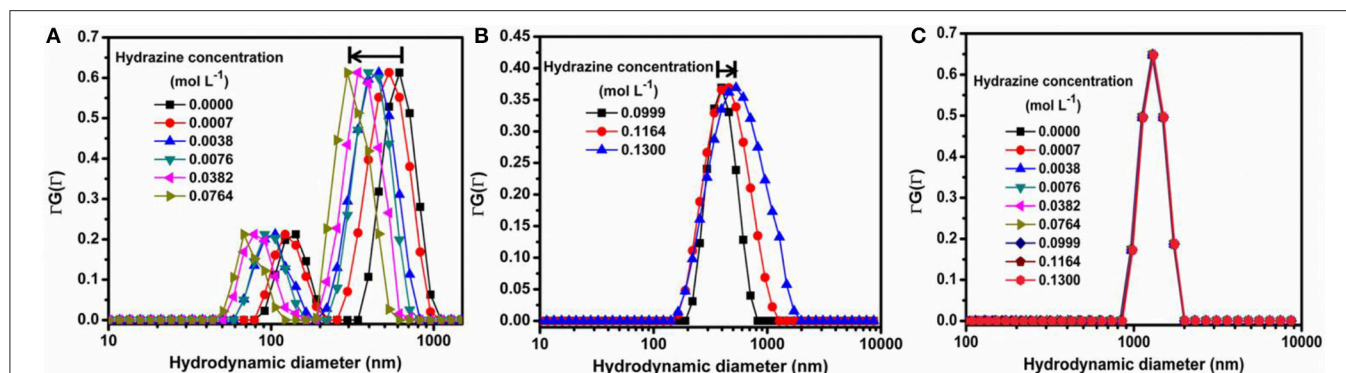


FIGURE 3 | Dynamic Light Scattering (DLS) experiments for (A) SOMs in 0.0000–0.0764 mol L⁻¹ hydrazine showing left shift, (B) SOMs in 0.0999–0.1300 mol L⁻¹ hydrazine showing right shift, (C) SiO₂ in 0.0000–0.1300 mol L⁻¹ hydrazine showing negligible shift.

therefore, are amongst the fastest (normalized by their size) of currently reported active particles.

In order to quantify the effect of loading of chemical fuel on motion of active SOMs we now increase in steps, the concentration of our fuel, hydrazine. With increase in hydrazine sulfate concentration up to 0.0746 mol L⁻¹ the velocity of SOMs also increase exponentially as is evident from **Figure 2**. At 0.0764 mol L⁻¹ of hydrazine sulfate concentration, velocity reaches a value of 348 ± 22 body lengths s⁻¹ (Supplementary video). Past that concentration, the velocity of SOM decreases even with increase in hydrazine concentration and at 0.13 mol L⁻¹ of hydrazine sulfate no significant motion of SOM is observed. These data are in well agreement with the diffusion coefficient and DLS distribution curves where the first a left shift is observed followed by a right shift indicating initial increase in velocity of SOMs with increasing concentration of fuel followed by the decrease in their velocity (**Figure 3** and Supplementary Figure 2).

The nonmonotonicity of the propulsion velocity as a function of hydrazine concentration has to be explained in terms of the changing nature of osmotic stress at the particle surface. The SOM particle has considerable asymmetry in terms of its surface structure. The anterior end of the SOM is capped like a pencil while the posterior end consists of a series of rod like protrusions. We believe that these exposed ends of the rods provide a more accessible reaction surface than the capped end. Therefore, hydrazine preferentially reacts at the posterior open end. At low concentrations, the spatial asymmetry of the intensity of chemical reaction produces a corresponding asymmetry in the distribution of osmotic stress. This leads to particle propulsion. With increasing hydrazine concentration, the amount of reaction increases more rapidly than the spatial asymmetry decreases. This leads to an overall increase in propulsion speed. However, at a critical concentration, the asymmetry decreases more rapidly than the increase in reaction centers. Thus, although more fuel is available, the reaction takes place across the entire body of the SOMs and this leads to a symmetric distribution of the osmotic stress. The particle can no longer propel in the resulting

symmetrically distributed flow, but, it does nonetheless produce a fluid flow around itself. On general grounds the flow must be as seen in dipoles and quadrupoles as seen in **Figure 5**. Any micro-swimmer that swims cannot have any net external force or net external torque. The swimming motion and generation of fluid flow associated with it, at low Reynolds number environment can be understood through an additional slip velocity on the surface of the micro-swimmer (Singh et al., 2015). Exploiting the linearity of Stokes flow (Navier-Stokes Equation in the viscous limit) and boundary conditions without isolating the details of internal mechanism, it has been shown that any generic slip velocity can be decomposed into irreducible multipoles (Singh et al., 2015). Different irreducible multipoles represent different modes of stress-generation and associate fluid-flows. These fluid-flows contain different internal structures and decay algebraically as the distance from the source decreases. The order of the algebraic decay increases with the increase of order of multipole. Using similar approach, the flow produced by motile neutrally-buoyant SOM must be seen as a combination of Stokes-dipole or stresslet and potential-dipole or degenerate quadrupole at leading order. We note that stresslet does not contribute in self-propulsion and the associate flowfield decays as $1/r^2$, whereas, degenerate quadrupole produces leading contribution for self-propulsion and the associated flow field decays as $1/r^3$, where r is the distance of field point from the source point.

In our experiment, we observe a transition from a symmetry-broken motile state of activity to a symmetric stalled state of activity as the reaction increases with the increase of hydrazine. Below the critical concentration of Hydrazine, we have observed that the SOMs are moving very fast in a particular direction (**Figure 4**). Therefore, keeping the strength of the stresslet approximately 10% (it can be even smaller), of the potential-dipole, the flow-field around the SOM can be predicted, as seen in **Figure 5**. Above the critical concentration of hydrazine, the spatial asymmetry of distribution of product and correspondingly distribution of osmotic stress decreases which in turn, leads to suppression of motile potential-dipole mode. Therefore, stalled SOM at high concentration of Hydrazine can

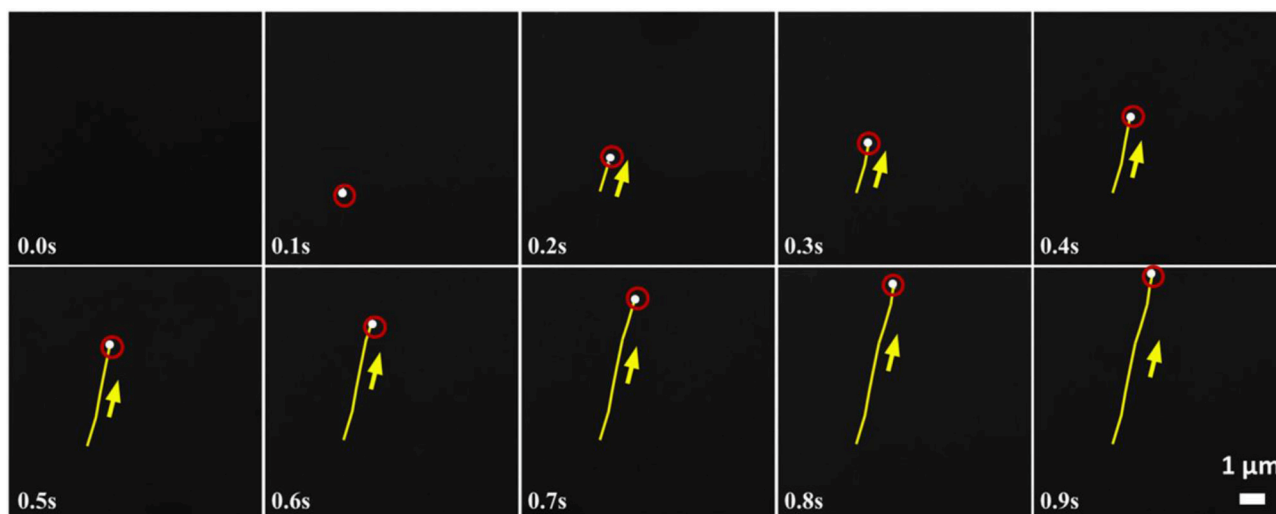


FIGURE 4 | Time lapse images of a moving heptamolybdate SOM in $0.0038 \text{ mol L}^{-1}$ of hydrazine sulfate. Direction of motion is shown by the arrows and yellow lines indicate the trace lines i.e., the position of SOM from the initial position at 0 s. Red circles help locating the white SOMs.

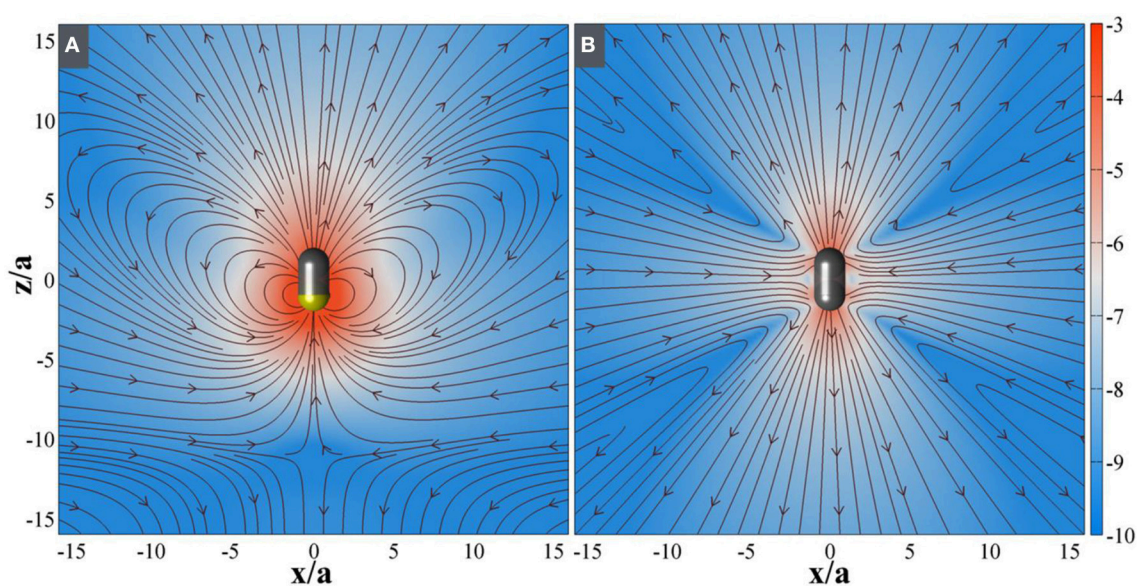


FIGURE 5 | Computed fluid flow around active SOM when (A) propulsive and (B) stalled. The streamlines show the direction of fluid motion and the background is pseudo-colored with logarithm of magnitude of the fluid velocity. In the (A), the flow around a SOM breaks the symmetry due to asymmetric surface slip and thus induces a propulsion motion. In the (B) the flow around a SOM restores the symmetry due to reduction of asymmetric surface slip both at very low, and high hydrazine concentration which results in decreasing propulsion efficiency.

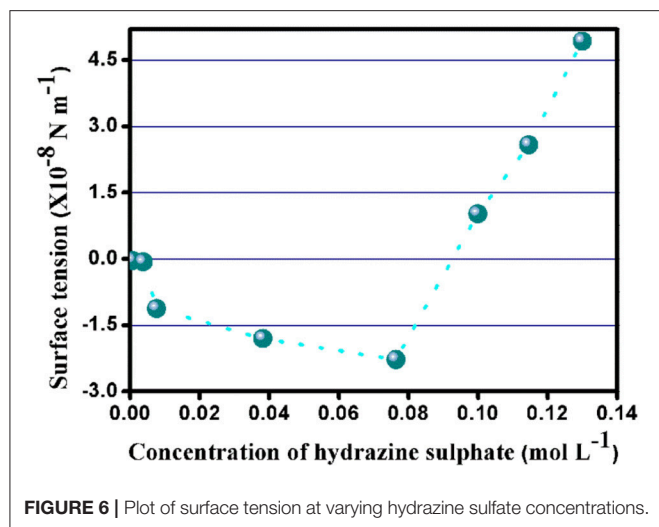
only have stresslet at leading order and the associated flow-field is displayed in **Figure 5**.

Surface Tension and the Direction of Propulsion of the SOM Nanomotors

The surface tension guides the direction of propulsion of the nanomotors i.e., it determines whether the motors tend to move along the gradient of the fuel or the gas evolved due to the

interactions between the SOM surface and the fuel. From the calculation of surface tension according to Kelvin's equation (from **Figure 6** and Supplementary Table 3) it can be seen that the surface tension has negative values upto $0.0764 \text{ mol L}^{-1}$ of hydrazine sulfate concentration.

Beyond this concentration, the surface tension becomes positive. From the negative values of surface tension we may infer that the SOM nanomotors move along the direction of the gas evolved. With the increase in hydrazine concentration



the value of surface tension becomes positive which leads to the movement of the motors in the opposite direction i.e., along the direction of the concentration gradient of the fuel.

Collective Motion

SOMs are charged particles with huge number of negative charges residing on the surface. On addition of hydrazine to the {Mo₇} SOMs, some Mo(VI) centers are reduced to Mo(V) (from equation 1) which generates more negative charge on the surface, enhancing their chance of agglomeration. SOMs are highly asymmetric rods (surface area at the anterior end is lesser than the posterior part as shown in **Figure 1E**), resulting in energy difference between the surfaces. To minimize the overall charge the SOM particles agglomerate to form bundles of such rods. This is more prominent at higher concentrations of hydrazine which stems schooling behavior in SOMs.

We now discuss the transition to collective motion that takes place when the fluid flow around the particles becomes symmetric from hydrodynamic viewpoint. When individual particle motility ceases due the symmetric distribution of osmotic stresses, there is still, as we discussed, hydrodynamic flow around the particle. On general grounds, it can be argued that this hydrodynamic flow must have dipolar symmetry. Particles aligned along the extensional axis of the flow are convected away from each other, while particles aligned along the contractile axis are convected toward each other. For sufficient strength of flow, this can lead to a flow-induced clumping of particles. The distribution of osmotic stresses in such a collection of particles, viewed as an aggregate entity, need no longer be symmetric. The aggregate as a whole can then propel itself, as seen from **Figure 7**, though at a much reduced speed. We see a clear signature of this transition to collective motility as a function of hydrazine volume fraction. Particles aggregate and travel in collective bands at a fraction of the speed of the individual particles. We believe such motion can be harnessed for transport of catalytic materials to large spatially distributed regions.

Surface Reaction Kinetics

In an effort to understand the surface reaction kinetics on the soft-oxometalate surface we have performed the electron absorption spectroscopy (EAS) studies. Loading of different concentrations of fuel, i.e., hydrazine sulfate leads to similar kind of kinetics with an initial increase in absorbance and then saturation. The plot of reaction rate vs. reactant concentration reveals how much reactant gets adsorbed on the soft- oxometalate surface, and from **Figure 8** we find that the kinetics resembles Michaelis-Menten kinetics which is one of the well-known enzyme kinetics. From the graph we may imply that the number of sites on SOM surface adsorbed by the gas increases initially but after a critical value, most of the sites are occupied and even though the amount of reactant increases the fraction of sites occupied by gas remains almost constant.

Power Conversion Efficiency of the SOM Nanomotors

The power conversion efficiency (η) (Wang et al., 2013) of these nanomotors can be defined as:

$$\eta = \frac{P_{mech}}{P_{chem}}$$

where, P_{mech} is the mechanical energy output and is determined by the equation:

$$P_{mech} = F_{drag}v = fv^2 = \gamma v^2$$

and P_{chem} is the chemical energy input provided by the redox reaction and is found out from the equation:

$$P_{chem} = n\Delta_r G_\gamma$$

For cylinders,

$$\gamma = \frac{2\pi\mu L}{\ln\left(\frac{L}{R}\right) - 0.72}$$

Here, F_{drag} is the drag force on the cylindrical SOM, γ is the drag coefficient, μ is the dynamic viscosity of water, L is the length of SOM, R is its radius, v is the motor speed, n is the nitrogen gas evolution rate in units of mol/(SOM·s) and $\Delta_r G_\gamma$ is the Gibbs free energy of the decomposition of dithionite. We calculate the values of P_{mech} and P_{chem} and find the energy efficiency of SOM nanomotors which is demonstrated in **Figure 9**. The power conversion efficiencies of the SOM nanomotors are found to be in the order of 10^{-7} (Supplementary Table 2) which is sufficiently high in the field of nanomotors (Wang et al., 2013). The highest efficiency is obtained for the hydrazine concentration of $0.0076 \text{ mol L}^{-1}$ which comes around 4.12×10^{-7} .

CONCLUSION

To summarize, in our current work we have used molybdenum based soft-oxometalates (SOMs) and employed hydrazine sulfate fuel to induce motility in these SOM nanorods. The directional

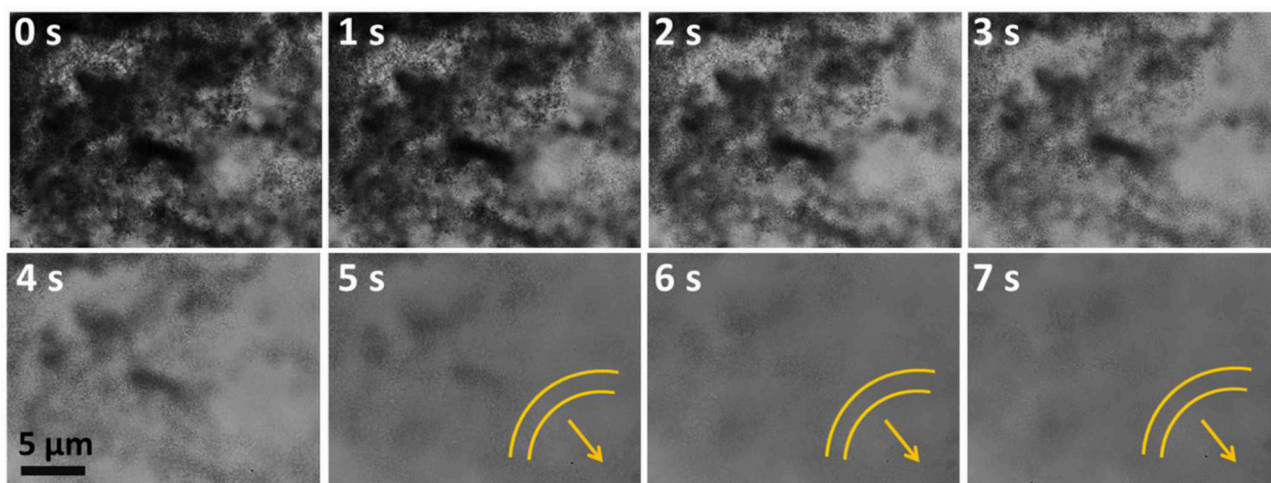


FIGURE 7 | Snapshots of collective motion of SOMs at $0.1910 \text{ mol L}^{-1}$ concentration of hydrazine sulfate from 0 to 7 s. Arrows denote the band formation.

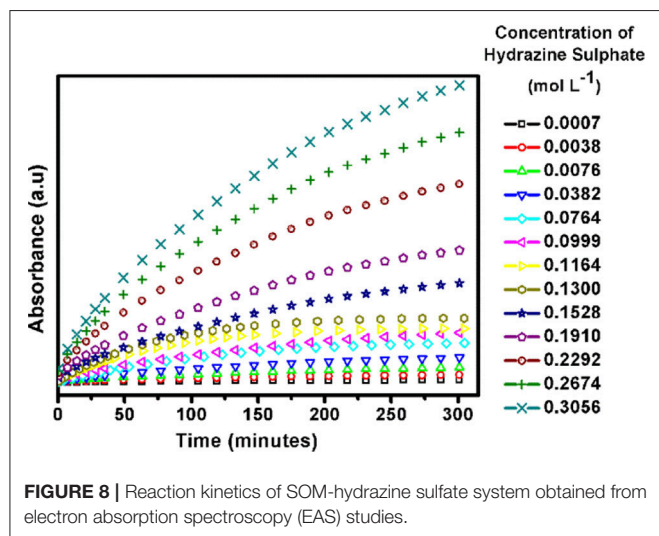


FIGURE 8 | Reaction kinetics of SOM-hydrazine sulfate system obtained from electron absorption spectroscopy (EAS) studies.

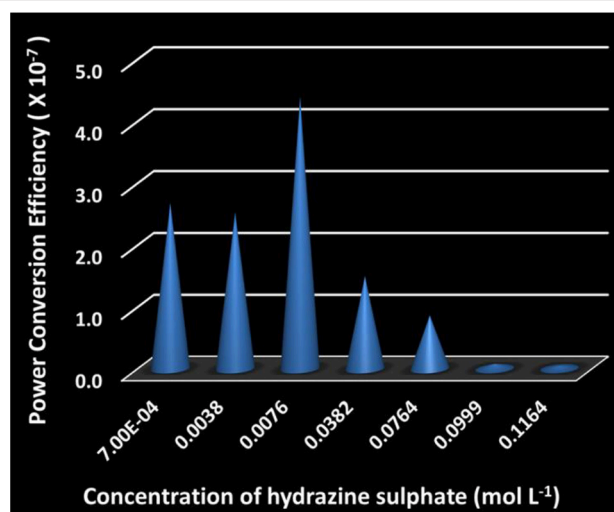


FIGURE 9 | Plot of power efficiency of SOMs at different hydrazine sulfate concentrations.

motility in these SOMs stems from the evolution of the nitrogen gas due to the reaction between $\{\text{Mo}_7\}$ surface and the fuel where hydrazine is oxidized to nitrogen gas and heptamolybdate type SOMs are reduced to molybdenum blue SOMs. Due to this reaction an osmotic boundary is generated between product i.e., the gas and the unreacted SOM surface. The chemical potential gradient between the surface of the heptamolybdate SOMs and the osmotic interface gives rise to a slip velocity to the SOMs propelling them with a high propulsion velocity of 369 body lengths per second. The velocity of the SOMs again decreases due to the viscous drag induced by nitrogen on the SOM surface. The velocity finally drops to zero when the viscous drag annuls the slip velocity. Observation of bands in our system which is totally non-living has been explained here. Such facile synthesis and high propulsion velocity of heptamolybdate SOMs hold considerable importance in the field of active matter and can be used in future for transport (del Mercato et al., 2014; Manna et al.,

2017) and catalysis (Li et al., 2014b) after properly controlling their direction of motion. We can further use these active SOMs for preparing nanocarpet utilizing their high velocity by immobilizing heptamolybdate on graphene sheets. Also we can use them for preparing raft by proper alignment of the SOM nanorods.

AUTHOR CONTRIBUTIONS

SR conceived, designed the experiments with RA. AM performed the experiments and characterizations. AM, AL, RA, and SR analyzed the data. AL and RA provided the hydrodynamic model. SR and RA wrote the manuscript with inputs from AM and AL. All authors read and approved the paper.

FUNDING

The work was supported by the Start Up and FIRE grants awarded to SR from IISER Kolkata. There was further supports from DST-Fast track grant and BRNS-DAE grants.

REFERENCES

- Allan, D. B., Caswell, T. A., and Keim, N. C. (2014). "Trackpy v0. 2." doi: 10.5281/zenodo.9971
- Brown, A., and Poon, W. (2014). Ionic effects in self-propelled Pt-coated Janus swimmers. *Soft Matter* 10, 4016–4027. doi: 10.1039/C4SM00340C
- Calvo-Marzal, P., Sattayasamitsathit, S., Balasubramanian, S., Windmiller, J. R., Dao, C., and Wang, J. (2010). Propulsion of nanowire diodes. *Chem. Commun.* 46, 1623–1624. doi: 10.1039/b925568k
- Chang, S. T., Beaumont, E., Petsev, D. N., and Velez, O. D. (2008). Remotely powered distributed microfluidic pumps and mixers based on miniature diodes. *Lab Chip* 8, 117–124. doi: 10.1039/B712108C
- Clemente-León, M., Ito, T., Yashiro, H., and Yamase, T. (2007). Two-dimensional array of polyoxomolybdate nanoball constructed by langmuir-blodgett semiamphiphilic method. *Chem. Mater.* 19, 2589–2594. doi: 10.1021/cm070436e
- del Mercato, L. L., Carraro, M., Zizzari, A., Bianco, M., Miglietta, R., Arima, V., et al. (2014). Catalytic self-propulsion of supramolecular capsules powered by polyoxometalate cargos. *Chem. Eur. J.* 20, 10910–10914. doi: 10.1002/chem.201403171
- Duan, W., Ibele, M., Liu, R., and Sen, A. (2012). Motion analysis of light-powered autonomous silver chloride nanomotors. *Eur. Phys. J. E Soft Matter* 35:77. doi: 10.1140/epje/i2012-12077-x
- Eelkema, R., Pollard, M. M., Vicario, J., Katsonis, N., Ramon, B. S., Bastiaansen, C. W., et al. (2006). Molecular machines: nanomotor rotates microscale objects. *Nature* 440, 163–163. doi: 10.1038/440163a
- Esteban-Fernández de Ávila, B., Angell, C., Soto, F., Lopez-Ramirez, M. A., Báez, D. F., Xie, S., et al. (2016). Acoustically propelled nanomotors for intracellular siRNA delivery. *ACS Nano* 10, 4997–5005. doi: 10.1021/acsnano.6b01415
- Gao, W., Kagan, D., Pak, O. S., Clawson, C., Campuzano, S., Chuluun-Erdene, E., et al. (2012a). Cargo-towing fuel-free magnetic nanoswimmers for targeted drug delivery. *Small* 8, 460–467. doi: 10.1002/sml.201101909
- Gao, W., Pei, A., Dong, R., and Wang, J. (2014). Catalytic iridium-based Janus micromotors powered by ultralow levels of chemical fuels. *J. Am. Chem. Soc.* 136, 2276–2279. doi: 10.1021/ja413002e
- Gao, W., Pei, A., and Wang, J. (2012b). Water-driven micromotors. *ACS Nano* 6, 8432–8438. doi: 10.1021/nn303309z
- Gao, W., Sattayasamitsathit, S., Uygun, A., Pei, A., Ponedal, A., and Wang, J. (2012c). Polymer-based tubular microbots: role of composition and preparation. *Nanoscale* 4, 2447–2453. doi: 10.1039/c2nr30138e
- Gao, W., Uygun, A., and Wang, J. (2011). Hydrogen-bubble-propelled zinc-based microrockets in strongly acidic media. *J. Am. Chem. Soc.* 134, 897–900. doi: 10.1021/ja210874s
- García-Gradilla, V., Orozco, J., Sattayasamitsathit, S., Soto, F., Kuralay, F., Pourazary, A., et al. (2013). Functionalized ultrasound-propelled magnetically guided nanomotors: toward practical biomedical applications. *ACS Nano* 7, 9232–9240. doi: 10.1021/nn403851v
- Ghose, S., and Adhikari, R. (2014). Irreducible representations of oscillatory and swirling flows in active soft matter. *Phys. Rev. Lett.* 112:118102. doi: 10.1103/PhysRevLett.112.118102
- Ghosh, A., and Fischer, P. (2009). Controlled propulsion of artificial magnetic nanostructured propellers. *Nano Lett.* 9, 2243–2245. doi: 10.1021/nl900186w
- Ibele, M., Mallouk, T. E., and Sen, A. (2009). Schooling behavior of light-powered autonomous micromotors in water. *Angew. Chem. Int. Ed.* 48, 3308–3312. doi: 10.1002/anie.200804704
- Ismagilov, R. F., Schwartz, A., Bowden, N., and Whitesides, G. M. (2002). Autonomous Movement and Self-Assembly. *Angew. Chem.* 114, 674–676. doi: 10.1002/1521-3757(20020215)114:4<674::AID-ANGE674>3.0.CO;2-Z
- Jurado-Sánchez, B., Wang, J., and Escarpa, A. (2016). Ultrafast nanocrystals decorated micromotors for on-site dynamic chemical processes. *ACS Appl. Mater. Interfaces* 8, 19618–19625. doi: 10.1021/acsami.6b05824
- Kim, K., Xu, X., Guo, J., and Fan, D. (2014). Ultrahigh-speed rotating nanoelectromechanical system devices assembled from nanoscale building blocks. *Nat. Commun.* 5:3632. doi: 10.1038/ncomms4632
- Kline, T. R., Paxton, W. F., Mallouk, T. E., and Sen, A. (2005). Catalytic nanomotors: remote-controlled autonomous movement of striped metallic nanorods. *Angew. Chem.* 117, 754–756. doi: 10.1002/ange.200461890
- Laochaeronsuk, R., Burdick, J., and Wang, J. (2008). Carbon-nanotube-induced acceleration of catalytic nanomotors. *ACS Nano* 2, 1069–1075. doi: 10.1021/nn800154g
- Laskar, A., Singh, R., Ghose, S., Jayaraman, G., Kumar, P. S., and Adhikari, R. (2013). Hydrodynamic instabilities provide a generic route to spontaneous biomimetic oscillations in chemomechanically active filaments. *Sci. Rep.* 3:1964. doi: 10.1038/srep01964
- Li, J., Gao, W., Dong, R., Pei, A., Sattayasamitsathit, S., and Wang, J. (2014a). Nanomotor lithography. *Nat. Commun.* 5:5026. doi: 10.1038/ncomms6026
- Li, J., Singh, V. V., Sattayasamitsathit, S., Orozco, J., Kaufmann, K., Dong, R., et al. (2014b). Water-driven micromotors for rapid photocatalytic degradation of biological and chemical warfare agents. *ACS Nano* 8, 11118–11125. doi: 10.1021/nn505029k
- Loget, G., and Kuhn, A. (2010). Propulsion of microobjects by dynamic bipolar self-regeneration. *J. Am. Chem. Soc.* 132, 15918–15919. doi: 10.1021/ja107644x
- Lu, A. X., Liu, Y., Oh, H., Gargava, A., Kendall, E., Nie, Z., et al. (2016). Catalytic propulsion and magnetic steering of soft, patchy microcapsules: ability to pick-up and drop-off microscale cargo. *ACS Appl. Mater. Interfaces* 8, 15676–15683. doi: 10.1021/acsami.6b01245
- Ma, X., Hortelao, A. C., Miguel-López, A., and Sánchez, S. (2016). Bubble-free propulsion of ultrasmall tubular nanojets powered by biocatalytic reactions. *J. Am. Chem. Soc.* 138, 13782–13785. doi: 10.1021/jacs.6b06857
- Mallick, A., Lai, D., and Roy, S. (2016). Autonomous movement induced in chemically powered active soft-oxometalates using dithionite as fuel. *New J. Chem.* 40, 1057–1062. doi: 10.1039/C5NJ01097G
- Mallick, A., and Roy, S. (2016). Autonomous movement in mixed metal based soft-oxometalates induced by CO₂ evolution and topological effects on their propulsion. *RSC Adv.* 6, 112158–112165. doi: 10.1039/C6RA24132H
- Mallick, A., and Roy, S. (2018). "Soft-oxometalates—a new state of oxometalates and their potential applications as nanomotors," in *Metal Nanoparticles: Synthesis and Applications in Pharmaceutical Sciences*, eds S. Thota and D. Crans. (Weinheim: Wiley-VCH), 83–99.
- Manna, R. K., Kumar, P. B., and Adhikari, R. (2017). Colloidal transport by active filaments. *J. Chem. Phys.* 146:024901. doi: 10.1063/1.4972010
- Minh, T. D., Safdar, M., and Jäms, J. (2017). Protection of platinum-based micromotors from thiol toxicity by using manganese oxide. *Chem. Eur. J.* 23, 8134–8136. doi: 10.1002/chem.201700788
- Mirkovic, T., Zacharia, N. S., Scholes, G. D., and Ozin, G. A. (2010). Fuel for thought: chemically powered nanomotors out-swim nature's flagellated bacteria. *ACS Nano* 4, 1782–1789. doi: 10.1021/nn100669h
- Morozov, K. I., and Leshansky, A. M. (2014). The chiral magnetic nanomotors. *Nanoscale* 6, 1580–1588. doi: 10.1039/C3NR04853E
- Muller, A., Das, K., Krickemyer, E., and Kuhlmann, C. (2004). Polyoxomolybdate clusters: giant wheels and balls. *Inorg. Synth* 34, 191–200.
- Orozco, J., Cheng, G., Vilela, D., Sattayasamitsathit, S., Vazquez-Duhal, R., Valdés-Ramírez, G., et al. (2013). Micromotor-based high-yielding fast oxidative detoxification of chemical threats. *Angew. Chem. Int. Ed.* 52, 13276–13279. doi: 10.1002/anie.201308072

SUPPLEMENTARY MATERIAL

The Supplementary Material for this article can be found online at: <https://www.frontiersin.org/articles/10.3389/fchem.2018.00152/full#supplementary-material>

- Palacci, J., Sacanna, S., Steinberg, A. P., Pine, D. J., and Chaikin, P. M. (2013). Living crystals of light-activated colloidal surfers. *Science* 339, 936–940. doi: 10.1126/science.1230020
- Patra, D., Sengupta, S., Duan, W., Zhang, H., Pavlick, R., and Sen, A. (2013). Intelligent, self-powered, drug delivery systems. *Nanoscale* 5, 1273–1283. doi: 10.1039/C2NR32600K
- Paxton, W. F., Kistler, K. C., Olmeda, C. C., Sen, A., St. Angelo, S. K., Cao, Y., et al. (2004). Catalytic nanomotors: autonomous movement of striped nanorods. *J. Am. Chem. Soc.* 126, 13424–13431. doi: 10.1021/ja047697z
- Paxton, W. F., Sundararajan, S., Mallouk, T. E., and Sen, A. (2006). Chemical locomotion. *Angew. Chem. Int. Ed.* 45, 5420–5429. doi: 10.1002/anie.200600060
- Rasband, W. S. (2011). *ImageJ*. Bethesda, MD: US National Institutes of Health. Available online at: <http://imagej.nih.gov/ij/>
- Roy, B., Ghosh, N., Panigrahi, P. K., Banerjee, A., Sahasrabudhe, A., Parasar, B., et al. (2014). Micro-optomechanical movements (MOMs) with soft oxometalates (SOMs): controlled motion of single soft oxometalate peapods using exotic optical potentials. *J. Mol. Engineer. Mater.* 2:1440006. doi: 10.1142/S2251237314400061
- Roy, S. (2011). “Soft Oxometalates” (SOMs): A Very Short Introduction. *Comments Inorg. Chem.* 32, 113–126. doi: 10.1080/02603594.2011.608443
- Roy, S. (2014). Soft-oxometalates beyond crystalline polyoxometalates: formation, structure and properties. *Cryst. Eng. Comm.* 16, 4667–4676. doi: 10.1039/C4CE00115J
- Ryu, J.-H., Hong, D.-J., and Lee, M. (2008). Aqueous self-assembly of aromatic rod building blocks. *Chem. Commun.* 1043–1054. doi: 10.1039/B713737K
- Safdar, M., Minh, T. D., Kinnunen, N., and Jänis, J. (2016). Manganese oxide based catalytic micromotors: effect of polymorphism on motion. *ACS Appl. Mater. Interfaces* 8, 32624–32629. doi: 10.1021/acsami.6b12024
- Safdar, M., Wani, O. M., and Jänis, J. (2015). Manganese oxide-based chemically powered micromotors. *ACS Appl. Mater. Interfaces* 7, 25580–25585. doi: 10.1021/acsami.5b08789
- Sattayasamitsathit, S., Gao, W., Calvo-Marzal, P., Manesh, K. M., and Wang, J. (2010). Simplified Cost-Effective Preparation of High-Performance Ag–Pt Nanowire Motors. *Chemphyschem* 11, 2802–2805. doi: 10.1002/cphc.201000348
- Schneider, C. A., Rasband, W. S., and Eliceiri, K. W. (2012). NIH Image to ImageJ: 25 years of image analysis. *Nat. Methods* 9, 671–675. doi: 10.1038/nmeth.2089
- Sengupta, S., Dey, K. K., Muddana, H. S., Tabouillot, T., Ibele, M. E., Butler, P. J., et al. (2013). Enzyme molecules as nanomotors. *J. Am. Chem. Soc.* 135, 1406–1414. doi: 10.1021/ja3091615
- Sengupta, S., Ibele, M. E., and Sen, A. (2012). Fantastic voyage: designing self-powered nanorobots. *Angew. Chem. Int. Ed.* 51, 8434–8445. doi: 10.1002/anie.201202044
- Sengupta, S., Patra, D., Ortiz-Rivera, I., Agrawal, A., Shklyae, S., Dey, K. K., et al. (2014). Self-powered enzyme micropumps. *Nat. Chem.* 6, 415–422. doi: 10.1038/nchem.1895
- Singh, R., Ghose, S., and Adhikari, R. (2015). Many-body microhydrodynamics of colloidal particles with active boundary layers. *J. Stat. Mech. Theory Exp.* 2015:P06017. doi: 10.1088/1742-5468/2015/06/P06017
- Soto, F., Wagner, G. L., Garcia-Gradilla, V., Gillespie, K. T., Lakshminpathy, D. R., Karshalev, E., et al. (2016). Acoustically propelled nanoshells. *Nanoscale* 8, 17788–17793. doi: 10.1039/C6NR06603H
- Teo, W. Z., and Pumera, M. (2016). Motion Control of Micro-/Nanomotors. *Chem. Eur. J.* 22, 14796–14804. doi: 10.1002/chem.201602241
- Teo, W. Z., Zboril, R., Medrik, I., and Pumera, M. (2016). FeO nanomotors in ton quantities (1020 units) for environmental remediation. *Chem. Eur. J.* 22, 4789–4793. doi: 10.1002/chem.201504912
- Tottori, S., Zhang, L., Qiu, F., Krawczyk, K. K., Franco-Obregón, A., and Nelson, B. J. (2012). Magnetic helical micromachines: fabrication, controlled swimming, and cargo transport. *Adv. Mater. Weinheim.* 24, 811–816. doi: 10.1002/adma.201103818
- Verhoeff, A. A., Kistler, M. L., Bhatt, A., Pigga, J., Groenewold, J., Klokkenburg, M., et al. (2007). Charge regulation as a stabilization mechanism for shell-like assemblies of polyoxometalates. *Phys. Rev. Lett.* 99:066104. doi: 10.1103/PhysRevLett.99.066104
- Wang, W., Chiang, T.-Y., Velegol, D., and Mallouk, T. E. (2013). Understanding the efficiency of autonomous nano-and microscale motors. *J. Am. Chem. Soc.* 135, 10557–10565. doi: 10.1021/ja405135f
- Yin, P., Li, D., and Liu, T. (2012). Solution behaviors and self-assembly of polyoxometalates as models of macroions and amphiphilic polyoxometalate-organic hybrids as novel surfactants. *Chem. Soc. Rev.* 41, 7368–7383. doi: 10.1039/c2cs35176e
- Zacharia, N. S., Sadeq, Z. S., and Ozin, G. A. (2009). Enhanced speed of bimetallic nanorod motors by surface roughening. *Chem. Commun.* 5856–5858. doi: 10.1039/b911561g
- Zhang, L., Petit, T., Lu, Y., Kratochvil, B. E., Peyer, K. E., Pei, R., et al. (2010). Controlled propulsion and cargo transport of rotating nickel nanowires near a patterned solid surface. *ACS Nano* 4, 6228–6234. doi: 10.1021/nn101861n
- Zhang, Q., Dong, R., Chang, X., Ren, B., and Tong, Z. (2015). Spiropyran-decorated SiO₂–Pt janus micromotor: preparation and light-induced dynamic self-assembly and disassembly. *ACS Appl. Mater. Interfaces* 7, 24585–24591. doi: 10.1021/acsami.5b06448
- Zhang, Q., Dong, R., Wu, Y., Gao, W., He, Z., and Ren, B. (2017). Light-Driven Au-WO₃@C janus micromotors for rapid photodegradation of dye pollutants. *ACS Appl. Mater. Interfaces* 9, 4674–4683. doi: 10.1021/acsami.6b12081
- Zheng, X., ten Hagen, B., Kaiser, A., Wu, M., Cui, H., Silber-Li, Z., et al. (2013). Non-gaussian statistics for the motion of self-propelled janus particles: experiment versus theory. *Phys Rev E* 88:032304. doi: 10.1103/PhysRevE.88.032304
- Zhou, D., Li, Y. C., Xu, P., McCool, N. S., Li, L., Wang, W., et al. (2017). Visible-light controlled catalytic Cu₂O–Au micromotors. *Nanoscale* 9, 75–78. doi: 10.1039/C6NR08088j

Conflict of Interest Statement: The authors declare that the research was conducted in the absence of any commercial or financial relationships that could be construed as a potential conflict of interest.

Copyright © 2018 Mallick, Laskar, Adhikari and Roy. This is an open-access article distributed under the terms of the Creative Commons Attribution License (CC BY). The use, distribution or reproduction in other forums is permitted, provided the original author(s) and the copyright owner are credited and that the original publication in this journal is cited, in accordance with accepted academic practice. No use, distribution or reproduction is permitted which does not comply with these terms.

Advantages of publishing in Frontiers



OPEN ACCESS

Articles are free to read
for greatest visibility
and readership



FAST PUBLICATION

Around 90 days
from submission
to decision



HIGH QUALITY PEER-REVIEW

Rigorous, collaborative,
and constructive
peer-review



TRANSPARENT PEER-REVIEW

Editors and reviewers
acknowledged by name
on published articles

Frontiers

Avenue du Tribunal-Fédéral 34
1005 Lausanne | Switzerland

Visit us: www.frontiersin.org

Contact us: info@frontiersin.org | +41 21 510 17 00



REPRODUCIBILITY OF RESEARCH

Support open data
and methods to enhance
research reproducibility



DIGITAL PUBLISHING

Articles designed
for optimal readership
across devices



FOLLOW US

[@frontiersin](https://twitter.com/frontiersin)



IMPACT METRICS

Advanced article metrics
track visibility across
digital media



EXTENSIVE PROMOTION

Marketing
and promotion
of impactful research



LOOP RESEARCH NETWORK

Our network
increases your
article's readership